



This work is protected by copyright and other intellectual property rights and duplication or sale of all or part is not permitted, except that material may be duplicated by you for research, private study, criticism/review or educational purposes. Electronic or print copies are for your own personal, non-commercial use and shall not be passed to any other individual. No quotation may be published without proper acknowledgement. For any other use, or to quote extensively from the work, permission must be obtained from the copyright holder/s.

**Sediment deposition and preservation in Aeolian Systems:  
A comparison of contemporary and ancient ergs**

**David Patrick Cousins**

**Doctor of Philosophy**

**June 2020**





## Abstract

Ancient and contemporary aeolian systems have been subject of important conceptual advances in recent years, however, a disconnect exists between the complexities inherent at the depositional surface and subsequent controls on preservation. At the fundamental level, the depositional environment consists of dune-fields, and the rock record is a stratigraphic architecture consisting of cross-strata and bounding surfaces. Vast outcrops of ancient aeolian strata display huge amounts of temporal variation manifest through dune-field evolution while the sedimentary record of contemporary ergs remain largely unknown. In order to bridge these gaps this research utilises a range of digitally based systems and techniques to analyse spatial data in order to unravel contemporary and ancient system evolutions. The study utilised the Wahiba Sand Sea of Oman and the Jurassic Navajo Sandstone of western USA as contemporary and ancient analogues respectively. Analysis of high to medium-resolution satellite and geophysical datasets demonstrate that antecedent topography has been a dominating allogenic boundary condition during the formation and growth of large linear bedforms in the Wahiba Erg. There appears to be a hierarchy of autogenic processes influenced by antecedent topography that imparts a uniqueness to the emergent dune-field pattern. The production of large-scale virtual outcrop models permitted broad spatial analysis of three sites across the Navajo Sandstone which represent marginal through central erg settings. Results show unique allogenic controls relating to system architectures at each outcrop, some of which provide validations to hypotheses made from observations within the contemporary analogue. The research demonstrates that in extracting signals of allogenic boundary conditions within which autogenic system processes evolved is the basis for the interpretation of geomorphic landforms and their stratigraphic record. The analogues represent a point on a spectrum of preservations styles recently detected in aeolian systems and provide additional examples with which to advance our knowledge.



# Contents

1	Introduction .....	1
1.1	Study Areas and Focus .....	3
1.1.1	Contemporary: The Wahiba Sand Sea .....	3
1.1.2	Ancient: The Jurassic Navajo Sandstone .....	4
1.1.3	Preservation .....	8
1.1.4	Linear dunes .....	8
1.2	Research Aims and Objectives .....	10
1.3	Thesis Structure .....	11
2	Aeolian Processes – Literature Review .....	15
2.1	Desert Aeolian System .....	16
2.2	Quaternary Aeolian sand Seas .....	18
2.3	Controls on Aeolian Systems .....	20
2.3.1	Construction .....	20
2.3.2	Accumulation .....	20
2.3.3	Preservation .....	21
2.4	Aeolian Bedforms .....	23
2.5	Particle Transport .....	24
2.6	Ballistic (aeolian) Ripples .....	25
2.7	Aeolian Dunes .....	27
2.7.1	Dune motion .....	31
2.7.2	Primary Stratification Types .....	35
2.7.3	Sets of Cross-strata .....	35
2.7.4	Aeolian Set Architecture .....	36
2.7.5	Interdunes .....	37
2.8	Water-Table .....	38
2.9	Draa / Megadune .....	39
2.10	Bounding surfaces .....	40
2.11	Supersurface .....	42
2.12	The Erg .....	42
2.12.1	Erg Margins and Interdune Bedforms .....	45
2.13	Chapter Summary .....	47
3	The Wahiba Sand Sea, Sultanate of Oman .....	51
3.1	Geological Setting .....	51
3.2	Geomorphic Regions .....	56
3.3	Climate .....	61

3.4	Stratigraphy .....	66
3.4.1	Core Sites .....	67
3.4.2	Aeolian Units.....	67
3.4.3	Internal architectures.....	71
3.5	Chapter Summary .....	74
4	An Investigation into Apparent Correlations .....	75
4.1	Site WDR-2 (Preusser <i>et al.</i> , 2002) .....	76
4.2	Site WDR-1 (Preusser <i>et al.</i> , 2002) .....	78
4.3	Site 4 (Hern <i>et al.</i> , 2018) .....	79
4.4	Concluding Remarks .....	79
5	Datasets .....	83
5.1	Landsat .....	83
5.2	ASTER .....	84
5.3	ALOS.....	85
5.4	GeoEye-1 and Worldview-3 .....	85
5.5	Ground Penetrating Radar (GPR) .....	86
6	Examining the Wahiba Sand Sea through Remote Sensing and Geospatial Techniques: Insights into Erg Geometry and Preservation .....	87
6.1	Relations between Dune Size and Spacing .....	89
6.1.1	Methods .....	92
6.1.2	Results .....	95
6.1.3	Discussion .....	99
6.2	Equivalent Sediment Thickness (EST), Base-level Topography and Dune-field Patterns.....	101
6.2.1	Methods .....	103
6.2.2	Results .....	106
6.2.3	Discussion .....	110
6.3	Relief Inspection .....	114
6.3.1	Methods .....	117
6.3.2	Results .....	119
6.3.3	Discussion .....	126
6.4	Geometry of Internal Architectures .....	130
6.4.1	Survey Location .....	130
6.4.2	Data Collection .....	132
6.4.3	GPR profile interpretation methods .....	133
6.4.4	Results and Interpretation.....	137
6.5	Vegetation Monitoring .....	148
6.5.1	Methods .....	149

6.5.2	Results .....	151
6.5.3	Discussion.....	156
6.6	Provenance Study .....	158
6.6.1	Methods .....	160
6.6.2	Results and Discussion .....	164
6.7	Summary .....	173
7	The Jurassic Navajo Sandstone, southwestern USA .....	177
7.1	Location .....	177
7.2	Stratigraphical Interval .....	177
7.3	Scope and Organisation.....	178
7.4	The Western Interior United States .....	181
7.4.1	The Colorado Plateau .....	181
7.4.2	Regional Tectonic Framework .....	184
7.4.3	Jurassic Basins .....	187
7.5	Stratigraphy of the Western Interior United States .....	190
7.6	Jurassic stratigraphy .....	191
7.6.1	Sedimentology of the upper Glen Canyon Group.....	194
7.7	The Navajo Erg .....	197
7.7.1	Palaeo-extent and Erg Development .....	197
7.7.2	Sources of the Lower Jurassic Sediments .....	197
7.7.3	Transport patterns.....	200
7.7.4	Architecture of the Navajo Erg .....	201
7.8	Summary: Controls on deposition .....	205
7.8.1	Tectonics .....	205
7.8.2	Climate.....	205
7.8.3	Eustatic Controls.....	206
8	Study Sites.....	209
8.1	Geological Setting .....	212
8.2	Summary .....	215
9	Lithofacies Analysis of Navajo Sandstone .....	217
9.1	Aeolian Dune Stratification Types .....	218
9.1.1	Wind-ripples facies (Wr) .....	218
9.1.2	Grainflow facies (Gfw).....	220
9.1.3	Grainfall facies (Gfl) .....	222
9.1.4	Adhesion strata (Adh) .....	224
9.2	Navajo Sandstone Facies .....	225

9.3	Facies Associations .....	237
9.3.1	FA1: Fluvial-channel and overbank association .....	238
9.3.2	FA2: Fluvial-aeolian interaction association.....	238
9.3.3	FA3: Flooded interdune and playa lake and association.....	238
9.3.4	FA4: Damp aeolian association .....	239
9.3.5	FA5: Erg-margin association .....	239
9.3.6	FA6: Erg-centre association .....	239
10	Facies architectures and controls on aeolian preservation of the Jurassic Navajo Sandstone 241	
10.1	Methods .....	242
10.1.1	Sedimentology .....	242
10.1.2	Photogrammetry .....	242
10.1.3	Image Processing.....	246
10.2	Site 1: Sevenmile Canyon .....	248
10.2.1	Study Site and Methods.....	249
10.2.2	Results and Interpretations .....	250
10.2.3	Discussion .....	260
10.3	Site 2: Hite .....	265
10.3.1	Study Site and Methods.....	266
10.3.2	Results .....	269
10.3.3	Interpretation and Discussion .....	277
10.4	Site 3: Johnsons Canyon .....	280
10.4.1	Study Site and Methods.....	281
10.4.2	Results and Interpretations .....	284
10.4.3	Discussion .....	296
10.5	Summary.....	298
11	Discussion and Synthesis .....	303
11.1	Study Methods.....	303
11.2	Antecedent Topography.....	307
11.3	Lessons from Linears .....	311
11.4	Preserved dune topography and stabilisation surfaces .....	315
12	Conclusions.....	317
12.1	Research Objectives .....	317
12.1.1	To examine, record and interpret the external environmental controls within which a contemporary aeolian dune-field pattern emerges.....	317
12.1.2	To examine and record the sedimentology and architectural elements at three sites across an ancient aeolian system representing spatial and temporal variations of erg evolution.	

At each site, elucidate the environmental controls in which the system preserved strata and formed a stratigraphic record .....	317
12.1.3 Compare the controls of preservation and bedform morphology within both systems where applicable .....	319
12.2 Recommendations .....	320
12.2.1 Wahiba Sand Sea .....	320
12.2.2 Navajo Sandstone .....	322
13 Reference List .....	325
14 Appendices .....	344

## List of Figures

- Figure 1.1: Location of study sites. (A) The contemporary Wahiba Sand Sea of the Sultanate of Oman. Google Earth™ image, 2016. (B) Palaeogeographic reconstruction of the Jurassic Navajo Sandstone at its maximum extent ~190 million years ago. The erg covered much of western Pangea. All studied outcrops are located in the State of Utah, USA outlined in black. Modified after Blakey and Ranney, 2017..... 6
- Figure 2.1: Dune, interdune, fluvial and sabkha environments in a desert (modified after Shepherd, 2009). .... 17
- Figure 2.2: Locations of the low and mid-latitude major inland sand seas/dune-fields and coastal carbonate aeolianite deposits with their associated tectonic settings (modified after Rodríguez-López et al., 2014)..... 19
- Figure 2.3: Kocurek (1999) considered three-phases (construction, accumulation and preservation) in the creation of the aeolian rock record. Modified after Rodríguez-López et al. (2014)..... 21
- Figure 2.4: End member aeolian system types displaying the accumulation space and the accumulation. Dry, wet and stabilising aeolian systems illustrate the role of aerodynamic configuration, water-table level and stabilising agent (e.g. vegetation) respectively (Kocurek et al., 1998). Modified after Rodríguez-López et al. (2014)..... 22
- Figure 2.5: Three groups of aeolian bedforms, namely ripple, dune and draa. Note the distinct gap in bedform size between the largest ripple and the smallest dune. Small aeolian ripples can be superimposed on both dunes and draa (Collinson et al., 2006; Nichols, 2009)..... 23
- Figure 2.6: Various modes of aeolian transport. Particles hop along the surface in a process known as saltation. The impacts of saltators can mobilize larger particles, causing them to hop, usually less than a centimetre, in a mode known as reptation. Alternatively, larger particles driven by impacts of saltating particles and wind drag force can roll or slide along the surface in a mode of transport known as creep. Modified after Nickling and Neuman (2009). .... 24
- Figure 2.7: (A) Formation of aeolian dunes by saltating sand grains. (B) Note the inverse grading between trough and crest of the ripple which is preserved in the laminae. (C) Ballistic ripple field formed in a coastal setting, Kenton-on-sea, South Africa. Branch ~30 cm long. (D) Coarse-grained wind ripples clearly showing the difference in grain size between troughs and crests. Centimetre scale bar. Schematic diagrams modified after Leeder (2012). Photograph (D) by D. Sumner (<http://mygeologypage.ucdavis.edu/sumner/gel109/sed-structures/Aeolian.html>). .... 26
- Figure 2.8: Simple aeolian dune classification scheme. Note the morphologies of some of these dune types are given in Figure 2.9a-f. Extracted from Wiggs (2019). .... 27
- Figure 2.9: Three-dimensional forms of some common aeolian dune morphologies. The arrows mark the dominant direction of the effective winds. Adapted after Collinson et al., 2006; Nichols, 2009; Boggs, 2011; Argüello Scotti and Veiga, 2019. .... 30
- Figure 2.10: The controls that differentiate dune types. Modified after Wasson and Hyde (1983)..... 31
- Figure 2.11: Hydrodynamic instability that leads to the formation of a sand dune. The schematic shows the streamlines of the wind flow over a Gaussian profile or 'bump'.  $\tau_{max}$  and  $q_{max}$  show the positions of maximum shear stress and maximum sand flux respectively. The saturation length ( $L_{sat}$ ) gives the horizontal distance of relaxation of the flux towards its saturated value due to the variation in the wind flow along the profile. The bump will grow if the maximum flux is reached upwind of the bump's crest (Kok et al., 2012). Modified after Fourrière et al. (2010)..... 32
- Figure 2.12: Dunes migrate as strong winds pick up grains of sand from the stoss (upwind or windward) side of the dune, blowing them across the crest and brink. Erosion occurs on dune slopes which experience the accelerating or divergent winds. Deposition takes place in two settings: where flow separation occurs, rapid and large-volume deposition on the lee-side avalanche faces; in areas where sand transport rates decrease downwind as a result of flow convergence or local flow expansion, slow deposition occurs. Adapted from Clarke (2017) – Keele lecture slides. .... 33

Figure 2.13: Schematic diagram showing the distribution of stratification types in a small dune. Photographs show examples of these primary sedimentary structures. Diagram modified after Hunter (1977), photographs taken from Lancaster (2005).....	34
Figure 2.14: The sets of cross-strata generated by climbing dunes. Modified after Kocurek (1991).....	35
Figure 2.15: Large and small-scale aeolian dunes truncated at different levels. Note how this may greatly influence the geological record of the dunes. Grainfall deposits are less frequently preserved in sets representing large dunes while they dominate in sets of much smaller dunes where the grainfall apron extends to the base of the dune. Modified after Kocurek and Dott, 1981.....	36
Figure 2.16: Schematic examples of aeolian set architectures showing (A) climb, (B) downlap and (C) scour-and-fill geometries. Schematics are extracted directly from Cardenas et al., 2019 and are based on illustrations from Allen (1970) and Rubin and Hunter (1982).....	37
Figure 2.17: A summary of sedimentary architecture and other features characteristic of interdune deposits and the range of depositional conditions under which they form. Observations from contemporary dune-fields and the ancient Entrada Sandstone of western USA. Modified after Kocurek, 1981.....	38
Figure 2.18: Interaction and significance between a migrating dune and interdune. Water-table fluctuations give rise to a variety of damp and wet sedimentary structures both within the interdune and advancing dune toe-sets. Modified after Mountney and Thompson (2002).....	39
Figure 2.19: Bounding surfaces labelled (A) Idealised effect on a dune with seasonal changes in wind direction. Strong winter winds cause the dune to migrate on the interdune surface creating the first order bounding surface. During summer, weaker winds do not reverse the migration of the dune, but rather alter the structure of the dune, both eroding into the lee slope at the brink and forming a smaller superimposed dune migrating down the stoss slope of the dune, marking the second order bounding surface. On return of the stronger winter winds, deposition is reactivated on the lee slope and a third order bounding surface is apparent. (B) Migration of simple dunes and interdune areas. (C) Migration of compound/complex dunes and interdune areas. Modified after Lancaster (2005) and Neuendorf et al. (2006).....	41
Figure 2.20: Conceptual model of the migrating erg with stratigraphic sequence of an idealised erg. Modified after Porter (1986) and Pye and Tsoar (2008).....	43
Figure 2.21: Tectonic, climatic and eustatic influences on erg deposition produces a distinctive variation or modification of the idealized erg facies sequence (modified after Porter, 1987).....	44
Figure 2.22: Erg margins and idealised vertical sequences. (A) Adjacent to an ephemeral stream alternating wet/dry conditions prevail. (B) Low-angle aeolian deposits of the sand sheet occurring peripheral to the erg and forming a transitional lithofacies which intercalates with high-angle dune deposits. Modified after Leeder (2011) and Fryberger et al. (1979).....	46
Figure 2.23: A water-table rise promotes the accumulation of sediment within the erg. A fall in the water-table from the level of the interdunes will leave more sediment available for transportation and thus removal from the area of the erg. Modified after Nichols (2009).....	47
Figure 3.1: A) The geological setting of northern Oman and approximate position of the Wahiba Sand Sea. The Gulf of Oman is floored by Cretaceous oceanic crust currently subducting northward below the Makran active continental margin of Eurasian continental lithosphere. In northern Oman, the oceanic lithosphere is thrust onto the continental margin forming the Oman Mountains. The Wahiba erg has accumulated south of the Oman Mountains. Foreland basin system terminology is that of DeCelles and Giles (1996). B) Structural profile A-A' through the Oman Mountains. The section includes the stratigraphic units from the Gulf of Oman to Fahud oil field. Adapted after Hanna (1990). For information on rock types, see Table 3.1. A) and (B) are modified after Burg (2018) ( <a href="http://www.files.ethz.ch/structuralgeology/JPB/files-/English/Omaneng.pdf">http://www.files.ethz.ch/structuralgeology/JPB/files-/English/Omaneng.pdf</a> ) and Hansman et al. (2017) respectively.....	54

Figure 3.2: A) Satellite image (Landsat -8 panchromatic 15m, LC08\_L1TP\_157045\_20190527\_20190605\_01\_T1\_B8, ©USGS) with schematic inset showing the location and extent of the Wahiba Erg. The N-S trending white line is the seismic line profile shown in Figure 3.3. The red box in the NW corner of the sand sea is the location of the GeoEye-1 and Worldview-3 dataset of section 5.4. B) Digital Surface Model 30 m (Advanced Land Observing Satellite AW3D30, ©JAXA) showing the principle geomorphological regions of the Wahibas (High Sands, Low Sands, Al Jabin and Coastal Sands). The two datasets were displayed in GIS software and measurements incorporated into a GIS database. UTM coordinate grid with 25 km spacing for scale..... 58

Figure 3.3: Interpreted seismic line (white line shown in Figure 3.2A) across the Wahiba Basin (Radies et al., 2004). The cross-section shows a down-warped basin with up to ~250 m of Barzaman (alluvial fan deposits) and aeolian strata in the High Sands..... 59

Figure 3.4: The megadune morphology in the A) High Sands and B) Low Sands. The DSM has been overlain onto the orthophoto to clearly differentiate the megadune and interdune morphology. Note the faint N-S trending lineation's representing the superimposed dunes..... 60

Figure 3.5: Examples of common wind vectors that affect the Wahiba Sand Sea (outlined in black). In summer, the strong and prevalent south to southeast winds that occur with the Indian monsoon act as the dominant winds that affect the Wahibas. In winter, the intense but short duration winter Shamal winds from the northwest act as the subordinate winds that affect the Wahibas. The weak but persistent monsoonal northeasterlies have little influence in winter. The ITCZ is approximately marked by the merging winds and its position is crucial in the movement and divergence of winds across the region. Extracted from [www.ventusky.com](http://www.ventusky.com). .... 62

Figure 3.6: A) Annual drift potentials (sand moving power of the wind) and B) directional variability of the wind (RDP/DP) contoured across Oman. Maps modified after Fryberger et al., 2016a, b..... 64

Figure 3.7: Average temperatures (degrees Celsius) for the Ash Sharqiyah Governate of Oman. Data Source: National Centre for Statistics and Information, Sultanate of Oman (<https://data.gov.om/>) ..... 65

Figure 3.8: Average rainfall for the Ash Sharqiyah north and south Governates of Oman. Known storms that have brought heavy rain are marked on the chart. Source: National Centre for Statistics and Information, Sultanate of Oman (<https://data.gov.om/>)..... 65

Figure 3.9: Location of three sites where stratigraphic dating occurred (reported in section ). WDR-1 and WDR-2 (yellow pins) are core locations of Preusser et al. (2002). Site 4 (blue pin) is a trench and GPR site of Hern et al. (2018). Table 4.1 provides precise coordinates of sites. Google Earth™ image (2016). .... 66

Figure 3.10: Plotted IRSL dates including error bars for cores WDR-1 and WDR-2 (raw data extracted from Preusser et al., 2002 supplementary files). Twenty-one dates extracted from core WDR-2 (blue circles) drilled through the crest of a linear megadune (302 m – 242 m ASL) and thirty-five dates extracted from core WDR-1 (orange circles) drilled through an interdune (240 m – 125 m ASL). The red dashed line highlights time-gaps between constructional phases of megadune building. The hiatus' may either represent periods where scouring and erosion occurred or, alternatively, periods of dune stabilisation and preservation prior to the next phase of deposition. While a hiatus is inferred between the Hawiyah and Al Hibal Units' the large errors in IRSL dating shows much overlap and the stratigraphy is rather associated with marine isotope stages in which the errors fall. The Barzaman Formation underlies the Al Batha Unit and is not shown here as no dates were extracted. .... 69

Figure 3.11: West to East schematic of the Wahiba Sand Sea including the stratigraphic units described in the text. The three stacked aeolian units of the High Sands megadunes include the Hawiyah (~71 Ka), the Qahid (~20 Ka) and the Holocene Unit (~1.8 Ka). See text for more details on ages. Not to scale. Modified after Radies et al., 2004..... 70

Figure 3.12: Radargram profile collected at 500 MHz on the crest of a complex linear draa in the Wahiba Sand Sea. Buried accreted whaleback or rounded ridge (highlighted) with self forms above accreting along its former axis. Image from Nursaidova (2009)..... 72

Figure 3.13: GPR radargrams acquired at the megadune containing Site 4 of Hern et al. (2018). A) A 250 MHz line from the start of the megadune stoss to its crest (full methodology provided in section 5.5). The inset Google Earth™ image shows the west to east trending GPR traverse. Red highlighted sections (b-e) show the approximate locations of the resolved radargrams used for interpretation in this study (section 6.4). Note the areas of high reflectivity punctuated by dimmed zones without signal loss. (B) to E) are the tentative interpretations of internal architectures in Hern et al., (2018): B) Stacked trough-cross bedded sets. C) Well-preserved transverse dunes forming above and below the dated stabilised surface. Note the relationships with bedform preservation and local dimming. D) The opposing slopes of a buried seif dune. E) Wind ripple dominated flank of the megadune. Figures are modified after Hern et al., (2018)..... 73

Figure 4.1: Google Earth™™ oblique view of a typical asymmetric linear megadune in the High Sands at the northern margin of the Wahiba erg. The dune measures approximately 70 m in height and 800 m in width. The east facing stoss slopes contain prominent knick-points or terraces flanked by superimposed dunes (marked in red arrows). Note the spatial relationship of the erg termination, the Wadi Batha and the Oman Mountains. . 75

Figure 4.2: The drilled megadune of the core WDR-2. A) Panchromatic Landsat-8 orthophoto with the precise location of core WDR-2 and surrounding megadunes. B) In cross-section, prominent knick-points (1, 2, and 3) on the stoss slope seem to correlate to stratigraphic units of Radies et al. (2004). C) Google Earth™ image (3x V.E.) view to the south shows the two interdunes that lie at the correlated elevations of core stratigraphy. The western-most interdune (Qahid level) lies ~21 m above the surface of the interdune to the east (Al Hibal level). ..... 77

Figure 4.3: A) Panchromatic Landsat-8 orthophoto showing the adjacent megadunes and precise location for core WDR-1. Note the east-facing stoss slopes of most megadunes are riddled with NNE-SSW trending linear ridges. B) Cross-section x-x' shows the position of core WDR-1 and suggested Al Hibal topography. C) Google earth view to the south (3 x V.E.) showing core location. The black dashed lines mark the topography and linear terraces that extend NNE-SSW along the stoss slope. The Al Hibal unit lies at the same elevation as the lowermost terrace and the topography making up the crescentic form to the south marked by the gridded lines and blue dots. .. 78

Figure 4.4: A) The location of Site 4 (S4) of Hern et al. (2018) and cores WDR-1, 2 of Preusser et al. (2002). S4 includes an OSL date taken on a prominent terraced surface of 18.1 Ka ±2.3 Ka. B) Oblique aerial view to the north of the terraced surface (the knick-point in cross-section) at site S4. C) The terraced surface of S4 where the OSL sample was acquired. D) Trench dug for the OSL sample at S4 taken at ~1 m depth. Note the easterly dipping relict dune cross strata. Photographs C and D are courtesy of Robin Westerman and Dominic Tatum..... 80

Figure 4.5: The cross-section x-x' traverses' S4 through to WDR-2 (Figure 4.4) slicing the megadunes oblique to their trend. Note knick-points are common on the stoss slope in almost all dune profiles crossed (red arrows). S4 OSL date is captured ~1 m below the knick-point surface (~10 m below crest) with correlative dates produced at knick-point level in core WDR-2 (~30 m below crest). The knick-points are interpreted here as exposure of the older core morphologies (Qahid Unit?), overlain by younger sands. The dashed line approximates this correlation between the two sites. .... 81

Figure 6.1: The relationships between dune height and spacing vary between dunes and from one sand sea to another, as well as from one dune type to another in the same sand sea. Modified after Lancaster (1988a, b, 2013)..... 91

Figure 6.2: Wahiba Sand Sea divided into zones 1 to 3 with line profiles A through F. The cross sections for each line profile are shown in Figure 6.4. .... 93

Figure 6.3: Close-up of two linear mega dunes of the Wahiba erg including definitions of the terminology used in this chapter to describe their geometry. In transects perpendicular to the dune trend (shown here by X-X'), cross sections were used to calculate dune height, dune wavelength, dune spacing and interdune width..... 94

Figure 6.4: Cross sections of lines A-A' through F-F' as shown in Figure 6.2. Elevation data was extracted using ASTER GDEM. Dune attributes were calculated through visual inspection and extraction of points along each line profile..... 97

Figure 6.5: Dune height vs. dune wavelength for line profiles A – F. Dune heights exhibits a positive correlation with bedform wavelength and spacing. .... 99

Figure 6.6: The blue lines show relationship between dune type, directional variability of the wind, and sand supply as determined by Wasson and Hyde (1983). This study (green lines) and a study on the Namib Sand Sea (Lancaster, 1989) found that similar dune types occurred where the wind was less variable. Figure modified after Lancaster (2013). Wahiba EST calculations are detailed below, RDP/DP values are extracted from Fryberger et al. (2016) in Figure 3.6..... 102

Figure 6.7: The sequence of images illustrates the process of deriving a map of Equivalent Sediment Thickness (EST). Each step produces a map that can be used to better analyse dune-field boundary conditions. (A) The cropped DSM only including the area of interest (ALOS AW3D30, ©JAXA). (B) The smoothed topography representing the interdune base level surface. (C) The base level surface is subtracted from the original dune topography and yields a map that excellently reveals areal patterns. (D) The map in (C) is filtered in order to approximate the local EST for a 15 km radius around grid cells. .... 105

Figure 6.8: (A) The smoothed base-level map after applying the mean filter. The base-level appears as a mound-like shape with common breaks in slope. (B) A 3D visualisation of the base-level topography. Dunes partly bury the Hawasina Group highlands in the northwest corner. The erg terminates abruptly at the northern, eastern margins and western margins where the wadis dominate. .... 106

Figure 6.9: Comparison of cropped DSM maps. (A) Standard DSM map of the dune-field area. (B) DSM where base-level is removed and the dunes rest on a flat surface. With base-level removed, heights and pattern heterogeneity become more apparent. .... 108

Figure 6.10: Spatial variation of equivalent sediment thickness overlain onto panchromatic Landsat-8 orthophoto for reference. Note how the spatial variability correlates with the dune-field patterns in Figure 6.9. Well-defined tall linear complex dunes are concentrated in areas with thicker sediment piles, while thinner sediment spread is associated with subdued compound dunes in the south. The contours mark the thickest sediment build-up (>45 m). .... 109

Figure 6.11: The coloured DSM map represents base-level which is overlain by EST contours. The maps are produced independently from one another but note how they approximately conform. Sediment thickness trends similarly with the underlying topography. Rapid increases in thickness generally tends to occur in conjunction with the topographic breaks-in-slope. Both maps are superimposed onto Landsat -8 panchromatic orthophoto..... 112

Figure 6.12: A) A 3D visualisation of base-level with line profile transects X, Y and Z taken approximately parallel, perpendicular and oblique to the general linear megadunes trend respectively. B) The profiles show base-level, dune topography and EST line profiles along north to south (X-X'), west to east (Y-Y') and a southwest to northeast (Z-Z') transects. Dashed arrows mark the breaks in slope at base-level and are commonly associated with increased EST and higher dune profiles, usually leeward of the terrace. .... 113

Figure 6.13: Shaded relief maps showing the results of residual relief separation the Badain Jaran desert.( A) The original surface with three dune generations. (B) The residual surface (medium-size dunes). (C) The smoothed underlying host bedform topography (large-sized dunes). (D) The discrimination of different dune generation showing the original surface (black line), residual surface (dotted line) and the underlying surface (grey lines). Modified after Hugenholtz and Barchyn (2010). .... 116

Figure 6.14: The high-resolution orthophoto (0.5 m) and accompanying DSM (1 m) of GeoEye-1 and Worldview-3. Red boxes show areas of interest reported in text. The location of these high-resolution datasets is shown in Figure 3.2. .... 118

Figure 6.15: (A) The panchromatic orthophoto shows the two linear megadunes MD1 and MD2 of Area (i). Subtle topographic variations identified in orthophoto and DSM were further inspected using the shaded relief technique (sun azimuth 180° at 25° altitude). The resulting map shows partial relicts of large crescentic bedforms, recognisable in the interdune area (see interpretation map). (B) South to north cross-sectional profiles: X-X' runs parallel along the interdune corridor and Y-Y' runs parallel to MD1's crest. Profile X-X' show the bedforms have

a gentle south facing slope and steep north facing slope. 'S' marks the small crescentic bedform superimposed on the larger bedform crossed in X-X'. Profile Y-Y' was generated using residual relief separation and shows the smoothed underlying surface (median filter radius = 50 m). This was done to minimise the effect of the superimposed dunes. The profile shows three offset highs (2-4) that are interpreted to be the western horn of the large crescentic bedforms, as shown in (A) and in profile X-X' ..... 120

Figure 6.16: A) Area (ii) displays the close relationship between the stoss slope of MD1 and the lee slope plinth of MD2. The interpreted lines on the Hillshade DSM (sun azimuth 190° at 20° altitude) were traced out using the highest points along DSM contours. The resulting interpretation reveals three large-scale arcuate lines (1-3), potentially fragments of crescentic bedforms. B) The zoomed in orthophoto shows megadune MD1 contains active seif dunes superimposed onto the well vegetated stoss slope. Under hillshade (sun azimuth 145° at 25° altitude), medium-scale crescentic bedform horns become apparent on MD1's stoss slope. Where they coincide, the active seif dunes trend along the crescentic bedforms. B) X-X' cross-sectional profile of MD1 shows prominent knick-points near the base of the stoss slope. The knick-point topography correlates with active seif dunes, as well as the crescent horns observed in the shaded relief map. Y-Y' cross-sectional profile perpendicular to the crescentic bedform (~2.5 m tall) shows a gentle south facing slope and a steep north facing slope. .... 122

Figure 6.17: A) The high-resolution orthophoto of megadune in area (iii). The shaded relief map shows the smooth underlying topography (5m radius mean filter applied; sun azimuth 180° at 04° altitude). Medium-sized crescentic forms are identified on the megadune stoss slope under residual relief. The purple box shows the site of 3D GPR acquisition (not analysed in this study) and OSL sampling of Hern et al. (2018). B) Zoomed in section of identified forms a and b with cross-section X-X' shows these forms have a gentle south-facing slope and steep north-facing slope. C) Zoomed in section of identified forms c and d, with cross-section Y-Y' shows peaks (c<sub>1</sub>, c<sub>2</sub>, d<sup>1</sup>, d<sup>2</sup>, d<sup>3</sup>) separated by troughs of what are thought to be horns and troughs of barchanoid forms. .... 125

Figure 6.18: A) Landsat-8 panchromatic orthophoto of the central High Sands (~800 km<sup>2</sup>). The surface pattern is dominated by linear megadunes. Crescentic bedforms are scattered and often fragmented B) Shaded relief map showing the underlying topography of the same area in (A). The abundance of crescentic forms becomes much clearer with this enhancement, occurring in almost all linear dunes. C) The northeastern margin of the erg is flanked by the fluvial Wadi Batha. The NE corner is easily distinguished by darker sediments and a disturbed surface pattern. D) Shaded relief map showing the underlying topography of the same area in (C). Medium-scale crescentic dunes dominate the disturbed pattern and fill linear interdune corridors. Maps (B) and (D) produced from ALOS AW3D30 DSM datasets. A 100m radius minimum filter was applied to investigate the underlying topographic expressions in (B) and (D) (sun azimuth 160° at 20° altitude). .... 129

Figure 6.19: Survey location for the 2D GPR profile. (A) The high-resolution orthophoto and zoomed-in study site in (B) showing the west – east GPR traverse on the eastern flank of the linear megadune. The purple box in (B) shows the site where trenching and OSL dates were acquired by Hern et al. (2018). The relative position of the high-resolution orthophoto in the Wahibas is shown in Figure 3.2 ..... 131

Figure 6.20: (A) Vehicle-towed GPR system. (B) Flight path of UAV to create a high-resolution DEM (overlay onto Google Earth Map with view to the north). Images courtesy Robin Westerman and Dominic Tatum. .... 132

Figure 6.21: Marked variations in moisture content in the primary depositional fabric are directly linked to GPR response. A positive reflection event (blue) results when convolved with a negative (red) reflection coefficient from a damp-over-dry (i.e. slow-over-fast) interface (Buckman et al., 2017). Image modified after Hern et al. (2018). .... 134

Figure 6.22: The drawing indicates the main types of reflector terminals (toplap, onlap and downlap). The terminations are used to identify radar sequence boundaries. Extracted from Gawthorpe et al. (1993). .... 135

Figure 6.23: Red highlights mark the approximate locations of 2D GPR radargrams tied to both the orthophoto and residual relief map. The dashed blue line represents the approximate traverse of the 250MHz GPR line between 60 m and 360 m. The black dashed box represents 3D GPR site acquisition (not analysed in this study). Orthophoto and GPR capture dates are 2 years apart (GPR acquisition 2015, orthophoto January 2017). .... 136

Figure 6.24: A) Example of concave-up reflections of RF1. (B) Example of convex-up reflections of RF2, typically increasing in amplitude with height. Example of near horizontal reflections of RF3. Approximately 2 X vertical exaggeration in all examples..... 140

Figure 6.25: Profile A-A' represents the west to east traverse on the crest of a linear megadune. A) Processed GPR data. B) Interpretation of the GPR profile reflectors. C) Dominated by RF1, the discontinuous concave-up reflections are interpreted as trough-cross strata likely to have been formed by crescentic superimposed dunes. Two orders of superimposed dunes exist at 8-9 m depth scouring into underlying stratigraphy that potentially represents the megadune, and at 2-3 m depth, scouring into the larger trough-cross sets below. Near-horizontal reflectors mark radar facies 3 as a blanket of wind-ripple strata resting on a deflationary 'supersurface' ..... 141

Figure 6.26: Profile B-B' represents the west to east traverse in a near horizontal terrace of a linear megadune. A) Processed GPR data. B) Interpretation of the GPR profile reflectors. C) Three stratigraphic units separated by the interpreted deflation surfaces exist in this profile. The top unit consists of RF3, interpreted as wind-ripple strata covering a deflationary surface. In the middle stratigraphic unit, an association exists between concave-up bounding surfaces of RF1 and the flanking convex-up bounding surfaces of RF2. Together the two radar facies are interpreted as well-preserved crescentic dunes. Due to the limitation of the profile, only the partial remains of this facies association can be identified in the oldest unit. The lower most deflation surface may be underlain by the megadune on which the overlying strata accreted, however, this is a tentative interpretation due to the loss of seismic reflectors at depth..... 142

Figure 6.27: Profile C-C' represents the west to east traverse on the stoss-slope of a linear megadune. A) Processed GPR data. B) Interpretation of the GPR profile reflectors. C) Two stratigraphic units are separated by deflation surfaces. The older unit consists of associated radar facies as identified in profile B-B', however only in partial view due to the limits of the profile. Together these two radar facies are interpreted as a partial crescentic dune. The comparable size of this interpreted bedform (~30 m horn) to that of the interpreted bedform in the lower stratigraphic unit of profile B-B' (~35 m horn), and both speculatively superimposed on an underlying megadune perhaps reveals that the dunes could be of the same genetic nature (e.g. medium-scale crescentic bedforms observed in Figure 6.15 and Figure 6.16). The upper-most deflation surface separates this unit from RF3, interpreted as a sheet of wind-rippled strata that covers much of the contemporary megadune. .... 143

Figure 6.28: Profile D-D' represents the west to east traverse on the stoss-slope of a linear megadune. A) Processed GPR data. B) Interpretation of the GPR profile reflectors. C) Two stratigraphic units RF3 and RF1 are separated by deflation surface. The older unit consists entirely of RF1 interpreted as grainflow strata potentially forming part of a large trough-cross set. The deflation surface cuts this set and is overlain by contemporary wind-ripple strata of RF1 that covers the megadunes' stoss slope. .... 144

Figure 6.29: A survey of a Barchan dune using GPR and satellite imagery reveals similar sub-surface structures to those interpreted in radargram profiles B-B' and C-C' in this study. A) The outlines of the migrating barchan dune in Morocco between 2005 and 2018. GPR profiles were collected parallel (X-X') and perpendicular (Y-Y') to the migration direction. (B) Radargram and interpretation of the barchan dune acquired perpendicular to migration direction (Y-Y'). Note the inclined strata from the barchan horns preserved on the dune margins (Radar facies 1). In this instance, ~5 m of the horn strata is apparent. The trough-cross set of the main barchan bedform is approximately 8m tall and is scoured by superimposed dunes migrating along the barchan crest. Images modified after Bristow (2019). .... 145

Figure 6.30: The areas from section 6.3 showing a close-up of proposed antecedent crescentic dunes. Note in area (i) and (ii) the crescentic dunes are superimposed onto a larger bedform, interpreted as the megabarchans that, in the contemporary configuration are thought to form the linear dune core. These dunes generations are suggested to make up the well-preserved crescentic bedforms interpreted in the subsurface stratigraphy. The superimposed dunes of Area (i) and (ii) are at an elevation of approximately 340-360 m on the megadune stoss slope and potentially make up the lower stratigraphic unit of GPR profile B-B' (Figure 6.26), and the interactions seen in C-C' (Figure 6.27) although speculative due to profile limitations. Area (iii) is closer to the dune crest at ~400 m elevation and potentially makes up the middle stratigraphic unit of B-B' where the relatively smaller sets of radar facies are situated. Identifiable in area (i) is the mega-crescentic bedform that encroaches into the linear megadune core. The western horn of this structure could potentially explain the apparent eastward dipping strata and large set size of profile D-D'. .... 147

Figure 6.31: Multi-temporal NDVI maps showing the extent of vegetation cover in the Wahibas in winter and summer months over a 5-year period. While minor variations are identified between seasons, the maps require further processing to examine the extent of well-to-poorly vegetated areas within the erg (see minimum and maximum NDVI values in Table 6.3). Note in all instances, the northeast corner and western margin show the lowest NDVI values of the erg. .... 150

Figure 6.32: NDVI overlain onto a high-resolution orthophoto. Blue values represent the vegetation index of dune-field components. Where vegetation is visible, NDVI values are high (green areas). In areas with low-to-no vegetation (Wadi Batha, basement outcrops and active sands), NDVI values are low (red areas). The exercise provides threshold values for further erg-wide analysis and proves that the NDVI technique is capable of analysing vegetated vs. non-vegetated areas in the very arid and sandy landscape. The dataset, however, is limited by its resolution and therefore will overestimate green space (note the distribution of green coverage includes the sandy areas between scattered vegetation). The yellow X marks the Sand Delight Camp shown in ground view in Figure 6.35. Pixel count = 3840, minimum = 0.03, maximum = 0.12, mean = 0.1, S.D. = 0.013. NDVI output map and orthophoto represent January 2019. .... 153

Figure 6.33: The extent of 'green-space' coverage through the studied seasons. The binary raster maps show the areas where NDVI values are greater (green) or lesser (red) than 0.095. The percentage coverage (erg only) is shown in Figure 6.34. .... 154

Figure 6.34: A) Mean NDVI classification trend (black line) show slight decreases between summer months (red dots) and winter months (black dot) over the two datasets, five years apart. Grey error bars show standard deviation from mean associated with classification values reported in ArcGIS statistics. NDVI values >0.095 were determined in classifying the poor-to-good vegetation coverage, cropped to fit the Wahiba erg, and is shown here as 'percentage covered' (green). An overall decrease occurs over the 5-year period, however, is not interpreted as a trend due to the short timescale. B) The precipitation averages from January 2013 to March 2014, and January 2018 to December 2018 for the Ash Sharqiyah region of Oman demonstrates the rainfall surrounding the two datasets (see Figure 3.8 for the full dataset). There is an average of 10 mm precipitation and 32% vegetation cover over the 2013/14 dataset vs. an average of 4 mm precipitation and 6% vegetation cover over the 2018/19 dataset. The agreement may represent the growth response in drier periods. .... 155

Figure 6.35: A photo of Sand Delight Camp on the northern edge of the Wahiba dune-field. The camp and surrounding dunes shows the abundance of stabilising vegetation between active seif dunes that are relatively devoid of vegetation. View is to the NNW. Refer to Figure 6.32 for plan view position and corresponding NDVI overlay. Photo by Petr Horacek (<https://lh5.googleusercontent.com/p/AF1QipOH7Z4ZoBrj6MtafNfrpD8fwNGh2k6zbKqs96hP=h1440>)..... 157

Figure 6.36: Absorption bands in the optical region (visible to shortwave infrared) that enable remote sensing mapping of mineral assemblages and rocks. VIS (visible spectrum), NIR (near infrared spectrum), SWIR (shortwave infrared spectrum). Modified after Gupta (2018). .... 158

Figure 6.37: Hypothetical reflectance curves depicting how ratios enhance minor reflectance variations. Adapted after Prost, 2013). .... 159

Figure 6.38: Method step to produce a map for each mineral occurrence. In this example, the produced map is grouped into five classes representing areas that contain a high occurrence (warm colours) vs. low to no occurrence (cold colours) of the mineral type. Once a threshold value is determined, a binary raster map is produced and finally superimposed onto an orthophoto for better spatial reference. .... 162

Figure 6.39: (A) Landsat-8 tiles surrounding the Wahiba Sand Sea were selected for regional-scale studies (within red-dashed box). (B) With solar corrections applied, the tiles were merged into a continuous dataset for each band. Fig (A) is extracted from <https://search.remotepixel.ca> ..... 163

Figure 6.40: Greyscale output maps of band ratios. Bright areas in each output map indicate likely target zones for associated mineral assemblages. A) B4/B2 iron oxide ratio is associated with hematite / goethite. B) B6/B5 ferrous mineral ratio associated with mafic minerals. C) B6/B7 clay / carbonate ratio associated with hydrous aluminosilicates and / or carbonates. As quartz has high reflectance in band 7 it is represented on the same map

by areas of very low reflectance. (D) Band ratios derived from image spectra 4/2-6/5-6/7 combined in RGB to produce a false colour composite. .... 166

Figure 6.41: (A) Separated mineral raster datasets. (B) Panchromatic map with all mineral overlay based on binary raster separations of the three mineral categories – ferric, ferrous and calcium carbonate/clays. Zones without colour are unclassified. .... 167

Figure 6.42: (A) Landsat-8 false-colour composite 7-4-2 (RGB) shows the location of the Wahiba dune-field in references to the surrounding Oman Mountains, Bajada and wadis, Hufq outcrop and Rub' al Khali desert at the Oman / Saudi Arabia border. The false-colour band combination shown here is typically used to highlight the geology of a region. (B) The same area in (A) showing the mineral occurrences as identified by the band ratio datasets. Red and blue arrows indicate the net annual resultant drift directions for summer and winter seasons respectively (relative strength by arrow length). Black dashed arrows represent simplified net annual sand flow directions based on dune orientations in the Rub' al Khali. Sand drift data is extracted from Fryberger et al., 2016a. .... 172

Figure 7.1: Physio-geographical provinces of the Western Interior United States include the high standing Colorado Plateau; the north-south trending Basin and Range Province characterised by narrow faulted mountain chains and flat arid valleys; the tall peaks and valleys of the Middle and Southern Rocky Mountains; and the inclined flat grasslands of the High Plains Province. Modified after Blakey (2008). .... 179

Figure 7.2: (A) Simplified Jurassic litho-stratigraphy of the Colorado Plateau showing the main aeolian deposits and major unconformities (see section 7.6). This work focuses on the Navajo Sandstone, the largest and most widespread aeolian deposit during Jurassic times (Modified after Allen et al., 2000; Beitler et al., 2005; Lucas et al., 2011). (B) Generalised stratigraphy and age assignments marking the Triassic-Jurassic boundary at ~201 Ma (Modified after Lucas and Tanner, 2014). .... 180

Figure 7.3: The outline of the Colorado Plateau tectonic Province. Large scale lineaments define much of the tectonic grain on the Colorado Plateau. The northwest-trending Olympic-Wichita Lineament appears to have had right-lateral strike-slip displacement and is bracketed to 1.72 – 1.46 Ga. The northeast-trending Colorado Lineament displaced basement rocks in a left-lateral sense and is dated at ~1.7 Ga. The two continental-scale rift systems form a conjugate set that bisect one another in the vicinity of Moab. The Cordilleran Hingeline (section 7.4.2) delineates the northwesterly extent of the Plateau and had its roots in Precambrian time. The Precambrian northwest-trending Walker Lane-Texas Lineament (not shown here) was one of the largest, longest, and most prominent lineaments on the N. American continent. On this map, limited features of this lineament are represented by the Mogollon Hingeline and Zuni Lineament. Modified after Foos, 1999 with information from Kelley, 1955; Baars and Stevenson, 1981; Blakey, 1988. .... 183

Figure 7.4: Palaeotectonic evolution of southwestern North America from the late Precambrian Period to the Jurassic Period with brief summaries of the subsequent depositions. Figures modified after Blakey, 2008 with summaries from Blakey, 1988; Marzolf, 1993, 1994; Blakey, 2008; Ingersoll, 2008; Miall, 2008. .... 186

Figure 7.5: Tectonic subsidence histories for Blanding in southeastern Utah and Zion in southwestern Utah. During Navajo times, subsidence was greatest in the west accounting for the thicker accumulation of aeolian sands. Modified after Allen et al. (2000). .... 188

Figure 7.6: General tectonic setting for the deposition of the Lower Jurassic. Modified after Blakey, 1994. .... 189

Figure 7.7: The Pennsylvanian to Jurassic systems of the Western Interior of the United States highlighting all known aeolian-bearing intervals (yellow). Unconformities are in grey with principal unconformities of the Jurassic labelled. The early works of this stratigraphical diagram shows the Triassic-Jurassic boundary to lie on the J-0 unconformity (see in-text for the correct boundary). Refer to section 7.6 for the positions of the J-sub-K and J-sup boundaries (not shown here). Modified after Blakey (1988). .... 190

Figure 7.8: Cross-section of the Jurassic rocks of western interior United States showing regional relations of the sequences and unconformities. Note the considerably different geometry between Navajo-Kayenta (drastically thickens to the southwest) and Wingate-Moenave (irregular sheet geometry). Modified after Blakey (2008). 192

Figure 7.9: Upper Glen Canyon fluvial-aeolian palaeoflow map. Fluvial systems of the Kayenta were sourced to the south and east. Opposed to obliquely opposed palaeocurrents of aeolian and fluvial systems intuitively argues for an exchange of sand between the two systems. Modified after Blakey (2008)..... 196

Figure 7.10: (A) Geometry and facies relations of Lower Jurassic aeolian deposit (Navajo, Nugget and Aztec) with superimposed generalized tectonic elements that influenced aeolian sedimentation. Tectonic boundaries are approximate and varied through time. Isopachs show thicknesses of the aeolian interval (dashed isopachs in southwestern Arizona are highly conjectural). Where the Navajo intertongues with the Kayenta Formation along the southern and southwestern margin of the outcrop, the thickness of Navajo is included without the intervening Kayenta Formation. Much of the data on the extent of the Navajo was early interpretation collected from literature dating back to 1927 and was developed as a framework for future research (see table 5 of Blakey et al., 1988). The tectonic elements shown (Blakey, 1988; Blakey et al., 1988; Bjerrum and Dorsey, 1995; Blakey, 2008) were generally well known, however are continually changing with new research, especially with regards to the adjacent Cordilleran arc. (B) The palaeo-extent of the erg was redefined during later work completed by Blakey and Ranney (2008). Note the source areas of the underlying Kayenta to the south and east of the erg. A and B are modified after Blakey et al. (1988) and Blakey and Ranney (2008) respectively..... 199

Figure 7.11: Transport patterns for sand circulation and recycling between fluvial and aeolian environments as envisioned by Blakey (1994). Modified after Blakey (1994). ..... 201

Figure 7.12: General facies in the Navajo erg. The gradational contact between Marzolf's (1983) wet and dry Navajo erg is marked by the dashed time line. Modified after Blakey (1994)..... 202

Figure 7.13: Cross-sections showing six hypothetical models of internal architecture of Navajo Sandstone and inferred timelines for each. Note that Figure 7.12 is compatible with any one of these schematics. .... 203

Figure 7.14: Palaeo-extent of the Navajo erg and thickness with the superimposed erg centre (shadowed) as depicted by Blakey (1988). Red question marks are placed by the author due to either areas falling out of Blakey's study area (e.g. the western margin and the northern extent of the erg), or where the two forms do not meet, and thicknesses are constant. .... 204

Figure 7.15: The southernmost winds are tropical westerlies as interpreted by Loope et al. (2004b). Shadowed regions demarcate the areas where evidence for wetter conditions are prevalent. Note the palaeolatitude of 10° N. Modified after Loope et al. (2004a). ..... 207

Figure 7.16: The chart compares sea-level curves (Ross and Ross, 1988; Haq, 2009), Sloss sequences (Sloss, 1988) and the stratigraphical sequences and unconformities of Blakey (2008). The Upper Glen Canyon, representing the Kayenta Formation and Navajo Sandstone, is highlighted in red. Asterisks signify high-water periods on the Colorado Plateau as marked by marine sequences that penetrated the dominantly continental section (for further details see Figure 37 of Blakey, 2008). Modified after Blakey (2008). ..... 208

Figure 8.1: Study sites of the Navajo Sandstone. Inset shows location within the 'four corner' States of southwestern USA – Utah (UT), Colorado (CO), Arizona (AZ), and New Mexico (NM). Following key observations, three key sites were selected including Sevenmile Canyon, Hite, and Johnsons Canyon for further large-scale examination by remote sensing (reported in chapter 10). A summary of site observations is provided in Table 8.1. Sedimentary logs are included in Appendix A2..... 210

Figure 8.2: Palaeogeographic map and cross-section of the known extent of Navajo Erg. The cross section highlights the westward thickening in the Utah-Idaho trough, interpreted as a retro-arc foreland basin system. Three study sites of the Navajo Sandstone (1-3) were analysed in a northeast to southwest transect from marginal to central basin. The positions of the studied sections on the schematic cross-section are approximate and largely for reference purposes. Palaeogeographic reconstruction modified after Blakey, 2008. Cross-section modified after Blakey, 1994..... 213

Figure 9.1: Wind-ripple facies A) Millimetre-scale wind-ripple laminated sand. The weathering of the outcrop accentuates the characteristic bimodal framework of the facies. A single massive grainflow laminae (Gfw) separates the pinstripe lamination. Navajo Sandstone at Mt Carmel Junction, Utah. B) The outcrop wall shows mm-scale crinkly pinstripe laminations. The weathered surface shows the preserved wind-ripples in plan-view.

GPS unit in is 15 cm in length. Navajo Sandstone at Goblins Valley State Park, Utah. C) Preserved ripple-foreset cross-laminae (arrow). Truncation of the rippleform laminae is indicative of subcritical climb. Note the inverse-grading. Navajo Sandstone at Kanab, Utah. D) Modern example of wind-ripple facies clearly shows the bimodality of grain-sizes. Mesquite dune-field in Death Valley National Park, California. Lens cap in (B) and (C) is 55 mm in diameter. .... 219

Figure 9.2: A) Aeolian dune cross-strata dominated by grainflow facies (Gfw). The grainflow strata are typically interbedded with wind-ripple facies (Wr) or thin grainfall laminae (Gfl). Note the wedge-like geometry at the toe of the grainflow strata and the interaction with wind-ripple facies forming dune plinth deposits. Navajo Sandstone at Kanab, Utah. B) The upper most set shows the lenticular geometry of grainflow strata in a section parallel to strike. Navajo Sandstone at Sevenmile Canyon, Utah C) Grainflow tongues pinching out into pinstriped wind-ripple strata. Cyclic interfingering is commonly referred to as compound crossbedding indicating seasonal wind reversals (Loope et al., 2004) . Navajo Sandstone, Goblins Valley State Park, Utah. D) Modern example of grainflow facies and the interaction with wind-ripple facies on the lee-slope plinth of a crescentic dune. Note the pinching out into wind-rippled strata as identified in (C). Mesquite dune-field in Death Valley National Park, California. Lens cap in A and C is 55mm in diameter. .... 221

Figure 9.3: A) The outcrop is dominated by grainfall facies interbedded with wind-ripple strata. The strata are laterally continuous along strike for several to tens of metres. A close-up image (B) shows the structureless tabular units rarely exceed 1 cm in thickness. Navajo Sandstone at Kanab, Utah. C) Thin sharply defined grainfall laminae (arrows) interbedded with thicker packages of grainflow strata. Navajo Sandstone at Kanab, Utah D) Modern example shows the process of grainfall deposition. Saltation of sand moves over the brink of a dune forming a suspended cloud. Deceleration of the airflow on the lee-slope results in falling out of suspension. Arrow shows wind direction. Coral Pink Sand Dunes State Park, Utah. .... 223

Figure 9.4: Adhesion strata. (A) Evidence of damp conditions throughout deposition. Wavy-crinkly beds occur in thick packages, along dune bottomsets and up cross-strata (arrow). The thick bed in this example could be followed for over 100 m. Pole has 20 cm divisions. Navajo Sandstone at Hite, Utah. (B) Adhesions strata marking out trough cross sets and individual cross-strata. Navajo Sandstone at Sevenmile Canyon, Utah. (C) Close-up of adhesions strata along cross-strata between grainflow strata. Arrows point to the wavy-crinkly surfaces. Navajo Sandstone at Kanab, Utah. (D) Contemporary example of adhesions strata occurring at a dune bottomset following precipitation. This surface will likely be buried by grainflow or wind-ripple strata leaving behind deposits similar to those seen in (B) and (C). Photo extracted from Kocurek, 1981 (Padre Island, Texas)..... 225

Figure 9.5: Facies SA1 cross-bedded sandstone. A) and B) Large sets of trough-cross bedded sandstone. C) Sets of wedge cross-strata. Red arrows mark tapered edges. D) Small to medium-sized tabular sets of cross-strata. E) Small to very-large sets ranging from ~1 m to 55 m in thickness of tabular cross-strata. The largest sets grades into soft sediment deformation structures (SA4) marked by dashed line. .... 227

Figure 9.6: A) Wind-ripple dominated dry interdune deposit. B) Dune plinth and toeset deposits and the association with cross-stratification marked by cycles of grainflow (Gfw) and wind-ripple (Wr) deposits. Commonly referred to as cyclic cross-bedding (Hunter and Rubin, 1983). C) Pinstripe laminations in a sandsheet deposit highlights the bimodal sorting of wind-ripples. Coarser grainsizes weather faster and their darker appearance indicates more oxidation (rusting) has occurred. .... 228

Figure 9.7: The above examples show the SA3 facies of damp interdune / sandsheet deposits. Examples of adhesion strata occurring directly on aeolian dunes is shown in Figure 9.4. A) An extensive horizontally laminated sandsheet contains discrete brown beds with wavy-crinkly distorted laminae of facies SA3. The sandsheet truncates an aeolian dune (SA1) with abundant rhizolith, bioturbation and soft sediment deformation, indicative of wet conditions possibly through a fluctuating water-table. B) Plan view surfaces shows adhesion wart casts of wavy-crinkly laminae. C) Adhesion laminae observed along discrete lenses of cross-stratified sets. .... 229

Figure 9.8: A) Large-scale trough cross bed grades into convoluted stratification commonly referred to as soft sediment deformation. D) Deformed cross-strata in a planar set and truncated by a damp interdune. .... 230

Figure 9.9: A) Laterally continuous structureless sandstone bed continues for hundreds of metres along outcrop strike. (B) Clastic dike hosts structureless sand and is connected to a wet interdune. Mound forms where dike breaches the surface and floods the interdune. .... 231

Figure 9.10: A) Channel form with cross-bedded sandstone sets. The channel cuts into a massive / deformed aeolian sand body. B) Laterally continuous tabular beds. Internally the beds contain planar to cross-stratified bodies. ....	232
Figure 9.11: Millimetre to centimetre-scale bedding ranging from faint or impersistent to sharp and laterally continuous. B) Faint cross-laminations evident in upper sandstone bed.....	233
Figure 9.12: A) Crudely laminated mudstone bed with cross cut by vertical burrow B) Mudcracks filled with sandstone derived from overlying aeolian sets.....	234
Figure 9.13: A) and B) show sets of massive sandy limestones associated with rhizoliths, bioturbation and algal mats of facies CL2. The two sites show the same bed which are spaced approximately 3 km apart. C) Lenticular sandy limestone approximately 60 m wide. ....	235
Figure 9.14: A) Algal crenulation and chert nodules of long-standing water associated with lacustrine deposits. B) Thinly laminated limestones interbedded with mudstones and wavy carbonate lenses.....	236
Figure 9.15: Examples of facies associations in contemporary dune-fields. A) Fluvial-channel and overbank association (FA1) of an erg-adjacent environment. Note at erg-margin areas (FA5), fluvial channels may beach interdune corridors. Mesquite dune-field, Death-Valley, California. B) Ephemeral fluvial incursion into a dune-field (FA2). Interdune corridors become locally flooded and a fluvio-lacustrine delta forms as flow terminates (FA3). Trarza Desert, Mauritania. (C) Flooded interdune ponds or playa lakes (FA3). The large dunes and lack of fluvial incursion indicate the lakes are water-table controlled in a central erg setting (FA6). Gobi Desert, Northern China. (D) Due toesets are preserved in interdune hollows behind migrating dunes. The water-table breaches the surface to the west of this image (not shown here) and must have been at or near the surface as this dune migrated leaving behind these surfaces that are indicative of damp conditions. Al Jafurah Desert, eastern Saudi Arabia. (E) Variation in dune morphology and distribution from marginal-erg (FA6) to central-erg (FA5) in a dominantly dry desert setting. Note the reduction in dune-size toward dune-field margins as the erg interacts with competing environment (FA1). Much of the information above is adapted from Al-Masrahy and Mountney, 2013, 2015. ....	240
Figure 10.1: Idealised image acquisition for photogrammetric processing. The shaded area represents the field of view for each camera with increased darkness representing increased overlap. This is done to make features more resolvable in a three-dimensional sense. Extracted from Bemis et al. (2014).....	243
Figure 10.2: The workflow followed for the generation of the ground-based 3D photogrammetric model of the Johnsons Canyon outcrop (section 10.4). The figures show a cropped portion of the full outcrop which was about 600 m in width and up to 50 m in height. A) Cameras spaced with >80% overlap were used to generate the sparse point cloud. B) Dense point cloud construction. C) A triangular mesh surface reconstruction was created from the dense point cloud. D) The final textured surface is created by projecting images onto the mesh.....	247
Figure 10.3: (A) Location of the remote outcrop at Sevenmile Canyon (red star). (B) Google earth oblique aerial view to the north. The figure shows the litho-stratigraphy of the site and separates the aeolian Navajo from the underlying older fluvial Kayenta Formation and the overlying J-2 unconformity that separates the younger dominantly marine Carmel Formation. The red square marks the area where UAV photogrammetry was acquired. (C) Ground-based photo panel of the Navajo sequence at Sevenmile Canyon. The grey triangles mark extensive first-order bounding surfaces and super surfaces.....	248
Figure 10.4: Composite log at Sevenmile Canyon. The log and data are derived from traditional sedimentological observations along observable transects, supplemented by the large-scale virtual outcrop models. ....	251
Figure 10.5: The georeferenced model used to observe bounding surface architectures. (A) Markers placed along outcrop-scale bounding surfaces to record precise coordinates and altitudes. The inset shows the plan view and approximate locations of each marker indicated by red x's. (B) The profile plots the altitudes of surfaces 1-3 and overlying marker surfaces (DS and SS) along a ~350 m transect, showing their apparent relief and relationships to one another. Surface 1 separates Unit T1 from the underlying Kayenta Fm, surface 2 separates Unit T1 from Unit T2 and surface 3 forms the upper bounds of Unit T2. Surface's 1 and 2 display scouring and truncate underlying units. The two marker beds above include the base of a thick damp sandsheet deposit (DS), and part	

of a super surface (SS) that truncates sets for tens of kilometres (refer to log in Figure 10.4). The channel location is placed to show the relationship of the fluvial presence with relief changes and is not drawn to scale. All surface altitudes were recalculated to account for regional tilt of approximately 3° to the west. .... 253

Figure 10.6: (A) Virtual outcrop model showing position of Unit T1 (red box). Scale bars have 20 cm divisions. (B) Interpreted outcrop panel showing the facies architectures and relationships with Surfaces 1 and 2 that bound Unit T1. Note the erosive nature of the contact between T1 and T2 sets (represented by blue polyline in the 3D model and thick black line in panel interpretation). .... 256

Figure 10.7: (A) Virtual outcrop model showing the positions of the lower aeolian unit T2 (red boxes). Scale bars have 20 cm divisions. Interpreted sedimentary structures in photo panels (B) and (C) were informed with on-site sedimentary logging and the virtual outcrop model. The outcrop-scale bounding surfaces (2 & 3) are showing by thick black lines. The fluvial channels cross-cut aeolian sets of Unit T2 and disrupted much of their internal architectures as represented by the abundance of facies SA4 (structureless to contorted sandstone). (B) In a direction perpendicular to migration aeolian set widths conforms with Surface 2 scour (arrow) and indicate scour occurred with bedform migration. Where present, aeolian sets scour into underlying fluvial channels fill and form topographic relief of up to 40 cm. (C) The depth variation evident in set troughs by scalloped bounding surfaces truncating adjacent sets is characteristic of a scour-and-fill geometry (Figure 2.16). .... 259

Figure 10.8: (A) Local relief of Surface 1 plotted against the thickness of Unit T1. The inverse relationship shows that the basal relief of Surface 1 controls the preservation of Unit T1. This provides partial evidence in favour of the hypothesis that the antecedent relief of Kayenta topography was a dominant control in preservation of early-phase dune accumulations (T1) by preventing full reworking of the later phase larger scouring dunes (T2). (B) Low correlation between the number of stacked sets in Unit T2 and the local thickness of the Unit indicates the quantity of sets do not control the Unit thickness as would be expected in an aggradational setting. The observation favours a scour-and-fill type geometry with variable scour depths between sets. Data in (A) and (B) is extracted from the virtual outcrop model with mm-scale accuracy..... 262

Figure 10.9: Local relief changes calculated by deducting the altitude at each point along the transect from the lowest altitude in the transect (where relief equals zero in the profile). The vertically exaggerated pattern shows an approximate mimicking of relief changes between the two surfaces. As Surface 2 approximately mimics the antecedent topography, it indicates the further translation of this control into the overlying preservation.... 263

Figure 10.10: Schematic of the relationships between set architectures and outcrop-scale bounding surfaces parallel to the migration direction of bedforms. In the studied outcrop Basal Unit sets climb off a planar surface and fill topographical lows. In contrast, Lower Unit T2 sets dominantly show scour-and-fill geometries interpreted to have formed with the passage of many dunes with variable scour depths. The antecedent topographical relief of Kayenta Topography translates into outcrop-scale Surfaces 2 and 3 and is suggested to a key play a role in the preservation of overlying Units..... 263

Figure 10.11: (A) Location of the remote outcrop at Hite (red star). (B) Google earth oblique aerial view to the south. The figure shows the litho-stratigraphy of the site which includes the fluvial Kayenta Formation, overlain by aeolian Navajo Sandstone which is separated by the overlying marine Carmel Formation by the J-2 unconformity. The red square marks the area where UAV photogrammetry was acquired. (C) Ground-based photo panel of the top ~50 m of the Navajo sequence (location in shaded red in (B)). The blue triangles mark lenticular wet interdune surfaces that are typically found at Hite. .... 265

Figure 10.12: Composite log at Hite. The log and data are derived from traditional sedimentological observations along observable transects, supplemented by the large-scale virtual outcrop models. Surfaces A-D are described in text..... 267

Figure 10.13: (A) Virtual outcrop model produced from 1035 UAV photographs of the outcrop. Scaled poles have 5m divisions. (B) A planar orthomosaic produced from a view to the southwest using the virtual outcrop model in (A). The surfaces (A - D) and units (1-2) are detailed in this study. The lenticular purple shaded regions are lacustrine deposits (facies CL1 and CL2)..... 268

Figure 10.14: Survey points along surfaces A-D along an approximate SE to NW traverse (compare with Figure 10.13). Shaded region indicates lacustrine deposit. .... 269

Figure 10.15: (A) Unit 1 at its thinnest with the preservation of a relatively thin set (<1 m) bound by surface A and B. Surface A shows relatively thin deposits of adhesion strata and is associated with root casts and load structures that cut into and disrupt underlying sets. Interdune deposition of surface B and C is missing in this section and rather interfingering of wind ripple strata and grainflow strata (see annotation) is evident at dune toesets. (B) Surface A and B bounds two tabular planar sets containing tangential cross-strata (select annotated). Surface B forms a mound shape with overlying deposits wrapping around the mound indicative of post depositional deformation. Below the mound massive sands in the shape of a vertical dike cross-cuts the two sets. (C) Typically, interdune deposits of surfaces A-C show a massive and distorted appearance, with load casts into underlying sets, capillary rise draping tangential foresets that downlap into the interdune. In this instance, sand dikes extend from the interdune and cross cut overlying strata. (D) In places, interdune deposits are better bound and consist of wavy-crinkly laminae characteristic of damp interdune (facies SA3). In this example the overlying sets scour into the damp interdune..... 273

Figure 10.16: Interpreted sedimentary structures of unit 2. At this outcrop, internal stratification shows well-developed top sets and foresets indicating preservation of dune topography (see tracing and arrows in inset (i) and (ii)). Cross-strata indicates migration to the SE. Vertical pillar structures are evident in at least three places across this image (two labelled here). Features of the pillar structure on the left side of the image is shown in more detail in Figure 10.17B. Letters A-D indicate outcrop scale surfaces. Refer to Appendix A3 for high-resolution figure. .... 274

Figure 10.17: Common pillar structures and associated features at the Hite outcrop. (A) Surface D truncates underlying stratigraphy leaving a near planar surface. Pillar structure shows branching geometries and are typically associated with structureless sand or contorted laminae. In this instance two branches terminate at surface D. (B) Two pillar structures cross cut both Units, both of which are associated with massive sands draped over the topography that lies directly above a carbonate lens. On the left of the image the pillar structure terminates at surface D with planar bedded carbonates. (C) and (D) shows the pillar structures leading up to the lacustrine carbonate lens at surface D. The inset of (D) was taken from a carbonate bed at the same stratigraphical level while logging and shows well-preserved algal mats common in the carbonate beds indicating long-standing water. (E) The pillars are crossing sets below Unit 1. Note the intense deformation of the strata on the pillar structures. A dome shaped mound is evident where the pillar structure meets surface A and terminates. Zoomed in image at (F) shows how more permeable strata act as fluid conduits through the relatively small compound climbing sets predominantly consisting of grain-flow strata. Replacement textures of the compound sets are thought to be by carbonate bearing fluids as identified by differential weathering and elephant skin texture common of carbonate deposits. .... 276

Figure 10.18: Schematic models that envision Hite development (not to scale). Time 1: The stratigraphic record shows sand dikes and associated mounds appear at every major surface on which dune sets climb. Surface C was likely a slowly rising water-table that was periodically static. Renewed deposition occurred with a lower water-table, however, reactivated dikes from lower surfaces brought water-lain sediments that periodically flooded the interdune corridors and in some instances covered and preserved active dunes which were eventually buried by larger downwind dunes. Time 2: Reactivated dikes shows periodic sediment disruption within the larger dunes as they advanced. Reactivated dikes flooded the next generation of interdune corridors. Pondered water deposited up to 4m of lacustrine sediments exposed directly below surface D. As the water-table rose to a new level, it led to large-scale deflation and super surface formation (surface D)..... 279

Figure 10.19: (A) Location of the roadside outcrop at Johnsons Canyon (red star). (B) Google earth oblique aerial view to the north. The figure shows the litho-stratigraphy of the site showing the J-2 unconformity that separates the overlying younger dominantly marine Carmel Formation. The red square marks the area where ground-based photogrammetry was acquired. (C) Ground-based photo panel of the outcrop displaying the top ~50 m of the Navajo sequence. The yellow triangle marks a thick dry sandsheet surface. .... 280

Figure 10.20: The thickness of the 'main body' of the Navajo Sandstone. This outcrop approximately overlies the Tenney Canyon Tongue of the fluvial Kayenta Formation and represents erg advancement and the deposition of large-scale aeolian bedforms. The studied outcrop includes the top ~50 m of this unit in a road exposure about 2 km northwest. .... 282

Figure 10.21: (A) Stitched photo panels of the outcrop shown in Figure 10.19. The panels are divided here to fit the page and a continuous length panel is provided in digital Appendix A4. The red numbered boxes are cross-

referenced in Figure 10.23, Figure 10.24 and Figure 10.27. (B) Traced and interpreted architectural complexes of photo panels in (A). The schematic diagram is shown in Figure 10.22 ..... 283

Figure 10.22: Schematic diagram of outcrop at Johnsons Canyon. Rose diagrams are colour-coded to each Complex and contain foreset orientation. The grey base contains sets that are covered by vegetation and do not form part of this study..... 285

Figure 10.23: (A) Portion of complex 1 showing the geometry of the set bodies with marked examples of individual sets showing apparent upslope and downslope apparent dip directions. The inset stereonet and rose diagram shows this approximate oblique bimodality. Set colours are for visual effect only. (B) The complex is bound by a lower sandsheet deposit hosting protodunes and an upper interdune deposit of the overlying Complex 2. Asymptotic foreset fill scoured basal depressions as the bedforms advanced. (C) Migration of the superimposed bedforms form scalloped surfaces with intersecting troughs (yellow arrows). The red numbers are cross-referenced from Figure 10.21..... 287

Figure 10.24: (A) Snapshot from the virtual outcrop model looking towards the NW. The data shows these cross-beds dip SW (towards the viewer). The foresets consist dominantly of wind-ripple / grainfall couplets (Wr / Gfl) as shown in detail in Figure 10.25. Reactivation is common in set bodies as a result of opposing winds. (B) Low-angle wind-ripple dominated plinth deposits transition into the thick wind-rippled interdune deposits (~2.5m). (C) Yellow arrows point out downlapping cross-strata indicating active slipface conditions. These sets are lenticular with maximum thicknesses ranging between 10 - 85cm with apparent widths up to 20 m. Cross sets dip steeply (>35°) towards SSW (n=3; inset rose diagram). The red dashed line marks the interpreted overlying bounding surface. The distribution of these bodies is shown in yellow in complex 2 of interpreted panel (Figure 10.21) - note their abundance below interpreted bounding surfaces. The red numbers are cross-referenced from Figure 10.21. .... 291

Figure 10.25: Tabular foreset bodies within sets typically appear structureless on their weathered surface, however consist of wind-ripple (Wr) / Grainfall (Gfl) couplets and thicker sets of preserved ripple-foreset cross-laminae. It appears that each 'massive' tabular body is separated by stacked wind-rippled strata (pin-striping) in a pattern that indicates cyclicity (black arrows). The mobile phone used for scale is 146 mm tall by 72 mm wide. .... 291

Figure 10.26: Sedimentological model of Complex 2. The simulation of migration and accumulation of a simple linear bedform whereby components of migration occur in a direction parallel to bedform crestline and transverse to crestline. Input parameters are provided in Appendix A5. Produced in BEDFORMS 4.0 (Rubin and Carter, 2006). .... 293

Figure 10.27: (A) Intermediate-scale trough-cross sets of complex 3. The set sizes, position within the section and nature of erosive contact suggests the migration of superimposed dunes over the large-scale underlying Complex. These bounding surfaces may therefore be interpreted as second order (superimposition) surfaces. (B) Nature of the contact between Complex 2 & 3. The superimposed sets of Complex 3 are found best preserved extending over the interpreted sinuosity axis of the linear mega-dune (indicated by the dotted red line). The red numbers are cross-referenced from Figure 10.21. .... 295

Figure 11.1: Examples of methods used to investigate the internal structures of contemporary dunes. (A) Large-scale trenching through a dune. In this study, trenches were dug perpendicular and parallel through a transverse dune in White Sands National Monument, USA (after McKee, 1966). (B) Small-scale trenching using a shovel. Multiple trenches were dug along the stoss and lee slope of this dune in Rub' AL-Khali desert, UAE (after Fryberger et al., 2017). (C) Well-developed cross-bedding of a transverse dune exposed by wind-erosion in the Rub' Al-Khali desert, UAE (after Al-Masrahy and Mountney, 2013). (D) Auger hole exposing mm-scale laminations in the Strzelecki desert, South Australia (after Telfer and Hesse, 2013). (E) An example of 2D ground penetrating radar acquisition to image the subsurface of a dune in the Wahiba Sand Sea, Oman (after Tatum et al., 2019). .... 305

Figure 11.2: Examples of methods used to broaden spatial observations in aeolian outcrops. (A) One of the first studies to accurately measure bounding surfaces used a tacheometer (top left inset) to survey over a continuous 2.7 km 3D outcrop of the aeolian Entrada Sandstone (USA). This allowed for mathematical planes of correlated surfaces to be determined (bottom right inset) (after Crabaugh and Kocurek, 1993). (B) A Global Positioning

System (GPS) is used to tracks points along bounding surfaces over a continuous outcrop. The study was able to characterise the well-preserved morphology of a linear megadune (inset) in the Troncoso Inferior Member (Argentina) (after Argüello Scotti and Veiga, 2015). (C) Terrestrial Light Detection And Ranging (LiDAR) and (D) UAV photogrammetry capture continuous outcrops in 3D for the production of georeferenced virtual outcrop models. These models can be examined in 3D data visualisation and interpretation software for accurate measurements of sedimentary architectures. Figures (C) after Rarity et al. (2013). Figure (D) shows a virtual outcrop model produced from UAV drone (inset) photogrammetry in the Navajo Sandstone (USA)..... 306

Figure 11.3: Google Earth™ Image in (A) and residual relief map of the same area in (B) shows the intimate relationship between the linear draa and mega-crescentic dunes between N-S trending interdraa corridors. Note under residual relief in (B), the configuration of the crescentic bedforms appear to shape three linear draa crests and create an undulating south-to-north topography on the draa flanks. The arrow in both (A) and (B) points to the east facing stoss flank of a linear draa evidently not containing any mega-crescentic bedforms within the interdraa but showing a similar undulating flank to those that do west of it and possibly indicates partial preservation of antecedent bedforms. South to north profile X-X' is taken on a linear dune not closely associated with the mega-crescentic dunes and is shown in Figure 11.4. Based on evidence provided in chapter 6 , this study hypothesises that these mega-crescentic bedforms are antecedent and a subsequent change in the wind regime favoured the linear configuration seen today. The mega-crescentic bedforms were probably well stabilised prior to the growth of the linear draa and their topography played an important role over phases of accumulation that is apparent on the contemporary geomorphic surface. Relief map produced from ALOS AW3D30 DSM dataset (sun azimuth 160° at 20°altitude)..... 308

Figure 11.4: South to North trending topographic profile of a 60 m tall linear draa shown in Figure 11.3. The undulating topography on the draa crests shows up to 10 m of relief. This undulating relief is thought to be translated from the draas core topography suggested to be partial remains of stabilised antecedent crescentic bedforms. A similar style of relief translation was identified in the ancient Navajo Sandstone at Sevenmile Canyon ..... 309

Figure 11.5: Interpreted GPR radargram from the Wahiba Sand Sea near the crest of the draa (refer to section 6.4). Deflation / stabilisation surfaces have been labelled as outcrop-scale surfaces in reference to the observations at Sevenmile Canyon (ancient Navajo Sandstone). As in the Navajo, the individual sets of cross-strata are defined by upper and lower set bounding surfaces that are less continuous than the 'outcrop-scale surfaces'. Focus is placed on the sets above surface 2 which contain up to 4.2 m of relief in this section. The well-preserved bedforms occur in areas of low topographic relief, while those at higher-relief have a lower preservation potential and are deflated by outcrop-scale surface 3. Locally high topographic relief overcomes autogenic tendency of dune scour that would otherwise remove older units. If Surface 1 is a stabilisation surface of the draa core that forms the 'geomorphic container', the above lying configuration is expected as observed in the Navajo architecture at Sevenmile Canyon. Note how all three outcrop-scale surfaces approximately follow the same apparent trend (dipping to the east →B')..... 310

Figure 11.6: Aerial photograph of a complex linear draa of the Namib Sand Sea. The system hosts dune types of linear, transverse and star morphologies. Circled numbers in the foreground are hypothesised contemporary examples of the Complexes (1-3) identified in the study at Johnsons Canyon (section 10.4). Smaller sinuous to linear bedforms show opposing slipfaces and are commonly arranged oblique to the draa crest (Complex 1 type) and rest on the undulating wind-ripple dominated draa flanks. Hypothesised transverse migration of very large undulating bedforms deposit sets of Complex 2 type (wind-ripple dominated slipfaceless draa). Intermediate scale sinuous linear to transverse(?) superimposed dunes of Complex 3 type are observed on the draa crests. The image is modified after Romain, 2016..... 311

Figure 11.7: Example of the stabilised aeolian system of the Strzelecki Desert, Australia. Linear dune developed from underlying transverse bedforms. The along-dune profile shows multiple episodes of vertical dune accretion spanning the past 120Ka. 'II' to 'VII' indicate marine isotope stages. From Cohen et al. (2010). Image modified after Rodríguez-López et al., 2014..... 313

Figure 11.8: Two models for aeolian aggradation. (A) **Model 1:** Bedform climb on a low-relief horizontal to subhorizontal depositional surface explains the preservation of continuous beds of aeolian sandstone and the growth of compound / complex dunes. (T1) Dunes migrate across a partially vegetated, stabilised horizontal surface. This 'supersurface' provides the primary surface from which dunes aggrade. (T2) The dunes aggrade

through climb on first-order bounding surfaces (interdune-migration surfaces). (T3) A temporary reduction in sediment supply results in a bypass surface to form as dunes are cut by nonclimbing migration. The interruption to climb may make the first-order bounding surfaces difficult to recognise. (T4) Aggradation of complex dunes through climb on first-order surfaces. Reactivation surfaces (3<sup>rd</sup> order surfaces of Brookfield, 1977) mark dune slipface reworking and second-order surfaces (superimposition surfaces) formed through superimposed barchanoid dunes migrating down the slipface of the draa. Reactivation and downwind dipping surfaces create complex internal stratigraphy. (B) **Model 2:** An alternate explanation for the preservation of aeolian sandstone in which the depositional surface is the upper surface of a draa or large dune form. Dunes aggrade laterally from this constructed topography. (T1) Note the discontinuous first-order bounding surfaces indicating bedform climb was only a local phenomenon. Draa and interdrea deposits lap directly down onto the supersurface. (T2) A stabilisation surface drapes the draa and sandsheets accumulate on both flanks. (T3) The interdrea fills with strata separated by downwind-descending surfaces that mark accretion from the side of the draa. Figures modified after Langford et al. ( 2008). ..... 314

## List of Tables

Table 1.1: Outline of key features in the Wahiba and Navajo aeolian systems .....	7
Table 2.1: Aeolian bedforms morphology and classifications (adapted after McKee, 1979; Brookfield, 1992; Boggs, 2001).....	40
Table 3.1: Simplified stratigraphy of the Oman Mountains. Compiled from Hopson et al., 1981; Hanna, 1990; Allen, 2007; Stern and Johnson, 2010; Hansman et al., 2017.....	54
Table 4.1: Core location of Preusser et al., (2002) and trenched Site 4 of Hern et al., (2018).....	76
Table 5.1: Landsat 8 band specifications .....	84
Table 5.2: Satellite sensors and datasets acquired for the study.....	86
Table 6.1: Measurements of megadune features for each line profile including number of dunes (N), minimum (min), maximum (max), average (ave) and standard deviation (SD) of each line profile. ....	98
Table 6.2: Constants, exponents and correlation coefficient of power functions in Figure 6.5 .....	98
Table 6.3: NDVI classification statistics and green-space coverage. ....	152
Table 8.1: Outcrops and key observations of the initial field season. Highlighted sites were chosen for further study and are examined in chapter 10. See Figure 8.1 for locations.....	211
Table 9.1: Erg-scale facies of the Navajo Sandstone .....	226
Table 9.2: Facies associations of the Navajo Sandstone.....	237
Table 10.1: Summary of the eleven models produced between the three outcrops.....	245
Table 10.2: Observations of outcrop-scale surfaces and Units over the outcrop shown in Figure 10.5. The stratigraphical position of the bounding surfaces can be seen in the composite log (Figure 10.4).....	254
Table 10.3: Fluvial channel dimensions .....	259
Table 10.4: Difference in scale, geometry and migration vectors for the three architectural Complexes at Johnsons Canyon. ....	285



## Acknowledgements

I would like to acknowledge Stuart (Stu) Clarke for welcoming me into the Basin Dynamics Research Group (BDRG) following an unexpected change in circumstances. Stu's aptitude for field training and excellent knowledge on the sedimentology and stratigraphy of the Western USA excited my interest and made this project meaningful.

I extend my gratitude to Keele University, particularly Peter Andras and Kelly Montana-Williams for their assistance during difficult times and in securing the funding to continue my studies at Keele.

A big thank-you to Caroline Hern and Shell Exploration and Production Company for supplying the high-resolution datasets and GPR data integral to the Wahiba Sand Sea study. Caroline's unwavering encouragement, time input, and insight, particularly during the collaborative presentation at AAPG 2019 is greatly appreciated.

Thanks to Gary Kocurek for enlightening discussions on the Wahibas, the Navajo and aeolian system processes. The scope of my knowledge and depth of interest in this field has multiplied as a result. To Robin Westerman and Dominic Tatum for providing the processed radargrams and thought-provoking discussions. To Dave Hodgetts for providing Virtual Reality Geological Studio (VRGS). Dave's training and quick response-time regarding software enhancements made working with this programme stress-free.

To all members of the BDRG with special mention to my field colleagues – Andrew Mitten, Ross Pettigrew and Charlotte Priddy who made the months of camping and working in western U.S. a pleasurable task. I couldn't have asked for a better team of geologists.

Lastly, I am sincerely grateful to my wife, Camilla, for her constant, solid and unconditional support while undertaking this PhD. Camilla kept me sane, well fed and motivated during long hours of thesis writing.



# 1 Introduction

For an aeolian dune system, a fundamental process is a wind event with basic external environmental controls, or boundary conditions, of sediment supply, sediment availability, and the transport capacity of the wind known as its 'sediment state' (Kocurek, 1999; Ewing and Kocurek, 2010). Ultimately, dune-field patterns emerge through a series of autogenic processes which include a series of interactions between its elements (i.e. flow and grains, flow and dunes, and dune and dunes) (Kocurek and Ewing, 2016). The system evolves from an unpatterned to a patterned state, self-organising as a result of the interactions among these elements (Werner, 1999). As a basic example, where dune-fields originate on a planar surface, protodunes develop into a field of many small dunes that eventually evolve (or coarsen) into fewer, larger and more widely spaced dunes (e.g. Kocurek *et al.*, 2010; Gao *et al.*, 2015). As self-organisation occurs within the complexities of the external environment, a change in these conditions may initiate a new constructional phase of dunes upon an existing, or antecedent, dune pattern (Kocurek and Day, 2019). The existing dunes then provide the sand supply and are reworked into a new pattern, once again through a series of interactions (Werner and Kocurek, 1997; Kocurek and Ewing, 2015).

The boundary conditions begin at some initial state and then may continue to evolve over the time period that the aeolian system exists and ultimately develop a stratigraphic record (Kocurek and Ewing, 2016). This requires that the dune-field leaves an accumulation but is not always the case as dunes typically bypass along a surface or they are reworked by subsequent environments (Kocurek, 1999). If accumulation persists, then aeolian strata record kinematics of all interaction through the phases of development (e.g. Brothers *et al.*, 2017). The presence or absence of preserved accumulations associated with different growth phases are useful for interpreting the external environmental and autogenic forces that lead to accumulation and preservation (Kocurek and Day, 2018; Cardenas *et al.*, 2019).

At the fundamental level, the aeolian depositional environment consists of dune-field patterns, and the rock record is a stratigraphic architecture consisting of cross-strata and bounding surfaces (Kocurek and Ewing, 2016). In a contemporary setting, the dune-field pattern is an obvious feature which, when viewed from satellite imagery, reveals a temporal ‘snapshot’ of its configuration. Although the study of dune-field patterns may reveal the boundary conditions in which a contemporary aeolian system evolved (e.g. Ewing *et al.*, 2006; Ewing and Kocurek, 2010), their sedimentary record remains largely unknown and only fragmentary glimpses of sedimentary architectures are available (Rodríguez-López *et al.*, 2014). On the other hand, the ancient rock record represents huge amounts of temporal variation through dune-field evolution but incurs spatial limitations by the observer. Broadening spatial observations are necessary if the discussion of autogenic processes and allogenic forcings is to be considered (e.g. Kocurek and Day, 2018; Cardenas *et al.*, 2019). While it is possible to effectively describe the morphological characteristics of modern bedforms and dune-fields as well as the geometry of architectural elements of ancient aeolian successions, several difficulties persist regarding the controlling mechanisms behind their ultimate preservation. This is particularly true in cases where large compound and complex morphologies form through multiple generations of construction, developing upon existing or antecedent patterns. The need arises to advance knowledge in these areas through coordinated research that seeks to link dune processes to the sedimentary record.

The primary aim of this research is to determine the controls on deposition and preservation in aeolian systems and to understand how the effects of these controls may be recognised in contemporary and ancient successions. This aim is achieved by 1) conducting a high-resolution remote sensing study (satellite and subsurface) on the contemporary Wahiba Sand Sea of Oman revealing spatial and temporal parameters of the system, and 2) through a sedimentological and stratigraphic study of the Jurassic Navajo Sandstone in southwestern USA, broadening spatial and temporal observations through the capture of large-scale 3D digital outcrop models. The starting points for these investigations are outlined below.

## 1.1 Study Areas and Focus

The sites for this study include the contemporary Wahiba Sand Sea of the Sultanate of Oman and the ancient Jurassic Navajo Sandstone exposed within the State of Utah in the western United States. A brief summary of each sand sea and key focal points of this study is provided below.

### 1.1.1 Contemporary: The Wahiba Sand Sea

Occupying the eastern part of the interior basin of Oman, the Wahiba Sand Sea is a relatively small (~16 000 km<sup>2</sup>), elongate sand sea containing a great variety of dune forms but largely dominated by large linear megadunes (Figure 1.1A). The Wahiba Sand Sea provides a study area where the developing stratigraphy and surface geomorphology can be coupled with the Quaternary evolution of the region (Preusser *et al.*, 2002) (Table 1.1). The evolution of the sand sea occurred within a set of boundary conditions that include climatic forcing of fluvial, aeolian and eustatic cycles within an active tectonic basin (Radies *et al.*, 2004). Over a period of approximately 160 Ka, this basinal setting and sediment influx into the basin generated a stratigraphic record onto which the contemporary dune-field pattern emerged. Existing data for the Wahiba Sand Sea suggests that the switching between glacial and interglacial periods resulted in multiple generations of aeolian construction that were punctuated by periods of dune stabilisation / deflation and enhanced fluvial activity respectively (Preusser *et al.*, 2002; Radies *et al.*, 2004; Fryberger *et al.*, 2016a; Hern *et al.*, 2018). Studies on the Wahiba Sand Sea have benefited from the luminescence dating of a 200m drill-core allowing a long sequence of dune records to be achieved (Preusser *et al.*, 2002). This provides an excellent temporal control on preservation through erg evolution.

Datasets acquired and investigated include: 1) medium-resolution (30 m) public-access satellite imagery and digital elevation models covering the full extent of the Wahiba erg and surrounds, 2) focussed high-resolution (0.5 m) commercially acquired satellite imagery and digital elevation models covering 100 km<sup>2</sup> of the erg, and (3) ground penetrating radar datasets capturing the subsurface architectures of a linear megadune. The examination takes full advantage of these remote sensing datasets and digitally based systems, provides reviews of current methodologies and applies a variety

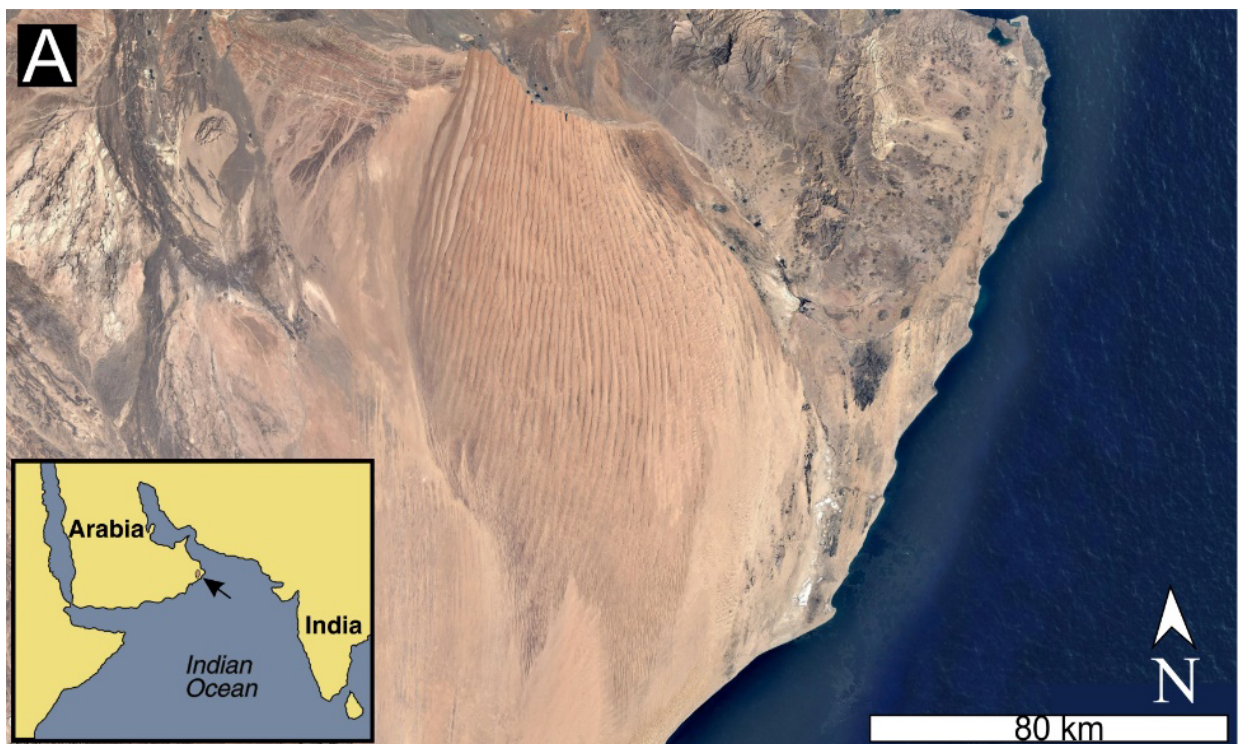
of geospatial techniques in order to examine dune-field and dune characteristics. Discussions include aspects such as spatial and topographic variance of dunes and dune-field patterns, basin geometry, sediment availability, internal architectures, dune-field stability and provenance.

Complex morpho-dynamics of time and space underpins aeolian dune development and the Wahiba megadunes integrate wind regimes over vast periods of time, exhibiting a range of shapes and sizes with superimposed patterns. Because this geomorphological signature is retained, this research will investigate if it is possible to reveal wide-scale temporal evolutions through the examination of the contemporary geomorphic surface.

### 1.1.2 Ancient: The Jurassic Navajo Sandstone

The Navajo Sandstone, remnant of an early Jurassic (Pliensbachian – Toarcian) aeolian system that stretched over most of the western United States for several million years, belongs to one of several thick and geographically widespread Jurassic aeolian erg successions (Figure 1.1B; Chapter 0) (Verlander, 1995). Palaeogeographic and palaeoclimatic reconstructions place the Navajo erg over western Pangea within the tropics, where dunes were subject to cross-equatorial winds and annual monsoonal conditions (Kocurek and Dott; 1983; Loope *et al.*, 2004). A close balance between sediment supply, accumulation rate and subsidence resulted in the generation of thick intervals of aeolian stratigraphy, of which the Navajo represents a period of approximately 10 Ma of the Lower Jurassic (Blakey, 1994; Blakey, 2008). The well-studied Navajo Sandstone has received much attention for over five decades and as such literature covering its spatial and temporal evolution is broad and encompassing (Chapter 0). This research considers that accumulation in the rock record may occur because of several parameters that can be broadly associated with types of dune-fields (e.g. wet, dry and stabilizing aeolian systems) (Kocurek and Havholm, 1993; Kocurek, 1999, Mountney, 2012) and utilises three sites across the Navajo succession in order to capture variations during system evolution (Chapter 8). Known diversity within the system allowed for a selection that represents a broad range of configurations characterising marginal to central erg conditions.

Remote sensing methods, detailed in this thesis, allowed for the production of large-scale three dimensional georeferenced virtual outcrop models as key datasets with which to study architectural elements in high detail. Because studies on bounding surfaces that define the limits of preserved aeolian successions have become a key research focus recently (e.g. Kocurek and Day, 2018; Argüello Scotti and Veiga, 2019; Cardenas *et al.*, 2019; Swanson *et al.*, 2019) the study investigates if the analysis of large-scale virtual outcrop models can elucidate the expression of allogenic and autogenic features within preserved sequences.



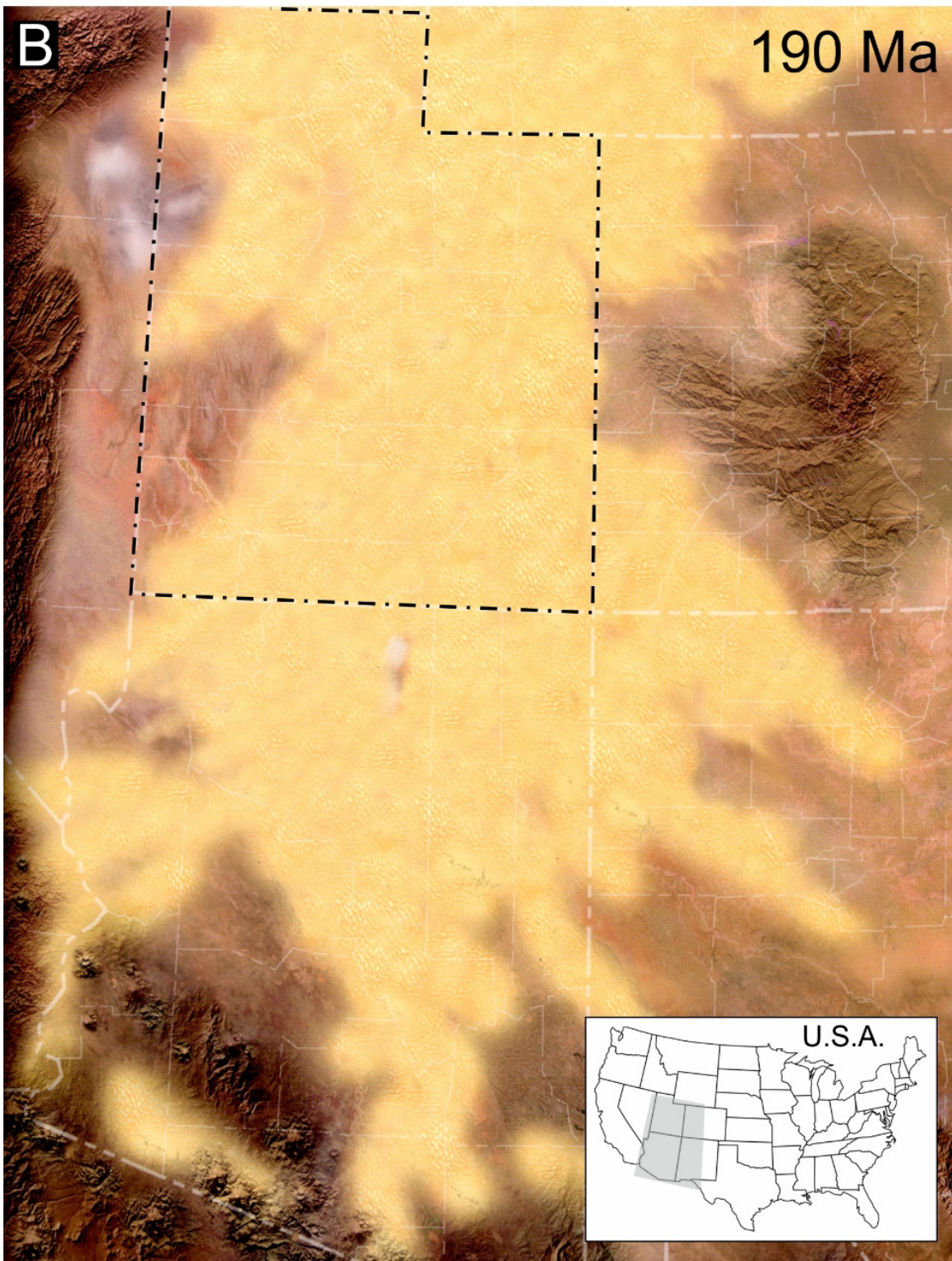


Figure 1.1: Location of study sites. (A) The contemporary Wahiba Sand Sea of the Sultanate of Oman. Google Earth™ image, 2016. (B) Palaeogeographic reconstruction of the Jurassic Navajo Sandstone at its maximum extent ~190 million years ago. The erg covered much of western Pangea. All studied outcrops are located in the State of Utah, USA outlined in black. Modified after Blakey and Ranney, 2017.

Table 1.1: Outline of key features in the Wahiba and Navajo aeolian systems

Location	Period, Epoch / Age	Additional name/correlative Fms	System Type	Basin Setting	Thickness	Extent / Morphologies	Key References
<b>Wahiba Sand Sea</b>							
Sultanate of Oman	Quaternary, Pleistocene to Holocene	Al Sharqiyah Sands	Multiple generations of aeolian construction evident. Accumulation occurring in dry glacial stages & sub-stages. Dune stabilisation / pedogenesis and enhanced fluvial activity occurring in humid interglacial stages & sub-stages.	Backbulge basin (in the terminology of DeCelles and Giles, 1996)	Up to 150 m in the 'High Sands'	The erg covers ~16 000 km <sup>2</sup> and is bound by wadis and the Indian Ocean. Dominated by crescentic dunes and complex to compound linear megadunes up to 70m above the interdune surfaces.	Goudie <i>et al.</i> (1987) Glennie (1998) Juyal <i>et al.</i> (1998) Preusser <i>et al.</i> (2002) Radies <i>et al.</i> (2004) Robinson <i>et al.</i> (2007) Preusser (2009) Fryberger <i>et al.</i> (2016)
<b>Navajo sandstone</b>							
Western United States of America	Lower Jurassic, Pliensbachian to Toarcian	Glen Canyon Sandstone, Nugget Sandstone, Aztec Sandstone	Formation of the Glen Canyon Group. Overlies fluvial Kayenta Formation. May be transitional and Intertonguing with Kayenta, marking periods of erg advancement and contraction. Preservation of a lower wet aeolian system (water table controlled) transitioning to an upper dry aeolian system.	Retro-arc foreland basin; flexural basin	Up to 650 m in western Utah, thinning to the east and pinching out in western Colorado.	Preserved remnants of large erg(s) (~ 265 000 km <sup>2</sup> ) covering much of western Pangea. Individual aeolian dune sets sizes can from sub-metre to > 30 m. Former existence of transverse bedforms are well reported in the literature. Compound linear bedform is reported in this study.	Pipiringos and O'Sullivan (1978) Marzolf (1983) Blakey (1994, 2008) Allen <i>et al.</i> (2000). Loope <i>et al.</i> (2001, 2012) Lucas and Tanner (2014) Bryant <i>et al.</i> (2016) Parrish <i>et al.</i> (2017) Hassan <i>et al.</i> (2018)

### 1.1.3 Preservation

The variables that impact each phase of rock record creation (construction, accumulation and preservation) are largely independent of one another, but are strongly influenced by antecedent conditions and dynamic interactions with other variables or boundary conditions (Kocurek, 1999). Because of the wide variety of factors that affect the evolution of aeolian systems means that each system has a significant degree of uniqueness (Kocurek, 1999). Within both the contemporary and ancient systems, the study demonstrates how allogenic controls in the form of antecedent topography and the water table may influence the overall stratigraphic architecture in aeolian system development. Supplementing available literature with the remote sensing application of this study, and, in utilising the stratigraphic record of an ancient system as an example with which to investigate a variety of controls on preservation further facilitated interpretation and speculation surrounding the sedimentary record in the contemporary environment. The investigations on the Wahiba and Navajo demonstrate how their record represents a point on this spectrum of preservation styles and thus serve as additional examples with which to understand aeolian systems.

### 1.1.4 Linear dunes

One fundamental problem that remains in relation to the interpretation of original dune type from the stratigraphic architecture preserved in the rock record is that successions representing linear (or longitudinal) bedform types remain apparently under-recognized (Rodriguez-Lopez *et al.*, 2014). Linear dunes are the most abundant bedform type in Earth's sandy deserts (Lancaster, 1982), and establishing the dominant characteristics of the sedimentary architecture associated with the bedform type has been a topic of interest for several decades (McKee, 1979; Tsoar, 1982; Arguello Scotti and Veiga, 2015, 2019; Besley *et al.*, 2018). Principally, linear bedforms transport sediment in an orientation close to parallel to the trend of their crestlines, however, GPR studies (Bristow, 2000, 2007) have convincingly demonstrated that a minor component of transverse motion occurs such that bedforms favour the preferential preservation of cross-strata that dip in the direction of the transverse component of migration. Conversely, vertical accretion of linear dunes is recognised where growth occurs through

the reworking of underlying dunes of a transverse type and long-distance sand transport plays a less significant role in their formation (e.g. Cohen *et al.*, 2010). This makes them very difficult to recognise in the sedimentary record and accounts for the apparent scarcity of linear dunes in the geological record as initially recognised by Rubin and Hunter (1985). The above opens questions about their long-term behaviour and specific set of controlling conditions that allow for bedform climb *versus* episodic sequence of accumulation and preservation.

As large complex linear megadunes dominate the Wahiba Sand Sea, it provides the opportunity to document their construction and morphology. Rubin and Hunter (1983) and Rubin (1987) recognised the characteristics of longitudinal / oblique bedforms in outcrops of the Navajo Sandstone and, given that there is no reason to suspect that these bedforms were less abundant in the geological past, investigations within Navajo set architectures is a focal point in this thesis.

## 1.2 Research Aims and Objectives

This aim of this thesis is to forward our knowledge and understanding of the complex depositional processes and preserved sedimentary architectures considered typical of aeolian systems. The study will highlight the use of digitally based systems and analytical techniques of spatial data in order to achieve the following objectives:

- 1) To examine, record and interpret the external environmental controls within which a contemporary aeolian dune-field pattern emerges.
- 2) To examine and record the sedimentology and architectural elements at three sites across an ancient aeolian system representing spatial and temporal variations of erg evolution. At each site, elucidate the environmental controls in which the system preserved strata and formed a stratigraphic record.
- 3) Compare the controls of preservation and bedform morphology within both systems where applicable.

### 1.3 Thesis Structure

The successive chapters of this thesis are divided into four parts as follows:

Chapter	Title	Description
<b>PART A: Aeolian Processes</b>		
2	Literature Review	Provides a summary evaluation of sedimentological research into aeolian processes and desert systems. The chapter investigates the fundamental geomorphological processes and theory behind small to large scale aeolian bedform development.
<b>PART B: A Contemporary Aeolian System</b>		
3	The Wahiba Sand Sea, Sultanate of Oman	Provides a detailed literature review of the Wahiba Sand Sea of Oman including the geological setting, geomorphology, climate and resolved stratigraphy of the dune-field.
4	An Investigation into Apparent Correlations	Observations within the literature review show that a chronological tie can be made across the sand sea. Utilising the position of these correlations on the dune form, this chapter presents a hypothesis.
5	Datasets	Provides a review of the digital datasets utilised in studying the Wahiba Sand Sea.
6	Examining the Wahiba Sand Sea through Remote Sensing and Geospatial Techniques: Insights into Erg Geometry and Preservation	Applies the datasets from the previous chapter and provides detailed methodologies into the techniques utilised in examining the Wahiba Sand Sea. The examination reveals the controls on dune-field pattern heterogeneity, hypothesises the configuration of a relict erg on which the contemporary geomorphic surface built upon, details geometries of internal architectures and their control on active bedforms, provides the vegetation coverage and implication for dune-field stability, and provides a provenance study. Each aspect is individually assessed and discussed.
<b>PART C: An Ancient Aeolian System</b>		
7	The Jurassic Navajo Sandstone, southwestern USA	Provides a detailed literature review of the Jurassic Navajo Sandstone. The chapter reveals the regional geology, stratigraphy, palaeogeographic reconstruction and controls on deposition and preservation.
8	Study Sites	Details the investigation for study area selection in order to capture the variations in Navajo system evolution. Three key study sites were selected and are placed into context for the study.
9	Lithofacies Analysis of the Navajo Sandstone	Describes and interprets the strata typical of Navajo Sandstone bedforms and tabulates a detailed facies analysis from observations across the erg. Genetically related facies are grouped into several facies associations. The findings are placed into context in the following chapter.

10	Facies Architecture and Controls on Aeolian Preservation of the Jurassic Navajo Sandstone	The chapter provides detailed methodologies, specifically into the application of remote sensing and analytical techniques used to create high resolution virtual outcrop models. The controls on deposition and preservation at each site are individually assessed and discussed.
<b>PART D: Synthesis and Conclusion</b>		
11	Discussion and Synthesis	The ancient and contemporary ergs utilised in this thesis are placed into context providing motive for the chosen methodologies and the necessity for comparing ancient and contemporary aeolian systems. It places focus on integrating the research ideas in Part B and C and outlines the broader contributions to the academic discourse.
12	Conclusions	Provides a summary of how the primary research objectives of the thesis have been addressed and considers the way in which our understanding of the controls on deposition and preservation in aeolian systems have been advanced. The chapter proposes recommendations for future study in both the contemporary and ancient systems.

# PART A : AEOLIAN PROCESSES



## 2 Aeolian Processes – Literature Review

The erosion, transport, and deposition of material due to wind action at or near the Earth's surface are termed aeolian processes, after the Greek God Aeolus, the keeper of the winds (Allaby, 2013). Aeolian processes occur wherever there is a supply of granular material and atmospheric winds of sufficient strength to move them. As the wind moves sand size particles more effectively than coarser or finer material, it works most readily where there is material of this size at the surface (Livingstone and Warren, 1996). The scale of aeolian processes can vary greatly, from the entrainment of a single grain of dust, to the movement of dune-fields, incorporating many hundreds of thousands of tonnes of sand present in the world's major sand seas (Pye and Tsoar, 2008).

Because of their sensitivity to climatic change, aeolian deposits have long been used to extract climatic information of the Earth's past, from the Late Quaternary (e.g. Tchakerian and Lancaster, 2002) to as far back as the Precambrian (e.g. Ross, 1983). Previous works have been able to extrapolate information such as the interrelationships of climate, sediment supply, and relative sea-level change from ancient aeolian units (e.g. Kocurek and Havholm, 1993; Carr-Crabaugh and Kocurek, 1998; Mountney and Thompson, 2002). Modern, inaccessible aeolian deposits have been studied using remote sensing in which morphological changes in the distribution of aeolian bedforms and interdunes are tracked (Breed and Grow, 1979; Hugenholtz *et al.*, 2012; Al-Masrahy and Mountney, 2013).

Aeolian sandstones also have important economic applications in that they form important aquifers (e.g. Permian Bridgnorth Sandstone Formation of the Cheshire Basin) and can contain substantial hydrocarbon reserves (e.g. Permian Rotliegend Group of the North Sea). A major part of the recent approach to reservoir characterization and flow modelling is based upon the architecture of ancient aeolian rocks (e.g. Goggin *et al.*, 1992; Mountney and Jagger, 2004; Romain and Mountney, 2014; Romain, 2016, Besly *et al.*, 2018). The study of modern analogues has been useful in extracting valuable information with which to improve our understanding of the likely arrangement of architectural elements in ancient preserved successions (Al-Masrahy and Mountney, 2013). Although our

understanding of aeolian systems has improved, complexities have also become apparent and many basic questions remain unanswered (Kocurek, 1996; Rodríguez-López *et al.*, 2014).

## 2.1 Desert Aeolian System

Vast concentrations of deserts lie within the 30° belts centred on the Tropics of Cancer and Capricorn. Here, the climate is dominated by the subtropical high-pressure cells in the atmosphere. The trade winds diverging from these cells consist of air that is descending and stable, and therefore unlikely to produce rain (Kocurek, 1996). Additional factors such as the position of the high-pressure cells over the oceans, orographic barriers (mountain belts) and cold upwelling ocean currents all contribute to enhanced aridity and promote desert conditions. Large-scale wind patterns are responsible for large-scale patterns of aeolian activities, for instance, the winter trade winds (Harmattan) are credited for the patterns of sand flow throughout the Saharan sand seas (Livingstone and Warren, 1996). Not all deserts are vast areas of wind-blown sand: present-day deserts have a diverse array of environments that differ widely due to tectonic setting, coastal or inland location, local climate, and their past conditions (Livingstone and Warren, 1996).

Conditions that produce aridity affect approximately one third of all land surface and include three major sedimentary environments, 1) alluvial fans and ephemeral streams, 2) inland sabkhas or playas, and 3) sandy deserts, more commonly known as “sand seas” or ergs (Figure 2.1) (Walker and James, 1992). Aeolian sand systems with dune-fields and their larger counterparts, the erg, cover only about 20% of modern deserts and occur mostly inland (Kocurek, 1996). Aeolian sand systems occur on all continents and at all latitudes, with major inland ergs occurring between 45°N and 45°S (Figure 2.2). Major sand seas are most extensive in the old-world deserts of the Sahara, Arabia, central Asia, Australia and southern Africa (Figure 2.2). In these locations, they occupy between 20 and 45% of the land area that is classified as arid (Nickling and Neuman, 1999).

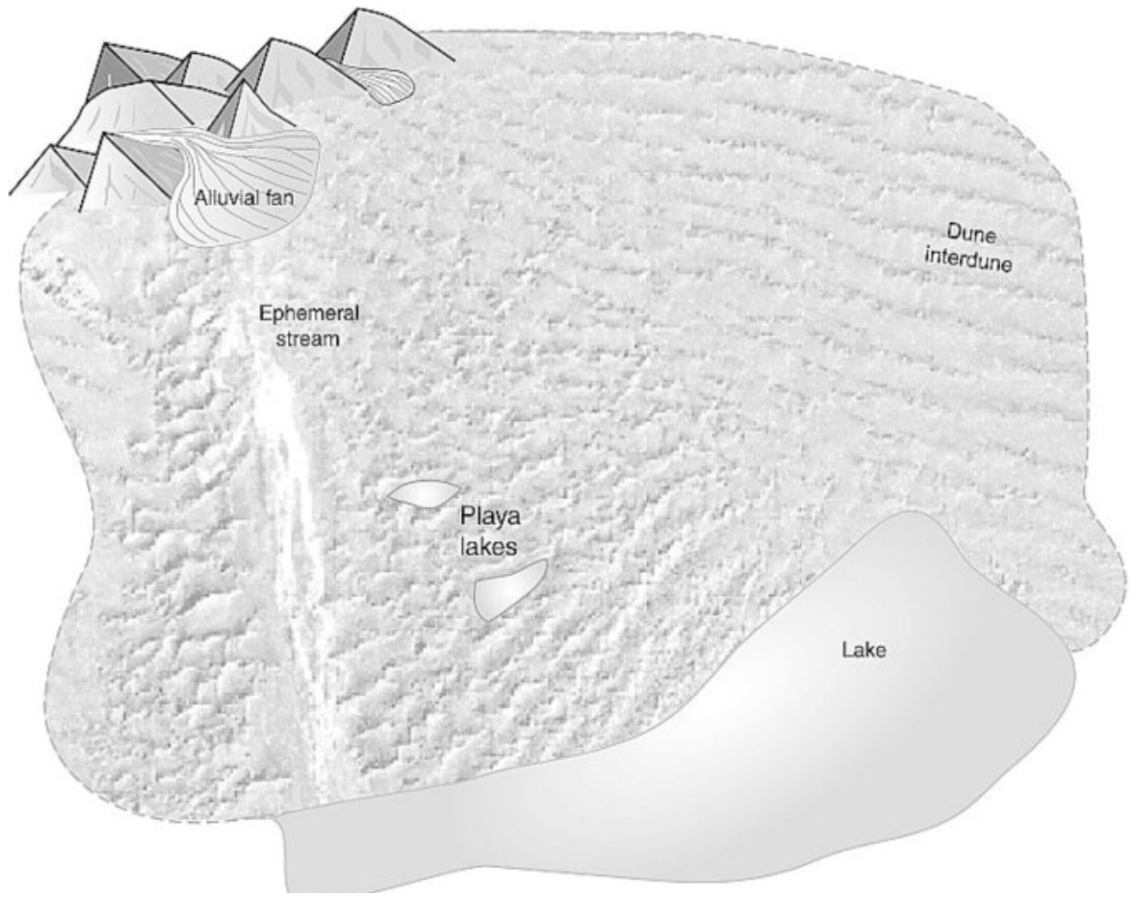


Figure 2.1: Dune, interdune, fluvial and sabkha environments in a desert (modified after Shepherd, 2009).

## 2.2 Quaternary Aeolian sand Seas

During the Quaternary Era significant changes in climate and sea-level relating to glacial-interglacial activity affected the supply, availability and mobility of sediments (Pye and Tsoar, 2008). Today, the accumulation and preservation of sand seas largely reflect these changes in addition to modern processes (Rodríguez-López *et al.*, 2014). In arid deserts, the degree of aeolian-sand development will typically reflect the sediment supply, therefore, if sand supply wanes over a period of time, sand systems will contract allowing adjacent environments to expand (Kocurek, 1996; Lancaster, 2013). As with other systems, aeolian sand seas are sensitive to global and regional changes in tectonism, sea level and climate (Kocurek, 1996). The tectonic setting of major modern sand seas vary, with many in Africa, Australia and Arabia occurring in cratonic basins; central Asian and South American ergs, by contrast, are located mostly in foreland basins (Figure 2.2).

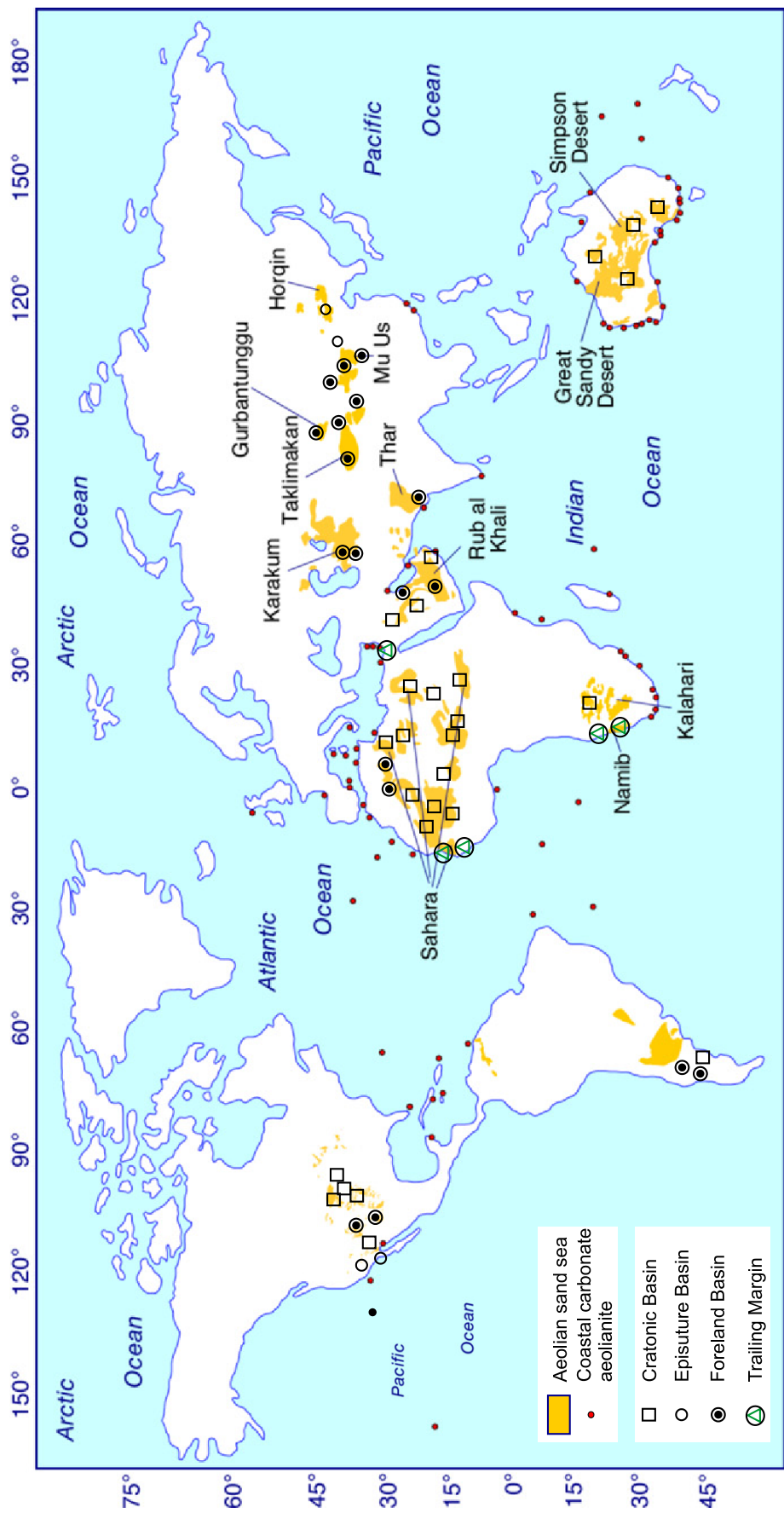


Figure 2.2: Locations of the low and mid-latitude major inland sand seas/dune-fields and coastal carbonate aeolianite deposits with their associated tectonic settings (modified after Rodríguez-López et al., 2014).

## 2.3 Controls on Aeolian Systems

Kocurek (1999) noted that the creation of an aeolian rock record can be viewed as occurring in three phases (Figure 2.3): (1) sand sea construction; (2) accumulation of a body of strata; and (3) preservation of the accumulation.

### 2.3.1 Construction

Construction of aeolian systems is a function of three separate controls: (i) sediment supply, (ii) sediment availability and (iii) transport capacity of the wind. Together these controls define the sediment state of the system (Kocurek and Lancaster, 1999). The sediment supply is the volume of a suitable grain size generated that contemporaneously or at some later point serves as source material for system construction (Kocurek, 1999). Whether or not this supply will be utilised in dune construction is a function of the availability of the sediment to aeolian deflation (Kocurek, 2003). Due to the range of factors involved that affect sediment availability (i.e. vegetation cover, moisture content, surface binding and cementation, grain sorting), Kocurek and Lancaster (1999) have proposed that the actual aeolian sediment transport rate (volume per time) is a functional definition of sediment availability. In contrast, every wind has a potential transport rate, solely a function of wind power given also as volume per time (Kocurek, 2003).

### 2.3.2 Accumulation

Accumulation here is referred to as the build-up of a body of strata, such that the accumulation surface upon which the bedforms rest rises over time (Kocurek, 1999). The space generated for the accumulations, by the rise of the accumulation surface, is termed the 'accumulation space' (Kocurek and Havholm, 1993). Shifting from a surface of accumulation to one of erosion or bypass results in a supersurface (Kocurek, 1988). The accumulation of a sand sea requires specific conditions that satisfy the principle of continuity, the dynamics of which rest with the three basic types of aeolian systems (dry, wet and stabilizing - Figure 2.4) (Kocurek, 1999).

### 2.3.3 Preservation

The incorporation into the rock record of a body of accumulated strata refers to preservation (Kocurek, 2003). The space for the preserved accumulation is termed the 'preservation space' and for aeolian systems it can differ from the accumulation space (Kocurek and Havholm, 1993). For sand sea accumulations, preservation occurs with subsidence and burial and/or a rise in the water-table through the accumulation (Kocurek, 1999). Subsidence with burial is necessary to avoid deflation, hence a continued saturated aeolian influx into the system is necessary to prevent removal of aeolian accumulations (Kocurek, 2003). A rising water-table (absolute or relative) through the accumulation may also effectively shield it from deflation (Kocurek, 2003).

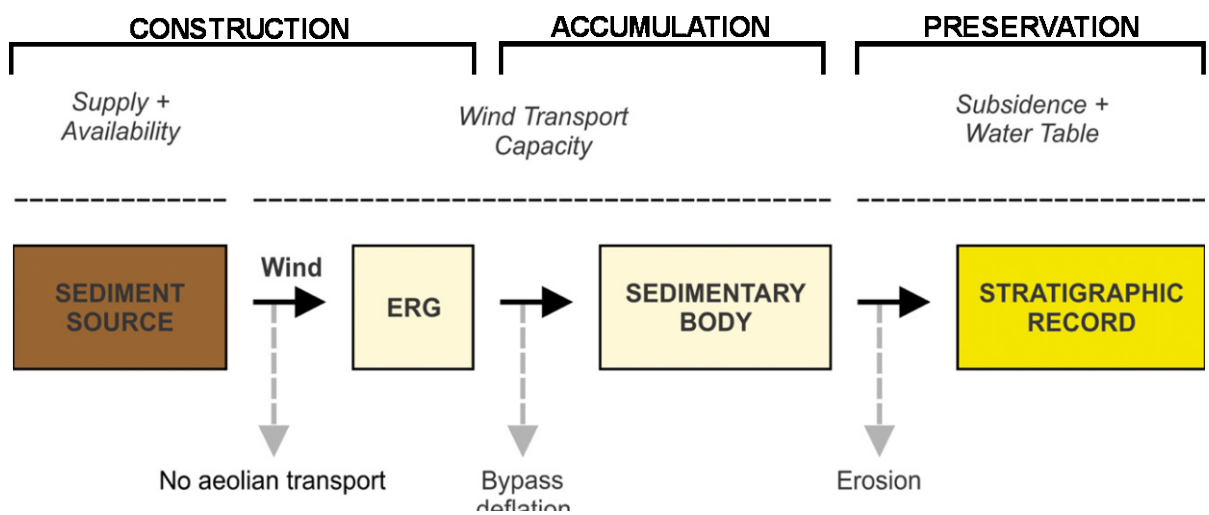


Figure 2.3: Kocurek (1999) considered three-phases (construction, accumulation and preservation) in the creation of the aeolian rock record. Modified after Rodríguez-López et al. (2014).

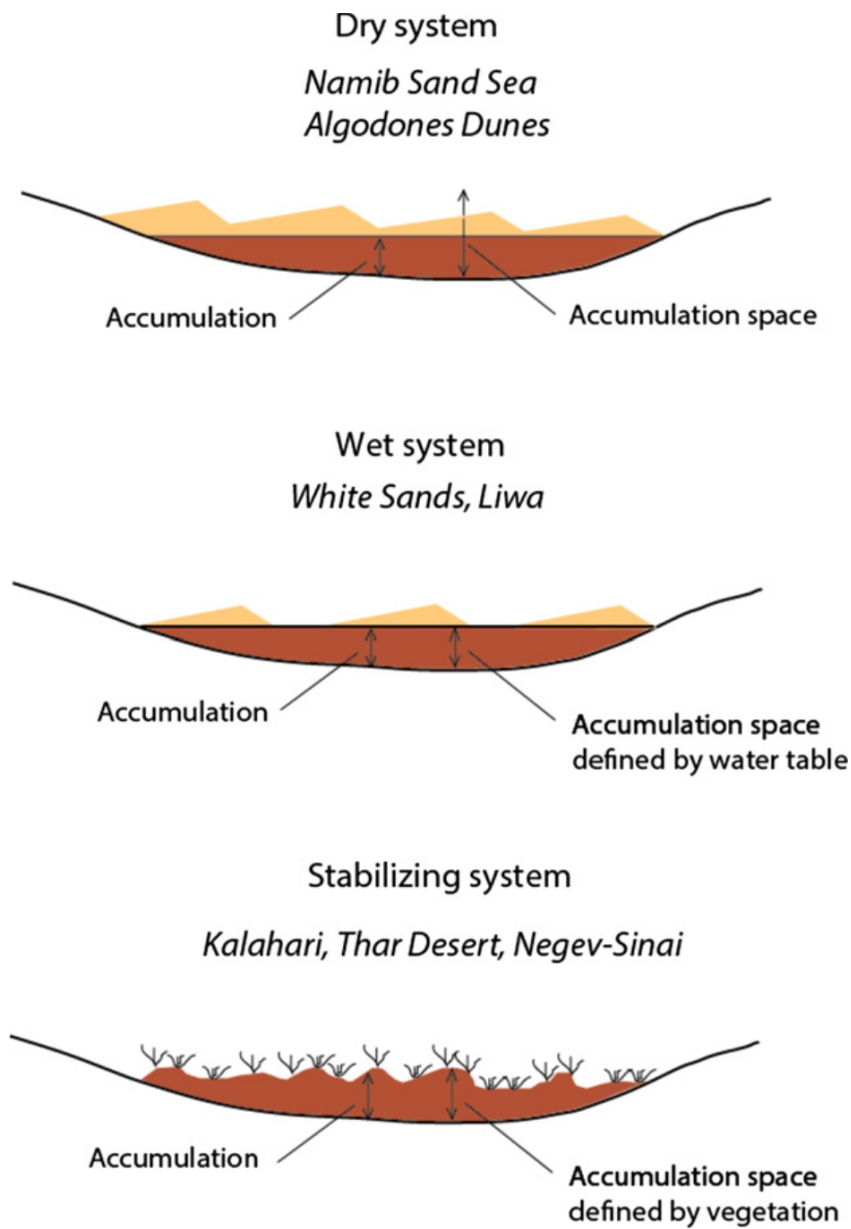


Figure 2.4: End member aeolian system types displaying the accumulation space and the accumulation. Dry, wet and stabilising aeolian systems illustrate the role of aerodynamic configuration, water-table level and stabilising agent (e.g. vegetation) respectively (Kocurek et al., 1998). Modified after Rodríguez-López et al. (2014)

## 2.4 Aeolian Bedforms

Deserts contain the most extensive of aeolian deposits and the dune-fields existing within these large-scale sediment systems comprise bedforms of different morphological types and sizes (Walker and James, 1992; Rodríguez-López *et al.*, 2014). Wilson (1972) proposed three groups of aeolian bedforms based on their size distribution (Figure 2.5): (1) aeolian ripple; (2) aeolian dune; and (3) draa (also called megadune). These three distinct scales of structures represent a hierarchy, within which similar features coexist at different sizes and spacing suggesting the presence of equilibrium bedforms (Collinson *et al.*, 2006). Dunes and draa regularly have ripples migrating across many parts of their slopes (Goudie, 2013).

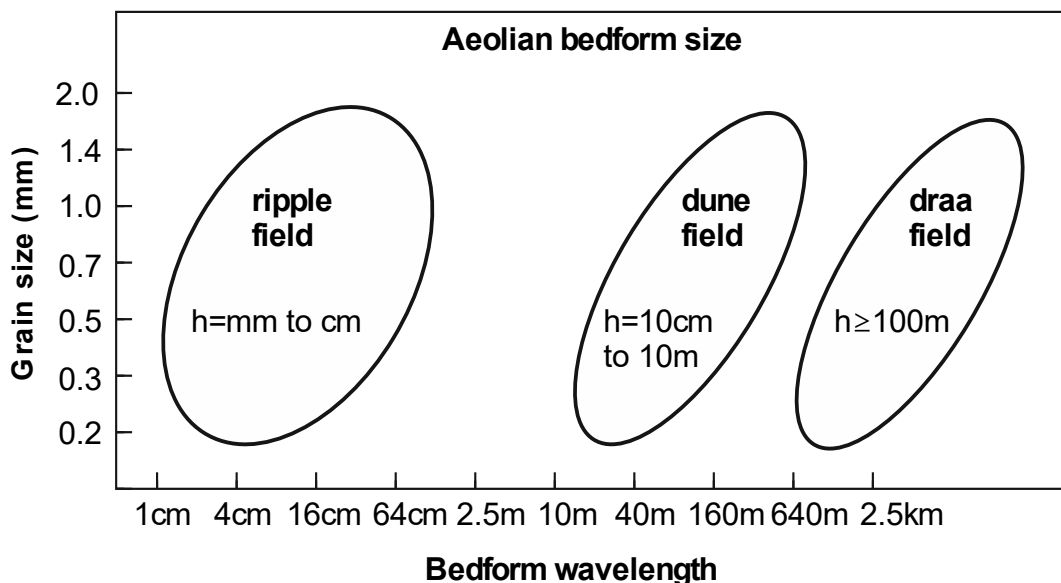


Figure 2.5: Three groups of aeolian bedforms, namely ripple, dune and draa. Note the distinct gap in bedform size between the largest ripple and the smallest dune. Small aeolian ripples can be superimposed on both dunes and draa (Collinson *et al.*, 2006; Nichols, 2009).

## 2.5 Particle Transport

When the wind blowing over a sand bed exceeds a certain velocity threshold, the particles of the bed can be set into motion and transported away (Durán *et al.*, 2011). Due to its low density and viscosity, the wind is a highly effective sorting agent of sediments with the ability to entrain a narrow range of grain sizes within its flow (Kocurek, 1996). Depending on particle size and wind speed, the transport can occur in several modes. Sand grains will move by suspension, creep, saltation and reptation and form a thin carpet of moving sand (Figure 2.6) (Bagnold, 1941; Nichols, 2009).

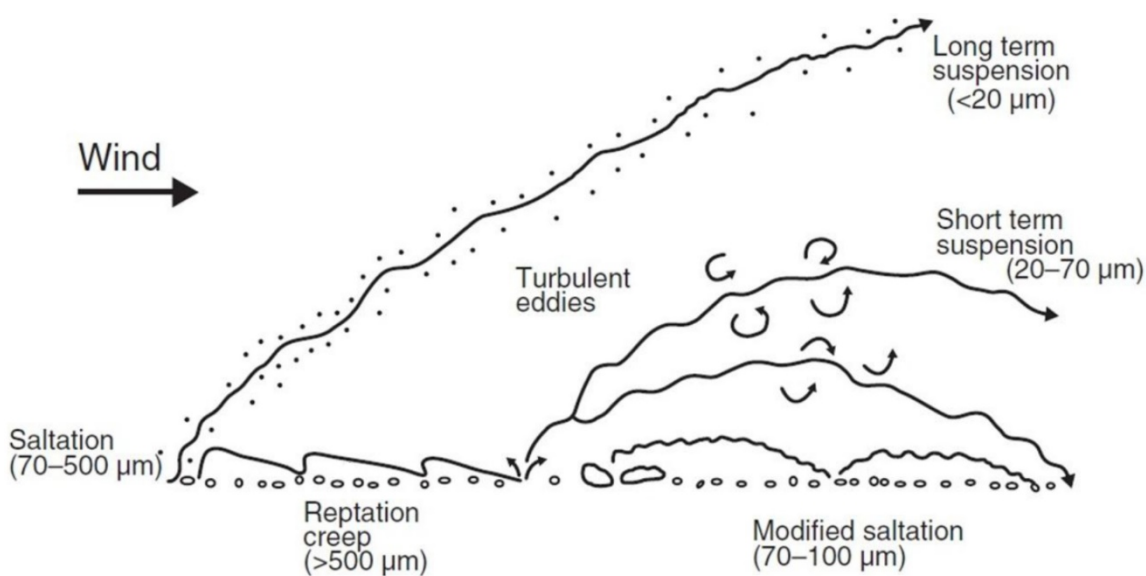


Figure 2.6: Various modes of aeolian transport. Particles hop along the surface in a process known as saltation. The impacts of saltators can mobilize larger particles, causing them to hop, usually less than a centimetre, in a mode known as reptation. Alternatively, larger particles driven by impacts of saltating particles and wind drag force can roll or slide along the surface in a mode of transport known as creep. Modified after Nickling and Neuman (2009).

## 2.6 Ballistic (aeolian) Ripples

Ripples that form under aeolian conditions can be distinguished from subaqueous ripples due to characteristic inverse grading as a result of ripple migration of coarse crests over finer-grained troughs and due to the higher ripple indices (wavelength: height ratio) (Anderson, 1990). They form when saltating grains collide obliquely onto a sand bed, generating a small depression on the surface, which then develop a chain of rough, small-scale undulations of asymmetric profile (gentle windward slope and steep lee slope) (Figure 2.7a) (Kok *et al.*, 2012; Leeder, 2012). Each collision results in the ejection of many (larger) reptating particles that move forward several grain diameters. The upwind side receives more impacts of saltating grains than the downwind surface areas or “shadow-zone” (Figure 2.7a). Particles in the shadow zones are shielded from impacts and thus accumulation and subsequent growth of the perturbations occurs (Kok *et al.*, 2012). Aeolian ripples should have a wavelength roughly equal to characteristic saltation path (Leeder, 2012). The role of saltating particles for ripple formation is to furnish energy to the motion of low-energy particles through reptation, in effect the transport mechanism of ripples. Due to the saltation bombardment and less advancement by leeside avalanches, there is no clear internal structure of cross lamination in ballistic ripples (Figure 2.7b) (Leeder, 2012).

As fine sand and silt particles tend to become concentrated in the ripple troughs during ripple migration it forms a very fine-grained layer at the base of each climbing translational ripple stratum. The fine deposits become preferentially cemented during early diagenesis and gives rise to distinctive pin-stripe lamination when the deposits are exposed in outcrop (Pye and Tsoar, 2008). Pin-stripe laminations may also form in grain-flow deposits owing to the concentration of fine grains near the basal shear plane.

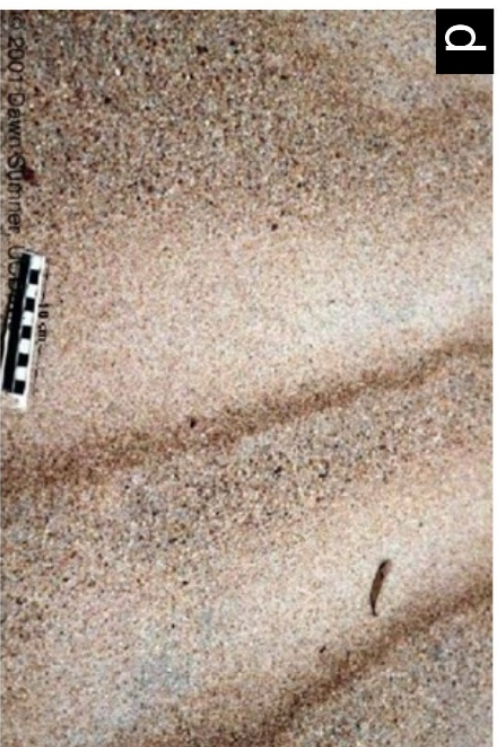
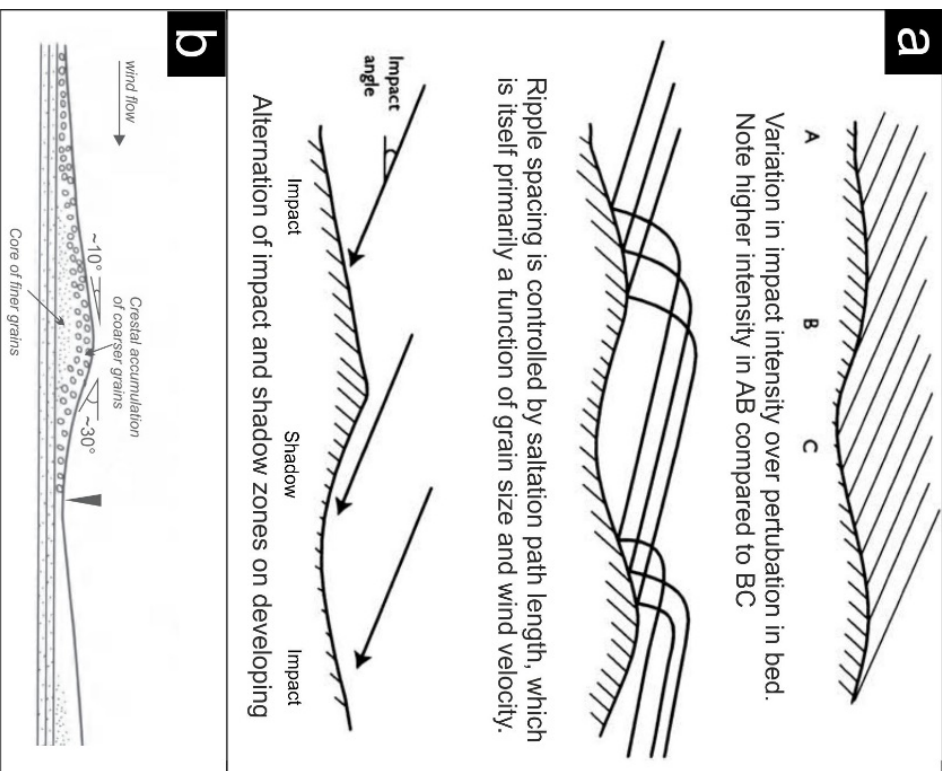


Figure 2.7: (A) Formation of aeolian dunes by saltating sand grains. (B) Note the inverse grading between trough and crest of the ripple which is preserved in the laminae. (C) Ballistic ripple field formed in a coastal setting, Kenton-on-sea, South Africa. Branch ~30 cm long. (D) Coarse-grained wind ripples clearly showing the difference in grain size between troughs and crests. Centimetre scale bar. Schematic diagrams modified after Leeder (2012). Photograph (D) by D. Sumner (<http://mygeologypage.ucdavis.edu/summer/gel1109/sed-structures/Aeolian.html>).

## 2.7 Aeolian Dunes

There are some basic dune types that are prevalent in many of the world's deserts, their morphology of which depends on wind speed and directional variability, sand supply and availability (Pye and Tsoar, 2008; Goudie, 2013). Dune classification has been found to be problematic and no single classification scheme successfully captures the inherent complexities apparent in dune form or process of development (Wiggs, 2019). A very simplistic geomorphic classification was devised by Livingston and Warren (1996) and distinguishes between dunes that are 'anchored' and those considered to be 'free' and form only by aeolian action of loose sand (Figure 2.8). These dune types can be further divided by their morphology into the major dune types evident in sandy deserts (Figure 2.8, Figure 2.9A-F).

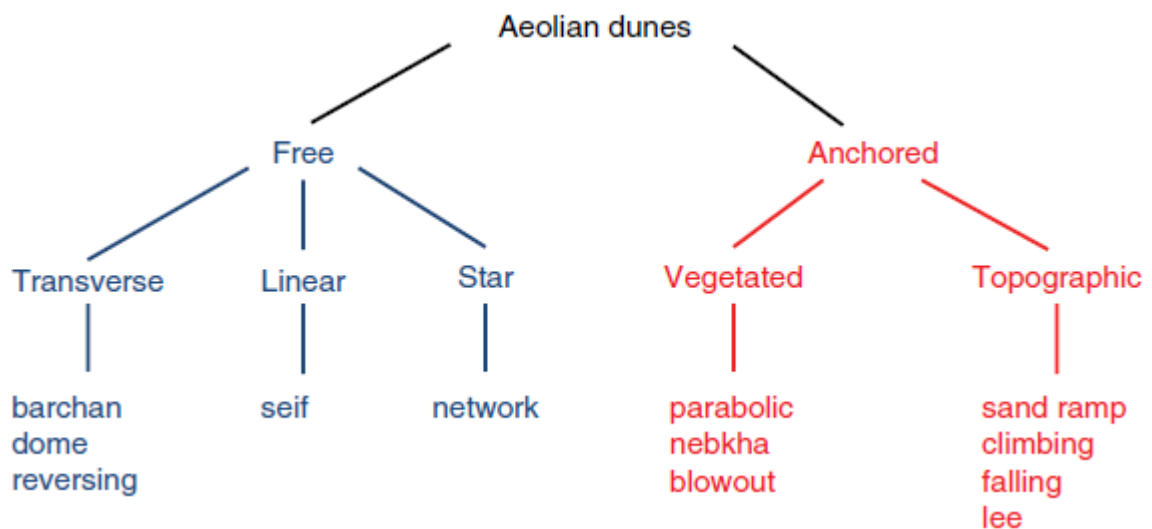


Figure 2.8: Simple aeolian dune classification scheme. Note the morphologies of some of these dune types are given in Figure 2.9a-f. Extracted from Wiggs (2019).

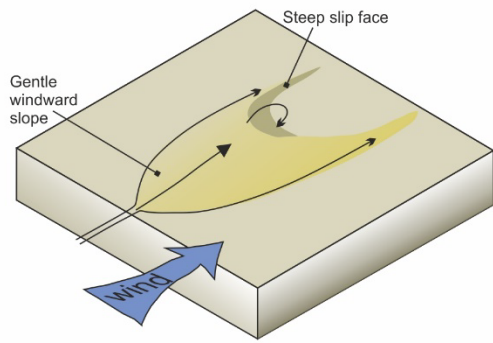
Aeolian dunes have a diversity which may vary between and across dune-fields (Goudie, 2013). Simple dunes (e.g. transverse and barchan) are characterized by a single gentle windward stoss slope (inclination of 8-16°) and a steep lee slope (inclination of 20-34°) comprising a slipface (i.e. a foreset slope), inclined at or close to the angle of rest (Figure 2.13) (Collinson *et al.*, 2006). Aeolian dunes that occur superimposed on and migrating over larger bedform structures which are themselves migratory are known as compound and complex dune forms (Collinson *et al.*, 2006) (Figure 2.9G-H). Complex

dunes are composed of a number of dunes of a different type but at different scales superimposed onto each other, while compound dunes consist of superimposed dunes of the same type (McKee, 1979; Figure 2.9G-H).

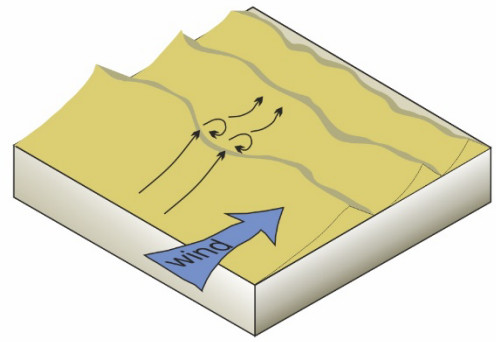
Wasson and Hyde (1983) simplistically demonstrated that dune shape (e.g. transverse, linear, star) is a manifestation of sand availability and wind direction variability (Figure 2.10). For instance, in areas of low sand supply and low wind directional variability barchan dunes will form. An increase in sand supply results in the coalescence of barchan dunes into transverse ridges and dune networks such as aklé patterns (Figure 2.9E) which are made up of crescent-shaped sections that alternately face the wind (linguoid) and back to the wind (barchanoid) (Allaby, 2013). An increase in the wind directional variability will result in the formation of linear dunes in a bi-directional wind regime and, where both sand supply and directional variability are at their greatest, star dunes are apparent (Figure 2.10). The developments in dune forms are most apparent at the dune field scale from a coastal system, where sand supply is low and winds are uni-directional, to an inland basin where sand supply is greater and wind regimes are more complex (Wiggs, 2019).

The simplicity of the classification scheme of Wasson and Hyde (1983) (Figure 2.10) conceals the complex morpho-dynamics of time and space which underpins dune development. For example, the Wahiba Sand Sea of Oman consists of complex linear dune forms hosting smaller seif and barchan dunes superimposed onto their flanks and crests (Goudie *et al.*, 1987). This complexity arises as dunes of different sizes adjust to changing wind patterns at different rates, which is not considered in the classification of Figure 2.10 (Wiggs, 2010). The difference in response and readjustment time for different scales of dunes has been described as 'dune memory' (Warren and Kay, 1987), such that large dunes retain a geomorphological signature of previous winds (Wiggs, 2019).

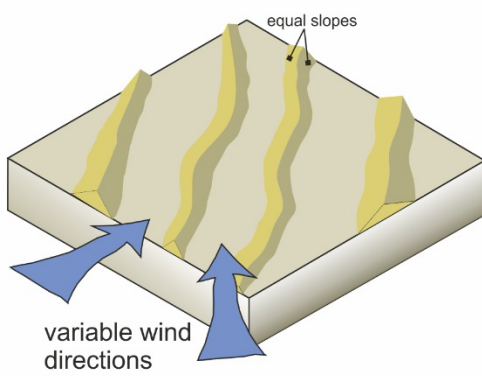
(a) Barchan dune



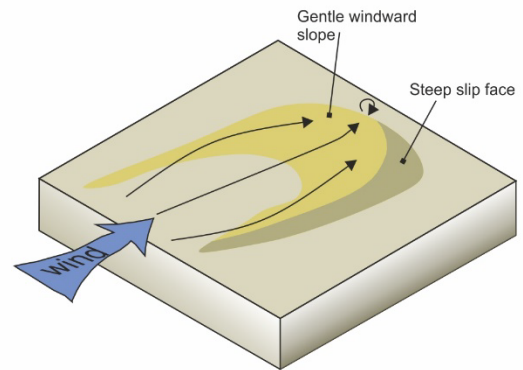
(b) Transverse dune



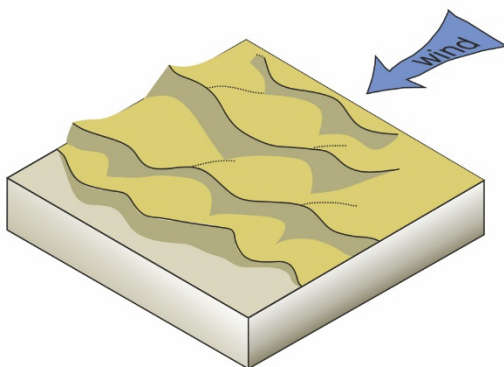
(c) Longitudinal / linear / seif dune



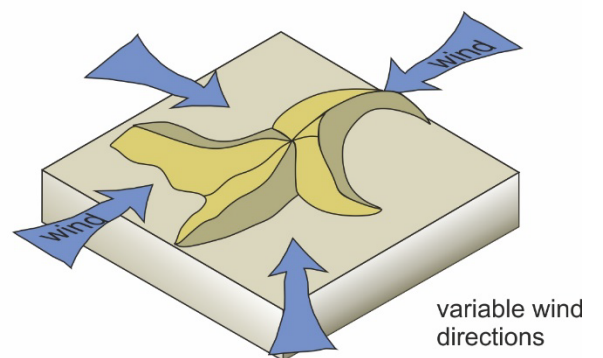
(d) Parabolic (blowout) dune



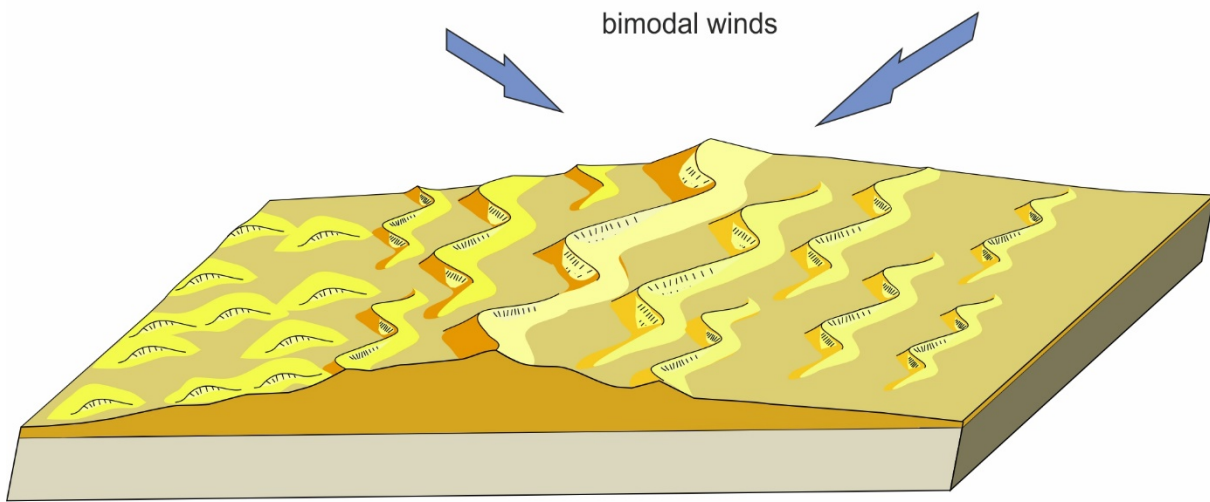
(e) Aklé dunes



(f) Star dune



(g) Complex linear dunes



(h) Compound crescentic dunes

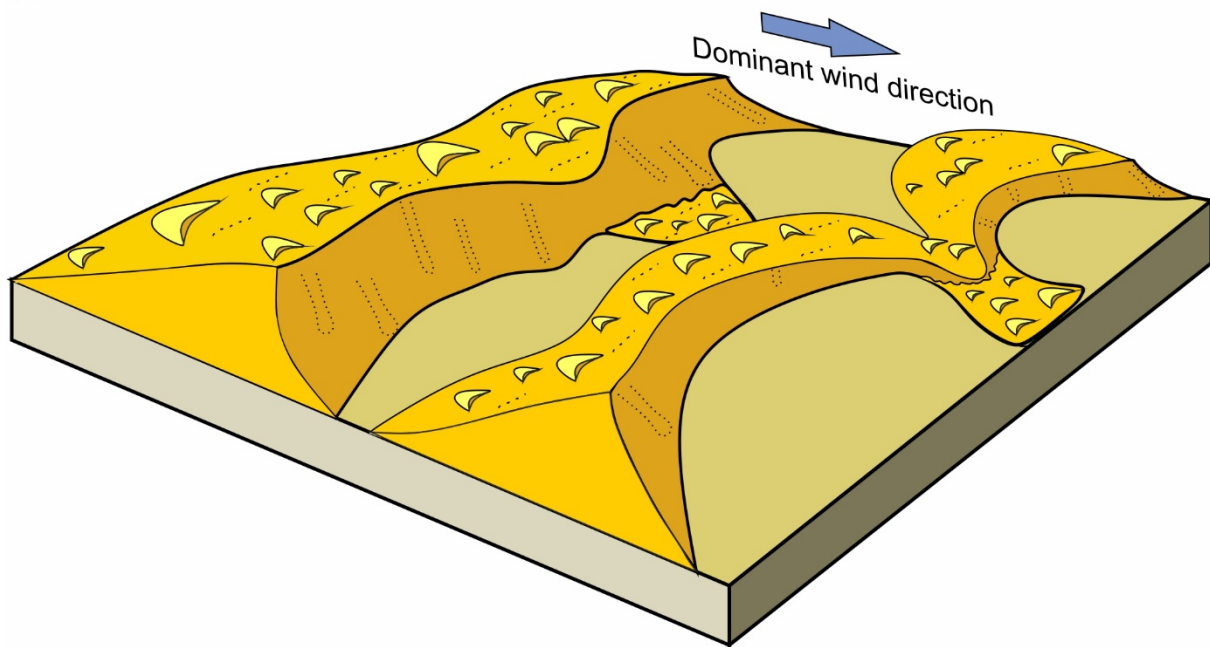


Figure 2.9: Three-dimensional forms of some common aeolian dune morphologies. The arrows mark the dominant direction of the effective winds. Adapted after Collinson et al., 2006; Nichols, 2009; Boggs, 2011; Argüello Scotti and Veiga, 2019.

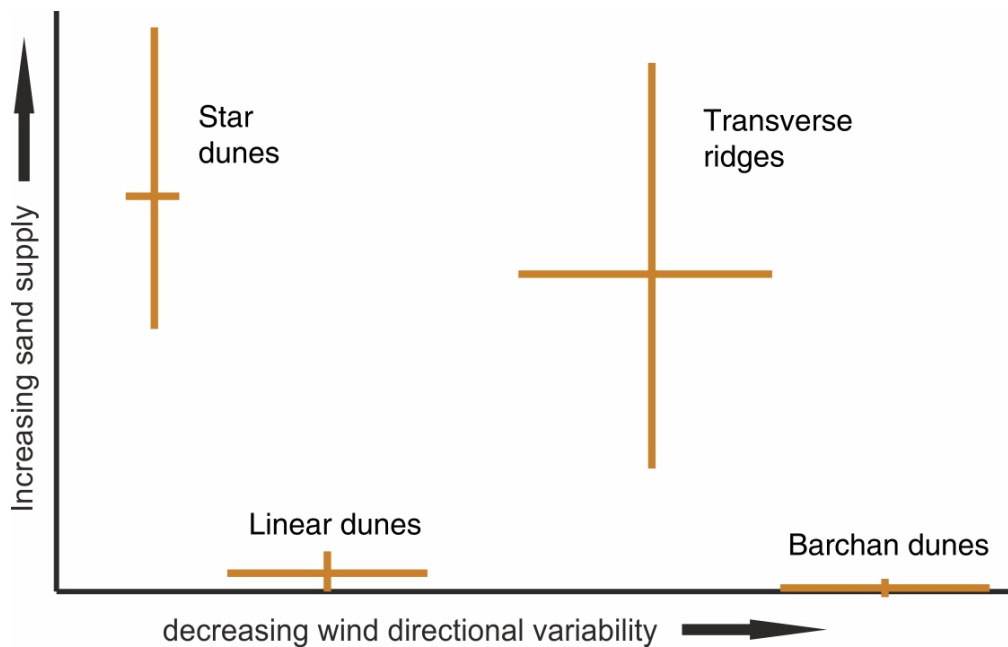


Figure 2.10: The controls that differentiate dune types. Modified after Wasson and Hyde (1983).

### 2.7.1 Dune motion

The wavelength at which a dune pattern emerges from a flat sand bed is controlled by the sediment transport saturation length. This is the length required for the sand flux to adapt to a change of wind strength (Andreotti *et al.*, 2008). Dune nucleation is largely attributed to the transport capacity of the wind and the saturation length (Elbelrhiti *et al.*, 2005). The presence of a bump or small hill on the ground induces a modification in the logarithmic fluid flow profile of the wind (Figure 2.11) (Fourrière *et al.*, 2010). The coupling between erosion and deposition and fluid dynamics results in an asymmetric dune profile to form with a gentle windward slope and steep lee slope (Kok *et al.*, 2012).

With dune growth and increase surface curvature, the negative pressure perturbation at the crest does not suffice to keep the flow attached to the topography and flow separation occurs thus reducing its transportation capacity and causing deposition on the lee slope (Figure 2.12). As a dune grows, the sand accumulates at its crest, when the slope at the lee exceeds the angle of repose of the sand ( $\sim 34^\circ$ ) the surface relaxes through avalanches and a slip face forms (Figure 2.12) (Kok *et al.*, 2012). Dune motion thus consists of saltating grains climbing up the windward side, accumulating on the crest and

thereafter rolling down the slip face being deposited at the bottom on the lee side of the dune (Figure 2.12).

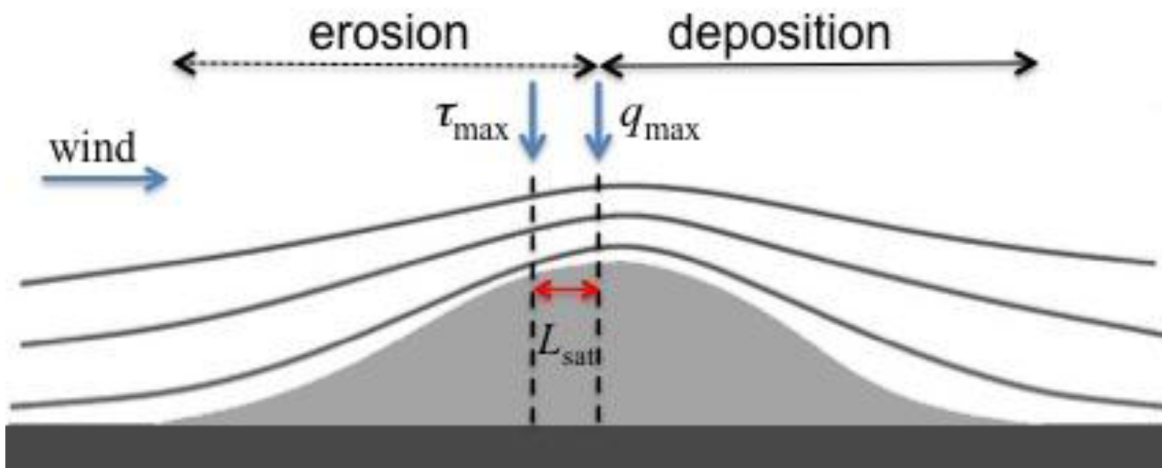


Figure 2.11: Hydrodynamic instability that leads to the formation of a sand dune. The schematic shows the streamlines of the wind flow over a Gaussian profile or 'bump'.  $\tau_{max}$  and  $q_{max}$  show the positions of maximum shear stress and maximum sand flux respectively. The saturation length ( $L_{sat}$ ) gives the horizontal distance of relaxation of the flux towards its saturated value due to the variation in the wind flow along the profile. The bump will grow if the maximum flux is reached upwind of the bump's crest (Kok et al., 2012). Modified after Fourrière et al. (2010).

Repeated avalanches build up a set of cross-beds which may be preserved if there is a net accumulation of sand (Nichols, 2009). At high wind speeds some sand grains are in temporary suspension and are blown directly over the crest of the dune and fall out onto the lee slope. These grainfall deposits accumulate on the lee slope, but they will usually be reworked from the upper slope by grain flows. Some may be preserved at the toe bedded with grain flow deposits. Grainflow strata have specific characteristic morphologies consisting of tabular shape, with upwards tapering edges (Figure 2.13) and typically display inverse grain size grading, caused by shear sorting during the flow (Kocurek, 1991).

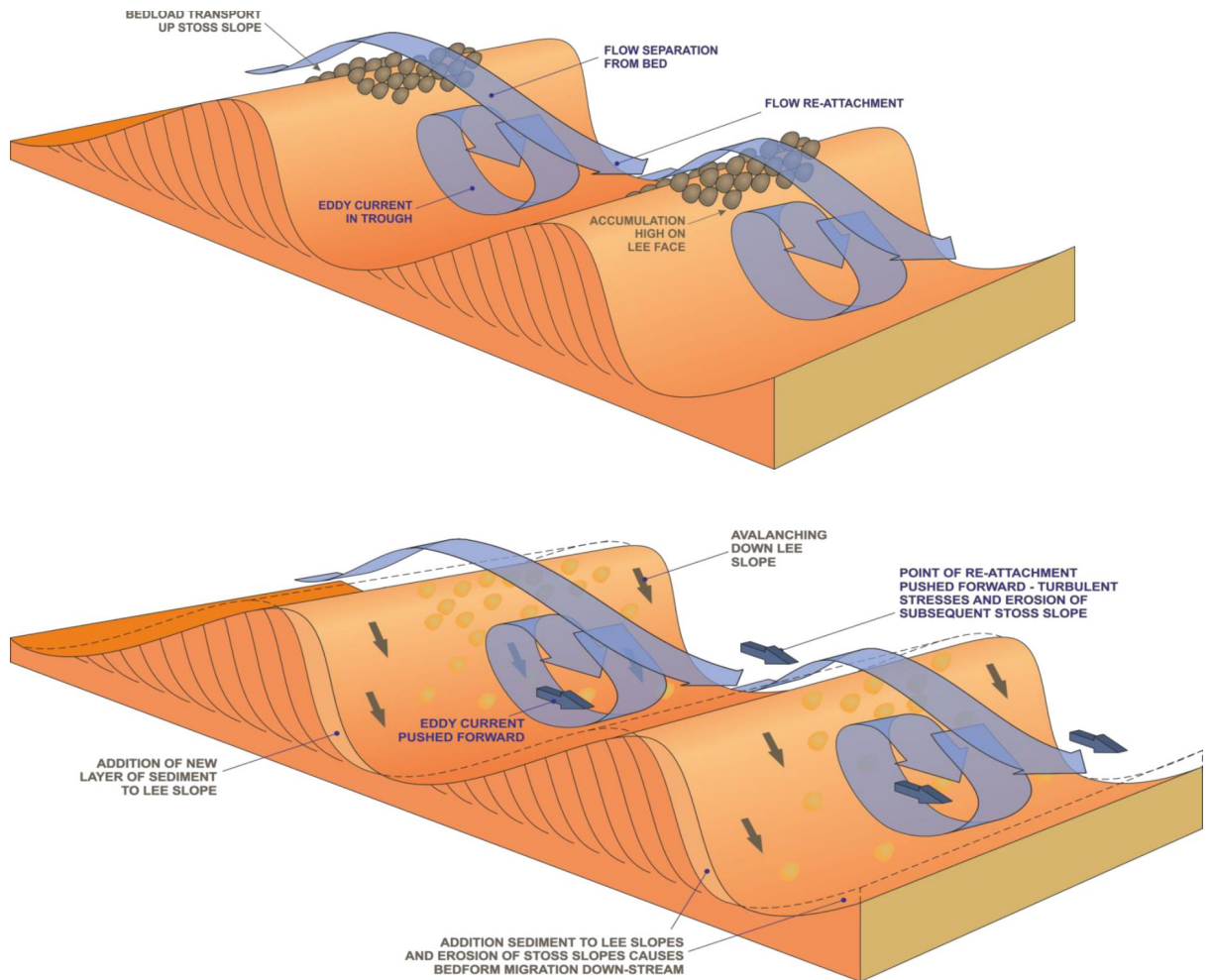


Figure 2.12: Dunes migrate as strong winds pick up grains of sand from the stoss (upwind or windward) side of the dune, blowing them across the crest and brink. Erosion occurs on dune slopes which experience the accelerating or divergent winds. Deposition takes place in two settings: where flow separation occurs, rapid and large-volume deposition on the lee-side avalanche faces; in areas where sand transport rates decrease downwind as a result of flow convergence or local flow expansion, slow deposition occurs. Adapted from Clarke (2017) – Keele lecture slides.

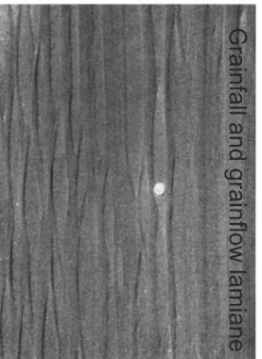
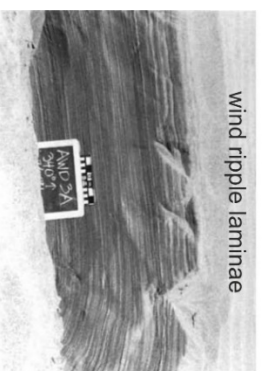
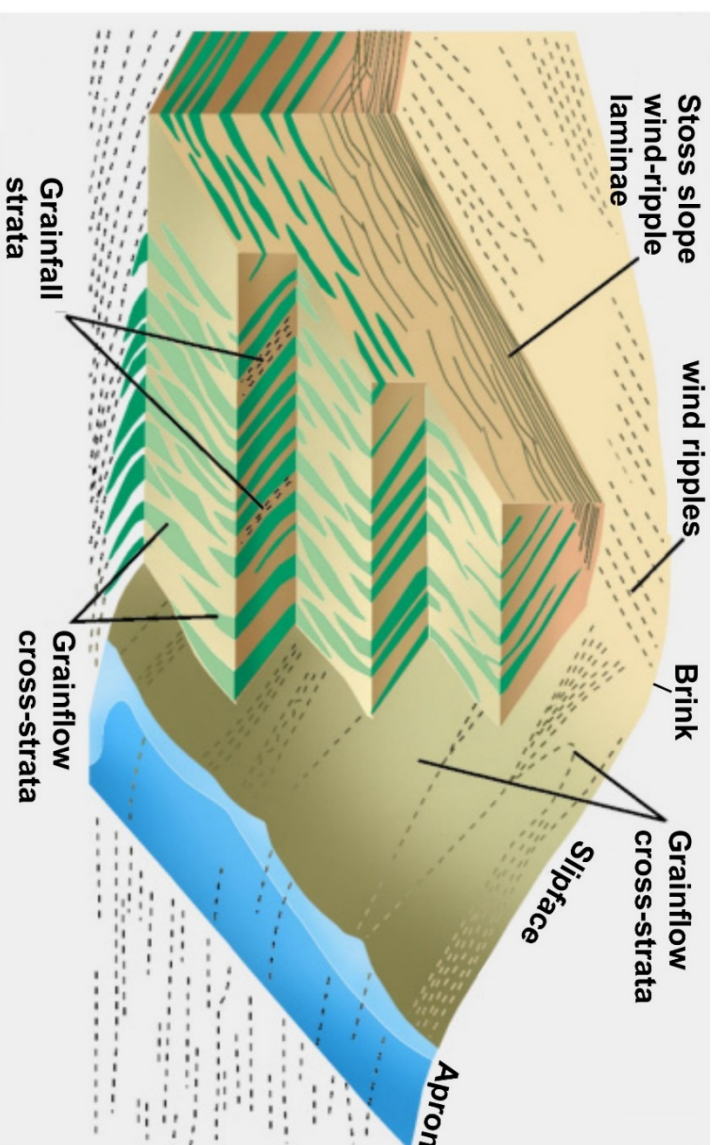


Figure 2.13: Schematic diagram showing the distribution of stratification types in a small dune. Photographs show examples of these primary sedimentary structures. Diagram modified after Hunter (1977), photographs taken from Lancaster (2005).

### 2.7.2 Primary Stratification Types

Hunter (1977) identified three main modes for deposition on dunes: 1) migration of wind ripples, 2) fallout from temporary suspension in the flow separation zone (lee of the crest), and 3) avalanching on the lee slope of the dune. These processes form the three major types of aeolian structures (Figure 2.13) (Kocurek and Dott, 1981): 1) climbing translant strata (wind ripple laminae), 2) grainfall laminae, and 3) grainflow cross-strata.

### 2.7.3 Sets of Cross-strata

The basic deposit of an aeolian dune is a set of cross-strata, formed by depositional processes of the dune through time (Kocurek, 1991). Where bedforms migrate and leave behind a deposit, they necessarily move upward or climb with respect to this surface (Hunter, 1977). The resultant sets of cross strata are climbing translant strata, which cross-depositional surfaces and are time transgressive (Kocurek, 1991). Barring uncommon cases, aeolian dunes are represented in the rock record by subcritically climbing translant strata, and typically only small fractions of the original dune heights are preserved (Rubin and Hunter 1982, Kocurek 1981). The stratification types may provide clues as to original bedform size. For instance, the common presence of grainfall deposits between strata indicates smaller dunes where grainfall deposits of observable thickness extended to the base of the set (Figure 2.15) (Hunter, 1977; Kocurek and Dott, 1981).

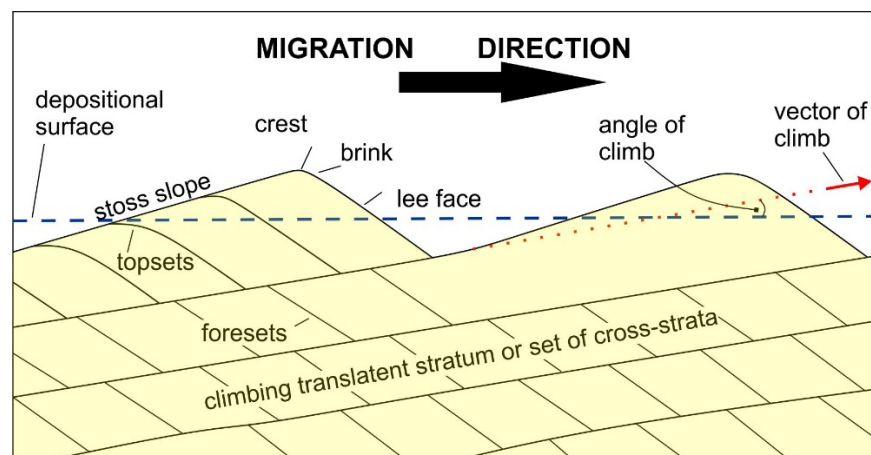


Figure 2.14: The sets of cross-strata generated by climbing dunes. Modified after Kocurek (1991).

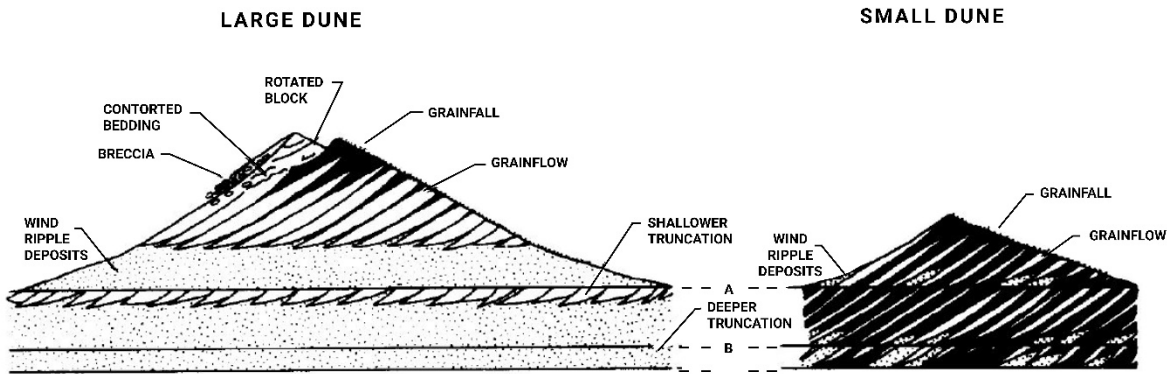
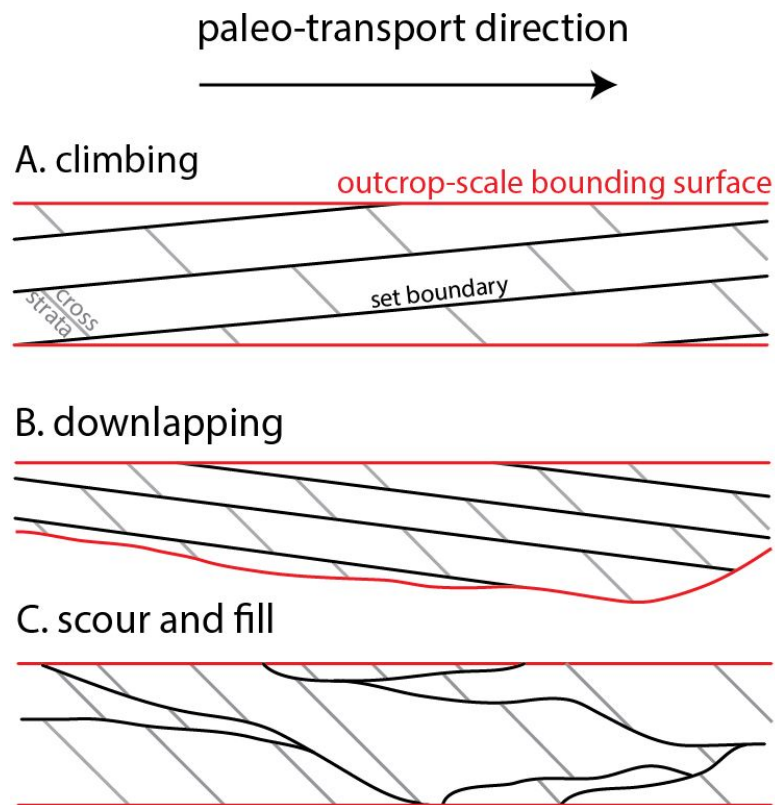


Figure 2.15: Large and small-scale aeolian dunes truncated at different levels. Note how this may greatly influence the geological record of the dunes. Grainfall deposits are less frequently preserved in sets representing large dunes while they dominate in sets of much smaller dunes where the grainfall apron extends to the base of the dune. Modified after Kocurek and Dott, 1981.

#### 2.7.4 Aeolian Set Architecture

Aeolian set architectures preserve a record of the dune-field dynamics as the bedforms migrated and interacted with one another (Figure 2.16) (Rubin and Hunter, 1982; Allen, 1970; Cardenas *et al.*, 2019). In the examples shown in Figure 2.16, sets are bound by more extensive surfaces labelled 'outcrop-scale bounding surfaces' that truncate the sets of cross-strata. Trains of migrating dunes may climb over the accumulation of downwind bedforms, their set boundaries originate from a lower outcrop-scale bounding surface and climb at some measurable angle (Figure 2.16A). In cases where sets are migrating down into and in the process filling pre-existing topographic lows, the sets' boundaries originate from an upper outcrop-scale bounding surface and downlap onto a lower outcrop-scale surface (Figure 2.16B). Lastly, variable depth of trough scour creates space that is later filled by smaller dunes in the train. Set boundaries are discontinuous and cut by adjacent sets, rather than the outcrop-scale surfaces (Figure 2.16C). Observations of set architectures can aid in the reconstruction of the filling history and environmental controls in which the dune-field emerged (e.g. Cardenas *et al.*, 2019)



*Figure 2.16: Schematic examples of aeolian set architectures showing (A) climb, (B) downlap and (C) scour-and-fill geometries. Schematics are extracted directly from Cardenas et al., 2019 and are based on illustrations from Allen (1970) and Rubin and Hunter (1982).*

#### 2.7.5 Interdunes

Aeolian dune deposits are universally punctuated by various bounding surfaces, the most extensive of which are commonly overlain by horizontal interdune deposits (Kocurek, 1981). Interdune surfaces are formed by the migration of dunes and sediment aggradation, resulting in preservation of sections of interdune sediments between sets or cosets of cross-strata (Bristow and Mountney, 2013). Bounding surfaces and interdune deposits provide keys for detailed interpretations of the development, shape, type, wavelength and angle of climb of aeolian bedforms, as well as overall erg conditions (Figure 2.17) (Kocurek, 1981). The environmental condition may be dry and display near horizontal wind-ripple strata, or damp to wet indicating an interaction with the water-table and display cohesion of sand or cementation by evaporates (Bristow and Mountney, 2013). Interdune bedforms are further detailed in section 2.12.

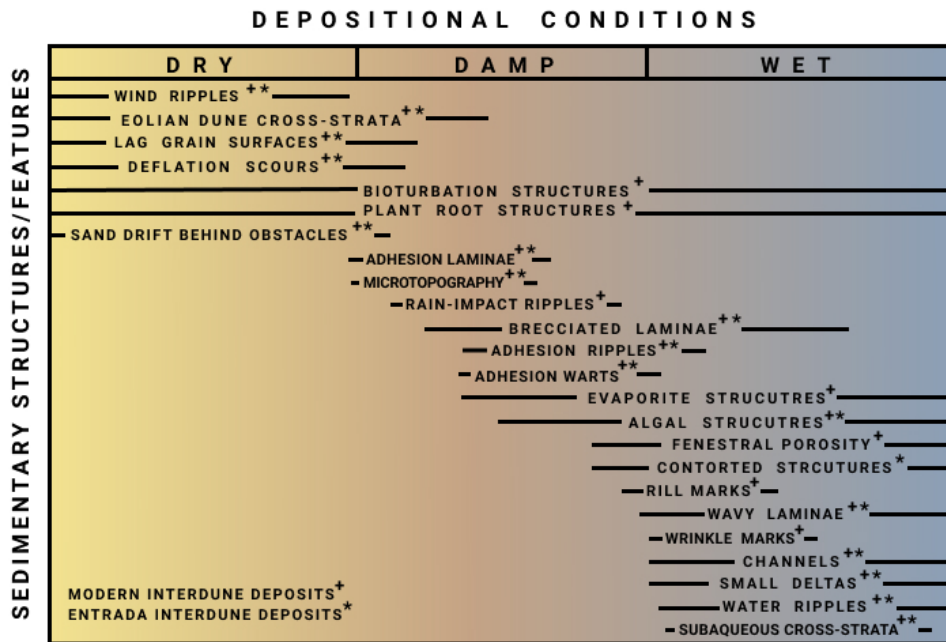


Figure 2.17: A summary of sedimentary architecture and other features characteristic of interdune deposits and the range of depositional conditions under which they form. Observations from contemporary dune-fields and the ancient Entrada Sandstone of western USA. Modified after Kocurek, 1981

## 2.8 Water-Table

The land surface in a sandy desert is mainly dry, however if the substrate is porous rock or sediment there will be groundwater. The water-table level is determined by the amount of water charging the water-bearing strata, the aquifer, and the nearest lake or sea (Figure 2.18). A rise in the water-table will affect aeolian processes in the erg. If the water-table rises to the level of the interdune, flat areas between individual bedforms, wet sediment will not be picked up by the wind and unavailable for aeolian reworking (Nichols, 2009). Figure 2.18 details some of the features present in the rock record following a static/rising water-table.

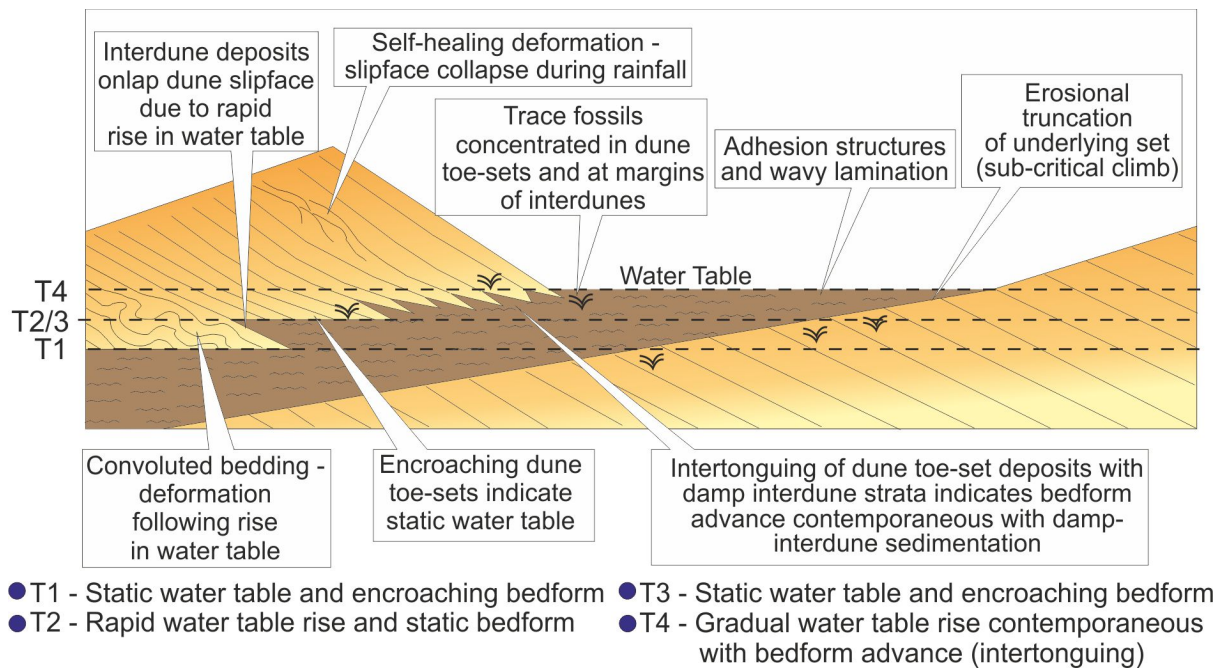


Figure 2.18: Interaction and significance between a migrating dune and interdune. Water-table fluctuations give rise to a variety of damp and wet sedimentary structures both within the interdune and advancing dune toe-sets. Modified after Mounthey and Thompson (2002)

## 2.9 Draa / Megadune

*Draa* is a North African word for a large sand hill (Pye and Tsoar, 2008). Draas cannot always be distinguished from dunes on the basis of grain size, and there is a continuum of scale between the two (Wasson and Hyde; 1983). Havholm and Kocurek (1988) suggested that draa should be used as a purely morphological term for any aeolian bed form with smaller superimposed dunes. The dune-draa distinction is not universally accepted and the term “megadune” is often used to describe very large aeolian bed forms (Brookfield, 1992; Collinson *et al.*, 2006; Pye and Tsoar, 2008). More recently, Livingston and Warren (2019) refer to larger dune bedforms with superimposed bedforms as ‘megadunes or draa’. A descriptive classification based on form and complexity of the aeolian bedform is given in Table 2.1 below.

The term ‘draa’ is maintained in this thesis and is used interchangeably with ‘megadune’. More commonly, the space between two large megadunes will be referred to as ‘interdraa’ so as to avoid confusion in distinguishing the interdune space between smaller superimposed bedforms.

Table 2.1: Aeolian bedforms morphology and classifications (adapted after McKee, 1979; Brookfield, 1992; Boggs, 2001).

Morphology	Slipfaces	Name	Associations
Sheet-like	0	Sand sheet	
Thin elongate strips	0	Streaks	COMPOUND - two or more of the same type combined by overlap or superimposition (*Wilson's draa).
Circular to elliptical mound, dome shaped	0	Dome	
Crescent in plan	1	Barchan	
Connected crescents	1	Barchanoid ridge	
Asymmetrical ridge	1	Transverse ridge	COMPLEX - two different basic types occurring together, either superimposed
Symmetrical ridge	2	Linear (seif)	
Central peak with arms	3 or more	Star (pyramidal)	(*Wilson's draa), or adjacent.
U-shaped	1 or more	Parabolic	

\*Wilson (1971, 1972)

## 2.10 Bounding surfaces

A bounding surface is an erosional surface within or between sets of cross-strata usually formed as bedforms climb at angles lower than their windward slopes (Brookfield, 1992; Kocurek, 1996). The underlying and preceding bedforms are eroded leading to the formation of bounding surfaces that define sets of cross-strata (Brookfield, 1992). Commonly a hierarchy is applied to bounding surfaces (i.e. 1<sup>st</sup>, 2<sup>nd</sup> and 3<sup>rd</sup>-order surfaces), however these are not used in all publications as may not be universally distinct (Kocurek, 1996). The ordering is included in the descriptions and figures below for reference. The most common bounding surfaces are recognized by the following mechanisms (Brookfield, 1992; Fryberger, 1993; Kocurek, 1996; Neuendorf *et al.*, 2005):

**Interdune migration surface:** May be labelled as first-order surfaces. Near horizontal bedding planes cutting across all underlying aeolian structures, attributed to the migration of the megadune. The surface originates with erosion that begins on the stoss-side and progresses to the depth of scour defined by the passage of the interdune trough. Further erosion may take place as an interdune surface. As dry sand is less resistant to erosion than wet/moist sand, the water-table may control the extent of the interdune erosion.

**Superimposition surface:** May be labelled as second-order surfaces. Attributed to the migration of one dune over another dune (i.e. superimposed dune). The surface may occur without erosion occurring on the underlying dune. Examples include transverse dunes climbing down the lee slopes of a megadune, or lateral migration of linear dunes across a megadune lee slope.

**Reactivation surface:** May be labelled as a third-order surface. Form the boundaries of bundles of laminae within co-sets of cross-bedding. The surface is created when the depositional process is temporarily interrupted by fluctuations in wind direction causing erosion. The eroded surface becomes a reactivation surface if renewed deposition occurs in the original direction.

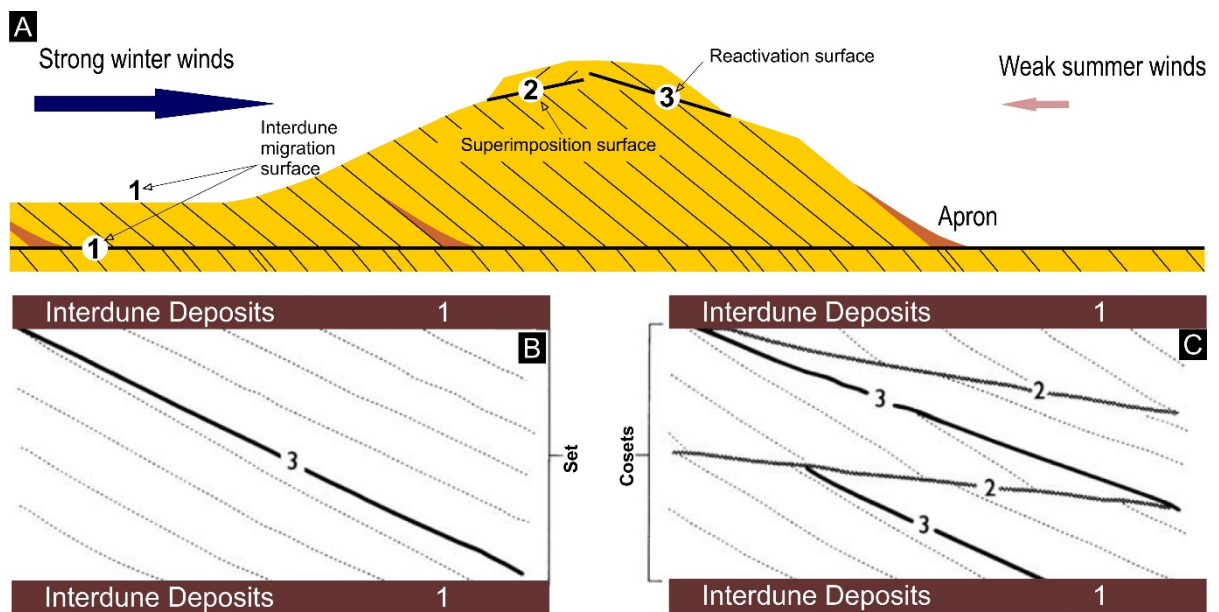


Figure 2.19: Bounding surfaces labelled (A) Idealised effect on a dune with seasonal changes in wind direction. Strong winter winds cause the dune to migrate on the interdune surface creating the first order bounding surface. During summer, weaker winds do not reverse the migration of the dune, but rather alter the structure of the dune, both eroding into the lee slope at the brink and forming a smaller superimposed dune migrating down the stoss slope of the dune, marking the second order bounding surface. On return of the stronger winter winds, deposition is reactivated on the lee slope and a third order bounding surface is apparent. (B) Migration of simple dunes and interdune areas. (C) Migration of compound/complex dunes and interdune areas. Modified after Lancaster (2005) and Neuendorf et al. (2006).

## 2.11 Supersurface

Synchronous horizons that cut all earlier surfaces are known as supersurfaces (Kocurek, 1981). These major stratigraphic surfaces extend for many kilometres through an erg (Miall, 2016). The supersurface may only consist of a thin coarse lag between identical aeolian horizons and may therefore be difficult to detect (Brookfield, 1992). The supersurface delineates a bounding discontinuity which can be used to place aeolian deposits within the context of allostratigraphy and sequence stratigraphy (Brookfield, 1992). Kocurek (1988) placed supersurfaces into three broad categories (not mutually exclusive of one another): a) Climatic change, b) changes in relative sea level or tectonic setting and c) the migration of the erg.

## 2.12 The Erg

Wilson (1972) established ergs to be large accumulations of wind-deposited sands, with a minimum area from 1 - 40 km<sup>2</sup> and covering at least 20% of the ground. In many cases, these major sand seas show a clear spatial pattern of dune types, dune size and spacing, and sediment thickness (Lancaster, 2013). They include superimposed deposits of large dunes at the centre, with other facies typically occurring closer to the margins (Miall, 2016). In a study on the sedimentary record of sand seas, Porter (1986) conceptualised an ideal model of the migrating erg by dividing the facies sequences into three components (downwind fore-erg, a central erg, and an upwind back-erg) (Figure 2.20). The central areas of the sand sea are occupied by large compound and complex dunes that represent the major area of sediment accumulation (Lancaster, 2013). Most erg margins are characterised by small barchanoid or transverse dune-fields, zibars, sand sheets and gravel pavements (Porter, 1986).

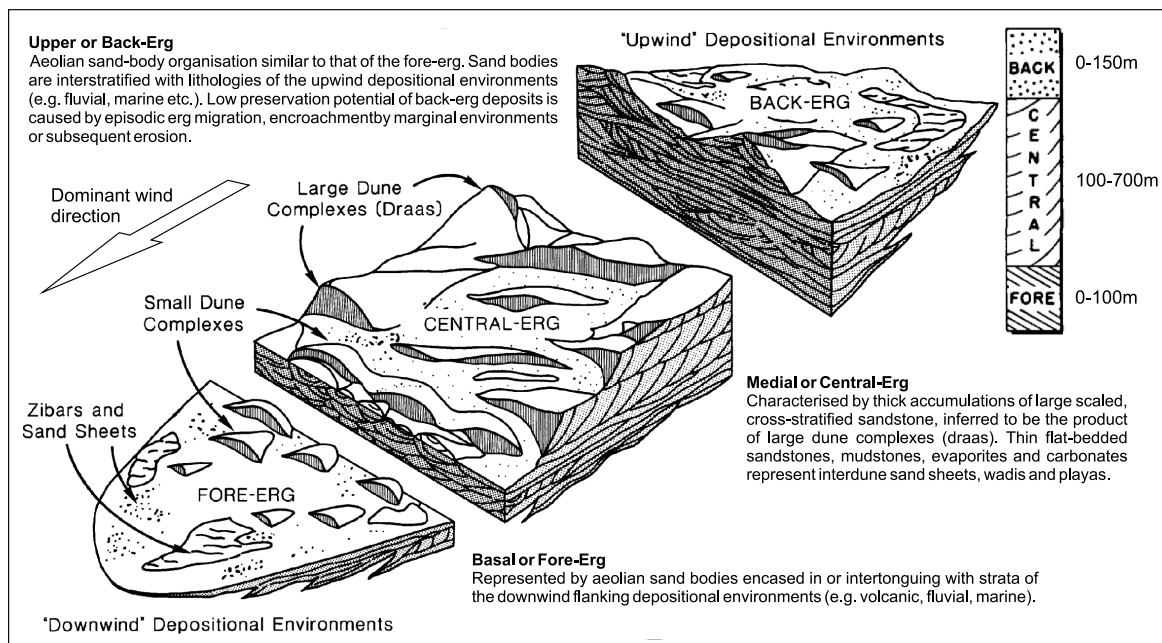


Figure 2.20: Conceptual model of the migrating erg with stratigraphic sequence of an idealised erg. Modified after Porter (1986) and Pye and Tsoar (2008).

The erg margins may be periodically encroached by fluvial, marine or volcanic processes, resulting in a complex interstratification of aeolian and non-aeolian deposits (Porter, 1986). These influences create variations to the basic erg facies sequences (Figure 2.21). Non-marine influenced cases create intertonguing of the fore-erg and central-erg strata, while marine influenced cases either create thin or absent fore-erg and back-erg (single transgression) or expanded fore-erg division (multiple-transgressions (Porter, 1986; Porter, 1987).

ERG MODEL	TYPE	INFLUENCE	FACIES SEQUENCE	EXPLANATION	EXAMPLES
	NON-MARINE	VOLCANIC		Expanded fore-erg of the idealised sequence. In tectonically active settings, volcanism may punctuate the non-marine erg. Poor back erg preservation.	Aztec Ss Botacatu Fm Clarens Fm
		FLUVIAL		Expanded fore-erg of the idealised sequence. Sandstone and mudstone deposits typical in the fore-erg division. Very large scale (5-30m) cross-stratification in the central erg. Back erg preservation enhanced by basin subsidence (rapid burial by transgressing fluvial or lacustrine environments).	Navajo-Kayenta Ss Unkpapa Ss New Red-Keuper Ss
	MARINE	SINGLE TRANSGRESSION		Abrupt facies transition on the erg margin. During lowstand the thickness and type of central-erg deposits depends upon rate of sand supplied or removed from erg, bedform organisation and duration of sea-level drop. Back-erg likely to be thin (<20m) with moderate sea-level rise or missing entirely with extremely rapid transgression.	Weissliegend Ss Entrada Ss Wonewoc Ss St. Peter Ss
		MULTIPLE TRANSGRESSION		Fore-erg division is expanded and shows a characteristic facies repetition of aeolian sandstone and marine sandstones and carbonates. Thickness of central-erg deposits vary with magnitude of sea-level change and sediment supply. Back-erg typically absent so that erg sequence is typically capped by a major unconformity.	Morgan-Weber Fm Schnebly Hill- Coconino Ss Minnelusa Fm

Figure 2.21: Tectonic, climatic and eustatic influences on erg deposition produces a distinctive variation or modification of the idealized erg facies sequence (modified after Porter, 1987).

### 2.12.1 Erg Margins and Interdune Bedforms

The margins of many ergs are marked by relatively thin sand accumulations, so-called sand sheets (Figure 2.22). Additionally in many ergs, areas of interdune or interdraa deposition occur that have many similarities to the deposits of sand sheets. The characteristics of these deposits are outlined below.

#### *Sand Sheets*

Margins of many ergs are marked by relatively thin sand accumulations known as sand sheets which form a transitional facies between aeolian dunes and non-aeolian deposits (Figure 2.22) (Leeder, 2011). Kocurek and Nielson (1986) defined sand sheets as 'areas of predominantly aeolian sand where dunes with slip faces are generally absent'. The deposit exhibits small dunes, aeolian ripple remnants, granule ridges, surface lag deposits, internal low-angle erosion surfaces and climbing ripple laminae (Figure 2.22) (Fryberger, 1979). Some sand sheets display the development of low amplitude, typically transverse ridges without slip faces known as zibar (Pye and Tsoar, 2008). Zibar are long-wavelength migrating bed forms whose surfaces are usually covered by ripples or megaripples (Pye and Tsoar, 2008).

Commonly, sand sheets occur peripherally to the main dune area, but may also be surrounded by dunes (Fryberger *et al.*, 1979). They may also form when the erg margin is bordered by a high water-table area where permanent or ephemeral streams rework erg bedforms (Leeder, 2011). Depending on their environment of formation, the thickness of sand sheet deposits ranges from a few centimetres to several tens of metres (Pye and Tsoar, 2008). The grain size of these deposits ranges from fine sand, occasionally with a significant silt component, to poorly sorted coarse sand (Pye and Tsoar, 2008). With few exceptions, sand sheet deposits have a bimodal grain size distribution and can be classified as poorly sorted (Fryberger *et al.* 1979; Pye and Tsoar, 2008).

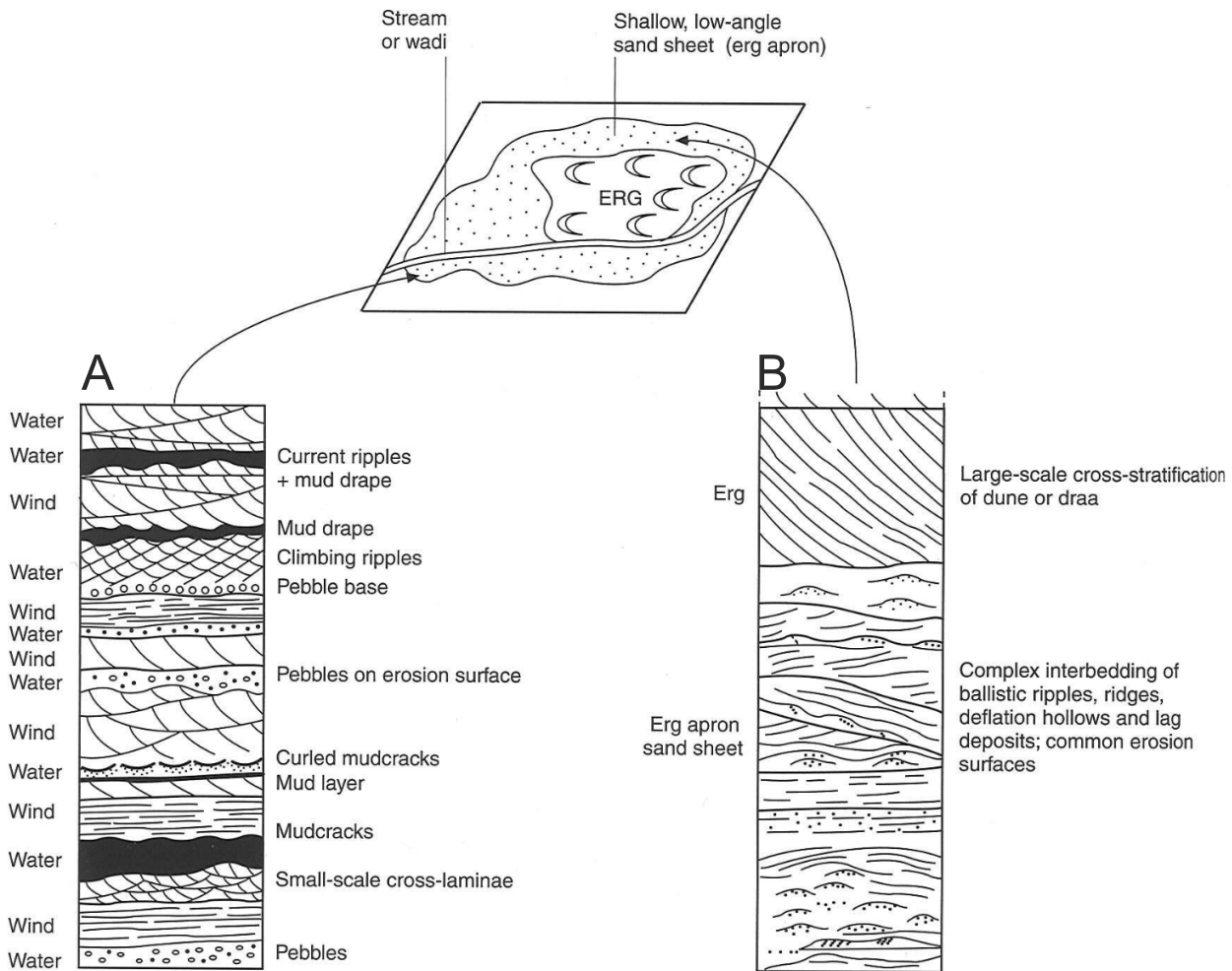


Figure 2.22: Erg margins and idealised vertical sequences. (A) Adjacent to an ephemeral stream alternating wet/dry conditions prevail. (B) Low-angle aeolian deposits of the sand sheet occurring peripheral to the erg and forming a transitional lithofacies which intercalates with high-angle dune deposits. Modified after Leeder (2011) and Fryberger et al. (1979).

### Interdune Areas

The precise nature of interdune areas depends upon the availability of sand, moisture content of the depression floor brought about by changes in the water-table level, river flooding, saline groundwater invasion or marine incursion in coastal ergs (Leeder, 2011). Sparse sand availability under dry conditions will lead to dune or draa migration over the areas of immobile sediments and non-preservation of interbedform sediment (Figure 2.23). Wet interdunes show ample evidence for deposition and commonly result from passive rise of the local water-table or rapid flooding from

adjacent ephemeral rivers (Leeder, 2011). Careful analysis of interbedform deposits can provide valuable evidence for palaeogeographical and palaeoclimactic conditions (Leeder, 2011).

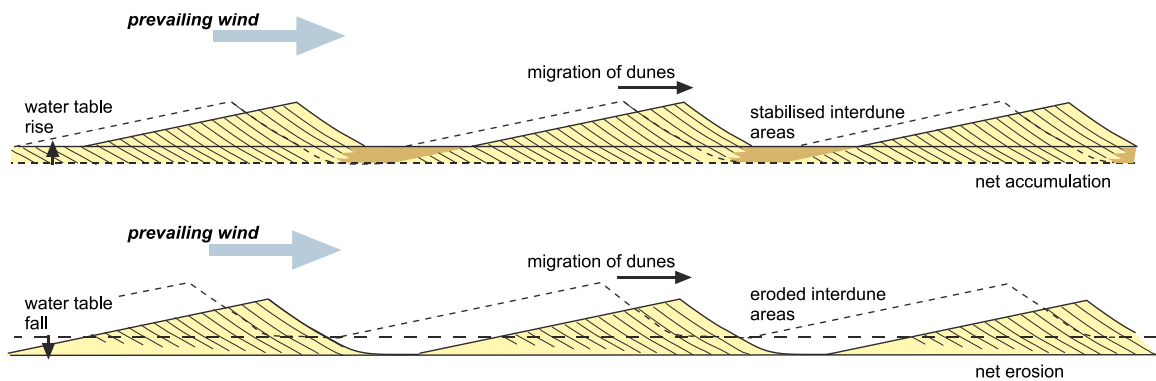


Figure 2.23: A water-table rise promotes the accumulation of sediment within the erg. A fall in the water-table from the level of the interdunes will leave more sediment available for transportation and thus removal from the area of the erg. Modified after Nichols (2009).

## 2.13 Chapter Summary

- Majority of worlds deserts lie within the 30° belts centred on the Tropics of Cancer and Capricorn, where climate is dominated by subtropical high-pressure cells with diverging trade-winds consisting of air that is descending, stable, and unlikely to produce rain.
- Glacial-interglacial activity causing significant changes in climate and sea-level over the Quaternary affected the availability and mobility of sediments, largely reflected in modern sand seas.
- Simplistically, the creation of an aeolian rock record occurs in three phases, namely sand sea construction, accumulation of a body of strata, and preservation of the accumulation.
- A hierarchy of aeolian bedforms is recognised namely wind-ripples, dunes, and draa (or megadunes). Bedforms are observed to coexist at different sizes and spacing. Compound and complex dunes form where smaller dunes are superimposed onto larger dunes.

- A variety of dune morphologies exist which is largely a manifestation of sand availability and wind direction variability.
- Dune migration occurs as sand particles saltate up the windward slope, accumulate at the crest and, upon reaching the angle of repose of sand ( $\sim 34^\circ$ ), avalanche and deposit on the lee slope. The play between erosion and deposition on the windward and lee side of a dune respectively causes the forward migration downstream.
- Three main modes for deposition on dunes includes migration of wind-ripples forming wind-ripple strata, fallout from temporary suspension in the flow separation zone forming grainfall strata, and avalanching down the lee slope of a dune forming grainflow strata.
- Commonly aeolian dunes are represented in the rock record by sets of subcritically climbing translational strata with only a fraction of the dune height is preserved. Aeolian set architectures preserve all dune-field dynamics as bedforms migrate and interact with one another.
- Aeolian bounding surfaces are erosional surfaces recognisable in preserved aeolian outcrops. These surfaces include interdune migration surface, superimposition surface and reactivation surface.
- Super surfaces are synchronous horizons and form major stratigraphic horizons delineating a bounding discontinuity that can be used to place aeolian deposits within the context of allostratigraphy and continental sequence stratigraphy.
- An erg or sand sea is a large continuous accumulation of wind-deposited sands that commonly show clear spatial patterns of dune types, dune size and spacing, and sediment thickness. Ergs may be periodically encroached by competing environments (fluvial, lacustrine, marine or volcanic) resulting in complex interstratification of aeolian and non-aeolian deposits.
- Erg margins are usually marked by relatively thin sand sheets that form a transitional facies between aeolian and non-aeolian deposits.

**PART B : A CONTEMPORARY AEOLIAN  
SYSTEM**



### 3 The Wahiba Sand Sea, Sultanate of Oman

This chapter will provide a literature review of the Wahiba Sand Sea of Oman including the geological setting, geomorphology, climate and stratigraphy. Observations within the literature have led to a hypothesis given in Chapter 4. The chapter will provide context to further analysis through remote sensing in Chapter 6.

#### 3.1 Geological Setting

The Wahiba Sand Sea covers ~16 000 km<sup>2</sup> and is located on the southeast coast of the Arabian Peninsula in the Sultanate of Oman (Figure 3.2). The erg is bound by ephemeral fluvial systems (wadis) to the west, north and east, and by the Indian Ocean at the southern rim. The accumulation of sand is attributed to deceleration of southerly winds at the foot of the Oman Mountains, accommodated in the northern sector by regional subsidence between the Oman Mountains and the Huqf Anticline (Radies *et al.*, 2004; Robinson *et al.*, 2007; Figure 3.1). The configuration has led to the creation of a sedimentary basin which extends over an area of ~10 000 km<sup>2</sup> and is filled with up to 150 m of aeolian deposits (Figure 3.3; Radies *et al.*, 2004).

The regional tectonics are primarily controlled by the subduction of the Arabian Plate under the Eurasian plate, characterised by continent-continent collision along the Zagros Mountains Suture in the west, and by subduction of remnant oceanic plate (neo-Tethys) at the Makran Subduction Zone in the Gulf of Oman (Figure 3.1) (Stern and Johnson, 2010). Initial uplift and subaerial weathering of the Oman Mountains occurred with Late Cretaceous thrusting of the Tethys oceanic lithosphere onto the Arabian continental margin (Figure 3.1; Rollinson *et al.*, 2014). Although the Persian Gulf is well understood as occupying the peripheral portion of the foreland basin that extends to the Arabian Shield (DeCelles and Giles, 1996), the tectonic setting of sedimentary systems south of the Oman Mountains is less defined owing to the complex development thereof. If the Oman Mountains represents a forebulge, the sedimentary systems south of the mountains occupy the backbulge basin (Figure 3.1).

The mountains comprise three major tectono-stratigraphic units (Table 3.1; Hanna, 1990): 1) a pre-Permian basement (Huqf Supergroup) overlain unconformably by mid-Permian to Cenomanian platform carbonates of the former Arabian margin (Hajar Supergroup); 2) Relating to the initial uplift and weathering of the Oman Mountains when at least 300 km of nappe thrusting occurred (Searle and Cox, 1999): Permian to Cenomanian rocks composed of relative autochthonous and allochthonous units (Sumeini, Hawasina and Semail groups); 3) The upper unit of neo-autochthonous sedimentary cover of Late-Campanian to Tertiary age (Aruma, Hadhramaut, Dhofar and Fars Group). Tectonic extension by normal faulting facilitated deposition of latest Cretaceous to early Miocene sediments (Dhofar and Fars Groups) (Fournier *et al.*, 2006).

Post-obduction uplift of the Oman Mountains is taken at the Eocene-Oligocene boundary, the dynamics of which remain debated (see discussion in Hansman *et al.*, 2017). An estimated 2 km of uplift of the Oman Mountains occurred since the Late Eocene, 400 m since the middle Miocene, and 100-500 m during the Quaternary (Hansman *et al.*, 2017; Kusky *et al.*, 2005). Neotectonics include Quaternary displacement along faults (Kusky *et al.*, 2005), structural controls evident in wadi drainage patterns (Robinson *et al.*, 2007), vertical motion forming marine terraces (Yuan *et al.*, 2016), and historical records of earthquakes since 879 AD (El-Hussain *et al.*, 2012).

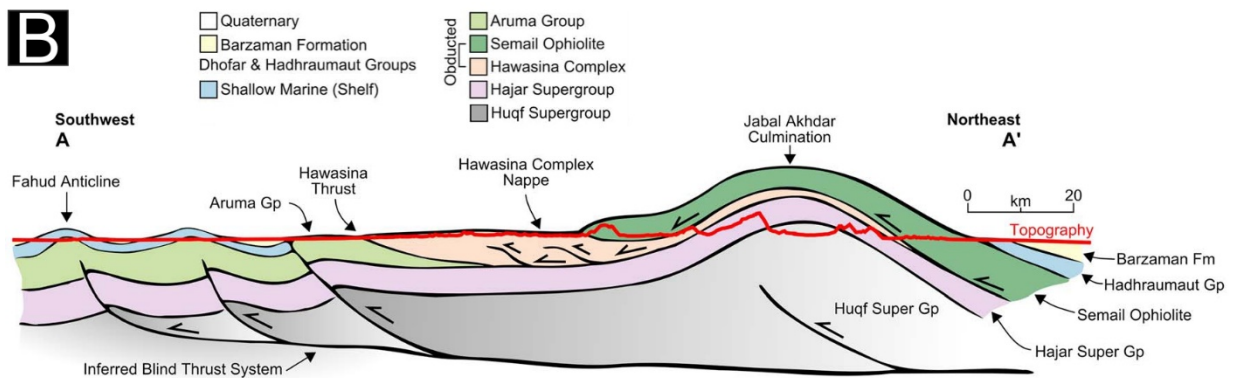
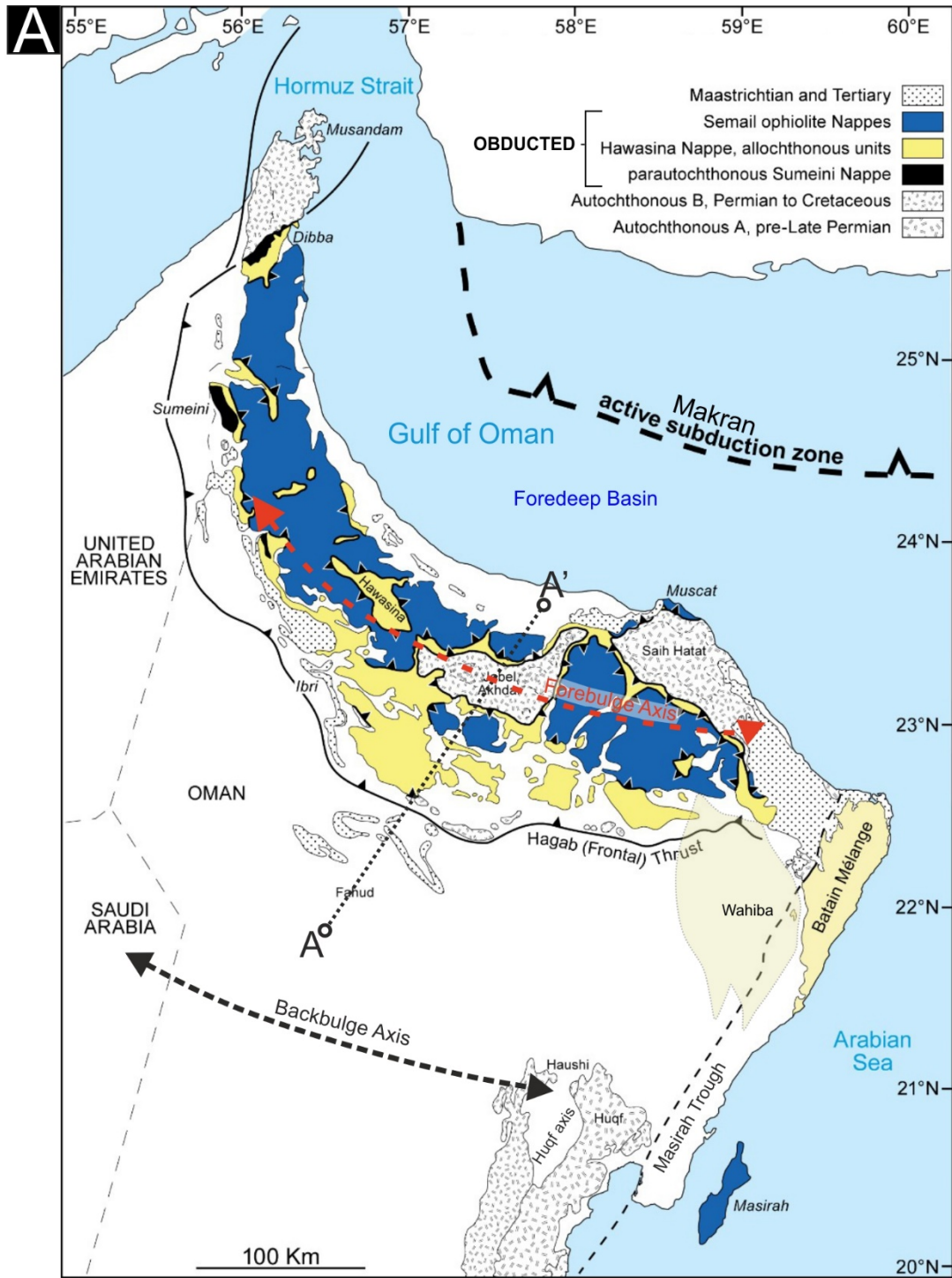


Figure 3.1: A) The geological setting of northern Oman and approximate position of the Wahiba Sand Sea. The Gulf of Oman is flooded by Cretaceous oceanic crust currently subducting northward below the Makran active continental margin of Eurasian continental lithosphere. In northern Oman, the oceanic lithosphere is thrust onto the continental margin forming the Oman Mountains. The Wahiba erg has accumulated south of the Oman Mountains. Foreland basin system terminology is that of DeCelles and Giles (1996). B) Structural profile A-A' through the Oman Mountains. The section includes the stratigraphic units from the Gulf of Oman to Fahud oil field. Adapted after Hanna (1990). For information on rock types, see Table 3.1. A) and (B) are modified after Burg (2018) (<http://www.files.ethz.ch/structuralgeology/JPB/files-/English/Omaneng.pdf>) and Hansman et al. (2017) respectively

Table 3.1: Simplified stratigraphy of the Oman Mountains. Compiled from Hopson et al., 1981; Hanna, 1990; Allen, 2007; Stern and Johnson, 2010; Hansman et al., 2017.

Tectono and lithostratigraphic units		Period / Epoch	Emplacement / Depositional Environment	Rock Types
3	Fars Group	Tertiary	Deep marine slope to shallow marine shelf deposition	Limestones, shale, conglomerates
	Dhofar Group			
	Hadhramaut Group			
	Aruma Group	Late Cretaceous	Syn-to-post-orogenic cover (terrigenous to shallow marine)	Conglomerates and shallow water limestones
	Semail Nappe		Oceanic lithosphere	Ophiolitic sequence: Ultra-mafic to mafic igneous
2		Permian to Late Cretaceous	Ocean basin: Proximal to distal deep-sea deposition	Limestones and chert, may be locally interlayered with minor (<50m thick) basaltic rocks (Hopson et al., 1981)
				Haybi Melange: Shale, volcanics, exotic limestones, chert
			Sumeini Nappe	Carbonate slope deposition
1	Hajar Supergroup	Pre-Permian	Continental shelf deposition	Limestones, dolomites and sandstones
	Huqf Supergroup		Basement rocks	Schists only exposed in relatively small windows

As a result of the tectonic and climatic setting of the Oman Mountains, vast low gradient Bajada cover the interior of northern Oman (Rodgers and Gunatilaka, 2003). The Bajada comprises old fan successions of inferred Miocene to Pliocene age, termed the Barzaman Formation, that are overlain by a thin veneer of Quaternary alluvial fan and wadi deposits (Blechsmidt *et al.*, 2009). Alluvial fans systems, coastal sands and sabkha are inferred to be the main sediment sources of the Wahiba (Pease and Tchakerian, 2002). Through observations of sand colour both on the ground and in satellite imagery, Goudie *et al.* (1987) hypothesised the Wahibas were primarily derived from pale coastal sands and secondarily from dark wadi sediments in the northeast and west. Following mineralogical, geochemical and grain-size studies Pease and Tchakerian (2002) divided the sediment sources suggesting the sands in the northern sector were derived primarily from the wadis that drain the adjacent Oman Mountains (limestones and basic rocks), while in the southern sector sediments are more likely derived from surrounding sabkha deposits, the underlying reworked aeolianites, and carbonate rich coastal sands to the south of the sand sea. Radies *et al.* (2004) showed that the oldest aeolian deposits were associated with both a rich and diverse assemblage of coastally derived bioclastic grains and a significant continental component of quartz, feldspars, pyroxene and a suite of heavy minerals. Further regional remote sensing studies conducted by Robinson *et al.* (2007) concluded that northwest to southeast trending faults dominated the landscape in humid climatic phases and structurally controlled the fluvial systems from the Oman Mountains, providing much of the original sediment that filled the Wahiba basin. This fill was subsequently reworked by aeolian processes in more arid periods.

## 3.2 Geomorphic Regions

The Wahiba erg has been divided into various zones depicting geomorphic regions by numerous authors in the past (e.g. Goudie *et al.*, 1987; Jones *et al.*, 1988; Preusser *et al.*, 2005; Glennie *et al.*, 2011). Two major zones covering the analysed megadune topography are reported here using remote sensing observations (see datasets section 0) and published literature (Figure 3.2 and Figure 3.4):

(1) The 'High Sands' in the north, composed of N-S trending ( $350^{\circ}$ -  $020^{\circ}$ ) megaridge topography separated by flat corridors clearly visible from satellite imagery. The megaridges are asymmetrical complex linear megadunes up to 100 m in height and spaced on average 1.5 km apart. The asymmetry is commonly characterised by a gentle east facing slope, a bulged crestal region and a steep west facing slope, however, the reverse configuration is also observed in some instances. The flat corridors, or interdunes are the remains of former lakes (Figure 3.11) (Preusser *et al.*, 2005) with some containing freshwater gastropods (Radies *et al.*, 2004). On the northwestern margin of the erg, low bedrock outcrops of the Permian to Middle Cretaceous Hawasina Group are exposed in interdune corridors (Figure 3.2B). Both megadunes and interdunes are crossed obliquely by long meso-scale bedforms (seif dunes) that trend north to north-northwest ( $000^{\circ}$  -  $340^{\circ}$ ). The megadunes in the High Sands host both seif dunes and crescentic dunes superimposed onto their stoss slopes.

(2) The 'Low Sands' to the south are composed of north-northeast to south-southwest trending ( $010^{\circ}$ -  $020^{\circ}$ ) subdued compound linear megadunes. In cross-section, the megadunes show both symmetrical and, more commonly, asymmetrical geometries. The megadunes are up to 60 m in height and spaced on average 1.9 km apart. Where the dunes are asymmetrical, a steeper east facing lee slope is frequently present. The megadunes and interdunes are crossed by long, narrow north-south trending seif dunes, 4–6 m high and spaced on average 160 m apart (Goudie *et al.*, 1987). The seifs dominate the topography as they traverse interdune corridors and are superimposed onto the main bedform. At

the resolution of the satellite imagery, no superimposed crescentic dunes, comparable to those observed commonly in the High Sands, are apparent.

Surrounding the High and Low Sands there are a number of sandy marginal areas which have been termed the peripheral sands (Figure 3.2B) (Goudie *et al.*, 1987; Pease and Tchakerian, 2002). These sands host both active and inactive dunes interspersed with areas of desert pavement and outcrops of bedrock and 'aeolianite' (weakly cemented aeolian sandstone) (Goudie *et al.*, 1987). The western part of the peripheral sands, known as the Al Jabin Plateau, contains outcrops of older aeolianites (informally labelled 'Al Jabin Unit') exposed by fluvial erosion of the Wadi Andam, and a widespread deflated aeolian surface (Radies *et al.*, 2004). The coastal sands to the east (Figure 3.2B) contain active transverse dunes with numerous outcrops of younger aeolianites (informally labelled 'Qahid Unit') in the interdunes and exposed in sea cliffs up to 20 m high (Goudie *et al.*, 1987; Gardner, 1988; Radies *et al.*, 2004).

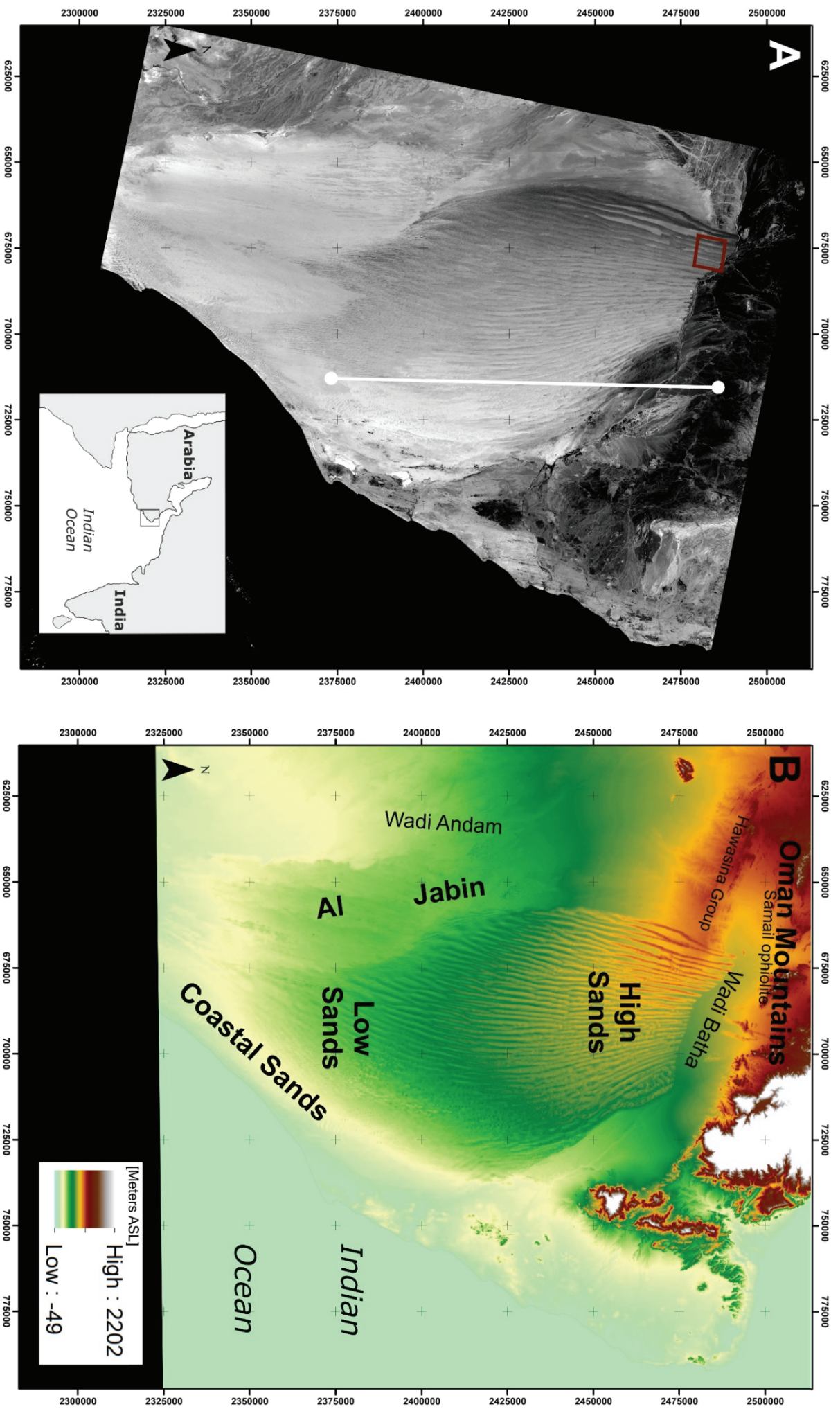


Figure 3.2: A) Satellite image (Landsat-8 panchromatic 15m, LC08\_L1TP\_157045\_20190527\_20190605\_01\_T1\_B8\_@USGS) with schematic inset showing the location and extent of the Wahiba Erg. The N-S trending white line is the seismic line profile shown in Figure 3.3. The red box in the NW corner of the sand sea is the location of the Geofeye-1 and Worldview-3 dataset of section 5.4. B) Digital Surface Model 30 m (Advanced Land Observing Satellite AW3D30, @JAXA) showing the principle geomorphological regions of the Wahiba (High Sands, Low Sands, Al Jabin and Coastal Sands). The two datasets were displayed in GIS software and measurements incorporated into a GIS database. UTM coordinate grid with 25 km spacing for scale.

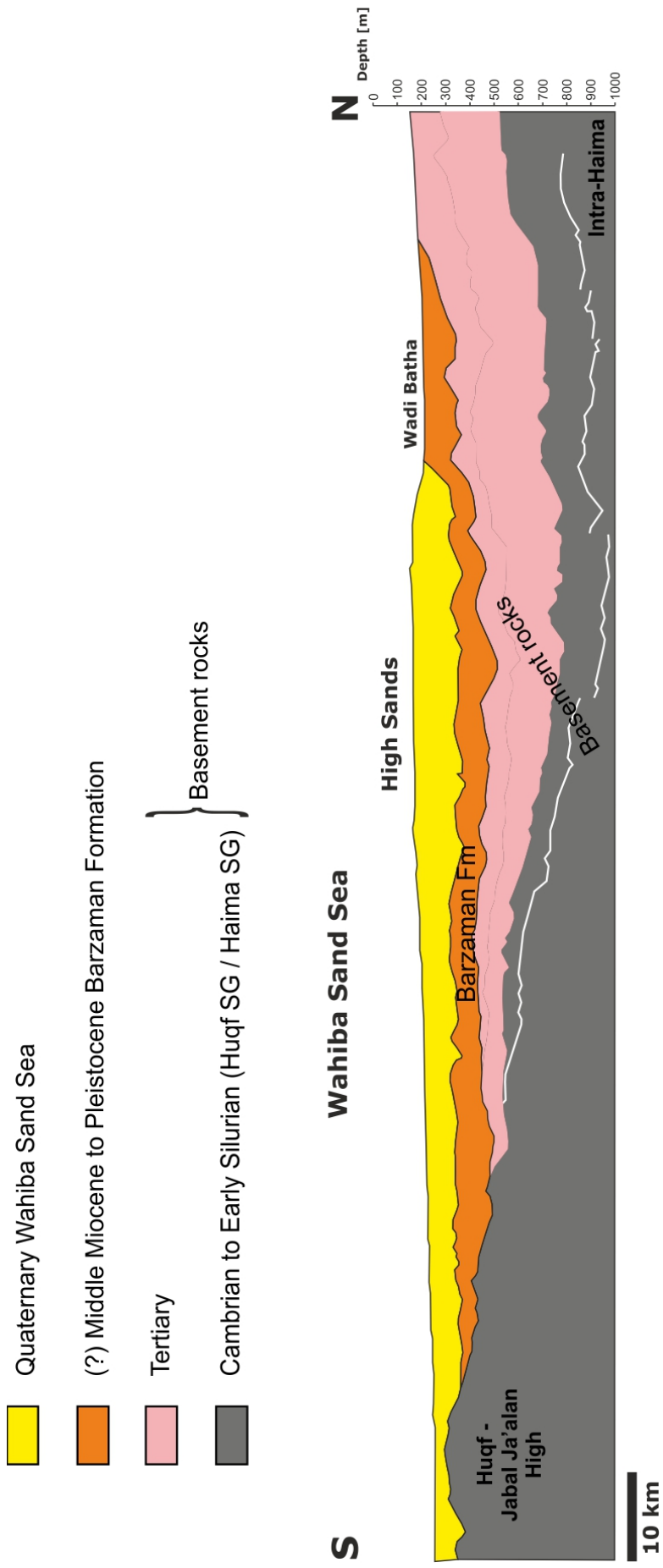


Figure 3.3: Interpreted seismic line (white line shown in Figure 3.2A) across the Wahiba Basin (Radies et al., 2004). The cross-section shows a down-warped basin with up to ~250 m of Barzaman (alluvial fan deposits) and aeolian strata in the High Sands.

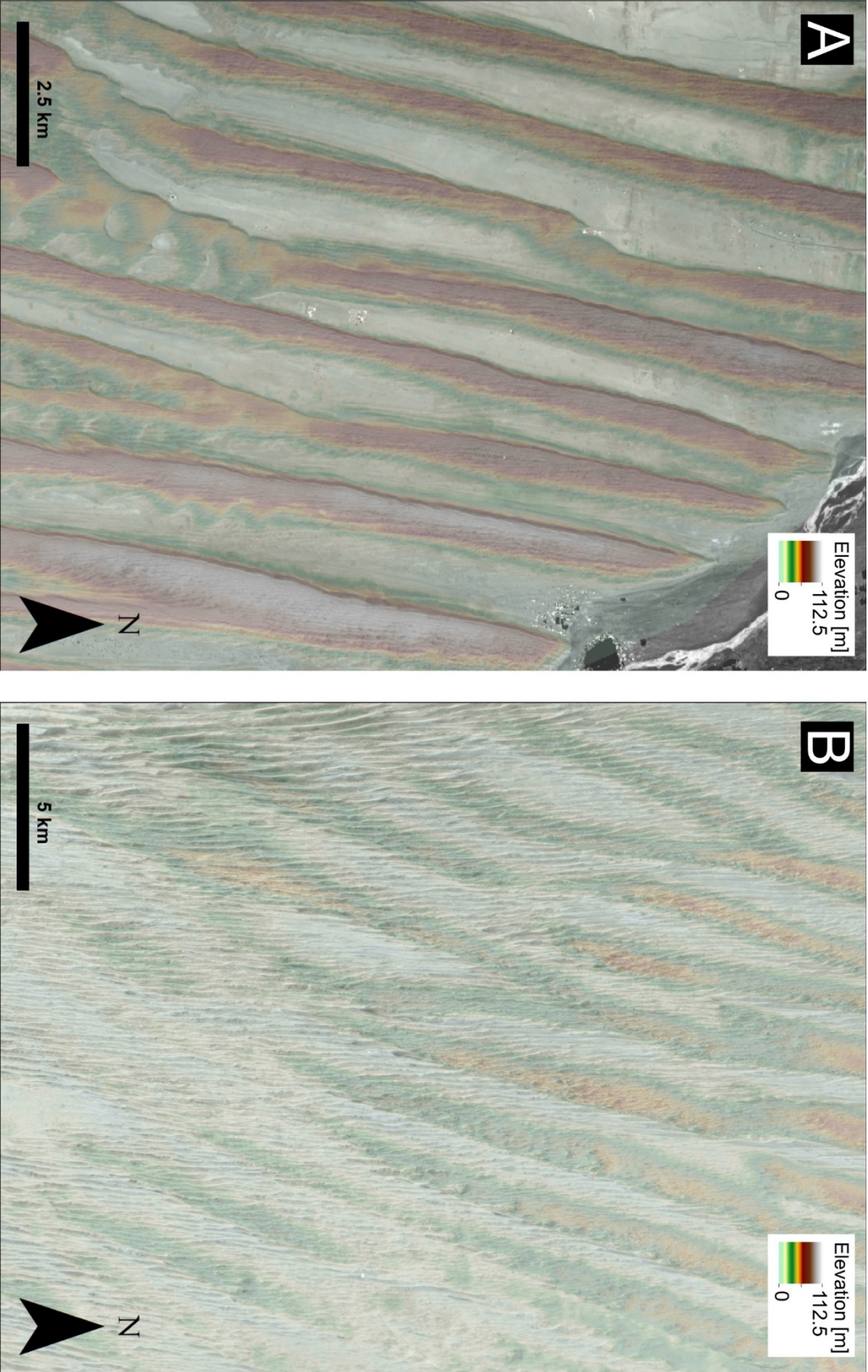


Figure 3.4: The megadune morphology in the A) High Sands and B) Low Sands. The DSM has been overlain onto the orthophoto to clearly differentiate the megadune and interdune morphology. Note the faint N-S trending lineation's representing the superimposed dunes.

### 3.3 Climate

#### *Wind Regime*

The winds across the globe are largely driven by differences between the cold polar regions of high atmospheric pressure and the equatorial zone of low-atmospheric pressure, also known as the Intertropical Convergence Zone (ITCZ) (Lashkari *et al.*, 2017). Located in the sub-tropics, the winds acting on the Wahiba erg are largely resultant from the Indian monsoon and the position of the ITCZ (Lashkari *et al.*, 2017). The major wind systems are the summer/winter monsoonal and 'Shamal' winds (Figure 3.5).

The development of the summer Indian monsoon corresponds to the northward migration of the ITCZ which forms a belt of low pressure over southwest Asia. The development of a high pressure over the Arabian Sea causes regional energetic and persistent south to southwesterly winds to form (Chaichitehrani and Allahdadi, 2018). On the eastern Arabian Peninsula, the ITCZ is positioned approximately parallel to the coast from May to September and shifts as far inland as the Oman-Saudi Arabia border from July to August (Lashkari *et al.*, 2017). Over this period of maximum incursion, the strong south to southwesterly monsoonal winds deflect inland to merge with the ITCZ. This results in the formation of the dominant south to southeasterly winds that affect the Wahibas over the summer monsoonal period (Figure 3.5A,B). The summer Shamal winds are associated with severe dust storms and occur in response to high pressure over the eastern Mediterranean and a low pressure over Iran, Pakistan and northwest India (Hamidi *et al.*, 2013). The north to northwesterly winds are deflected to merge with the ITCZ forming periodic but strong southwesterly winds over the Wahibas (Figure 3.5C).

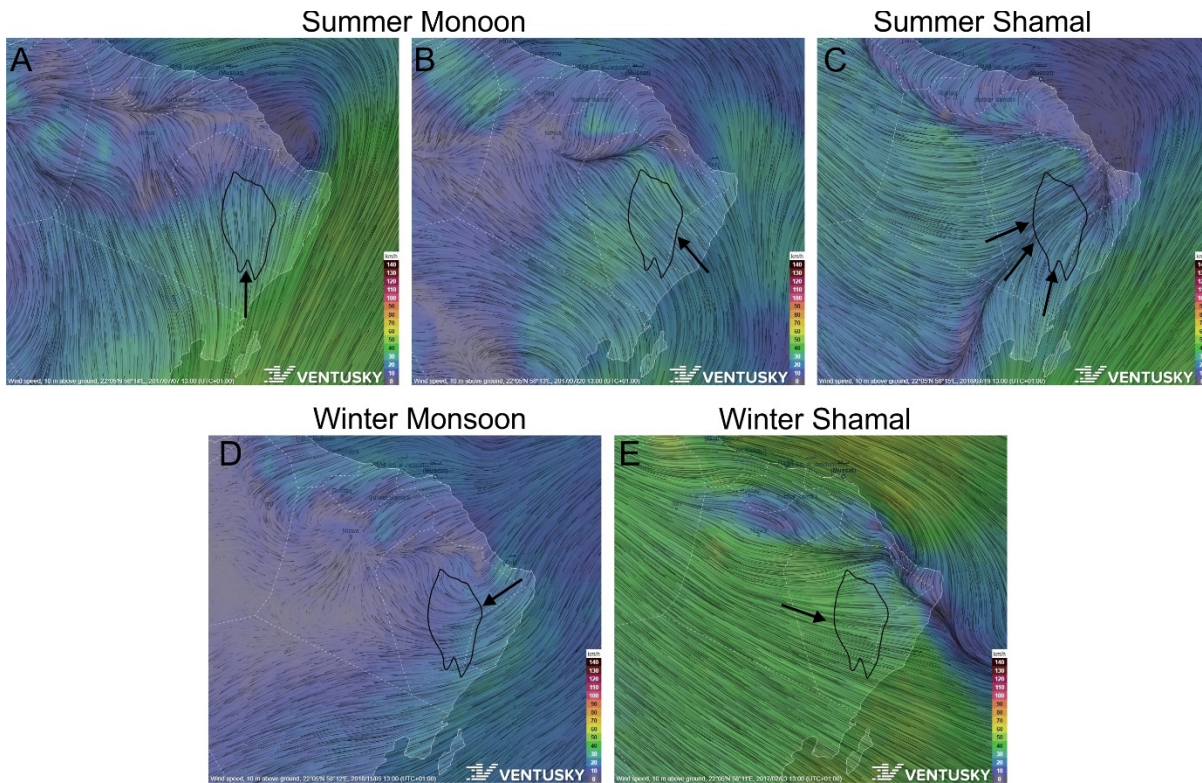


Figure 3.5: Examples of common wind vectors that affect the Wahiba Sand Sea (outlined in black). In summer, the strong and prevalent south to southeast winds that occur with the Indian monsoon act as the dominant winds that affect the Wahibas. In winter, the intense but short duration winter Shamal winds from the northwest act as the subordinate winds that affect the Wahibas. The weak but persistent monsoonal northeasterlies have little influence in winter. The ITCZ is approximately marked by the merging winds and its position is crucial in the movement and divergence of winds across the region. Extracted from [www.ventusky.com](http://www.ventusky.com).

In the winter period (November to April) the ITCZ migrates southwards and the locations of the high and low-pressure systems are reversed. A low-pressure system is persistent over the Indian Ocean while the centre of the high-pressure system moves over the continental landmass north of the Indian Ocean (Chaichitehrani and Allahdadi, 2018). This seaward pressure gradient is weak and contributes to low velocity north to northeasterly winter monsoonal winds over the Wahibas (Figure 3.5D). Following the passage of a cold front the high-pressure system is strengthened and, in conjunction with a deep trough of low pressure maintained in areas east of the Persian Gulf, a strong north to northwesterly wind forms and extends over Oman (Hamid Ali, 2009). These northwesterly Shamal winds (Figure 3.5E) are short but intense and while they act as the dominant winds affecting the Wahibas over the winter period, they are subordinate to the summer monsoon winds.

## *Drift Potential*

Sand drift is the process of sand movement across the desert as a result of surface winds. Sand drift can be quantified (refer to Fryberger, 1979) with values reflecting the sand-moving capacity for a given time-period of wind summary. This is known as the drift potential (DP) and is numerically expressed in vector units (VU). Vector unit totals from different directions may be resolved into a single resultant, referred to as resultant drift direction (RDD). The magnitude of the RDD is known as the resultant drift potential (RDP) and expresses, in vector units, the net sand transport potential when winds from various directions interact (Fryberger, 1979). The ratio of the resultant drift potential to drift potential (RDP/DP) is an index of directional variability (between 0 and 1) (Fryberger, 1979). A RDP/DP index of 1 indicates unidirectional winds. The lower the value is below 1, the higher the directional variability of the wind (Fryberger, 1979). Although vector units imply dimensionless values (Fryberger, 1979), the drift potential equation shows that DP are in fact equivalent to wind speed units cubed, e.g. (m/s)<sup>3</sup> (Livingstone *et al.*, 2019).

A belt of high wind energy occurs on the east coast of Oman (Fryberger *et al.*, 2016b; Figure 3.6). A wind energy gradient exists in the Wahibas with values decreasing from ~850 VU on the eastern margin to <500 VU on the western margin. Directional variability is also shown to decrease from the east to west with an index of ~0.8 in the east, decreasing to 0.6 on the western margin (Fryberger *et al.*, 2016b). The wind regime along the coast are thought to be regionally compatible with dune morphologies (Fryberger *et al.*, 2016a), however, longer term monitoring is required for more meaningful interpretations.

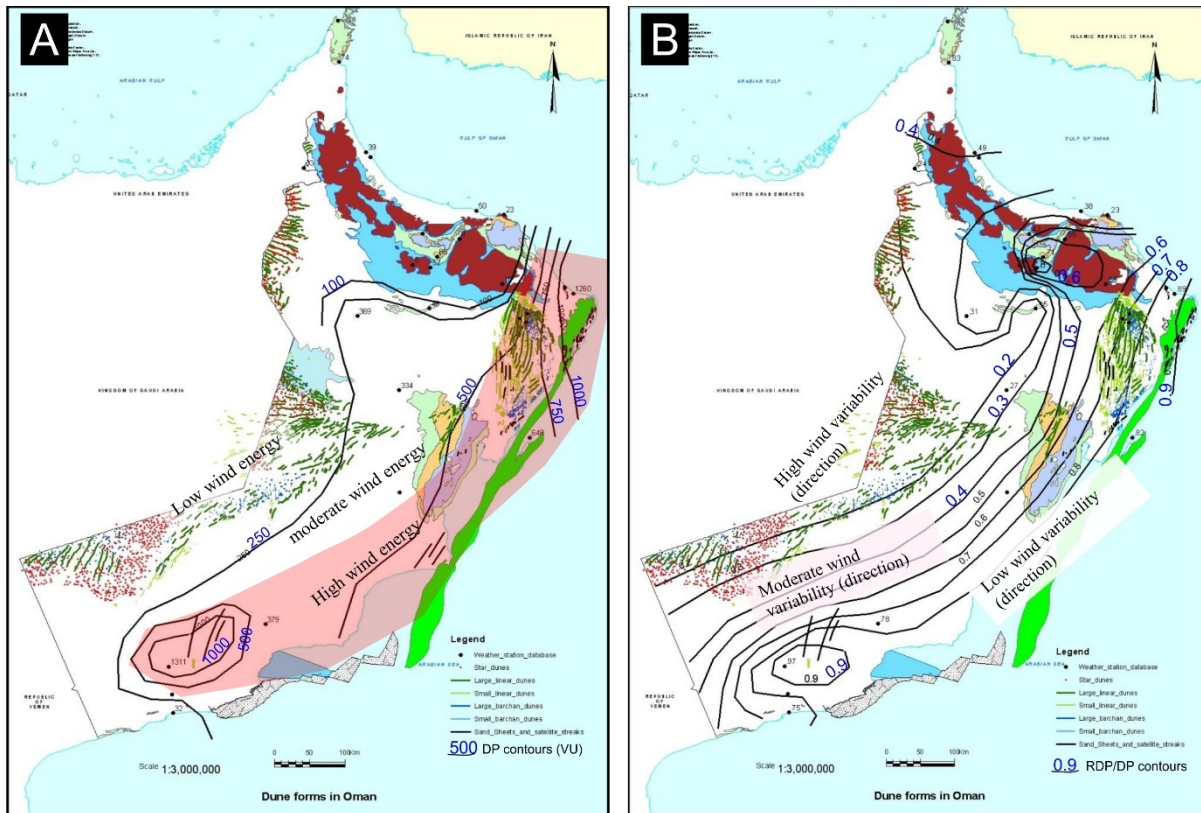


Figure 3.6: A) Annual drift potentials (sand moving power of the wind) and B) directional variability of the wind (RDP/DP) contoured across Oman. Maps modified after Fryberger et al., 2016a, b.

### Temperature and Precipitation

The temperature pattern over Arabia differs considerably between summer and winter. In summer, mean July isotherms show a belt of high temperature above the 30 °C isotherm. During winter, average temperatures are much more variable (as exemplified by January in Figure 3.7), ranging between 10 °C and 20 °C. Nevertheless, the greatest effect on the desert climate of Arabia is caused by the temperature differential extremes between day and night. These variations can be so great that it causes rocks to crack and exfoliate, contributing to the fragmental material that fills piedmonts and dune-fields (Edgell, 2006).

Arabia lies in a subtropical zone where its climate is influenced by the descending cool dry air of a Hadley Cell, which dynamically suppresses convection and warms as it rises with clouds being

suppressed. Rainfall is irregular from year to year; when it falls it is usually during the winter months and is less than 100 mm classifying the region as hyper-arid (Figure 3.8) (Ghazanfar, 1992; Edgell, 2006). Small pockets in the central core of the Oman Mountains have rainfall of up to 350 mm annually, but most of this mountain arc receives between 100–200 mm and can be classed as arid. The primary rain mode is winter to early spring (January to April) with a secondary mode occurring during the summer (July to August). Due to its location and long coastline along the Arabian Sea, Oman is regularly impacted by tropical cyclones which can bring several days of heavy rain (Figure 3.8).

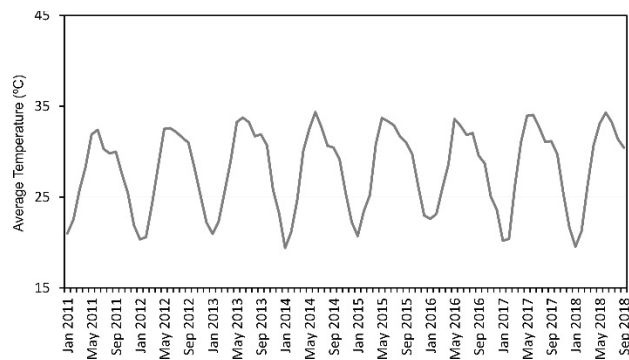


Figure 3.7: Average temperatures (degrees Celsius) for the Ash Sharqiyah Governate of Oman. Data Source: National Centre for Statistics and Information, Sultanate of Oman (<https://data.gov.om/>)

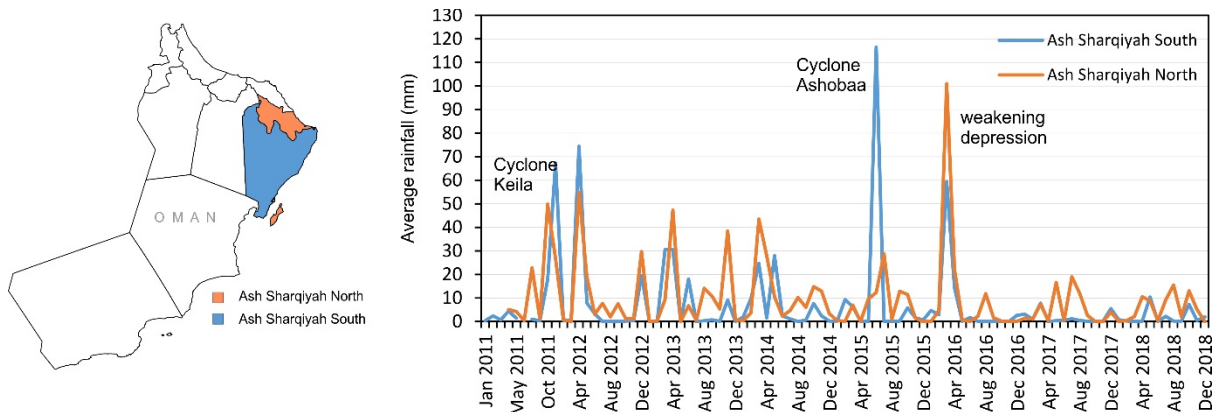


Figure 3.8: Average rainfall for the Ash Sharqiyah north and south Governates of Oman. Known storms that have brought heavy rain are marked on the chart. Source: National Centre for Statistics and Information, Sultanate of Oman (<https://data.gov.om/>).

### 3.4 Stratigraphy

The Wahiba stratigraphy has been resolved through seismic (Radies *et al.*, 2004; Figure 3.3), studies of outcropping aeolianites (Juyal *et al.*, 1998; Fryberger *et al.*, 2016a), trenching (Fryberger *et al.*, 2016a; Hern *et al.*, 2018), core extraction (Preusser *et al.*, 2002), luminescence dating (Juyal *et al.*, 1998; Glennie and Singhvi, 1998; Preusser *et al.*, 2002, 2005; Radies *et al.*, 2004; Hern *et al.*, 2018) and ground penetrating radar (GPR) (Nursaidova, 2009; Tatum *et al.*, 2012; Hern *et al.*, 2018). The most complete vertical record of the High Sands subsurface was carried by means of two cores drilled into a megadune crest and associated interdune (WDR-1 and WDR-2 of Preusser *et al.*, 2002; Radies *et al.*, 2004; Preusser, 2009) (Figure 3.9). One additional OSL date was obtained by trenching on a linear dune stoss slope (Site 4 of Hern *et al.*, 2018) (Figure 3.9).

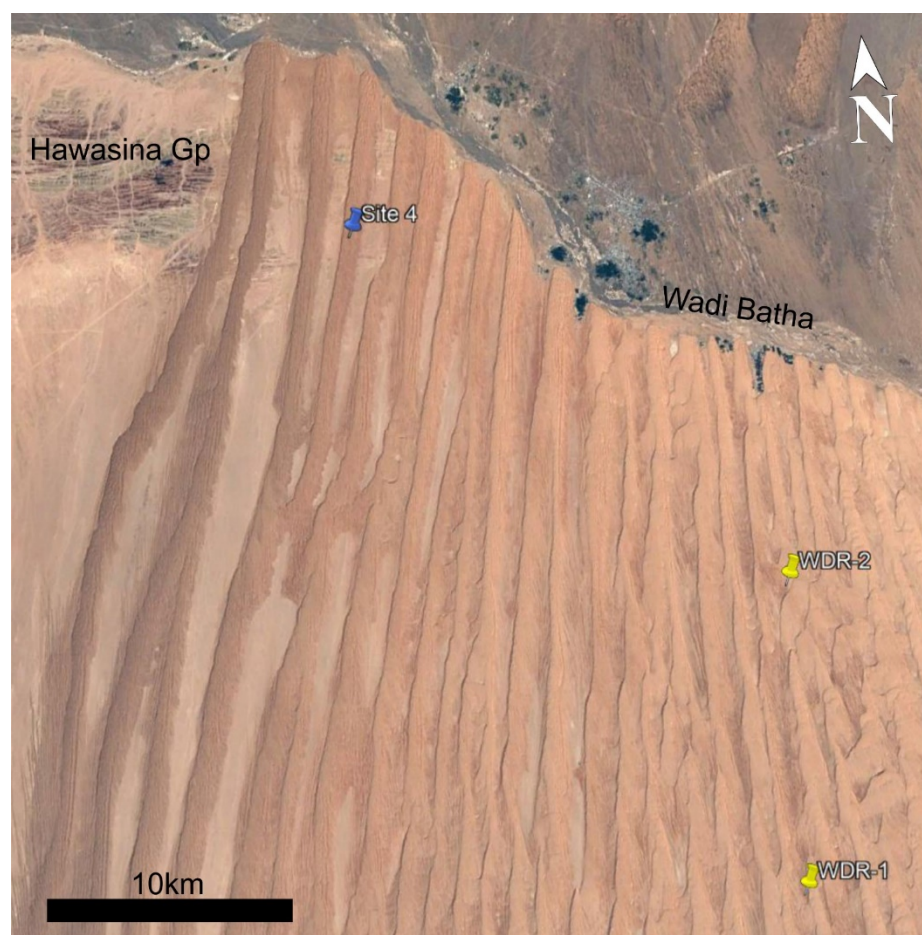


Figure 3.9: Location of three sites where stratigraphic dating occurred (reported in section ). WDR-1 and WDR-2 (yellow pins) are core locations of Preusser *et al.* (2002). Site 4 (blue pin) is a trench and GPR site of Hern *et al.* (2018). Table 4.1 provides precise coordinates of sites. Google Earth™ image (2016).

### 3.4.1 Core Sites

Figure 3.9 shows the locations of the two cores described below. Core WDR-1 is located in the High Sands approximately 22 km south of the dune-field's northern boundary and was drilled down from interdune level to a depth of 144 m. Core WDR-2 was drilled 66 m through a 70 m high linear megadune approximately 12 km north of core WDR-1. The cores were logged and sampled approximately every 3 m for dating using infrared stimulated luminescence (IRSL) techniques. Methodology of the dating procedure with results are reported in supplementary data section of Preusser *et al.* (2002) and the plotted data are presented here in Figure 3.10. The sedimentary logs of both cores can be found in Figure 3 of Radies *et al.* (2004) with key observations outlined below.

Based on sedimentological observations, IRSL-dating and petrographical data, five aeolian units and two fluvial units were identified (Radies *et al.*, 2004). The oldest fluvial unit consists of the (?)middle Miocene – Pleistocene Barzaman Formation unconformably overlying Tertiary basement rocks (Figure 3.3). The Al Batha Unit disconformably overlies the Barzaman Formation and is intercepted in Core WDR-1 although with very poor age constraints but approximated at 125 Ka (Figure 3.10) (Radies *et al.*, 2004).

### 3.4.2 Aeolian Units

Four aeolian units were intercepted in cores WDR-1 and WDR-2 (Figure 3.10). Excepting the oldest and fifth aeolian unit (Al Jabin Unit), the below section mainly focuses on IRSL ages extracted from the two cores in the active dune-field. From oldest to youngest, the five informal aeolian units making up Wahiba stratigraphy are:

- 1) The Al Jabin Unit (130 – 160 Ka; mean 153 Ka) on the western periphery studied through sections of aeolianites on the edge of the Al Jabin Plateau (Juyal *et al.*, 1997; Figure 3.2). In core, the unit consists of intervals of aeolian sets (0.5 – 6 m thick) separated by bioturbated or calcrete paleosol horizons and sediment. Foreset dip directions range between 320° – 040°

indicating northward dune migration. The unit is capped by a sabkha deposit with pedogenic overprint, which separates it from the overlying Al Hibal Unit (Preusser, 2009).

- 2) The Al Hibal Unit (84 – 133 Ka; mean 109 Ka) is intercepted in the lowermost 3 m of core WDR-2 as well as 82 m of core WDR-1 and is correlated with erosional aeolianite remnants on the Al Jabin Plateau (94 – 131 Ka). In core, the unit consists of sets of cross-strata (~1 m thick) with four pedogenic calcretes (1-1.5 m thick). Northward bound dune migration is recognised, and the unit is taken to generally represent the body of aeolian sand below the current interdune level (Preusser *et al.*, 2002; Radies *et al.*, 2004; Preusser, 2009).
- 3) The Hawiyah Unit (63 – 80 Ka; mean 71 Ka (n=4); outlier at 90 Ka) is intercepted in 17 m of core WDR-2 and is not identified in any surrounding outcrops. The unit consists of cross-bedded sets, contains no soil horizons and considered to be a period of minor deposition with reduced aeolian accumulation (Radies *et al.*, 2004; Preusser, 2009). Due to the quality of the core, palaeoflow is unknown.
- 4) The Qahid Unit (18 – 22 Ka; mean 20 Ka) is intercepted in 15 m of core WDR-2 and correlated with the aeolianites in the peripheral coastal sands. It is divided into three subunits from surrounding outcrops with dates ranging from 35 – 8 Ka (Radies *et al.*, 2004). While no accurate measurements are available, Radies *et al.* (2004) alludes to a northerly transport direction based on an exposed outcrop on the northern tip of the dune-field (sample location WBT1/2). The correlative coastal aeolianites however indicate transport towards the E to ENE (Preusser *et al.*, 2002; Radies *et al.*, 2004). A more recent study carried out in the High Sands (Site 4 of Hern *et al.*, 2018) acquired a sample for optically stimulated luminescence (OSL) age dating from a 1 m deep trench on the stoss slope of a megadune ~22 km NW of core WDR-2 (Figure 3.9). The sample is dated at 18.1 Ka  $\pm$  2.3 Ka placing the surface within the Qahid Unit (see section 4).
- 5) A Holocene Unit (2Ka to present; mean age of 1.8Ka) comprises the upper 27 m of core WDR-2. The above 'Unit' however shows a single basal age of 12.3  $\pm$  0.9 Ka (Figure 3.10).

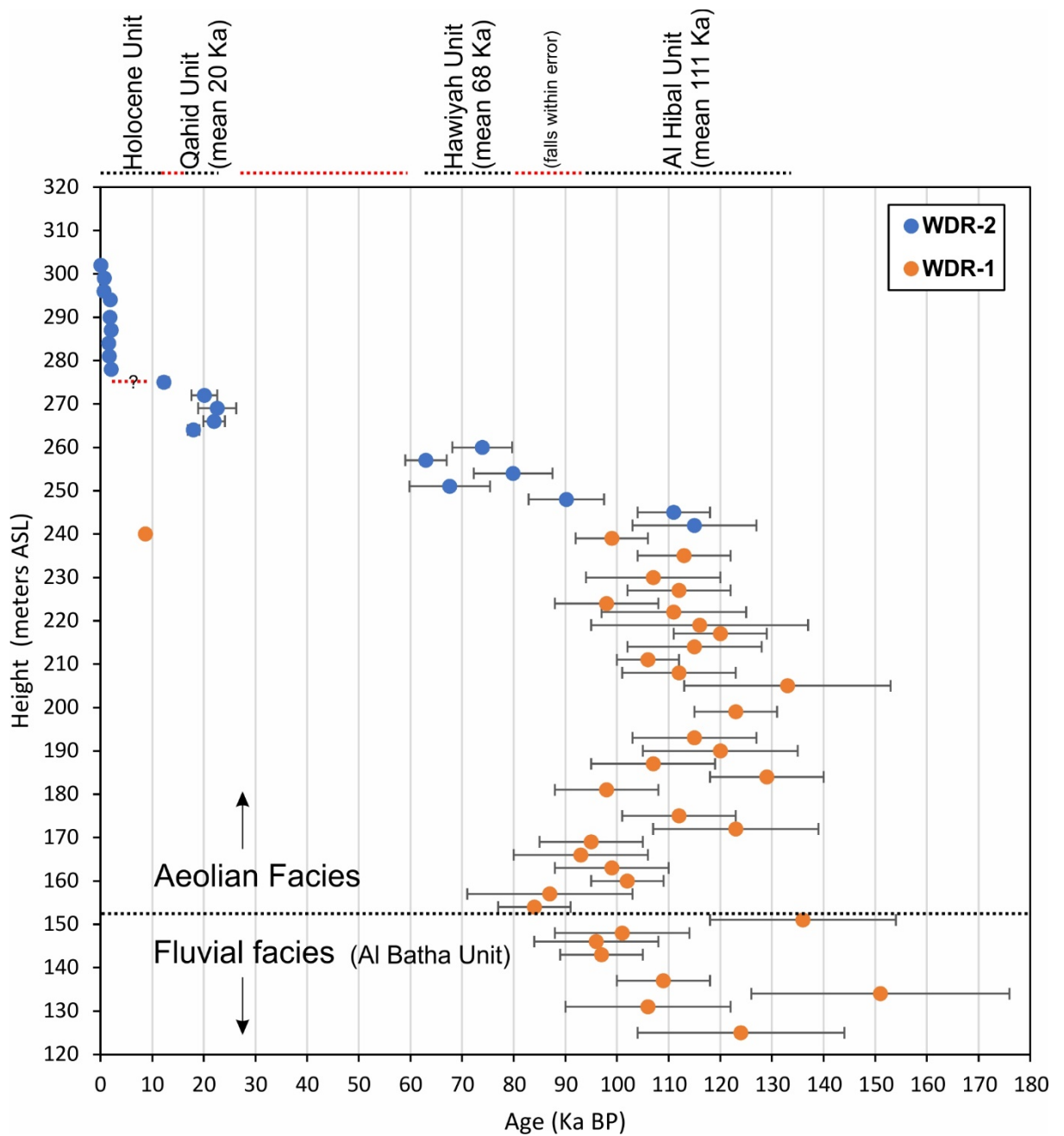


Figure 3.10: Plotted IRSL dates including error bars for cores WDR-1 and WDR-2 (raw data extracted from Preusser et al., 2002 supplementary files). Twenty-one dates extracted from core WDR-2 (blue circles) drilled through the crest of a linear megadune (302 m – 242 m ASL) and thirty-five dates extracted from core WDR-1 (orange circles) drilled through an interdune (240 m – 125 m ASL). The red dashed line highlights time-gaps between constructional phases of megadune building. The hiatus' may either represent periods where scouring and erosion occurred or, alternatively, periods of dune stabilisation and preservation prior to the next phase of deposition. While a hiatus is inferred between the Hawiyah and Al Hibal Units' the large errors in IRSL dating shows much overlap and the stratigraphy is rather associated with marine isotope stages in which the errors fall. The Barzaman Formation underlies the Al Batha Unit and is not shown here as no dates were extracted.

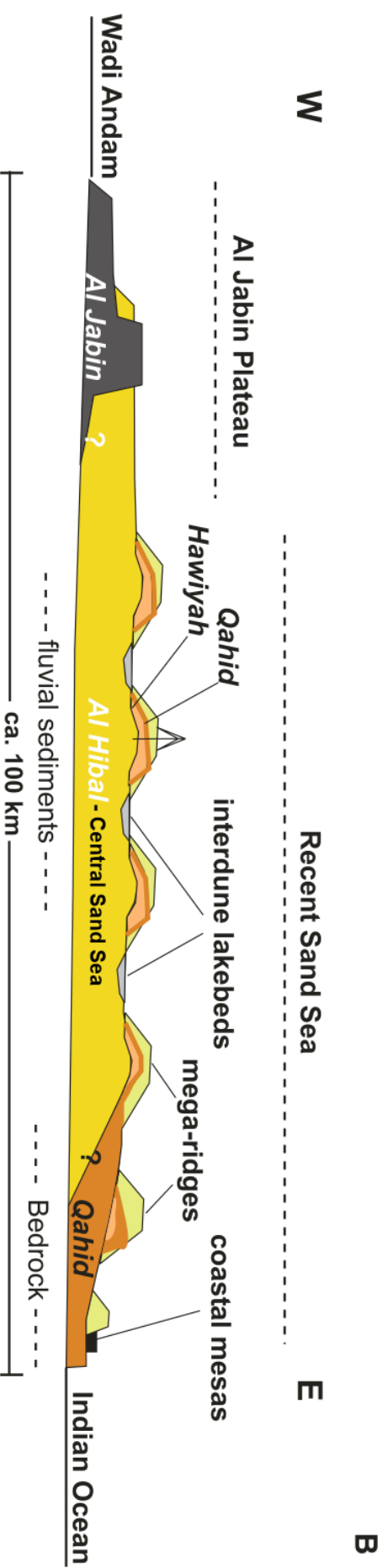


Figure 3.1.1: West to East schematic of the Wahiba Sand Sea including the stratigraphic units described in the text. The three stacked aeolian units of the High Sands megadunes include the Hawiyah (~71 ka), the Qahid (~20 ka) and the Holocene Unit (~1.8 ka). See text for more details on ages. Not to scale. Modified after Radley et al., 2004.

### 3.4.3 Internal architectures

Because of their resistance to change, megadunes generally have long growth histories, thus creating complex internal stratigraphy (Fryberger *et al.*, 2016a). The internal stratification of the Wahiba megadunes have been studied by means of GPR surveys at various sites across the High Sands (Nursaidova, 2009; Tatum *et al.*, 2012; Fryberger *et al.*, 2016a; Hern *et al.*, 2018; Tatum *et al.*, 2019). It is demonstrated that the draa contain internal architectures of a linear nature, similar in form and direction to the contemporary seif dunes found across the draa flanks (Figure 3.12) (Nursaidova, 2009). The preserved composite seif dune is observed above a rounded ridge (termed a 'whaleback core') that seems to have acted as a template with seif accretion along its axis (Hern *et al.*, 2018). Mapping and interpretation of Wahiba radargrams have allowed the quantification of 3D geometry, the spatial distribution of the main bounding surfaces and variability of stratification types (Nursaidova, 2009, Tatum *et al.*, 2012).

Acquired by Shell E&P, the GPR profiles shown in Figure 3.13 all fall within Site 4 of Hern *et al.* (2018) (refer to Figure 3.9 for site location). The preserved architectures at Site 4 are tentatively interpreted by Hern *et al.* (2018) as stacked transverse dunes, seif dunes superimposed onto relict stabilized surfaces (Figure 3.13B, C, D), and wind ripple preservation on the megadune stoss flank (Figure 3.13E). Some bedforms appear to be complete and excellently preserved, formed both above and below an interpreted Pleistocene stabilisation surface (OSL age of 18.1 Ka; Hern *et al.*, 2018) (Figure 3.13C). Areas of high reflectivity are commonly interspersed with transparent areas without loss of signal (Hern *et al.*, 2018). A speculative cause for the variation in reflectivity response is through the action of microbially altered clays that may form stabilising soil crusts (Buckman *et al.*, 2017). The resulting effect is both gross stabilisation of relict bedforms or 'cores' (e.g. whaleback structure of Figure 3.12), and the excellent preservation of aeolian bedforms in the subsurface (Buckman *et al.*, 2017; Hern *et al.*, 2018).

Expressed above, these initial GPR interpretations of radargrams in Figure 3.13 by Hern *et al.* (2018) are tentative and require additional age constraints and trenching at each location (Hern, *pers comms*). As the radargrams in Figure 3.13 best complement the high-resolution satellite datasets that cover this particular linear megadune (analysed in section 6.3), the thesis places them under further scrutiny. The presentation of the methodology of the GPR acquisition and processing, along with the reinterpretation of these 2D profiles is given in section 6.4.

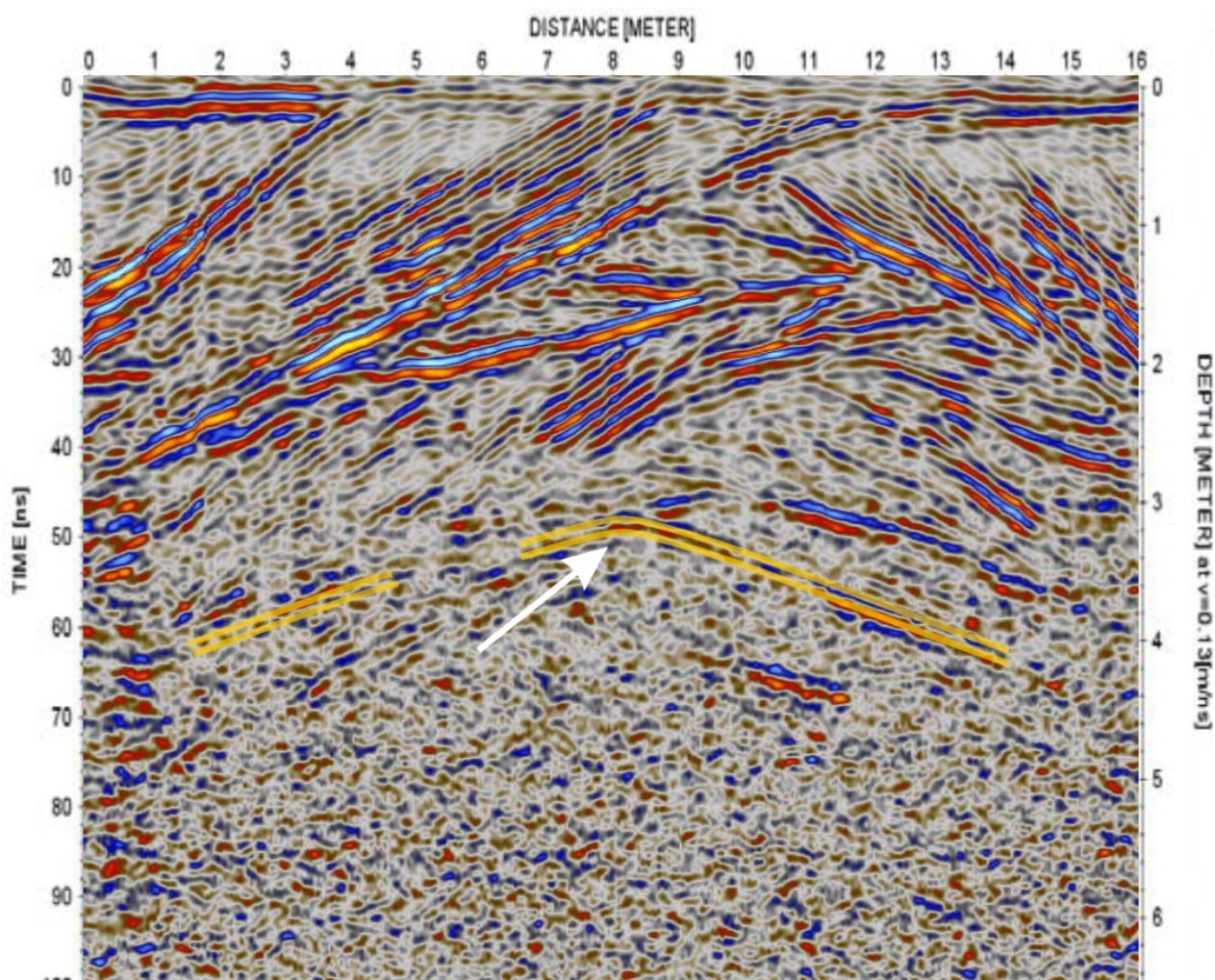


Figure 3.12: Radargram profile collected at 500 MHz on the crest of a complex linear dune in the Wahiba Sand Sea. Buried accreted whaleback or rounded ridge (highlighted) with seif forms above accreting along its former axis. Image from Nursaidova (2009).

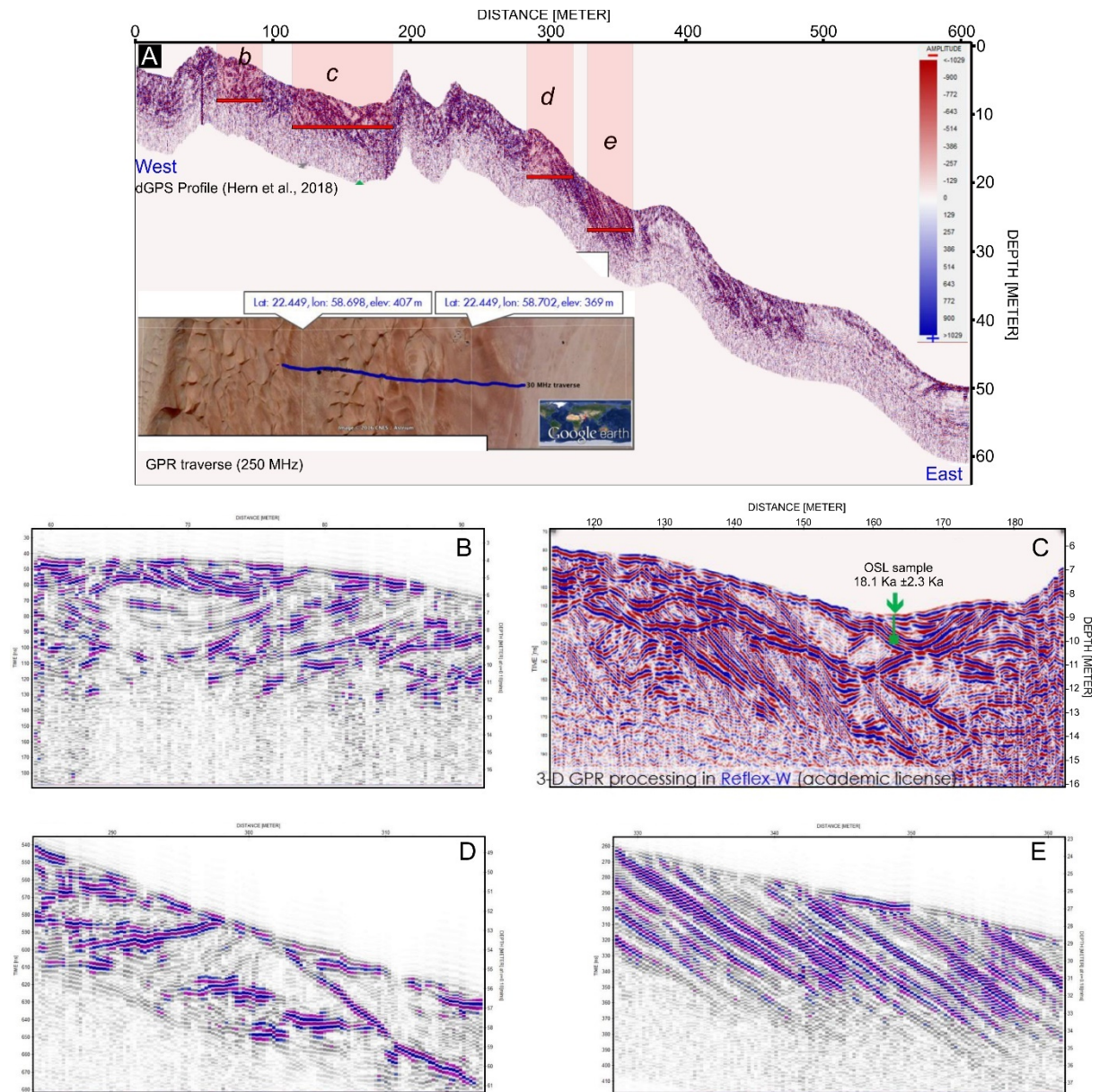


Figure 3.13: GPR radargrams acquired at the megadune containing Site 4 of Hern et al. (2018). A) A 250 MHz line from the start of the megadune stoss to its crest (full methodology provided in section 5.5). The inset Google Earth™ image shows the west to east trending GPR traverse. Red highlighted sections (b-e) show the approximate locations of the resolved radargrams used for interpretation in this study (section 6.4). Note the areas of high reflectivity punctuated by dimmed zones without signal loss. (B) to E) are the tentative interpretations of internal architectures in Hern et al., (2018): B) Stacked trough-cross bedded sets. C) Well-preserved transverse dunes forming above and below the dated stabilised surface. Note the relationships with bedform preservation and local dimming. D) The opposing slopes of a buried seif dune. E) Wind ripple dominated flank of the megadune. Figures are modified after Hern et al., (2018).

### 3.5 Chapter Summary

- Located on the southeastern coast of the Arabian Peninsula, the Wahiba erg overlies vast bajada and alluvial fans formed in response to the uplift of the Oman Mountains. Wahiba sediment is derived from the surrounding alluvial, sabkha and coastal systems.
- The two main geomorphic regions of the Wahiba system include the High Sands and Low Sands generally containing both complex and compound linear megadunes respectively.
- The two main winds acting on the dune-field are the dominant south to southeast summer monsoonal winds and the subordinate northwest Shamal winds. Annual drift potential decreases inland from the coast and the directional variability of the wind increases inland from the coast. Precipitation is generally low (<100 mm) and the region is classed as hyper-arid.
- The High Sands megadunes are made up of four informal chrono-and-litho-stratigraphic aeolian units. The ages of the younger units (<22 ka) are well resolved while high errors and greater uncertainty exists in precisely defining older units.
- Internal architectures of GPR radargrams show relict topographies play a key role in the position and dynamics of subsequent deposition and accretion.

## 4 An Investigation into Apparent Correlations

High-resolution orthophotos and DSMs of the High Sands (section 5.4) allowed for a more detailed study of the complex linear megadune. In cross-section, these asymmetric megadunes typically show knick-points on their stoss slope (Figure 4.1). In plan-view, these knick-points trend north-south and host active seif dunes. Due to the angle variance between the seifs and draa crest, they approach the draa brink-line and deflect near parallel on approach.

The presence of these knick-points are suggested to form either by 1) scouring, initiated by the dominant summer monsoonal southerlies (section 3.3) or 2) preserved remnants of relict bedforms on which the active dunes migrate and accrete (e.g. templates of Hern *et al.*, 2018). These past preserved bedforms are thought to play a role in the position and dynamics of the active bedforms in a process termed ‘antecedent templating’ (Hern *et al.*, 2018). The latter proposal is preferred as ground observations commonly revealed these surfaces (templates) to be well-vegetated and stabilised (e.g. Buckman *et al.*, 2017), reducing the effects of erosion and wind scour.

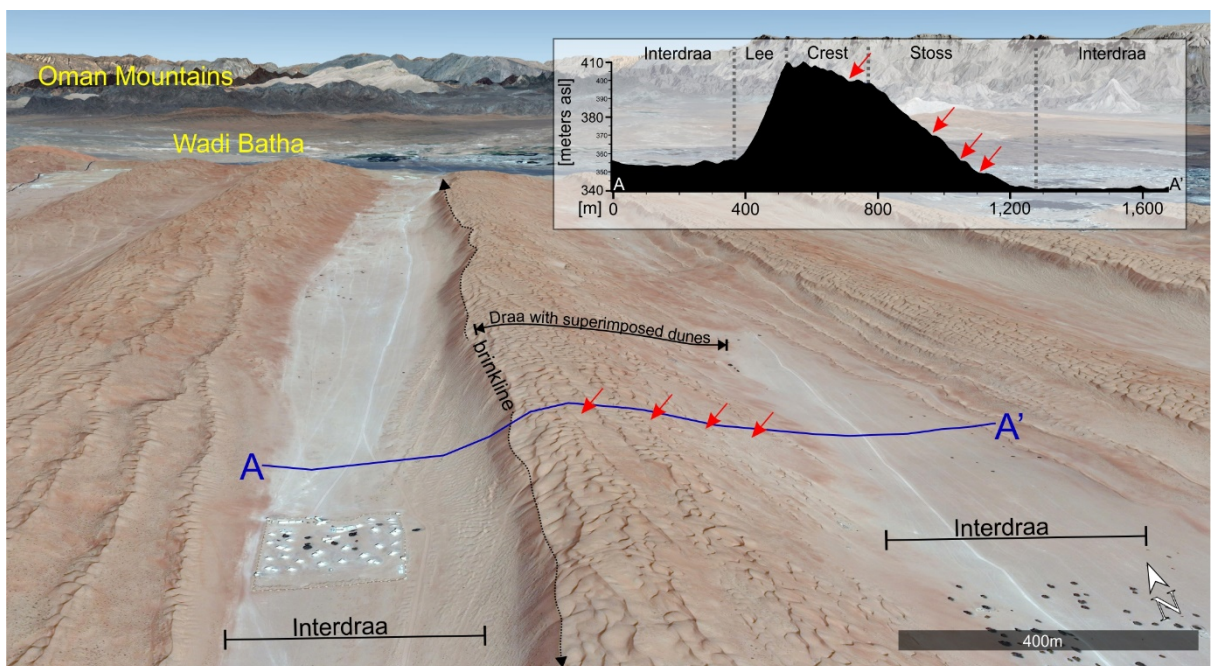


Figure 4.1: Google Earth™™ oblique view of a typical asymmetric linear megadune in the High Sands at the northern margin of the Wahiba erg. The dune measures approximately 70 m in height and 800 m in width. The east facing stoss slopes contain prominent knick-points or terraces flanked by superimposed dunes (marked in red arrows). Note the spatial relationship of the erg termination, the Wadi Batha and the Oman Mountains.

Following these observations, three previously well-studied sites in the High Sands were further evaluated (Table 4.1 and Figure 4.4A). The sites include: Core sites' WDR-1 and WDR-2 of Preusser *et al.* (2002). The sedimentological units of these two cores are detailed in Radies *et al.* (2004) and summarised in section 3.4.2. A third site that included trenching and an OSL aged strata labelled 'Site 4' of Hern *et al.* (2018) (section 3.4.2). All 'Units' mentioned in the sections below are the informal aeolian units of Radies *et al.* (2004) (see section 3.4.2)

Table 4.1: Core location of Preusser *et al.*, (2002) and trenched Site 4 of Hern *et al.*, (2018).

Core / Site	Latitude (°)	Longitude (°)
WDR-1	22.194363	58.853248
WDR-2	22.307881	58.857305
Site 4	22.449	58.698

#### 4.1 Site WDR-2 (Preusser *et al.*, 2002)

In order to assess the local topography and stratigraphic units, a 2500 m west to east line profile  $\gamma$ - $\gamma'$  (Figure 4.2) crossed the site where core WDR-2 was drilled. The cross-section covers two megadunes, the eastern most containing WDR-2 which penetrated four aeolian units (section 3.4.2). At the resolution of the dataset, the cored megadune is about 60 m in height and 1170 m wide. Figure 4.2 shows that the stoss slope of the drilled dune consists of a series of knick-points labelled 1-3. Below the interdune surface, to the lower most knick-point (1) marks the Hawiyah Unit while knick-points 2 and 3 mark the Qahid Unit with overlying deposits representing the Holocene Unit. Although speculative, these apparent local topographic correlations could indicate that the surface features within the interdunes that flank the megadune to the west of the drill site represent the Al-Hibal Unit and the Qahid Unit (Figure 4.2C).

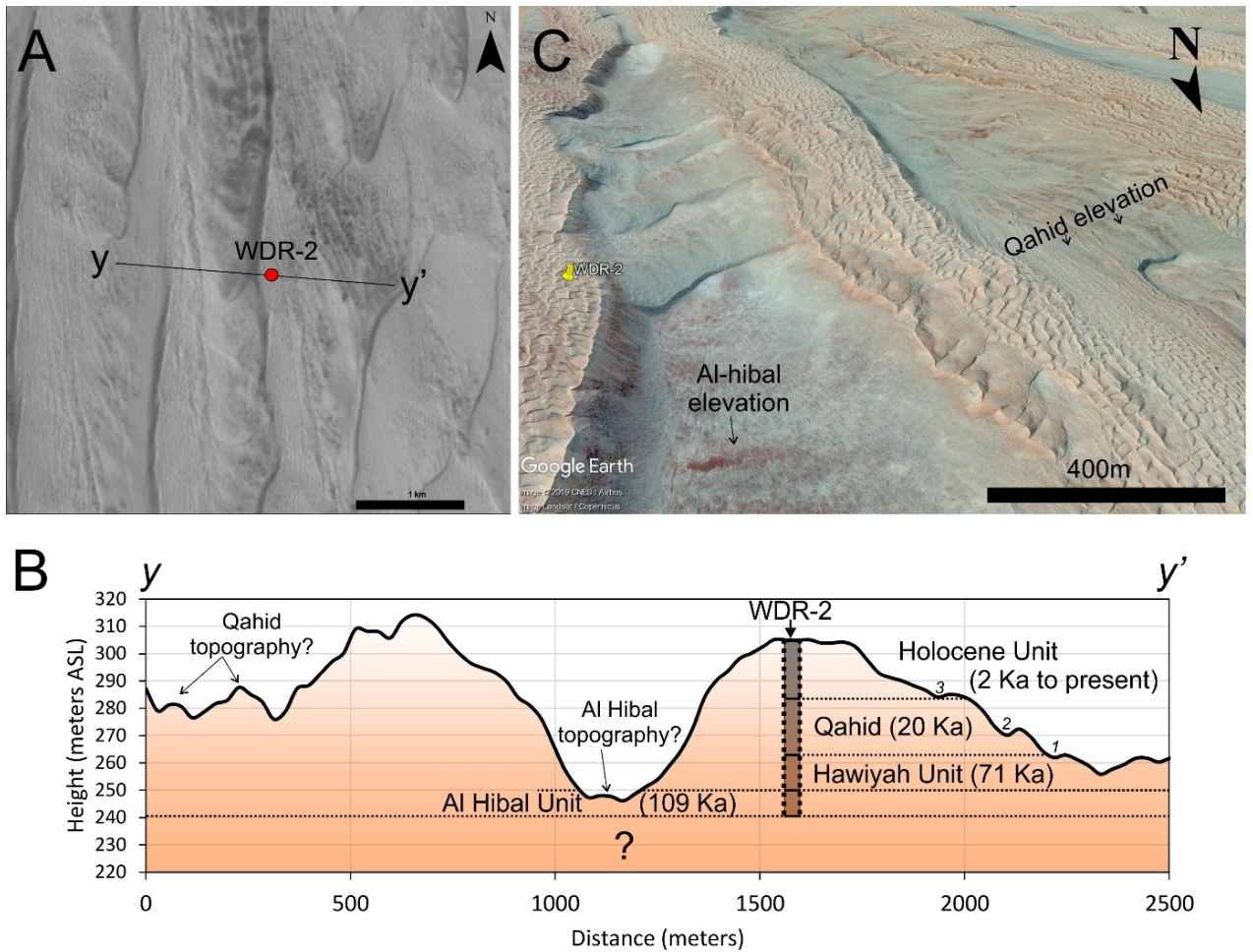


Figure 4.2: The drilled megadune of the core WDR-2. A) Panchromatic Landsat-8 orthophoto with the precise location of core WDR-2 and surrounding megadunes. B) In cross-section, prominent knick-points (1, 2, and 3) on the stoss slope seem to correlate to stratigraphic units of Radies et al. (2004). C) Google Earth™ image (3x V.E.) view to the south shows the two interdunes that lie at the correlated elevations of core stratigraphy. The western-most interdune (Qahid level) lies ~21 m above the surface of the interdune to the east (Al Hibal level).

## 4.2 Site WDR-1 (Preusser *et al.*, 2002)

Precise coordinates for core location WDR-1 in Preusser *et al.* (2002) indicate the core was drilled on a terraced east facing stoss slope, ~27 m above the lower-most interdune surface (coordinates placed in Landsat-8 with 15 m positional accuracy; Figure 4.3A). The megadune itself (LR2 in Figure 4.3B) is ~77 m in height (eastern interdune to crest) and links by a mega crescent to the linear megadune LR1 to the west of it. The core intercepts the Al Hibal Unit at ~6 m subsurface and correlates to the lowermost knick-point of the megadunes stoss as well as surface features located within the flanking interdune (Figure 4.3B). The lowermost topography that makes up a large crescentic dune with a north-facing lee slope, located ~400 m SSE in the interdune corridor also lies at the same elevation as the Al Hibal Unit (Figure 4.3C).

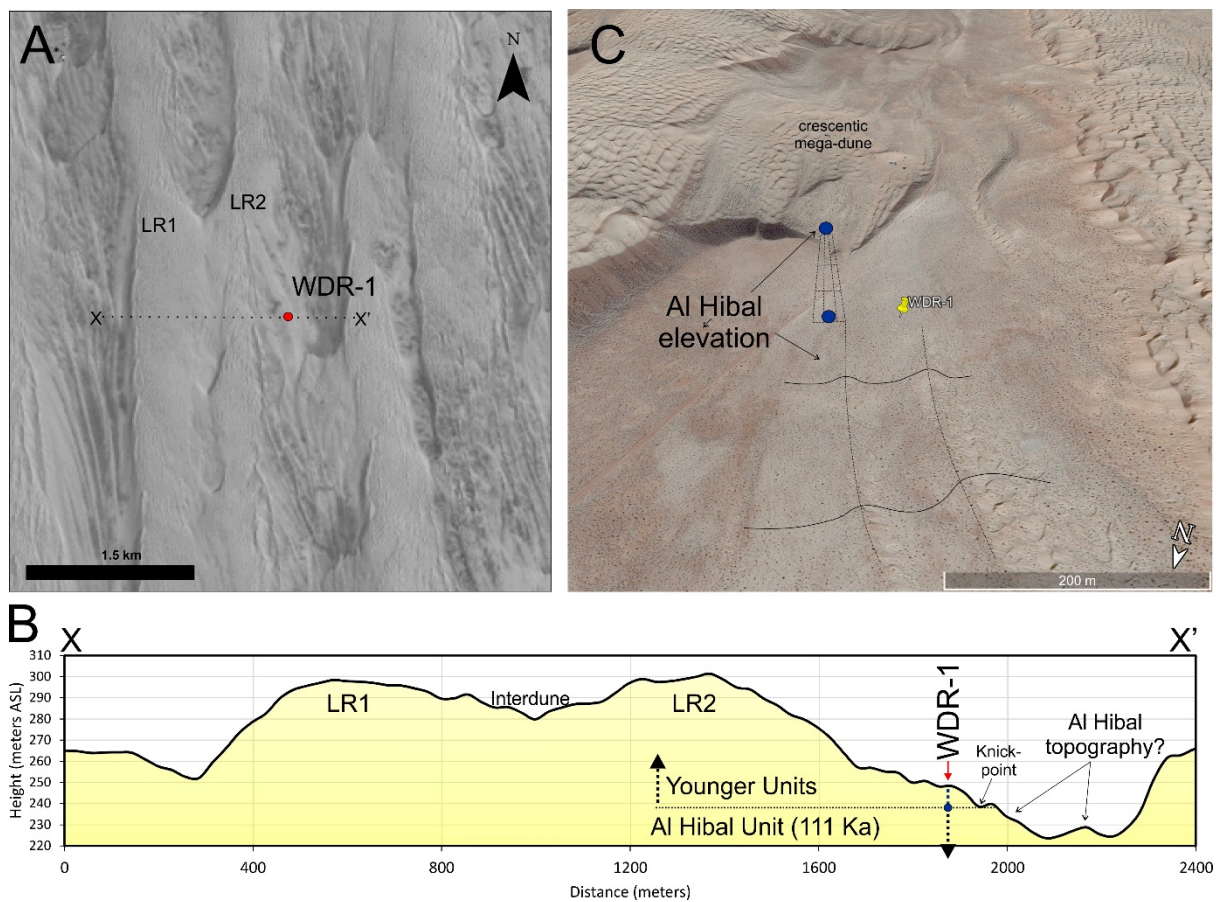


Figure 4.3: A) Panchromatic Landsat-8 orthophoto showing the adjacent megadunes and precise location for core WDR-1. Note the east-facing stoss slopes of most megadunes are riddled with NNE-SSW trending linear ridges. B) Cross-section x-x' shows the position of core WDR-1 and suggested Al Hibal topography. C) Google earth view to the south (3 x V.E.) showing core location. The black dashed lines mark the topography and linear terraces that extend NNE-SSW along the stoss slope. The Al Hibal unit lies at the same elevation as the lowermost terrace and the topography making up the crescentic form to the south marked by the gridded lines and blue dots.

### 4.3 Site 4 (Hern *et al.*, 2018)

An OSL dated sample was extracted from Site 4 (S4) of Hern *et al.* (2004). The sample was dated at 18.1 Ka, correlative to the Qahid Unit (WDR-2 of Radies *et al.*, 2004). Site 4 is located approximately 22 km northwest of core WDR-2 (Figure 4.4). The sample was extracted from 1 m trench dug within a prominent knick-point on the stoss slope of a megadune (Figure 4.4B, C, D). Under the assumption that the knick-points at Site 4 and WDR-2 represent the surface of a relict core, their age correlations suggest the surfaces are related. If these associations do indeed indicate relict dune topographies, the surfaces could potentially be used to pinpoint stratigraphic units within megadunes across the field (Figure 4.5).

### 4.4 Concluding Remarks

Observations reveal that these local topographic expressions or 'knick-points' can be approximately correlated to the stratigraphy. Where topographic correlations are made, the hypothesis here is that the antecedent bedforms are the cause of the surface features (knick-points) identified in orthogonal cross-sections (Figure 4.1; Figure 4.2; Figure 4.3; Figure 4.5). Further scrutiny of the relationship between mega-crescentic dunes present within the interdune corridors (e.g. Figure 4.2 and Figure 4.3) and the linear dunes is provided in Chapter 6.

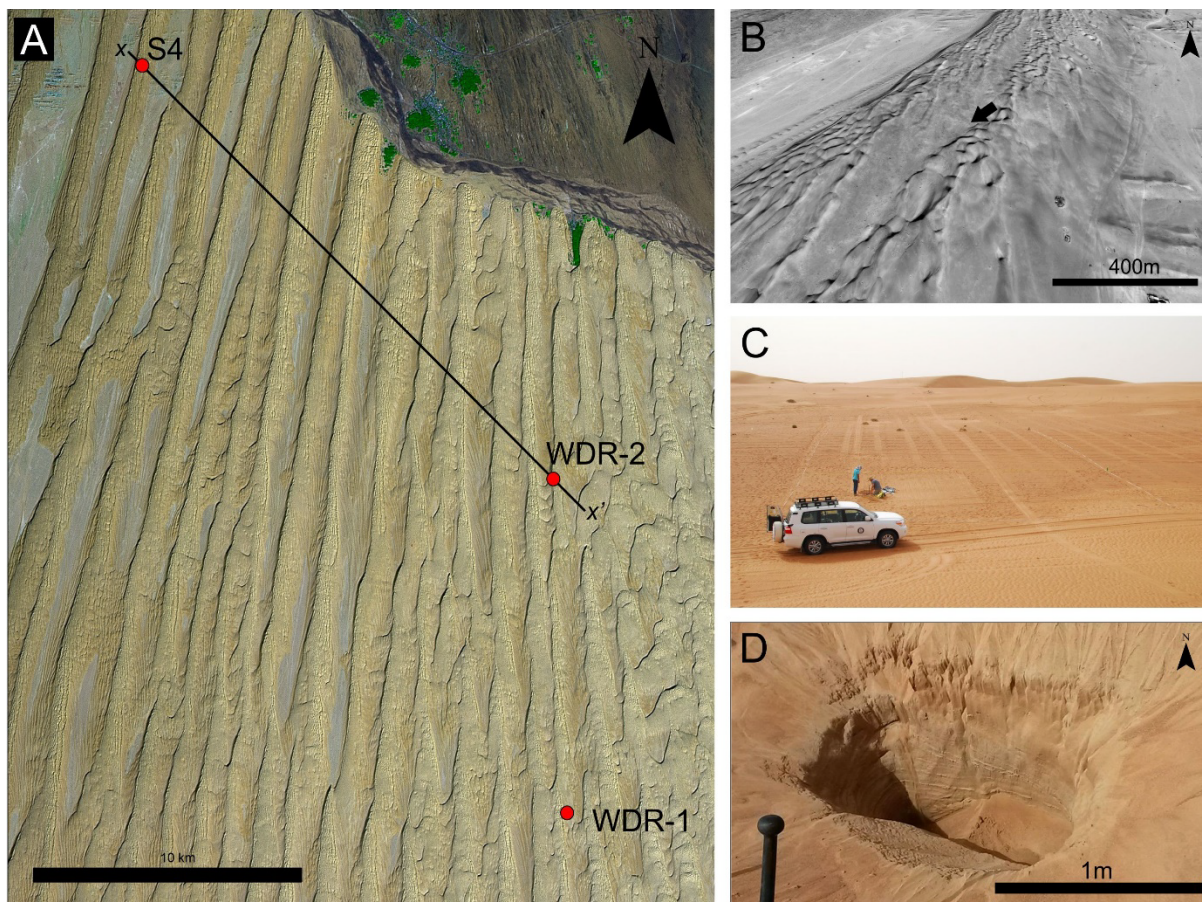


Figure 4.4: A) The location of Site 4 (S4) of Hern et al. (2018) and cores WDR-1, 2 of Preusser et al. (2002). S4 includes an OSL date taken on a prominent terraced surface of  $18.1 \text{ Ka} \pm 2.3 \text{ Ka}$ . B) Oblique aerial view to the north of the terraced surface (the knick-point in cross-section) at site S4. C) The terraced surface of S4 where the OSL sample was acquired. D) Trench dug for the OSL sample at S4 taken at  $\sim 1 \text{ m}$  depth. Note the easterly dipping relict dune cross strata. Photographs C and D are courtesy of Robin Westerman and Dominic Tatum.

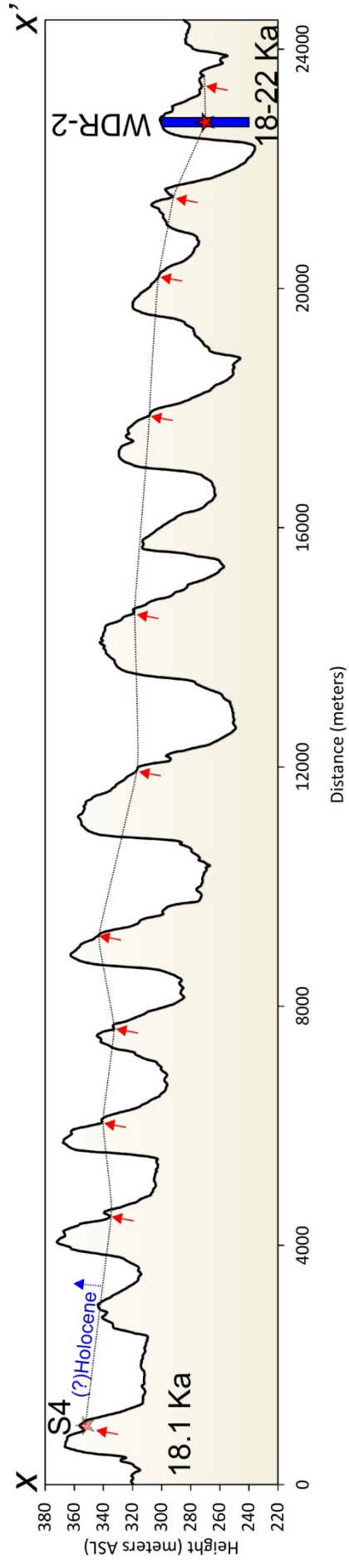


Figure 4.5: The cross-section x-x' traverses' S4 through to WDR-2 (Figure 4.4) slicing the megadunes oblique to their trend. Note knick-points are common on the stoss slope in almost all dune profiles crossed (red arrows). S4 OSL date is captured ~1 m below the knick-point surface (~10 m below crest) with correlative dates produced at knick-point level in core WDR-2 (~30 m below crest). The knick-points are interpreted here as exposure of the older core morphologies (Qahid Unit?), overlain by younger sands. The dashed line approximates this correlation between the two sites.



## 5 Datasets

The following chapter provides a background to the remote sensing datasets used in this study. Datasets from three medium-resolution and two high-resolution Earth resource satellites were utilised. Additionally, processed ground penetrating radargrams (GPR) complemented high-resolution satellite imagery and digital surface models (DSM).

### 5.1 Landsat

Launched in 1972, the Earth Resources Technology Satellite 1 (ERTS-1) was the first unmanned satellite designed to acquire data about earth resources on a systematic, repetitive, medium resolution, multispectral basis. Designed as an experimental system to test the feasibility of collecting information from unmanned satellites, ERTS was subject to an 'open skies' policy of non-discriminatory access to data acquired, inviting all nations to take part in evaluating them with overwhelmingly favourable results (Lillesand *et al.*, 2008). Renamed the "Landsat program" in 1975 with the launch of the second satellite, all subsequent satellites in the series carried the Landsat designation. To date and since 2013, seven Landsat satellites have been launched successfully, namely Landsat-1 to -5 and Landsat-7 to-8, with Landsat-6 failing to reach orbit following technical difficulties (Viets, 1995). The Landsat-8 Operational Land Imager (OLI) and Thermal Infrared Sensor (TIRS) provide seasonal coverage of the global landmass at a spatial resolution of 30 m in the visible, near infrared and short-wave infrared spectrums, a 100 m resolution in the thermal spectrum, and a 15 m resolution in the panchromatic spectrum (Masek, 2020). Bands 2-8 of Landsat-8 were acquired in order to study spatial characteristics of the panchromatic image (15 m) and multi-spectral composites (30 m).

Table 5.1: Landsat 8 band specifications

Sensor	Band		Spectral Resolution ( $\mu\text{m}$ )	Spatial Resolution (m)
<b>OLI</b>	1-	Coastal	0.435–0.451	30
	2-	Blue	0.452–0.512	30
	3-	Green	0.533–0.590	30
	4-	Red	0.636–0.673	30
	5-	NIR	0.851–0.87	30
	6-	SWIR-1	1.566–1.651	30
	7-	SWIR-2	2.107–2.294	30
	8-	Pan	0.503–0.676	15
	9-	Cirrus	1.363–1.384	30
<b>TIRS</b>	10-	TIR-1	10.60–11.19	100
	11-	TIR-2	11.50–12.51	100

## 5.2 ASTER

The Japanese sensor known as the Advanced Spaceborne Thermal Emission and Reflection Radiometer (ASTER) was launched into Earth orbit aboard the NASA Earth Observing System (EOS) in 1999. A collaboration between Japan and the USA, the satellite provides fourteen bands of electromagnetic spectrum with resolutions ranging between 15 and 90 m<sup>2</sup> per pixel. Given its ability to change viewing angles and collect stereoscopic images, ASTER produces detailed terrain height models (Thome, 2020). Open-access to the ASTER Global Digital Elevation Model (GDEM; also known as ASTGTM) was given in 2009 and replaced NASA's Shuttle Radar Topography Mission (SRTM) as the most comprehensive mapping of the earth surface (99% coverage). Improvements to the GDEM were released in 2011 (version 2) and 2016 (version 3) to produce maps with vertical root mean square error (RMSE) accuracies generally between 10 and 25 m (e.g. Luana *et al.*, 2015; Gesch *et al.*, 2016). ASTER GDEM datasets allow a detailed study of topographies and give insight through a three-dimensional perspective.

### 5.3 ALOS

The Japanese Aerospace Exploration Agency (JAXA) launched the Advanced Land Observing Satellite (ALOS) in 2006. ALOS has three remote-sensing instruments: (1) the Panchromatic Remote-sensing Instrument for Stereo Mapping (PRISM) for digital elevation mapping, (2) the Advanced Visible and Near Infrared Radiometer type 2 (AVNIR-2) for precise land coverage observation, and (3) the Phased Array type L-band Synthetic Aperture Radar (PALSAR) for day-and-night and all-weather land observation. In 2015 the ALOS World 3D-30 m (AW3D30) became publicly available, providing global coverage of 30 m resolution digital surface models (Advanced Land Observing Satellite, 2020). Further processing of image archives have produced DSM datasets with vertical RMSE accuracies as low as 5 m (Takatu *et al.*, 2014). The ALOS AW3D30 datasets complemented the panchromatic imagery in this study.

### 5.4 GeoEye-1 and Worldview-3

At the time of its launch in 2008, GeoEye-1 was the world's highest resolution commercial Earth-imaging satellite, providing commercially accessible data with 0.5 m panchromatic and 1.84 m multispectral resolutions (Satellite Imaging Corporation GeoEye-1, 2017). The Worldview-3 satellite launched in 2014 and, in addition to super-spectral data, provides commercially available 0.3 m resolution panchromatic imagery (Satellite Imaging Corporation WorldView-3, 2017). Co-registered and orthorectified panchromatic stereo image pairs collected from these two satellites allowed the production of a high-resolution (1 m) digital surface model. Provided courtesy of Shell Exploration and Production Company (Shell E&P), these commercially acquired, fully processed high-resolution datasets cover 100 km<sup>2</sup> within the area of study (Wahiba Sand Sea) and complement the medium-resolution public-access Landsat, ASTER and ALOS datasets analysed in this chapter.

Table 5.2: Satellite sensors and datasets acquired for the study

Satellite: Sensor	Datasets	Resolution
Landsat-8: OLI	Bands 1-8	15m - 30m
Earth Observing System: ASTER	Global digital elevation model (GDEM)	10-25m
ALOS – PRISM	Digital surface model (DSM): AW3D30	30m
GeoEye-1 and Worldview-3	Panchromatic band, digital surface model	0.5m, 1m

## 5.5 Ground Penetrating Radar (GPR)

Popular in sedimentological studies, ground-penetrating radar (GPR) is a non-invasive geophysical technique designed primarily for subsurface investigations (Robinson *et al.*, 2013). Using discrete pulses of high frequency electromagnetic (EM) energy (usually 10-1000 MHz), a GPR system will detect changes in electrical properties commonly associated with lithological properties of the subsurface (Neal, 2004; Tatum *et al.*, 2012). The times between transmission and reception of signals are a function of the velocity of electromagnetic wave propagation through the sediments and the depth to the reflecting horizon (Bristow, 1996). The depth of penetration relies on the frequency used, the amount of power delivered, and the complex dielectric properties of the sediments (Gawthorpe *et al.*, 1993; Tatum *et al.*, 2012). GPR has previously been used to investigate the internal structures of modern and ancient aeolian sediments (e.g. Bristow *et al.*, 1996; 2000; 2005; 2007; 2019; Jol and Bristow, 2003; Tatum *et al.*, 2010; Tatum and Francke, 2012; Robinson *et al.*, 2013).

This thesis will further examine and interpret processed GPR data acquired by Shell E&P (Hern *et al.*, 2018; Tatum *et al.*, 2019). The need for reinterpretation followed the analysis of the complementary high-resolution satellite datasets of section 5.4. Processing and interpretation methodologies are provided in section 6.4.

## 6 Examining the Wahiba Sand Sea through Remote Sensing and Geospatial Techniques: Insights into Erg Geometry and Preservation

'Remote sensing' is defined as "...the science and art of obtaining information about an object, area, or phenomenon through the analysis of data acquired by a device that is not in contact with the object, area, or phenomenon under investigation." (Lillesand *et al.*, 2015). Significant advances in aeolian dune research have been made through the application of remote sensing over the past four decades (e.g. Breed and Grow, 1979; Bristow 2000; Al-Masrahy and Mountney, 2013; Dong *et al.*, 2013). Satellite imagery provided a base for qualitative studies of large-scale aeolian landforms in widely distributed sand seas. More recent advances in sensor technology and software have allowed for a more quantitative approach to resolve dune form evolution and pattern development (e.g. Hugenholtz *et al.*, 2012; Baitis *et al.*, 2014).

With the improved spatial and spectral resolutions of freely-available, medium-resolution, remote sensing and satellite data (e.g. Landsat, ASTER, ALOS) in conjunction with commercially acquired high-resolution datasets (satellite and ground penetrating radar), this chapter aims to provide deeper insights into the geometry and preservation of a contemporary sand sea hosting large, linear bedforms. The examination takes advantage of digitally based systems and analytical techniques for spatial data to provide detailed insights into the methodology and application thereof.

The distribution of large aeolian bedforms or 'draa' reflect long-term patterns of deposition which relate to complex boundary conditions (Ewing and Kocurek, 2010). Linear draa are the most common desert dune type worldwide (Lancaster, 1982) and, compared to smaller, more mobile, and migratory dune forms, tend to store sediment and thereby capture a history of dune accumulation events (e.g. Thomas and Shaw, 1991). To this end, the chapter presents a detailed review of the aeolian bedforms of the Wahiba Sand Sea and its large linear draa. The Wahibas have a well-documented stratigraphy with growth events spanning over 160 Ka (Preusser *et al.*, 2002; Radies *et al.*, 2004). The chapter

evaluates this growth history and pattern of development and considers the influence of complex boundary conditions inherent in dune evolution.

The following section reviews and applies a variety of geospatial techniques utilising the remote sensing datasets. In the context of the Wahiba Sand Sea, the section will discuss aspects such as spatial and topographic variances of dunes, sediment availability, base-level geometry, internal architectures, dune-field stability and provenance.

## 6.1 Relations between Dune Size and Spacing

A range of sizes of aeolian bedforms occurs in sand seas worldwide and spatial variabilities of dune and interdune morphologies have been well documented (Wilson, 1972; Breed and Grow; 1979; Lancaster, 1982; 1983; 1988; 2013; Ewing *et al.*, 2006; Ewing and Kocurek, 2010; Al-Masrahy and Mountney, 2013; Baitis *et al.*, 2014). Dune height and spacing relationships have been shown to reflect the amount of sand incorporated in the bedform of an area (Lancaster, 1988a, b). These have been analysed using the concept of allometry which uses the relative rates of change of two parts of a system (Lancaster, 1988a, b; 2013). In using allometry to characterise dune patterns, Lancaster (1988a, b; 2013) found strong correlations in the dune height/spacing relationships in a variety of sand seas and between compound/complex and simple dunes (Figure 6.1).

The general form of the relationships between dune height and dune spacing is expressed as a power function (Lancaster, 1988a):

$$D_H = cD_s^n \quad [1]$$

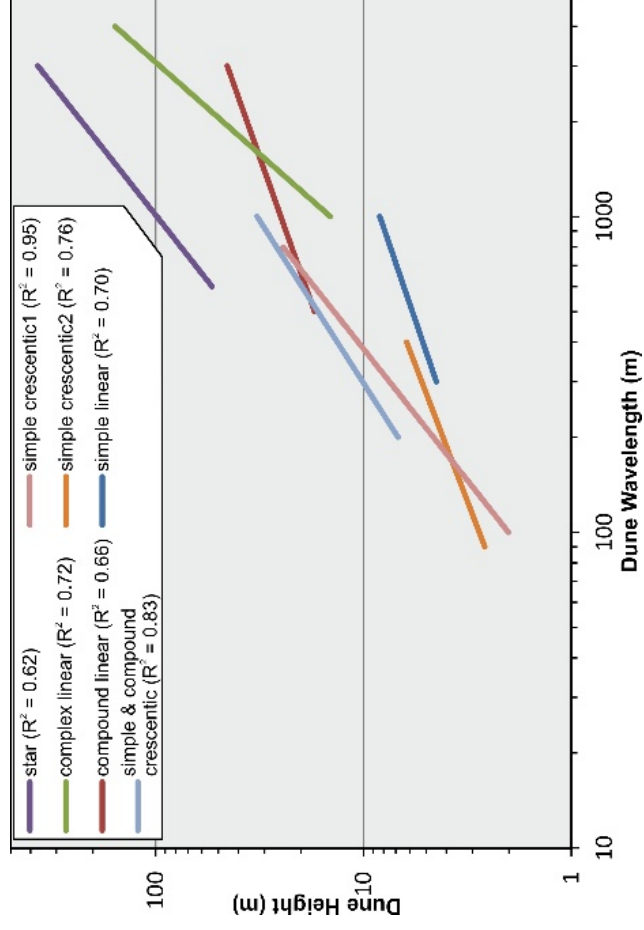
Where

- $D_H$  is dune height,
- $D_s$  is dune spacing,
- $c$  is a constant, and
- the exponent  $n$  is a measure of the rate of change of the dependent variable relative to the rate of the independent variable (slope of regression).

Three possible allometric models explain the dune height / spacing relationships (Lancaster, 1988a, b). An exponent of 1 (isometry) indicates dune height increases at the same rate as wavelength and that a given amount of sand can be formed into a few widely spaced dunes or many small closely spaced dunes. Exponents greater than 1 (positive allometry) indicate dune height increases more rapidly than

spacing and thus a vertical growth of the dune. This is indicative of a high sediment supply and wind regime promoting deposition on dunes. Exponents less than 1 (negative allometry) indicate dune height grows slower than dune spacing, and dune size may be limited by sand availability. Such relationships appear to reflect both the availability of sand for building and wind regime characteristics, which determine whether dunes will accrete vertically (e.g. star and complex dunes), migrate (simple crescentic dunes), or extend (many simple and compound linear dunes) (Lancaster, 1988a, b; Lancaster, 2013).

Using public-release, medium-resolution orthophotos and digital elevation models allows for the easy extraction of height-spacing relationships within a dune-field. These relationships can be measured and compared in the central and marginal portions of the erg in order to spatially assess their geomorphic complexities.



	Constant (c)	Exponent (n)	R <sup>2</sup>
<b>Namib Sand Sea</b>			
Crescentic dunes	0.040	0.97	0.83
Compound linear dunes	0.600	0.54	0.66
Complex linear dunes	0.001	1.72	0.72
Star dunes	0.002	1.20	0.62
<b>Skeleton Coast crescentic dunes</b>	0.008	1.40	0.95
<b>Grand Desierto crescentic dunes</b>	0.192	0.58	0.76
<b>Simpson-Strzelecki sand sea seif dunes</b>	0.011	1.06	0.67
<b>Great Sandy Desert seif dunes</b>	0.230	0.52	0.70
<b>Southwestern Kalahari seif dunes</b>	0.014	1.10	0.81

Figure 6.1: The relationships between dune height and spacing vary between dunes and from one sand sea to another, as well as from one dune type to another in the same sand sea. Modified after Lancaster (1988a, b, 2013)

### 6.1.1 Methods

The Wahiba Sand Sea was divided into three zones representing the High Sands (zones 1 and 2) and the Low sands (zone 3) (Figure 6.2). In the contemporary wind regime, this zone division approximately follows the three-component erg succession of an upwind back-erg (zone 1), a central erg (zone 2), and downwind fore-erg (zone 3) (Porter, 1986). Six cross-sections were taken (two per zone) trending about west to east directed approximately perpendicular to the trend of the linear megadunes. The data from each line profile were extracted from the DSM in order to analyse dune wavelength, dune spacing and dune height (Figure 6.4). The results were plotted, and exponential lines of best fit were determined with resulting equations and correlation coefficients reported in Figure 6.5 and Table 6.2.

Following terminology used in published literature (Al-Masrahy and Mountney, 2013), the following definitions of terminology were applied. Dune wavelength is defined here as the length of the bedform from the base of the lee slope to the base of the stoss slope, perpendicular to the crestline (Figure 6.3). Dune spacing is defined here as the distance between successive dunes in a train measured, for example, between consecutive dune crests and includes the interdune that joins them (Figure 6.3). Bedform height is defined as the difference in relief between the crest of a bedform and the general level of the desert surface and is calculated here as the average between the interdune surfaces on either side of the linear megadune (Figure 6.3).

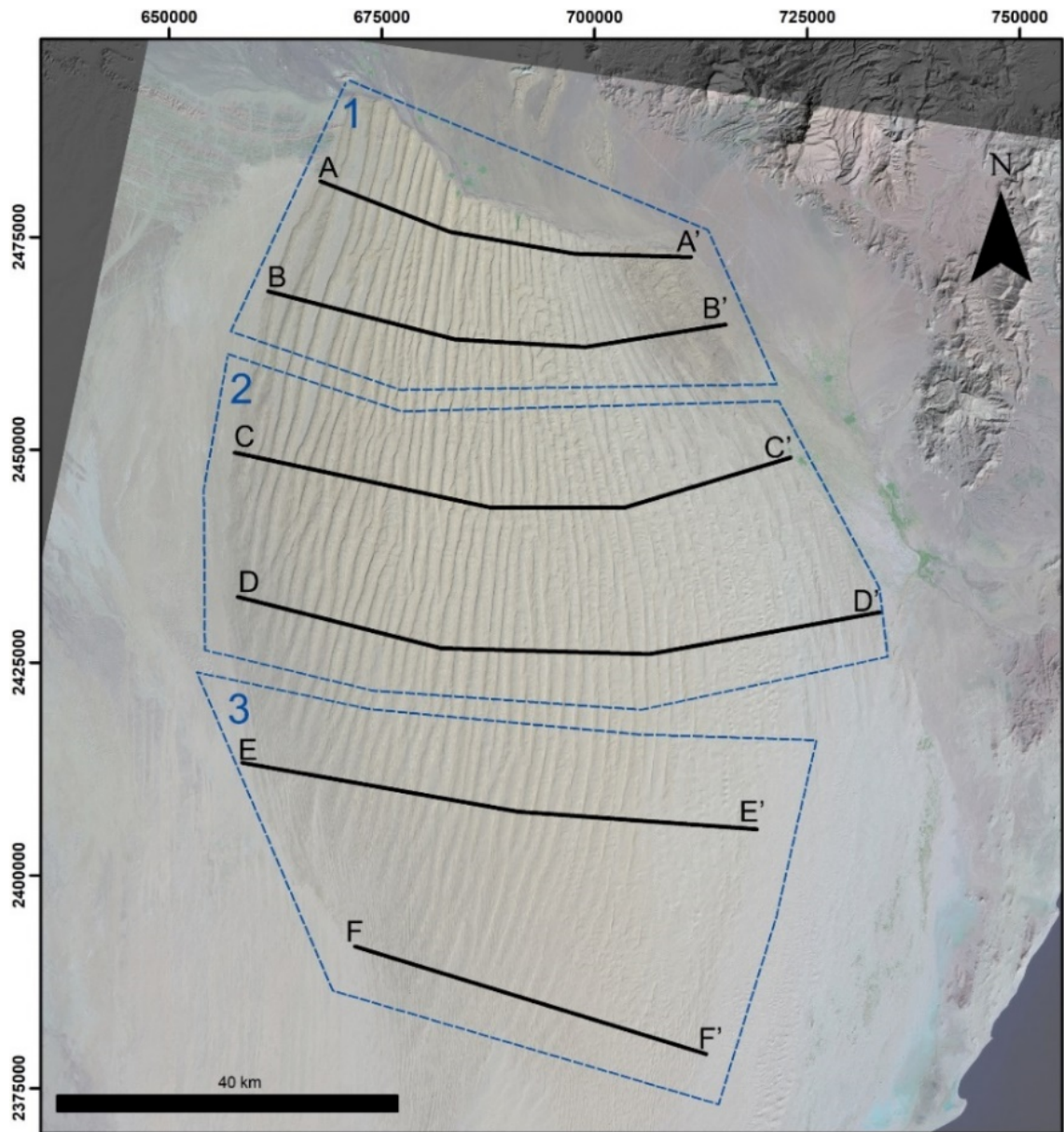


Figure 6.2: Wahiba Sand Sea divided into zones 1 to 3 with line profiles A through F. The cross sections for each line profile are shown in Figure 6.4.

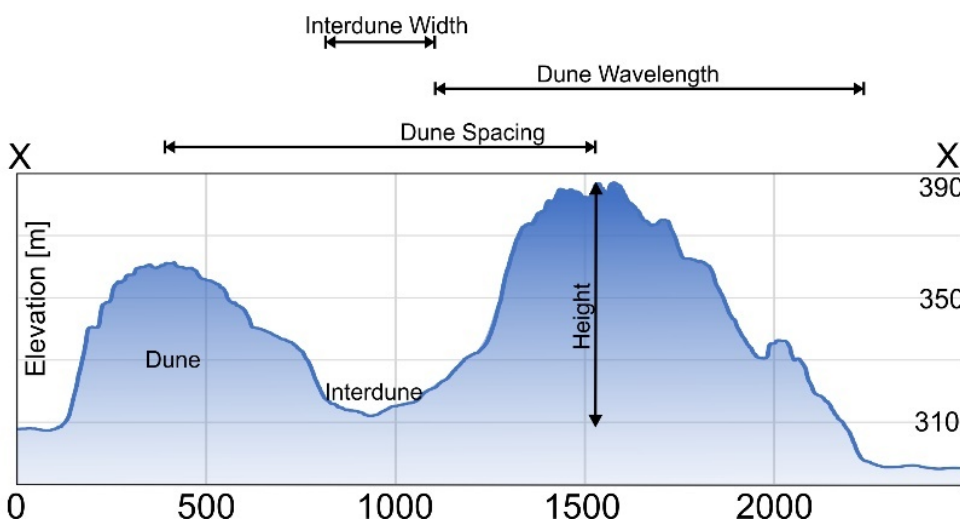
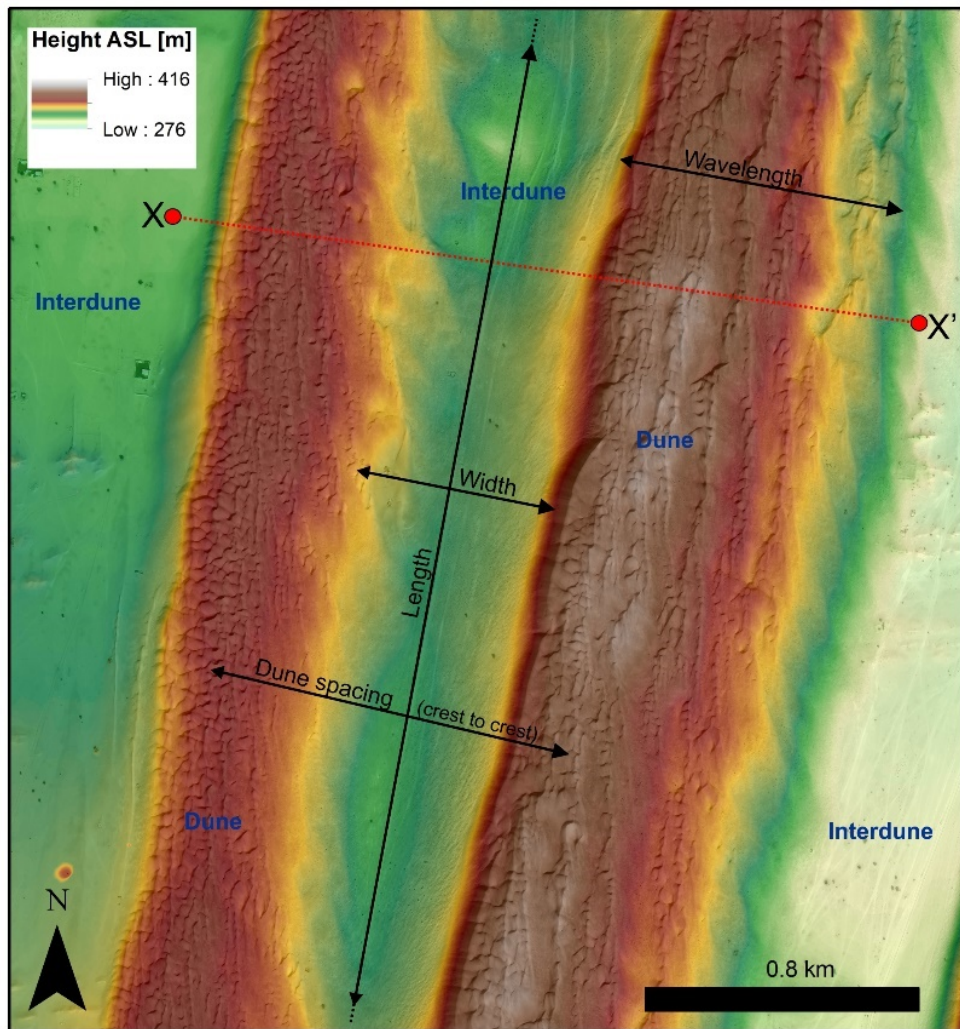


Figure 6.3: Close-up of two linear mega dunes of the Wahiba erg including definitions of the terminology used in this chapter to describe their geometry. In transects perpendicular to the dune trend (shown here by X-X'), cross sections were used to calculate dune height, dune wavelength, dune spacing and interdune width.

## 6.1.2 Results

A total of 215 dunes were intersected by line profiles A through F in zones 1 to 3 of the analysed area. Values from statistical analysis for each cross-section are reported in Table 6.1 with values for each zone reported in the text below.

### *Zone 1*

Sixty-five dunes in line profiles A-A' and B-B' were intercepted in zone 1. Visual inspection of zone 1 (Figure 6.2) reveals variations in megadune crest morphology, particularly towards the eastern margin of the dune-field (also note darker colours in the NE). These have been previously labelled as sand mounds / megabarchans (Goudie *et al.*, 1987), however the peaks and troughs of the linear megadune form is still maintained as seen in the in the cross section, albeit with a large amount of superimposition onto the profiles (Figure 6.4A, B). Average dune wavelength in zone 1 is 1309.2 m with a standard deviation of 438.1 m. Average dune spacing is 1495.4 m with a standard deviation of 488.5 m. Average dune height is 49.7 m with a standard deviation of 16.2 m.

### *Zone 2*

Ninety-nine dunes in line profiles C-C' and D-D' were intercepted in zone 2. Visual inspection of zone 2 (Figure 6.2) reveals similar variations in the megadune crests morphology towards the eastern margin as seen in zone 1, and is also observed in the cross-sections (Figure 6.4). Average wavelength in zone 2 is 1322 m with a standard deviation of 521.2 m. Average dune spacing is 1441.7 m with a standard deviation of 554.5 m. Average dune height is 40.4 m with a standard deviation of 19.1 m. The higher standard deviations in zone 2 compared with zone 1 are probably attributed to larger sections of the morphological variance captured in cross-section.

### *Zone 3*

Fifty-one dunes in line profiles E-E' and F-F' were intercepted in zone 3 (Low Sands). Visual inspection of zone 3 (Figure 6.2; Figure 6.4) reveals a distinctive topography, different from that in the High Sands. Profile E demonstrates a transition in topography on the west and east margins, while profile F is entirely different. The zone is dominated by long, narrow linear seifs which obliquely cross the NNE trending linear megadunes and embed a strong overprint onto the line profiles (Figure 6.4). Average wavelength in zone 3 is 1761.2 m with a standard deviation of 637.8 m. Average dune spacing is 1899.2 m with a standard deviation of 598.2 m. Average dune height is 26.7 m with a standard deviation of 14.1 m.

### *Relationships*

The exponents of the power function as shown in eq. 1 vary from 0.18 to 1.11 increasing systematically from lines A to C, peaking at line D with lower values in lines E and F (Table 6.2). The values of constants range from 0.0103 to 7.4336 with no obvious trend in the changes. The strongest correlation coefficients ( $R^2$ ) are found in zone 2 with moderate values in zone 1 and the weakest correlations in zone 3.

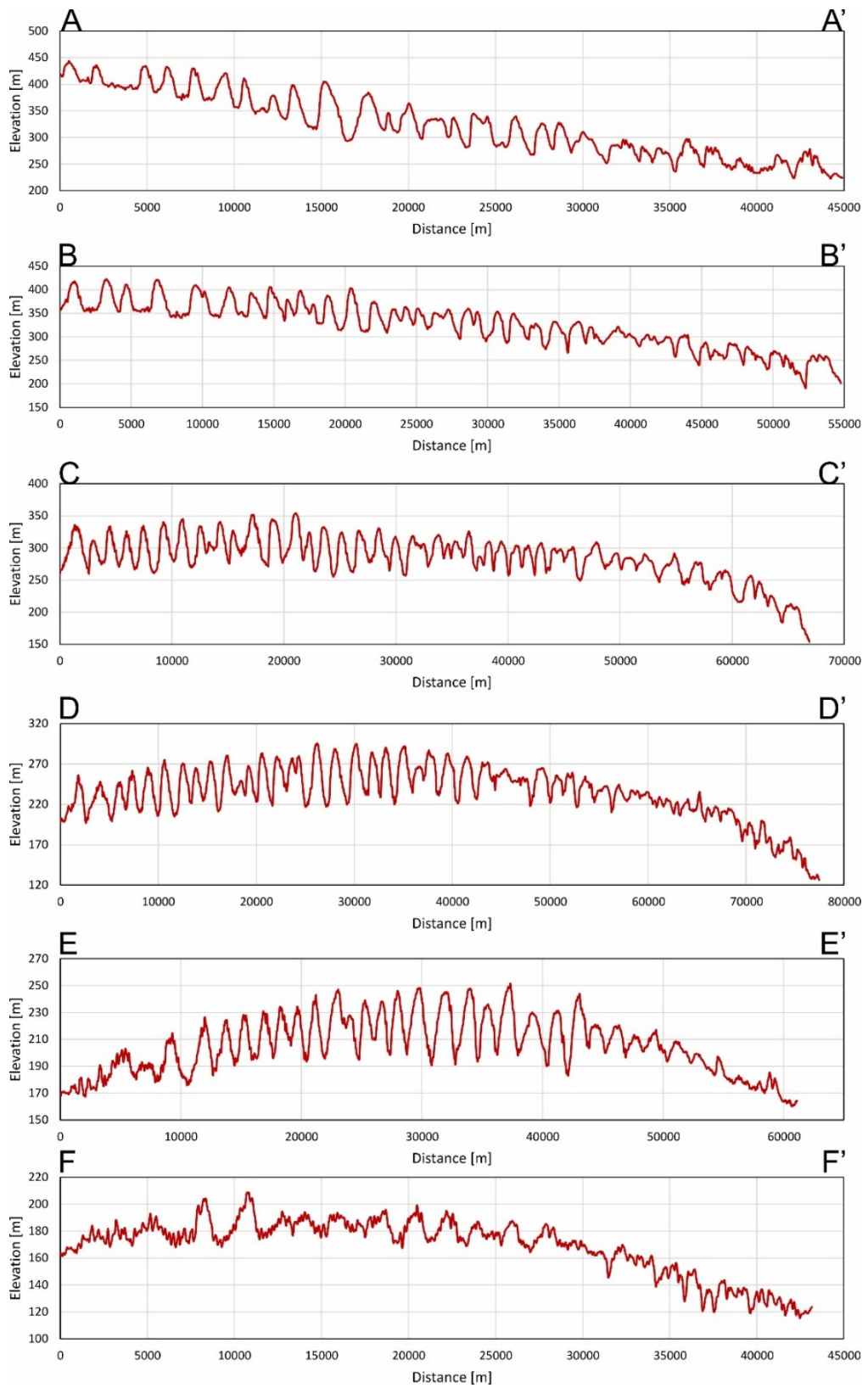


Figure 6.4: Cross sections of lines A-A' through F-F' as shown in Figure 6.2. Elevation data was extracted using ASTER GDEM. Dune attributes were calculated through visual inspection and extraction of points along each line profile.

Table 6.1: Measurements of megadune features for each line profile including number of dunes (N), minimum (min), maximum (max), average (ave) and standard deviation (SD) of each line profile.

Zone		1		2		3	
Line Profile		A-A'	B-B'	C-C'	D-D'	E-E'	F-F'
No. of dunes (N)		28	37	44	55	32	19
Wavelength (m)	min	511	512	631	391	902	1083
	max	2102	2617	2556	3579	3310	4482
	ave	1300.0	1316.2	1415.3	1247.4	1611.1	2013.8
	SD	396.5	472.5	460.0	558.4	488.8	781.6
Spacing (m)	min	751	661	631	391	993	1113
	max	2497	2736	2767	3940	2646	4482
	ave	1554.3	1451.2	1499.9	1395.3	1728.0	2194.2
	SD	410.3	541.4	485.3	604.5	392.7	769.8
Height (m)	min	24.5	17.5	15	7	7.5	9.5
	max	100	89.5	75.5	75.5	55.5	32
	ave	49.9	49.4	47.4	34.8	32.5	17.0
	SD	16.5	16.1	16.3	19.5	14.3	6.6

Table 6.2: Constants, exponents and correlation coefficient of power functions in Figure 6.5

Line Profile	N	Constant	Exponent	R <sup>2</sup>
A	27	2.0867	0.43	0.15
B	36	0.7776	0.57	0.31
C	43	0.2294	0.72	0.35
D	54	0.0103	1.11	0.58
E	31	7.4336	0.18	0.01
F	18	0.6978	0.41	0.11

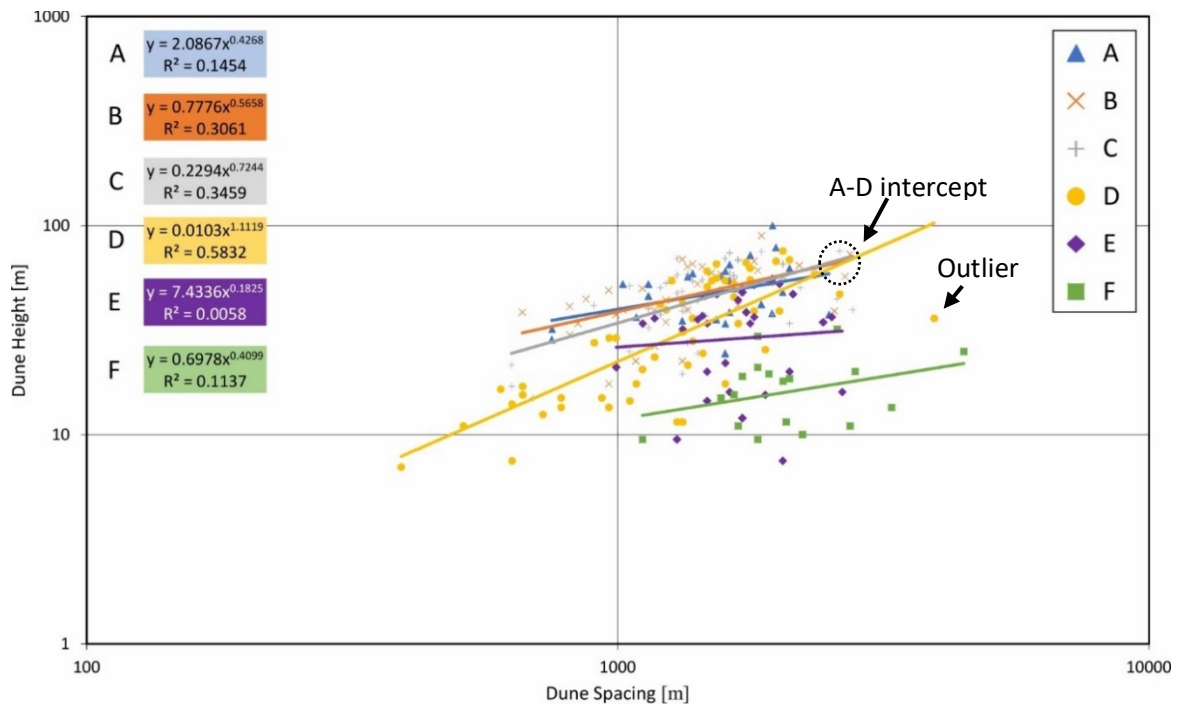


Figure 6.5: Dune height vs. dune wavelength for line profiles A – F. Dune heights exhibits a positive correlation with bedform wavelength and spacing.

### 6.1.3 Discussion

Dunes types exhibiting negative allometry have been found to occur where the annual total and resultant potential sand transport rates are higher (e.g. Namib Sand Sea in Lancaster, 1988b). It is also suggested that negative allometric relationships may characterise dunes in zones of active through-going sand transport resulting in dune extension or migration, while positive allometric relationships indicate areas of net deposition and dune growth (Lancaster, 1988a, b). The dunes crossed in line profile D is the only area where positive allometry is shown and, in the above sense, indicates a strong tendency for vertical growth without an equivalent change in dune spacing. The differences seen between the profile transects in this study highlight the sensitivity of transect placement and pattern heterogeneity within the dune-field.

Viewing all allometric relationships (Figure 6.5), the profile slopes of A-D approximately intercept at the trendline terminations or maximum values (when excluding outlier in line profile D - the result of an infilled interdune area), suggesting there is an upper limit of dune height-spacing relationship within the High Sands. Low correlation coefficients ( $R^2$ ) in line profiles A, E and F are possibly due to a combination of low sample numbers and influences of pattern heterogeneity. Furthermore, the strong superimposition seen on the short, widely spaced dunes of the Low Sands negatively affects the data acquisition as peaks and troughs are difficult to identify. Consequently, care must be taken with the interpretation of profiles within the Low Sands.

Allometric relationships are known to vary from one sand sea to another, as well as from one dune type to another in the same sand sea (Lancaster, 1988a, b; Lancaster, 2013). Although the Wahiba High Sands commonly exhibit complex and compound linear dunes in the High and Low Sands respectively, further morphological heterogeneity exists within each geomorphic region. In the above case, the eastern and western margins, all grouped into the calculations will play a role in the differences in allometric relationships and undermine averaging procedures. Further factors to be considered must include topographic heterogeneity (e.g. Ewing and Kocurek, 2010; Baitis *et al.*, 2014), wind regime and sediment supply (e.g. Fryberger *et al.*, 2016a), and dune stability (e.g. Levin *et al.*, 2006). These controlling factors are known contributors to pattern heterogeneity and will be further investigated in this study.

## 6.2 Equivalent Sediment Thickness (EST), Base-level Topography and Dune-field Patterns

Sand supply is an important variable in dune building as it pertains to the assessment of sand influx and outflow, storage and overall sand budget. While sand availability has been considered a significant factor influencing dune morphology, it is not the only one. Wasson and Hyde (1983) conceptualised the quantification of sediment supply in using an equivalent sediment thickness (EST) model, defined as the thickness of a continuous sheet of sand which results from the hypothetical spreading out of dunes over a specified area. When plotting EST against the directional variability of the wind (RDP/DP as in section 3.3), the study concluded such parameters could clearly discriminate dune types (Figure 6.6). In a later study, Lancaster (1989) found similar relationships in the Namib Sand Sea, however all dune types observed occur in wind regimes that are less variable than the samples of Wasson and Hyde (Figure 6.6). Lancaster (2013) established that EST is not a measure of sand supply but rather of the volume of sand contained in the dunes and may only provide a reflection of the dune type. Other factors should be taken into consideration such as the interplay between boundary conditions which impose a strong influence on dune type and dune-field pattern development (e.g. Ewing and Kocurek, 2010; Baitis *et al.*, 2014).

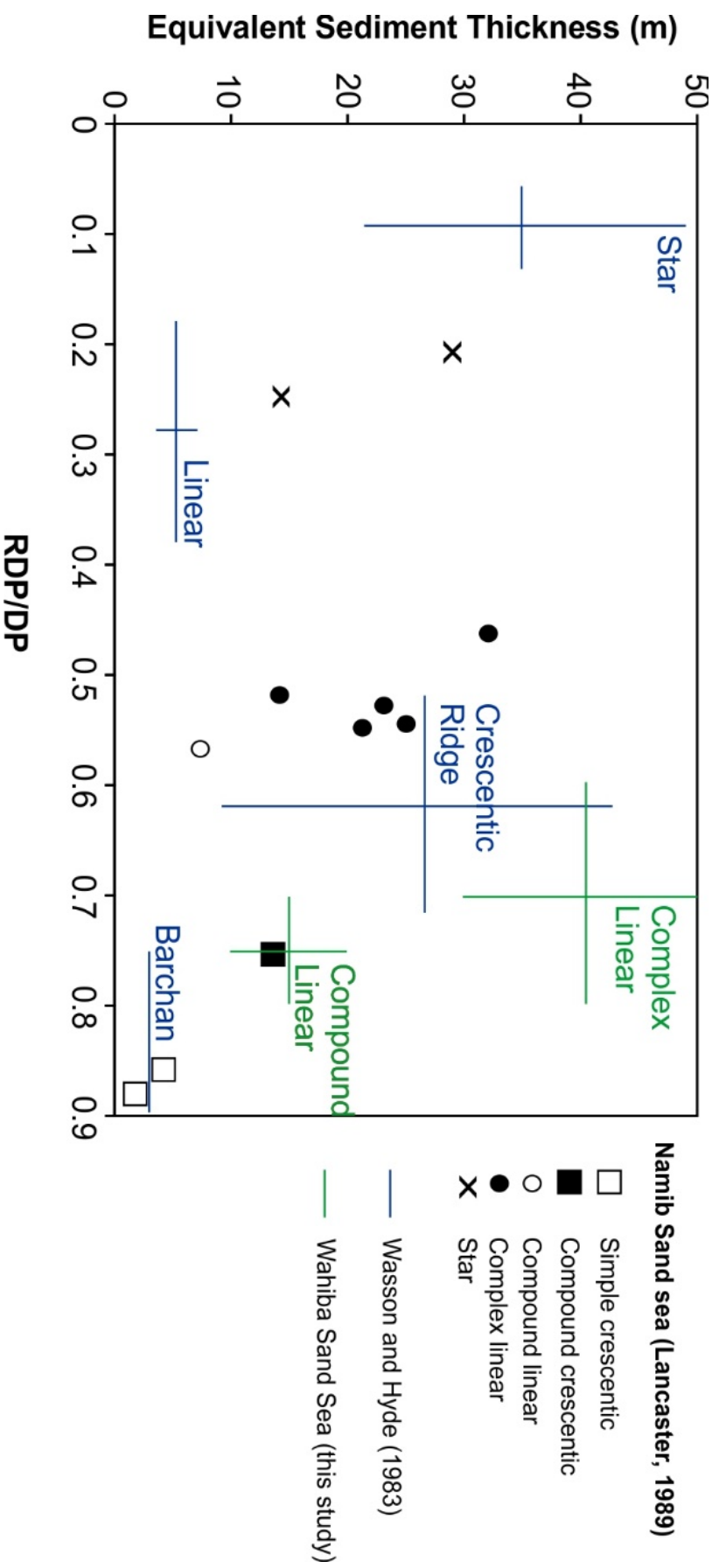


Figure 6.6: The blue lines show relationship between dune type, directional variability of the wind, and sand supply as determined by Wasson and Hyde (1983). This study (green lines) and a study on the Namib Sand Sea (Lancaster, 1989) found that similar dune types occurred where the wind was less variable. Figure modified after Lancaster (2013). Wahiba EST calculations are detailed below, RDP/DP values are extracted from Fryberger et al. (2016) in Figure 3.6.

### 6.2.1 Methods

With the aid of modern-day digital elevation models and GIS, an approach to quantify EST has been developed and applied with success to the Rub' Al Khali and Badain Jaran deserts (Hugenholtz and Barchyn, 2010; Yang *et al.*, 2011; Hugenholtz *et al.*, 2012). In resolving EST, the computer-aided process identifies local minima in order to strip off the dunes from their base-level. This produces maps that showcase the base-level topography, better definitions of dune-field patterns and the EST across the field.

The following single equation outlines the procedure used to calculate EST for focal cell  $i$ :

$$EST_i = \text{avg}_{d_{i,j} < 15000}$$

$$\{Z_i - \text{avg}_{d_{i,j} < 1500}[\min_{d_{i,j} < 1000}(\text{med}_{d_{i,j} < 90}(Z_j))]\} \quad [2]$$

Where:

- $Z_i$  : elevation of the focal cell
- $\text{Avg}_{d_{i,j} < 15000}$  : average of cells where distance ( $d_{i,j}$ ) between focal cell  $i$  and adjacent cell  $j$  is less than 15000m\*
- $\min_{d_{i,j} < 1000}$  : minimum of all cells within 1000 m\* of focal cell
- $\text{med}_{d_{i,j} < 90}$  : median of all cells within 90 m\* of the focal cell
- $Z_j$  : elevation of adjacent cells

\*The values provided in metres are examples and must be manipulated according to the local dune-field being analysed.

A local minimum surface is determined based upon dune-field parameters (the above equation uses a 1000 m filter) and creates a map that represents an approximation of base-level (subdune topography), or the surface upon which the dunes rest. Subtracting this surface from the original elevation model removes the dunes from their base-level and produces a map that better defines dune-field patterns. Using the dune height map, EST can be calculated by kernel density estimation. All tools required to produce these maps are commonly available in GIS software.

The application of Equation. 2 was carried out in ArcGIS 10.6 using the spatial analyst plugin. The DSM raster file was clipped to only include the area of interest in the Wahiba erg (Figure 6.7A). Using the focal statistics tool, the clipped file was run through a median filter with a circular radius of 90 m. This was carried out to smooth the interdune surface of spurious pits in the dataset (as suggested in Hugenholtz and Barchyn, 2010). A local minimum surface was created using a value of 1500 m (average interdune spacing) which was subsequently smoothed with a mean filter to better connect interdune surfaces. This map represents an approximation of the base-level on which the dunes surfaces lie (Figure 6.7B). A dune height map was calculated using the raster calculator and subtracting the topography from the base level surface (Figure 6.7C). A 2000 x 2000 m fishnet was created on this map and each label point was given a height value using the 'multi-values to point' tool. Finally, these points were run through the 'kernel density estimation' tool with a search radius of 15000 m to produce a smooth surface representing EST (Figure 6.7D). Lower values were found to retain topographical expressions of the dunes and not a well-levelled surface as originally inferred in the definition of EST (Wasson and Hyde, 1983; Lancaster and Greely, 1990).

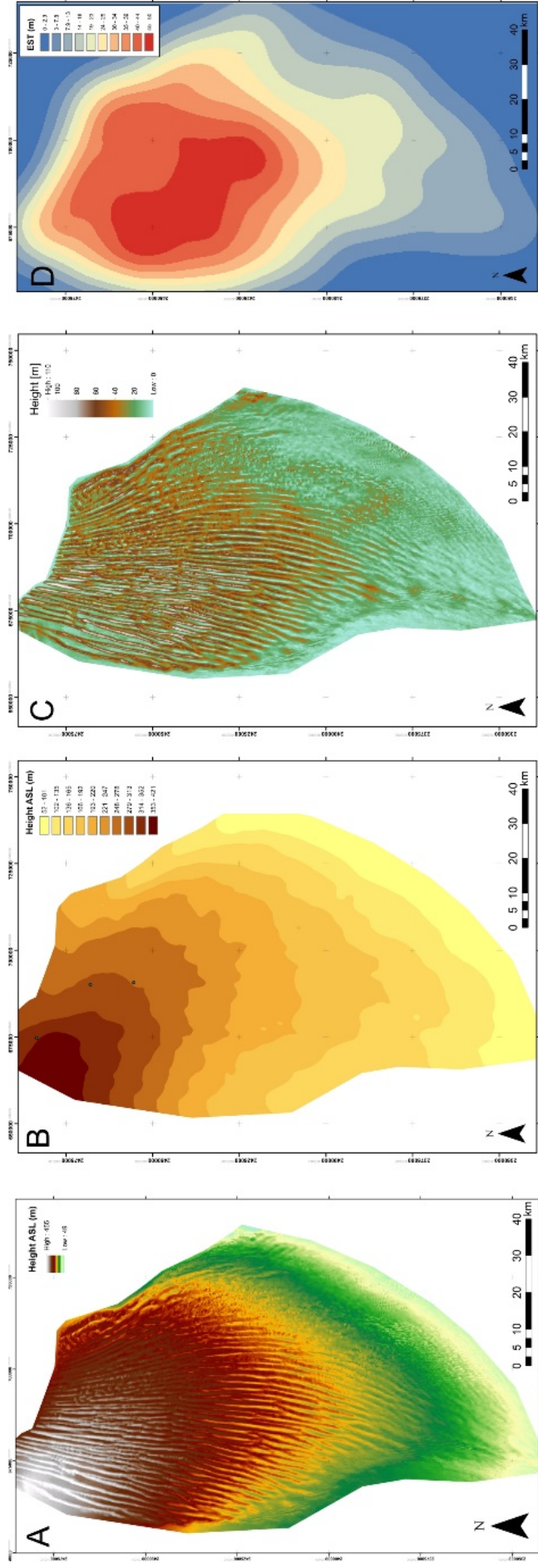


Figure 6.7: The sequence of images illustrates the process of deriving a map of Equivalent Sediment Thickness (EST). Each step produces a map that can be used to better analyse dune-field boundary conditions. (A) The cropped DSM only including the area of interest (ALOS AW3D30, ©JAXA). (B) The smoothed topography representing the interdune base level surface. (C) The base level surface is subtracted from the original dune topography and yields a map that excellently reveals areal patterns. (D) The map in (C) is filtered in order to approximate the local EST for a 15 km radius around grid cells.

## 6.2.2 Results

Three separate maps are produced following the above methodology that defines the dune-fields 'base-level', elucidates pattern heterogeneity, and provides the spatial distribution of sediment (and therefore supply) within the sampled erg.

### *Base-level topography map*

Removal of the dunes reveals the extent of heterogeneity in the underlying topography, the most obvious being the breaks-in-slope (Figure 6.8). The highest elevations occur in the northwestern corner where the erg covers a portion of the Hawasina Group outcrops. Elevations at the northwestern margin are in excess of 400 m, steadily decreasing eastwards to ~220 m in the NE corner and sharply dropping to 130 m along the northeastern margin. A relatively gentle decrease in elevation occurs from the northern to southern boundaries. The southern and southeastern margins have the lowest elevations ranging between 60 m and 90 m.

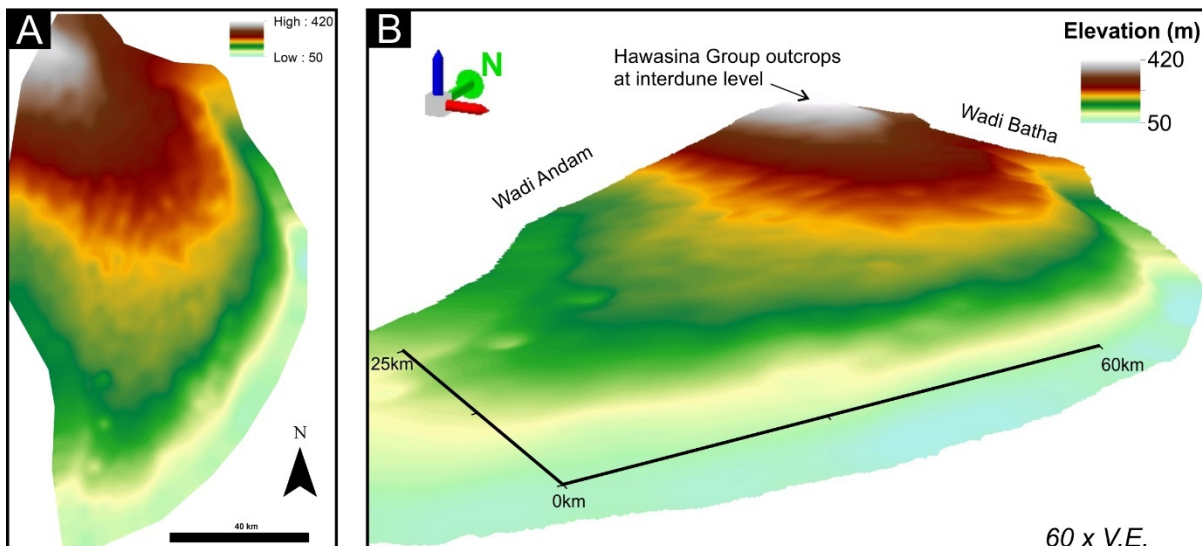


Figure 6.8: (A) The smoothed base-level map after applying the mean filter. The base-level appears as a mound-like shape with common breaks in slope. (B) A 3D visualisation of the base-level topography. Dunes partly bury the Hawasina Group highlands in the northwest corner. The erg terminates abruptly at the northern, eastern margins and western margins where the wadis dominate.

### *Dune-field Patterns*

Dune pattern heterogeneity becomes most obvious with the removal of base-level (Figure 6.9). A strong linear megadune footprint is evident in the central to western portions of the High Sands. Disruption in this pattern occurs most notably within the eastern half of both the High and Low Sands. In the High Sands, dune heights are commonly in excess of 80 m (range 30 m – 90 m), peaking in the central western parts with highs up to 110 m. The lowest dune heights occur in the northwest corner where the dunes cover the Hawasina Group outcrops (30-40 m) and in the central to eastern parts where the strong disruption in patterns exists (elevations as low as 30 m). Along the northeast margin, however, an increase in dune width is evident and the most easterly dunes which reach up to 90 m in height. In the Low Sands, dunes generally decrease from 40 m at the northern margin to 10 m in the south and southeast. Along the central eastern margin the linear footprint is subtle or not visually apparent at all.

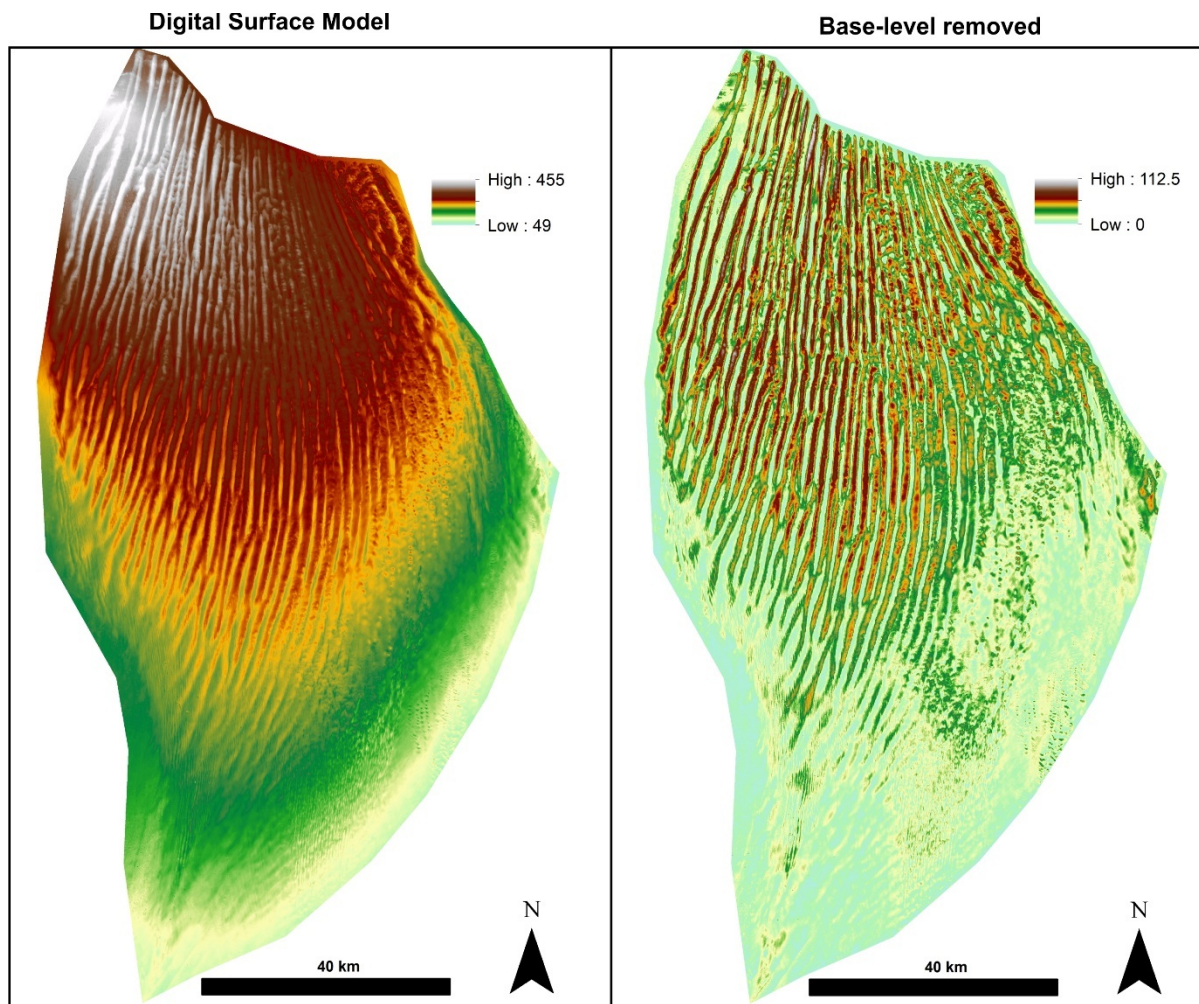


Figure 6.9: Comparison of cropped DSM maps. (A) Standard DSM map of the dune-field area. (B) DSM where base-level is removed and the dunes rest on a flat surface. With base-level removed, heights and pattern heterogeneity become more apparent.

#### Equivalent Sediment Thickness (EST)

The EST map forms a mound-like shape with relatively steep slopes (average 0.26%) from the central sands to the erg terminations in the west, north and east. A much gentler slope (average 0.06%) occurs towards the Low Sands and erg termination in the south (Figure 6.10). The thickest pile of sediment (>45 m) occurs along the eastern-central High Sands, covering approximately 750 km<sup>2</sup> in an oblong shape with long axis trending NW-SE (Figure 6.10). In general, EST ranges between 30 m to 50 m in the High Sands, thinning southwards as it transitions into the Low Sands and ranges between 10 m and 20 m.

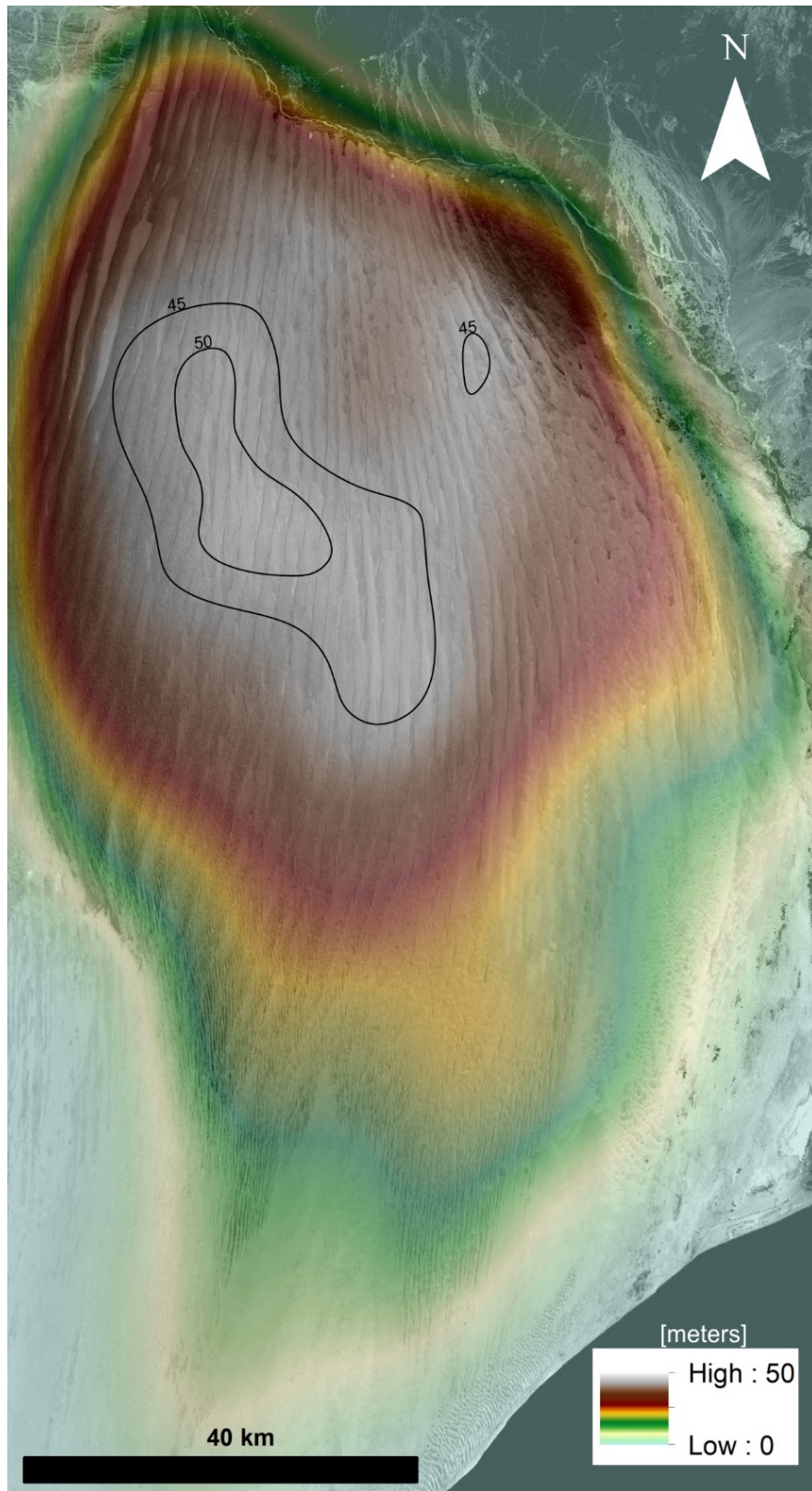


Figure 6.10: Spatial variation of equivalent sediment thickness overlain onto panchromatic Landsat-8 orthophoto for reference. Note how the spatial variability correlates with the dune-field patterns in Figure 6.9. Well-defined tall linear complex dunes are concentrated in areas with thicker sediment piles, while thinner sediment spread is associated with subdued compound dunes in the south. The contours mark the thickest sediment build-up (>45 m).

### 6.2.3 Discussion

The base-level, dune-field pattern and EST maps provide an excellent tool with which to study the influence of dune-field boundary conditions. In comparing the base-level map (Figure 6.8) with dune-field patterns (Figure 6.9) simple associations become apparent. Note for instance dunes size is drastically decreased at the northwest erg limits due to the sudden increase in elevation from the Hawasina outcrops. By contrast, at the northeastern erg limits, dune size is significantly increased associated with a sudden topographical low and increase in accommodation space along the eastern margin (Masirah trough?).

Topography is known to influence wind flow patterns through topographic steering that promotes/inhibits aeolian deposition across the landscape (Hay, 2018). Aeolian sediments are preferentially deposited at the first point(s) where the interaction between wind flow and topography promote deposition (i.e. accommodation space) (Hay, 2018). At the erg scale, spatial associations become apparent when comparing EST with the underlying topography where distinct terracing coincides with sediment build (Figure 6.11). These pronounced breaks-in-slope also tend to agree with the identified heterogeneity seen in dune profiles and should be considered to play a role in the dune-field pattern development (Figure 6.12). These are not the first observations of terracing in the Wahiba Sand Sea, which have been previously described on the western flanks of the Sand Sea (Radies *et al.*, 2004), attributed to northwest to southeast trending faults utilised for ancient drainage with some explaining the linearity of the southwestern and northeastern edges of the Wahiba Sand Sea (Kusky *et al.*, 2005; Robinson *et al.*, 2007; Blechschmidt *et al.*, 2009). These faults may provide some explanation to the nature of subdune topography of the Wahiba Sand Sea.

Similar relationships have been found on a smaller scale in the White Sands dune-field, New Mexico where the consideration of wind regime, source-area geometry and sediment supply by themselves were insufficient to account for dune-field patterns (Ewing and Kocurek, 2010). Baitis *et al.* (2014) found pronounced breaks in slope when determining base-level and interpreted them to be paleo-shorelines formed by the late Pleistocene retreat of Lake Otereo. The study found elevated bands of higher, more closely spaced dunes were found to occur just leeward of the terraced paleo-shorelines (Baitis *et al.*, 2014). The elevated bands are proposed as sand ridges, formed at the upwind margins of dune-fields.

While this preliminary work suggests that antecedent conditions are a major player in early Wahiba dune pattern development, additional controls such as wind regime, sediment supply and source-area geometry should also be considered (e.g. Ewing and Kocurek, 2010). If sediment reworking is the dominant player in the contemporary development of the Wahiba dune-field (i.e. 'plane source area' in the terminology of Ewing and Kocurek, 2010), the EST map could be further used to determine source area geometries.

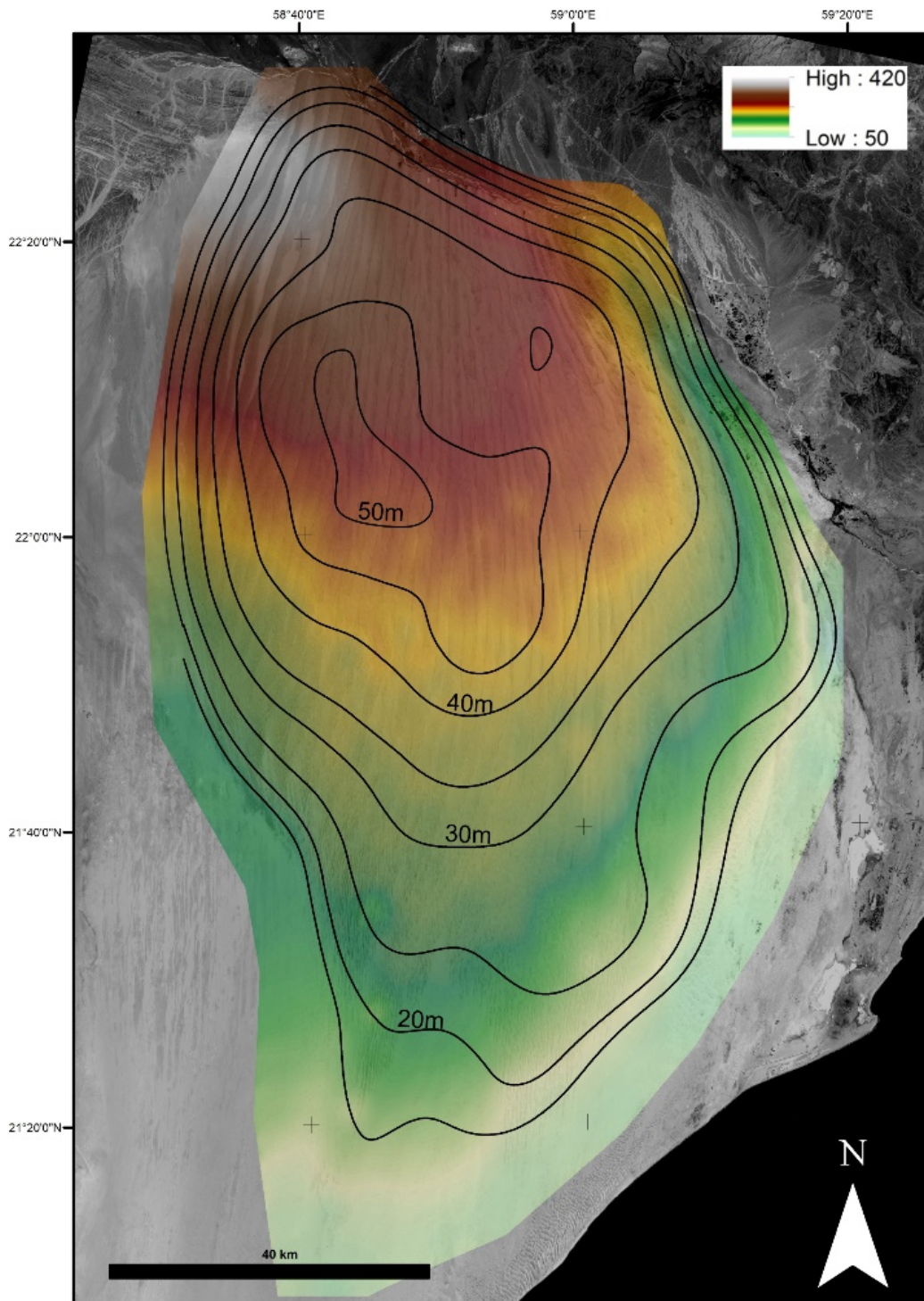


Figure 6.11: The coloured DSM map represents base-level which is overlain by EST contours. The maps are produced independently from one another but note how they approximately conform. Sediment thickness trends similarly with the underlying topography. Rapid increases in thickness generally tends to occur in conjunction with the topographic breaks-in-slope. Both maps are superimposed onto Landsat -8 panchromatic orthophoto.

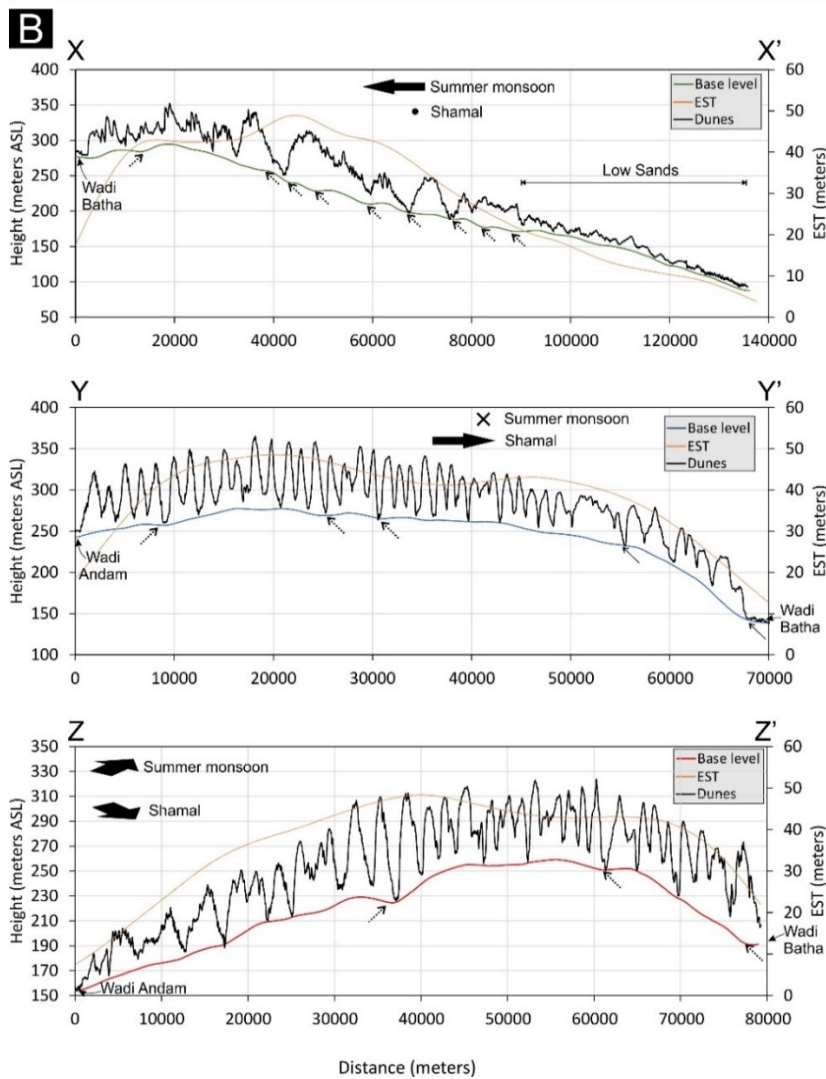
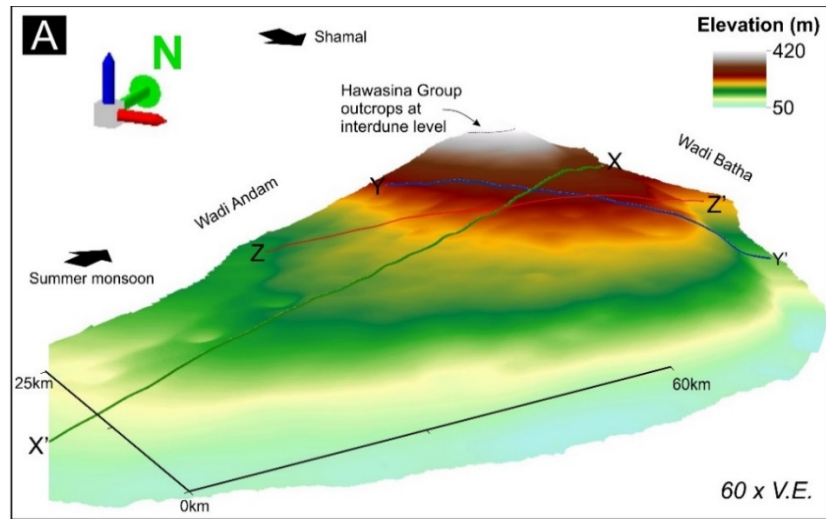


Figure 6.12: A) A 3D visualisation of base-level with line profile transects X, Y and Z taken approximately parallel, perpendicular and oblique to the general linear megadunes trend respectively. B) The profiles show base-level, dune topography and EST line profiles along north to south (X-X'), west to east (Y-Y') and a southwest to northeast (Z-Z') transects. Dashed arrows mark the breaks in slope at base-level and are commonly associated with increased EST and higher dune profiles, usually leeward of the terrace.

### 6.3 Relief Inspection

Digital Elevation Models (DEM) and Digital Surface Models (DSM) provide the opportunity to collect data on the three-dimensional shape of the land surface in an area. This section provides insights into representing this data by means of shaded relief maps. It will outline, apply and discuss a technique in which the manipulation of the datasets can assist in 'stripping away' the overlying topographic 'noise' in order to reveal the nature of an underlying surface. This is particularly useful in an aeolian system where a bedform hierarchy exists (i.e. complex dune forms).

#### *Shaded Relief Maps*

To visualize topographic data, this simple technique applies shading on a digital elevation model to create what is known as the 'hillshade effect' (Figure 6.13A). This is essentially a simulation of the pattern of shading that would be expected from a three-dimensional surface under a given set of illumination conditions (Lillesand *et al.*, 2015). The simulated light source or 'sun' can be manipulated on a 360° stage with altitude between 0-90°. This offers the ability to change the intensity of both primary and diffuse sources of lighting in order to highlight features under investigation. Flat areas will have uniform tone in shaded relief maps while slopes facing into the light source will appear brighter than those facing away from it. A shaded relief map provides a useful and quick image interpretation tool that can reveal subtle topographic changes otherwise overlooked using standard DSM maps.

#### *Residual relief maps*

Previous studies have shown that dune generations can be discriminated by means of visual examination of the imagery and elevation models (e.g. Lancaster *et al.*, 2002), statistical distributions of crest orientations (e.g. Ewing *et al.*, 2006) and residual relief separations (e.g. Hillier and Smith, 2008; Hugenholtz and Barchyn, 2010). In carefully separating, these dune hierarchies can be examined with respect to dune pattern evolution and/or palaeoenvironmental reconstruction (Kocurek and Ewing, 2005; Lancaster, 1992).

The term ‘geomorphic backstripping’ (of Hugenholtz and Barchyn, 2010) essentially refers to the unstacking of dune generations and reveals the subtle evolution of geometries. The technique filters the digital elevation data to create a smoothed surface representing the topography of the larger underlying dunes. This surface can then be subtracted from the raw DSM, revealing the topographic variability below the spatial scale of the filter. Hugenholtz and Barchyn (2010) outline the procedure to calculate residual relief (RES) for focal cell  $i$  using the following equation:

$$RES_i = Z_i - \text{avg}_{d_{i,j} < x}(Z_j) \quad [3]$$

Where:

- $Z_i$  : elevation of the focal cell
- $\text{Avg}_{d_{i,j} < x}(Z_j)$  : average elevation of all adjacent cells  $Z_j$  where the distance ( $d_{i,j}$ ) between focal cell  $i$  and adjacent cell  $j$  is less than the filter radius  $x$

Successfully separating dune hierarchies is dependent on the resolution of the datasets. Using public-access medium-resolution ASTER GDEM datasets, Hugenholtz and Barchyn (2010) demonstrated the separation of medium sized barchanoid dunes ( $\leq 107$  m high) from megadunes up to 480 m in height. Those dunes that are superimposed onto the medium-sized bedforms (<15 m high), were too small to resolve with the ASTER GDEM dataset and would require high-resolution datasets. Using these two above mentioned relief inspection techniques on a local and regional scale, one can compare the original surface representing larger dunes with superimposed dunes, the residual surface representing the superimposed dunes, and the smoothed underlying host bedforms (Figure 6.13).

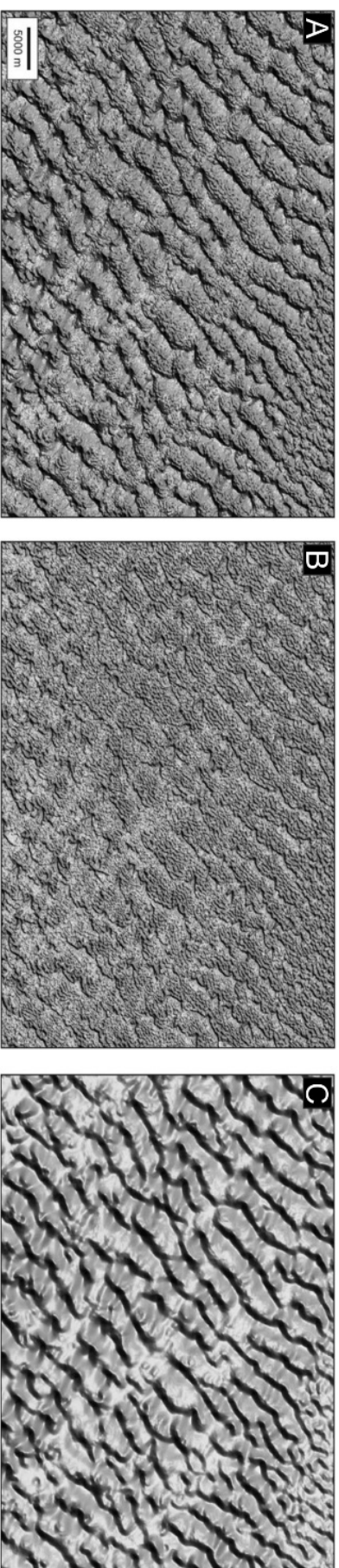


Figure 6.13: Shaded relief maps showing the results of residual relief separation the Badain Jaran desert. (A) The original surface with three dune generations. (B) The residual surface (medium-size dunes). (C) The smoothed underlying host bedform topography (large-sized dunes). (D) The discrimination of different dune generation showing the original surface (black line), residual surface (dotted line) and the underlying surface (grey lines). Modified after Hugenholtz and Barchyn (2010).

### 6.3.1 Methods

Shaded relief maps are produced in ArcGIS 10.6 using the spatial analyst plugin. Datasets were loaded as input raster files for shaded relief map production. Illumination conditions (azimuth and altitudes) are reported with each produced map and were determined according to the area of interest and bedforms under scrutiny.

Residual relief maps were created through the application of Equation 3 via ArcGIS 10.6 using the spatial analyst plugin. To produce the smoothed underlying host bedform surfaces, the DSM was run through a median filter using the focal statistics tool with a circular radius determined according to the dataset resolution and area of interest (reported with figures). The residual surface, representing the superimposed dune generation, was created using the raster calculator by subtracting the host bedforms from the raw DSM file.

Using the 100 km<sup>2</sup> high-resolution orthophoto and accompanying DSM located on the northwest corner of the Wahiba dune-field, megadunes were analysed by visual inspection for topographic variations (Figure 6.14). Three areas of interest were chosen for closer investigations: Area (i) for the topographic variability identified in the interdune corridor; Area (ii) displays pronounced transitional variability at the interdune-stoss boundary; Area (iii) focuses on the site where GPR investigations took place (section 3.4.3).

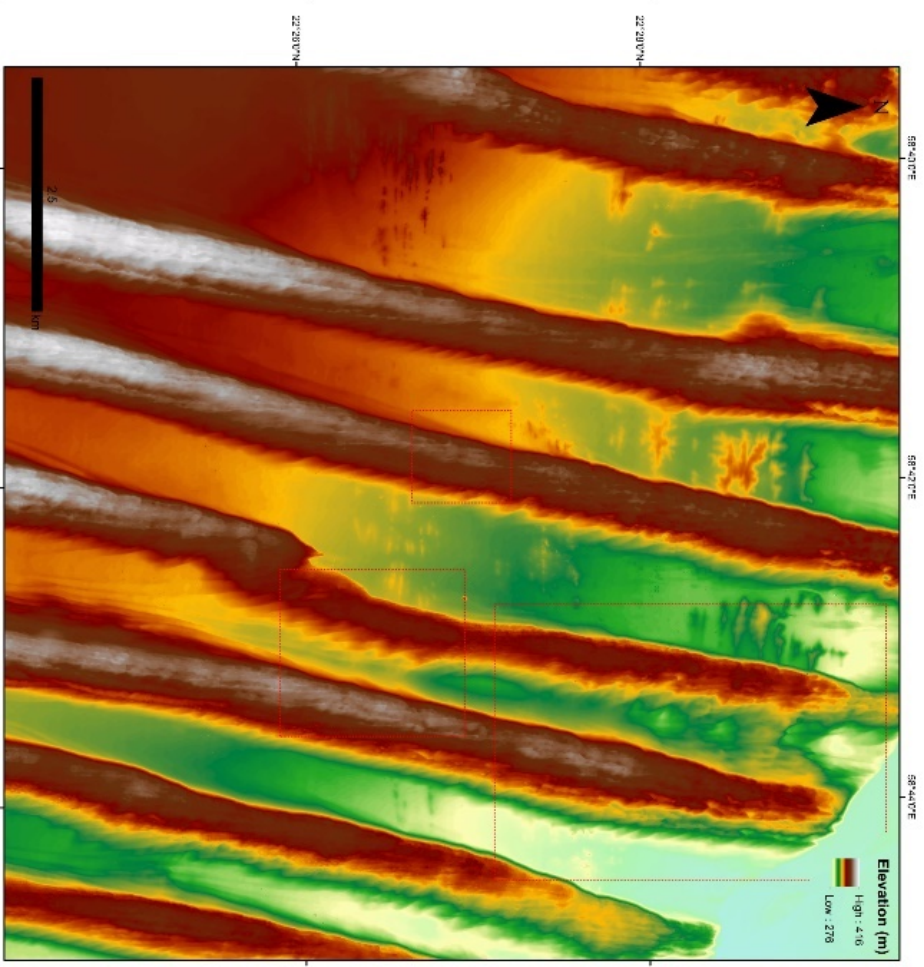
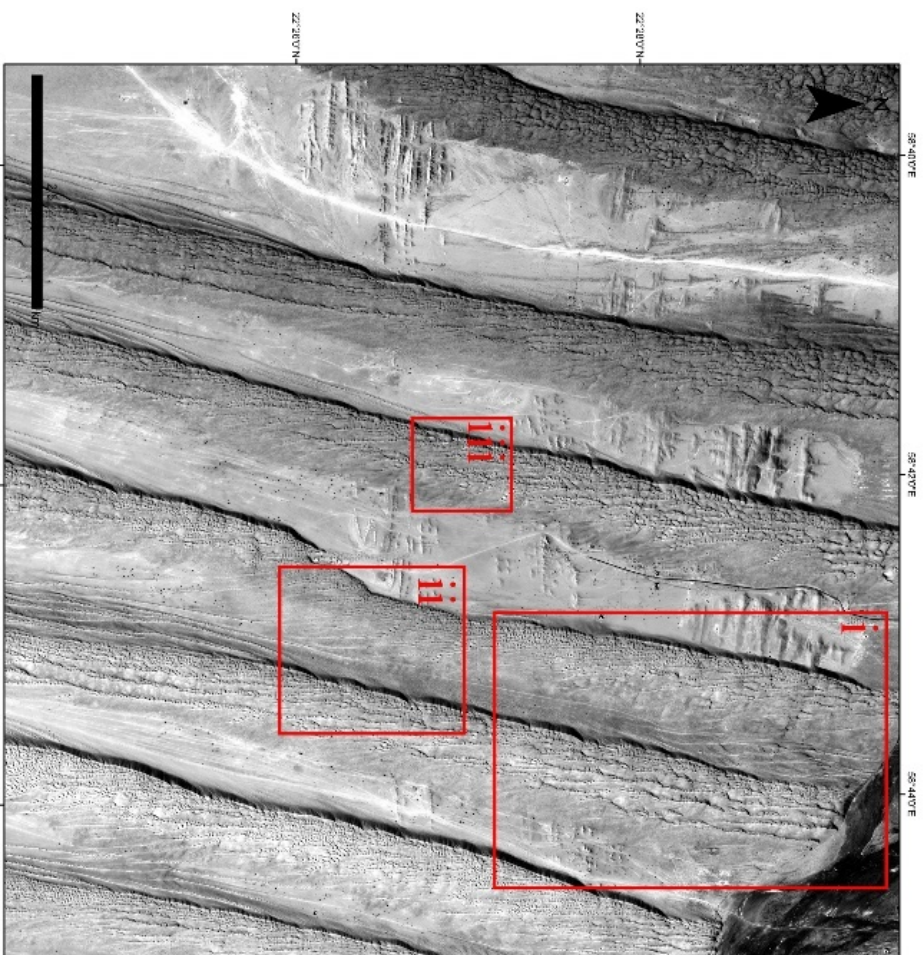


Figure 6.14: The high-resolution orthophoto (0.5 m) and accompanying DSM (1 m) of GeoEye-1 and Worldview-3. Red boxes show areas of interest reported in text. The location of these high-resolution datasets is shown in Figure 3.2.

### 6.3.2 Results

Area (i) includes two linear megadunes labelled here as MD1 and MD2 (Figure 6.15A). The megadunes are spaced approximately 1150 m apart and show active seif bedforms in an otherwise stabilised and vegetated interdune corridor (Figure 6.15A orthophoto). Five large crescentic bedforms (labelled 1-5) within the interdune are recognisable when relief shading is applied (Figure 6.15A hillshade and interpretation). Four of the crescentic forms are intercepted in cross section X-X' and display a gentle south facing slope with a steeper north facing slope. The crescentic forms range in height between 8 m and 19 m (apparent interdune-to-crest) and are spaced between 660 m and 690 m (apparent crest-to-crest). The eastern horn of the crescentic forms terminates at the lee slope of MD2 while the western horns are observed by fluctuations in the stoss/crest topography of MD1 (profile Y-Y' in Figure 6.15B). Profile Y-Y' was produced with the residual relief removed (i.e. superimposed dunes) to reduce the effects they have on the topography. Along this profile, the crest spacing ranges between 130 m and 616 m. The mean trend of the western horn is SSE-NNW (335°; n=5). Five smaller crescentic bedforms are identified on the gentle south-facing slope of bedform 4 (Figure 6.15A interpretation). The crescent lengths range between 157 m and 386 m (n=5). Perpendicular to crescent, the bedform are oriented between 327° and 001° (n=5).

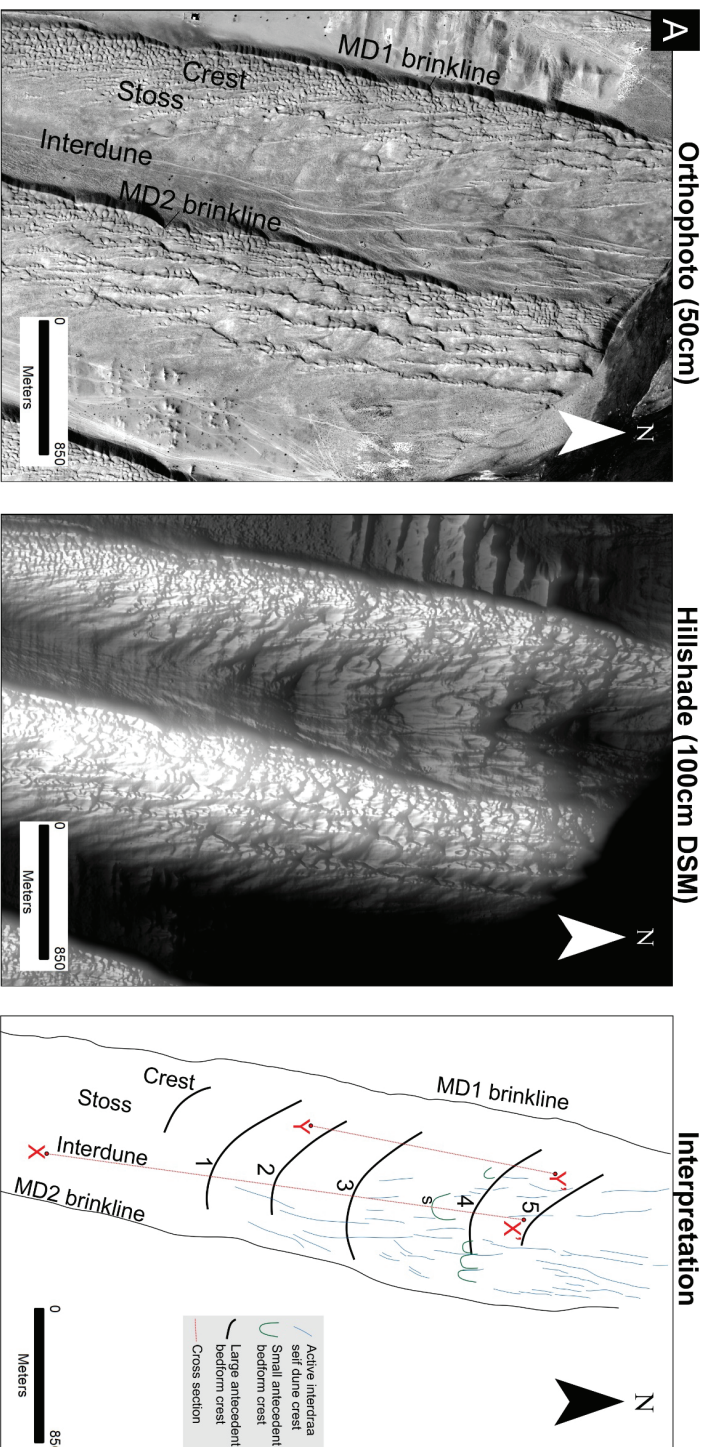


Figure 6.15: (A) The panchromatic orthophoto shows the two linear megadunes MD1 and MD2 of Area (I). Subtle topographic variations identified in orthophoto and DSM were further inspected using the shaded relief technique (sun azimuth 180° at 25° altitude). The resulting map shows partial relicts of large crescentic bedforms, recognizable in the interdune area (see interpretation map). (B) South to north cross-sectional profiles: X-X' runs parallel to MD1's crest. Profile X-X' show the bedforms have a gentle south facing slope and steep north facing slope. 'S' marks the small crescentic bedform superimposed on the larger bedform crossed in X-X'. Profile Y-Y' was generated using residual relief separation and shows the smoothed underlying surface (median filter radius = 50 m). This was done to minimise the effect of the superimposed dunes. The profile shows three offset highs (2-4) that are interpreted to be the western horn of the large crescentic bedforms, as shown in (A) and in profile X-X'.

Area (ii) displays MD1 and MD2 approximately 2 km south of Area (i). Topographic heterogeneity at the stoss-interdune boundary was identified in the DSM (Figure 6.14) and scrutinised using the relief shading (Figure 6.16A, B). The width of MD1 in Area (ii) is greater than that in Area (i) (850 m *versus* 600 m respectively) and forms a narrower interdune. The orthophotos show a well vegetated stoss slope with thin (~20 m wide) N-S trending active seif dunes. Three large-scale features interpreted as crescentic bedform fragments (1-3) are observed forming part of MD1's stoss slope and connect to MD2's lee-slope plinth (Figure 6.16A hillshade). Within the stoss-interdune boundary of MD1, the large crescentic features show gentle south facing slopes and steeper north facing slopes (Figure 6.16A hillshade). The most obvious and complete crescentic bedform (3) is ~15 m in height (crest peak to trough). Bedform 3's western horn forms part of MD1's stoss and crest and extends toward 354°, sub-parallel to the linear megadune brinkline (MD1) of 009°. Its eastern horn forms part of MD2's plinth and is associated with a break in the megadunes brinkline (see arrow in Figure 6.16A hillshade map).

Observed atop the large crescentic bedforms (1 and 2) are four medium-scale crescentic bedforms superimposed onto their gentle south facing slopes. (Figure 6.16B Hillshade and Interpretation). These four crescentic forms themselves display a gentle south facing slope and a steeper north facing slope (Figure 6.16C, Y-Y'). The bedform heights range between 1 and 2.5 m (n=4) with a crest spacing of ~400 m when observed in train (n=1). The crescent horns are spaced about 70-93 m apart (mean 83 m; n=4). The crescent lengths range between 126 m and 276 m (n=4). Perpendicular to crescent, the bedform are oriented between 339° and 007° (n=4). An approximate perpendicular cross-sectional profile of the host megadune (X-X') reveals the topographies as knick-points, which form terraces along the stoss-slope (Figure 6.16C). These knick-points host active seif dunes which extending along these terraces (Figure 6.16B Orthophoto).

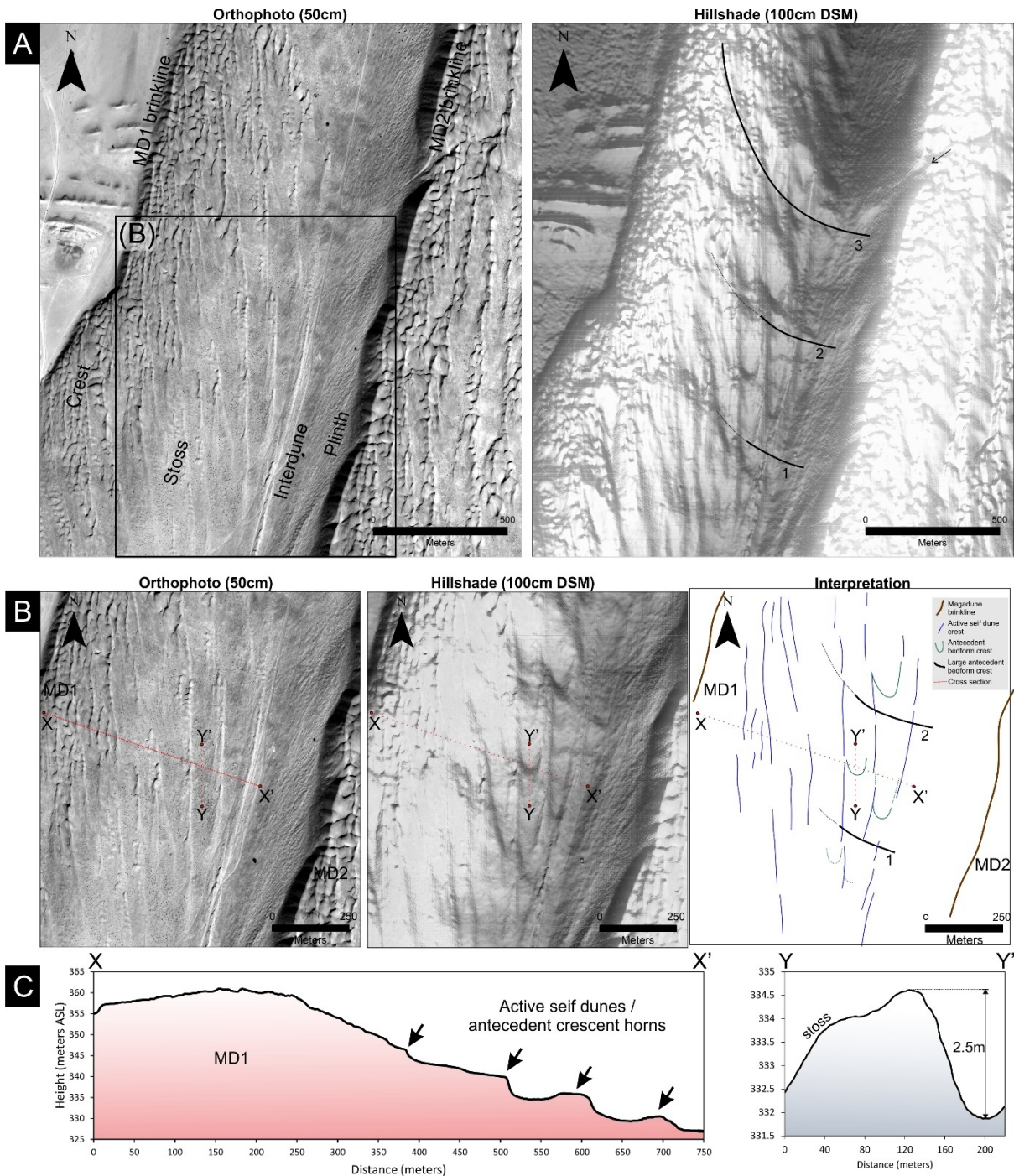


Figure 6.16: A) Area (ii) displays the close relationship between the stoss slope of MD1 and the lee slope plinth of MD2. The interpreted lines on the Hillshade DSM (sun azimuth  $190^\circ$  at  $20^\circ$  altitude) were traced out using the highest points along DSM contours. The resulting interpretation reveals three large-scale arcuate lines (1-3), potentially fragments of crescentic bedforms. B) The zoomed in orthophoto shows megadune MD1 contains active seif dunes superimposed onto the well vegetated stoss slope. Under hillshade (sun azimuth  $145^\circ$  at  $25^\circ$  altitude), medium-scale crescentic bedform horns become apparent on MD1's stoss slope. Where they coincide, the active seif dunes trend along the crescentic bedforms. B) X-X' cross-sectional profile of MD1 shows prominent knick-points near the base of the stoss slope. The knick-point topography correlates with active seif dunes, as well as the crescent horns observed in the shaded relief map. Y-Y' cross-sectional profile perpendicular to the crescentic bedform ( $\sim 2.5$  m tall) shows a gentle south facing slope and a steep north facing slope.

Area (iii) was analysed to scrutinise the megadune crest. Additionally, GPR acquisition at this site allows the inspection of internal architectures (GPR Site 4 of Hern *et al.*, 2018; section 3.4.3). The megadune consists of superimposed seif and crescentic bedforms (Figure 6.17A Orthophoto). A 90-100 m wide terraced surface devoid of any active dunes is present on the east flank of the megadune. The shaded relief map was produced with a mean filter of 5 m to remove the superimposed topography and produce a surface that best represents the smoothed underlying topography. The surface revealed obvious crescentic bedforms on the stoss slope, four of which (labelled a-d) were analysed in detail (Figure 6.17B, C). Results reported below will include the depth of the interpreted bedforms from the height of the GPR zone (purple box in Figure 6.17A).

Bedform A: Partial exposure of a crescentic bedform with a well-defined crest and trough (Figure 6.17B). The western horn of the bedform dips below the surface or is eroded. The eastern horn extends towards 031°, terminating at the rear of proceeding crescentic bedform. Both peak and trough fall below GPR elevation between 1.1 m to 8.9 m. Perceived height of the bedform is 2.1 m (crest to trough).

Bedform B: Poorly exposed, although in plan-view a crescentic form is apparent (Figure 6.17B). Horns either dip below the surface or are eroded and no directions were acquired. Both peak and trough fall below GPR elevation (between 2.6 m to 8.6 m). Perceived height of the exposed bedform is 0.3 m (crest to trough).

Bedform C: Good exposure of a crescentic bedform in plan-view (Figure 6.17C). The eastern horn extends towards 021° and western horn towards 348°. The deepest trough to the highest peak occurs at the bedform crescent with a perceived height of 3.9 m. While the bedform lies well above the elevation of the GPR site (2 m to 8.2 m), the deepest trough extends 1.4 m below the maximum height of the GPR surface. The bedform is orientated at 005° perpendicular to crescent.

Bedform D: Excellent exposure of a crescentic bedform in plan-view (Figure 6.17C) with a well-preserved crest, trough and horns. The eastern horn ( $d_2$ ) of the bedform extends towards  $031^\circ$  and is interpreted to connect with the eastern horn of the preceding bedform. The western horn ( $d_1$ ) extends towards  $356^\circ$  and terminates at the rear of the preceding bedform (Figure 6.17C). The bedform is perceived to be 3.2 m in height (crest to trough) and is oriented towards  $015^\circ$  (perpendicular to crescent). The bedforms horns protrude up to 2.6 m above the minimum GPR surface and up to 3.2 m below the maximum GPR surface elevation. The bedform trough always falls below GPR elevation between 0.6 m and 6.3 m (profile Y-Y' Figure 6.17C). An adjacent crescentic bedform horn ( $d_3$ ) is identified in plan-view and in profile Y-Y' (Figure 6.17C). The full shape of the bedform is not distinguished as the stoss of the megadune steepens to the east.

Analysis of 13 additional crescentic bedforms at the approximate elevations of bedforms A, B and D showed average bedform orientation perpendicular to crescent of  $352^\circ$  ( $n=16$ ). The average direction for the eastern horns is towards  $013^\circ$  and the western horn towards  $336^\circ$ .

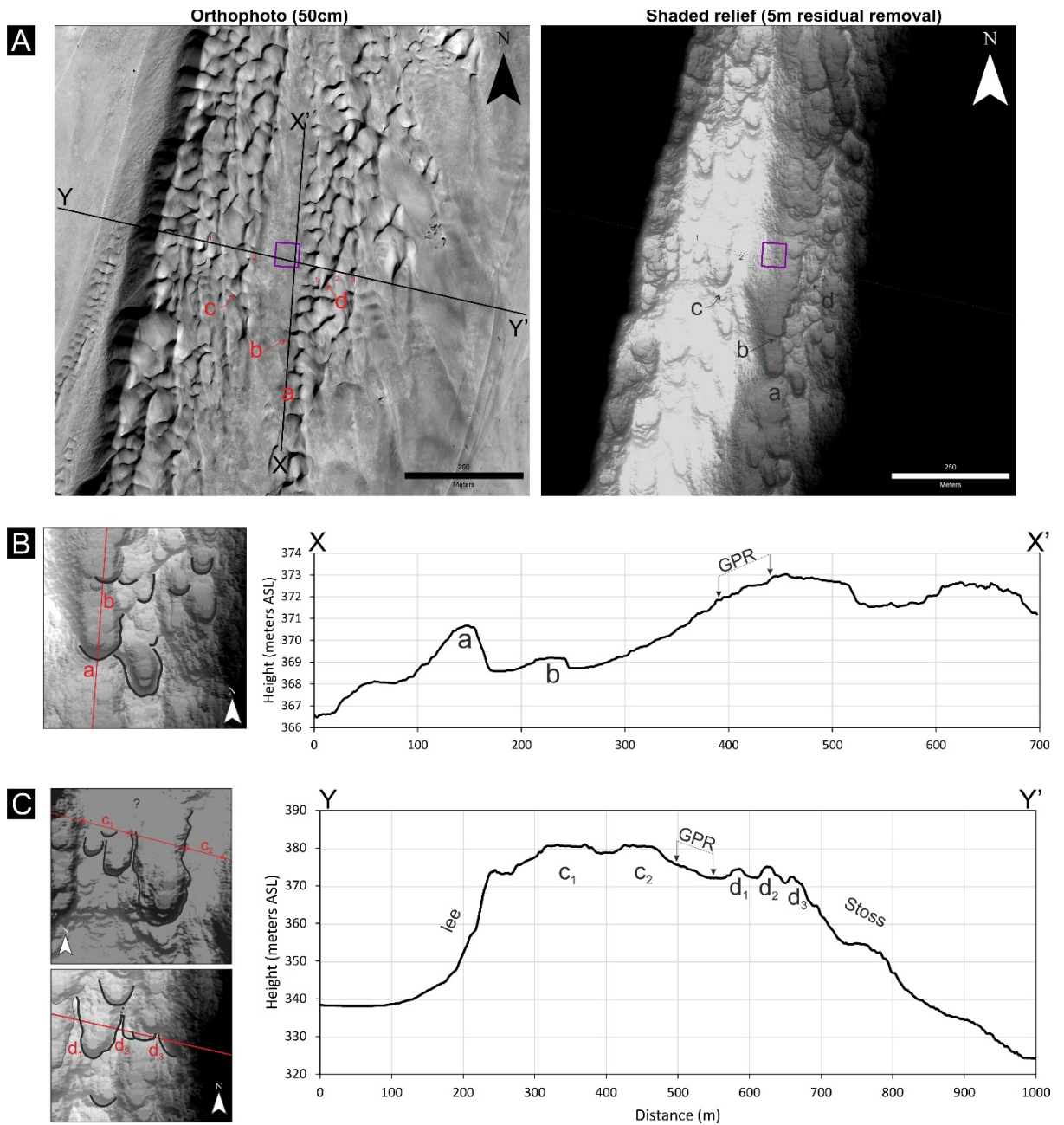


Figure 6.17: A) The high-resolution orthophoto of megadune in area (iii). The shaded relief map shows the smooth underlying topography (5m radius mean filter applied; sun azimuth 180° at 04° altitude). Medium-sized crescentic forms are identified on the megadune stoss slope under residual relief. The purple box shows the site of 3D GPR acquisition (not analysed in this study) and OSL sampling of Hern et al. (2018). B) Zoomed in section of identified forms a and b with cross-section X-X' shows these forms have a gentle south-facing slope and steep north-facing slope. C) Zoomed in section of identified forms c and d, with cross-section Y-Y' shows peaks (c<sub>1</sub>, c<sub>2</sub>, d<sub>1</sub>, d<sub>2</sub>, d<sub>3</sub>) separated by troughs of what are thought to be horns and troughs of barchanoid forms.

### 6.3.3 Discussion

#### *Areas (i) and (ii): Large-to-medium-scale bedforms*

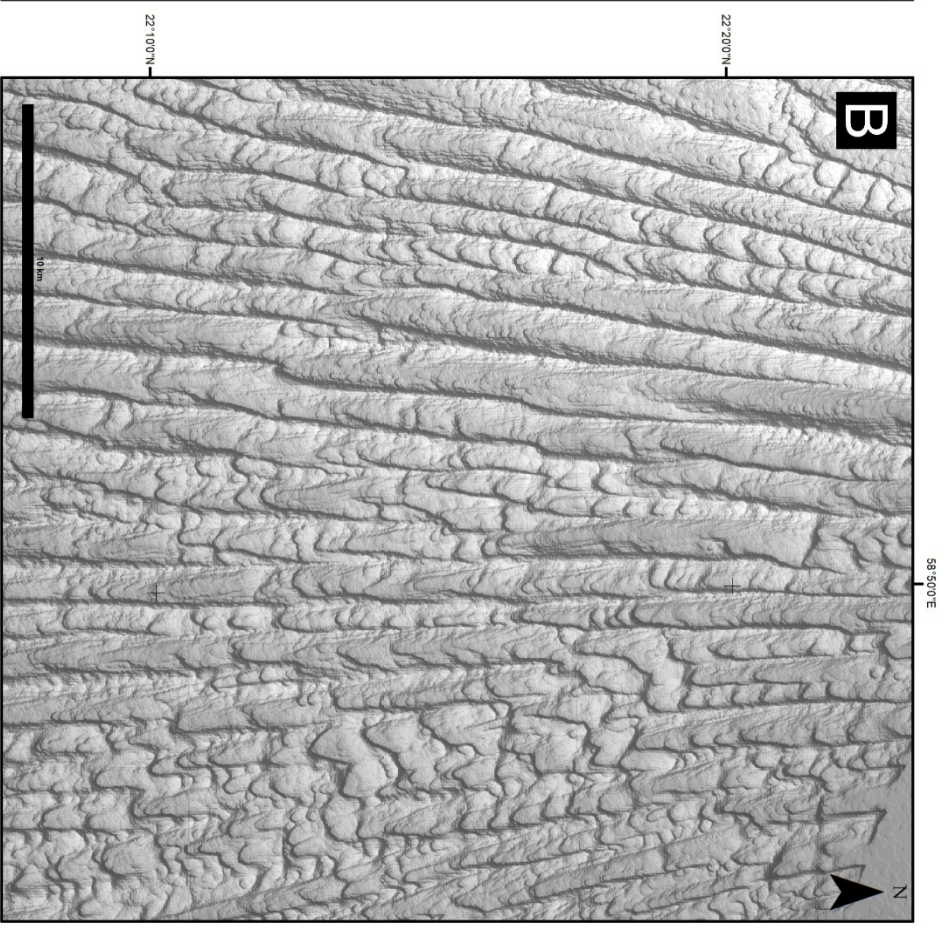
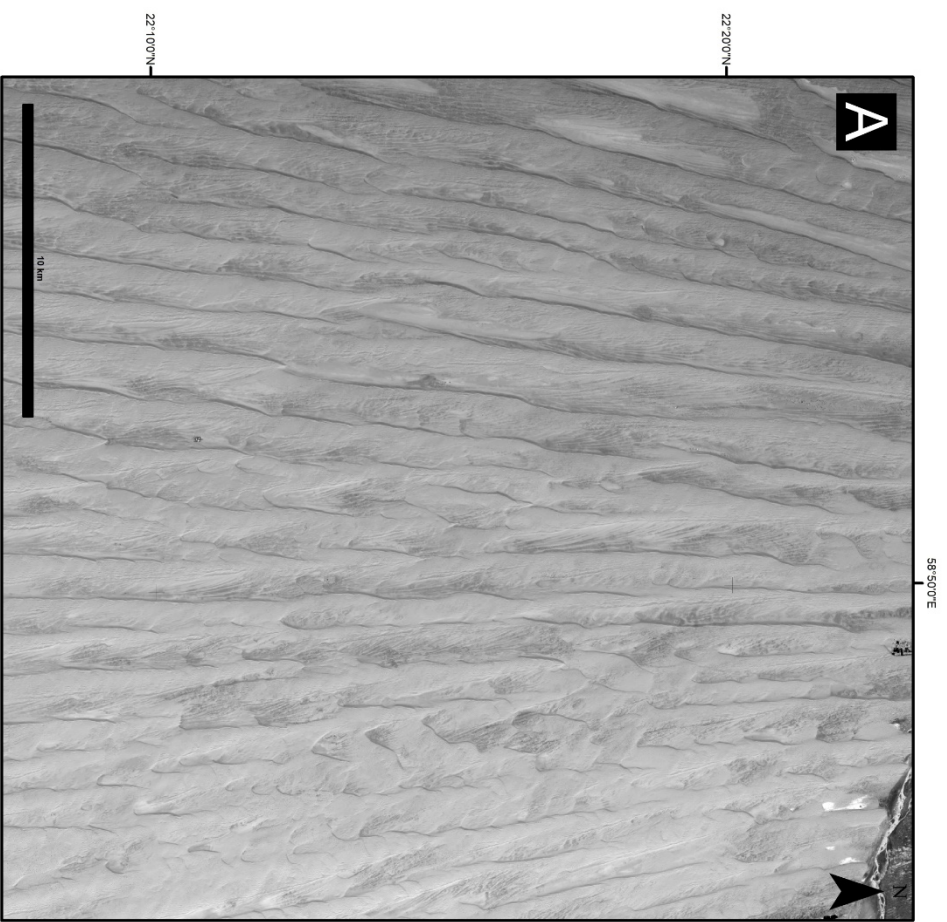
Mega-crescentic dunes are common and well-known bedforms of the Wahibas (Figure 4.2; Figure 4.3; Figure 4.4; Goudie *et al.*, 1987; Glennie *et al.*, 2011; Fryberger *et al.*, 2016a). In the High Sands, these bedforms have been classed as ‘mega-transversals’ inferred to have developed under the modern wind regime (Goudie *et al.*, 1987). These bedforms are typically observed within interdune areas, flanked by the linear dunes, and have large barchanoid crescentic lee slopes facing northwards (e.g. Figure 4.2; Figure 4.3). Linear crests that break up into complex aklé patterns (overlapping barchans) are also observed throughout the High Sands (Goudie *et al.*, 1987). On the eastern margin, it is thought that the barchan dunes form through the gradual reworking of large linear dunes (Fryberger *et al.*, 2016a). Evidence from area (i) and (ii) using the high-resolution datasets shows that these mega-barchans exist as subdued, well-stabilised bedforms falling below interdune elevation. From this evidence, two possibilities are suggested: (1) these crescentic bedforms are developed under the current wind regime as proposed by Goudie *et al.* (1987). In the instance of area (i) and (ii), they have recently (Holocene period) been stabilised by vegetation and/or soil crusts (note their proximity to the fluvial Wadi Batha) and will reactivate with increased sediment supply, as seen in other portions of the dune-field (e.g. Figure 4.2; Figure 4.3; Figure 4.4). (2) The exhumed topography reveals relict megadunes, potentially evidence of the ancient erg configuration (Pleistocene period) where the wind regime was dominantly unimodal (southerlies). In this scenario their horns, observed encroaching into the linear megadunes that flank them form the contemporary linear megadune core. Under the current wind regime, linear dune development was favoured and built from this core, which acted as an antecedent template. Atop, the medium-scale crescentic forms are superimposed dunes and occurred either contemporaneously with the active megadune or followed a stabilisation event (similar to the contemporary superimposed dunes migrating on the linear megadune axis).

Supporting evidence from a larger area using the medium-resolution datasets better represents the abundance of the crescentic forms in the High Sands when viewed using shaded residual relief maps (Figure 6.18). In some instances, a considerable portion of the linear megadune core consist of large-scale crescentic topography (Figure 6.18A, B). The northeast corner is distinguished by darker sediments where a disturbed pattern exists (Figure 6.18C). Under residual relief shading medium-scale barchan topography covers the disturbed pattern and fills the linear interdune corridors (Figure 6.18D). The distinct variation here may be explained by the variation in subdune topography as discussed in section 6.2 which would have had an effect on growth and dune evolution, extending into variations observed in the contemporary morphology.

*Area (iii): Megadune crest*

Care must be taken in the interpretation of the underlying host bedforms identified. The automated method used a 5 m circular radius to classify minimum surface heights and thus produces noise in the form of 10 m wide circular pits as seen in Figure 6.17. Testing was conducted under varying conditions (2 m minimum, 5 m mean and 10 m mean) and produced similar results. In all iterations, the main crescentic bedforms (a-d) analysed in Figure 6.17 were reproduced.

Under the assumption that the interference of the contemporary bedforms are reduced by the residual relief technique, these bedforms form the template on which the current superimposed dunes migrate/accumulate. As most of the bedforms fall near to and below the (proposed) relict surface on which the GPR was acquired, they may be of use when interpreting the processed radargrams.



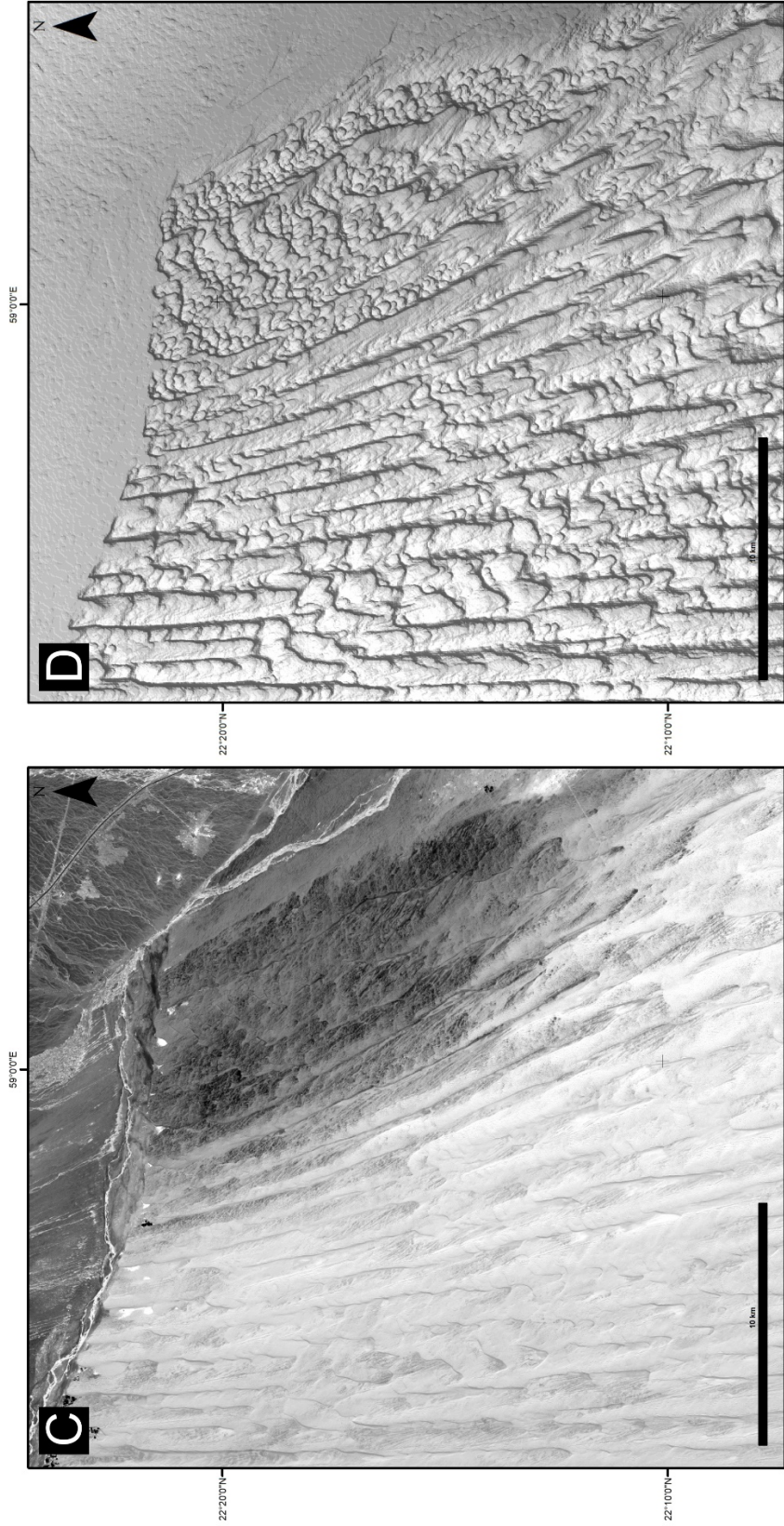


Figure 6.18: A) Landsat-8 panchromatic orthophoto of the central High Sands (~800 km<sup>2</sup>). The surface pattern is dominated by linear megadunes. Crescentic bedforms are scattered and often fragmented B) Shaded relief map showing the underlying topography of the same area in (A). The abundance of crescentic forms becomes much clearer with this enhancement, occurring in almost all linear dunes. C) The northeastern margin of the erg is flanked by the fluvial Wadi Batha. The NE corner is easily distinguished by darker sediments and a disturbed surface pattern. D) Shaded relief map showing the underlying topography of the same area in (C). Medium-scale crescentic dunes dominate the disturbed pattern and fill linear interdune corridors. Maps (B) and (D) produced from ALOS AW3D30 DSM datasets. A 100m radius minimum filter was applied to investigate the underlying topographic expressions in (B) and (D) (sun azimuth 160° at 20° altitude).

## 6.4 Geometry of Internal Architectures

Techniques used to understand the internal architectures of aeolian bedforms include mechanical excavation (e.g. McKee, 1966), hand dug trenches (e.g. McKee, 1979; Fryberger, 2017), coring (e.g. Radies *et al.*, 2004); measurements of deflating dunes (e.g. Hunter, 1977; McKee, 1979) and numerical modelling (Rubin and Hunter, 1985). Ground Penetrating Radar (GPR) allows the quickest and least intrusive way to image sub-surface dune strata (section 5.5). Aeolian sediments can be good targets for GPR surveys because they have high resistivity allowing for good penetration, and they contain large-scale sedimentary structures that can be resolved through GPR (Bristow *et al.* 2005).

### 6.4.1 Survey Location

This study presents results from a GPR survey conducted on a linear megadune containing Site 4 of Hern *et al.* (2018) (see section 4.3). The survey site is located in the northwestern corner of the Wahiba Sand Sea, approximately 7 km from the northern margin and 6 km from the western margin of the erg (Figure 6.19). The studied megadune is a complex linear bedform that trends about north-northeast to south-southwest and supports many smaller superimposed linear seif and crescentic bedforms (Figure 6.19B). The megadune is asymmetric in cross-section with a well-developed brinkline along the western margin of the dune (Figure 6.19B). The gentle sloping eastern flank of the megadune is undulating, a result of many superimposed dunes, while the steeper western flank is relatively smooth with less superimposed bedforms. A 600 m approximately east-west GPR traverse was conducted perpendicular to the linear megadune trend (Figure 6.19B). The site was selected due to its position relative to the town of Wasil (~ 8 km), the ease of access to the site's eastern flank for OSL dating (Figure 4.4), and the high quality of GPR profiles that represent the architectural diversity in sections along the traverse as presented in section 6.4.4. In addition, the site is complemented by high-resolution datasets examined in section 6.3 which was an important contribution to the interpretation of the profiles.

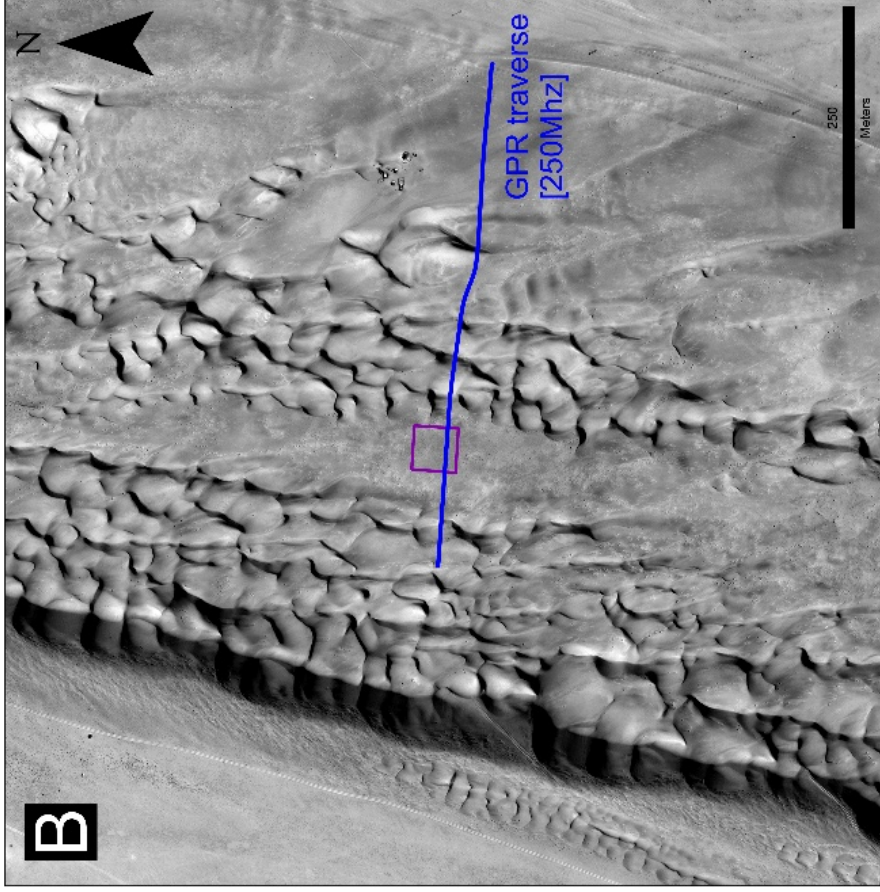
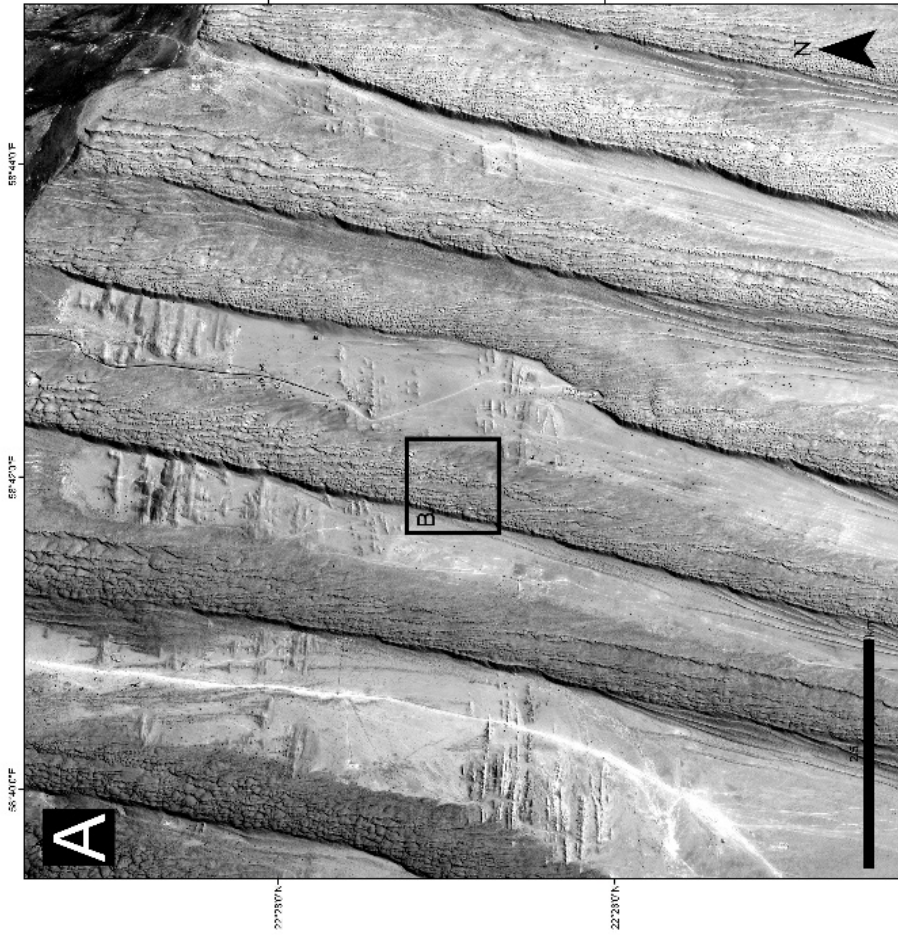


Figure 6.19: Survey location for the 2D GPR profile. (A) The high-resolution orthophoto and zoomed-in study site in (B) showing the west – east GPR traverse on the eastern flank of the linear megadune. The purple box in (B) shows the site where trenching and OSL dates were acquired by Hern et al. (2018). The relative position of the high-resolution orthophoto in the Wahibas is shown in Figure 3.2

## 6.4.2 Data Collection

Primary data for GPR profiles were collected using a MALÅ Geoscience RAMAC system with a 250 MHz shielded antenna. The antennas were placed on the ground in the parallel broadside configuration with 0.36 m separation. Measurements were taken at 0.25 m intervals with 4 stacks at each point. The system was vehicle-towed with a trailing encoder wheel used to trigger readings (Figure 6.20). An on-board GPS system recorded XYZ data, while a separate at-time-of-acquisition UAV survey was used to capture a true DEM in order to overcome any GPS limitations (Figure 6.20B). Two-way-time (TWT) velocity analysis was carried out using a buried metal can at 1 m depth and a playa calcrete that is overlapped by the draa margin, flattened beneath sand of variable depth. The velocity was calculated at 0.155 m ns<sup>-1</sup> which is within range for dry sand (Reynolds, 2011). Resolution can be taken as one-quarter of the wavelength ( $\lambda$ ) of incident radiation (Reynolds, 2011). Therefore, using a velocity of 0.155 m ns<sup>-1</sup> with a 250 MHz antenna gives a wavelength of 0.62 m and a resolution of ~16 cm at one-quarter wavelength. The GPR data was processed in REFLEX-W with the treatment procedures reported in Appendix A1.

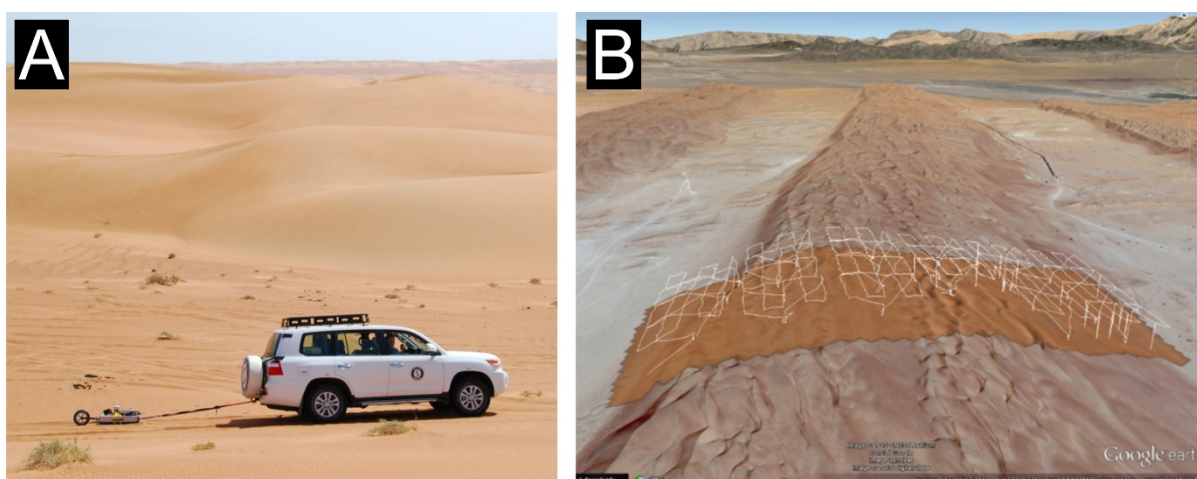


Figure 6.20: (A) Vehicle-towed GPR system. (B) Flight path of UAV to create a high-resolution DEM (overlain onto Google Earth Map with view to the north). Images courtesy Robin Westerman and Dominic Tatum.

### 6.4.3 GPR profile interpretation methods

Radar data or radargrams of GPR surveys superficially resemble that of a seismic reflection profile, however, their interpretation commonly involves the deciphering of interference patterns rather than the discrete reflections and diffractions characteristic of seismic (Gawthorpe *et al.*, 1993). GPR reflection coefficients in sediments mainly depend on moisture content due to the high dielectric permittivity of water (Buckman *et al.*, 2017). As an example, the radar responses in the Wahibas have been attributed to variations in permittivity, magnetic susceptibility and moisture, which have been ground-truthed through vertical trench profiles (Buckman *et al.*, 2017; Hern *et al.*, 2018). The resulting radargrams reflect damp-over-dry interfaces that represent primary sedimentary structures (Figure 6.21).

Radar sequence and radar sequence boundaries were first introduced by Gawthorpe *et al.* (1993). Following stratigraphic interpretation principles, it is necessary to identify reflection terminations to identify radar sequence boundaries (Figure 6.22; e.g. Bristow, 2005; Tatum and Francke, 2012). Terminations or truncations mark breaks in time and successive radar sequences can be used to construct a relative chronology following the laws of superposition and cross-cutting relations (Bristow, 2005). Radar sequence boundaries allow the identification of radar stratigraphic units (RSU), a group of which may assist in identifying a genetic unit (Gawthorpe *et al.*, 1993). A genetic sedimentary unit is an association of facies that are positionally related and have a discrete geometry (Tatum and Francke, 2012).

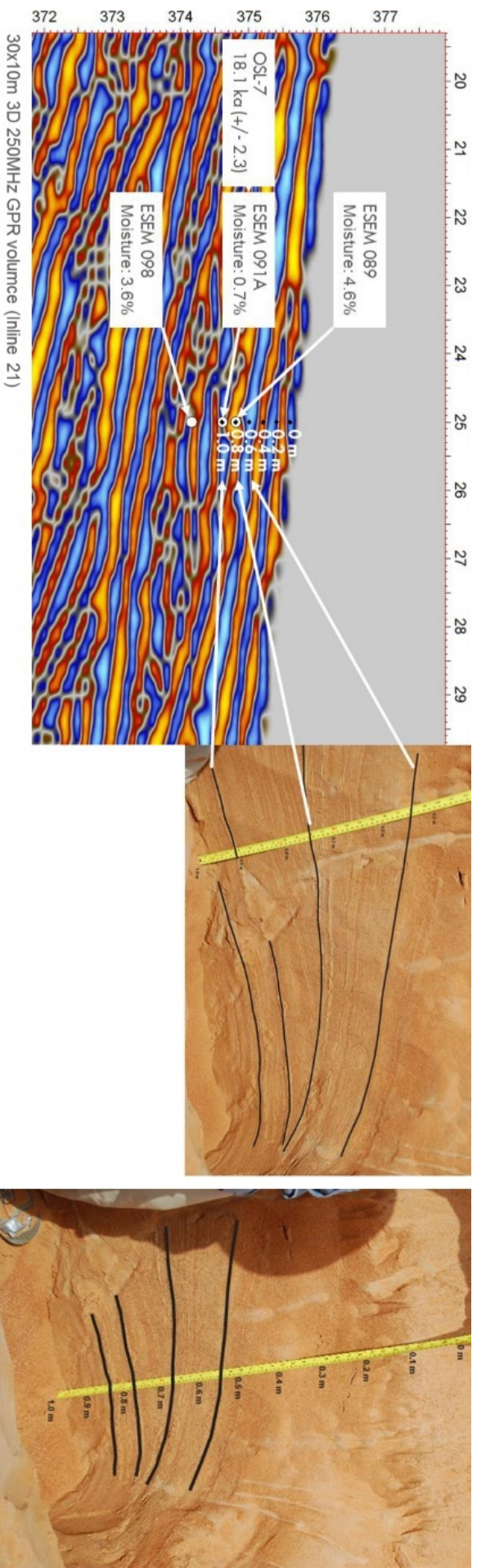


Figure 6.21: Marked variations in moisture content in the primary depositional fabric are directly linked to GPR response. A positive reflection event (blue) results when convolved with a negative (red) reflection coefficient from a damp-over-dry (i.e. slow-over-fast) interface (Buckman et al., 2017). Image modified after Herr et al. (2018).

The study employed the above principles in order to reinterpret the GPR profiles of Hern *et al.* (2018) (section 3.4.3). Major reflections were detected and traced. Identification and characterisation of reflection terminations (e.g. downlap, onlap, toplap; Figure 6.22) were used to determine radar sequence boundaries. Significant radar reflection patterns allowed the location of bedding planes, bedsets and cross-stratification. The reflection patterns with similar geometry were then grouped into radar facies in order to interpret them into their genetic sedimentary units.

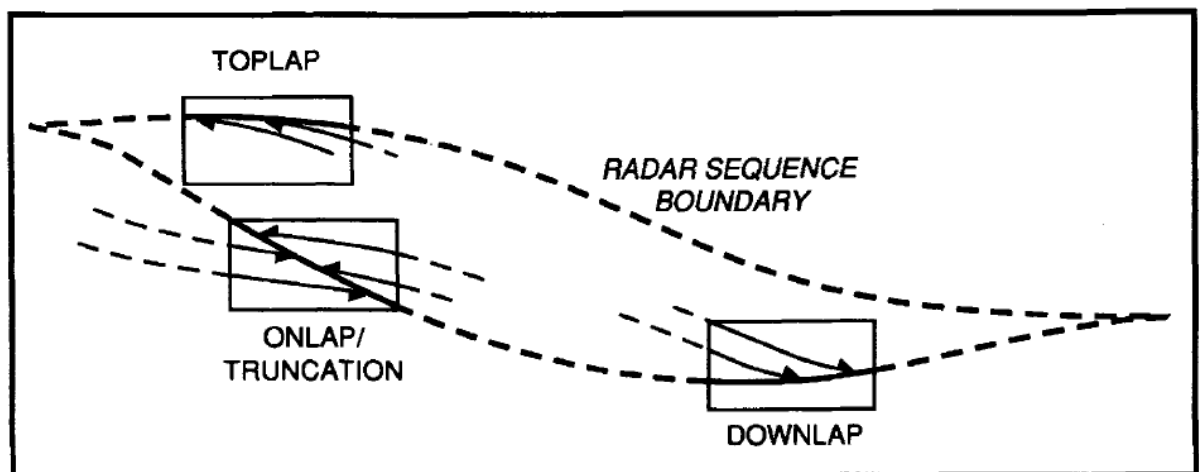


Figure 6.22: The drawing indicates the main types of reflector terminals (toplap, onlap and downlap). The terminations are used to identify radar sequence boundaries. Extracted from Gawthorpe *et al.* (1993).

West-to-east trending radargram transects extracted from Hern *et al.* (2018) (section 3.4.3) are tied to the high-resolution orthophoto and residual relief map of the GPR site (area (iii) of section 6.3.2) in order to compare them to the surface and residual surface topographies (Figure 6.23). No active dunes were crossed in the four radar intercepts (A-D in Figure 6.23) and the uppermost (groundwave) surface of the profiles represents the contemporary megadune surface.

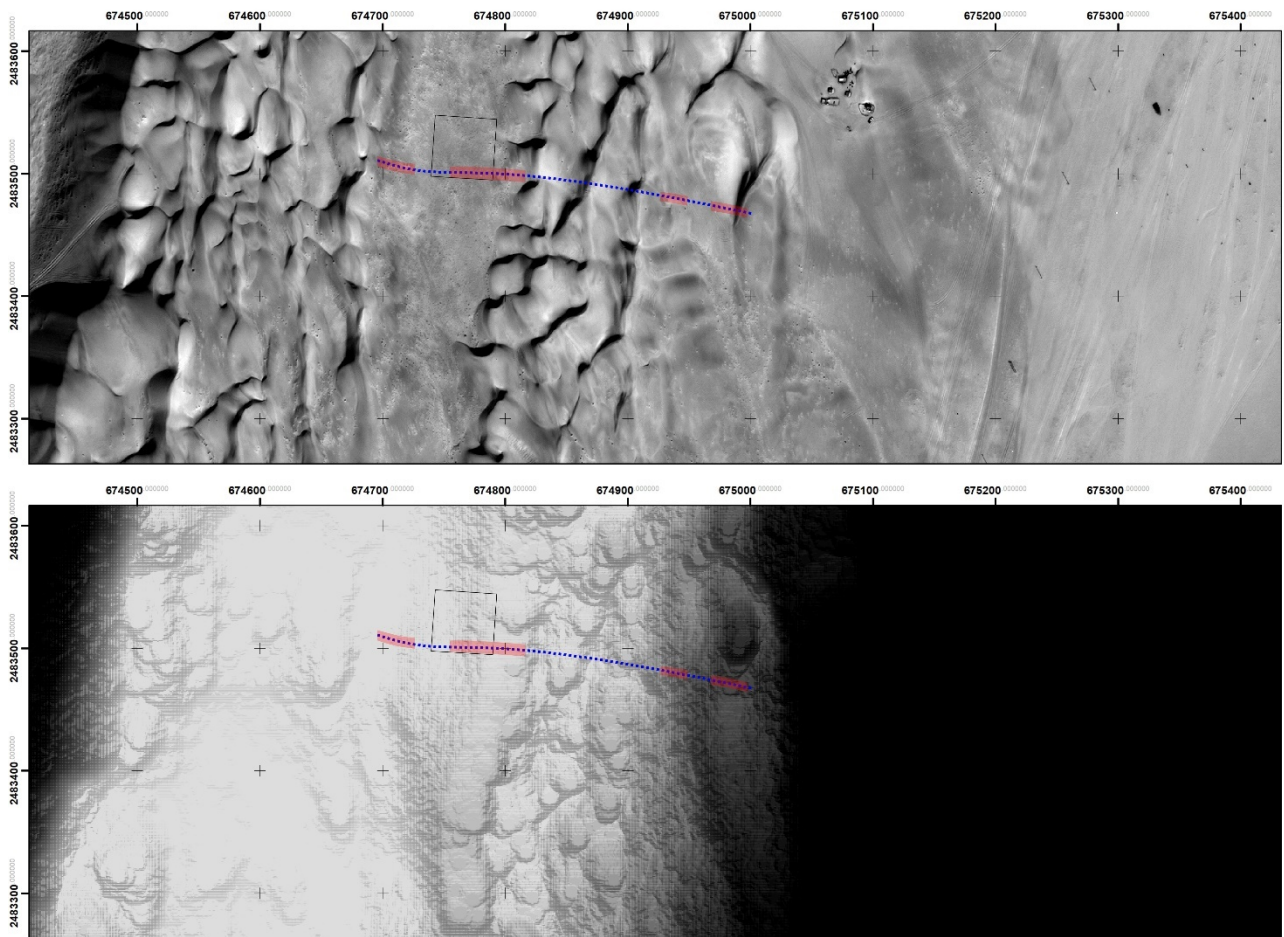
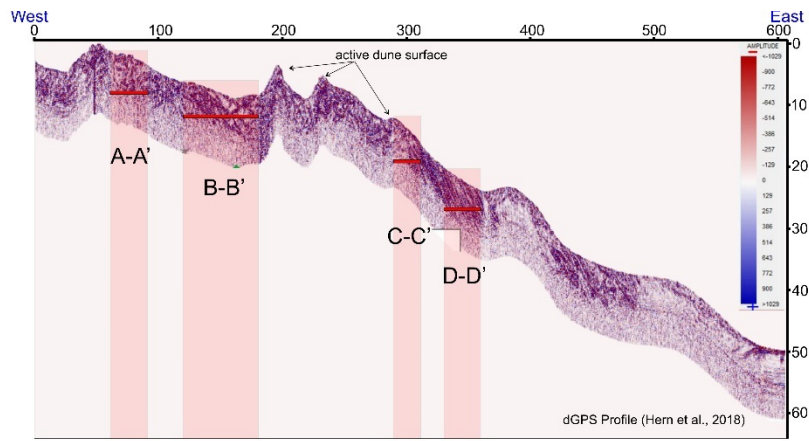


Figure 6.23: Red highlights mark the approximate locations of 2D GPR radargrams tied to both the orthophoto and residual relief map. The dashed blue line represents the approximate traverse of the 250MHz GPR line between 60 m and 360 m. The black dashed box represents 3D GPR site acquisition (not analysed in this study). Orthophoto and GPR capture dates are 2 years apart (GPR acquisition 2015, orthophoto January 2017).

#### 6.4.4 Results and Interpretation

The GPR transect covers a total of 600 m roughly perpendicular to the linear megadune trend. Four radargrams (A-A', B-B', C-C' and D-D') along this transect are captured between 60 m and 360 m (dune crest and upper-stoss slope) and their coverage ranges between about 30 m and 70 m (Figure 6.23). Three types of reflection patterns, or radar facies, became apparent (Figure 6.24): Radar facies 1 (RF1) are strong, laterally discontinuous concave-up reflections. Their internal reflections consist of low-angled trough-shaped to asymptotically dipping reflections that can also occur in small (~1 m thick) lens-shaped packages. Internal reflections are sometimes associated with a dimmed signal. RF1 is interpreted as trough cross-stratification associated with the migration of crescentic dunes. Radar facies 2 (RF2) are strong, laterally discontinuous convex-up reflections. Internally they consist of mound-shaped packages that tend to increase in amplitude with height. The internal reflections are commonly associated with a dimmed signal. RF2 is interpreted as either dune spurs or erosion surfaces between troughs. The former interpretation is preferred due to the continuity of each reflector's convex-up arch and their architectural association with RF1 in profile descriptions below. Radar facies 3 (RF3) are horizontal to low-amplitude undulating reflections. They are commonly continuous within the bounds of each profile. They always occur above the upper-most deflationary surfaces and mark the top surface of the radargram profiles. They are typically less than 1m thick. RF3 is interpreted as wind-ripple deposits that blanket the contemporary megadunes. Low-amplitude undulating reflections represent small slipfaceless zibar deposits.

**Profile A-A'** covers 30 m across the megadune crest (traverse from 60 m to 90 m) located approximately 48 m above the interdune surface. The radargram reveals near-surface aeolian architecture to a depth of about 10 m and consists of RF1 below a thin slice of RF3 (<0.5 m). Figure 6.25C reveals trough cross-stratification of RF1, interpreted here as superimposed crescentic dunes. The lowermost bounding surfaces are partial reflectors interpreted as trough-scour surfaces, produced by a crescentic dunes that migrated over the underlying stratigraphy. The discontinuous concave-up

reflectors within the upper part of this set are interpreted as sets of trough cross-strata formed by smaller superimposed dunes. Likely clues to the surface morphology of the lower-most bounding surface is shown by bedform 'c' in the residual relief map of Figure 6.17. The image shows a crescentic dune with a trough of approximately 45 m in width. The radargram profile limit is ~30 m wide and therefore does not show the full extent of the bounding surface. Separated by a deflationary surface, the overlying RF3 is interpreted as contemporary wind-ripple strata.

**Profile B-B'** covers 72 m across a pronounced megadune terrace (traverse from ~114 m to 186 m) located approximately 40 m above the interdune surface. The radargram reveals near-surface aeolian architecture to a depth of about 9 m and consist of three stratigraphic units separated by interpreted deflationary surfaces (Figure 6.26). The upper-most unit, consisting solely of RF3, is interpreted as contemporary wind-ripple strata that covers the most recent deflationary surface. Small and sporadic slipfaceless mounds may also be present in this unit. The lower two units consist of RF1 and RF2, with the upper most deflation surface separating RF3. Figure 6.26C reveals that RF1 and RF2 commonly flank each other with RF2 always resting on a deflation surface. In the instance of the middle stratigraphic unit, dated at ~18 Ka, trough-cross reflectors of RF1 dip away from either side of the flanking convex-up bounding surfaces and internal reflectors of RF2. Together, RF1 and RF2 are interpreted as well-preserved crescentic dunes. The concave-up reflections are interpreted to have been formed on the inside horns of the dune where they merge on the slipface. They show convergent dips from the slipface curvature and are preserved at the base of the crescentic bedform as the dune overrides its horns. Such relationships between the two radar facies have been previously identified in GPR profiles across a barchan dune (Figure 6.29; Bristow, 2019). In this case the bedforms may be best represented by the crescentic dunes of similar widths that flank this profile to the east (e.g. bedform 'd' of Figure 6.17). In the lower stratigraphic unit, a relatively larger set of RF2 is cut into on its eastern flank by a set of RF1. Both of these relatively larger sets are cut into by smaller sets of RF1 trough-cross stratification. The profile limitations restrict the interpretation, however, if the same relationships are true as in the stratigraphic unit above, then the relatively larger sets represent a portion of a crescentic

dune that is scoured into by smaller superimposed crescentic dunes. If this is the case, the sedimentology could be predicted further to the east (i.e. large flanking sets of RF1 and RF2).

**Profile C-C'** covers 30 m across the east-facing megadune stoss slope (traverse from 286 m to 316 m) located approximately 30-35 m above the interdune surface. The radargram reveals near-surface aeolian architecture to a depth of about 7 m and consists of two stratigraphic units separated by interpreted deflationary surfaces (Figure 6.27C). The lower unit consists of radar facies 1 and 2. The concave-up reflectors of RF1 are observed flanking the convex-up reflectors of RF2 in a similar association seen in the middle stratigraphic unit of profile B-B' although only a portion is evident in this profile. The profile limitations restrict interpretation, however, consistent with profile B-B', the associated radar facies potentially show a partial view of a preserved crescentic dune. In this case, one horn of the dune is identified by the presence of RF2 and is flanked by trough-cross strata of RF1 as the crescentic bedforms overriding the horn on either side. The bedform may be up to three times larger than those identified in profile B-B' and could rest upon underlying megadune stratigraphy. The youngest unit consisting solely of RF3 is interpreted as wind-ripple strata that covers the deflationary surface. Undulations in RF3 may represent slipfaceless zibar.

**Profile D-D'** covers 30 m across the east-facing megadune stoss slope (traverse from 330 m to 360 m) located 14 m east of radargram C and approximately 25-30 m above the interdune surface. The radargram reveals near-surface aeolian architecture to a depth of about 8 m. A deflation surface separates RF1 and RF3. RF1 consists of asymptotic reflectors with apparent eastward dips of up to 33°. In this profile RF1 is interpreted as grainflow strata and may be portion of a larger trough-cross set. The extents of the bounding surface at the base of this unit is speculative, as is all underlying stratigraphy due to the loss of signal at depth. RF3 rests above a deflation surface and is interpreted as wind-ripple facies along the megadune stoss slope.

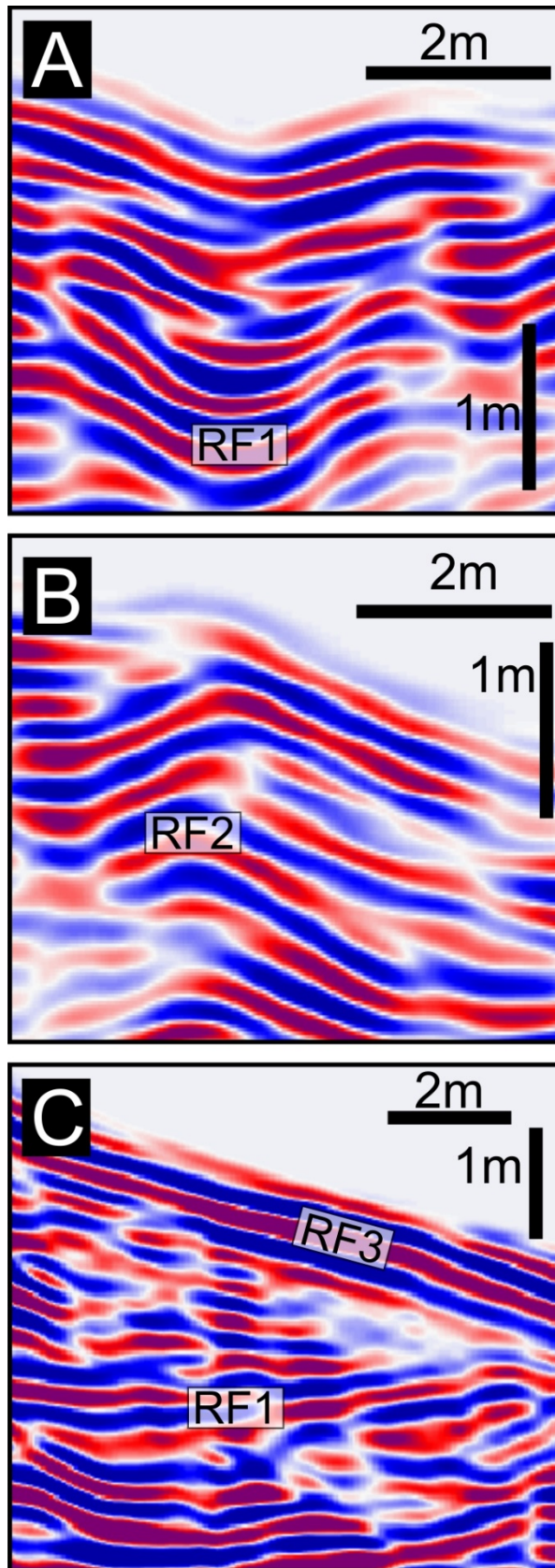


Figure 6.24: A) Example of concave-up reflections of RF1. (B) Example of convex-up reflections of RF2, typically increasing in amplitude with height. Example of near horizontal reflections of RF3. Approximately 2 X vertical exaggeration in all examples

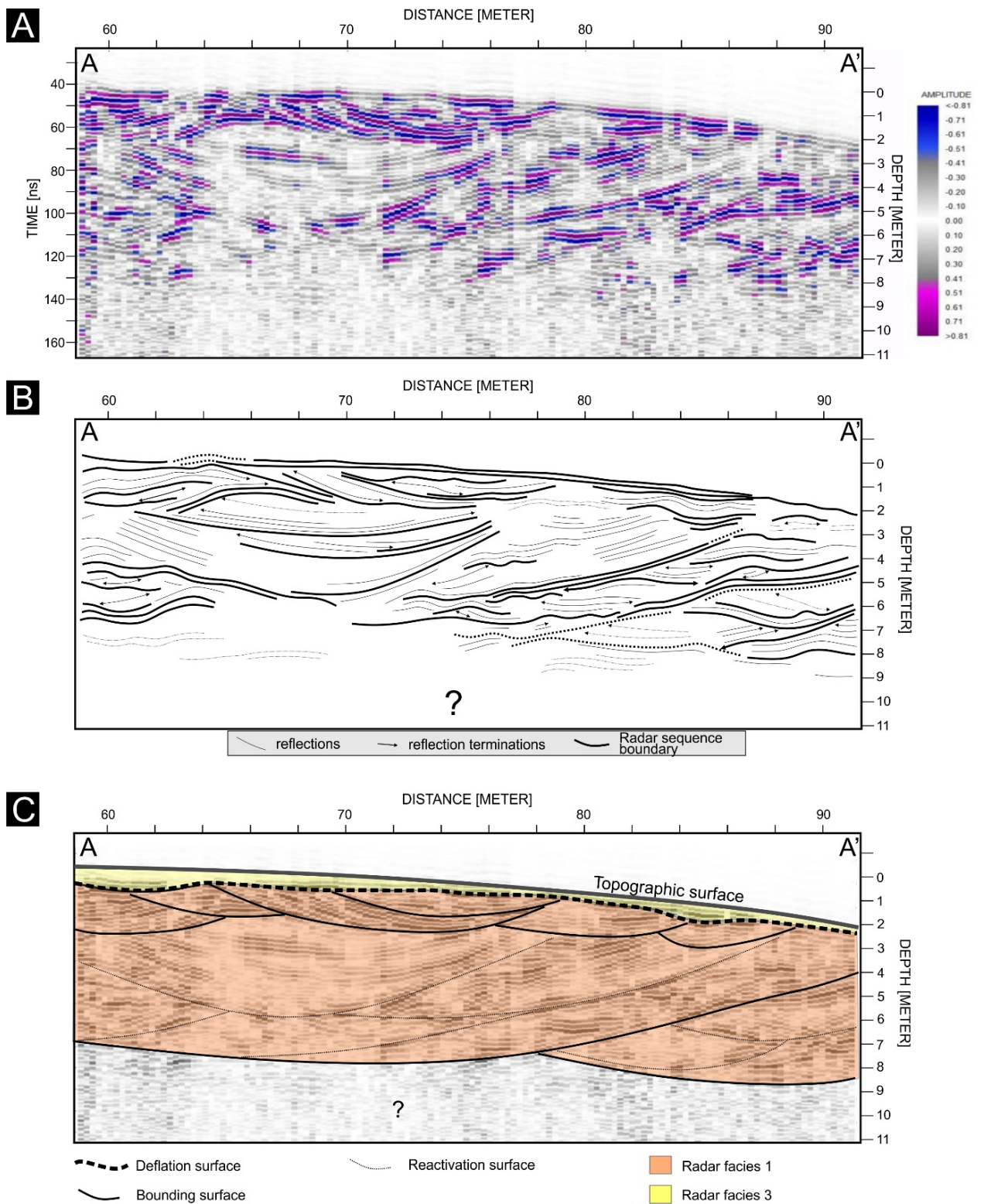


Figure 6.25: Profile A-A' represents the west to east traverse on the crest of a linear megadune. A) Processed GPR data. B) Interpretation of the GPR profile reflectors. C) Dominated by RF1, the discontinuous concave-up reflections are interpreted as trough-cross strata likely to have been formed by crescentic superimposed dunes. Two orders of superimposed dunes exist at 8-9 m depth scouring into underlying stratigraphy that potentially represents the megadune, and at 2-3 m depth, scouring into the larger trough-cross sets below. Near-horizontal reflectors mark radar facies 3 as a blanket of wind-ripple strata resting on a deflationary 'supersurface'.

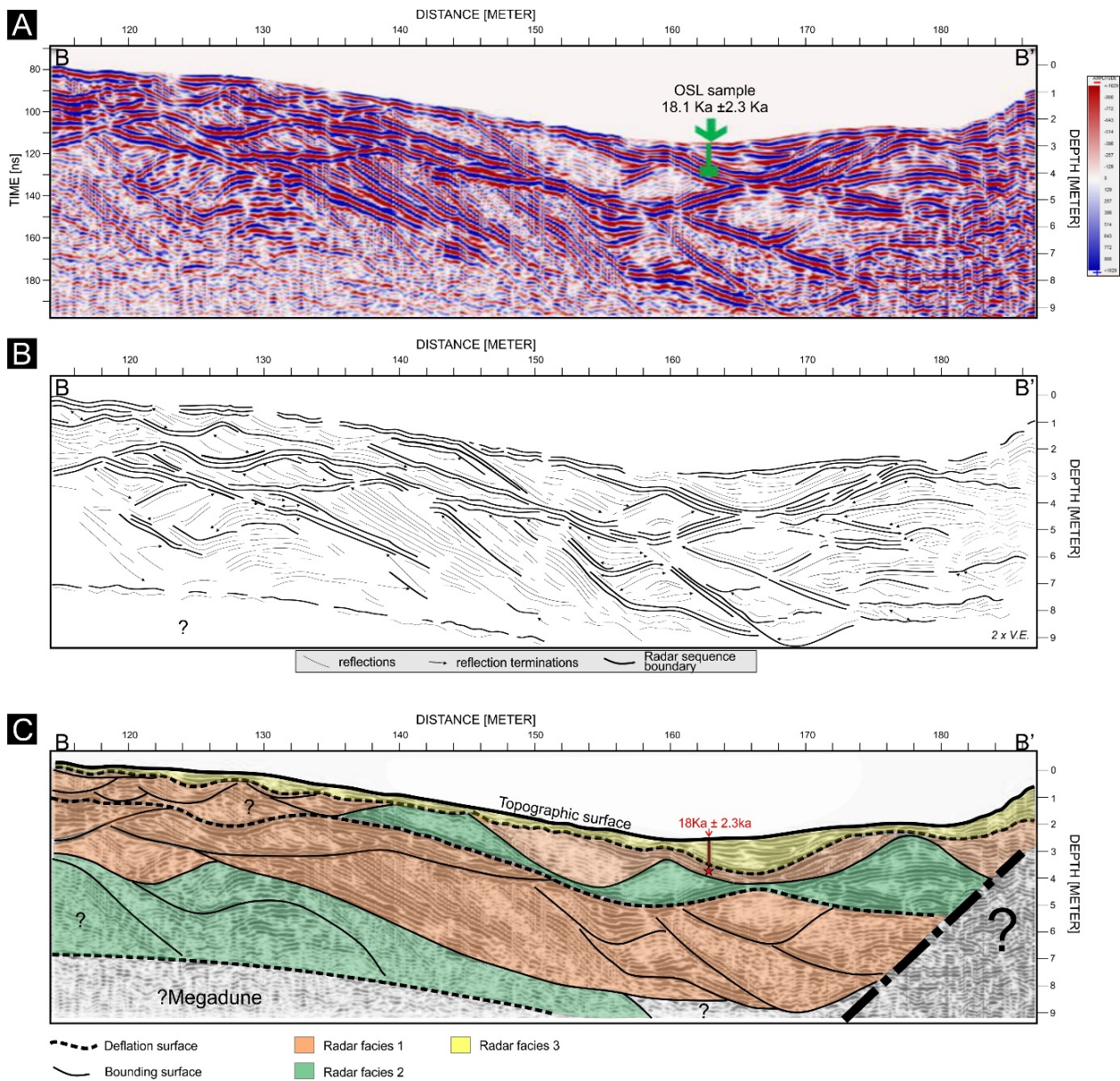


Figure 6.26: Profile B-B' represents the west to east traverse in a near horizontal terrace of a linear megadune. A) Processed GPR data. B) Interpretation of the GPR profile reflectors. C) Three stratigraphic units separated by the interpreted deflation surfaces exist in this profile. The top unit consists of RF3, interpreted as wind-ripple strata covering a deflationary surface. In the middle stratigraphic unit, an association exists between concave-up bounding surfaces of RF1 and the flanking convex-up bounding surfaces of RF2. Together the two radar facies are interpreted as well-preserved crescentic dunes. Due to the limitation of the profile, only the partial remains of this facies association can be identified in the oldest unit. The lower most deflation surface may be underlain by the megadune on which the overlying strata accreted, however, this is a tentative interpretation due to the loss of seismic reflectors at depth.

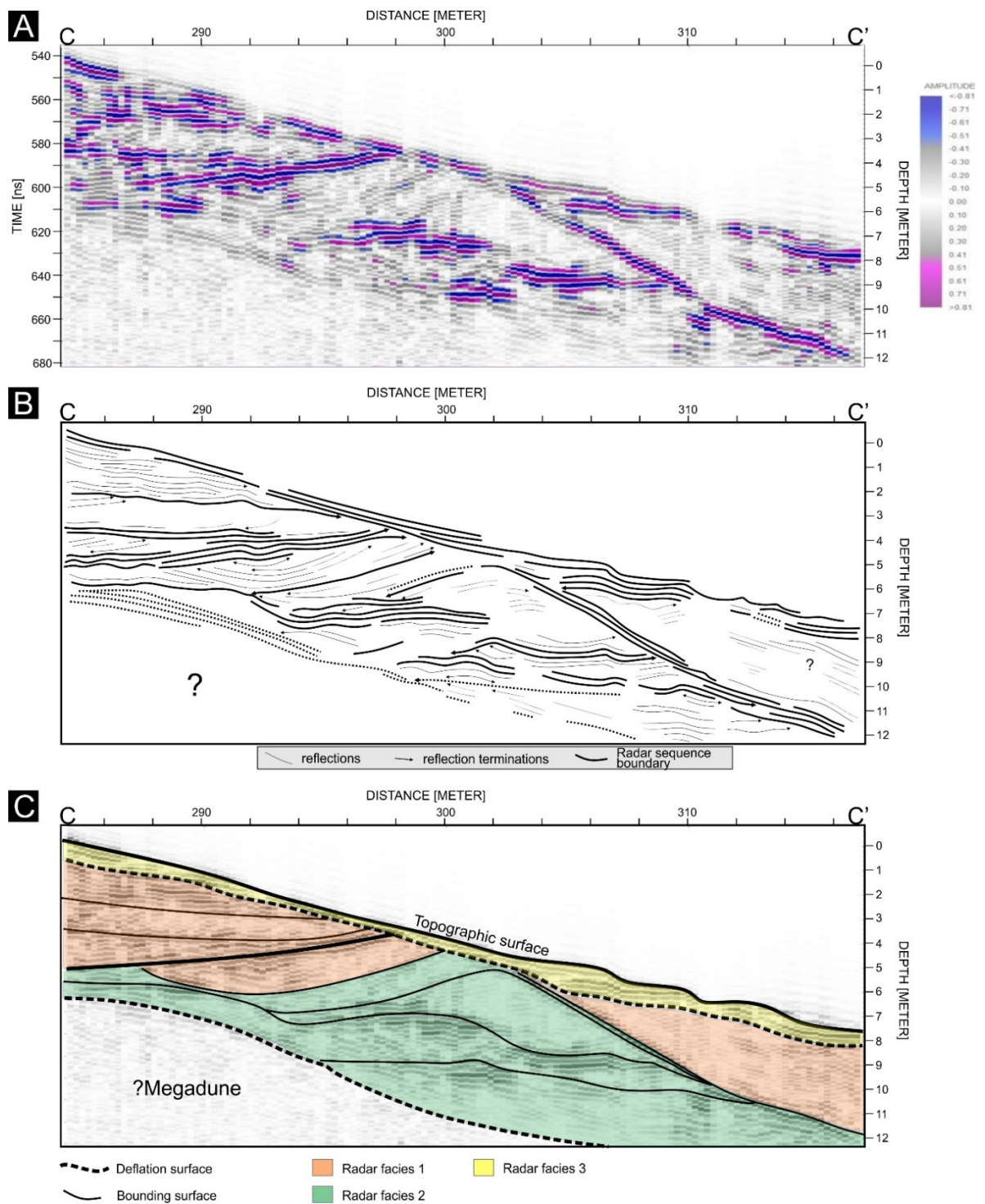


Figure 6.27: Profile C-C' represents the west to east traverse on the stoss-slope of a linear megadune. A) Processed GPR data. B) Interpretation of the GPR profile reflectors. C) Two stratigraphic units are separated by deflation surfaces. The older unit consists of associated radar facies as identified in profile B-B', however only in partial view due to the limits of the profile. Together these two radar facies are interpreted as a partial crescentic dune. The comparable size of this interpreted bedform (~30 m horn) to that of the interpreted bedform in the lower stratigraphic unit of profile B-B' (~35 m horn), and both speculatively superimposed on an underlying megadune perhaps reveals that the dunes could be of the same genetic nature (e.g. medium-scale crescentic bedforms observed in Figure 6.15 and Figure 6.16). The upper-most deflation surface separates this unit from RF3, interpreted as a sheet of wind-rippled strata that covers much of the contemporary megadune.

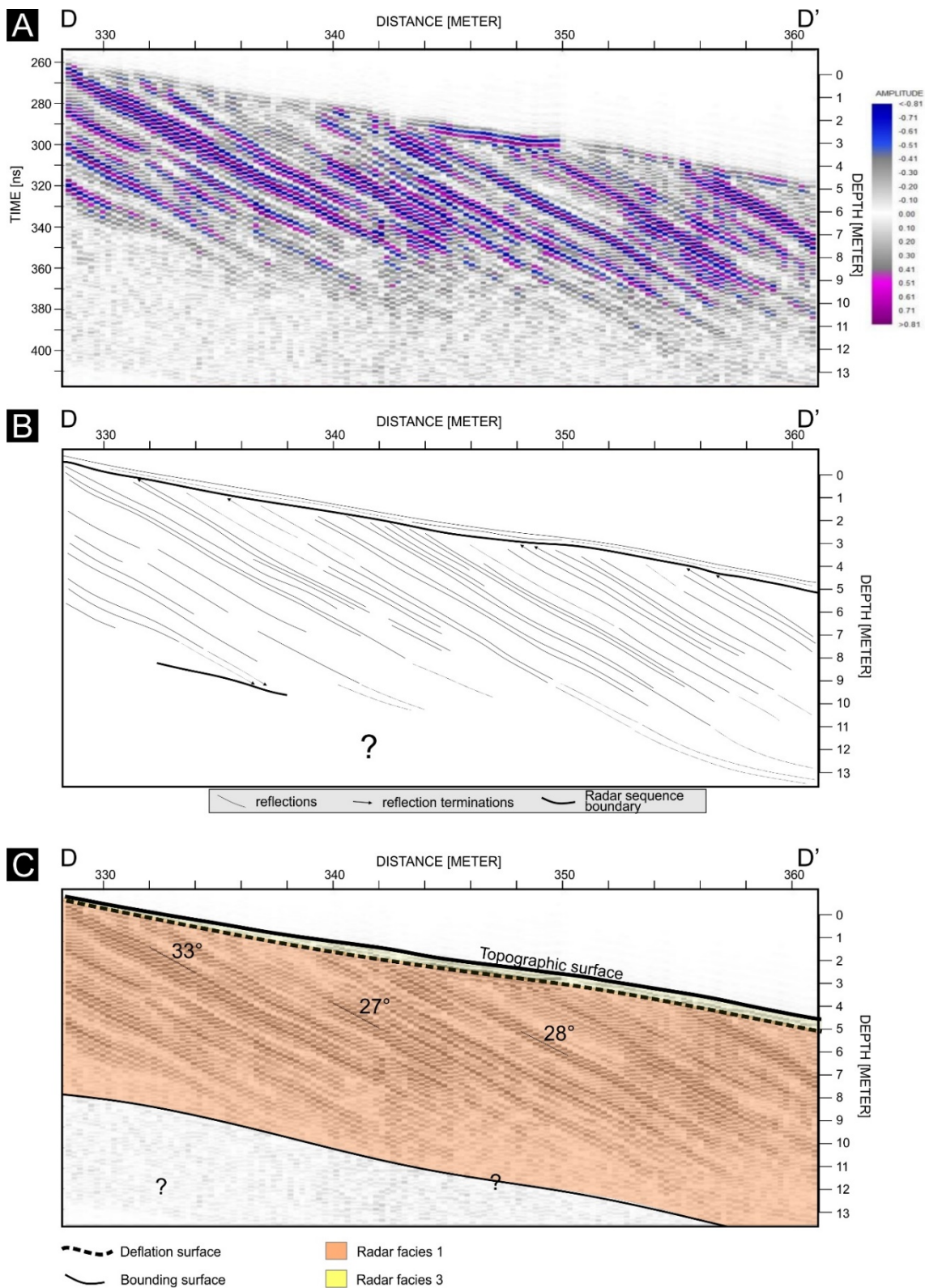


Figure 6.28: Profile D-D' represents the west to east traverse on the stoss-slope of a linear megadune. A) Processed GPR data. B) Interpretation of the GPR profile reflectors. C) Two stratigraphic units RF3 and RF1 are separated by deflation surface. The older unit consists entirely of RF1 interpreted as grainflow strata potentially forming part of a large trough-cross set. The deflation surface cuts this set and is overlain by contemporary wind-ripple strata of RF1 that covers the megadunes' stoss slope.

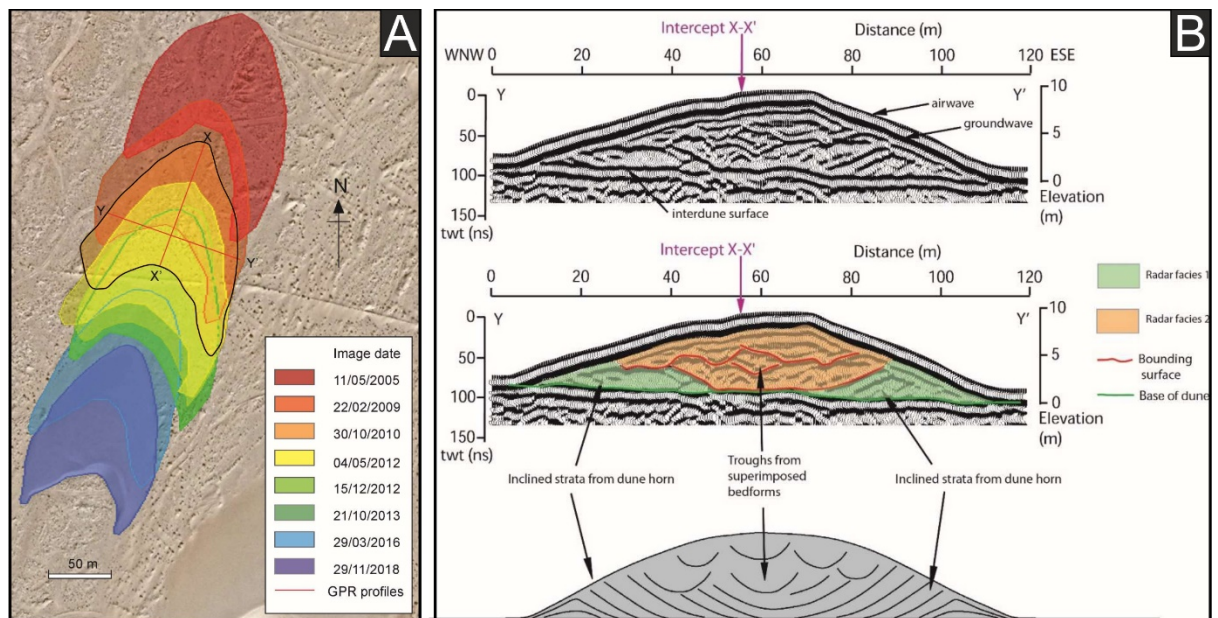


Figure 6.29: A survey of a Barchan dune using GPR and satellite imagery reveals similar sub-surface structures to those interpreted in radargram profiles B-B' and C-C' in this study. A) The outlines of the migrating barchan dune in Morocco between 2005 and 2018. GPR profiles were collected parallel (X-X') and perpendicular (Y-Y') to the migration direction. (B) Radargram and interpretation of the barchan dune acquired perpendicular to migration direction (Y-Y'). Note the inclined strata from the barchan horns preserved on the dune margins (Radar facies 1). In this instance, ~5 m of the horn strata is apparent. The trough-cross set of the main barchan bedform is approximately 8m tall and is scoured by superimposed dunes migrating along the barchan crest. Images modified after Bristow (2019).

#### 6.4.4.1 Discussion

The GPR interpretations, along with evidence from the residual relief maps in section 6.3 reveal that crescentic bedforms may have been a major component of the linear megadunes accretion as illustrated in trough-cross bedding in profile A-A' and the proposed fully preserved crescentic bedforms. These suggested fully preserved crescentic bedforms in the GPR profiles rely solely on the evidence provided from Bristow's (2019) survey of a barchan dune in Morocco and only the middle stratigraphic unit of profile B-B' mimics the full extent of these relationships. In McKee's (1966) study of a crescentic bedform in the White Sands dune-field, trenched perpendicular to its migration direction, these relationships were not apparent. Bristow (2019) attributed the lack of horn preservation in McKee's trench to the greater curvature of the Moroccan barchan and dimensions that favour horn preservation. It was demonstrated that the sedimentary architecture of the dune studied in White Sands were barchanoid, rather than that of a true barchan as observed in Morocco (Bristow, 2019).

Under residual relief in plan-view, the interpreted antecedent bedforms of the Wahibas display a similar nature to that of a 'true' barchan (independent from one another and with high curvatures) (Figure 6.30). If the subsurface 'well-preserved' bedforms are genetically linked to those subtly evident under residual relief, then the radar facies architectures interpreted herein (specifically within profile B-B' of Figure 6.26) could be expected, as evidenced in Bristow's true barchan dune in Morocco (Bristow, 2019).

In profile D-D' the thickness of the set and the nature of the high angle strata suggests an active slipface was present on a relatively larger bedform than those identified in other profiles. Profile C-C' overlies and cross-cuts these strata and is therefore chronologically younger and may represent the portion of a superimposed dune migrating on the suggested larger bedform. The largest of the interpreted antecedent bedforms under residual relief identified in section 6.3 occurred in Area's (i) and (ii) (Figure 6.30). These bedforms have heights of up to 19 m, host superimposed dunes, and are observed encroaching into the western flank of the contemporary linear megadune. If these bedforms do indeed make up the core stratigraphy of the linear megadunes, the western horn of a large crescentic bedform may provide an explanation for the apparent eastward dipping steep nature of this strata, large set size (~8 m), and overlying superimposed bedform (e.g. Area (i) of Figure 6.30).

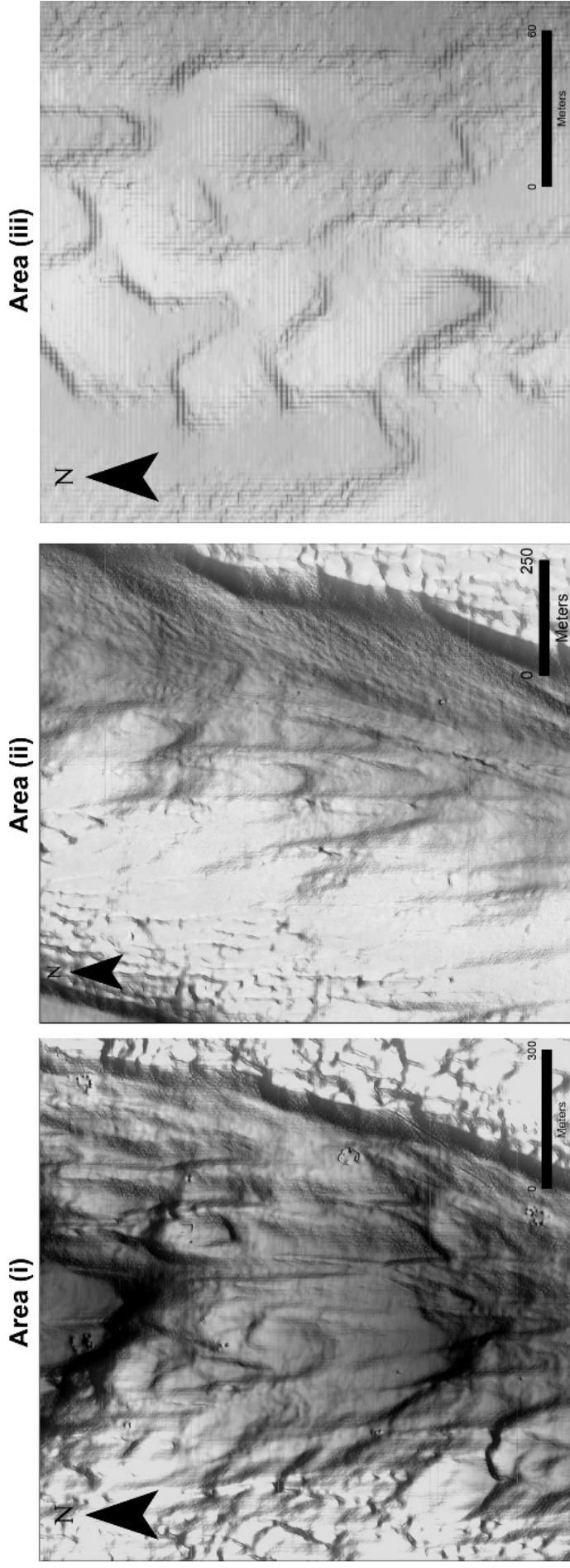


Figure 6.30: The areas from section 6.3 showing a close-up of proposed antecedent crescentic dunes. Note in area (i) and (ii) the crescentic dunes are superimposed onto a larger bedform, interpreted as the megabarchans that, in the contemporary configuration are thought to form the linear dune core. These dunes generations are suggested to make up the well-preserved crescentic bedforms interpreted in the subsurface stratigraphy. The superimposed dunes of Area (i) and (ii) are at an elevation of approximately 340-360 m on the megadune stoss slope and potentially make up the lower stratigraphic unit of GPR profile B-B' (Figure 6.26), and the interactions seen in C-C' (Figure 6.27) although speculative due to profile limitations. Area (iii) is closer to the dune crest at ~400 m elevation and potentially makes up the middle stratigraphic unit of B-B' where the relatively smaller sets of radar facies are situated. Identifiable in area (i) is the mega-crescentic bedform that encroaches into the linear megadune core. The western horn of this structure could potentially explain the apparent eastward dipping strata and large set size of profile D-D'.

## 6.5 Vegetation Monitoring

Previous studies have shown the importance of vegetation in limiting the availability of sand for transport (e.g. Levin *et al.*, 2006; Li *et al.*, 2007; Tsoar, 2008). Panchromatic aerial photographs have been used to great advantage in temporally discriminating vegetation cover over dune-fields with reasonably high spatial resolution (e.g. Tsoar and Blumberg, 2002; Hugenholtz and Wolfe, 2005). While aerial photographs provide an invaluable context for monitoring dune activity changes through time, additional information can be acquired with multispectral imagery.

Large-area vegetation monitoring is possible by measuring the difference between the near-infrared spectrum (NIR) which is strongly reflected by vegetation, and red light which vegetation absorbs. Various mathematical combinations of spectral bands are found to be sensitive indicators to the presence and condition of green vegetation. The mathematical quantities are referred to as vegetation indices and two forms are routinely calculated from multispectral datasets – a simple vegetation index (VI) and a normalised difference vegetation index (NDVI). NDVI is one of the most widely adopted (Hugenholtz *et al.*, 2012 and references therein) and therefore is preferred over VI for vegetation monitoring because of its ability to compensate for changing illumination conditions, surface slope, aspect, and other extraneous factors. NDVI is a band ratio technique (see section 6.6 for more details) and is calculated as follows:

$$\text{NDVI} = (\text{NIR} - \text{Red}) / (\text{NIR} + \text{Red}) \quad (4)$$

Generally, areas that are well-vegetated will yield positive values because of their relatively high NIR reflectance and low visible reflectance. Areas that have larger visible reflectance over NIR (e.g. clouds, water and snow) will yield negative values and areas with similar visible-to-NIR reflectance (e.g. bare rock and soil) will yield an index close to zero (Lillesand *et al.*, 2015). Hugenholtz *et al.* (2012) views the approach of using vegetation indices to be under-utilised as a means of predicting spatio-temporal patterns of aeolian sand transport and dune activity.

### 6.5.1 Methods

The spectral enhancement best suited for monitoring vegetation is the normalised difference vegetation index (NDVI). The Landsat 8 files used include spectral bands 4 (red) and 5 (near infrared) with less than 0.04% cloud cover on land. Multi-temporal images were used to compare vegetation through the summer and winter months of 2013-2014 and 2018-2019. The application of equation (4) was carried out in ArcGIS 10.6 using the raster calculator in the spatial analyst plugin. In order to visualise the NDVI values, the symbology was adjusted to a red-to-green colour ramp representing low-to-high vegetation content respectively (Figure 6.31). The output maps can be used for visual examination and statistics can be acquired in the maps' layer properties. The layers' statistics allow for further processing and the production of enhanced qualitative maps as well as quantification of the NDVI classes for comparison across the seasons (Figure 6.33; Figure 6.34; Table 6.3).

Because vegetation is only identifiable in the high-resolution orthophoto, a visual examination was carried out using a cropped NDVI output map and corresponding orthophoto for January 2019 (Figure 6.32). This is done to identify NDVI values associated to dune-field components (e.g. basement outcrops, superimposed dunes, interdunes *etc.*) and ultimately determines a threshold value that qualitatively represents the level of vegetation within certain areas. This threshold value is input into the raster calculator to create a new binary raster layer that represents vegetation intensities. The attributes of the binary raster layer are then used to determine a relative percentage of vegetation coverage (Figure 6.33).

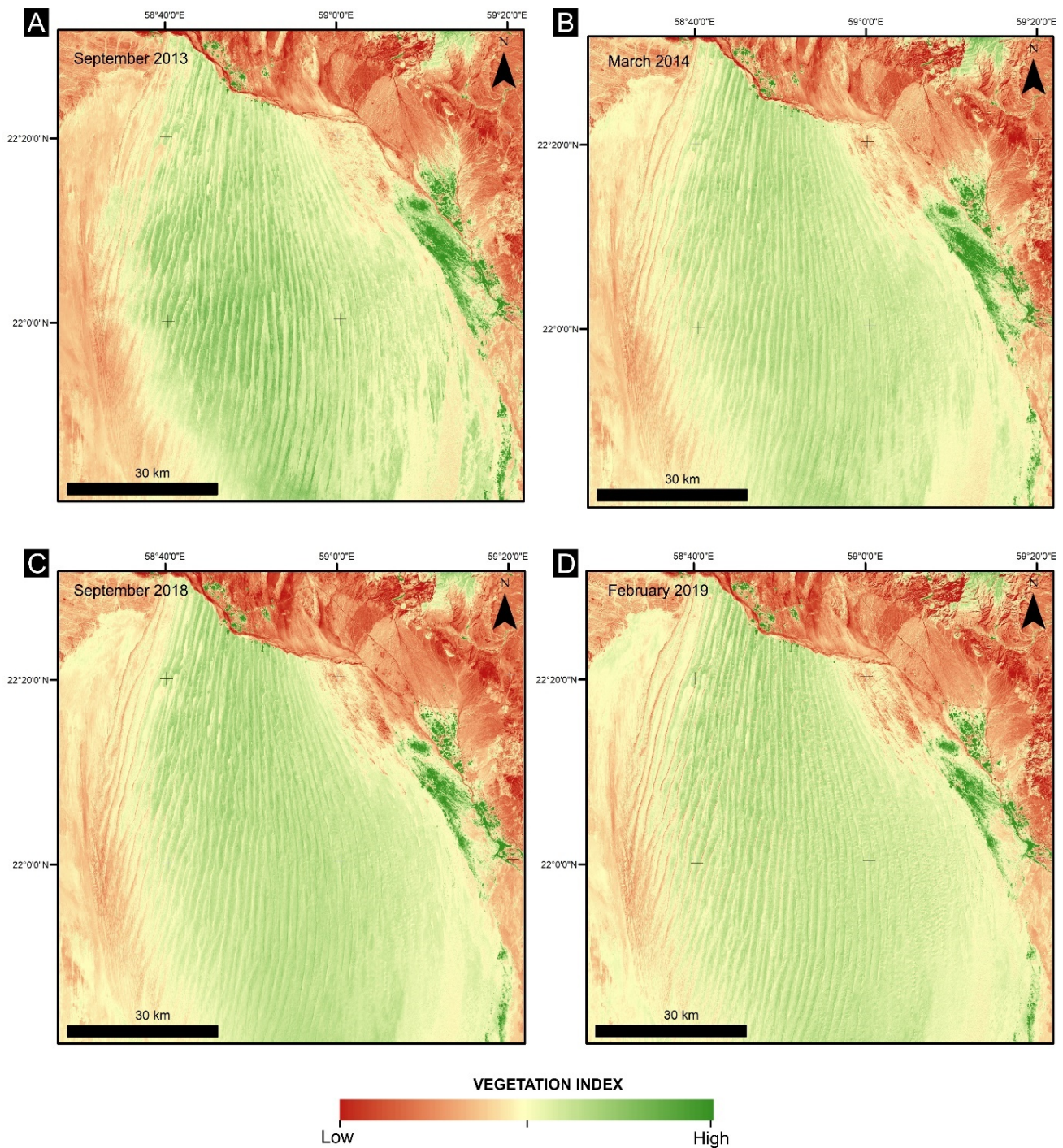


Figure 6.31: Multi-temporal NDVI maps showing the extent of vegetation cover in the Wahibias in winter and summer months over a 5-year period. While minor variations are identified between seasons, the maps require further processing to examine the extent of well-to-poorly vegetated areas within the erg (see minimum and maximum NDVI values in Table 6.3). Note in all instances, the northeast corner and western margin show the lowest NDVI values of the erg.

## 6.5.2 Results

Variations between the datasets are identified within the layer statistics for the maps produced in Figure 6.31 (Table 6.3). The mean NDVI values range between 0.076 and 0.092, with summer months having consistently higher values against their corresponding winter months (Figure 6.34). Wider minimum-to-maximum NDVI ranges occur within the 2013-2014 datasets (-0.11 to 0.56) compared with the 2018-2019 datasets (-0.05 to 0.56). These range differences will influence the colour ramps in Figure 6.31 and visually reduce the maps' effect of NDVI variations between seasons. Standard deviations are consistent across all datasets with values averaging at 0.02.

Figure 6.32 was used as the representative sample dataset for determining threshold values with the following results. The lowest NDVI values ( $\sim 0.03$ ) occur in the fluvial Wadi Batha where no visible vegetation is identified. Basement outcrops show values of about 0.07 and occur with very-sparse vegetation coverage. Active sands on the megadune stoss slopes and dune crests hold values of between 0.07 and 0.08. The active sands are composed of superimposed crescentic and seif dunes and a single pixel may cover both a non-vegetated dune and their very-sparsely vegetated interdune. Pixels that cover the wider interseif corridors show NDVI values of up to 0.1. The wide interdunal corridors show sparse to good vegetation coverage with values between 0.095 and 0.12 with lower values due to the presence of active sands, generally in the form of small seif dunes (<20 m wide).

Based off the above observations a threshold value of 0.095 was determined and used to create the binary raster maps (Figure 6.33). Pixels with values lower than 0.095 (red coverage) will contain areas with very sparse to no vegetation while pixels with values greater than 0.095 (green coverage) will contain areas with sparse to well vegetated areas. The maps in Figure 6.33 shows the variations between the two-yearly summer and winter periods. Green coverage decreases by a factor of 3.9 between the summer month of September 2013 and the winter month of March 2014. A decrease in green coverage by a factor of 11 occurs between the summer month of September 2018 and winter month of January 2019. Over the five-year period there is a decrease in green coverage by a factor of 4.6 and 13 in the summer and winter months respectively.

*Table 6.3: NDVI classification statistics and green-space coverage.*

<b>Layer</b>	<b>Pixels</b>	<b>Min</b>	<b>Max</b>	<b>Mean</b>	<b>S.D.</b>	<b>Green cover (erg only)</b>
<b>Sep-13</b>	9811074	-0.11	0.54	0.092	0.021	51.29%
<b>Mar-14</b>	9811074	-0.11	0.56	0.085	0.020	13.05%
<b>Sep-18</b>	9811074	-0.05	0.55	0.084	0.019	10.99%
<b>Jan-19</b>	9811074	-0.06	0.56	0.076	0.020	1.03%

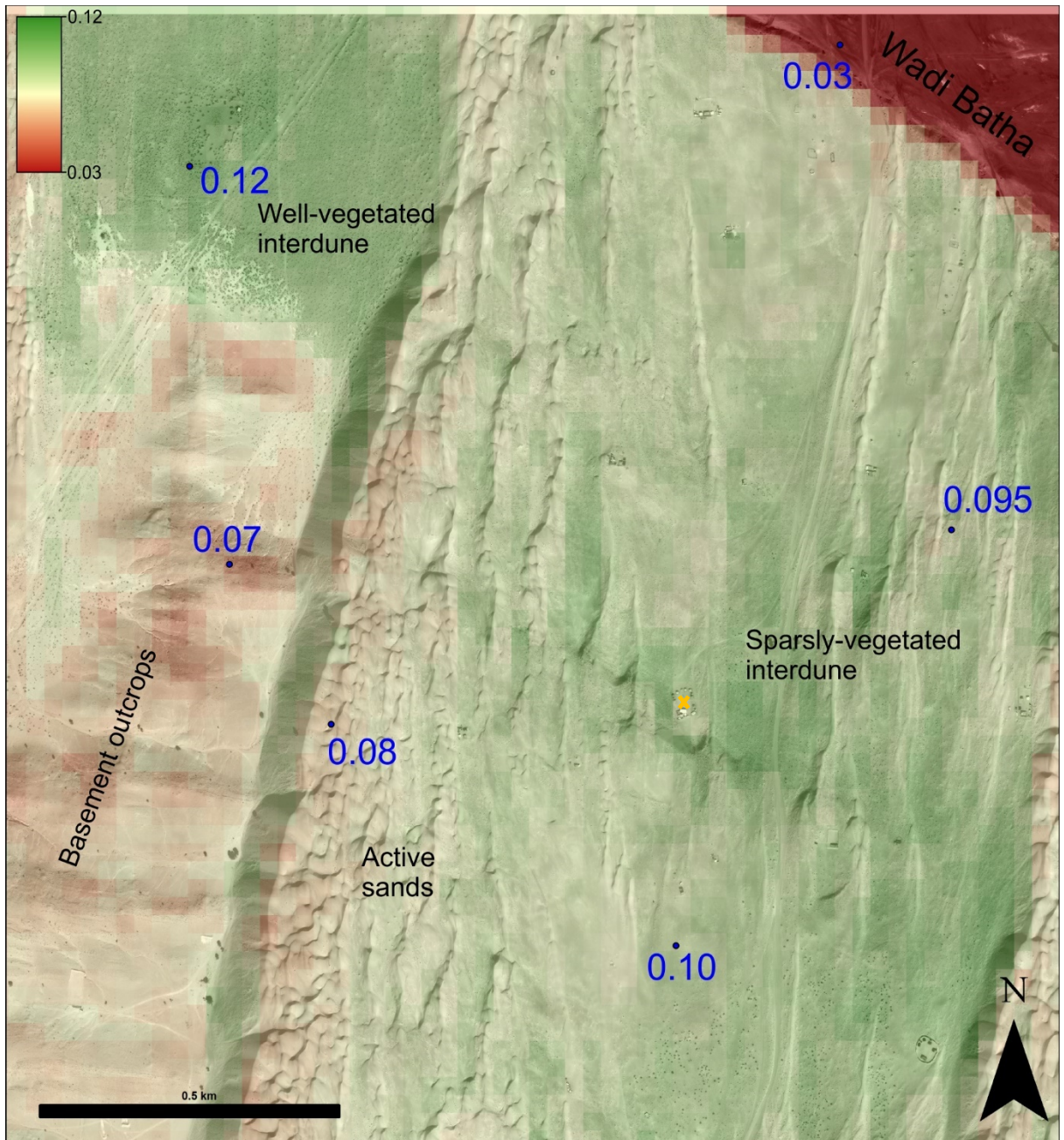


Figure 6.32: NDVI overlay on a high-resolution orthophoto. Blue values represent the vegetation index of dune-field components. Where vegetation is visible, NDVI values are high (green areas). In areas with low-to-no vegetation (Wadi Batha, basement outcrops and active sands), NDVI values are low (red areas). The exercise provides threshold values for further erg-wide analysis and proves that the NDVI technique is capable of analysing vegetated vs. non-vegetated areas in the very arid and sandy landscape. The dataset, however, is limited by its resolution and therefore will overestimate green space (note the distribution of green coverage includes the sandy areas between scattered vegetation). The yellow X marks the Sand Delight Camp shown in ground view in Figure 6.35. Pixel count = 3840, minimum = 0.03, maximum = 0.12, mean = 0.1, S.D. = 0.013. NDVI output map and orthophoto represent January 2019.

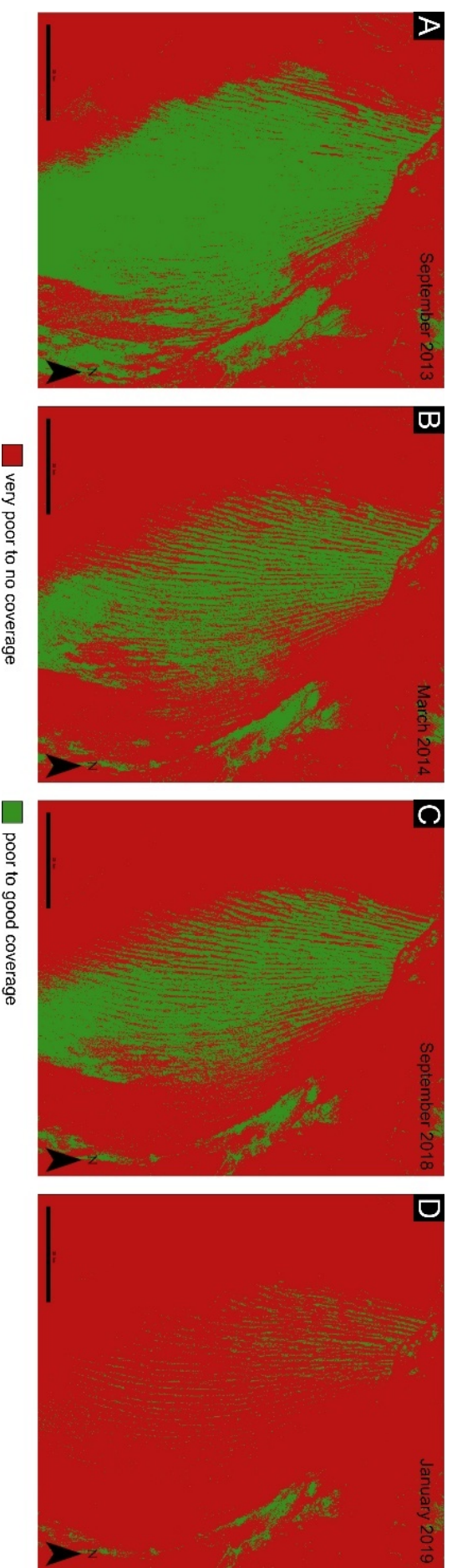


Figure 6.33: The extent of 'green-space' coverage through the studied seasons. The binary raster maps show the areas where NDVI values are greater (green) or lesser (red) than 0.095. The percentage coverage (erg only) is shown in Figure 6.34.

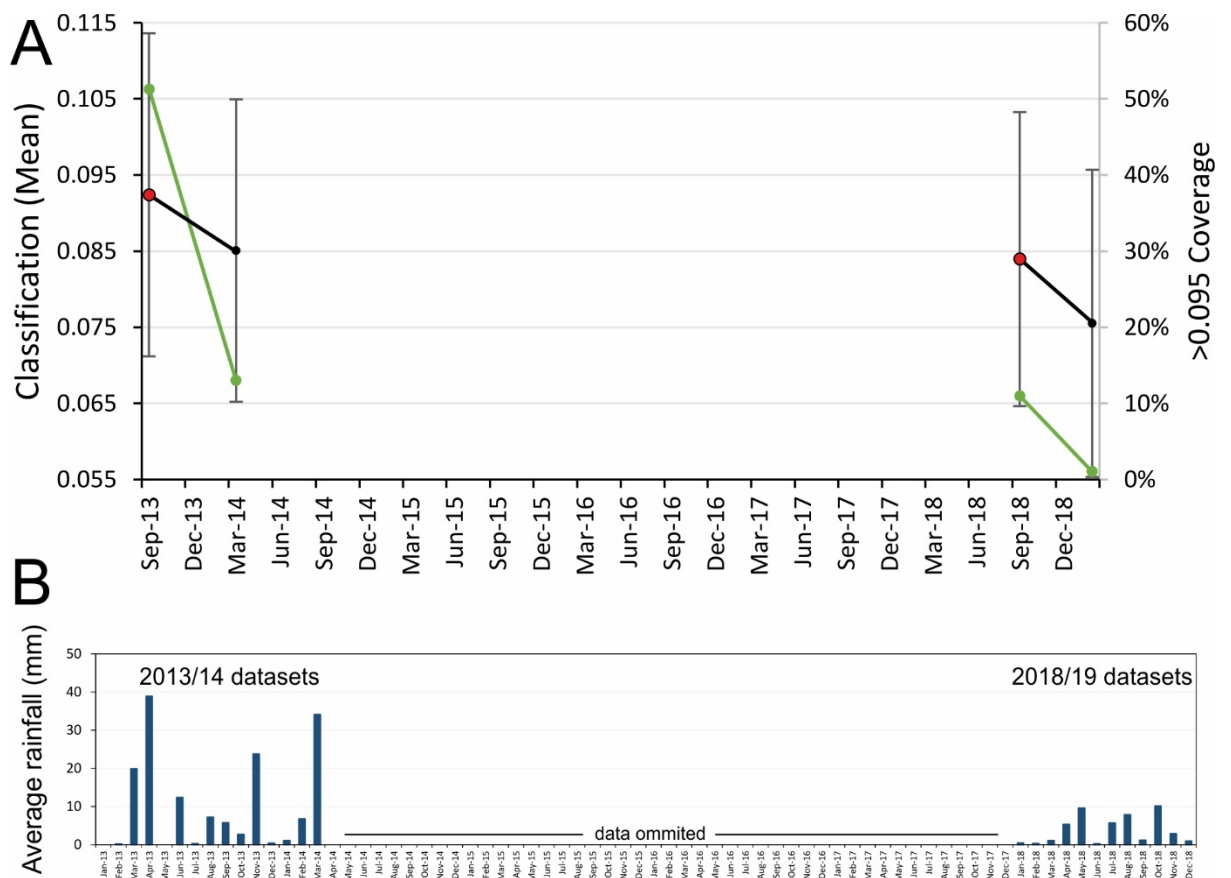


Figure 6.34: A) Mean NDVI classification trend (black line) show slight decreases between summer months (red dots) and winter months (black dot) over the two datasets, five years apart. Grey error bars show standard deviation from mean associated with classification values reported in ArcGIS statistics. NDVI values >0.095 were determined in classifying the poor-to-good vegetation coverage, cropped to fit the Wahiba erg, and is shown here as 'percentage covered' (green). An overall decrease occurs over the 5-year period, however, is not interpreted as a trend due to the short timescale. B) The precipitation averages from January 2013 to March 2014, and January 2018 to December 2018 for the Ash Sharqiyah region of Oman demonstrates the rainfall surrounding the two datasets (see Figure 3.8 for the full dataset). There is an average of 10 mm precipitation and 32% vegetation cover over the 2013/14 dataset vs. an average of 4 mm precipitation and 6% vegetation cover over the 2018/19 dataset. The agreement may represent the growth response in drier periods.

The comparison of the produced NDVI dataset with the high-resolution orthophoto shows that this technique is suited to map out the vegetated area of the dune-field (Figure 6.32). Additionally, the map provides a means to semi-quantitatively detect variations in NDVI between dune-field components and place a threshold value on the density of vegetation. Because absolute density is not determined due to the low resolution of the NDVI maps, binary raster maps are better suited for determining a relative change in vegetation cover between seasons rather than absolute coverage.

### 6.5.3 Discussion

The Wahiba Sand Sea belongs to the Arabian regional subzone where 50% of the flora is Saharo-Arabian and 5% is endemic to the Arabian Peninsula (Ghanzanfar, 1992). Although richness of species and cover is relatively low, vegetation growth along the slopes of the megadunes is commonly observed (Munton, 1988). The results here show that vegetation occurs erg-wide in both summer and winter seasons and probably persists all year-round. The relative density of the vegetation is shown to increase within the summer months and seems to respond to the annual precipitation averages with more cover observed in the wetter year. Sand dunes worldwide generally do not show a direct relationship between the amount of rainfall and vegetation due to the high rate of infiltration in dune sand (Tsoar *et al.*, 2008). The relationship seen in the Wahibas may be coincidental (dataset bias), or possibly reflects pedogenesis and therefore a degree of dune stabilisation. Additional factors that may play a role in stabilisation or moisture retention is the suggested presence of biological soil crusts (Buckman *et al.*, 2017). As an example, in the semi-to-hyper-arid Negev desert, the dunes are observed fully stabilised by the combination of vegetation (17% coverage) and biological soil crusts which commonly occurs between shrubs (Tsoar and Karnieli, 1996; Hugenholtz *et al.*, 2012).

Interestingly, the western margin and the northeast corner of the dune-field show very low NDVI values. This is consistent with zones where more active sands fall within the dune-field (e.g. Figure 6.32) and may infer a degree of reworking where consistent erosion prevents seeds from germinating (e.g. Tsoar *et al.*, 2008). Alternatively, these zones are subject to greater sediment input which covers the vegetation, masking any NDVI signatures.

Although this study only provides a relatively short temporal baseline of vegetation observations and measurement (5 years), it forms the basis for an extended approach. The Landsat programme provides almost five decades of multispectral data acquisition in which to study the dunes morphodynamic response to vegetation change and consequent sand availability. In addition to detecting different successional stages across a vegetated or semi-vegetated dune-field, the ability to resolve vegetation type may link empirical observations with numerical models to understand the degree of forcing required to reactivate stabilised or stabilising dunes (e.g. Baas and Nield, 2007). As sand dunes are known to be (1) free of vegetation and active, (2) partly vegetated and active or (3) fully vegetated and fixed (Tsoar, 2008), persistent vegetation in the Wahibas suggests a degree of stability which would have a direct effect on sand availability and dune pattern evolution (Figure 6.35). In conjunction with a comprehensive field study, the nature of dune stabilisation and sand mobility of the Wahiba Sands could be better resolved.



*Figure 6.35: A photo of Sand Delight Camp on the northern edge of the Wahiba dune-field. The camp and surrounding dunes shows the abundance of stabilising vegetation between active seif dunes that are relatively devoid of vegetation. View is to the NNW. Refer to Figure 6.32 for plan view position and corresponding NDVI overlay. Photo by Petr Horacek (<https://lh5.googleusercontent.com/p/AF1QipOH7Z4ZoBrij6MtafNfrpD8fwNGh2k6zbKqs96hP=h1440>).*

## 6.6 Provenance Study

When using conventional multispectral sensors, band ratioing is a simple and powerful technique used to discriminate and map surface rocks/sediments and is commonly used to inform mineral exploration targets (e.g. Spatz, 1997; Nouri *et al.*, 2012). Considering that each object has a unique spectral reflectance curve in each wavelength of the electromagnetic spectrum, spectral or band ratioing can be used to emphasize the anomaly of a target object by determining the band at which the reflectance is high or at a point of highest absorption (Jensen, 2015; Lillesand *et al.*, 2015). It is therefore possible to depict an overview of the broad mineral-absorption bands (Figure 6.36). Additionally, band ratioing can reduce the effects when differences in brightness values from identical surface materials are caused by topographic slope and aspect, shadows or seasonal changes in sunlight illumination angle and intensity, and therefore enhance differences between the spectral responses of each band (Rajesh, 2004; Nouri *et al.*, 2012; Jensen, 2015).

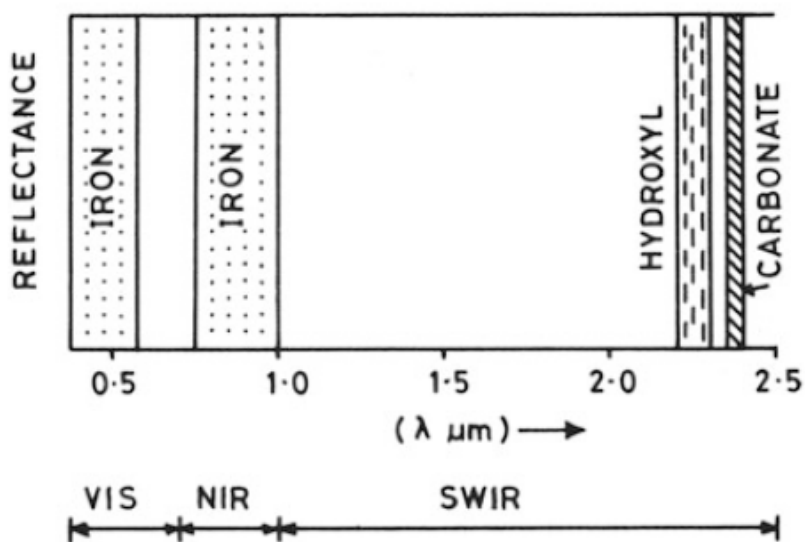


Figure 6.36: Absorption bands in the optical region (visible to shortwave infrared) that enable remote sensing mapping of mineral assemblages and rocks. VIS (visible spectrum), NIR (near infrared spectrum), SWIR (shortwave infrared spectrum). Modified after Gupta (2018).

The simplest method to computing spectral ratios is known as the linear spectral slope (Gupta, 2018). In this approach, ratioing is based on the division of every pixel value of one band by the homologous pixel of the other band and is computed as follows (Prost, 2013):

$$\text{Spectral Ratio} = \text{DN}_B / \text{DN}_A \quad (5)$$

$\text{DN}_A$  and  $\text{DN}_B$  are the digital numbers of the two spectral bands of interest. Applying the formula will generate images showing the distribution of specific minerals based on their unique spectral curves (Figure 6.37). These curves are characterized by “absorption bands” (reflectance or emissivity minima) caused by the presence of OH,  $\text{Fe}^{2+}$ ,  $\text{Fe}^{3+}$ ,  $\text{CO}_3$ ,  $\text{SO}_4$ , CH, and  $\text{SiO}_2$ . Due to chlorophyll, vegetation has an absorption band at wavelengths shorter than 750 nm. Ferric iron leads to strong absorption in the UV to blue wavelength region, while ferrous iron is known to exhibit some absorption effect around 0.85  $\mu\text{m}$ . Clay minerals have a characteristic absorption features of 2.1–2.4  $\mu\text{m}$  and shifts slightly depending on the clay type. Calcium carbonates have absorption features at 2.32 and 2.51  $\mu\text{m}$  in the short-wave infrared (SWIR) region and at 11.45–11.75  $\mu\text{m}$  and 13.92–14.0  $\mu\text{m}$  in the thermal region. Both clays and calcium carbonate have reflectance features of 1.55–1.75  $\mu\text{m}$  (Prost, 2013; Pour and Hashim, 2015; Gupta, 2018).

Ratio ( $\lambda$ )	Material A	Material B
$\frac{0.4}{0.6}$	$\frac{15}{25} = 0.6$	$\frac{20}{55} = 0.36$
$\frac{0.7}{0.9}$	$\frac{26}{35} = 0.74$	$\frac{71}{53} = 1.34$
$\frac{1.2}{1.6}$	$\frac{34}{36} = 0.94$	$\frac{92}{113} = 0.81$

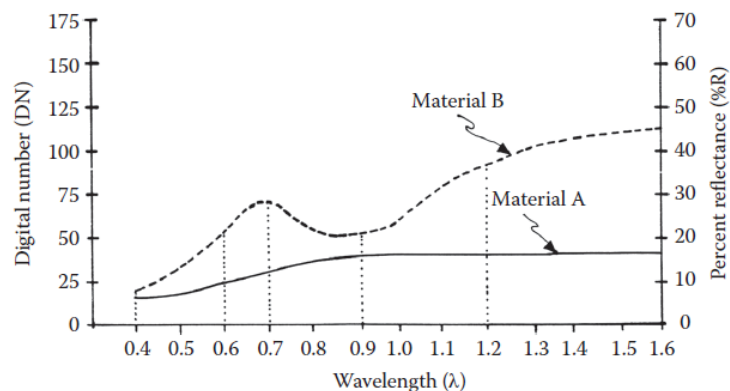


Figure 6.37: Hypothetical reflectance curves depicting how ratios enhance minor reflectance variations. Adapted after Prost, 2013).

To date, the composition of the Wahiba dune-field and surrounds has been relatively well studied by means of ground-based sampling, geochemical and remote-sensing analysis (e.g. Goudie *et al.*, 1987; Pease *et al.*, 1999; Pease and Tchakerian, 2002; Radies *et al.*, 2004; Blechschmidt *et al.*, 2009) (refer to section 3.1). The most recent and relevant work related to this study is that of Pease *et al.* (1999), and Pease and Tchakerian (2002) who determined sediment composition of the sand sea using Landsat-5, trained by sediment sampling. Using the latest Landsat-8 datasets, the study provides a broad outlook through observations on a regional-scale for provenance interpretations.

#### 6.6.1 Methods

The study used Landsat 8 bands (Table 5.1) for data transformation and applied the most commonly used ratios for mineral identification (Pease *et al.*, 1999; Prost, 2013; Pour *et al.*, 2015, Manuel *et al.*, 2017; Gupta, 2018):

- Band 4 / band 2: the iron oxide or ferric ratio allows the contrast between FeO and non-FeO minerals (e.g. Hematite, Goethite, Jarosite).
- Band 6 / band 5: the ferrous mineral ratio is used to enhance iron-bearing minerals (e.g. Olivine, pyroxenes, amphiboles).
- Band 6 / band 7: Clay and/or calcium carbonate ratio commonly used for distinguishing Al-OH, Mg-OH, OH and CaCO<sub>3</sub> bearing minerals (e.g. clay minerals, micas, calcium carbonates). Additionally, because quartz's reflectance is high in the second short-wave infrared band (band 7), this ratio is also useful in identifying it.

Figure 6.38 outlines the method step to produce the mineral occurrence raster datasets. The application of equation (5) was carried out in ArcGIS 10.6 using the raster calculator in the spatial analyst plugin in order to produce the band ratio datasets. Each band ratio map was grouped into classes, separating their reflectance values. Known geological outcrops (i.e. limestones, mafic rocks, chert rich units) are utilised to adjust class intervals and determine a threshold value for each mineral type. These values were cross-checked with the geochemically trained Landsat-5 images of Pease *et al.* (1999) with good agreement in most instances. Using the raster calculator, threshold values are used to create a binary raster dataset for each band ratio. In the case of band ratio 6/7, clay / carbonate was determined by high reflectance values and quartz was determined by low reflectance (high absorption) values. Each binary raster volume was overlain onto a panchromatic orthophoto of the erg to spatially represent the zones of likely mineral occurrence. A false colour composite was generated by applying the 4/2 band ratio to red, 6/5 band ratio to blue, and 6/7 band ratio to green (Figure 6.41).

Nine Landsat-8 tiles were merged in order to analyse mineral occurrences on a regional-scale (Figure 6.39). A solar correction was applied to each raster dataset in order to minimise the effect of variations in date, time and latitude when the datasets were captured (e.g. Young *et al.*, 2017). The datasets were merged using the 'mosaic raster' operator in the Data Management toolbox of ArcGIS 10.6. Band ratios were applied following the same procedure as above and, using the pre-determined threshold values as a reference point, regional scale binary raster maps were produced for each mineral type, all overlain onto a panchromatic orthophoto. Area-for-area the final map produced (Figure 6.42) was cross-checked against the erg-scale map (Figure 6.40D) with good agreement.

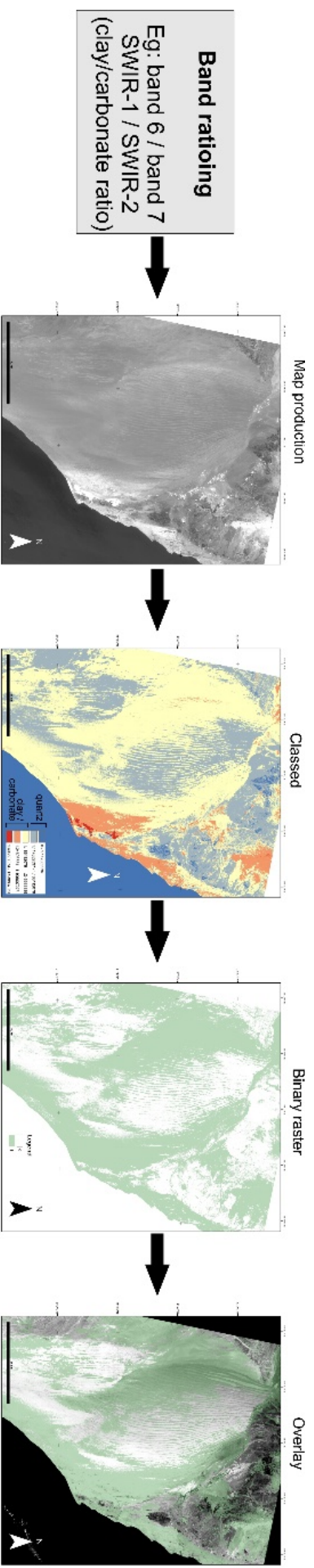


Figure 6.38: Method step to produce a map for each mineral occurrence. In this example, the produced map is grouped into five classes representing areas that contain a high occurrence (warm colours) vs. low to no occurrence (cold colours) of the mineral type. Once a threshold value is determined, a binary raster map is produced and finally superimposed onto an orthophoto for better spatial reference.

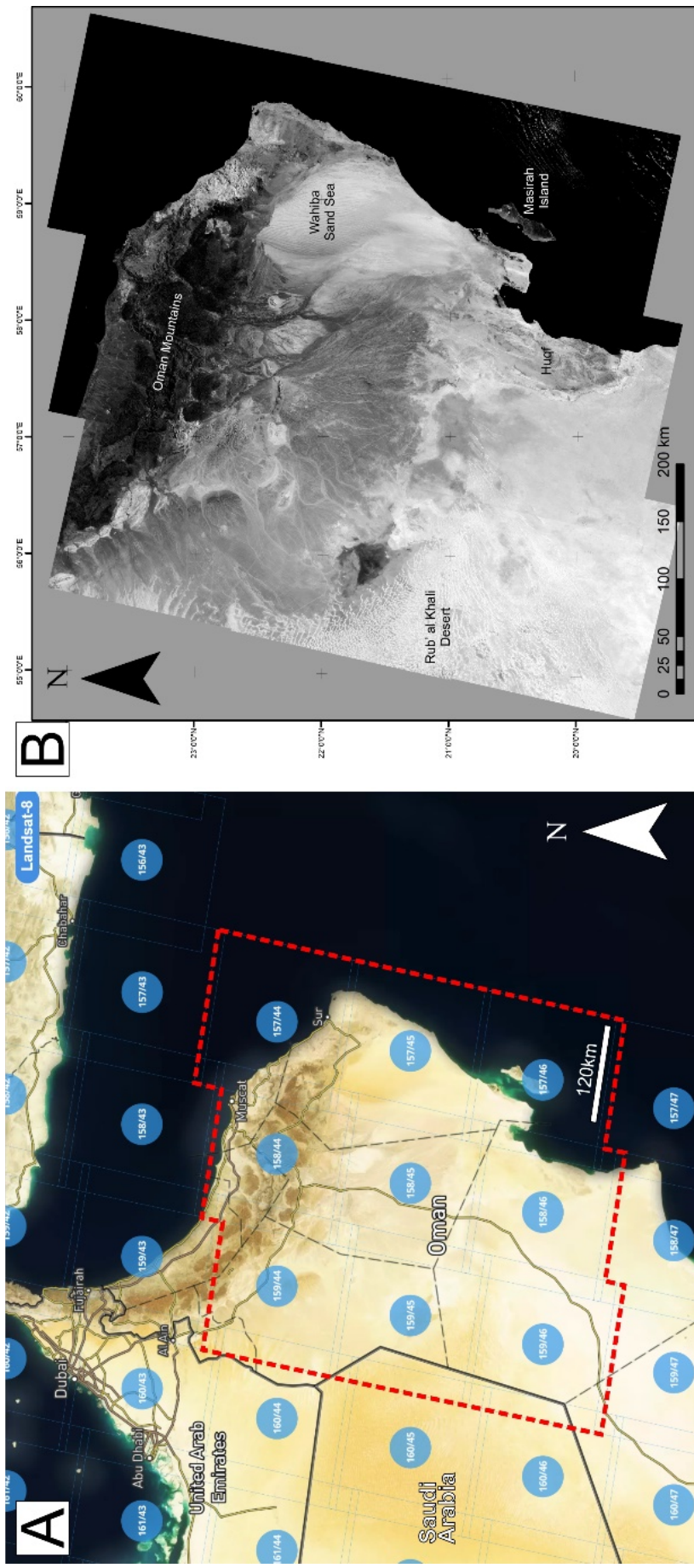


Figure 6.39: (A) Landsat-8 tiles surrounding the Wahiba Sand Sea were selected for regional-scale studies (within red-dashed box). (B) With solar corrections applied, the tiles were merged into a continuous dataset for each band. Fig (A) is extracted from <https://search.remotepixel.ca>

## 6.6.2 Results and Discussion

### *Erg-Scale*

The individual band ratio maps provide a means to quickly identify the zones of likely mineral occurrence revealed by high reflectance values (Figure 6.40A-C). Under band ratio 4/2 (ferric ratio) (Figure 6.40A), high reflectance is common on the erg and only decreases on its western margin and northeastern corner. Variable reflectance is observed on the western periphery and along the coastal portion of the erg.

The highest reflectance in band ratio 6/5 (ferrous ratio) (Figure 6.40B) is observed on the Semail Ophiolites that lies to the north and northeast of the erg and within linear bands of the Hawasina group outcrops on its northwestern margin. The associated alluvial fans and wadis of these highlands also show varying degrees of reflectance which extends into the erg, especially on the western margin and the northeastern corner. The reflectance of the 6/5 ratio are almost inverse to the observations of the ferric ratio.

Band ratio 6/7 (clay and / or calcium carbonate ratio) (Figure 6.40C) shows the highest reflectance on mountainous zones at the maps' northern border (Hawasina Nappe Limestones), along the southeastern erg margin (coastal sediments), and scattered spots occur where urban structures are observed. The erg itself shows relatively high reflectance along the east and west margins which fades inward. Variable reflectance is also observed in wadis and low sands that surrounding the erg. Zones with poor reflectance are more common on this map and is an indicator of the abundance of quartz.

A false colour composite represents the spatial distributions of ferric (red colours), ferrous (blue colours) and clay / carbonate minerals (green colours) in a single map (Figure 6.40D). On the erg, cyan to green colours dominate in the NE corner and western margin with similar colours observed in the surrounding wadis. Colours fade from yellowish in the west to a reddish orange in the east. Hues of purple dominate the southeastern margin and fade gently into the erg. Shades of bright green dominate in the northern mountainous region and their associated drainage basins. While the colour variances of the false colour composite reveal the degree of spectral signature overlap, especially within the erg, binary raster maps provide a more useful means to show their spatial variability on the erg and interaction with its immediate surroundings (Figure 6.41).

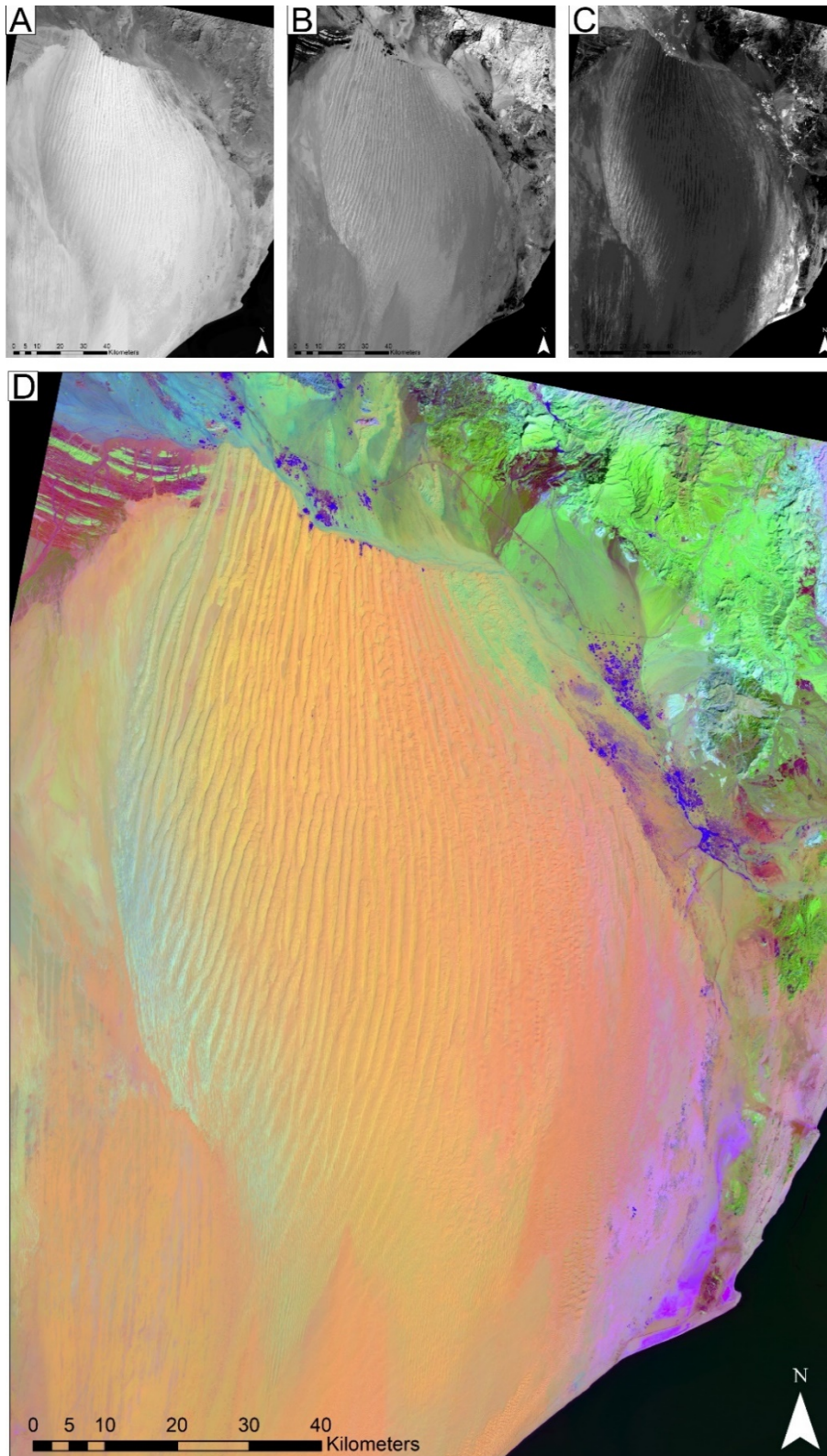


Figure 6.40: Greyscale output maps of band ratios. Bright areas in each output map indicate likely target zones for associated mineral assemblages. A) B4/B2 iron oxide ratio is associated with hematite / goethite. B) B6/B5 ferrous mineral ratio associated with mafic minerals. C) B6/B7 clay / carbonate ratio associated with hydrous aluminosilicates and / or carbonates. As quartz has high reflectance in band 7 it is represented on the same map by areas of very low reflectance. (D) Band ratios derived from image spectra 4/2-6/5-6/7 combined in RGB to produce a false colour composite.

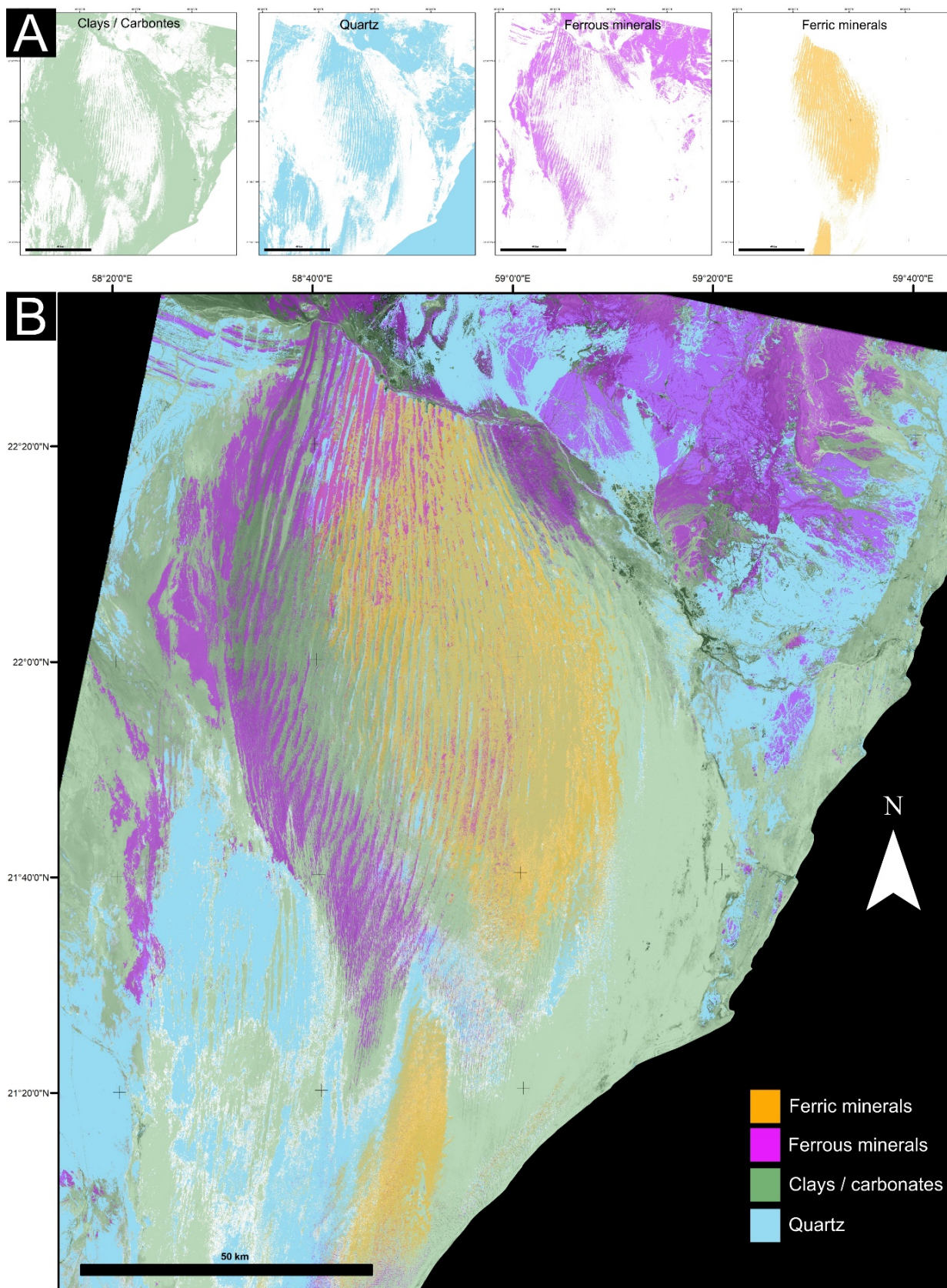


Figure 6.41: (A) Separated mineral raster datasets. (B) Panchromatic map with all mineral overlay based on binary raster separations of the three mineral categories – ferric, ferrous and calcium carbonate/clays. Zones without colour are unclassified

Because band ratio 6/7 does not differentiate between clay minerals and calcium carbonates, it cannot be separated on the map (Figure 6.41). Silt and clay sands in the Wahibas have been reported to be low, ranging between 0.0 and 6.4% (mean = 1.38%) with even lower values reported at the linear megadune crests (Goudie *et al.*, 1987). On the other hand, carbonate content of Wahiba dune sands is reported to be high ranging between 14.17 and 64.12% (mean = 33.36%) (Goudie *et al.*, 1987). Band ratio 6/7 response is more likely a cause of the presence of carbonate rich sediment than those of clays. The largest source is thought to be from beach sands with elevated proportions of bioclastic material from the coastal shelf in addition to limestones sourced from the adjacent Oman Mountains (Goudie *et al.*, 1987; Pease and Tchakerian 2002; Radies *et al.*, 2004). The 6/7 response within the wadis is probably a combination of clays, recycled dune sands, and weathered materials from the limestone-rich source of the Oman Mountains. The high response from urban structures is probably due to lime-rich cement.

Due to the application of the same threshold value to distinguish spectral signatures of carbonates and quartz, the two maps are the exact inverse to one another. This is not conclusive of the two minerals occurrences together and care should be taken when interpreting the maps. A meaningful interpretation rather lies in the relative abundances of carbonates compared to that of quartz in their respective zones of occurrence. Looking at the sand sea, carbonates dominate the east and west margins and, while both minerals are evident in the erg centre.

A strong response of ferrous minerals on the northeast corner is probably terrestrially derived material weathered from the local basic rocks (Semail ophiolites) on the northern mountains with the same spectral response (Figure 6.41). This zone is thought to have a long history of reworking (Goudie *et al.*, 1987; Fryberger *et al.*, 2016a; Hern *et al.*, 2018). The sediment here is likely derived from the southeastern portion of the Wadi Batha system and blown onto the northeastern flank of the erg. Extensive bajada and alluvial fans sits to the west of the erg have the potential to provide a substantial source of the ferrous minerals that is observed on the western margin of the field and is discussed in more detail in the regional outlook. Interestingly these two zones on the erg that contain the ferrous

mineral responses, are zones which do not show any NDVI response (compare Figure 6.31 and Figure 6.41). This may be interpreted as either reduced soil fertility due to the presence of basic minerals that limit vegetation growth, or due to the constant reworking and increased sediment input offering less opportunity for germination and/or growth.

The ferric mineral response is dominantly found enclosed in the erg centre where it overlaps with quartz' signature and similarly excludes the interdune corridors and lower stoss slopes where carbonates' signature dominates (Figure 6.41). It also occurs in a north-south trending elongate band separated from the main erg in the southern peripheral sands. Microscope and ESEM examinations reveal iron-oxide coatings are common on individual quartz and feldspar grains within the High Sands (Goudie *et al.*, 1987; Hern *et al.*, 2018). Chemical/biogeochemical weathering of the mafic content derived from the Oman Mountains provides a potential source of iron, however, the positioning of the iron-stained sediments is enigmatic. These reactions are known to occur in aqueous suspension (e.g. Scheidegger *et al.*, 1993) and as such the signature would be expected surrounding wadi sediments. Tentative thoughts are that this signature is erg-wide, however, its presence on the eastern and western margins is masked as a consequence of reworking and/or fresh sediment input into the margins.

### *Regional-Scale*

Figure 6.42 shows the position of the Wahiba Sand Sea and in relation to its regional surroundings. To the far west and west-southwest (~350 km) lies the margin of the Rub' al Khali Sand Sea, dominated by the ferrous and ferric spectral signatures. These signature extends from the Rub' al Khali erg eastwards in a relatively thin band towards the Hufq outcrops lying to the southwest of the erg (~80 km). The extensive bajada of northern Oman's interior comprises the Barzaman Formation and Quaternary alluvial fans which dominate the plain between the Wahiba and Rub' al Khali desert. Draining the Oman Mountains to the north, these major systems comprise mafic minerals of the Semail ophiolites and siliciclastics, limestones and cherts of the Hawasina Nappes and parautochthonous units (Blechs Schmidt *et al.*, 2009).

Southerly winds are suggested to have provided the Al Jabin Unit with most of its biogenic coastal carbonate content, as well as Huqf derived mafic minerals (Radies *et al.*, 2004) and may partly explain the carbonate response and limited ferrous response on the ergs southern periphery where Al Jabin aeolianites are exposed. The mineralogical nature of the exposed fans to the west of the erg provides insight into the oldest aeolian unit (Al-Hibal) and underlying alluvial and fluvial systems (Barzaman and Al-Batha unit). It is suggested that northeast to southwest trending faults structurally controlled the fluvial systems that deposited much of the material into the Wahiba Basin and was reworked by southerly winds in more arid times (Robinson *et al.*, 2007). In the oldest aeolian units of the High Sands, Radies *et al.* (2004; their table 3) reports high quantities of quartz, (38.5% average from 8 core samples), feldspar and pyroxenes making up the reworked terrestrial content, as well as a large input of bioclasts (38% average from 8 core samples) potentially coastally derived as the southerly winds dominated. These signatures are evident in the erg centre, where carbonates and quartz signatures dominate interdunes and the lower megadune stoss slopes. Additionally, the presence of carbonates on the lower stoss slopes in the erg interior is also controlled by the strong input of southerly derived bioclastic material from a period of low sea level and a well-exposed shelf forming the Qahid Unit (Radies *et al.*, 2004).

Annual resultant drift data, although limited, provide the pathways of contemporary regional sediment movement (Figure 6.42B). Strong southerlies have the potential to move vast quantities of sediment from the south. The apparent extension of Rub' al Khali sands towards the Wahiba (ferric, ferrous and quartz) suggests some form of linkage. Infrequent but strong Shamal sand storms can move vast quantities of sediment from the Rub' al Khali to the Wahiba Sand Sea (e.g. <https://earthobservatory.nasa.gov/images/92522/sandy-shamal-season>). Radies *et al.* (2014) infers a link between the Wahiba Sand Sea, the Hufq and the Rub' al Khali erg, caused by small shifts in the ITCZ, allowing southwesterlies to move sediment. Yu *et al.* (2016) supports this and reported 68 non-Shamal 'dust days' between May – August (2000-2013) where strong southwesterly winds moved sediments between the two ergs.

Fans and wadis to the west of the Wahibas are the likely source of the ferrous mineral occurrence at its western margin. These minerals are likely to be transported from the wadis by the north to northwesterly winter winds and westerly summer winds (Shamal) (Figure 6.42B). These links are also supported by geochemical and mineralogical analysis in the literature (Goudie *et al.*, 1987; Pease and Tchakerian 2002). The westerly sourced ferrous minerals are likely the dominant contemporary terrestrial source to the Wahibas.

The mineralogy determined through remote sensing analysis provides insight into the spatial and temporal patterns of mineral distribution both locally and regionally to the Wahiba dune-field. Source area geometries are recognised to have the ability influence the formation of dune-field patterns (e.g. Ewing and Kocurek, 2010). This type of data combined with higher resolution sand drift data has the potential to constrain (and semi-quantify) sediment input, reworking and resolve dune pattern evolution. Further insights may be gained through the acquisition of hyperspectral datasets which can better constrain mineralogical variances.

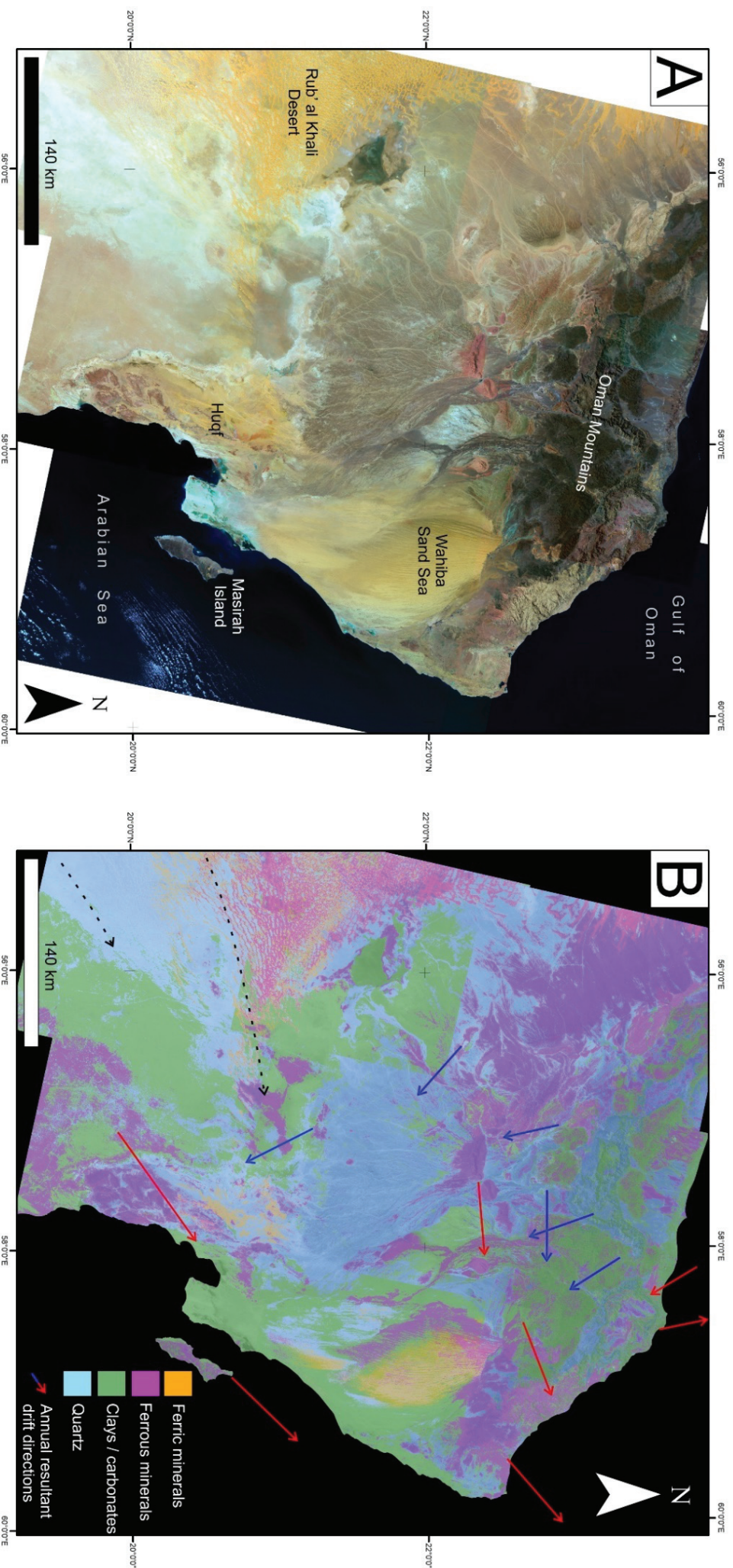


Figure 6.42: (A) Landsat-8 false-colour composite 7-4-2 (RGB) shows the location of the Wahiba dune-field in references to the surrounding Oman Mountains, Bojada and wadis, Huqf outcrop and Rub' al Khali desert at the Oman / Saudi Arabia border. The false-colour band combination shown here is typically used to highlight the geology of a region. (B) The same area in (A) showing the mineral occurrences as identified by the band ratio datasets. Red and blue arrows indicate the net annual resultant drift directions for summer and winter seasons respectively (relative strength by arrow length). Black dashed arrows represent simplified net annual sand flow directions based on dune orientations in the Rub' al Khali. Sand drift data is extracted from Fryberger et al., 2016a.

## 6.7 Summary

- Relationships between dune size and spacing, in conjunction with base-level representing the antecedent topography appear to control sediment distribution and reveal dune-field pattern heterogeneity.
- Large to medium-scale subdued crescentic antecedent bedforms revealed below interdune corridors are hypothesised as relicts of the ancient dune-field that the current configuration evolved from.
- Internal architectures on dune crests reveal well-preserved bedforms are buried in the subsurface. The topography from these bedforms play a key role in the position and dynamics of migrating contemporary bedforms.
- Vegetation occurs year-round on the dune-field and can be correlated with rainfall patterns.
- Mineral identification indicates sediment input dominates on the western erg margin and within the northeast erg corner. Regional maps show the Rub 'al Khali may also provide a substantial amount of sediment to the Wahiba erg.



## PART C : AN ANCIENT AEOLIAN SYSTEM



## 7 The Jurassic Navajo Sandstone, southwestern USA

The ancient Navajo Sandstone of western USA and equivalents (Aztec Sandstone, Glen Canyon Sandstone and Nugget Sandstone) are considered the remnants of the most extensive desert system ever to have existed in the history of the Earth (Blakey *et al.*, 1988; Verlander, 1995). The Navajo sand sea once covered an area up to 265,000 km<sup>2</sup>, and probably contained the largest sand dunes that ever moved across the surface of the planet (Verlander, 1995; Blakey and Ranney, 2008). The formation is exposed extensively and forms many of the cliffs and canyons of western interior United States.

### 7.1 Location

Today the sedimentary rocks of the western interior United States are exposed in a variety of high desert intermontane terrains (Figure 7.1). The greatest concentration of the aeolian-bearing formations occur on the Colorado Plateau in south-central Utah and adjacent Arizona (Blakey *et al.*, 1988). The Plateau along with the Southern Rocky Mountain region has been uplifted some 2000 m during the Cenozoic Period (Morgan, 2003). The Colorado River and its tributaries have carved the landscape over the last 5 – 10 million years revealing continuous, well-exposed, undeformed sections of Palaeozoic through Cenozoic, often accessible across fairly small areas (Blakey, 2008). In particular, the Navajo Sandstone offers an excellently preserved exposure of facies and architectural elements in three dimensions.

### 7.2 Stratigraphical Interval

The deposition of aeolian strata began in the late Carboniferous Period (early-to-middle Pennsylvanian), reaching an initial climax during the Permian Period, waning during the Triassic Period, and attained a second climax during early-to-middle Jurassic Period. By late Jurassic times, these aeolian systems were declining and were completely absent from the Cretaceous record (Figure 7.2) (Blakey *et al.*, 1988). Over ~160 Ma of sedimentation, aeolian deposits dominated vast areas of the western United States.

The Lower and Middle Jurassic rocks of the Colorado Plateau probably contained the greatest concentration of aeolian sandstone in the global rock record (Blakey; 1988). At the time of deposition this area was a broad flat plain near sea level behind a developing arc complex that provided a vast area for sand flow paths and aeolian accumulation (Kocurek and Dott, 1983; Riggs and Blakey, 1993; Blakey, 1994).

This chapter briefly covers regional stratigraphical patterns during the Jurassic Period and uncovers the major depositional successions that are divided by major bounding unconformities (Pipiringos and O'Sullivan, 1978; Blakey, 1994; Blakey *et al.*, 1996). This work will highlight the stratigraphical record of the Lower Jurassic deposition, with focus on the aeolian deposits of the upper Glen Canyon Group (Figure 7.2). Emphasis throughout will be placed on the extensive erg system of the Navajo Sandstone.

### 7.3 Scope and Organisation

This review is organised as follows: (1) examination of the Colorado Plateau as the locus for the Navajo Sandstone exposures followed by summary of the tectono-sedimentary evolution of the western interior of the United States from late Precambrian to Jurassic periods. Emphasis will be placed on Jurassic basin development and deposition; (2) summary of the stratigraphy of the Colorado Plateau, with further emphasis on the bounding unconformities of the Jurassic strata and sedimentology of the upper Glen Canyon Group; (3) palaeogeographical reconstruction of the Navajo Sandstone with focus on the erg development, evolution and architecture; (4) summary on the control of deposition of the Navajo Sandstone.



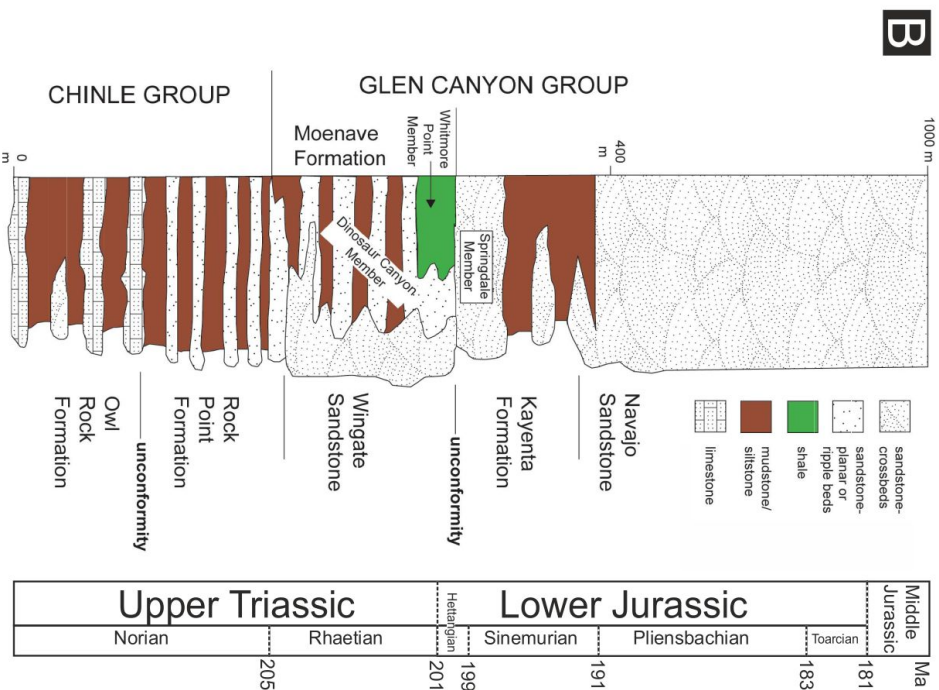
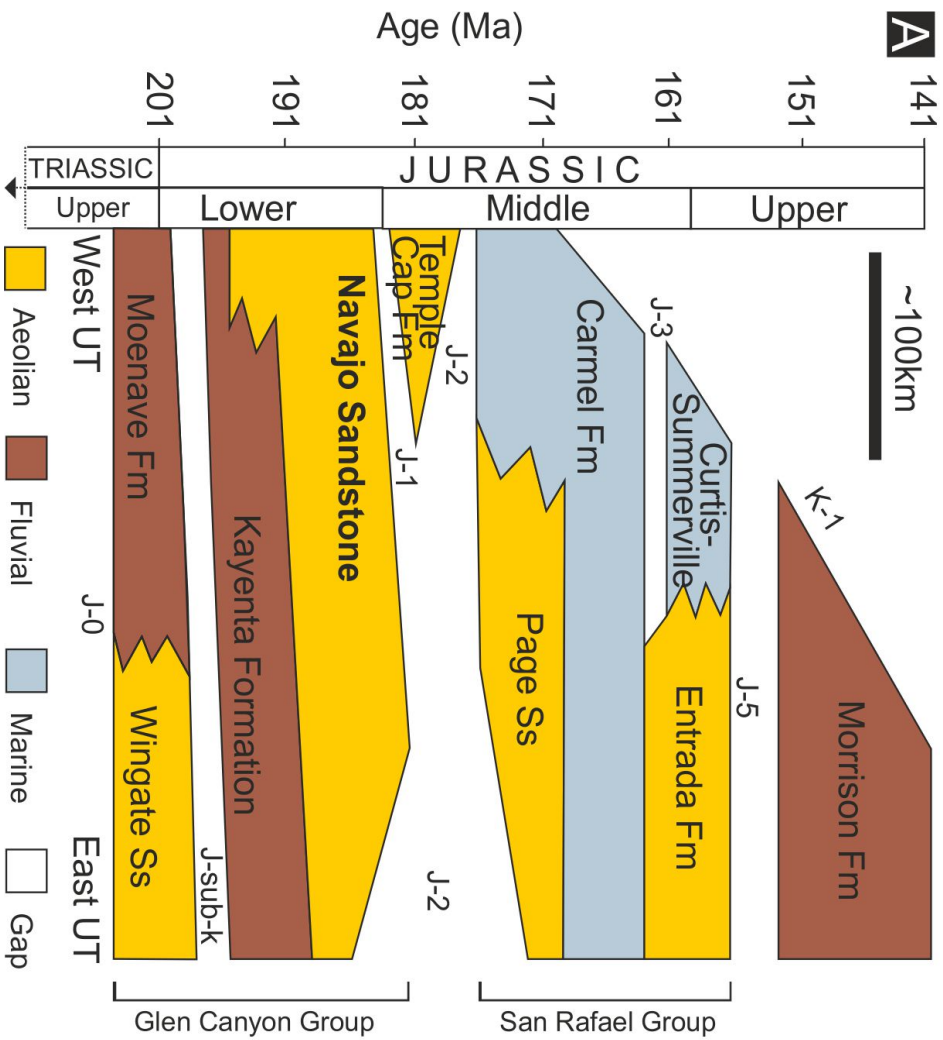


Figure 7.2: (A) Simplified Jurassic litho-stratigraphy of the Colorado Plateau showing the main aeolian deposits and major unconformities (see section 7.6). This work focuses on the Navajo Sandstone, the largest and most widespread aeolian deposit during Jurassic times (Modified after Allen et al., 2000; Beiter et al., 2005; Lucas et al., 2011). (B) Generalised stratigraphy and age assignments marking the Triassic-Jurassic boundary at ~201 Ma (Modified after Lucas and Tanner, 2014).

## 7.4 The Western Interior United States

The Navajo Sandstone is best exposed on the Colorado Plateau in the western interior United States. This section points out the important features of the Plateau (Figure 7.3), unravels the tectonic history of the western U.S.A. (Figure 7.4), and highlights the formation (Figure 7.5) and overall significance (Figure 7.6) of the Jurassic basins to the Glen Canyon Group deposits.

### 7.4.1 The Colorado Plateau

The Colorado Plateau is composed of Neoproterozoic, Palaeozoic, and Mesozoic sedimentary rocks overlying mechanically heterogeneous Palaeoproterozoic and Mesoproterozoic crystalline basement containing shear zones (Davis and Bump, 2009). It forms an irregular ovate stable block of North America, offset by major structural trends that separate it from mountainous regions in all directions (Baars, 2000). It has been affected by, and responded to, major plate-generated movements and stresses, but it was never strongly deformed and marks a relatively flat-lying, high-standing geological province in the southwestern United States (Figure 7.3) (Liu and Gurnis, 2010).

Much of the underlying tectonic grain of the Colorado Plateau and the adjacent Southern Rocky Mountains (Figure 7.1) was established during the Proterozoic assembly of southwestern North America (Blakey, 2008). The North America continent was part of the growing Laurentian craton and around this time global-scale collisional events were forming the supercontinent Columbia (Hoffman, 1988; Zhao *et al.*, 2002). Contractional amalgamation of juvenile continental lithosphere occurred between 1.8 - 1.65 Ga and produced major northeast-striking tectonic boundaries across North America (Karlstrom and Humphreys, 1988). A northwest-trending grain on the Plateau may also be inherited from Precambrian Period tectonics along with wrench tectonics that affected North America for long periods of time (Blakey, 2008).

Today, this tectonic grain can be seen on the Colorado Plateau in the form of prominent lineaments that trend northeast and northwest across most of North America (Figure 7.3) (Baars and Stevenson, 1981). The lineaments are host to complicated swarms of faults, originating in the Precambrian Period,

which have been reactivated numerous times over the geological history of the Plateau and account for much of the orientation of the structural features seen today (Figure 7.3) (Foos, 1999).

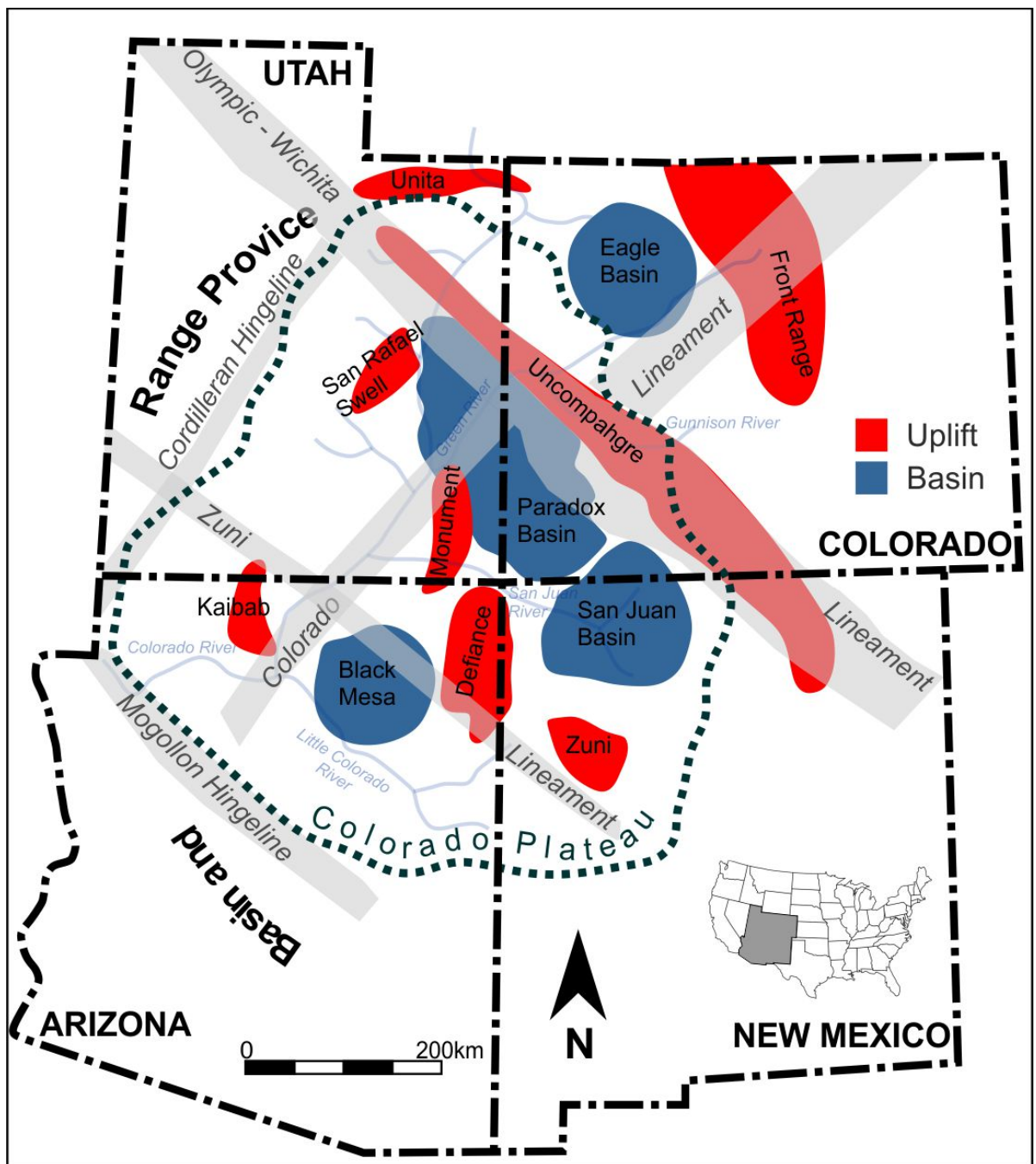


Figure 7.3: The outline of the Colorado Plateau tectonic Province. Large scale lineaments define much of the tectonic grain on the Colorado Plateau. The northwest-trending Olympic-Wichita Lineament appears to have had right-lateral strike-slip displacement and is bracketed to 1.72 – 1.46 Ga. The northeast-trending Colorado Lineament displaced basement rocks in a left-lateral sense and is dated at ~1.7 Ga. The two continental-scale rift systems form a conjugate set that bisect one another in the vicinity of Moab. The Cordilleran Hingeline (section 7.4.2) delineates the northwesterly extent of the Plateau and had its roots in Precambrian time. The Precambrian northwest-trending Walker Lane-Texas Lineament (not shown here) was one of the largest, longest, and most prominent lineaments on the N. American continent. On this map, limited features of this lineament are represented by the Mogollon Hingeline and Zuni Lineament. Modified after Foos, 1999 with information from Kelley, 1955; Baars and Stevenson, 1981; Blakey, 1988.

#### 7.4.2 Regional Tectonic Framework

The geological history of western North America has been and continues to be shaped by its position on the eastern rim of the Pacific Ocean (Cannings *et al.*, 2011). The modern Pacific Ocean's basin is the successor to the original ocean which split Laurentia away from the rest of the Precambrian supercontinent Rodinia. This opened a seaway that widened until it became the Panthalassan Ocean in late Palaeozoic time (Cannings *et al.*, 2011). Western North America has always faced the same active ocean basin and, over a 700-million-year period of time, has been affected by multi-episodic rifting followed by plate-margin subduction and transcurrent faulting (Cannings *et al.*, 2011).

The schematics of Figure 7.4 give a brief palaeotectonic and depositional history of southwestern North America from the Precambrian to Jurassic Periods. Prior to summarising these images, it is important to note two tectonic features:

1) The Wasatch Line (also known as the Cordilleran hingeline/miogeocline) has been defined as a linear feature related to the late Precambrian rifting of the North American continent (Picha and Gibson, 1985). Marshall Kay (1951), the first to describe the Wasatch, defined it as "the flexure that defined the miogeosyncline in the Cambrian continued as the site of differential movement through the Palaeozoic and earlier Mesozoic" (Stokes, 1976). The Wasatch Line has been repeatedly reactivated as structural uplifts, ramps, strike-slip faults, and extensional detachments. (Stokes, 1976; Picha and Gibson, 1985). Although it is recognised as a major feature of North American Geology, the true nature, origin and present-day extent of the Wasatch remains equivocal.

2) The Cordilleran Orogen is a mountain chain of western North America and forms a segment of the Circum-Pacific orogenic belt. It was established when subduction was initiated between early and late Triassic time along a continental margin that had been delineated by Neoproterozoic rifting during the breakup of Rodinia (Wasatch Line), and later modified in late Palaeozoic and earliest Mesozoic time by the emplacement of oceanic allochthons upon the edge of the continental block during the final assembly of Pangea (Dickinson, 2004). Older rock assemblages exposed within the mountain chain

record preceding tectonic regimes of different character (e.g. Grenville orogenesis and the Gondwanide orogenic belt) (Dickinson, 2004).

From the early Palaeozoic Period through to the Mesozoic Period, southwestern North America underwent several changes in tectonic setting (Blakey, 1997). Following the rifting between North America and Gondwana (late Precambrian through Devonian times), the region was part of a passive margin and received chiefly shallow marine and shoreline sedimentation (Figure 7.4A) (Miller *et al.*, 1992). Around the mid-Devonian Period, widespread subduction began along the continental margin, forming a series of intra oceanic island arcs (Cannings *et al.*, 2011). The late Devonian into the Mississippian periods signifies a change in tectonic setting as an arc collided with the western margin of the continent starting the Antler Orogeny (Figure 7.4A&B) (Ingersoll, 2008). A thick oceanic sequence of Mississippian through Permian chert, limestone, conglomerate, siltstone, shale, lava flows and pyroclastics accumulated in a trough west of the Antler orogenic belt in the Havallah Basin (Figure 7.4B)

During the late Palaeozoic Era southern Utah occupied a palaeolatitude just north of the equator along the western margin of the supercontinent of Pangaea (Condon, 1997; Rogers and Santosh, 2004). It is thought that a compressional tectonic regime developed in response to the collision of Gondwana and Laurussia (Ouachita-Marathon orogeny) resulting in the development of numerous thrust-bound structural uplifts in the region collectively known as the Ancestral Rocky Mountains (ARM) (Figure 7.4B) (Barbeau, 2003). However, Blakey (2008) has cautioned that the tectonic setting or cause of the ARM formation is not yet clearly understood. The ARM consisted of up to 20 flexural-controlled foreland basins, of which the Paradox foreland basin (Figure 7.3) is considered to be the largest, covering an area of approximately 50 000 km<sup>2</sup> across southeast Utah and western Colorado (Barbeau, 2003).

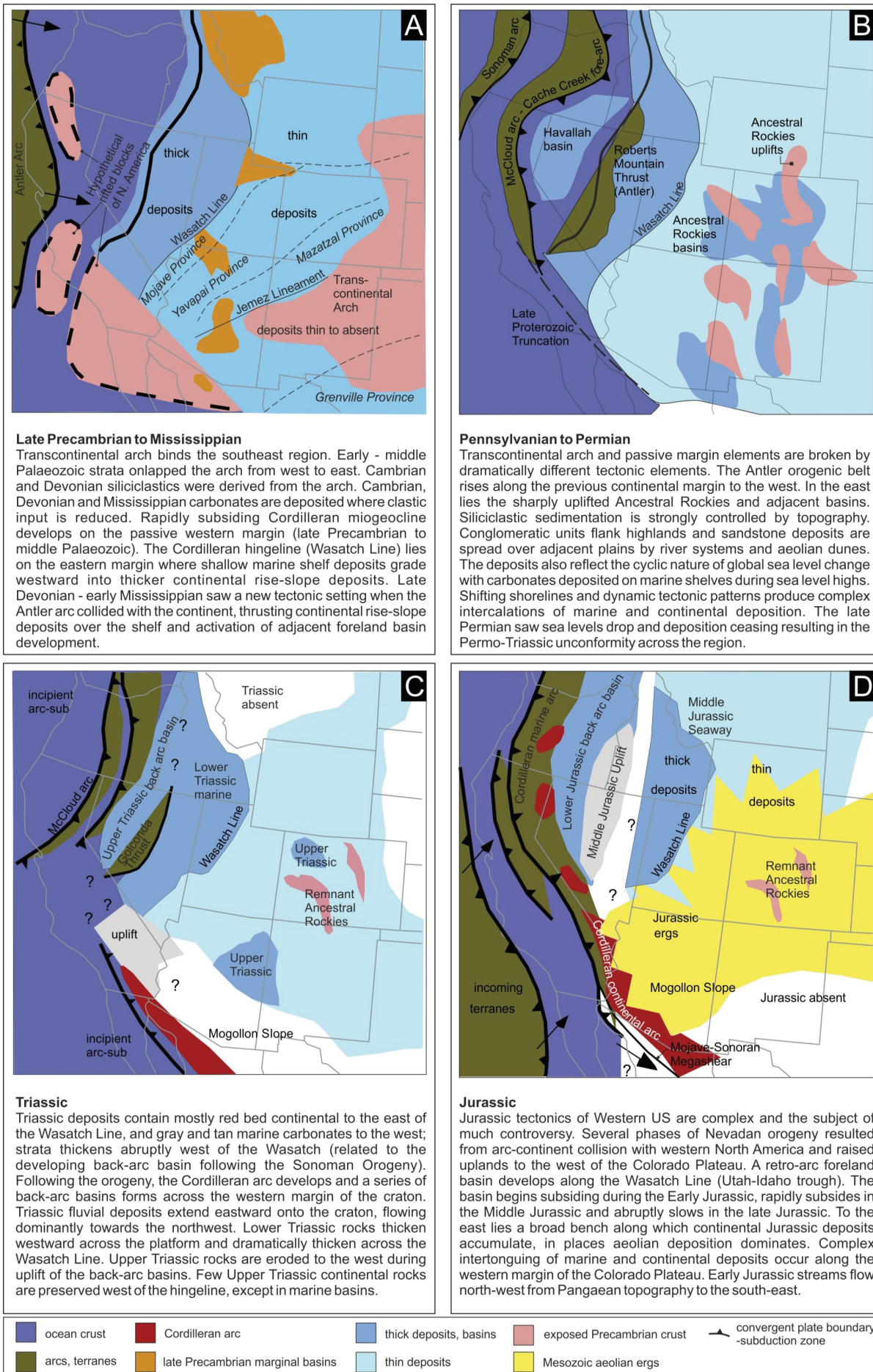


Figure 7.4: Palaeotectonic evolution of southwestern North America from the late Precambrian Period to the Jurassic Period with brief summaries of the subsequent depositions. Figures modified after Blakey, 2008 with summaries from Blakey, 1988; Marzolf, 1993, 1994; Blakey, 2008; Ingersoll, 2008; Miall, 2008.

By late Permian to early Triassic times another arc collided with the west edge of the continent forming the Sonoman Orogeny (west of area shown in Figure 7.4C) (Ingersoll, 2008). The Havallah Basin sediments were emplaced along the Golconda Thrust during this orogenic event (Figure 7.4C) (Ingersoll, 2008). Persistent subduction and collision marks the initiation of the Cordilleran orogenic system in the early Triassic Period (Figure 7.4C) (Dickinson, 2004).

The Jurassic Period saw a series of terranes colliding with the western margin of the continent and a radical change in the configuration of the Cordilleran arc (Figure 7.4D) (Blakey, 2008). The events collectively produced the Nevadan orogeny (west of area shown in Figure 7.4D). At a time between the Pennsylvanian and Upper Jurassic, the southwest margin of North America was truncated and apparently transported to the southeast into Mexico along the Sonoran-Mojave megashear (Blakey, 2008) (Figure 7.4D). Further details on the basins that formed in the Jurassic Period are given below.

#### 7.4.3 Jurassic Basins

From the early Triassic to middle Jurassic Period, sediments were deposited in the feature known as the Utah-Idaho Trough - an elongate basin most commonly interpreted as a retroarc foreland basin (Kocurek and Dott, 1983; Bjerrum and Dorsey, 1995; Allen *et al.*, 2000; Blakey, 2008). A fundamental feature of the Mesozoic history of the U.S. Cordillera is the evolution from Early Jurassic extension to Middle to Late Jurassic contraction (Allmendinger, 1992). However, a major shortening event also occurred between ~ 200 and 185 Ma in the Early Jurassic as indicated by pluton age dates in northwest Nevada (Wyld, 1996). The generation of shortening events in the early Mesozoic continental margin arc flexed the continental interior downward (Allen, 2000). Burial curves show that a slow and prolonged background subsidence with distinct superimposed convex up events at 205 – 185 Ma (Figure 7.5). The subsidence suggests that the Navajo preservation was fundamentally controlled by a combination of positive sand budget and downflexing in the retro-foreland basin system (Allen *et al.*, 2000). The combination of the creation of a wide topographic depression representing a retro-foreland basin, sheltered behind a mountain belt exerting a rain shadow effect, and a background dynamic

subsidence, produced optimum conditions for the preservation of thick aeolian deposits during the Jurassic (Verlander, 1995; Allen *et al.*, 2000).

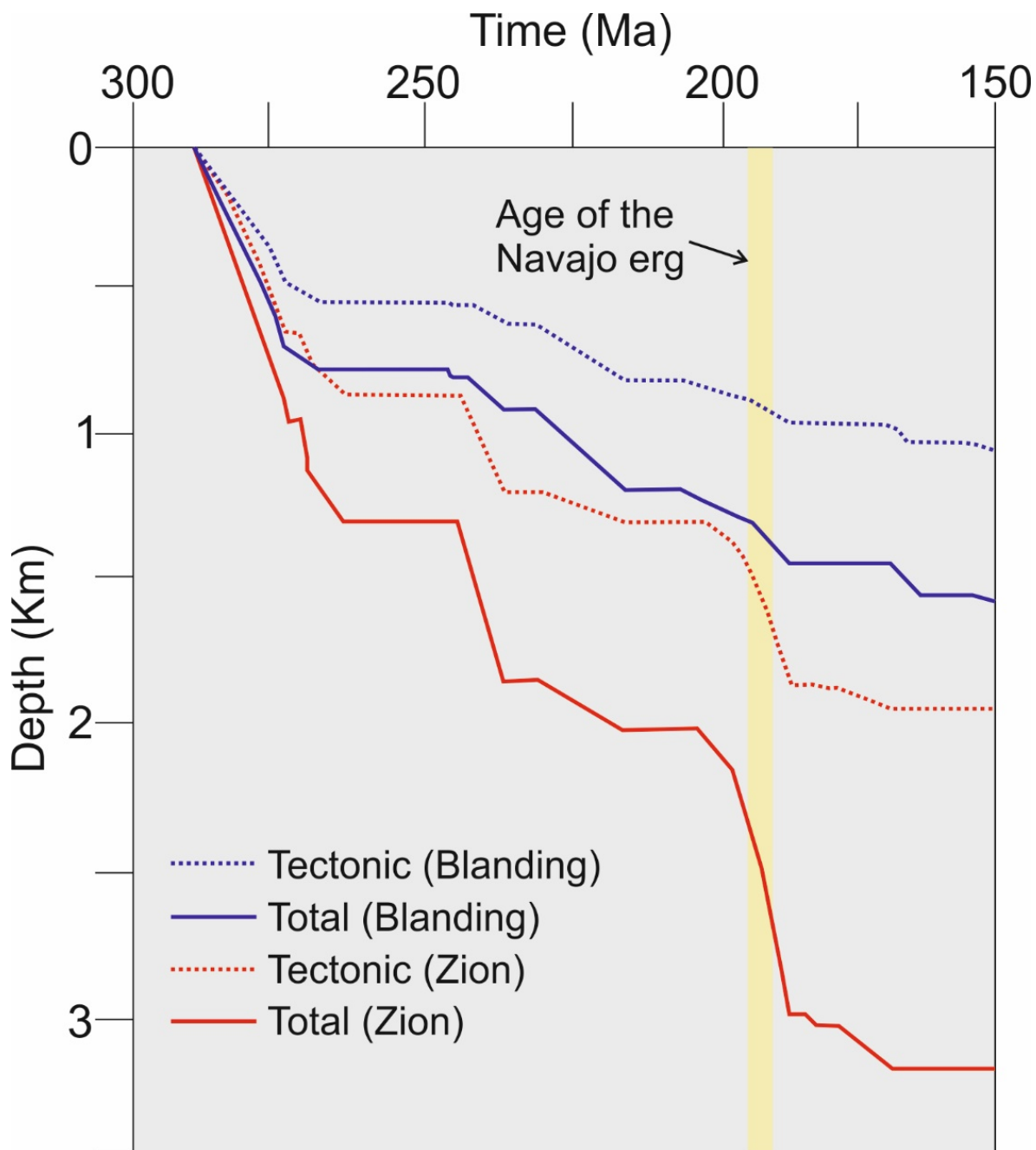


Figure 7.5: Tectonic subsidence histories for Blanding in southeastern Utah and Zion in southwestern Utah. During Navajo times, subsidence was greatest in the west accounting for the thicker accumulation of aeolian sands. Modified after Allen *et al.* (2000).

### Basin Locations

Two prominent basins developed during the Jurassic (Figure 7.6); (1) the Zuni Sag, trending northwest across the southwest Colorado Plateau, and (2) the Utah-Idaho Trough, trending along and west of the Wasatch Line (Blakey 1994; Peterson, 1994; Blakey, 2008). The Zuni Sag lies at the foot of the uplands area known as the Mogollon slope and was the locus of northwest flowing Glen Canyon streams that eventually flowed into the Utah-Idaho Trough (Blakey, 1994). Across the western interior US, the Utah-Idaho Trough has been referred to as the dominant sedimentary basin during Jurassic times (Peterson, 1994). Jurassic rocks thicken sharply into the trough beginning during Glen Canyon deposition, thinning eastwards and are generally truncated by sub-Cretaceous or sub-Tertiary unconformities (Figure 7.8) (Bjerrum and Dorsey, 1995; Blakey, 2008).

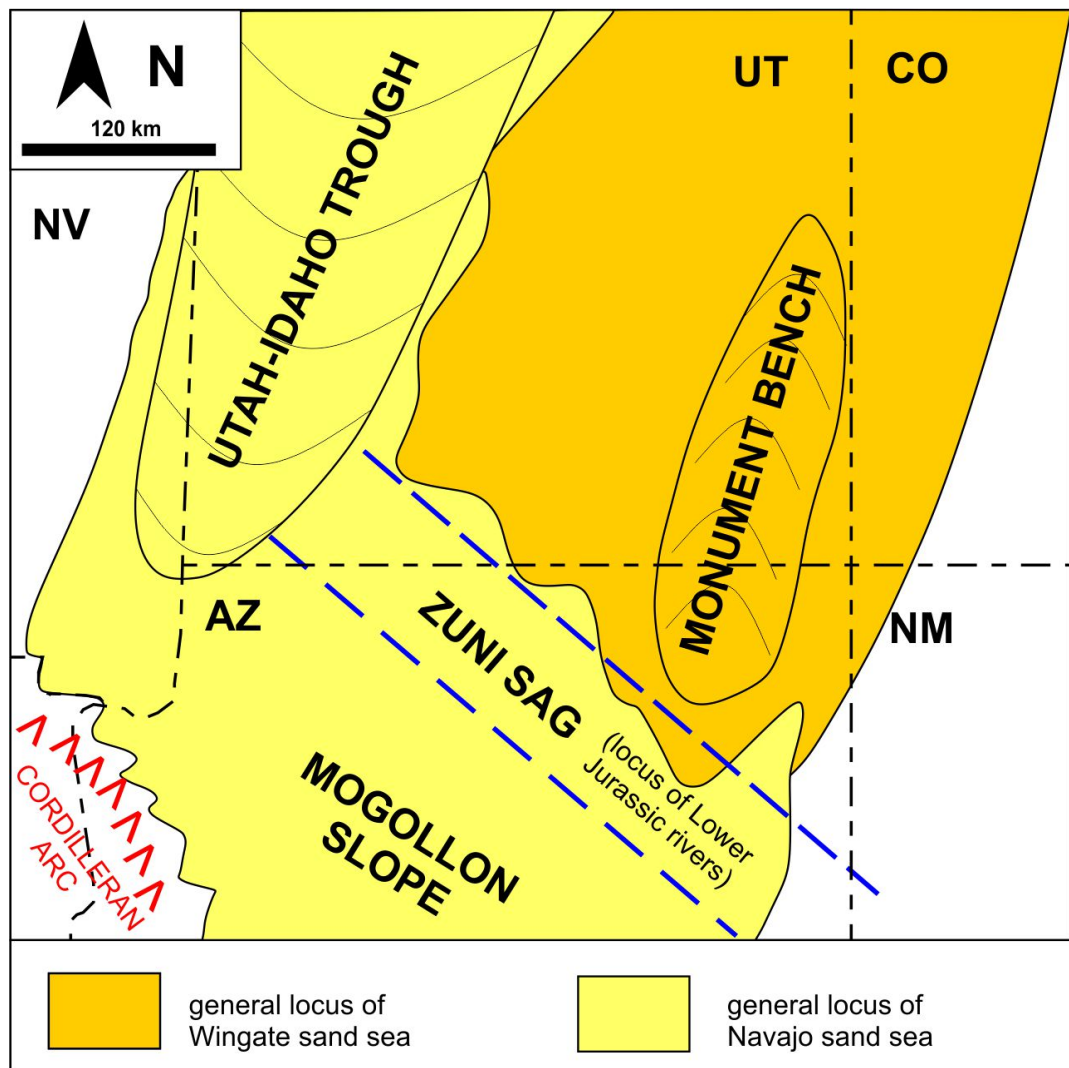


Figure 7.6: General tectonic setting for the deposition of the Lower Jurassic. Modified after Blakey, 1994

## 7.5 Stratigraphy of the Western Interior United States

Figure 7.7 shows the general regional stratigraphy of the late Palaeozoic and Mesozoic of the Western Interior. The Triassic and Jurassic rocks of the western United States were divided into unconformities which made for useful correlation of rock sequences in areas where fossil and age dates were lacking (Pipiringos and O’Sullivan; 1978). A lack of sufficient biostratigraphical data in certain areas made it difficult to determine whether the series boundaries lay exactly within stratigraphical intervals represented by the unconformity, as such they are considered approximate (Blakey, 2008). The numerals in the sequence boundaries (e.g. J-1, J-2 etc.) should not be taken as sequential as newly defined sequences cannot maintain a parallel system of nomenclature (e.g. the J-sub-K and J-sup fit below J-1 and J-3 respectively) (Blakey, 2008).

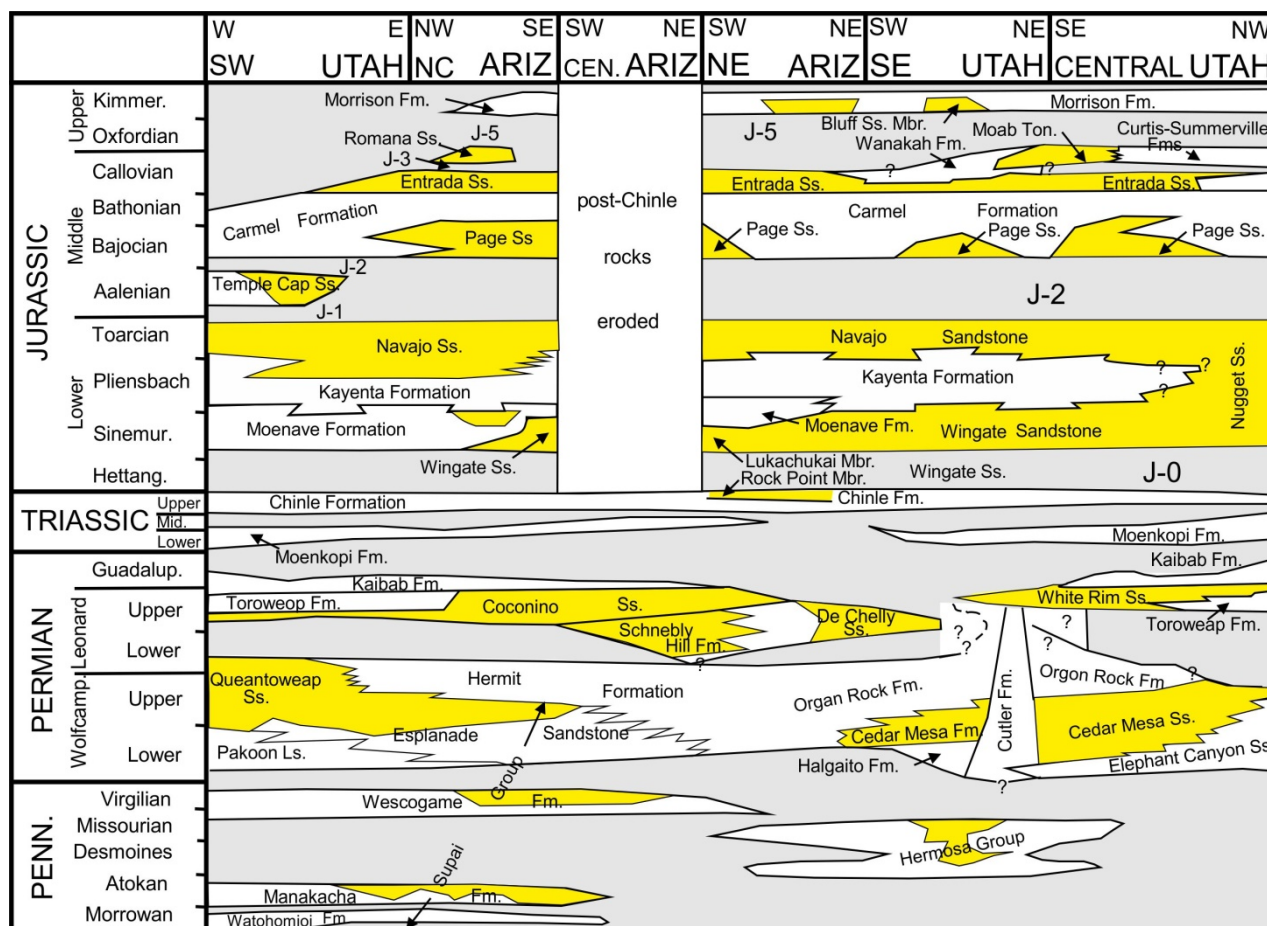


Figure 7.7: The Pennsylvanian to Jurassic systems of the Western Interior of the United States highlighting all known aeolian-bearing intervals (yellow). Unconformities are in grey with principal unconformities of the Jurassic labelled. The early works of this stratigraphical diagram shows the Triassic-Jurassic boundary to lie on the J-0 unconformity (see in-text for the correct boundary). Refer to section 7.6 for the positions of the J-sub-K and J-sup boundaries (not shown here). Modified after Blakey (1988).

The sediments deposited onto the Colorado Plateau during the Triassic and Jurassic periods are predominantly fluvial or aeolian in origin. From oldest to youngest these comprise the Moenkopi and Chinle Formation (Figure 7.7), the Glen Canyon Group, the San Rafael Group and the Morrison Formation (Figure 7.2A). The type-locality for the Glen Canyon Group deposits is the Glen Canyon National Park in southeast Utah where entire sections are visible (Peterson and Pippingos, 1979). Initially the Group was considered to be entirely Jurassic in age as shown in Figure 7.7 (Peterson and Pippingos, 1979), however, more recent biostratigraphical and magnetostratigraphical evidence place the Triassic-Jurassic boundary, with relative precision, in the middle part of the Whitmore Point Member of the Moenave Formation (Figure 7.2B) (Lucas *et al.*, 2011).

## 7.6 Jurassic stratigraphy

The Jurassic strata form the largest areal outcrop of any geological system across the Colorado Plateau which facilitates correlation and development of a consistent lithostratigraphical nomenclature across the region (Figure 7.7). Modern recognition and correlation of the Jurassic unconformities were used to create five sequences as follows (Riggs and Blakey, 1993; Blakey, 1994; Blakey, 2008):

Sequence 1 overlies unconformity J-0. The sequence includes the aeolian Wingate Sandstone and coeval fluvial deposits of the Moenave Formation (Dinosaur Canyon Member). Facies patterns suggest a complex fluvial-aeolian recycling between the two units with northwest stream flow and southeast dune migration (Blakey, 1994). Previously thought to mark the Triassic-Jurassic boundary (Pippingos and O'Sullivan, 1978), the J-0 unconformity falls in the early Rhaetian Stage of the late Triassic Period (Lucas *et al.*, 2011).

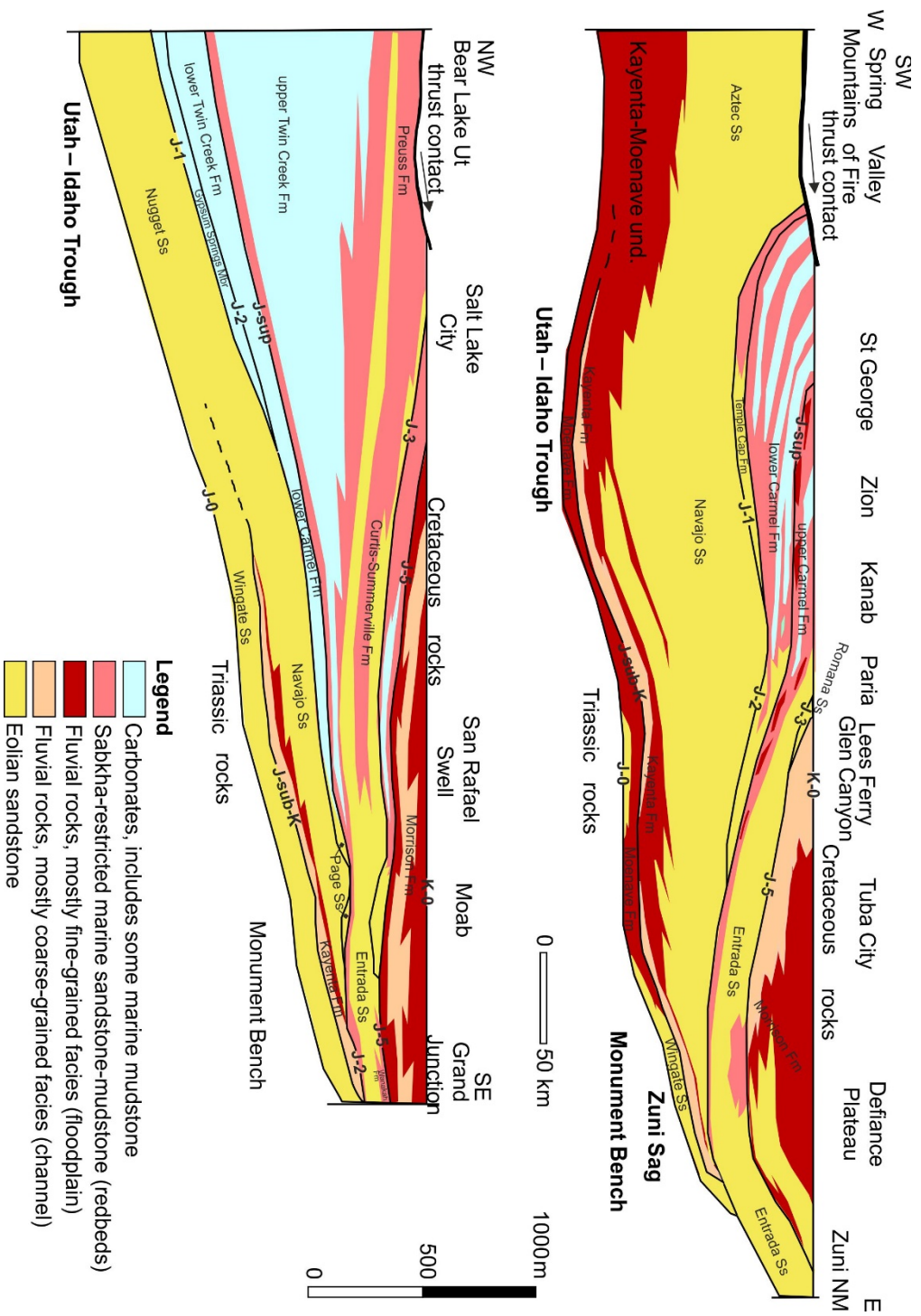


Figure 7.8: Cross-section of the Jurassic rocks of western interior United States showing regional relations of the sequences and unconformities. Note the considerably different geometry between Navajo-Kayenta (drastically thickens to the southwest) and Wingate-Moenave (irregular sheet geometry). Modified after Blakey (2008).

- Sequence 2 overlies unconformity J-sub-k (sub-Kayenta) of Blakey (1994) or the  $J_u$ - $M_{sb}$  unconformity of Marzolf (1994). The sequence is made up of the sandy facies of the Kayenta Formation and coeval Springdale Sandstone Member (Moenave Formation), the silty facies of the Kayenta Formation and coeval parts of the Navajo Sandstone, all overlain by the aeolian facies of the Navajo Sandstone (Figure 7.8) (Blakey, 2008). Previous workers have described the Wingate-Kayenta contact as interfingering and/or gradational, particularly in southwestern Utah, however such claims have been convincingly rejected in support that the J-sub-k contact is indeed a regional unconformity (Lucas and Tanner, 2014 and references therein). The surface marks an obvious break (sharp contact) between aeolian Wingate deposits below and fluvial Kayenta deposits above. Fluvial channels incise the cliff-forming aeolian sandstone forming local relief of up to 10 m (Blakey, 2008). Biostratigraphy and magnetostratigraphy suggest the hiatus to have lasted ~2 million years with the Wingate being no younger than earliest Hettangian and the Kayenta Formation Sinemurian (Figure 7.2B) (Lucas and Tanner, 2014). Without exception, the Navajo is overlain by an erosional unconformity and brings into question whether the preserved thickening is primarily from an increased westerly subsidence rate, uplift and truncation to the east, or a combination of both (Blakey, 2008).
- Sequence 3 overlies unconformity J-1. The sequence consists of red sandy mudstone of sabkha origin and tan cross-bedded sandstone of aeolian origin (Temple Cap Sandstone) (Peterson, 1994). The unit is related to the first mid-Jurassic transgression (Peterson and Pipiringos, 1979). The J-1 unconformity truncates the aeolian Navajo Sandstone with a planar surface at most outcrops, although it is rarely cleanly exposed (Blakey, 1994, 2008).
- Sequence 4 overlies unconformity J-2. The sequence extends throughout the western interior and comprises the aeolian Page Sandstone and coeval marine, sabkha and fluvial Carmel Formation of the San Rafael Group (Pipiringos and O'Sullivan, 1978; Blakey, 1994). The unconformity truncates the underlying Glen Canyon Group at the eastern edge of the Colorado

Plateau (Figure 7.8). The Page and Carmel intertongue throughout a 50-75 km-wide band and along with a series of supersurfaces, provides the basis for detailed regional correlation (Havholm *et al.*, 1993).

- Sequence 5 overlies unconformity J-sup (upper surface of the Page Sandstone). The sequence separates the lower and upper portions of the Carmel Formation and related rocks (Figure 7.8) (Blakey, 2008). Sequence 5 also includes the Entrada Sandstone which overlies the Upper Carmel Formation with a conformable and gradational contact (Blakey, 2008). The aeolian Entrada was deposited inland from a restricted marine seaway and is as widespread as the Navajo erg, however, does not approach Navajo thickness (Peterson, 1994; Blakey, 2008).

#### 7.6.1 Sedimentology of the upper Glen Canyon Group

The upper Glen Canyon Group consists of the fluvial Kayenta Formation and the aeolian Navajo Sandstone bound between the J-sub-k unconformity and J-2 unconformity (Figure 7.8).

##### *Kayenta Formation*

The Kayenta Formation represents the deposits of a fluvial plain that stretched west and southwest from the Uncompahgre Uplift of southwest Colorado (Miall, 1988). It is up to 300 m thick and becomes finer grained, from sand-dominated to silt-dominated to the southwest, toward central Arizona (Marzolf, 1983; Middleton and Blakey, 1983). The upper part of the Kayenta is interbedded with the aeolian Navajo Sandstone and was possibly deposited by flash flooding during more arid times (Middleton and Blakey, 1983; Luttrell, 1986). The characteristics of two types of Kayenta sandstone body on the Colorado Plateau have been reported (Bromley, 1992): 1) ephemeral deposits composed of high-regime horizontally-laminated sandstone, forming multiple-event storeys up to eight metres thick, formed by flash floods; 2) perennial deposits composed of planar cross-beds, deformed parabolic cross-beds and massive sandstone formed under low-regime flow from an active unconfined perennial river flow.

### *Navajo Sandstone*

The Navajo Sandstone is fairly uniform in texture and lithology throughout its distribution on the Colorado Plateau (Middleton and Blakey, 1983). The Navajo is composed mainly of well sorted fine-grained subrounded quartz-rich sand. Large scale features include wedge-planar and tabular-planar cross-bedding, contorted bedding, horizontally bedded sandstones and siltstones, and cherty limestones (Marzolf, 1983). Regional stratigraphical and palaeocurrent analysis suggests transport to the south (Figure 7.9) (Marzolf, 1983; Dickinson and Gehrels, 2003; Loope and Rowe, 2003). The aeolian origin of the Navajo has been questioned (see Visher, 1971; Freeman and Visher, 1975), however, facies relations with other units, small-scale stratification types, along with other data clearly delineate a depositional system consisting of large complex dunes and broad interdunal areas where locally, ponds may have developed in the depressions and freshwater carbonate accumulated (Middleton and Blakey, 1983).

### *Intertonguing Interval*

Intertonguing between the Navajo and Kayenta in southwestern is evident in Utah (Middleton and Blakey, 1983): the Shurtz Sandstone tongue of the Navajo thins from ~105 m near Cedar City, Utah to 19 m within a distance of 13 km towards the south, this occurs in conjunction with an overlying Cedar City tongue of the Kayenta which thickens to the south and thins to the north; in Kanab, Utah, the Lamb Point tongue of the Navajo, thickens to the northeast, eventually merging with the main body of the Navajo, thins to the southwest, grading into the silty facies of the Kayenta and is overlain by the Tenney Canyon tongue of the Kayenta (Figure 7.12).

The intertonguing was documented as a lower sandy fluvial complex grading upwards into an upper fluvial sandstone and mudstone, aeolian sandstone and lacustrine limestone (Blakey, 1994). On investigating an interval along the line between Echo and Vermillion cliffs, a facies change was noted between aeolian deposits to the northeast of the line that rise in section and intertongue with fluvial deposits to the southwest of the line (Blakey, 1994). These stacked zones of facies changes have been labelled the Zuni Trend (sag) (Blakey, 1988; 1994) (Figure 7.9; Figure 7.10A). This zone of facies changes

and associated succession of fluvial, aeolian and lacustrine strata varies laterally from southeast to northwest in the Zuni Sag (Figure 7.9; Figure 7.10A).

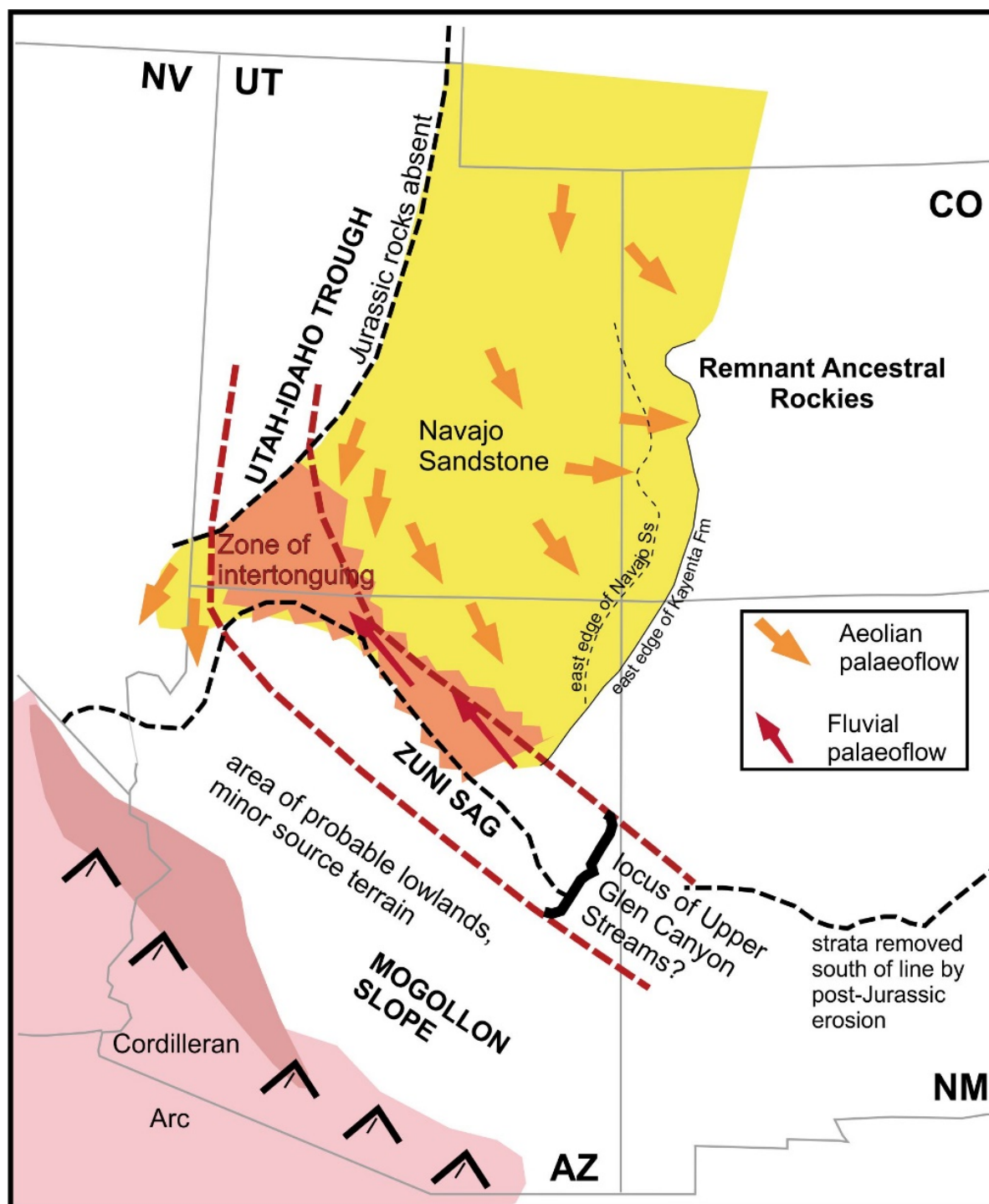


Figure 7.9: Upper Glen Canyon fluvial-aeolian palaeoflow map. Fluvial systems of the Kayenta were sourced to the south and east. Opposed to obliquely opposed palaeocurrents of aeolian and fluvial systems intuitively argues for an exchange of sand between the two systems. Modified after Blakey (2008).

## 7.7 The Navajo Erg

The Navajo sand sea was underway as dunes advanced across broad Kayenta floodplains. The Navajo Sandstone deposits cover much of the Colorado Plateau region and into surrounding regions. The Navajo erg has been labelled one of the great aeolian deposits in all of geologic time (Blakey and Ranney, 2009)

### 7.7.1 Palaeo-extent and Erg Development

The palaeo-extent of the Navajo Sandstone is depicted in the maps of Figure 7.9 and Figure 7.10. The maximum thickness of the Navajo (677 m) occurs in central Utah in parts of the Utah-Idaho Trough (Figure 7.10A) (Blakey *et al.*, 1988). The Kayenta-Navajo package thickens to over 800 m in southwestern Utah (see Fig. 28 in Blakey, 2008). Based on the lack of sedimentological evidence that the Navajo sandstone grades into a non-aeolian facies to the eastward extent of the erg (Figure 7.10A), it is possible that the Navajo erg flowed a considerable distance farther to the east (Blakey *et al.*, 1988). This was depicted in later works (Blakey and Ranney, 2008) where the erg is shown to extend eastward into the San Juan Basin of northwest New Mexico and much of western Arizona (compare Figure 7.10A with 10B).

Aeolian deposition of the Navajo Erg initiated in the northeast (Nugget Sandstone) and expanded southwestward with time (Blakey, 1994). Contraction and expansion occurred in response to the cycles in the fluvial systems to their southwest margins with the general pattern of two steps forward and one step back (Blakey, 1994). The Navajo Erg eventually overwhelmed the entire region by ~190 Ma it had encroached into the adjacent Cordilleran Arc (Figure 7.10B) (Riggs and Blakey, 1993).

### 7.7.2 Sources of the Lower Jurassic Sediments

Based on geological trends, known and inferred Mesozoic tectonic and palaeogeographical patterns south and east of the Colorado Plateau are likely to be the major source terrain for the Glen Canyon Group deposits (chiefly fine-grained quartz for both fluvial and aeolian deposits) (Blakey, 1994). Much of the source of sand was carried from the southeast by northwesterly flowing rivers, eventually

flowing northwards down the axis of the Utah-Idaho Trough (Blakey, 1994). The varied sources included:

#### A] Major orogenic belts

- Exposed and uplifted basement rocks of Gondwanaland composed of crystalline basement rocks.
- Ouachita thrust belt composed of folded, thrust and locally metamorphosed Palaeozoic rocks of a wide-ranging lithology. The broad piedmont from the Ouachitas was underlain by Triassic fluvial deposits, locally quartz-rich, and by Permian redbeds and carbonates, potentially sources for chert and fine-grained sands.
- Sonoman thrust belt.

#### B] Ancestral Rockies (elements below J-2 Unconformity)

- Precambrian crystalline basement rocks.
- Late Palaeozoic to Triassic quartzose sedimentary rocks.

#### C] Unnamed uplift (Pre J-0) (Marzolf, 1991)

- Folded late Palaeozoic rocks.
- Exposed Precambrian crystalline basement.

The above-mentioned sources may have provided a significant percentage of sand to the voluminous Jurassic aeolianites of the western interior US, most of which was probably supplied to the Colorado Plateau and vicinity from areas lying in the southeast (Blakey, 1994). Much of the sand in the Kayenta Formation is attributed to sources in the Ancestral Rockies of Colorado (Luttrell, 1987; 1993).

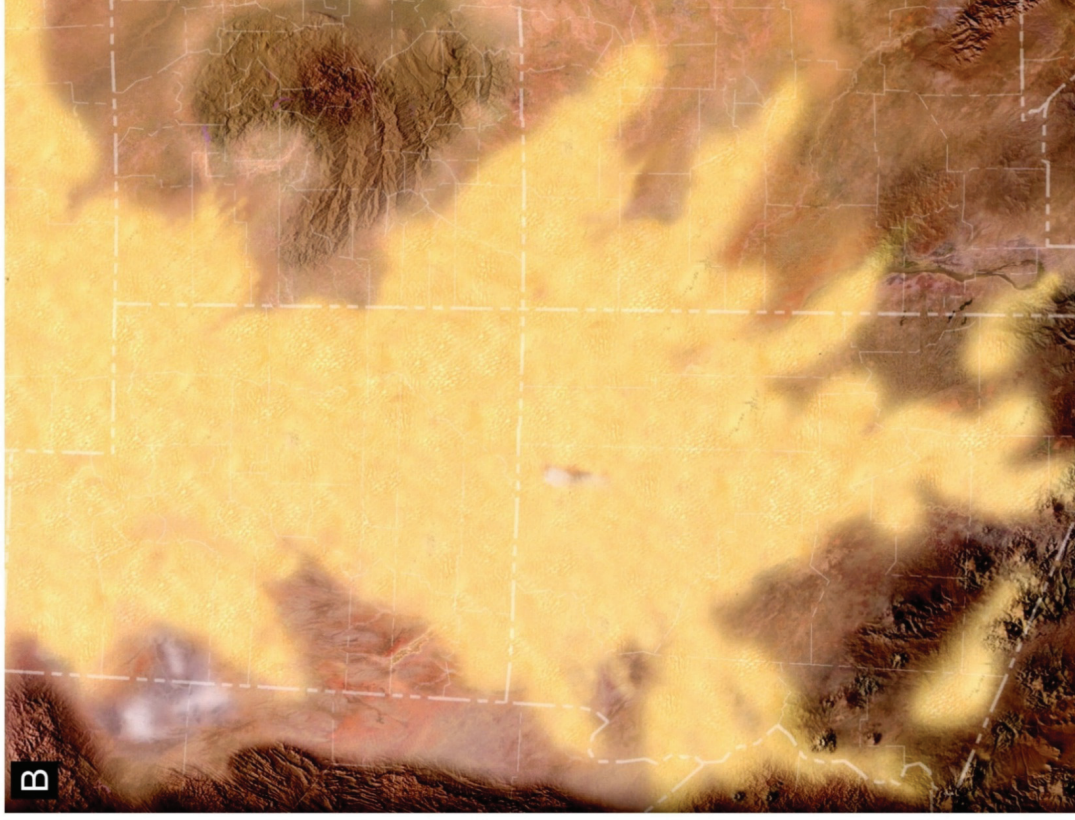
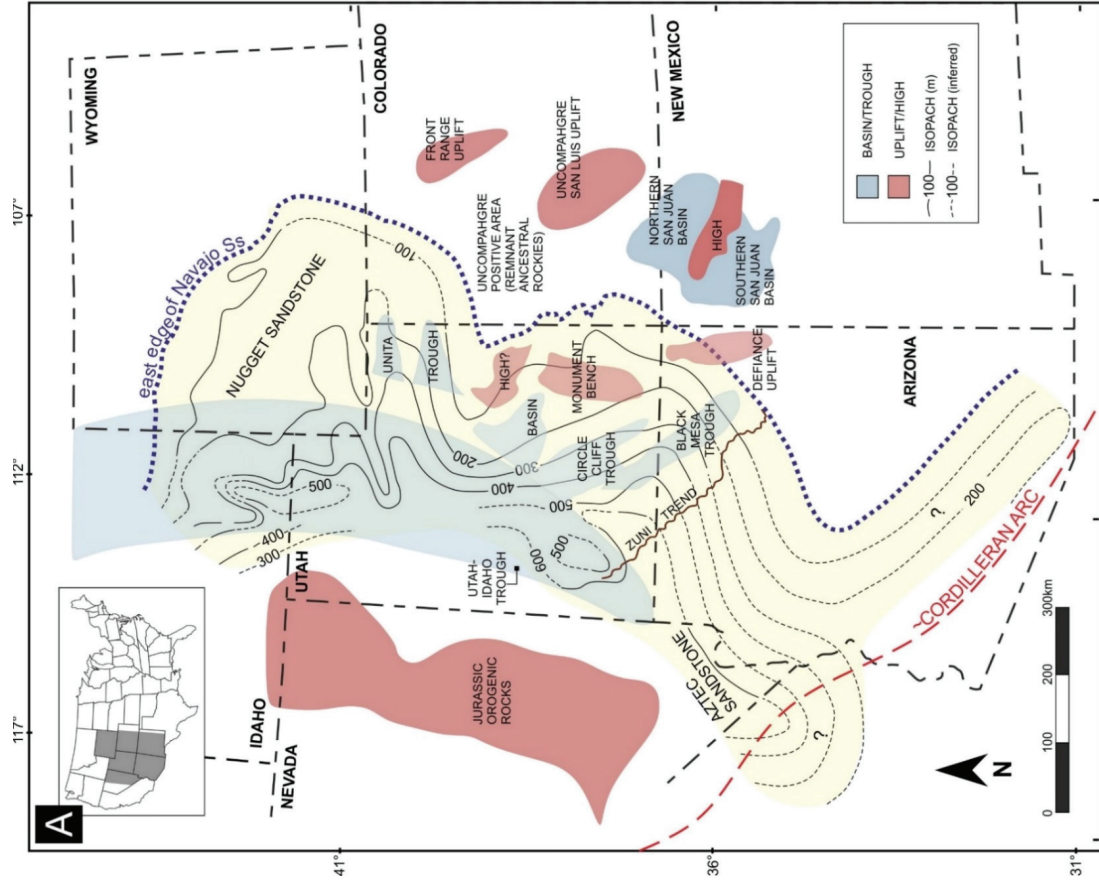


Figure 7.10: (A) Geometry and facies relations of Lower Jurassic aeolian deposit (Navajo, Nugget and Aztec) with superimposed generalized tectonic elements that influenced aeolian sedimentation. Tectonic boundaries are approximate and varied through time. Isopachs show thicknesses of the aeolian interval (dashed isopachs in southwestern Arizona are highly conjectural). Where the Navajo intertongues with the Kayenta Formation along the southern and southwestern margin of the outcrop, the thickness of Navajo is included without the intervening Kayenta Formation. Much of the data on the extent of the Navajo was early interpretation collected from literature dating back to 1927 and was developed as a framework for future research (see table 5 of Blakey et al., 1988). The tectonic elements shown (Blakey, 1988; Blakey et al., 1988; Bjerrum and Dorsey, 1995; Blakey, 2008) were generally well known, however are continually changing with new research, especially with regards to the adjacent Cordilleran arc. (B) The palaeo- extent of the erg was redefined during later work completed by Blakey and Ranney (2008). Note the source areas of the underlying Kayenta to the south and east of the erg. A and B are modified after Blakey et al. (1988) and Blakey and Ranney (2008) respectively.

### 7.7.3 Transport patterns

Evidence for the Lower and Middle Jurassic aeolian sandstones point to transcontinental transport via westward-flowing rivers from eastern and southern North America (Dickinson and Gehrels, 2003; Rahl *et al.*, 2003; Loope *et al.*, 2004). It was hypothesised that winds blowing from the west, northwest, north and northeast deflated sandy alluvial plains to feed the southward-migrating Navajo erg system (Blakey, 1994) (Figure 7.9; Figure 7.11). Sand blowing out of the main Navajo erg to the south was transported back to the northwest by the fluvial systems and eventually deflated from the fluvial systems back into the erg (Figure 7.9; Figure 7.11) (Blakey, 1994). The fluvial sand reaching the hypothetical coastal plains to the west and northwest margin of the continent was recycled by southeasterly wind and coastal currents, returning to the interior to feed the aeolian system (Loope *et al.*, 2004).

Preserved Jurassic fluvial systems of the Dinosaur Canyon Member (Moenave Formation) and the silty facies of the Kayenta have sand contents of approximately 30 – 50% while the sandy facies of the Kayenta has 80 – 90% sand content (Blakey *et al.*, 1988). Such systems were probably active for up to several million years each allowing deflation onto broad, arid alluvial plains and providing a significant source of sand to the Navajo erg (Blakey, 1994).

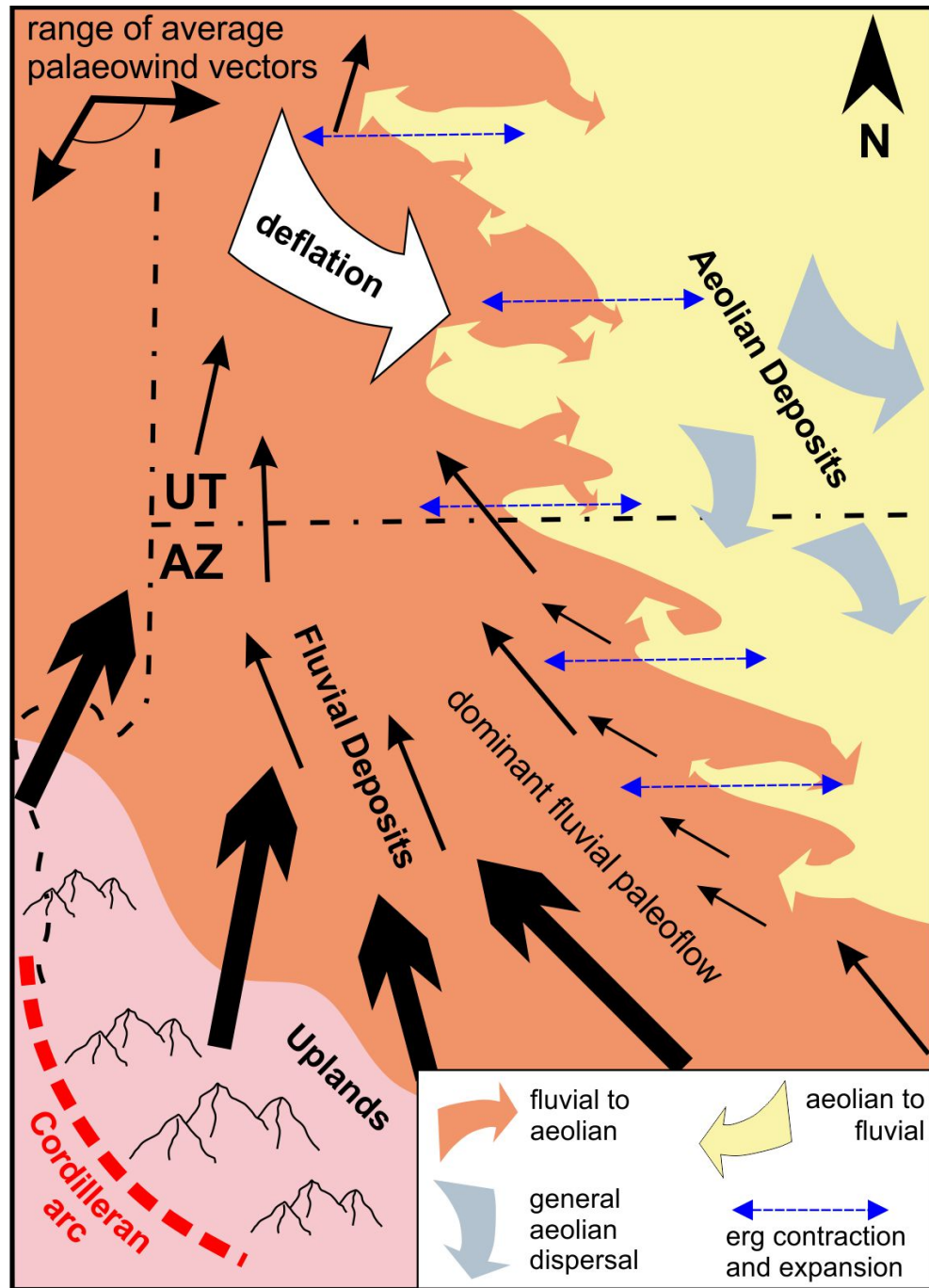


Figure 7.11: Transport patterns for sand circulation and recycling between fluvial and aeolian environments as envisioned by Blakey (1994). Modified after Blakey (1994).

#### 7.7.4 Architecture of the Navajo Erg

Two parts of the Navajo erg are recognised - a lower wet part and an upper dry part (Marzolf; 1983; Blakey, 1994) (Figure 7.12). The lower part is equivalent to and intertongues with fluvial deposits of the Kayenta Formation to the southwest, while the upper part consists of the Navajo Sandstone

overlying the youngest documented horizon of intertonguing (Blakey, 1994). The boundary between the divisions was picked at the top of the highest sequence of Navajo that contains features suggestive of wet depositional conditions, including limestone lenses, horizontal, subaqueous strata and contorted and structureless sandstone (Marzolf, 1983) (Figure 7.12). Blakey (1994) cautioned that the regional correlation within the Navajo Sandstone is yet to be established and presented several possibilities concerning the correlation (Figure 7.13).

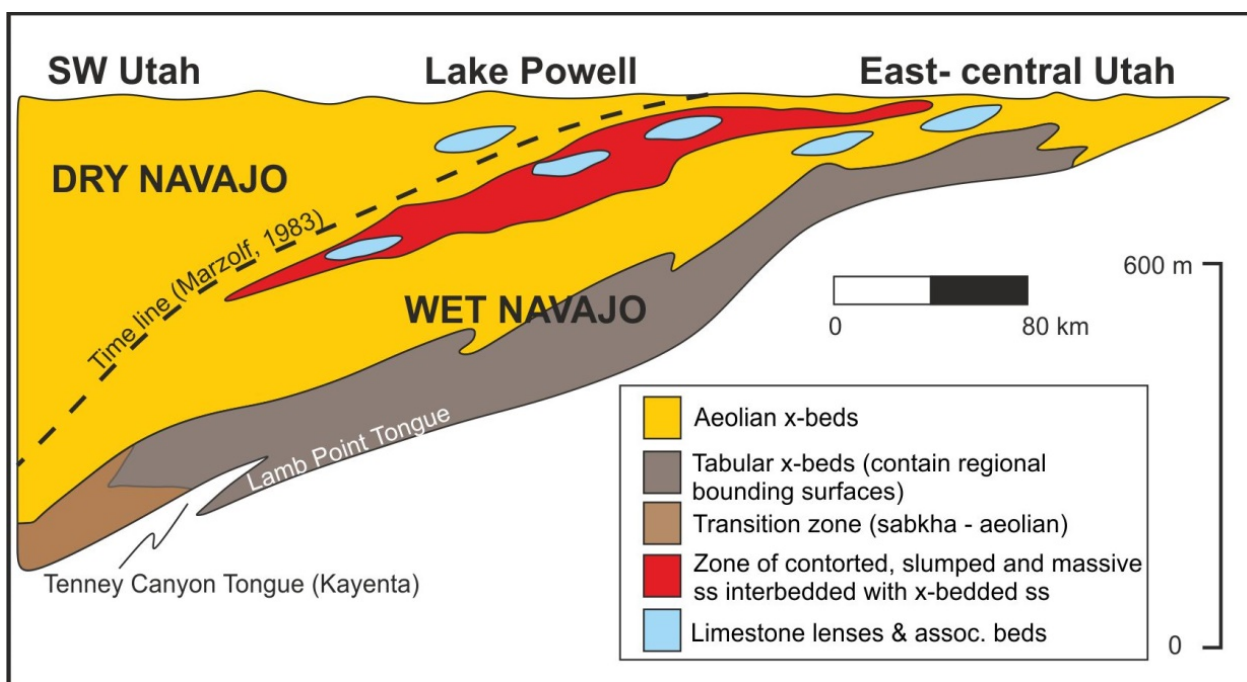


Figure 7.12: General facies in the Navajo erg. The gradational contact between Marzolf's (1983) wet and dry Navajo erg is marked by the dashed time line. Modified after Blakey (1994).

The alignment and distribution of facies in major erg deposits of Permian and Jurassic systems on the Colorado Plateau show remarkable coincidence with modern tectonic elements, indicating that precursors to the present tectonics were coeval with aeolian deposition and controlled erg geometry and facies distribution (Blakey, 1988). Areas with greater sand accumulation would be expected to be dominated by facies typical of erg centres and areas of lesser sand accumulation would be expected to be dominated by facies typical of erg margin and aeolian sand sheets (Blakey, 1988) (Figure 7.14).

In a study conducted on erg responses to basin tectonics (Blakey, 1988), the centre of the Navajo was roughly defined (Figure 7.14). This study was limited to the southern half of the Colorado Plateau and involved aeolian sequences from the Permian to Jurassic using data of erg thickness to average out contours. This has been the only attempt to define the relationship between the erg centre with its margins of the Navajo Sandstone (Figure 7.14).

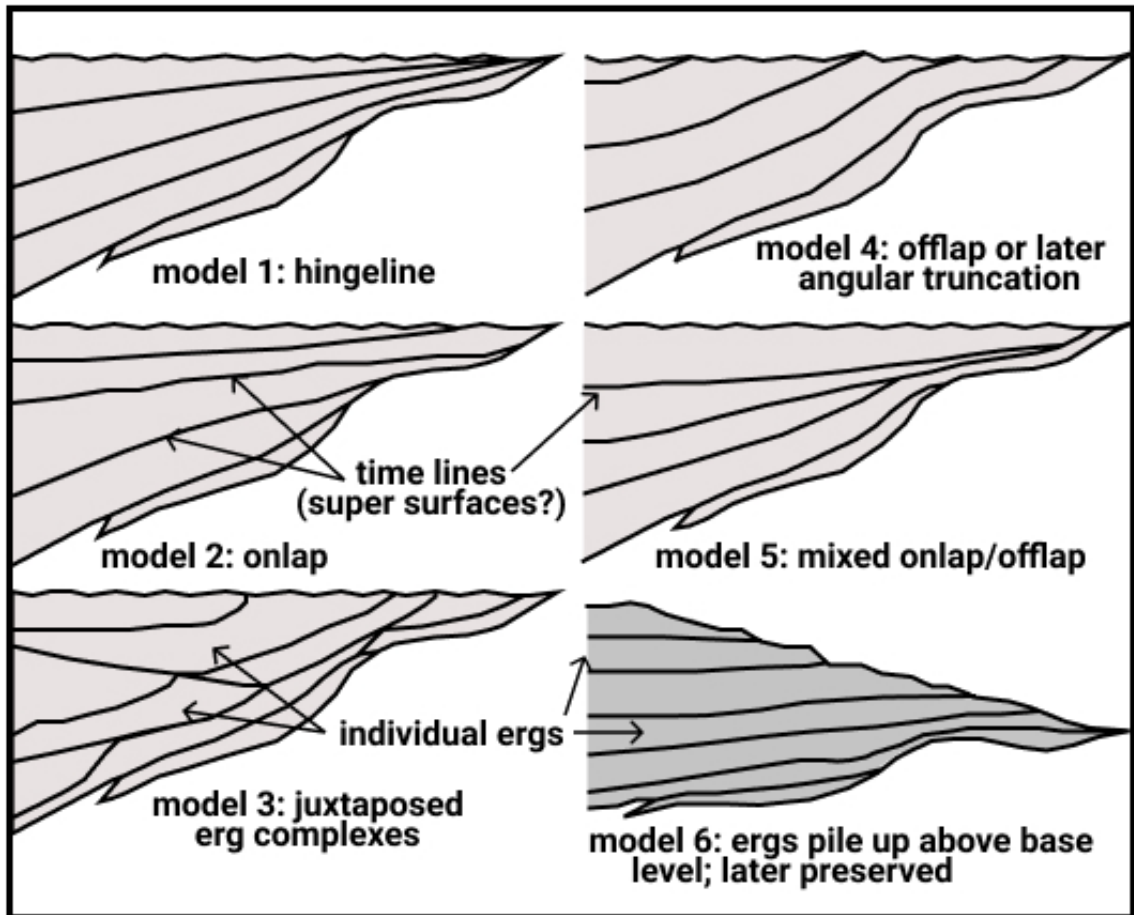


Figure 7.13: Cross-sections showing six hypothetical models of internal architecture of Navajo Sandstone and inferred timelines for each. Note that Figure 7.12 is compatible with any one of these schematics.

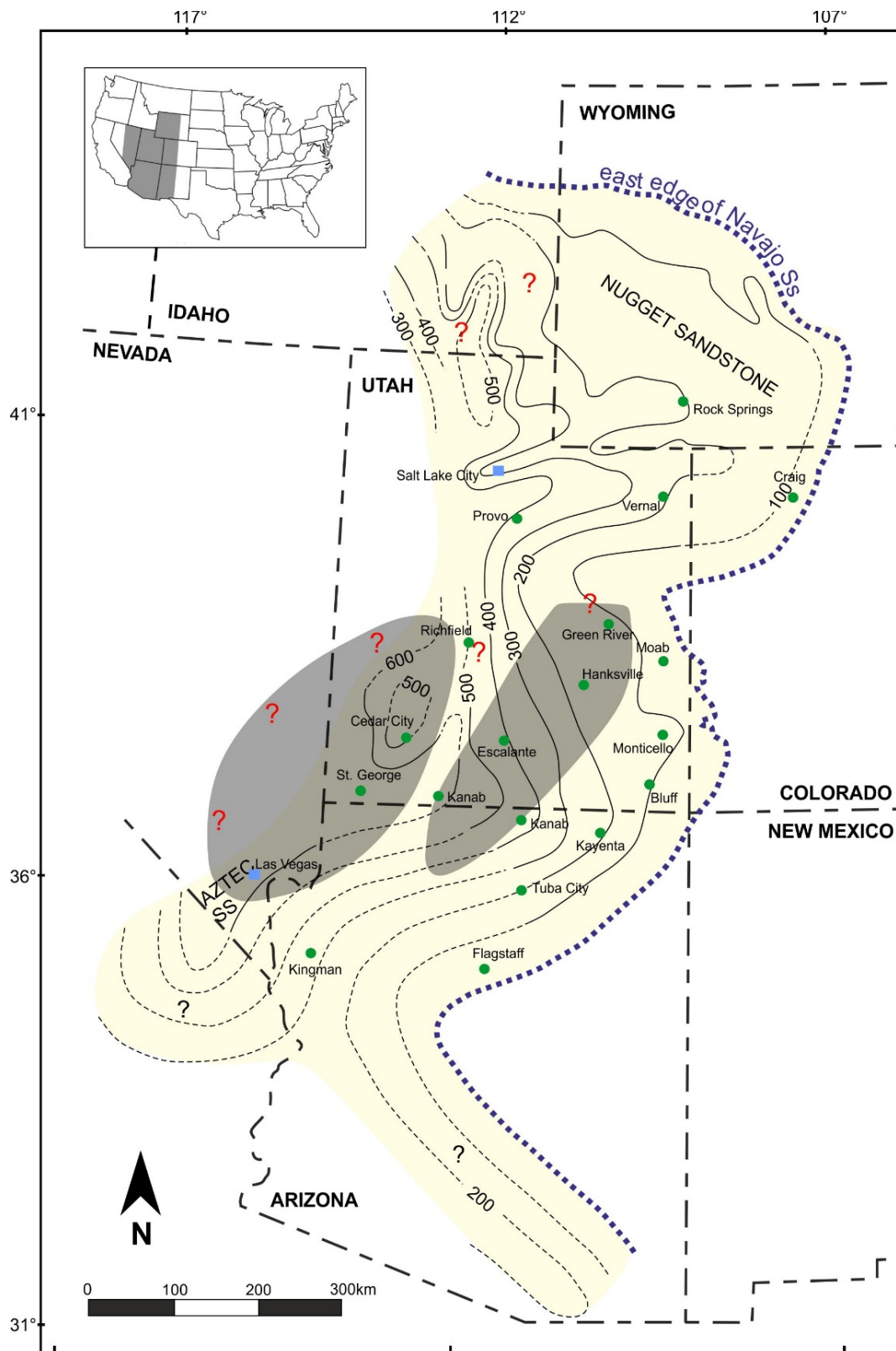


Figure 7.14: Palaeo-extent of the Navajo erg and thickness with the superimposed erg centre (shadowed) as depicted by Blakey (1988). Red question marks are placed by the author due to either areas falling out of Blakey's study area (e.g. the western margin and the northern extent of the erg), or where the two forms do not meet, and thicknesses are constant.

## 7.8 Summary: Controls on deposition

Unless otherwise stated, much of the following interpretation was taken from Blakey (1994) and Blakey (2008). The Upper Glen Canyon Group or 2 sequence was deposited during a low eustatic interval. Moderate subsidence rates across much of the western interior US may have created a topographic basin (Figure 7.10A), but without direct connection to the sea. The fluvial deposits of the coeval Kayenta drained into the basin (the start of the Utah-Idaho Trough) and deflated by winds from the northwest to feed the Navajo ergs (Figure 7.11). The topographic low coupled with low sea-level isolated the region from all other depositional systems, allowing the Navajo system to fill the basin over millions of years. Excessive loss of sediment resulted from a high water-table as the Kayenta River seeped into the porous sands. Eisenberg (2003) documents this high water-table with widespread fresh water carbonates and mass flow sand deposits. Based on zircon ages within the sandstones, a dominantly cratonic North American and Pangaeian source for the Navajo erg system is inferred (Dickinson and Gehrels, 2003).

### 7.8.1 Tectonics

The Triassic and Jurassic rocks of the western interior US were deposited on a relatively stable shelf that sloped to the west in Triassic time and to the northwest in Jurassic time (Pipiringos and O'Sullivan, 1978). This first-order tectonic grain of North America is reflected in the river systems of the time; rivers flowed west and northwest from the Appalachian continental divide towards the palaeo-Pacific Ocean (Blakey, 2008). Back-arc basin development, dynamic subsidence, and possibly early foreland basin subsidence are apparent across much of the Colorado Plateau during the late Triassic and Jurassic times (Ingersoll, 2008).

### 7.8.2 Climate

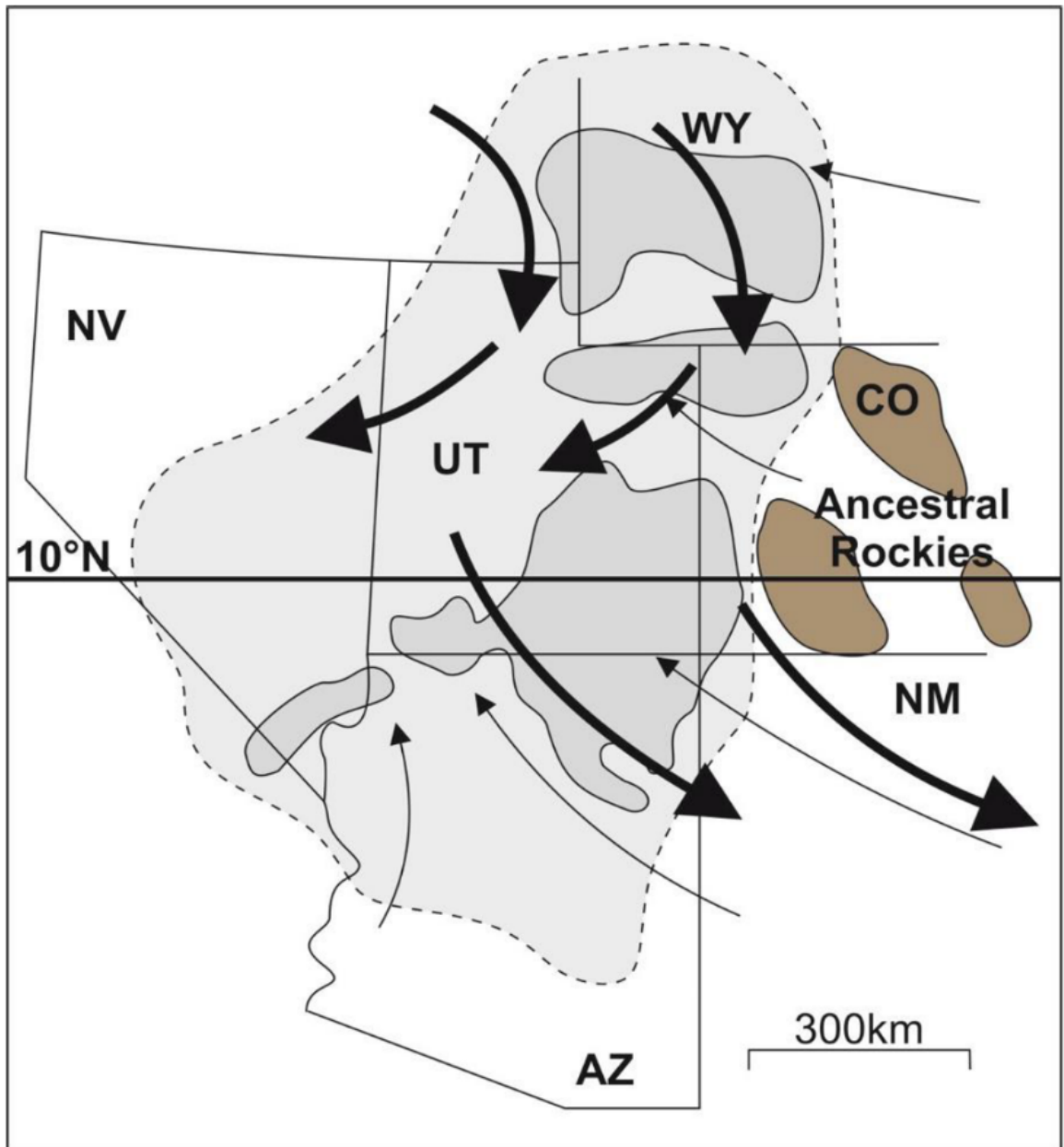
The Navajo erg was deposited in a generally arid environment, however, evidence for wetter conditions occur towards its southern and eastern margins (Figure 7.15) (Loope *et al.*, 2004a). Based on palaeowind directions it was initially thought that the palaeolatitude of the Four Corners (Utah-Colorado-New Mexico-Arizona) was  $\sim 18^\circ$  N and blew as mid-latitude westerlies (Runcorn, 1963).

Following palaeomagnetic studies of the Colorado Plateau, a new interpretation placed the Four Corners farther south at  $\sim 9^\circ$  N placing the affecting winds rather as tropical westerlies (Figure 7.15) (Loope *et al.*, 2004b). Today, such winds are developed only in monsoonal systems and depend on the development of a strong low-pressure zone across the equator, sustaining them for only 3 months of the year (Loope *et al.*, 2004a).

It is demonstrated that heavy monsoonal rains occurred at least on the southern side of the Navajo erg (Loope *et al.*, 2001). During the northern hemisphere summer, the ITCZ would have migrated northward to cover the Colorado Plateau and, with moist air available, the convergence would have generated enough lift needed for precipitation (Loope *et al.*, 2004b). Long-standing, northwest flowing, long distance Kayenta rivers provided much of the water to the southern margin (Blakey, 1994, 2008). The Ancestral Rockies along with westward flowing rivers from eastern North America may have also brought significant amounts of water to the Navajo erg on its eastern margin (Dickinson and Gehrels, 2003; Loope *et al.*, 2004a).

### 7.8.3 Eustatic Controls

Several marine marker beds penetrate continental sediments on the Colorado Plateau between Pennsylvanian and Jurassic times (Figure 7.16) (Blakey, 2008). However, the lack of marine incursion over 70 million years during Sloss's Absaroka 3 interval (covering the Glen Canyon Group) allowed over 400 m of continental strata to be preserved (Blakey, 2008). The incredible thickness of the Navajo Sandstone in the Utah-Idaho Trough suggests local-regional tectonic and sedimentologic conditions overrode the global eustatic signal (Blakey, 2008).



- ▶ fluvial sand delivery system
- ▶ paleo-wind direction
- depositional limit
- outcrop limit

Figure 7.15: The southernmost winds are tropical westerlies as interpreted by Loope et al. (2004b). Shaded regions demarcate the areas where evidence for wetter conditions are prevalent. Note the palaeolatitude of 10° N. Modified after Loope et al. (2004a).

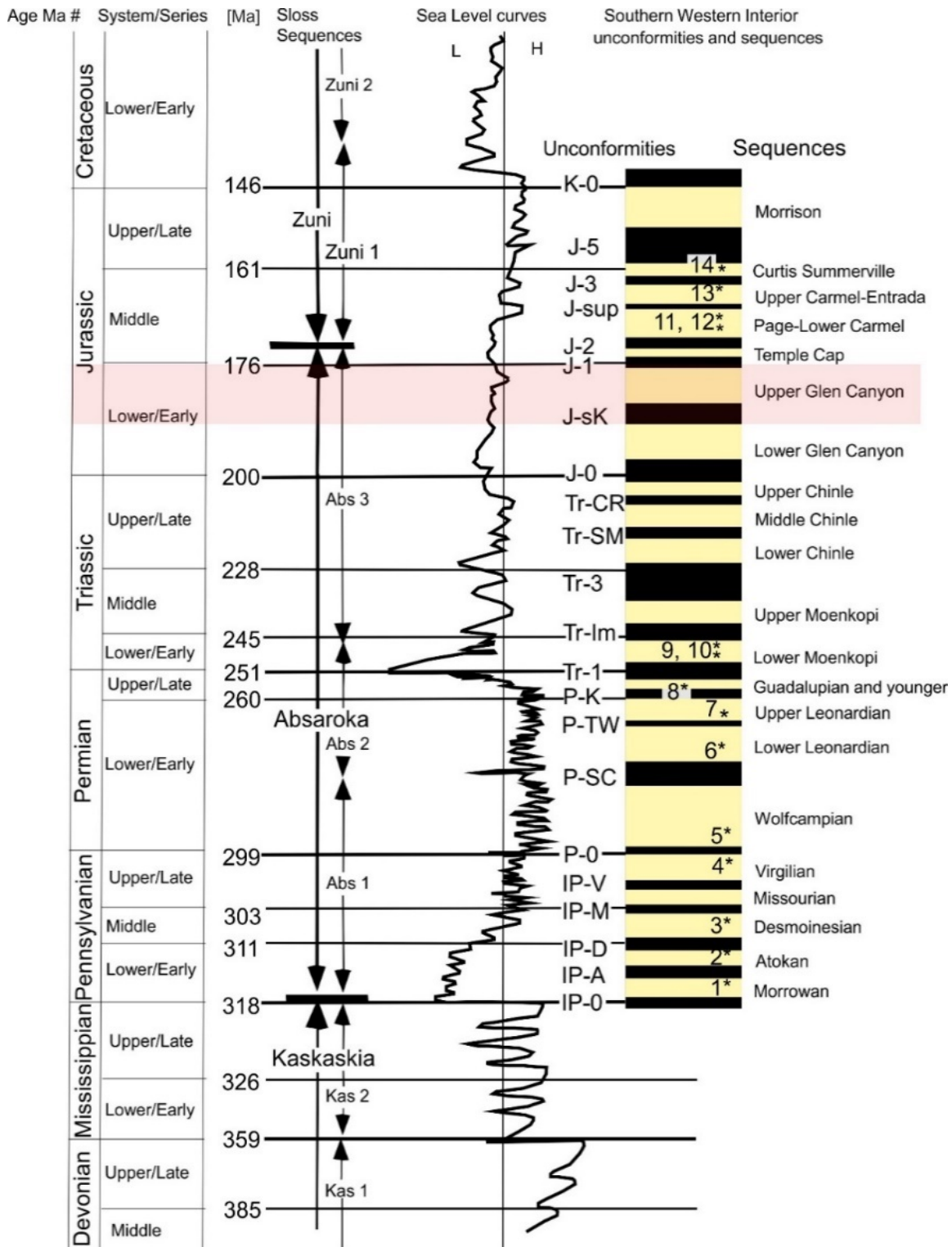


Figure 7.16: The chart compares sea-level curves (Ross and Ross, 1988; Haq, 2009), Sloss sequences (Sloss, 1988) and the stratigraphical sequences and unconformities of Blakey (2008). The Upper Glen Canyon, representing the Kayenta Formation and Navajo Sandstone, is highlighted in red. Asterisks signify high-water periods on the Colorado Plateau as marked by marine sequences that penetrated the dominantly continental section (for further details see Figure 37 of Blakey, 2008). Modified after Blakey (2008).

## 8 Study Sites

This research considers that accumulation in the rock record may occur because of several parameters that can be broadly associated with types of dune-fields (e.g. wet, dry and stabilizing aeolian systems) (Kocurek and Havholm, 1993; Kocurek, 1999, Mountney, 2012). As such, an investigation into key site selection was conducted in order to capture variations during system evolution. Planning was based on two field seasons, the first of which was designed to assess outcrops regionally for sedimentary logging and initial observations (Table 8.1; Figure 8.1). In order to cover the best possible regional transect, the study utilised the detailed literature review (chapter 0) in conjunction with remote desktop studies to visit eleven sites across southwestern USA where the Navajo was excellently exposed (Figure 8.1). The sites were chosen based on ability to successfully log outcrop faces with the best possible vertical continuity and, where possible, include the contacts with the underlying J-sub-k contact (Kayenta – Navajo), or overlying J-1 / J2 unconformity (Navajo – Temple Cap / Carmel). Furthermore, investigations of outcrops representing the deposits of large longitudinal bedforms in a central erg setting was vital for comparison with the linear outcrops of the contemporary Wahiba Sand Sea of Oman.

Following analysis of data collected during the initial field season, three key sites (Table 8.1; Figure 8.1) namely Sevenmile Canyon (site 1), Hite (site 2), and Johnsons Canyon (site 3) were selected for their definitive ties to stratigraphy (confined by well-known underlying and / or overlying Formations), and their position within the tectonic basin (Figure 8.2). The second field season was devised to take advantage of their excellent exposures and accessibility for photogrammetric recording of large-scale architectural elements in a three-dimensional sense. The following section places each study site into the context of the basin and provides a summary of their geological setting. A more detailed review of basin evolution in the context of the Navajo erg is provided in the Chapter 0.

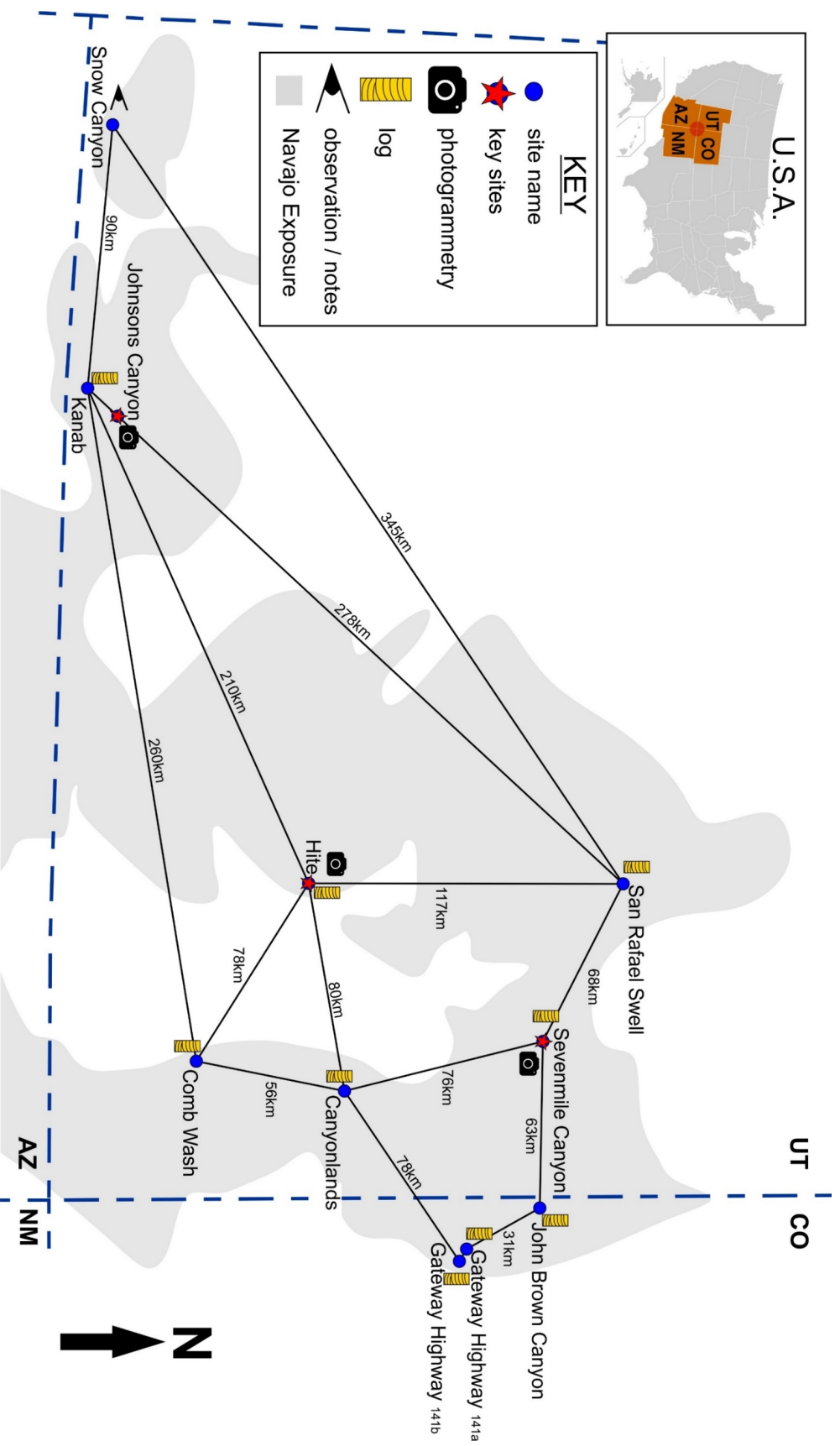


Figure 8.1: Study sites of the Navajo Sandstone. Inset shows location within the 'four corner' States of southwestern USA – Utah (UT), Colorado (CO), Arizona (AZ), and New Mexico (NM). Following key observations, three key sites were selected including Sevenmile Canyon, Hite, and Johnsons Canyon for further large-scale examination by remote sensing (reported in chapter 10). A summary of site observations is provided in Table 8.1. Sedimentary logs are included in Appendix A2.

Table 8.1: Outcrops and key observations of the initial field season. Highlighted sites were chosen for further study and are examined in chapter 10. See Figure 8.1 for locations.

Outcrop Name	Log (m)	Log Contact	Outcrop type, limitations and / or opportunities	Key characteristics of deposits / Additional information	Ref(s)
John Brown Canyon	23	none	Vertically continuous, 2D, highly vegetated limits continuous observations.	Erg margin, thick sand sheet deposits and deformed aeolian deposits (SSD).	Bromley, 1992
Gateway H'way 141a	11	J-sub-K	Vertically continuous, 2D, highway road cutting limits horizontal extent and observations.	Erg margin, aeolian-fluvial interactions. Highly deformed aeolian deposits (SSD).	Bromley, 1992
Gateway H'way 141b	3	J-sub-K	Small, scattered outcrops at Kayenta contact, mostly 2D, vertically continuous at highway road cutting. Limited horizontal extent.	Erg margin, aeolian-fluvial interactions. Highly deformed aeolian deposits (SSD).	Bromley, 1992
Sevenmile Canyon	73	J-sub-K J-2	Vertically and laterally continuous, 3D. Well-exposed and traversable. UAV photogrammetry possible.	Basal deposits erg margin setting (fluvial-aeolian interactions) evolving into dry erg centre in upper deposits. Extensive super surfaces present.	Sansom (1992; 2018)
Canyonlands	31	J-sub-k	Vertically continuous 3D. Sections covered by vegetation obstructs horizontal continuity.	Small aeolian sets at base punctuated by fluvial tongue (very high energy). Grades into dry erg central conditions. Extensive super surfaces present.	Loope <i>et al.</i> (2004)
Comb Wash	67	J-sub-k	Monocline dipping ~eastwards, 3D, highly weather sets in parts (structures absent). Inside National Park.	Basal deposits erg margin setting (fluvial-aeolian interactions) evolving into dry erg centre punctuated by high energy fluvial. Extensive super surfaces present.	Parrish <i>et al.</i> (2019)
San Rafael Swell	28	J-sub-k	Monocline dipping ~eastwards. Discontinuous sections logged.	Small aeolian sets at base punctuated by fluvial tongue. Grades into dry erg conditions. Super surfaces present.	Loope <i>et al.</i> (2004)
Hite	71	J-sub-K	Vertically and laterally continuous, 3D. Well-exposed and traversable in sections. UAV photogrammetry possible.	Very large sets, wet interdunes, large transverse dunes. Extensive (?)super surfaces present.	Marzolf, 1983
Johnsons Canyon	N/A	J-2	Vertically and laterally continuous, 3D, road cut. Roadside photogrammetry possible.	Dry erg centre, large sets, possible longitudinal /oblique dunes.	Rubin & Carter ('06)
Kanab	78	J-sub-k	Excellent exposure in 3D sections approx. along US H'way 89. Continuity punctuated.	Erg margin aeolian-fluvial interactions. Punctuated by ephemeral fluvial tongues	Hassan <i>et al.</i> (2018)
Snow Canyon	N/A	J-sub K	In sections ~ northwards. Vertical joints. State Park restricts close observations.	Very large dunes. Evolution from sabkha to dry central conditions.	Sansom (1992)

## 8.1 Geological Setting

Permian to Jurassic aeolian deposits of southwestern USA represent some of the largest accumulations in the geological record (Figure 7.2), the preservation of which required consistent and large-scale accommodation generation (Pipiringos and O'Sullivan, 1978; Blakey *et al.*, 1988; Rodríguez-López *et al.* 2014). The Late Triassic to early Jurassic breakup of Pangea transformed the south and western margin of North America from an island-arc setting to an Andean-type convergent margin, leading to the formation of a northwest -to- southeast aligned retro-arc foreland basin in southwestern USA called the Utah-Idaho Trough (Dickinson, 1976) (Figure 8.2).

Loading of the continental crust beneath the Cordilleran belt dates to the early Jurassic Period, with aeolian and non-aeolian sediments preserved at maximum accommodation generation (Hassan *et al.*, 2018). The basin fill is, as expected, thickest in the west with individual wedge-shaped successions separated by regional unconformities coeval with loading in the western Cordillera (Figure 8.2) (Allen *et al.*, 2000; Blakey, 2008). The Navajo Sandstone of the upper Glen Canyon Group is consistently truncated by the J-2 unconformity and therefore is difficult to say if the thickness increase to the west is solely a result of increased subsidence, uplift, and truncation towards the east, or a combination thereof (Figure 7.2; Figure 8.2) (Blakey, 1994).

The best-preserved erg margin conditions occur in southeastern Utah within the Lower Navajo succession (study site 1 and surrounds; Figure 8.2). Conditions here show a sequence of fluvial-aeolian interactions informally known as the Navajo – Kayenta transition zone (Luttrell, 1987; Sansom, 1992). This was followed by more arid times initiating erg expansion where aeolian conditions dominated and were periodically interrupted by relative water-table rise as evidenced by at least three super bounding surfaces in the region (Sansom, 1992; Blakey, 1994). Located close to the eastern edge of the erg, Site 1 (Sevenmile Canyon) is dominated by aeolian stratigraphy of about 54 m thick.

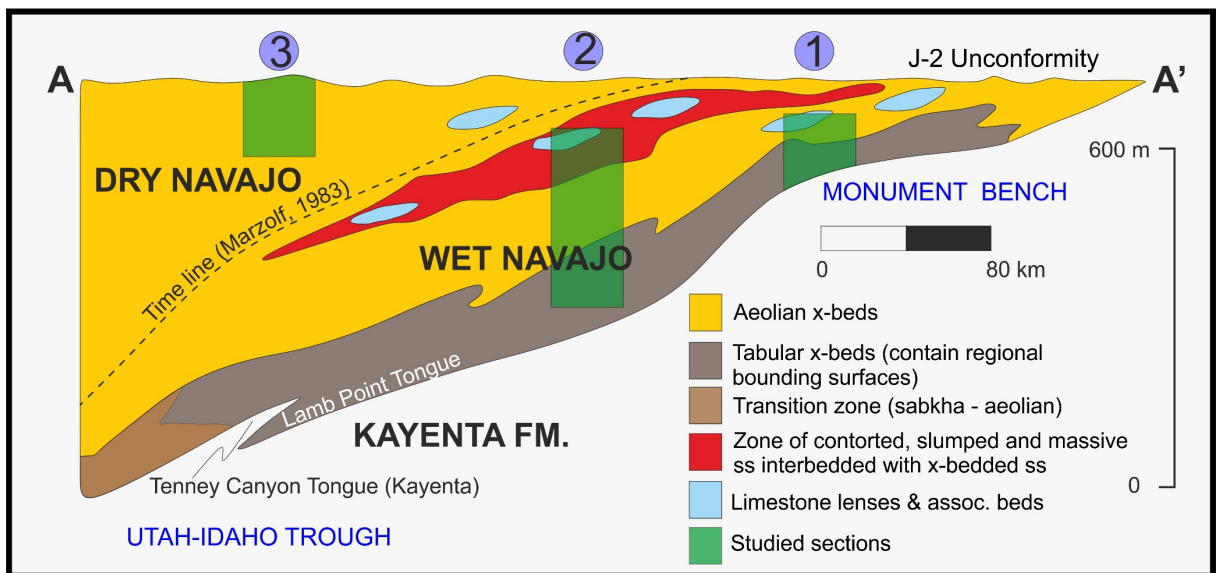
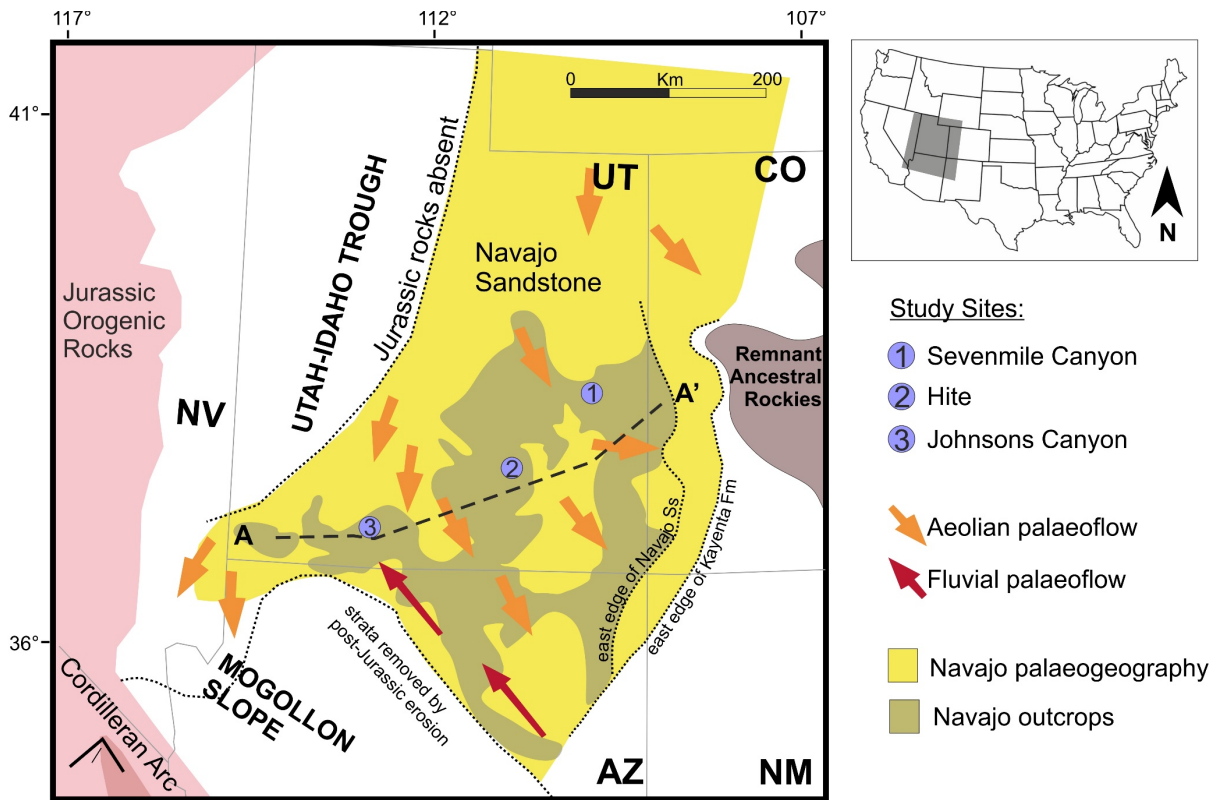


Figure 8.2: Palaeogeographic map and cross-section of the known extent of Navajo Erg. The cross section highlights the westward thickening in the Utah-Idaho trough, interpreted as a retro-arc foreland basin system. Three study sites of the Navajo Sandstone (1-3) were analysed in a northeast to southwest transect from marginal to central basin. The positions of the studied sections on the schematic cross-section are approximate and largely for reference purposes. Palaeogeographic reconstruction modified after Blakey, 2008. Cross-section modified after Blakey, 1994.

The pattern of Navajo erg deposition expanded south-westwards into the Utah-Idaho trough. Two parts to Navajo Sandstone deposition are recognised in the literature with the boundary picked between units intertonguing with fluvial deposits of the Kayenta Formation (Blakey, 1994), or at the highest gradational successions of Navajo that suggests wet depositional conditions such as limestone lenses, horizontal subaqueous strata, and contorted or structureless sandstone (Figure 8.2) (Marzolf, 1983). These wet conditions are typically identified within Navajo deposits in southeastern to south-central Utah and are sparsely addressed in the literature (Parrish *et al.*, 2017). Site 2 (Hite) investigates these features and Navajo deposition in a medial to central setting of erg expansion, dominated by large-scale aeolian sets and separated by and / or gradational with intermittent wet conditions.

The Navajo erg expanded and contracted in response to the cycles in the fluvial system at the southwest margins (intertonguing units described in section 10.4.1). The pattern of expansion and contraction was one of two steps forward and one step backwards, until eventually the Navajo erg overwhelmed the entire region and encroached into the adjacent Cordilleran Arc (Figure 8.2) (Blakey, 1996, 2008). Study site 3 (Johnsons Canyon) captures the uppermost 50 m of deposition well above the final intertonguing fluvial unit of the Kayenta Formation. The interval therefore represents Navajo deposition at its maximum encroachment in the dry central erg (Blakey, 1996).

## 8.2 Summary

Aeolian systems can be viewed as a spectrum in which end members are wet, dry or stabilised, each being distinct because the dynamic processes that give rise to the accumulations and their capping super surfaces vary in each system (Kocurek and Havholm, 1993). At the basin scale, the depositional evolution of the Navajo Sandstone occurred within a set of boundary conditions that include climatic forcing of fluvial, aeolian and eustatic cycles within an active tectonic basin (chapter 0) (Blakey, 1994; Verlander, 1995; Allen, 2000; Blakey, 2008). Because of the basinal setting and sediment flux into the basin, evolution of the geomorphic surface has been accompanied by the generation of a stratigraphical record. This record shows that aeolian deposition in the Navajo evolved from one in which wet conditions dominated, to one where more arid conditions dominated as the erg expanded (Figure 8.2) (Blakey, 1994). This study will make use of three key sites representing snapshots of erg evolution and provides insights into the mechanisms that promoted preservation.



## 9 Lithofacies Analysis of Navajo Sandstone

Facies analysis is a well-established means for the interpretation of preserved sedimentary deposits by describing sediments in terms of their lithology, sedimentary textures and structures (e.g. Clemmensen and Abrahamsen, 1983; Miall, 1985; Mountney, 2006a). The sedimentology of the Navajo Sandstone has been well established and described by many authors in the past and the variations in range and relative abundance of facies and facies associations have been well observed both spatially and temporally as the erg expanded, contracted and evolved. Published literature has typically focused on particular facies types, for example cyclic crossbedding (Hunter and Rubin, 1983), stromatolites (Eisenberg, 2003), ichnofacies (Ekdale *et al.*, 2007), soft sediment deformation (Bryant *et al.*, 2013, 2016), and carbonate beds (Dorney *et al.*, 2017). Alternatively, individual sites have been studied capturing snapshots of the temporally evolving system, for example the salt anticline region of southwestern Colorado (Bromley, 1992), the marginal erg setting of Moab, Utah (Sansom, 1992), the central erg deposits of Zion National Park, Utah (Loope *et al.*, 2012), and the interfingering deposits of with the fluvial Kayenta Formation in Kanab, Utah (Hassan *et al.*, 2018).

Intense debate in the sedimentological community was sparked following a reinterpretation of an aeolian origin of the Jurassic Navajo Sandstone in 1975 (Freeman and Visher, 1975). This led to detailed investigations, provoking widespread interest in the depositional facies and architectures of aeolian accumulations. In a pioneering study, Hunter (1977) documented the lamination types and associations that could have only been formed by aeolian bedform and this indisputably reassured the aeolian origin of the Navajo. The most common and characteristic feature of the Navajo Sandstone is the occurrence of huge, sweeping sets of cross-bedding and their internal laminations that documents the movements of dunes in an exceedingly complex aeolian system.

The following lithofacies analysis initially focusses on the stratification types typical of aeolian dunes and their stratification types. This includes wind-ripple stratification (Wr), grainflow stratification (Gfw), grainfall stratification (Gfl) and adhesion stratification (Adh). Following this, facies relevant to

the three key outcrops of chapter 8 is tabulated utilising observations made by both conventional means (sedimentary logging) and non-conventional means (virtual outcrop models). The two summaries will provide context to the outcrop analyses in chapter 10.

## 9.1 Aeolian Dune Stratification Types

The following section describes and interprets the individual aeolian strata typical of Navajo bedforms. Although the title implies these facies are restricted to aeolian dunes, wind-ripple and adhesion strata are abundant in the aeolian systems and are presented in context in section 9.2.

### 9.1.1 Wind-ripples facies (Wr)

*Description (Figure 9.1):* The deposits are characterised by reddish brown, orange to pale-yellow millimetre-scale laminated quartz arenite with grain sizes ranges from very fine to medium sand. The facies are strongly characterised by a bimodal grainsize separation between laminae such that packages of the wind-ripple facies reveal pinstripe laminations (*sensu* Fryberger and Schenk, 1981). Internally the laminae exhibit reverse grading, typically evident in weathering patterns due to the bimodality of grain sizes. The facies may occur on its own in centimetre to metre thick horizontal packages. It is also typically found coupled, interfingering or in a transitional relationship with grainflow laminae with dips up to 25° (Figure 9.2).

*Interpretation:* In a flow configuration where tractional transport dominates and becomes increasingly prominent with decreasing incidence angles, wind ripples form (Eastwood, 2012). In nature, aeolian ripples are easily distinguished by coarse-grained crests, fine-grained troughs, and thin veneers of coarse grains on the stoss slopes. Migration during net deposition results in characteristic inversely graded stratigraphy that distinguishes aeolian sandstones from those of a fluvial origin (Anderson and Bunas, 1993). The grain segregation and interlaminations of very fine and medium sand results in the deposits' pinstriping effect. Aeolian ripples form widespread deposits in sand sheets, in dry interdunes areas, at the dune-plinth area, and in low to moderately inclined dune and draa slopes (Mountney,

2006a). Where ripples occur on dune lee slopes, they typically have crests oriented parallel to the dip direction of the lee face as a function of along slope transport and gravity (Howard, 1977).

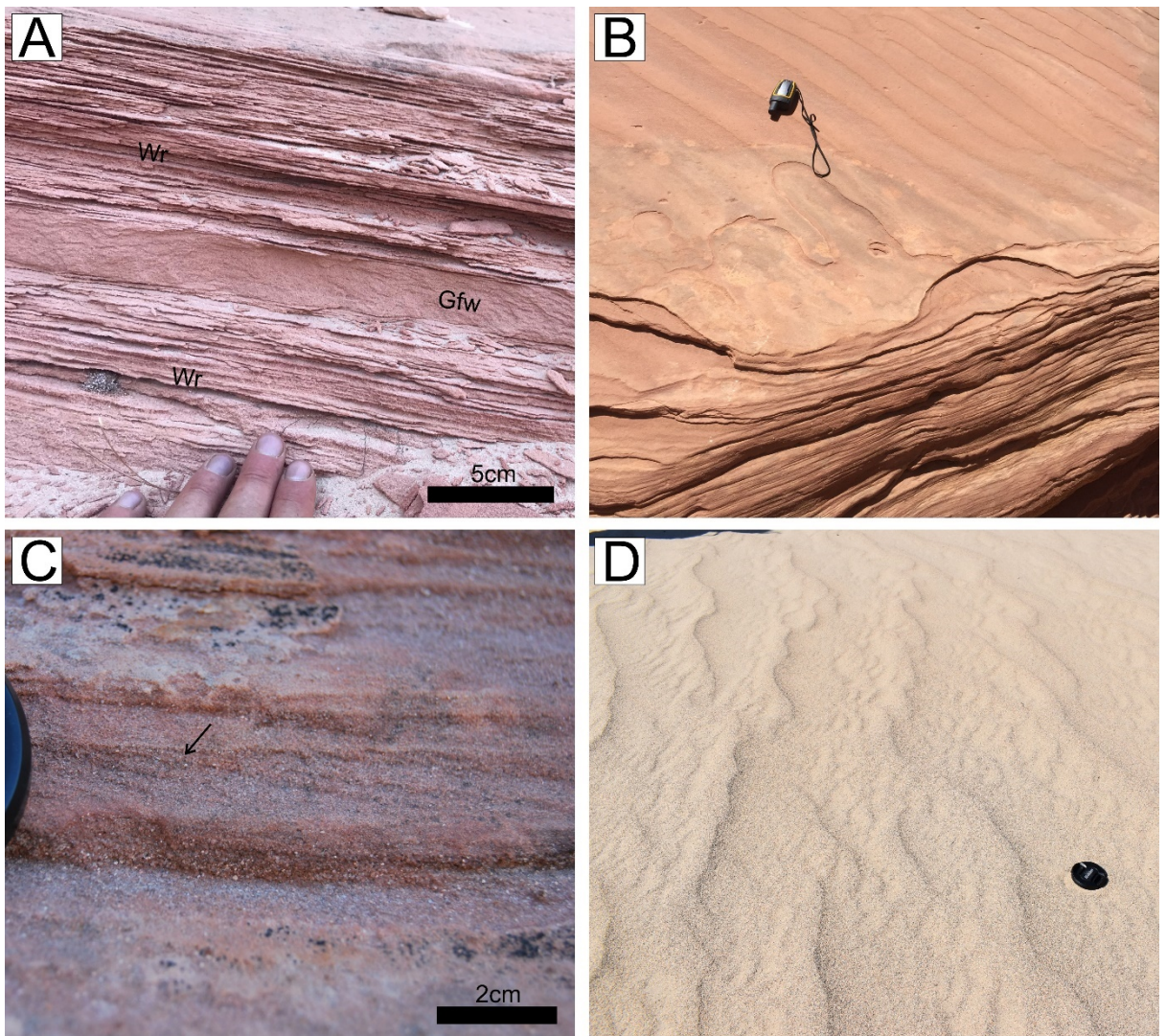


*Figure 9.1: Wind-ripple facies A) Millimetre-scale wind-ripple laminated sand. The weathering of the outcrop accentuates the characteristic bimodal framework of the facies. A single massive grainflow laminae (Gfw) separates the pinstripe lamination. Navajo Sandstone at Mt Carmel Junction, Utah. B) The outcrop wall shows mm-scale crinkly pinstripe laminations. The weathered surface shows the preserved wind-ripples in plan-view. GPS unit in is 15 cm in length. Navajo Sandstone at Goblins Valley State Park, Utah. C) Preserved ripple-foreset cross-laminae (arrow). Truncation of the rippleform laminae is indicative of subcritical climb. Note the inverse-grading. Navajo Sandstone at Kanab, Utah. D) Modern example of wind-ripple facies clearly shows the bimodality of grain-sizes. Mesquite dune-field in Death Valley National Park, California. Lens cap in (B) and (C) is 55 mm in diameter.*

### 9.1.2 Grainflow facies (Gfw)

*Description (Figure 9.2):* The deposits are characterised by reddish-brown, orange to pale-yellow, fine to medium grained quartz arenite with laminated cross-strata that ranges in thickness from 8 – 50 mm. Units are tabular, tapering-upward wedges of cross-strata that can occur as structureless as well as inversely graded units with depositional dips ranging between 18° and 30°. Along strike the laminae form lenticular bodies that may extend up to 2m (*Figure 9.2b*).

*Interpretation:* Where flow separation occurs at the dune brink, a cornice of sand accumulates high on the lee slope until an angle of initial yield is exceeded and a grainflow (sand avalanche) moves downslope (Loope *et al.*, 2012). The avalanching of this non-cohesive sand down the slipface forms the grainflow cross-strata (Hunter, 1981). Such a process is associated with sets composed internally of laminations formed by repeated avalanches coming to rest at the angle of repose for loose, dry sand. On modern dunes this angle is between 32° and 34°, however, preserved inclinations are lower (typically more than 17° and up to 26°) as a result of post-depositional compaction (Besly *et al.*, 2018). Inverse grading in laminations is a result of sorting during the avalanche process (Eastwood, 2012); additionally, coarser grains may outpace the finer grains and become concentrated at the toe of a set (Kocurek, 1991).

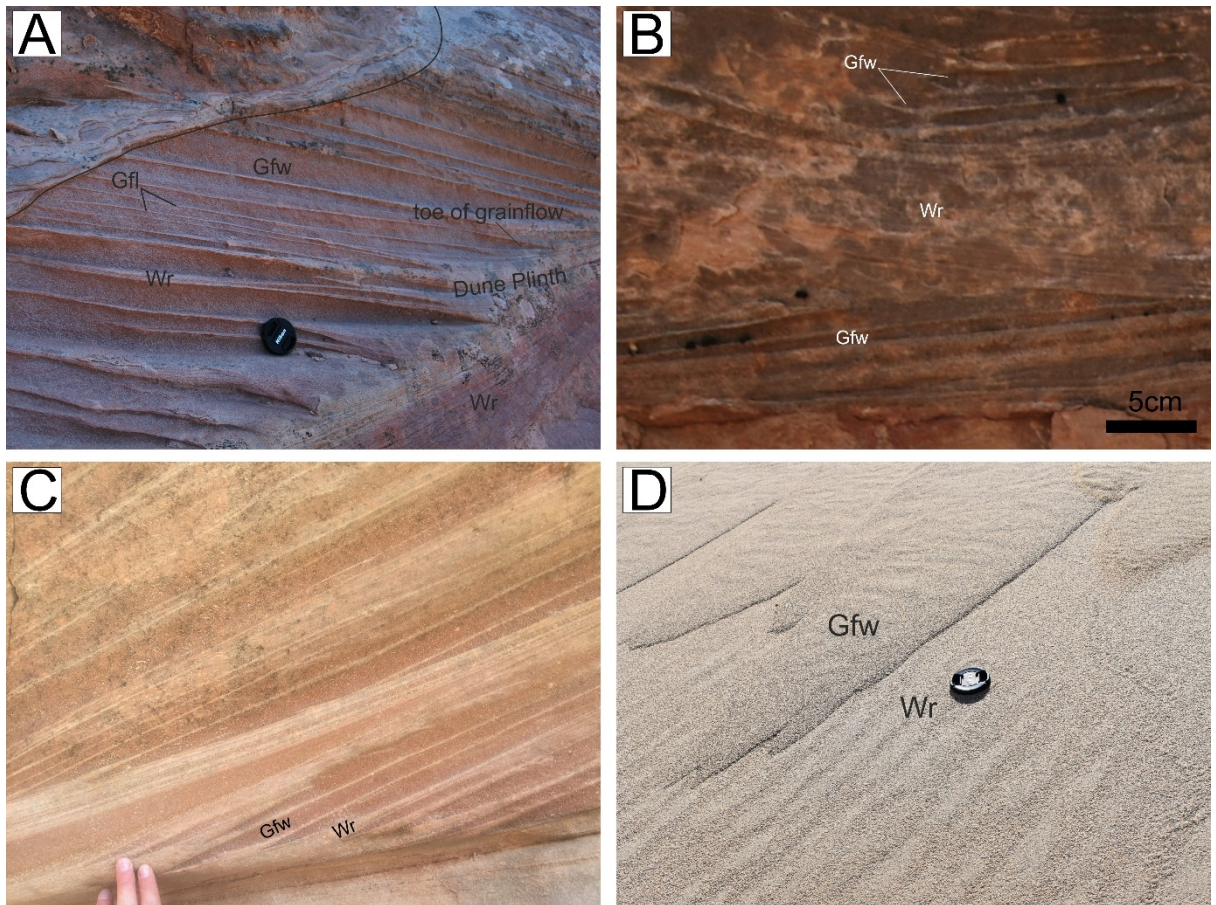


Figure 9.2: A) Aeolian dune cross-strata dominated by grainflow facies (Gfw). The grainflow strata are typically interbedded with wind-ripple facies (Wr) or thin grainfall laminae (Gfl). Note the wedge-like geometry at the toe of the grainflow strata and the interaction with wind-ripple facies forming dune plinth deposits. Navajo Sandstone at Kanab, Utah. B) The upper most set shows the lenticular geometry of grainflow strata in a section parallel to strike. Navajo Sandstone at Sevenmile Canyon, Utah C) Grainflow tongues pinching out into pinstriped wind-ripple strata. Cyclic interfingering is commonly referred to as compound crossbedding indicating seasonal wind reversals (Loope et al., 2004) . Navajo Sandstone, Goblins Valley State Park, Utah. D) Modern example of grainflow facies and the interaction with wind-ripple facies on the lee-slope plinth of a crescentic dune. Note the pinching out into wind-rippled strata as identified in (C). Mesquite dune-field in Death Valley National Park, California. Lens cap in A and C is 55mm in diameter.

### 9.1.3 Grainfall facies (Gfl)

*Description (Figure 9.3):* The deposits are characterised by orange to pale-yellow thinly laminated (typically < 7 mm) fine-grained quartz arenite. Deposits form structureless tabular units with a unimodal grain size distribution and tend to be laterally continuous along strike of cross-bedding (traced up to tens of metres). Deposits range in dip from horizontal (bottomsets) to foresets that approach the angle of repose.

Interpretation: Grainfall is the process of settling out of grains typically occurring at the lee of the dune as saltating grains enter the zone of flow separation (Hunter, 1977; Fryberger and Schenk, 1981). This pattern of grainfall results in a wedge of sediment that is thickest near the brinkline which thins downslope to its steepest part where it builds to the angle of initial yield, then avalanches downslope to form grainflow deposits (Kocurek, 1991). In the zone of flow separation of the lee slope of a dune where tractional transport of sand is aided by gravity, the wind speed is too weak to form ripples and lee slope smoothing occurs. This results in stratification indistinguishable from that produced purely by grainfall and therefore adds to grainfall deposits (Hunter, 1977). In the rock record, deposit typically occurs on the dune slipface or apron and are concordant with pre-existing dune topography (Kocurek and Dott, 1981). Distinguishing grainfall deposits from adjacent grainflow deposits may not be possible because the avalanching of grains incorporate and rework the grainfall deposits as they pass downslope over them. Accumulated intervals of grainfall facies tend to occur typically after wind storm events (Besly *et al.*, 2018).

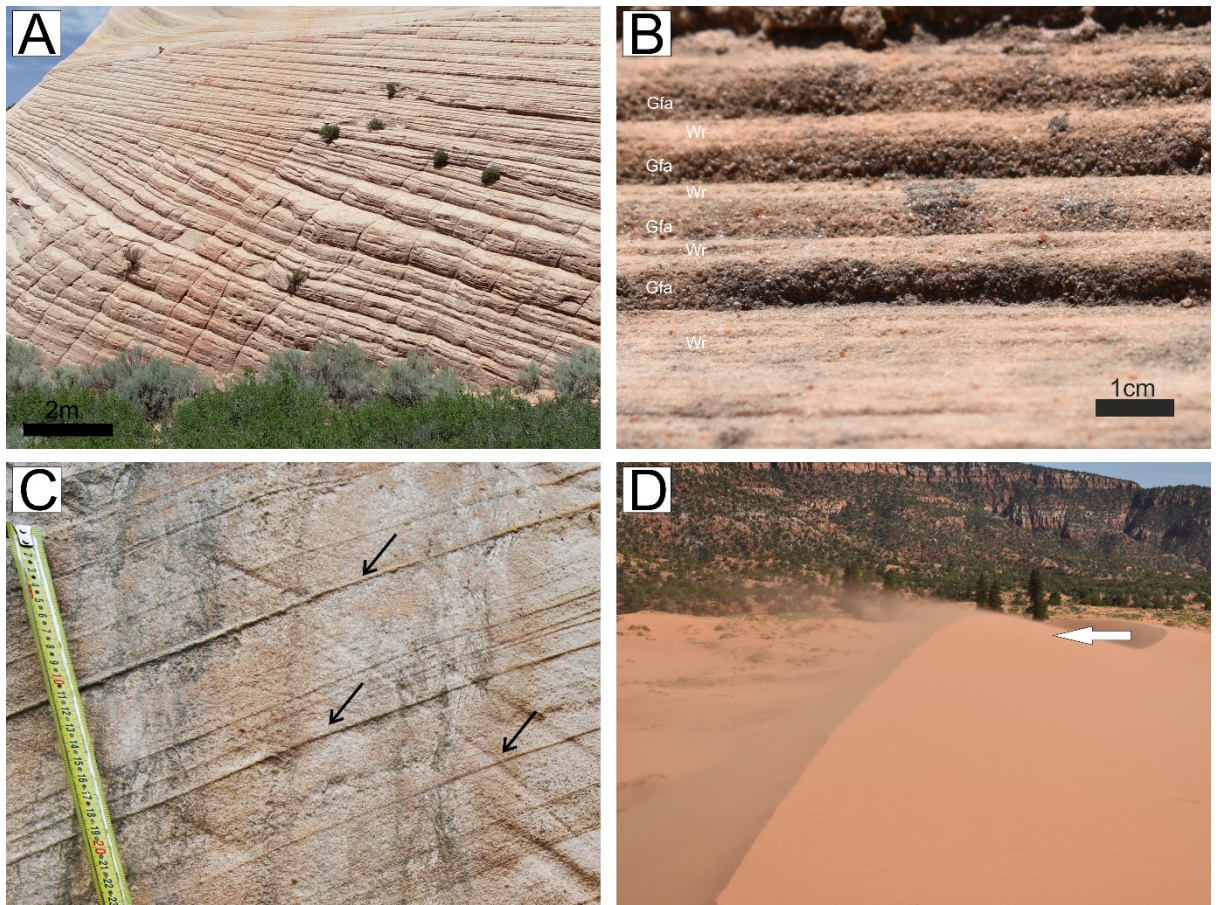


Figure 9.3: A) The outcrop is dominated by grainfall facies interbedded with wind-ripple strata. The strata are laterally continuous along strike for several to tens of metres. A close-up image (B) shows the structureless tabular units rarely exceed 1 cm in thickness. Navajo Sandstone at Kanab, Utah. C) Thin sharply defined grainfall laminae (arrows) interbedded with thicker packages of grainflow strata. Navajo Sandstone at Kanab, Utah D) Modern example shows the process of grainfall deposition. Saltation of sand moves over the brink of a dune forming a suspended cloud. Deceleration of the airflow on the lee-slope results in falling out of suspension. Arrow shows wind direction. Coral Pink Sand Dunes State Park, Utah.

#### 9.1.4 Adhesion strata (Adh)

*Description (Figure 9.4):* The deposits are characterized by dark brown to red crinkly, laminated to mottled, fine-to-medium-grained sand. Deposits typically occur in discrete laminae along low angle foresets into horizontal bottomsets. They may form extensive horizontal surfaces from a few centimetres wide to laterally continuous (tens to hundreds of metres).

*Interpretation:* When the accumulation surface is damp, transported grains generate a range of adhesion structures, adhesion plane beds, adhesion ripples (Kocurek & Fielder, 1982) and adhesion warts (Olsen *et al.*, 1989). Adhesion plane beds stick to a damp surface devoid of previous adhesion ripple or wart features, resulting in a smooth bed with faint, crinkly laminations only a few millimetres thick which although hard to recognise are distinct from other laminated deposits by thickness, faintness and crinkly laminations (Kocurek & Fielder, 1982). Adhesion ripples form by trapping wind-blown sand with their crests lying transversely to wind direction. Adhesion warts form small domes or oval bumps more randomly distributed than adhesion ripples. Wavy-crinkly bedding has also been explained by adhesion of silt and sand onto a moist sabkha surface (Glennie, 1970). Many of the adhesion structures present in the Navajo Sandstone occur with facies indicating the groundwater-table was close to the surface, in a generally arid setting. Adhesion strata is typically observed in erg-margin settings such as the Permian Cutler Group and Cedar Mesa Sandstone (Langford and Chan, 1989), as well as the erg-margin association within the Moenave-Wingate system (Clemmensen *et al.*, 1989).

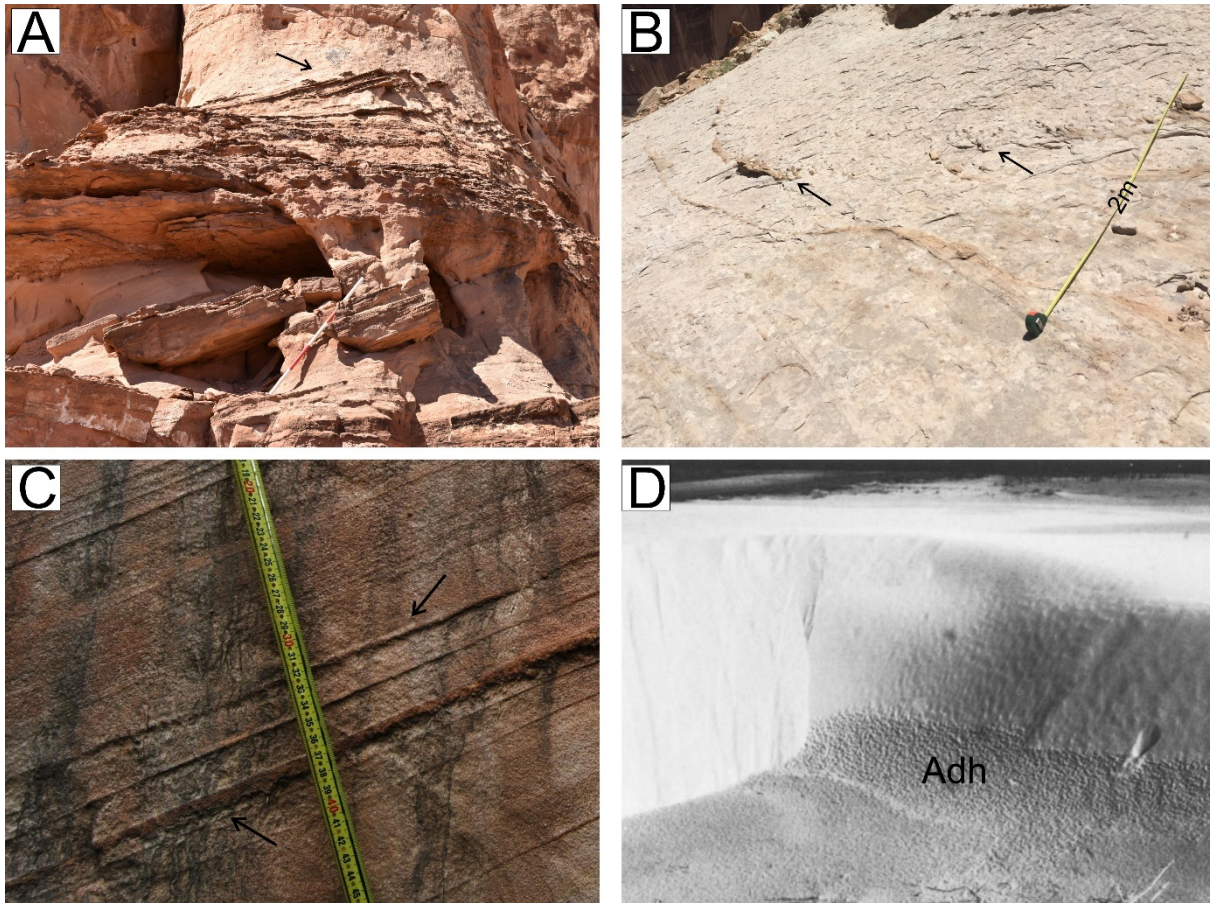


Figure 9.4: Adhesion strata. (A) Evidence of damp conditions throughout deposition. Wavy-crinkly beds occur in thick packages, along dune bottomsets and up cross-strata (arrow). The thick bed in this example could be followed for over 100 m. Pole has 20 cm divisions. Navajo Sandstone at Hite, Utah. (B) Adhesions strata marking out trough cross sets and individual cross-strata. Navajo Sandstone at Sevenmile Canyon, Utah. (C) Close-up of adhesions strata along cross-strata between grainflow strata. Arrows point to the wavy-crinkly surfaces. Navajo Sandstone at Kanab, Utah. (D) Contemporary example of adhesions strata occurring at a dune bottomset following precipitation. This surface will likely be buried by grainflow or wind-ripple strata leaving behind deposits similar to those seen in (B) and (C). Photo extracted from Kocurek, 1981 (Padre Island, Texas).

## 9.2 Navajo Sandstone Facies

Facies were simplified and summarised into seven sandstone (prefix -S), one mudstone (prefix -M) and two carbonate (prefix -C) facies as outlined in Table 9.1 and Figure 9.5 through Figure 9.14. The scheme then subdivides the facies into five ‘facies associations’ of dry desert environments representing key desert settings that apply directly to this study (section 9.3).

Table 9.1: *Frg-scale facies of the Navajo Sandstone*

Code	Facies	Structures	Other features	Interpretation	References / Figure
SA1	Fine to medium grained sandstone. Small to very large-scale cross-stratified. Reddish-brown, orange, pale yellow to off-white.	Small to very-large scale tabular cross-strata, wedge-cross-strata, trough cross-strata.	Sets may be dominated by either reverse-graded translent strata and grainfall laminae, or large proportion of grainflow stratification with minor translent strata. Large-scale sets (up to 15 m) to very-large-scale cross-stratified sets (up to 60 m thick) with variable cross-bedding styles are typically compound or complex in nature. Small to large simple sets composed of grainflow strata wedge out into tangential wind-ripple laminated sets.	Simple, compound to complex aeolian dunes or drias. Preserved dune bottomssets (transition into dry interdunes).	Brookfield, 1977 Hunter, 1977 Kocurek and Dott, 1981 Hunter and Rubin, 1983 Rubin and Hunter, 1983 Mounthey, 2006a Figure 9.5
SA2	Fine to medium grained sandstone. Millimetre-scale laminations. Reddish-brown, orange, pale yellow to off-white.	Reverse-graded wavy / crinkly pinstripe lamination	Horizontal to cross-stratified laminae. May be laterally continuous for 100s of metres in near-horizontal sets. Typically associated with facies SA1, occurring within cross-stratification laminae and into horizontal basal sets. Foreset cross-laminations sometimes observed within individual laminations.	Wind-ripples forming dry interdune, dune plinth and dune cross-stratification. Dry sandsheet deposits if laterally extensive.	Kocurek and Nielsen, 1986 Mounthey and Russel, 2004 Mounthey, 2006a Figure 9.6
SA3	Fine grained to silty sandstone. Crinkly laminated. Pale orange to brownish red.	Irregular wavy, crinkly and / or distorted laminae	Usually laterally continuous up to 100s of metres. Laminae is irregular and variable along strike and may pass laterally or vertically into wavy bedded limestones of facies CL1. Adhesion structures are common. Laminae also found occur along cross-stratification of facies SA1 (adhesion plane lamination). Rhizoliths and bioturbation may be present.	Capillary action from a shallow water-table forming damp interdune deposits. Water-table may restrict sediment availability inhibiting dune creation and form extensive sandsheets.	Kocurek & Fielder, 1982 Mounthey, 2006b Figure 9.7
SA4	Fine to medium grained sandstone. Contorted to massive. Reddish-brown, orange, pale yellow to off-white.	Small to large-scale contorted sandstone associated with structureless sandstone	Small-to-large-scale ductile deformation of cross-bedding closely associated with massive sands. Mostly isolated within sets of aeolian dune deposits but can cross through and affect all elements (e.g. interdune, sandsheet). Bioturbation may be present.	Modification of aeolian laminae and soft-sediment deformation probably a cause of overburden pressure of large advancing bedforms. Laminae may be disrupted by bioturbation. Associated with a fluctuating water-table.	Horowitz, 1982 Bryant <i>et al.</i> , 2013, 2016 Benan and Kocurek, 2000 Figure 9.8
SA5	Silty- to-very fine-grained sandstone. Dark red with carbonate cement	Structureless	Structureless horizontal and laterally extensive beds up to 2m thick. Typically associated with sharp vertically bound structures that truncate underlying sets and connect to the horizontal beds from below. Mound-shaped structures with draping strata occurs where they connect.	Confined Structureless deposits formed in wet interdune by rapid flooding. Vertical structures indicate paleohydrological influence and an upward injection of over pressurized water-plain sediment.	Chan <i>et al.</i> , 2007 Dorney <i>et al.</i> , 2017 Parrish <i>et al.</i> , 2017 Bryant <i>et al.</i> , 2013 Figure 9.9
SF1	Fine to coarse grained sandstone. Small to medium scale cross-stratified. White or purple-red.	Small to medium-scale tabular and lenticular sandbodies	Confined tabular beds typically laterally extensive. May show compound sandbodies built by vertical stacking and lateral linking of smaller cross-stratified bodies. Poorly cross-bedded to massive sandstone lenses.	Upper flow-regime plane-bed deposits, rapid deposition in fluvial channels	Miall, 1985, 1996 Luttrell, 1987, 1993 Hassan <i>et al.</i> , 2018 Figure 9.10
SF2	Silty to fine-grained sandstone. Horizontally laminated. White to grey	Tabular beds of sandstone sheets interbedded with mm-scale siltstones	Poorly to moderately sorted. Faint cross-strata to parallel laminated. Individual sets usually less than 1 m thick.	Shallow but persistent flows forming Sheetfloods deposits	Miall, 1985, 1996 Luttrell, 1987, 1993 Hassan <i>et al.</i> , 2018 Figure 9.11
M1	Massive mudstone. Brownish red to green	Massive to crudely parallel laminated	Typically associated with facies SF1 and SF2. V-shaped sand-filled fissures marking desiccation cracks or root casts common	Subaqueous deposition by suspension settling in ponded water. Low energy flooding	Bromley, 1992 Mounthey, 2006b Figure 9.12
CL1	Sandy Limestone/dolostone. Fine to medium sand in a calcareous matrix. Grey, light brown, light green	Planar horizontal lamination / massive	Occurs either as laterally continuous tabular sets or as lenticular bodies. Bioturbation, desiccation cracks and rhizoliths common. Almost always associated with CL2, spatially associated with SA3 and vertically associated (below and above) with SA4.	Calcium carbonate precipitation out of water column (lacustrine). Surrounding sediment input, intermittent drying and spatial association with damp aeolian facies indicates playa lake or ponded interdune.	Sansom, 1992 Dorney <i>et al.</i> , 2017 Parrish <i>et al.</i> , 2017 Figure 9.13
CL2	Laminated carbonate lenses	Wavy bedded lenticular limestones	Millimetre to centimetre-scale crystalgal laminates with sharp irregular base. Authigenic chert nodules typically present. Observed within CL1 facies.	Algal mat growth within long-standing lacustrine settings.	Bromley, 1992 Eisenberg, 2003 Figure 9.14

Facies SA1: Cross-bedded sandstone



*Figure 9.5: Facies SA1 cross-bedded sandstone. A) and B) Large sets of trough-cross bedded sandstone. C) Sets of wedge cross-strata. Red arrows mark tapered edges. D) Small to medium-sized tabular sets of cross-strata. E) Small to very-large sets ranging from ~1 m to 55 m in thickness of tabular cross-strata. The largest sets grades into soft sediment deformation structures (SA4) marked by dashed line.*

Facies SA2: Wind-ripple

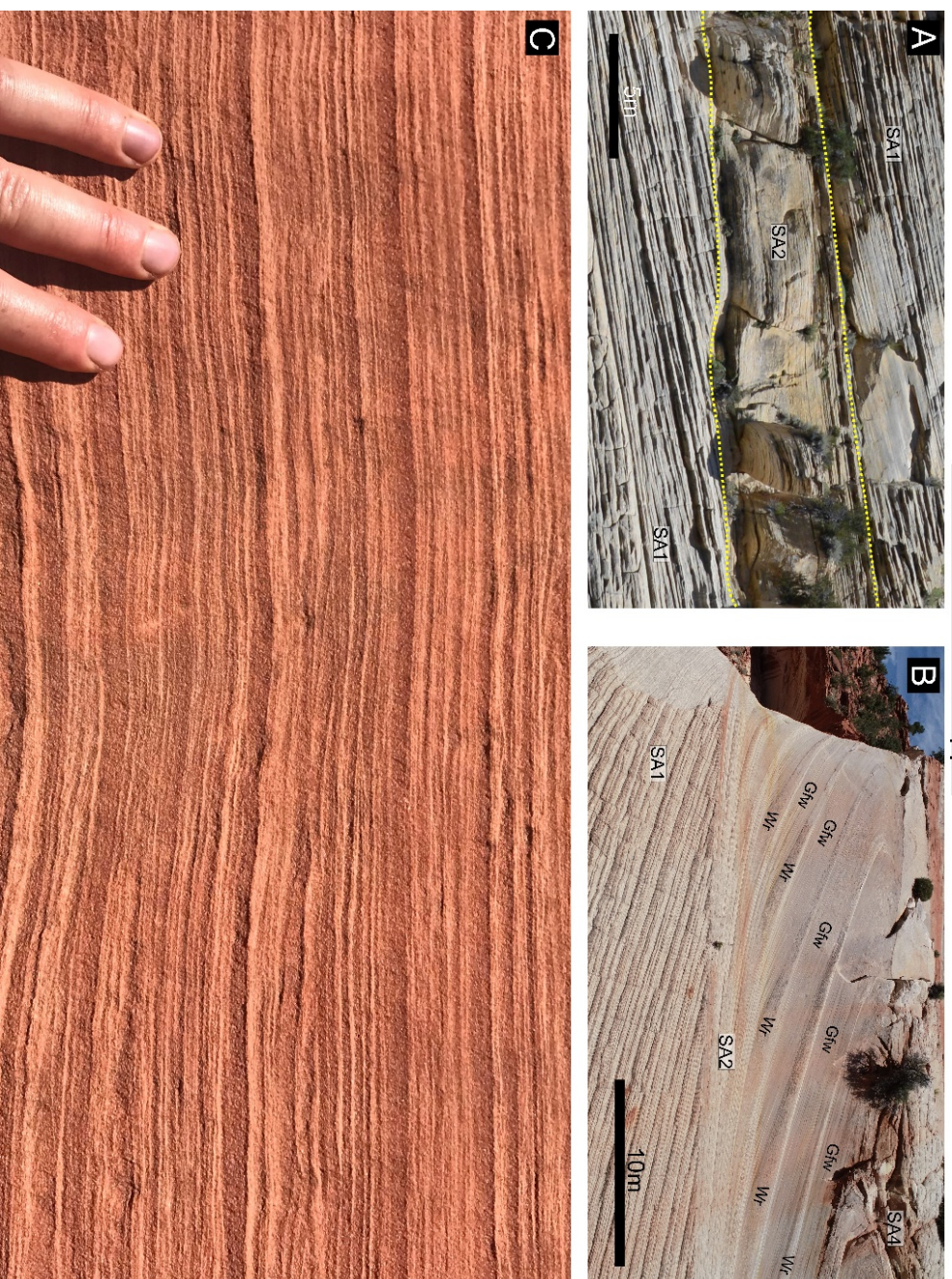


Figure 9.6: A) Wind-ripple dominated dry interdune deposit. B) Dune plinth and toeset deposits and the association with cross-stratification marked by cycles of grainflow (Gfw) and wind-ripple (Wr) deposits. Commonly referred to as cyclic cross-bedding (Hunter and Rubin, 1983). C) Pinstripe laminations in a sandsheet deposit highlights the bimodal sorting of wind-ripples. Coarser grain sizes weather faster and their darker appearance indicates more oxidation (rusting) has occurred.

**Facies SA3: Irregular wavy-crinkly laminated sandstone**

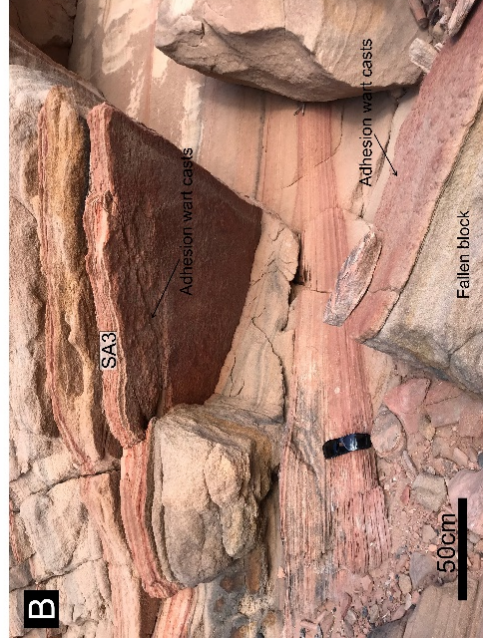


Figure 9.7: The above examples show the SA3 facies of damp interdune / sandsheet deposits. Examples of adhesion strata occurring directly on aeolian dunes is shown in Figure 9.4. A) An extensive horizontally laminated sandsheet contains discrete brown beds with wavy-crinkly distorted laminae of facies SA3. The sandsheet truncates an aeolian dune (SA1) with abundant rhizolith, bioturbation and soft sediment deformation, indicative of wet conditions possibly through a fluctuating water-table. B) Plan view surfaces shows adhesion wart casts of wavy-crinkly laminae. C) Adhesion laminae observed along discrete lenses of cross-stratified sets.

## Facies SA4: Contorted sandstone

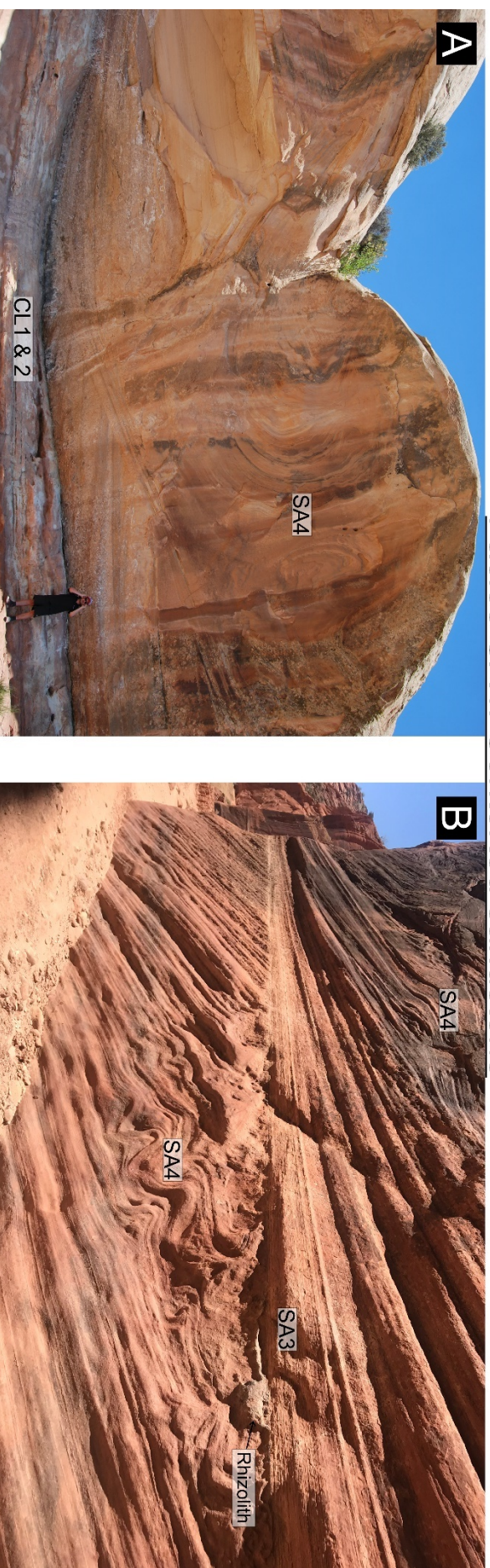


Figure 9.8: A) Large-scale trough cross bed grades into convoluted stratification commonly referred to as soft sediment deformation. D) Deformed cross-strata in a planar set and truncated by a damp interdune.

## Facies SA5: Structureless sandstone

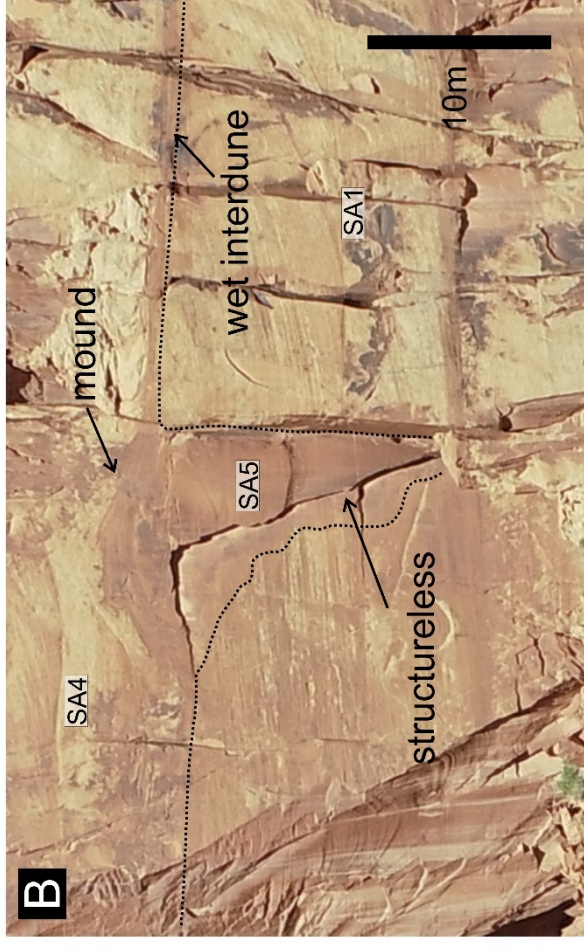
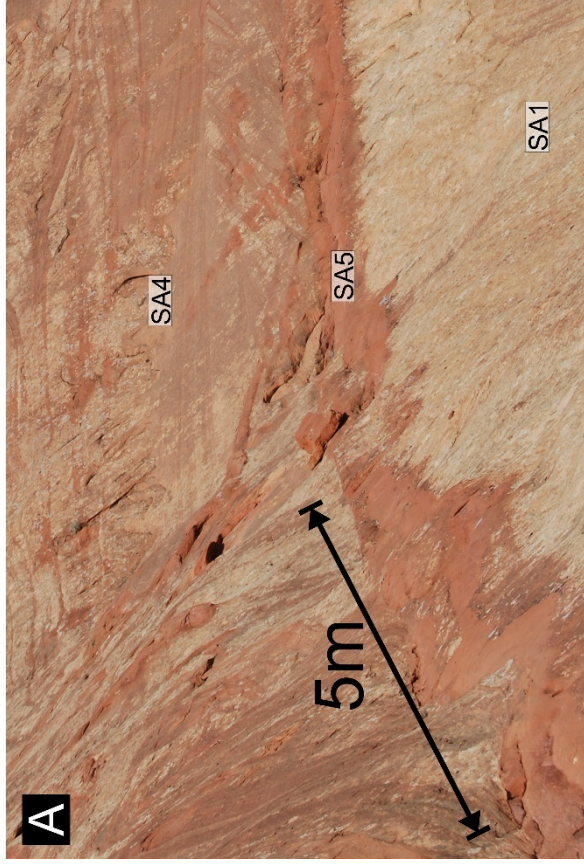


Figure 9.9: A) Laterally continuous structureless sandstone bed continues for hundreds of metres along outcrop strike. (B) Clastic dike hosts structureless sand and is connected to a wet interdune. Mound forms where dike breaches the surface and floods the interdune.

## Facies SF1: Tabular and lenticular sandbodies



*Figure 9.10: A) Channel form with cross-bedded sandstone sets. The channel cuts into a massive / deformed aeolian sand body. B) Laterally continuous tabular beds. Internally the beds contain planar to cross-stratified bodies.*

Facies SF2: Planar laminated sandstone

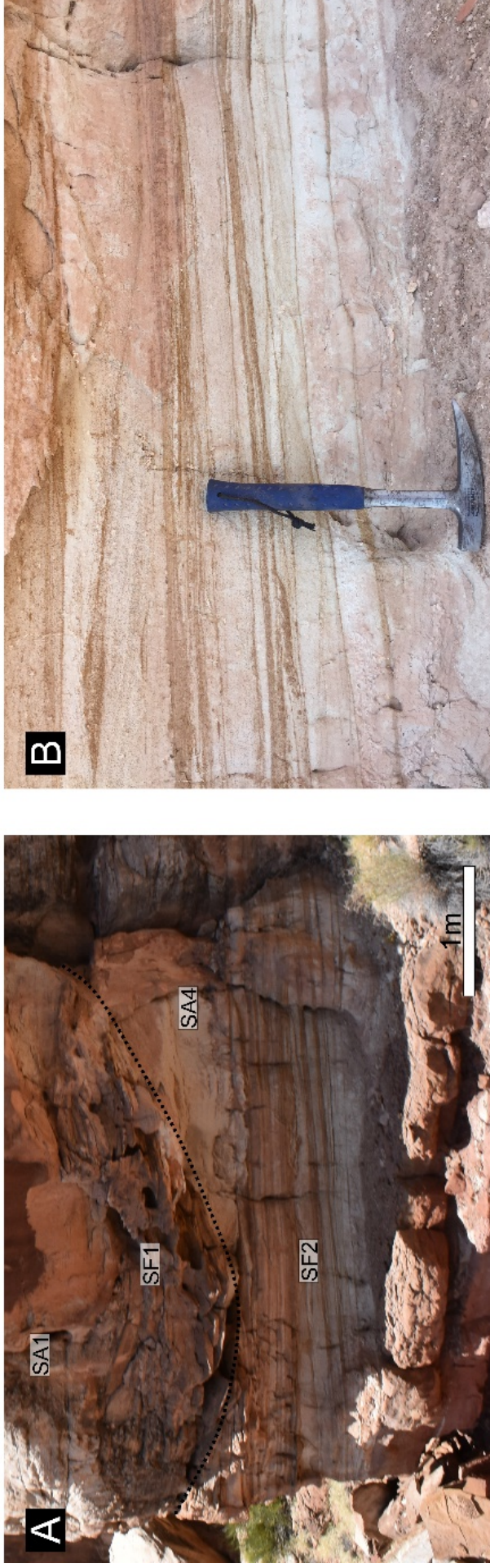


Figure 9.11: Millimetre to centimetre-scale bedding ranging from faint or impersistent to sharp and laterally continuous. B) Faint cross-laminations evident in upper sandstone bed.

**Facies M1: Massive mudstone**



*Figure 9.12: A) Crudely laminated mudstone bed with cross cut by vertical burrow B) Mudcracks filled with sandstone derived from overlying aeolian sets.*

## Facies CL1: Sandy limestone



Figure 9.13: A) and B) show sets of massive sandy limestones associated with rhizoliths, bioturbation and algal mats of facies CL2. The two sites show the same bed which are spaced approximately 3 km apart. C) Lenticular sandy limestone approximately 60 m wide.

Facies CL2: Laminated wavy carbonate lenses



*Figure 9.14: A) Algal cretulation and chert nodules of long-standing water associated with lacustrine deposits. B) Thinly laminated limestones interbedded with mudstones and wavy carbonate lenses.*

### 9.3 Facies Associations

To reconstruct the depositional setting of successions, genetically related facies are grouped into several facies associations, each representative of a different depositional environment within the Navajo Erg. Facies relationships are determined by correlation through virtual outcrop models, tracing individual beds where possible. The distribution of facies associations will be used to assess palaeogeographical distribution of depositional environments across the basin and discuss the controlling factors. Six facies associations were recognised in the study present between the three studied sites of chapter 8 (Table 9.2).

*Table 9.2: Facies associations of the Navajo Sandstone*

<b>Code</b>	<b>Facies Association</b>	<b>Facies included</b>
<b>FA1</b>	Fluvial-channel and overbank	SF1, SF2, M1
<b>FA2</b>	Fluvial-aeolian interaction	SF1, SA1, SA4, SA5
<b>FA3</b>	Flooded interdune and playa lake	SA3, SA4, SA5, CL1, CL2, M1
<b>FA4</b>	Damp aeolian	SA2, SA3, SA4
<b>FA5</b>	Erg-margin	SA1, SA2, SA3, CL1, M1
<b>FA6</b>	Erg-centre	SA1, SA2, SA4, CL1, CL2

### 9.3.1 FA1: Fluvial-channel and overbank association

Fluvial channel and overbank association includes lenticular sandbodies composed of facies SF1 and laterally equivalent overbank sands, silts and muds of SF2 and M1. The association typically forms the final stages of the dominantly fluvial Kayenta Formation (see Bromley, 1991; Hassan *et al.*, 2018 for more details) prior to increased aridity and Navajo expansion. The sediments were deposited in areas proximal to the dune-field (i.e. erg-fringe / extra-erg) in sheet-like fluvial systems emanating from multiple sources prior to erg expansion and accumulation (e.g. Figure 9.15A). This association is identified in the deposits of the Kayenta Formation and within the lowermost deposits of the Navajo Sandstone at Sevenmile Canyon region (Figure 8.2) and is discussed further in section 10.2.

### 9.3.2 FA2: Fluvial-aeolian interaction association

This association is characterised by lenticular fluvial sandbodies of facies SF1 surrounded by soft sediment deformed, massive and / or slumped sands of facies SA4. The channels are typically found isolated only affecting the immediate surrounding aeolian sands (facies SA4). Aeolian sandbodies of facies SA4 transition into facies SA1 which may range from highly continuous to lenticular depending on the spacing of fluvial channels. The sediments were deposited in distinct episodes of confined ephemeral fluvial-channels encroaching into an established dune-field (e.g. Figure 9.15B). There is typically a spatial association with FA3 as interdune areas are flooded periodically.

### 9.3.3 FA3: Flooded interdune and playa lake and association

Associations of this type are characterised by discontinuous planar wavy laminae and contorted structures of facies SA3 and SA4 respectively. Additionally, carbonate sediments (CL1), microbial mats (CL2) and mudstone facies (M1) may accumulate in long-lived ponds. Muddy, silty and / or sand may be supplied through aeolian or fluvial processes (e.g. Figure 9.15B). Intermittent drying is common and identified by desiccation cracks of facies M1. The sediments were deposited in interdune flats and depressions that occur between aeolian dunes where the water-table has risen above the level of the depositional surface or there is a hydrodynamic breach (SA5) at the surface (springs / water injection)

(e.g. Figure 9.15C). This association is common in the Hite region (Figure 8.2) and is discussed further in section 10.3.

#### 9.3.4 FA4: Damp aeolian association

The association is characterised by a range of adhesion structures of facies SA3 and deformed structures of SA4. Adhesion structures are typically found along aeolian dune toesets of facies SA1 and SA2 (e.g. Figure 9.15D). Deposition of these sediments occur in flats and hollows between aeolian dunes where the depositional surface is in contact with the capillary fringe of the water-table. Sedimentation is therefore strongly influenced by the presence of moisture. This may encourage the colonisation of plants and biogenic activity. There is typically a close temporal association with FA3. This association is observed in all studied sites of chapter 10 (Figure 8.2).

#### 9.3.5 FA5: Erg-margin association

The erg-margin association is characterised by small to medium tabular and trough-cross sets of facies SA1, separated by beds of facies SA2 or SA3 (dry or damp interdune). Varying amounts of carbonate facies CL1, lenticular mudstones of facies M1 and contorted sets of facies SA4 are present. The association is interpreted as deposits of a well-established erg-margin dune-field complete with extensive sandsheets and zibar, as well as small to medium-sized aeolian dunes where conditions switched between damp, wet and dry due to competing environments (e.g. Figure 9.15A,E). This association is common in Sevenmile Canyon region (Figure 8.2) and is discussed further in section 10.2.

#### 9.3.6 FA6: Erg-centre association

The erg-centre association is dominated by medium to very-large sets of aeolian dune and draa of facies SA1 and thick sandsheet deposits of facies SA2. These sediments were deposited in a well-developed erg-centre characterised by extremely large draa with dry interdune areas, far beyond the range of fluvial incursion (e.g. Figure 9.15E). In cases where wet conditions are observed, they are generally the cause of water-table and hydrological interactions near to the depositional surface (e.g.

Figure 9.15C). This association common in both the Hite and Johnsons Canyon regions (Figure 8.2), discussed further in section 10.3 and 10.4 respectively.

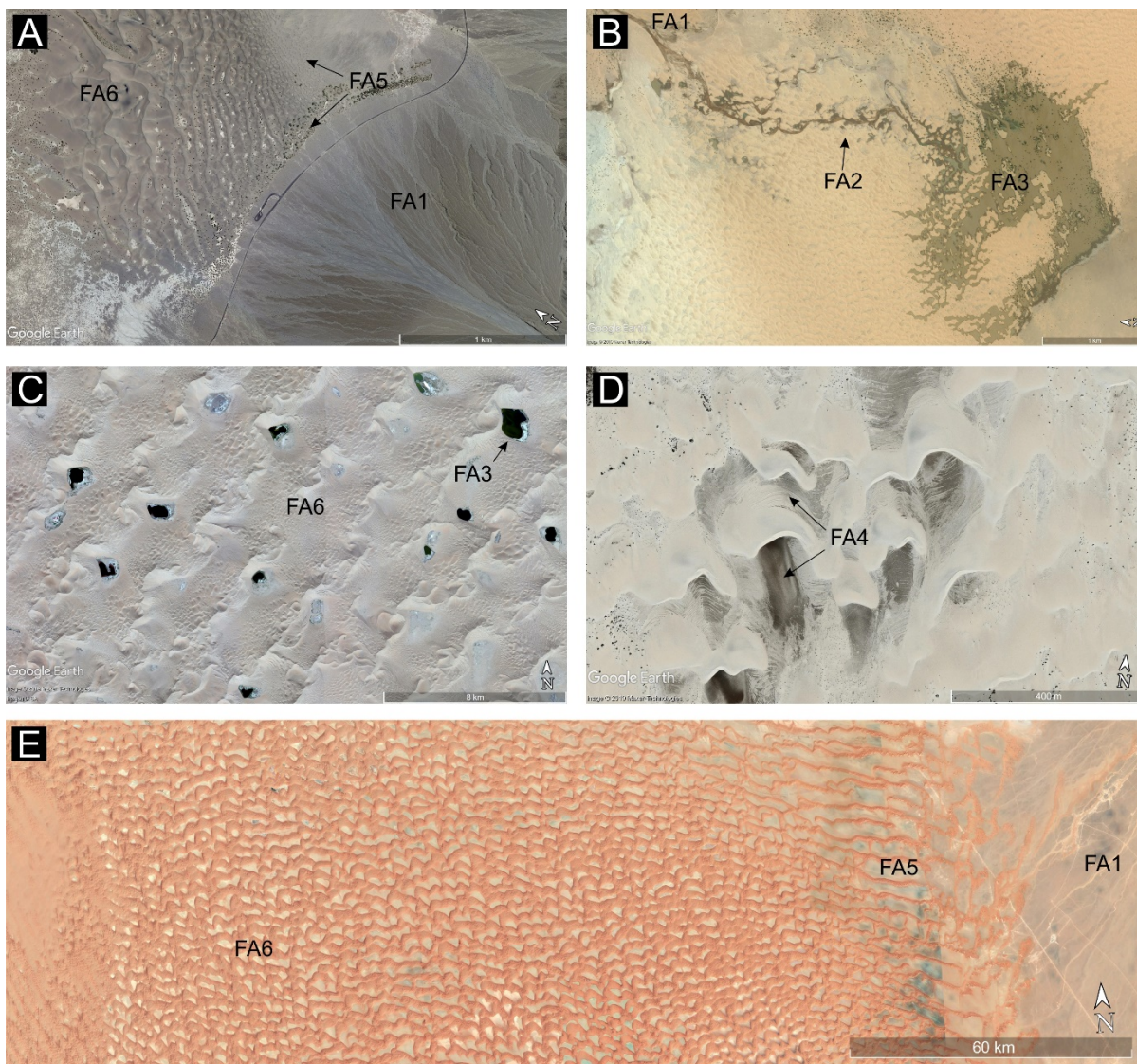


**Figure 9.15:** Examples of facies associations in contemporary dune-fields. A) Fluvial-channel and overbank association (FA1) of an erg-adjacent environment. Note at erg-margin areas (FA5), fluvial channels may beach interdune corridors. Mesquite dune-field, Death-Valley, California. B) Ephemeral fluvial incursion into a dune-field (FA2). Interdune corridors become locally flooded and a fluvio-lacustrine delta forms as flow terminates (FA3). Trarza Desert, Mauritiana. C) Flooded interdune ponds or playa lakes (FA3). The large dunes and lack of fluvial incursion indicate the lakes are water-table controlled in a central erg setting (FA6). Gobi Desert, Northern China. D) Due tosets are preserved in interdune hollows behind migrating dunes. The water-table breaches the surface to the west of this image (not shown here) and must have been at or near the surface as this dune migrated leaving behind these surfaces that are indicative of damp conditions. Al Jafurah Desert, eastern Saudi Arabia. E) Variation in dune morphology and distribution from marginal-erg (FA6) to central-erg (FA5) in a dominantly dry desert setting. Note the reduction in dune-size toward dune-field margins as the erg interacts with competing environment (FA1). Much of the information above is adapted from Al-Masrahy and Mounney, 2013, 2015.

## 10 Facies architectures and controls on aeolian preservation of the Jurassic Navajo Sandstone

Aeolian dune-field patterns evolve as a result of autogenic processes that occur in a set of external environmental (allogenic) conditions (Cardenas *et al.*, 2019). The external environmental controls are known as the boundary conditions and typically include the presence or absence of a near-surface water-table (e.g. Bryant *et al.*, 2016; Kocurek and Havholm, 1993), the sediment carrying capacity of the wind (magnitude and direction), the availability of sediment, and the geometry of the basin and sediment source (Ewing and Kocurek, 2010).

Nature, laboratory experiments and numerical models all show that where dune-fields originate on a planar surface, the general trend is for protodunes to evolve into a field of small closely spaced dunes, that coalesce into fewer, larger, more widely spaced dunes through constructive dune interactions (Kocurek and Day, 2018). These interactions are recorded in aeolian deposits with the potential to preserve strata within any phase of this development (e.g. Brothers *et al.*, 2017). Changes in boundary conditions may initiate new constructional phases of dunes upon an existing dune pattern (e.g. Langford *et al.*, 2008; Kocurek and Day, 2018). Inherited aeolian topography may influence subsequent deposition and existing dunes can serve as sediment sources that are eventually reworked into the new pattern through a series of interactions (Cardenas *et al.*, 2019; Swanson *et al.*, 2019).

This chapter provides deeper insight into the processes that promoted aeolian dune-field development, accumulation of strata, and the preservation of the accumulated strata in the Navajo Sandstone. As the boundary conditions are not consistent during the construction of the extensive Navajo system (Figure 7.13), the study considers the three key locations described in chapter 8 which provide spatial variance across the erg at different temporal intervals within the succession.

## 10.1 Methods

This section provides the general methods carried out during this study of the Navajo Sandstone. Because photogrammetry and virtual models were vital to this study, the production methods are extensively covered herein. Any additional methods carried out local to each site is provided within each study site section (sections 10.2, 10.3 and 10.4).

### 10.1.1 Sedimentology

Detailed sedimentological investigation of well exposed and accessible zones within the three sites was carried out. Section-logging at each site was conducted with the aim of characterising facies variations, palaeo-environments, and defining genetic depositional units. While conventional sedimentological analysis was carried out at all key sites, inaccessible zones were examined where possible by means of representative outcrops proximal to and along tracible stratigraphical horizons (e.g. Site 3). The sedimentological studies provided the basis for desk-based virtual outcrop analysis provided by photogrammetric acquisition.

### 10.1.2 Photogrammetry

Photogrammetry is used to compute georeferenced and coloured dense point clouds from a sequence of overlapping images taken from a variety of viewpoints (Vollgger and Cruden, 2016). It is a highly efficient alternative to light detection and ranging (LiDAR) for creating virtual outcrop models. Photogrammetric processing has the capacity for millimetre-to-centimetre-scale resolution over hundreds of metres with the ability to collect data from inaccessible or unsafe exposures (Bemis *et al.*, 2014). Previous studies have shown that photogrammetry can be utilised in sedimentological analysis to successfully extract grainsize information (e.g. Westoby *et al.*, 2015), analyse dune foreset cyclicity (e.g. Hayes *et al.*, 2017), morphologically characterise an ancient aeolian system (e.g. Argüello Scotti and Veiga, 2015; 2019), determine facies architectures and geometries of shoreface tongues (Olsen *et al.*, 1999), and generate quantitative geobody data in ephemeral fluvial systems (Priddy *et al.*, 2019).

The data acquisition involves taking high-resolution photographs in a continuous line in a direction approximately orthogonal to the outcrop surface, which is the optimal position for image acquisition over a relatively planar surface (Figure 10.1). Bemis *et al.* (2014) recommends a minimum of fifty percent overlap of images for successful photogrammetric processing. However, later studies by Dietrich (2016) and Cruden *et al.* (2016) recommended percentages from sixty to eighty-five for higher quality, more reliable models. The greater the overlap, the higher the precision and spatial accuracy of resulting digital models when using structure from motion (SfM) photogrammetry (Chelsey *et al.* 2017). Variable image texture, illumination changes and target interference can all make a feature appear differently between images and must be minimised during photogrammetric acquisitions (Kehl *et al.*, 2017).

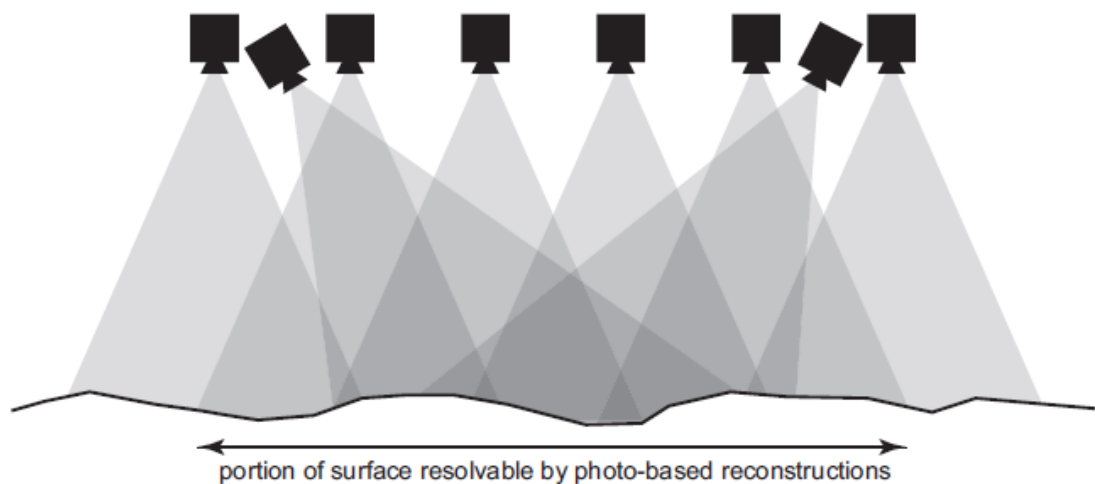


*Figure 10.1: Idealised image acquisition for photogrammetric processing. The shaded area represents the field of view for each camera with increased darkness representing increased overlap. This is done to make features more resolvable in a three-dimensional sense. Extracted from Bemis *et al.* (2014).*

Many of the remote outcrops in this study were only accessible on foot and as such lightweight equipment was required. For this reason, ground-based and UAV-based photogrammetric techniques were chosen over terrestrial LiDAR for data acquisition. Where possible, UAV-based techniques were

preferred over ground-based techniques in order to minimise perspective distortion obtained when photographing a tall object from ground level (Table 10.1).

Ground-based acquisition utilised a Nikon D800E hybrid digital single-lens reflex camera (HDSLR) with a 36.3 megapixel 8.6 cm<sup>2</sup> sensor and a 60 mm fixed focal length lens (Nikkor AF-S Micro 60mm F.2.8G ED). Images were captured approximately 10 – 30 m from the outcrop face with approximate 1 m spacings between photographs. To increase overlap and coverage of the uneven rugged outcrop surface, images were captured as the camera was ‘fanned’ approximately 20° – 40° to the left and right of orthogonal captures every 5 – 10 m. The first, last and every tenth photograph were georeferenced using a 12-channel Garmin GPSmap64 handheld Global Navigation Satellite System (GNSS) operating in the full Wide Area Augmentation System (WAAS) mode and using ground reference stations across the USA to correct for signal errors. Furthermore, measured targets placed on the outcrops were utilised to calibrate the models in a three-dimensional georeferenced space during post-production of the models.

The unmanned aerial vehicle (UAV) acquisition utilised a DJI Phantom 4 Pro drone with a 20-megapixel complementary metal oxide semiconductor sensor (CMOS) and an 8.8 mm / 24 mm fixed lens (35 mm format equivalent; f/2.8 - f/11 auto focus at 1 m to infinity, 84° field of view). Each photograph is georeferenced automatically utilising the drone’s built-in GPS (Global Positioning System) and GLONASS (Global Navigation Satellite System). Flights and acquisition were conducted after receiving a category 5 signal status (i.e. ‘very strong signal’ DJI GPS Signal Status). The cost-effective drone was chosen for the study due to its relatively lengthy flying time on a single battery (25 – 30 minutes), its multi-directional obstacle sensors, its automation in image capture and georeferencing, and its compact, lightweight nature for transport to remote sites. Each site was captured during manually operated flights, with sensors facing orthogonal to the outcrop surface. Typically, multiple runs along the outcrop face were conducted with variation in altitude and camera pitch and yaw for maximum coverage of the rugged surfaces. The drone allowed for closer inspection to the outcrop surface, generally ranging between 5 – 20 m depending on outcrop size and feature of interest. Image capture

was automated with a three second shutter at speeds up to 0.3 m s<sup>-1</sup> with results of overlap typically above 90%.

Photogrammetric models were produced for each site shown in Figure 8.2. While each outcrop was generally continuous, multiple models were typically constructed in order to isolate key areas of interest and produce high resolution models for analysis of facies architectures (Table 10.1). Models that relied on consistent tracking of laterally continuous bounding surfaces utilised full-scale models for consistency in georeferencing (e.g. SM1, H1, JC2 of Table 10.1). In the case of Johnsons Canyon only ground-based photogrammetry was conducted.

*Table 10.1: Summary of the eleven models produced between the three outcrops*

<b>Site</b>	<b>Model</b>	<b>Method</b>	<b>No. of Photos</b>	<b>No. of data points (Dense cloud)</b>	<b>Resolution</b>	<b>Outcrop horizontal coverage (m)</b>	<b>Outcrop true vertical thickness (m)</b>
<b>Sevenmile Canyon</b>	SM1	UAV	327	146463469	High	218	39
	SM2	UAV	61	6183536	Medium	144	51
	SM3	UAV	54	36863770	High	61	10
	SM4	UAV	43	2749201	Medium	80	9
	SM5	UAV & Ground	111	27297063	High	125	9
<b>Hite</b>	H1	UAV	1035	42200018	Medium	1470	170
	H1	UAV	333	15876441	Medium	659	170
	H2	UAV	352	13488101	Medium	911	162
	H3	UAV	75	4672715	Medium	490	128
<b>Johnsons Canyon</b>	JC1	Ground	170	15884638	Medium	335	42
	JC2	Ground	635	13813492	High	584	53

### 10.1.3 Image Processing

Image processing utilised Agisoft Metashape Professional (V. 1.5.3) in order to build every 3D virtual outcrop (Figure 10.2). The software utilized a structure-from-motion (SfM) multi-view stereo method, taking multiple overlapping images without the need for manual input of orientation or camera locations (Eltner *et al.*, 2016). Georeferenced photos were manually reviewed for consistency in overlap, illumination conditions and quality prior to importing them into the software. The initial stage undertakes camera alignment where common points of images are matched, thereby refining camera calibration parameters. This produces a sparse point cloud utilised in the production of the dense point cloud based on the estimated camera positions and images themselves. The dense cloud was edited to include only the outcrop, GPS markers and scale bars prior generating a triangular mesh surface. The mesh surface represents the object surface based on the dense point cloud and is necessary prior to overlaying the combined outcrop orthomosaics as a surface texture. Metashape supports setting a coordinate system based on ground control points and / or camera coordinates (pre-loaded to each photograph). Each virtual outcrop model was georeferenced based on the pre-loaded camera locations and additional GPS markers if deemed necessary. Setting the coordinate system provides precise scaling and orientation of the model in a real-world setting. This was a crucial stage prior to importing the model into a geoviewer or geoinformation software for outcrop analysis and interpretation.

Post processed models were imported into Virtual Reality Geological Studio (VRGS, V. 2.49; <https://www.vrgeoscience.com/>). This software provides 3D visualisation and interpretation utilities allowing analysis and accurate measurement of sets and all orders of bounding surfaces. This permits precise architectural element analysis on a large-scale where viewing areas are inaccessible by conventional means.

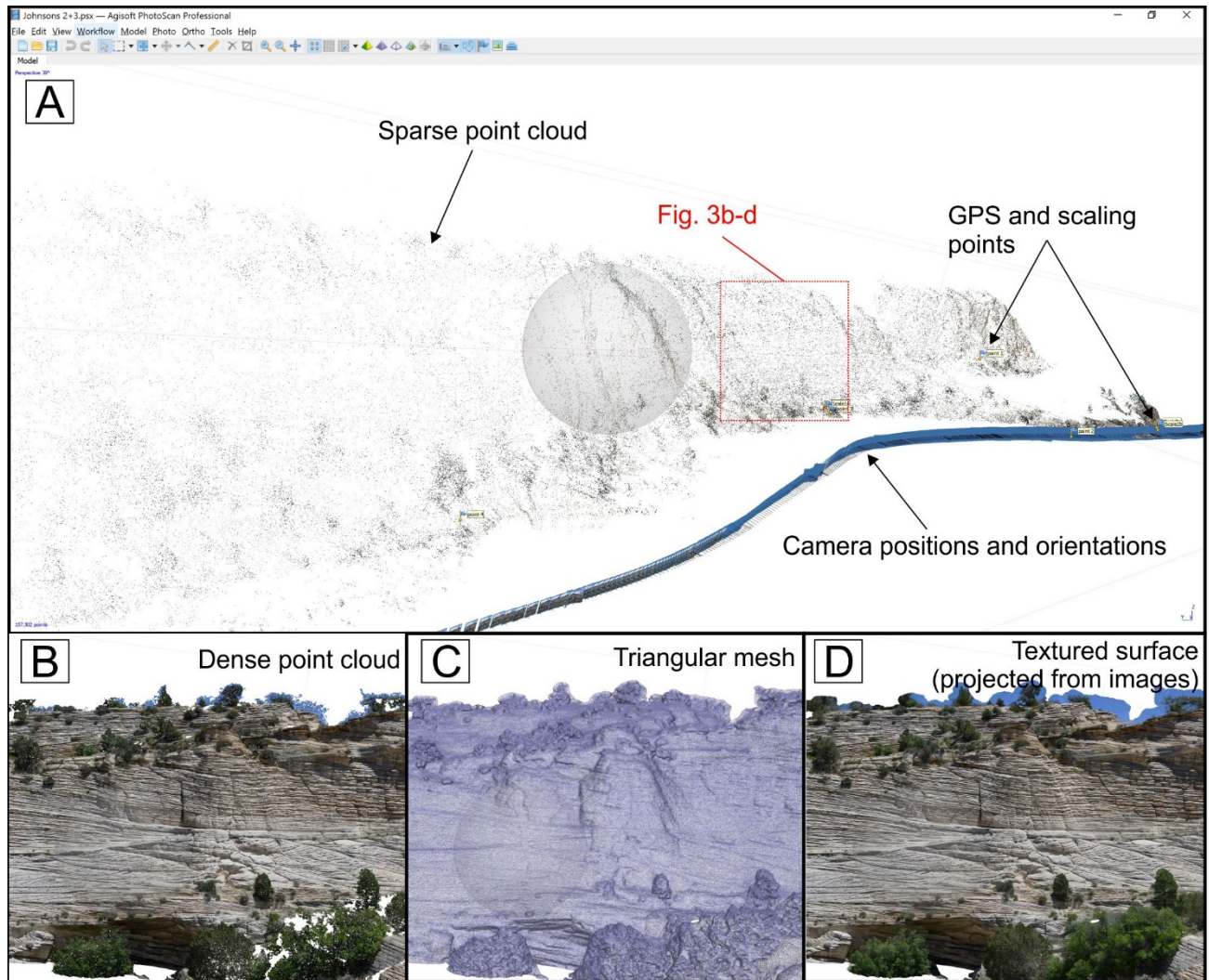


Figure 10.2: The workflow followed for the generation of the ground-based 3D photogrammetric model of the Johnsons Canyon outcrop (section 10.4). The figures show a cropped portion of the full outcrop which was about 600 m in width and up to 50 m in height. A) Cameras spaced with >80% overlap were used to generate the sparse point cloud. B) Dense point cloud construction. C) A triangular mesh surface reconstruction was created from the dense point cloud. D) The final textured surface is created by projecting images onto the mesh.

## 10.2 Site 1: Sevenmile Canyon

The section presented here focuses on an outcrop located approximately 20 km northwest of the town of Moab in central eastern Utah. Sevenmile Canon data acquisition covers segments of an outcrop of about 400m wide with a stratigraphical thickness of about 40 m (Figure 10.3). The area of focus is known as the Lower Navajo succession and basal deposits are associated with an erg-margin setting (Sansom, 1992; Blakey, 2008; Figure 8.2).

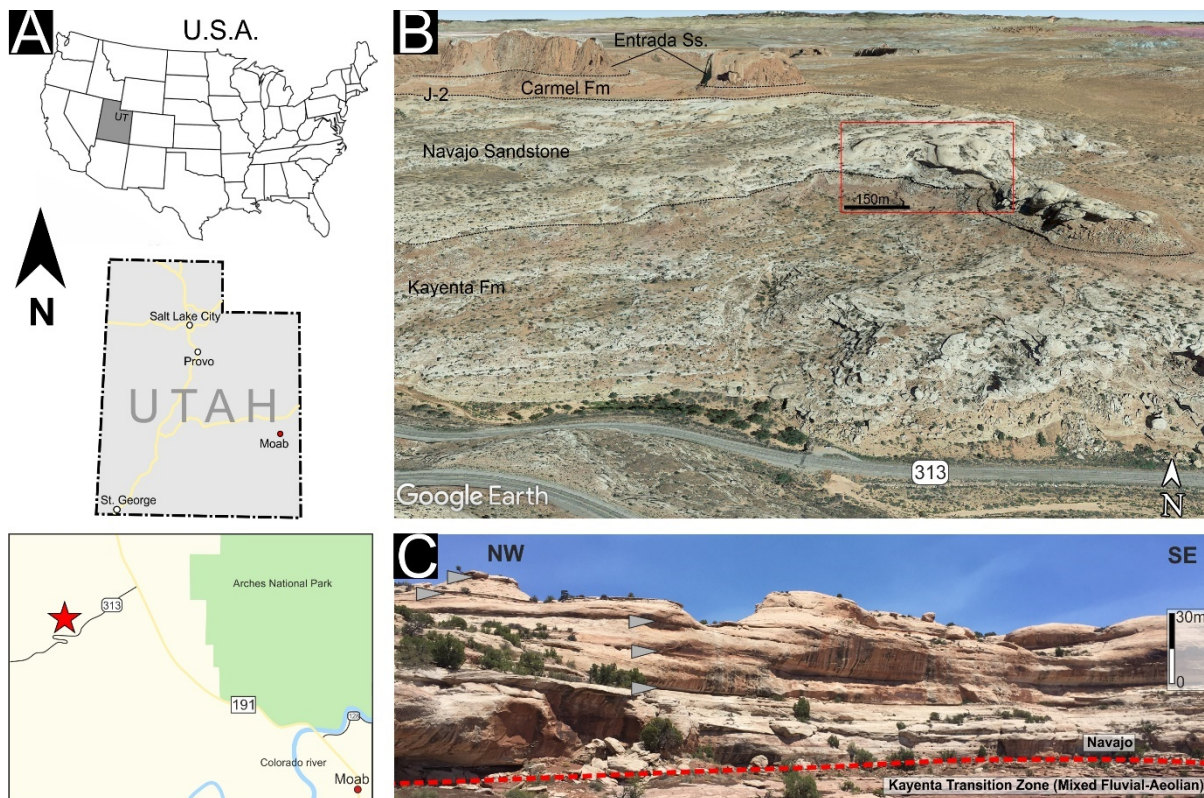


Figure 10.3: (A) Location of the remote outcrop at Sevenmile Canyon (red star). (B) Google earth oblique aerial view to the north. The figure shows the litho-stratigraphy of the site and separates the aeolian Navajo from the underlying older fluvial Kayenta Formation and the overlying J-2 unconformity that separates the younger dominantly marine Carmel Formation. The red square marks the area where UAV photogrammetry was acquired. (C) Ground-based photo panel of the Navajo sequence at Sevenmile Canyon. The grey triangles mark extensive first-order bounding surfaces and super surfaces.

### 10.2.1 Study Site and Methods

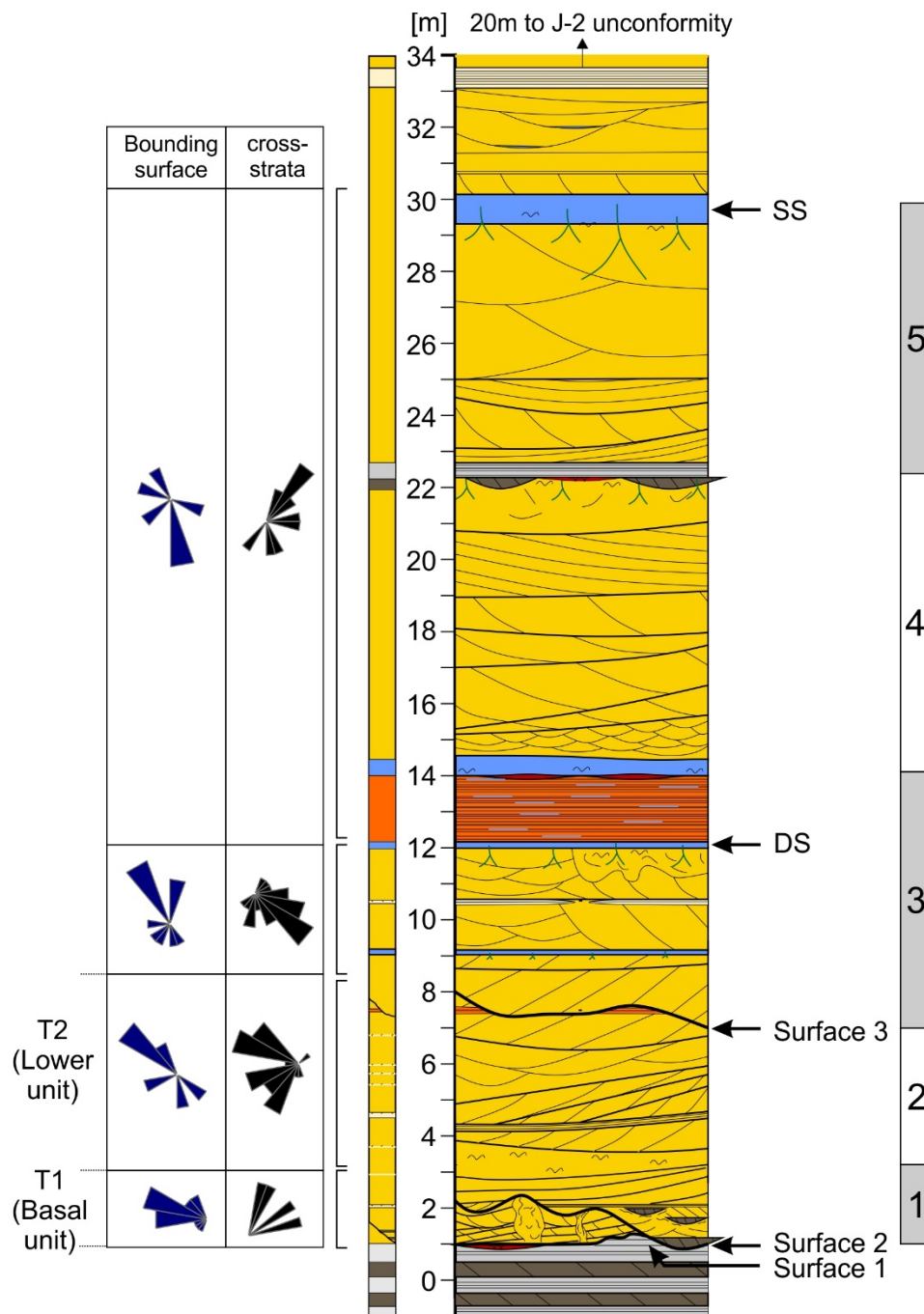
Sevenmile Canyon was chosen for this study as the lowermost deposits represent a marginal aeolian system (Sansom, 1992; 2018) marking the end of the fluvial system (Kayenta Fm) and into an era of increased aridity and the dominance of aeolian systems. In this region, the top of the Kayenta Formation forms a bench and is easily discernible by its reddish-brown colour and sudden change in topographical expression at the base of the first aeolian deposits (Figure 10.3). The Navajo Sandstone rises above this and largely consists of near-vertical outcrop faces (Figure 10.3C). Within the Navajo Sandstone, the succession is divided into five stratigraphical units based on the character of aeolian and non-aeolian sandbodies and the recognition of erosional bounding surfaces, some of which record large-scale deflation of the dune-field to a water-controlled planar surface (Figure 10.4).

Access for sedimentary logging occurred in short vertical sections, following contacts as best as possible. The UAV-based photogrammetric models later supplemented all observations in more detailed vertical and lateral sections in desk-based studies. Analysis of the virtual outcrop models captured true vertical thickness of sets, dip and dip direction of select cross-sets and bounding surface where exposed in a 3D sense. High-resolution photographs were selected to represent sections and used to trace all sedimentary structures (Figure 10.6; Figure 10.7). Georeferenced virtual outcrop models were used to extract location and altitude data in order to trace key surfaces that bound aeolian units (Figure 10.5). The apparent topographical relief from each surface was calculated using the altitudes of each marked location along the surface and deducting it from the lowest recorded altitude. All surface altitudes were recalculated to account for regional tilt of approximately three degrees to the west.

This section will detail two aeolian units, labelled the Basal Unit (T1) that marks the initial deposits of the Navajo Sandstone and the dominance of aeolian processes, and the Lower Unit (T2) that overlies and scours into Unit T1 (Figure 10.4; Figure 10.5). The surfaces that bound Units T1 and T2 (labelled Surface 1 – 3) are continuous on the scale of the virtual outcrop model and are studied in order to assess their relationship with the units' internal architectures (Figure 10.4 and Figure 10.5). Two additional outcrop-scale surfaces labelled 'DS' and 'SS' associated with damp to wet overlying sequences respectively were marked to assess the evolution of the system.

### 10.2.2 Results and Interpretations

At the two studied outcrops (Figure 10.6; Figure 10.7) the Navajo Sandstone is composed of sets of aeolian cross-strata partitioned and bound into 'Units' by prominent erosive surfaces traceable along the length of the virtual outcrop model. These are termed 'outcrop-scale surfaces' and labelled here as Surface 1, Surface 2, and Surface 3. Within the units that the surfaces bound individual sets of cross-strata are defined by upper and lower set-bounding surfaces that are less continuous than the outcrop-scale surfaces. The outcrop-scale surfaces (1-3), and internal architectures of two units (Basal Unit T1 and Lower Unit T2) are detailed and interpreted below.



## LEGEND

	SA1 Aeolian dune deposits		SA4 Soft sediment deformation, bioturbation, rhizoturbation, massive
	SF1, SF2 Fluvial channel, sheetflood / overbank		Rhizolith / bioturbation
	SA2 Dry interdune or sandsheet		Dune plinth deposits
	SA3 Damp interdune or sandsheet		M1 Mudstone (lenticular)
	CL1, CL2 Carbonate-rich lacustrine/playa deposits		Desiccation cracks

Figure 10.4: Composite log at Sevenmile Canyon. The log and data are derived from traditional sedimentological observations along observable transects, supplemented by the large-scale virtual outcrop models.

### *Outcrop-scale surfaces*

Figure 10.5 and Table 10.2 present the structure of the outcrop scale surfaces that bound aeolian Units T1 and T2. Surface 1 marks the boundary between Kayenta Formation and Navajo Sandstone and shows relief of up to 2.9 m. Where exposed, the aeolian deposits are observed overlying the surface with a sharp contact (Figure 10.6).

Surface 2 truncates aeolian sets in Unit T1 with a scalloped geometry (e.g. Figure 10.6). The surface is overlain by both fluvial and aeolian deposits that define its scouring nature. The surface shows relief of up to 2.8 m with the lowest recorded altitude coinciding with fluvial channel forms (shown on Figure 10.5) and marks an area where Surface 1 is entirely truncated. Along its length Surface 2 approximately mimics relief changes seen in Surface 1. Along the length of this studied outcrop, Surfaces 1 and 2 bound between 0 and 2.4 m of aeolian deposits of Unit T1.

Surface 3 truncates the upper most aeolian sets of Unit T2 and shows relief of up to 6.2 m with portions of the surface following similar relief changes along trend roughly mimicking Surface 2. Only aeolian deposits are recognised in sets directly above Surface 3 but they did not form part of this study. Surface 2 and 3 bound between 0.5 and 6.8 m of Unit T2 deposits.

Surfaces DS and SS are sharp and planar and show altitude changes of up to 2 m and 0.7 m along their length respectively. The two surfaces do not record continually changing altitudes as evident in Surfaces 1-3. The change in dip along their length translates to  $0.3^\circ$  towards the east for surface DS and  $0.2^\circ$  towards the west for surface SS.

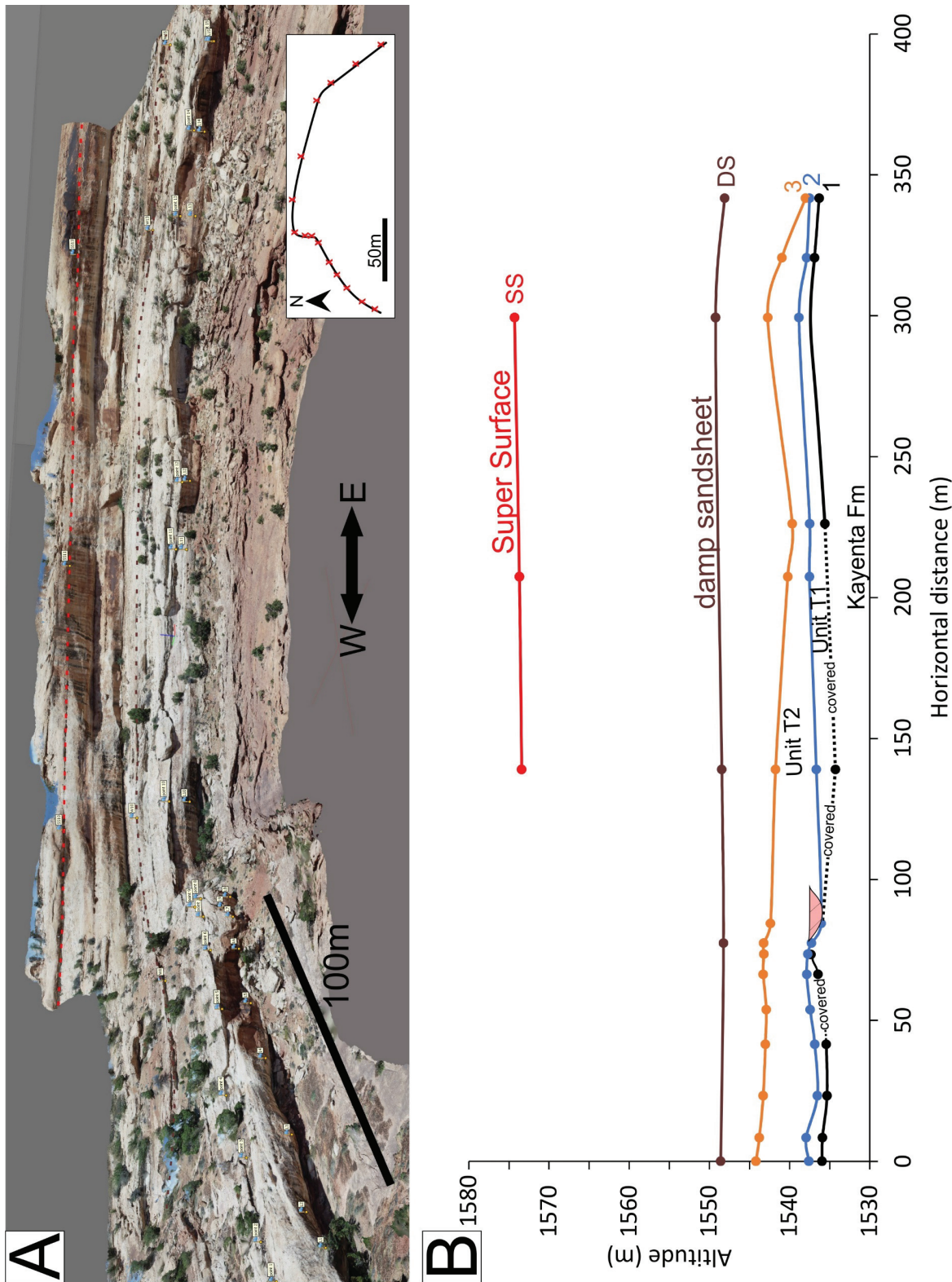


Figure 10.5: The georeferenced model used to observe bounding surface architectures. (A) Markers placed along outcrop-scale bounding surfaces to record precise coordinates and altitudes. The inset shows the plan view and approximate locations of each marker indicated by red x's. (B) The profile plots the altitudes of surfaces 1-3 and overlying marker surfaces (DS and SS) along a ~350 m transect, showing their apparent relief and relationships to one another. Surface 1 separates Unit T1 from the underlying Kayenta Fm, surface 2 separates Unit T2 and surface 3 forms the upper bounds of Unit T2. Surface's 1 and 2 display scouring and truncate underlying units. The two marker beds above include the base of a thick damp sandsheet deposit (DS), and part of a super surface (SS) that truncates sets for tens of kilometres (refer to log in Figure 10.4). The channel location is placed to show the relationship of the fluvial presence with relief changes and is not drawn to scale. All surface altitudes were recalculated to account for regional tilt of approximately 3° to the west.

Table 10.2: Observations of outcrop-scale surfaces and Units over the outcrop shown in Figure 10.5. The stratigraphical position of the bounding surfaces can be seen in the composite log (Figure 10.4).

Surface	Nature	Apparent relief (m)	Underlying set architecture	Ave. set thickness (m)	Type
1	Sharp	2.91	Stacked sets / Sheetfloods (Kayenta Fm)	unknown	Fluvial
2	Scour	2.77	Climbing sets	0.22	Transverse dunes
3	Scour	6.19	Scour-and-fill	0.52	Transverse dunes
DS	Planar	1.12	Crinkly horizontal laminae	2	Damp sandsheet
SS	Planar	0.7	massive to erosive	0.7	Flooding surface / bypass

#### Basal Unit T1

*Description:* The outcrop has a characteristic topographical expression distinct from overlying deposits in that it weathers more prominently than more resistant overlying aeolian Unit T2 (Figure 10.6). The basal aeolian deposits rest on a sharp sub-horizontal surface that directly overlies desiccated mudstone facies M1 with sand infill in the mudcracks. At this outcrop, Unit T1 ranges between 1 – 2.4 m thick, tapering towards the NNE where it is covered by scree (Figure 10.6A). Tabular to wedge planar climbing stacked sets typically separated by thin wind-rippled interdunes range in thickness between 8 – 69 cm (mean = 22.4 cm; N = 20) and exhibit tangential cross-stratification. The dips of the cross-strata range between 10° – 36° (mean = 23°; N = 8) with directions ranging between north-northeast and east-northeast (mean vector 042°; N = 4). Tangential cross-strata consist of grainflow strata, defined by their characteristic bladed shape towards the toesets, and are separated by mm-scale grainfall deposits. Dips of the set-bounding surface range between 1° – 27° (n = 16) with directions ranging between west and northwest (mean vector 283°). Soft sediment deformation (facies SA4) occurs near to diapiric structures that cross-cut vertically all sets. Soft sediment deformation is characterised by convoluted laminae and set surfaces as well as structureless sandstone (facies SA4).

*Interpretation:* Fluvial channels and sheetflood at the base of the outcrop marks the final deposition of the Kayenta Formation. Ponding followed by drying are indicated by the mud beds with cracked surface which were subsequently infilled by aeolian sands as dunes migrated over the surface (Bromley, 1992). The preserved mud beds were probably more resistant to erosion and no scouring is evident along the sharp and planar Surface 1. The weathering profile of Unit T1 is likely due to the higher arkosic nature of the rocks (higher feldspar and mica content) potentially as the underlying fluvial deposits are the dominant sediment supply reworked into aeolian dunes. Alternating packages of grainflow and grainfall along the length of the foresets indicate that aeolian bedforms did not grow very large, typically as the grainfall apron extends to the bases of smaller dunes (Kocurek and Dott, 1981). Dispersion of foresets and set-bounding surfaces is characteristic of climbing sinuous dunes migrating normal to their crestlines (Rubin and Carter, 2006) and migration of bedforms are approximated to be in a northeasterly direction. Variable thickness of wind-rippled interdunes indicate a variable migration rhythm by either grouped or solitary bedforms in dry conditions. Diapir-like soft sediment structures that cross-cut bounding surfaces and internal laminae were likely post-depositional, probably developed as escape features of over-pressurised water below the impermeable mud beds on which the aeolian sets lie (e.g. Hilbert-Wolf *et al.*, 2016). The post-depositional structures are truncated by larger overlying aeolian sets of T2 indicating a hiatus exists between the two units. Better evidence for water-table influence in Unit T1 is identified where Surface 2 appears sub-horizontal in Figure 10.5 (e.g. 150 – 200 m), however the nature of Surface 1 is unknown as it falls below ground-level.

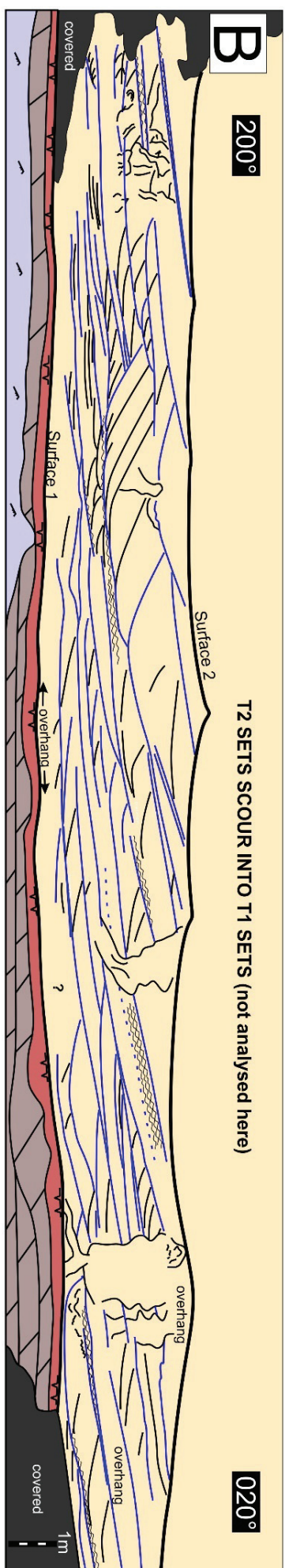


Figure 10.6: (A) Virtual outcrop model showing position of Unit T1 (red box). Scale bars have 20 cm divisions. (B) Interpreted outcrop panel showing the facies architectures and relationships with surfaces 1 and 2 that bound Unit T1. Note the erosive nature of the contact between T1 and T2 sets (represented by blue polyline in the 3D model and thick black line in panel interpretation).

### *Lower Unit T2*

*Description:* Unit T2 truncates basal unit T1 forming relief of up to 2.77 m. The erosive surface between the two units is traced to a well-exposed outcrop approximately seventy metres northeast of the outcrop shown in Figure 10.6, where it truncates Unit T1 entirely and into underlying sheetflood deposits (Figure 10.7). Two fluvial channels are identified at the base of the outcrop (facies SF1). Internally the channels contain a single isolated cross-bed set showing no coset formation and width-to-depth ratios of 5.1 and 7.8 (Table 10.3). The sedimentary structure within these channels are poorly preserved and no paleocurrent readings could be extracted.

Highly contorted and bioturbated aeolian sets surround fluvial channel forms with overlying sets scour into them forming topographic relief of up to 40 cm. Wedge planar to trough cross-bedded sets with tangential cross-strata dominate at this outcrop (Figure 10.7). Set-bounding surfaces are scalloped and discontinuous and show variable depths of scour into underlying sets. Set thicknesses are laterally variable due to the truncation of set surfaces by adjacent sets and range from 12 – 152 cm (mean = 51.6 cm; N = 17). The dips of the cross-strata range between 06° - 30° (mean = 21°; N = 24) with directions predominantly ranging between northwest and south-southwest (mean vector 255°). At set-bounding surfaces, interdune deposits may be absent as small basal scallops fill underlying sets with tangential grainflow strata. Where interdune surfaces are recognised they consist of thin wind-ripple strata (facies SA2) and wavy-crinkly strata with corrugated surfaces (facies SA3). Where present, the wind ripple plinth deposits interfinger with grainflow strata. The dip of the set-bounding surface ranges between 03° - 11° (mean 05°; N = 6) with directions ranging between northwest and southeast (mean vector 287°). Some aeolian sets may show massive and convoluted strata, soft-sediment deformation structures and bioturbation (facies SA4), but they are punctuated by sets that are dominated by grainflow deposition and scour depressions (facies SA1).

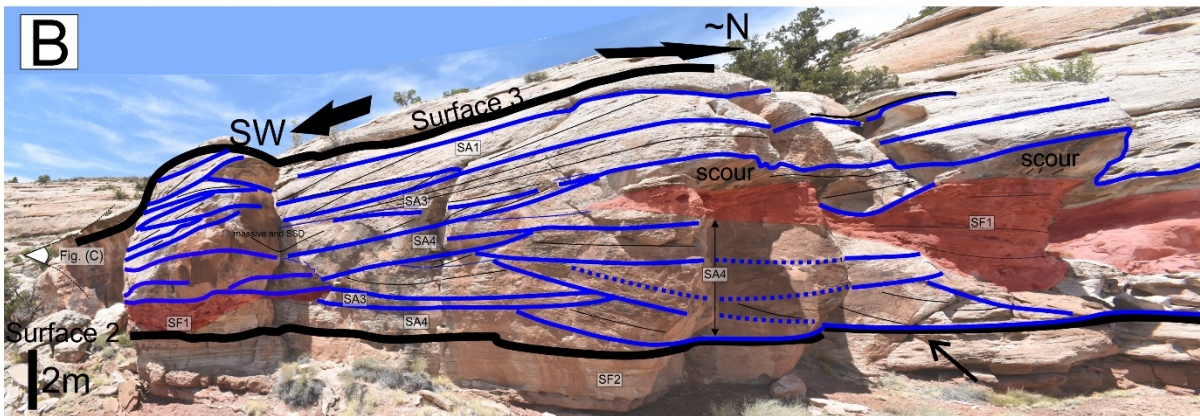
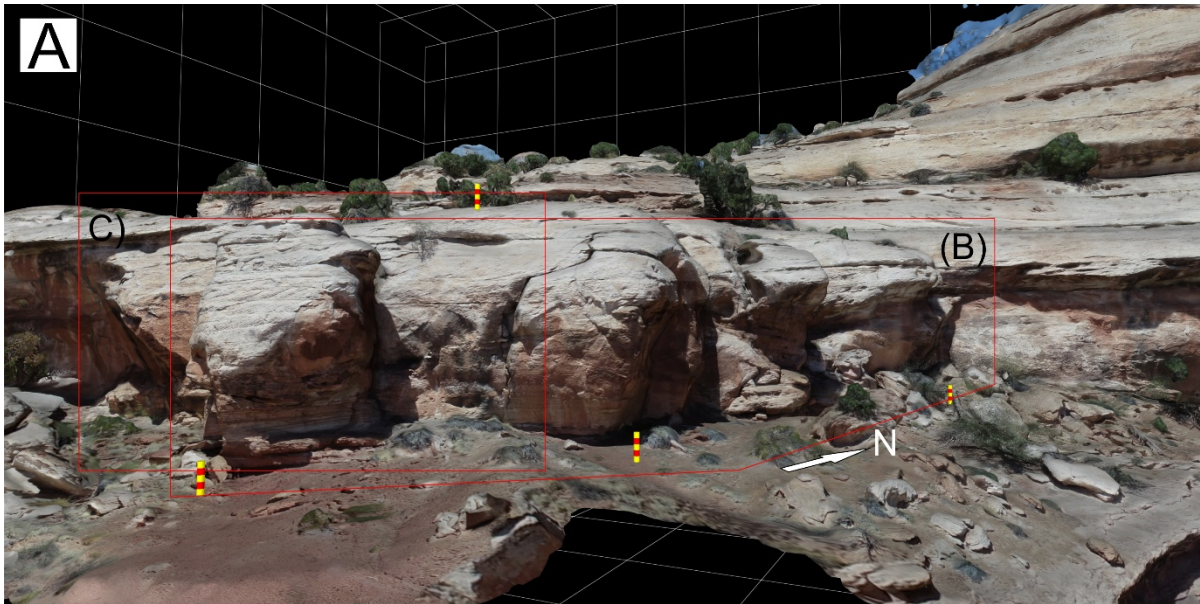


Figure 10.7: (A) Virtual outcrop model showing the positions of the lower aeolian unit T2 (red boxes). Scale bars have 20 cm divisions. Interpreted sedimentary structures in photo panels (B) and (C) were informed with on-site sedimentary logging and the virtual outcrop model. The outcrop-scale bounding surfaces (2 & 3) are showing by thick black lines. The fluvial channels cross-cut aeolian sets of Unit T2 and disrupted much of their internal architectures as represented by the abundance of facies SA4 (structureless to contorted sandstone). (B) In a direction perpendicular to migration aeolian set widths conforms with Surface 2 scour (arrow) and indicate scour occurred with bedform migration. Where present, aeolian sets scour into underlying fluvial channels fill and form topographic relief of up to 40 cm. (C) The depth variation evident in set troughs by scalloped bounding surfaces truncating adjacent sets is characteristic of a scour-and-fill geometry (Figure 2.16).

Table 10.3: Fluvial channel dimensions

Width (m)	Depth (m)	Width / Depth ratio
9.3	1.19	7.8 : 1
19.7	3.9	5.1 : 1

*Interpretation:* At this outcrop, the truncation of underlying sheetflood deposits indicate the complete erosion of basal Unit T1. Fluvial channels cut down into the sheetflood deposits and into aeolian dune sets, disrupting the surrounding dunes as evidenced by the contorted to massive aeolian sandstones surrounding the channel forms. Within the identified fluvial channels, poorly preserved sediment structure is indicative of high sediment load deposits suggesting a plastic, but still turbulent, flow. The width to depth ratios and pseudo-plastic flow deposition within the channel fills indicate that these channels are more like ephemeral alluvial fan top-modification channels found in arid environments (Hassan *et al.*, 2018).

Aeolian foreset dispersion reflects the span of dune troughs indicating these bedforms were likely sinuous three-dimensional dunes (Rubin and Carter, 2006). If dunes were migrating normal to their crestline, foreset and bounding surface dip direction indicate westward movement, by contrast to underlying T1 sets with a northeasterly migration.

Basal scallops indicate that periods of advance were punctuated by lee face reworking and subsequent fill by lee-face deposits (Kocurek, 1996). Grainflow strata interfingering with wind-ripple strata are typically identified as cyclic patterns due to seasonal changes in wind direction and are commonly referred to compound cyclic cross-strata (Hunter and Rubin, 1983; Loope *et al.*, 2001). The relatively larger set sizes of the Lower Unit (averages more than double than those in the Basal Unit), the dominance of grainflow strata over grainfall strata at toesets, and the presence of cyclic compound

cross-strata without evidence of crestline reorientation are indicators that dunes were larger than those in the Basal Unit (Hunter, 1977; Kocurek and Dott, 1981; Hunter and Rubin, 1983; Cardenas *et al.*, 2019).

Perpendicular to the migration direction (Figure 10.7B), set widths conform to the scalloped geometry of Surface 2 suggesting the scour occurred with the migration of dunes, or at least associated with dunes of the same size and of the same late phase of dune-field development. In sets viewed parallel to migration direction (Figure 10.7C), the variation in depth of set troughs and truncation of sets adjacent to one another is characteristic of an architecture consistent with a scour-and-fill geometry (e.g. Allen, 1970; Rubin and Hunter, 1982; Cardenas *et al.*, 2019).

Individual sets displaying convoluted strata, adhesion textures, corrugated surfaces and bioturbation are indicative of a fluctuating water-table (e.g. Crabaugh and Kocurek, 1983). This must have occurred with aggradation as autogenic processes of dune scour-and-fill alone would not result in the preservation of stacked multiple dune constructional periods (Cardenas *et al.*, 2019).

### 10.2.3 Discussion

Climbing stacked aeolian sets of Unit T1 fill and preserve in low relief areas of Surface 1. This is most evident within the initial ~70 m in Figure 10.5 as Unit T1 thins toward higher topographical relief on Surface 1. Where the highest altitude of Surface 1 exists, it coincides with the complete truncation of Unit T1 by Surface 2. Because dunes are observed gently climbing off Surface 1 with no evidence of dune scouring linked to the areas of low relief, it is hypothesised that Surface 1 is the antecedent topography of the Kayenta Formation. Depressions along this surface provide local accommodation space that were subsequently filled by small climbing dunes forming the thin sets of Basal Unit T1. Without any evidence of syndepositional moisture in Unit T1, the deposits likely aggraded there owing to local wind deceleration moving into the depression (Kocurek and Havholm, 1993). As all dunes from

both units were transverse in nature, the switch in migration directions between the Basal Unit and Lower Unit may indicate a variance in wind directions from southwesterlies to easterlies respectively. Palaeocurrent measurements show that westerly dune movement was subordinate within this region during Navajo times (Peterson, 1988), and the switch in migration direction is more likely attributed to wind steering within the topographically low areas of the antecedent Kayenta topography. Topographic wind steering is well recorded in modern environments with only small changes in the terrain (and air density within troughs) causing abrupt changes in the wind direction (e.g. Berry, 1981; Hesp and Pringle, 2001; Griffiths *et al.*, 2009 Hay, 2018).

The relationship between apparent surface relief and the thickness of Basal Unit is best shown by plotting the thickness of the unit against the relief change of Surface 1 at the same spatial reference (Figure 10.8A). The graph displays a negative correlation with good fit ( $R^2 = 0.66$ ) indicating the role the antecedent Kayenta topography had even as larger deep-scouring dunes from the Lower Unit T2 were unable to rework Unit T1 in low relief areas.

Sets of Unit T2 are suggested to represent a scour-and-fill type architecture with coeval development of relief formed on Surface 2. Little evidence of bedform climb and a lack of correlation between the number of stacked sets with unit thickness (Figure 10.8B) as expected in an aggradational scenario provides some confirmation of this geometry. Outcrop-scale Surface 2 that appears as continuous erosional relief could rather be defined as a lateral continuum of distinct scallops (e.g. Figure 10.6). The surface is interpreted to have formed with the passage of many dunes with variable scour depths, the ultimate relief reflecting the passage of the largest dunes with deepest scours. Deflation of Unit T1 appears to have been influenced by the antecedent topography as the erosional 'passage' roughly mimics relief changes in Surface 1, except in the case where fluvial channels are evident and the antecedent surface itself is scoured (Figure 10.5). The rapid fluvial incursion was likely channelled by the dunes and their associated troughs (Figure 10.5, Figure 10.7), however, with no evidence for fluvial palaeoflow this interpretation is speculative.

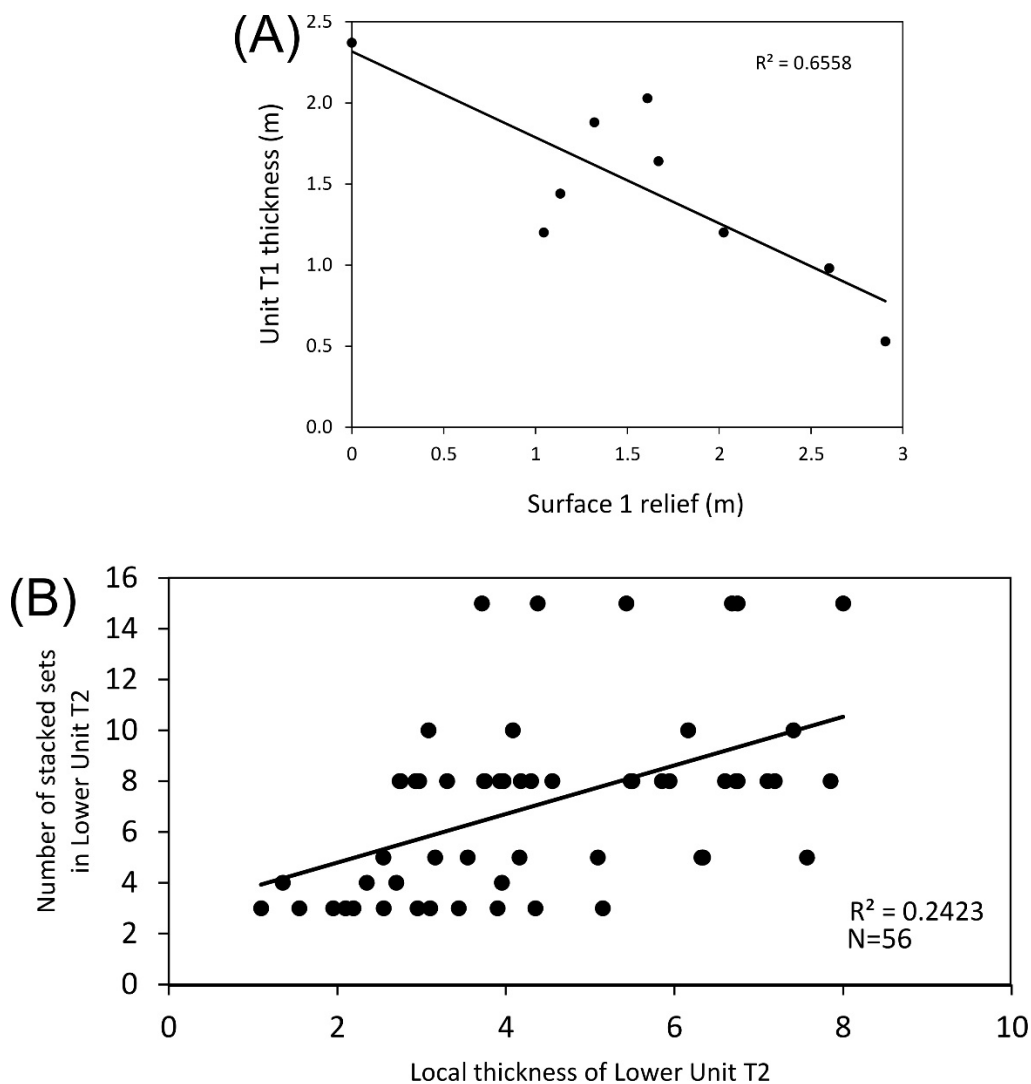


Figure 10.8: (A) Local relief of Surface 1 plotted against the thickness of Unit T1. The inverse relationship shows that the basal relief of Surface 1 controls the preservation of Unit T1. This provides partial evidence in favour of the hypothesis that the antecedent relief of Kayenta topography was a dominant control in preservation of early-phase dune accumulations (T1) by preventing full reworking of the later phase larger scouring dunes (T2). (B) Low correlation between the number of stacked sets in Unit T2 and the local thickness of the Unit indicates the quantity of sets do not control the Unit thickness as would be expected in an aggradational setting. The observation favours a scour-and-fill type geometry with variable scour depths between sets. Data in (A) and (B) is extracted from the virtual outcrop model with mm-scale accuracy.

Although the aeolian sets above Surface 3 were not part of this study, the mechanism of scour that created this outcrop-scale surface formed relief that approximately mimics Surface 2 (Figure 10.9). As Surface 2 is thought to be controlled by the underlying antecedent topography it suggests that this control translates even further into the second overlying outcrop-scale surface. Surface 3 is separated by at least two phases of dune growth with variation in architectures and overlies an average of 5.7 m of preserved aeolian stratigraphy above the antecedent topography (Figure 10.10).

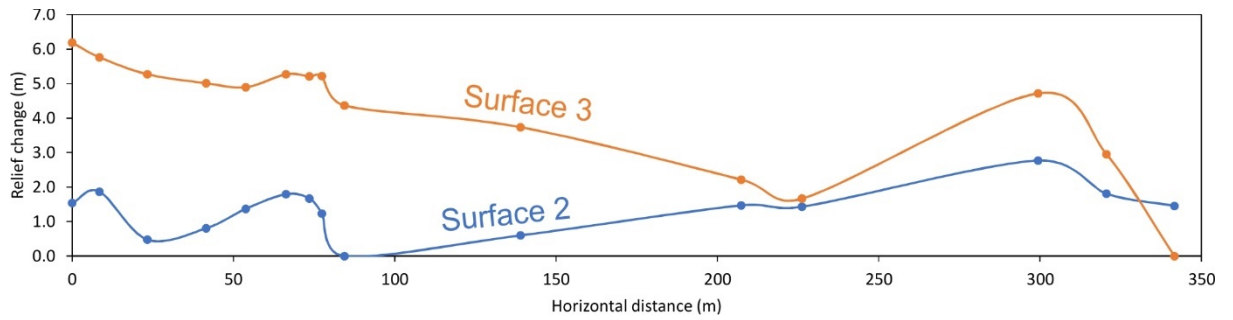


Figure 10.9: Local relief changes calculated by deducting the altitude at each point along the transect from the lowest altitude in the transect (where relief equals zero in the profile). The vertically exaggerated pattern shows an approximate mimicking of relief changes between the two surfaces. As Surface 2 approximately mimics the antecedent topography, it indicates the further translation of this control into the overlying preservation.

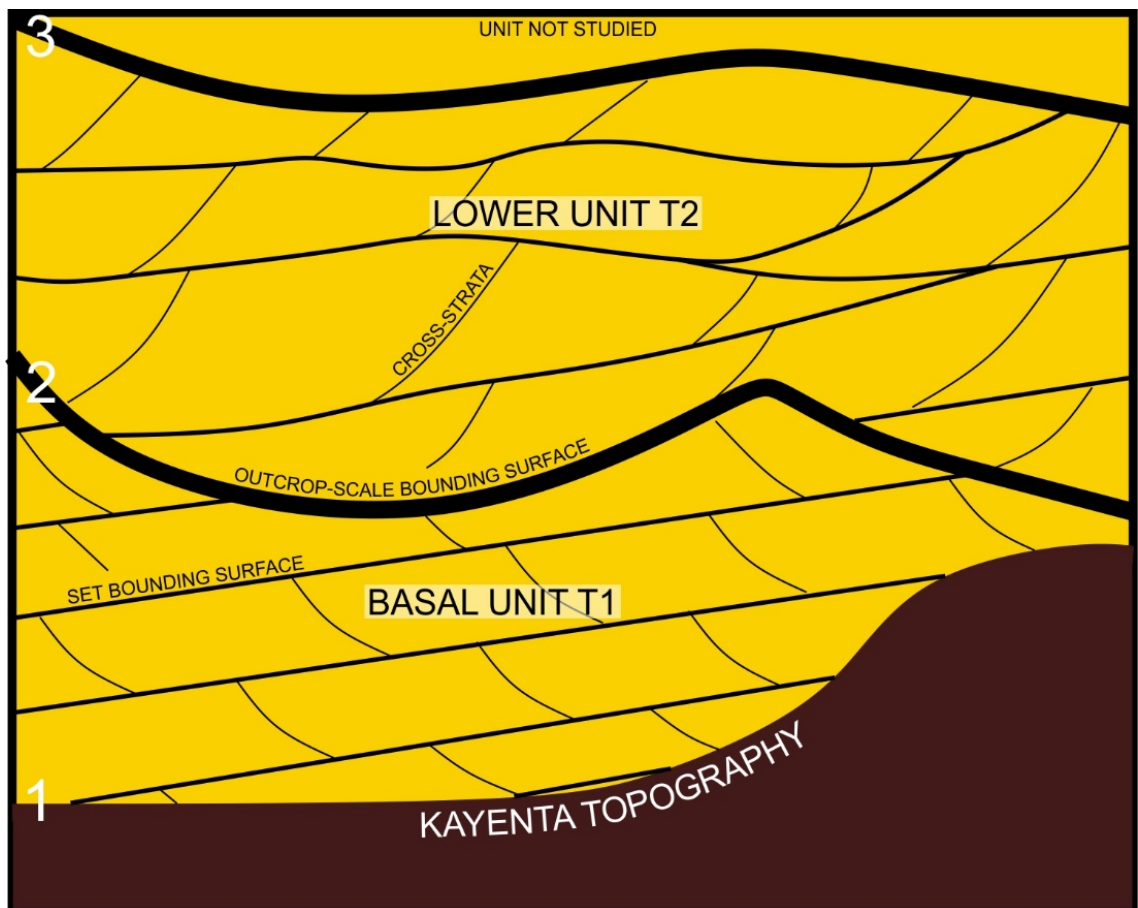


Figure 10.10: Schematic of the relationships between set architectures and outcrop-scale bounding surfaces parallel to the migration direction of bedforms. In the studied outcrop Basal Unit sets climb off a planar surface and fill topographical lows. In contrast, Lower Unit T2 sets dominantly show scour-and-fill geometries interpreted to have formed with the passage of many dunes with variable scour depths. The antecedent topographical relief of Kayenta Topography translates into outcrop-scale Surfaces 2 and 3 and is suggested to a key play a role in the preservation of overlying Units.

Aeolian sets that formed above the Lower Unit show abundant evidence for wet conditions and a rising water-table (see log in Figure 10.4). These conditions existed until the water-table became static and formed a laterally extensive and relatively horizontal surface, marked by abundant rhizoliths, bioturbation and separated by a thick damp sandsheet. This is indicative of a switch from preservation controlled by antecedent topography and a rising water-table, to one where the water-table became static. Two horizontal surfaces captured in DS and SS (Figure 10.5) mark a slowly rising water-table which eventually became static and led to large-scale deflation (Kocurek and Havholm, 1993). Subsequent deposition and preservation in the units overlying the horizontal surfaces do not show evidence for control of the Kayenta antecedent topography (Surface 1) and were primarily controlled by the relative position of the water-table with the depositional surface (Figure 10.4; Sansom, 1992).

Autogenically formed dune-scour topography may be differentiated from antecedent topography by following outcrop-scale surfaces, as this study shows. The dominant signatures of allogenic boundary conditions appear associated with antecedent surface topography and a variable water-table. The preservation of sets with scour-and-fill architecture and low bedform climb is likely to have been captured by a slowly rising water-table. The same relationships are evident in the aeolian Page Sandstone of northern Arizona where observations were backed by numerical modelling that demonstrates cannibalisation of early-phase strata is an expected outcome of autogenic dune growth and that early-phase strata is best preserved within antecedent depressions (Cardenas *et al.*, 2019; Swanson *et al.*, 2019).

### 10.3 Site 2: Hite

The section presented here focuses on an outcrop located approximately 15 km northwest of the historic town of Hite in southern Utah (Figure 10.11). Hite data acquisition covers an outcrop of approximately 900 m in width with a 3D face covering approximately 1900 m. The stratigraphical thickness of the Navajo Sandstone at the site is about 160 m. Previous regional studies on the Navajo Sandstone interpret the outcrops surrounding the region of Hite to display characteristics of a wet aeolian system (Marzolf, 1983; Blakey, 1994).

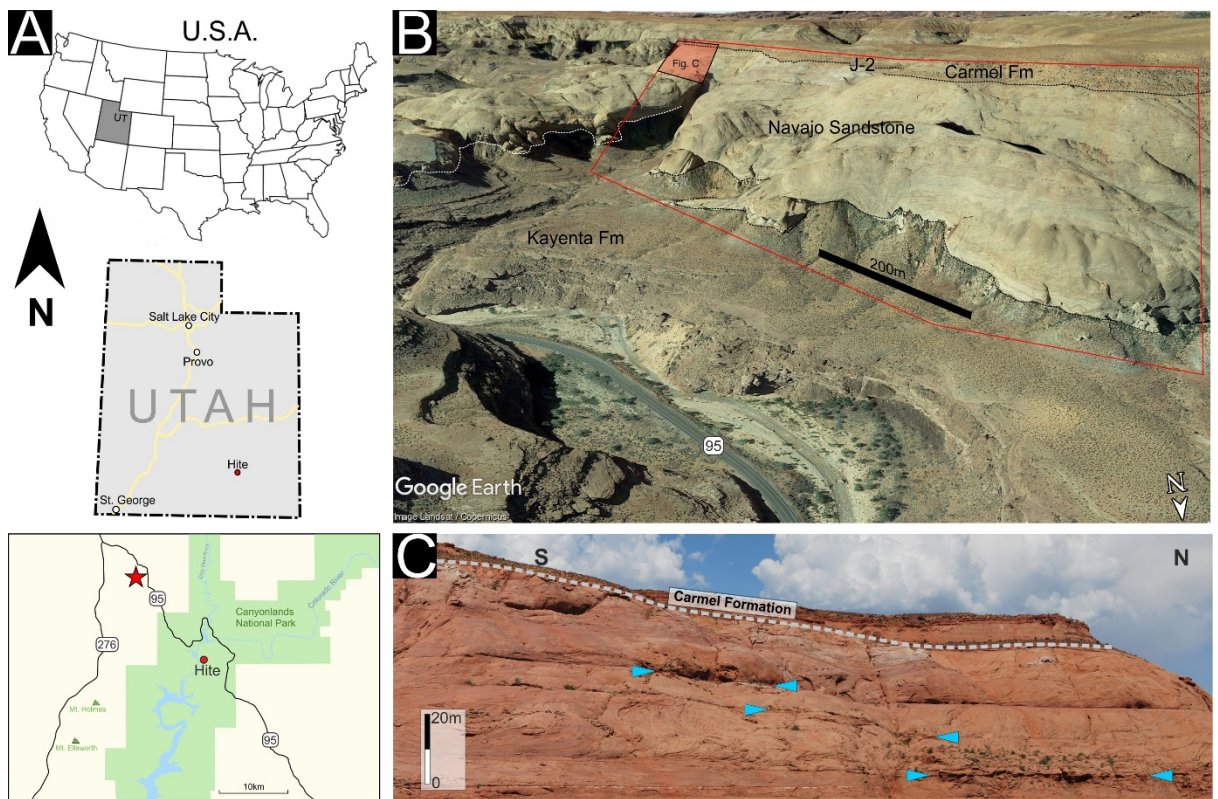


*Figure 10.11: (A) Location of the remote outcrop at Hite (red star). (B) Google earth oblique aerial view to the south. The figure shows the litho-stratigraphy of the site which includes the fluvial Kayenta Formation, overlain by aeolian Navajo Sandstone which is separated by the overlying marine Carmel Formation by the J-2 unconformity. The red square marks the area where UAV photogrammetry was acquired. (C) Ground-based photo panel of the top ~50 m of the Navajo sequence (location in shaded red in (B)). The blue triangles mark lenticular wet interdune surfaces that are typically found at Hite.*

### 10.3.1 Study Site and Methods

Hite was selected in order to characterise and interpret the facies architectures of a wet aeolian system located in medial to central erg setting. The study concentrates on four surfaces (labelled A-D) and bound units (1-2) chosen for their good exposure and lateral continuity, traceable along the entire length of the outcrop (Figure 10.12; Figure 10.13). The architectures of two units (1-2), separated purely for descriptive purposes with no implication of genetic association, are examined and detailed.

The three-dimensional study of the near vertical outcrop walls has benefited from the use of UAV-based photogrammetry. Traditional sedimentological studies were carried out where possible and complemented by observations using the virtual outcrop model to produce a composite log (Figure 10.12). Analysis of the virtual outcrop models (Table 10.1) captured true vertical thickness of sets, dip and dip direction of select cross-sets and bounding surfaces where best exposed. In addition, survey points placed on the georeferenced virtual models were used to extract spatial and altitude data in order to trace the surfaces that bound the studied aeolian units. In total eight survey points were taken for each surface A, C and D, and seven for surface B. The availability of this surveying technique allows a more accurate definition of the attitude of the extensive bounding surfaces and recognition of super surface candidates. The tectonic dip of the region is poorly constrained by regional geological maps reporting a dip of 2 - 3° towards the west-southwest, from a reading located approximately 15 km west of this outcrop. No 'flat' surfaces could be measured to confirm the data and the associations of the surfaces relative to one another are considered.

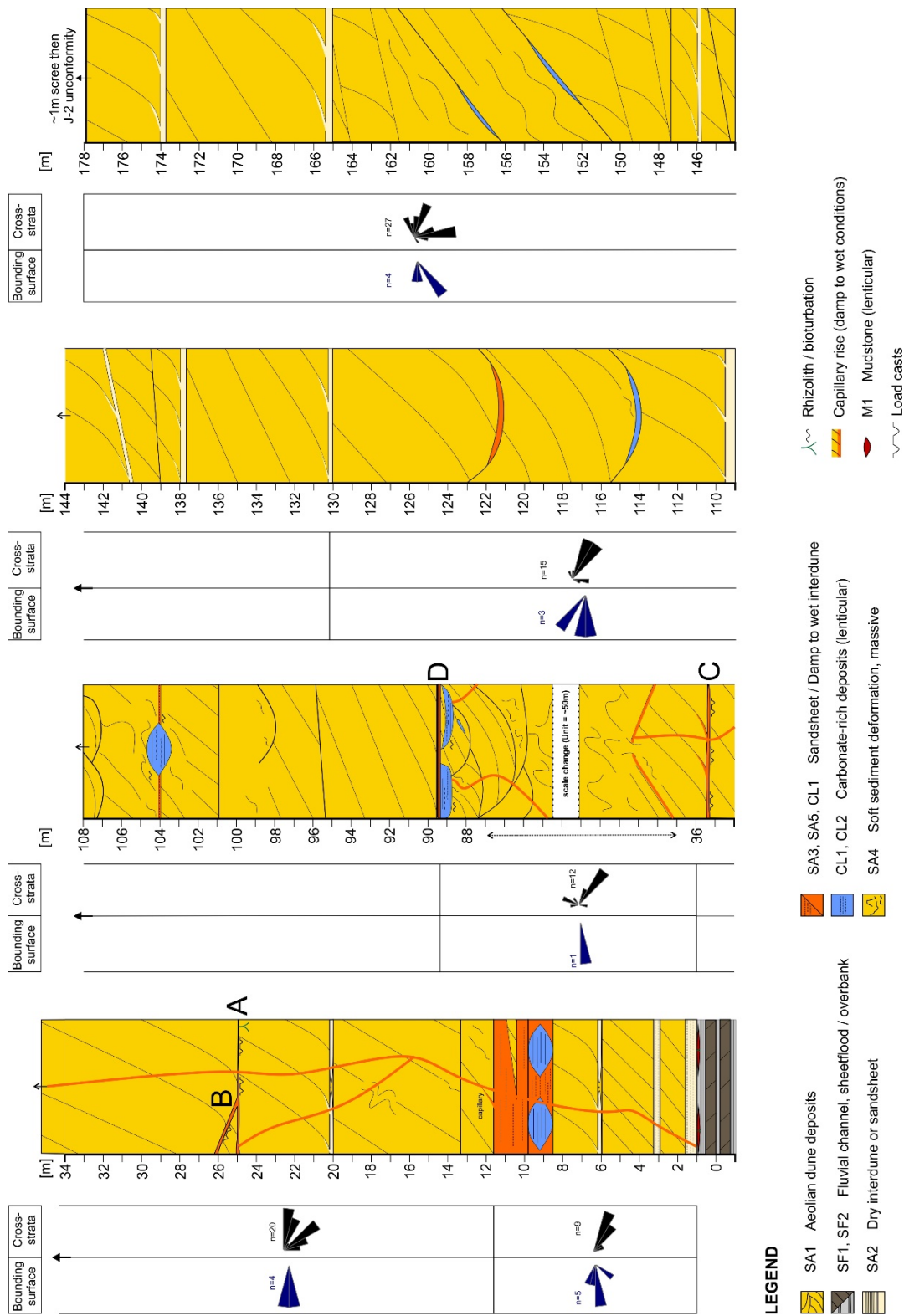


Figure 10.12: Composite log at Hite. The log and data are derived from traditional sedimentological observations along observable transects, supplemented by the large-scale virtual outcrop models. Surfaces A-D are described in text.

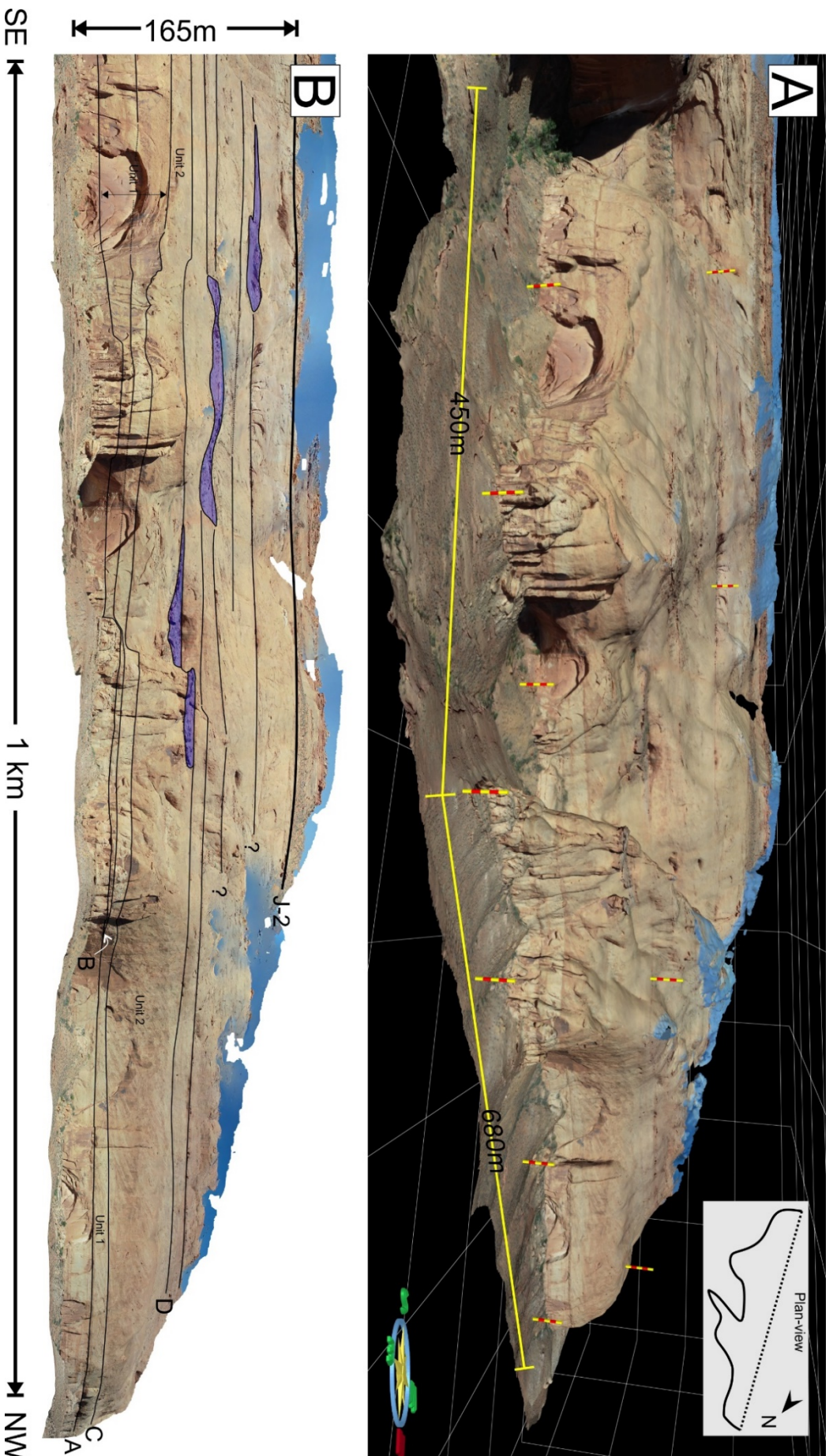


Figure 10.13: (A) Virtual outcrop model produced from 1035 UAV photographs of the outcrop. Scaled poles have 5m divisions. (B) A planar orthomosaic produced from a view to the southwest using the virtual outcrop model in (A). The surfaces (A - D) and units (1-2) are detailed in this study. The lenticular purple shaded regions are lacustrine deposits (facies CL1 and CL2).

### 10.3.2 Results

Bound by surfaces A and C, the lower division or Unit 1 widens from 10.8 m at the northwestern outcrop extent to its maximum thickness of 54.6 m at the southeastern extent (Figure 10.14). Unit 2 is bound by surfaces C and D and widens from 14.8 m thick on the southeastern outcrop extent to 46 m thick on northwestern extent. The opposing geometries reflect the relatively horizontal nature of surface A and D (Figure 10.14).

Surface A shows some undulations along its length but is relatively horizontal with an apparent dip of  $0.4^\circ$ . Unit 1 is divided by surface B, forming a wedge planar division rising off surface A on the northwest and widening to the southeastern outcrop extent with an apparent dip of  $2.1^\circ$ . Surface C approximately parallels surface B with an apparent dip of  $2.8^\circ$ . In contrast to the other surfaces, surface D truncates underlying strata, forming a planar surface along strike with an apparent dip calculated at  $1.1^\circ$  (see Figure 10.17A). Some relief is observed as shown by the survey points in Figure 10.14.

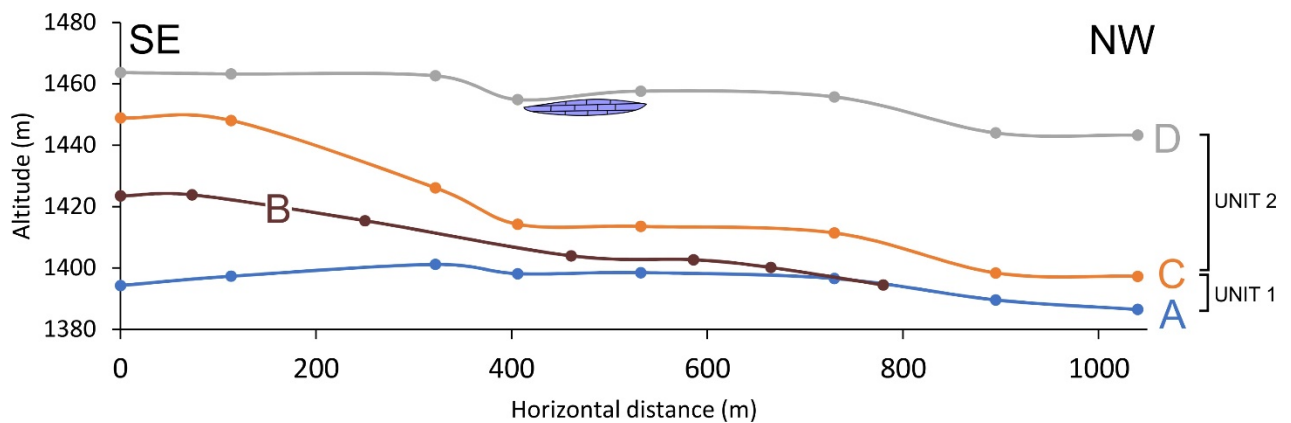


Figure 10.14: Survey points along surfaces A-D along an approximate SE to NW traverse (compare with Figure 10.13). Shaded region indicates lacustrine deposit.

The thickness of the interdune deposits above surfaces A, B and C vary considerably along strike (Figure 10.15). On the northwestern side of the outcrop, interdune deposition above surface A is very thin (mm-scale) showing signs of load cast structures and occasional rhizoliths at contacts. At this location, interdune deposition above surfaces B and C is conspicuously absent, except for tangential basal contacts and small plinths associated with some larger foresets (Figure 10.15A). Towards the southeast and roughly coinciding with surface B climbing off surface A (Figure 10.14), interdune deposits with damp (SA3) to wet (SA5) facies are evident ranging in thickness between 10 cm and 120 cm. Generally these interdune deposits are dark red in colour, massive and undulating (Figure 10.15B,C) (facies SA5), but may also be sharply bound and show cm-scale wavy-crinkly laminations of facies SA3 (Figure 10.15D). The wet interdune deposits of facies SA5 consist of silt to very-fine sub-rounded to sub-angular sand with a carbonate cement. Mound-shaped structures are observed along the surfaces and are associated with vertically bound massive sands directly below (Figure 10.15B). In places, dikes displaying branching and anastomosing geometry extend from interdune surfaces and cross-cut into overlying sets (Figure 10.15C). Capillary rise into toesets is common and easily recognisable with the striking colour variations between the red interdune surface and the yellowish-brown overlying aeolian dune sets.

#### *Internal Architectures*

At the northwestern half of the outcrop, sets within Unit 1 are generally tabular planar and exhibit tangential cross-stratification in a direction parallel to migration and trough cross-stratification in a plane perpendicular to this (Figure 10.15). Cross-strata show dip directions with a mean vector towards 130°. Complexity within co-sets occurs as surfaces climb and the unit increases in thickness. Within the southeastern half of the outcrop, superimposition surfaces become evident, however, no readings of internal strata could be taken from the virtual outcrop due to a combination of factors including the irregularity of the surface due to weathering / vertical joints, high reflectivity of the photography and lack of good exposure in three dimensions.

At its thickest (northwestern half), Unit 2 shows sets with tangential cross-stratification and well-developed top-sets with fully preserved dune topography (Figure 10.16). The mean dip direction of dune cross-strata is  $121^{\circ}$  (n=12). In places, the cross-strata and preserved topography are vertically cut by pillar structures showing highly deformed stratification or structureless sands (Figure 10.16). Planar stratification and / or structureless sands are also evident blanketing / draping the dune topography. Above the preserved topography, set architectures become increasingly difficult to identify with much of the space showing some form of deformation amongst southeasterly dipping cross-strata. Below surface D, Unit 2 is capped by trough cross sets that scour into the deformed strata below (Figure 10.16). Unfortunately, no readings were possible in these sets. Within the southeastern half, lenticular planar bedded carbonates hosting algal mats are evident directly below surface D (Figure 10.17B,C,D). The carbonate beds show an oblong shape with maximum observable extents of 178 m in length by 123 m width and are up to 4 m thick. As the thickness of Unit 2 decreases to the southeast, a single tabular planar set is evident (~11 m thick) scoured into by trough-cross sets (~3 m thick) bound by planar surface D.

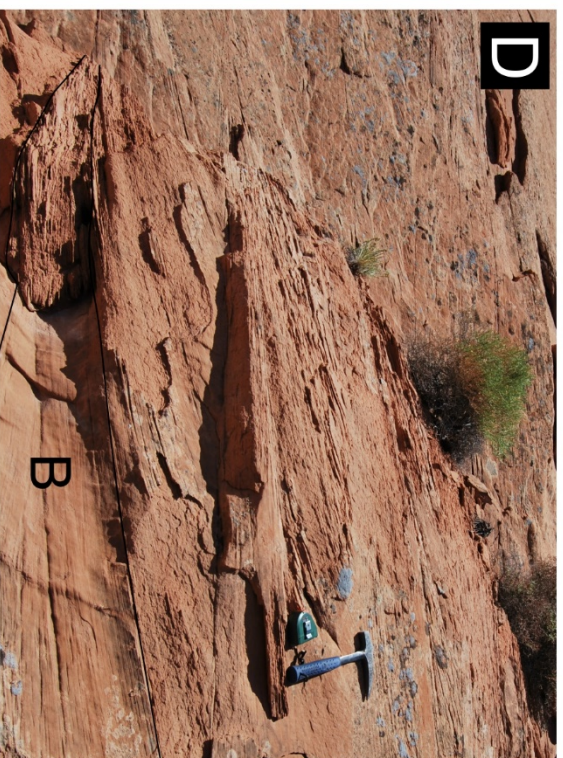
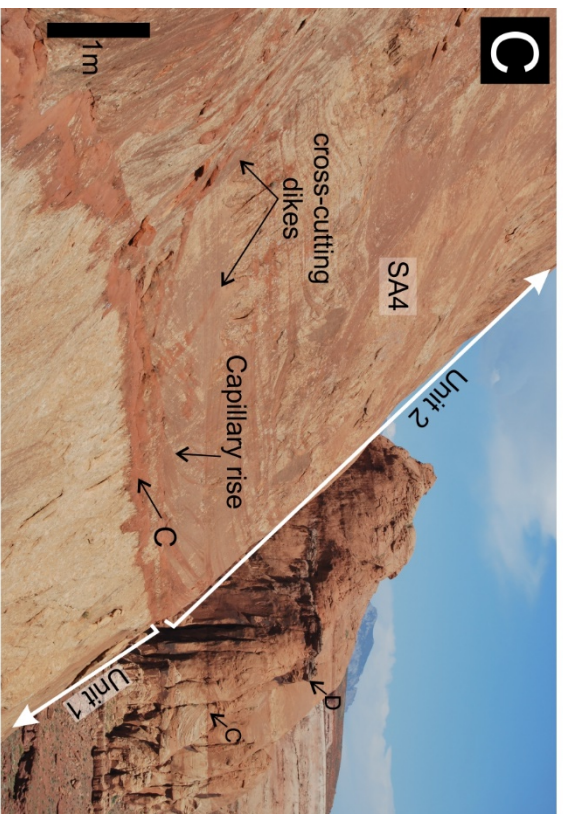
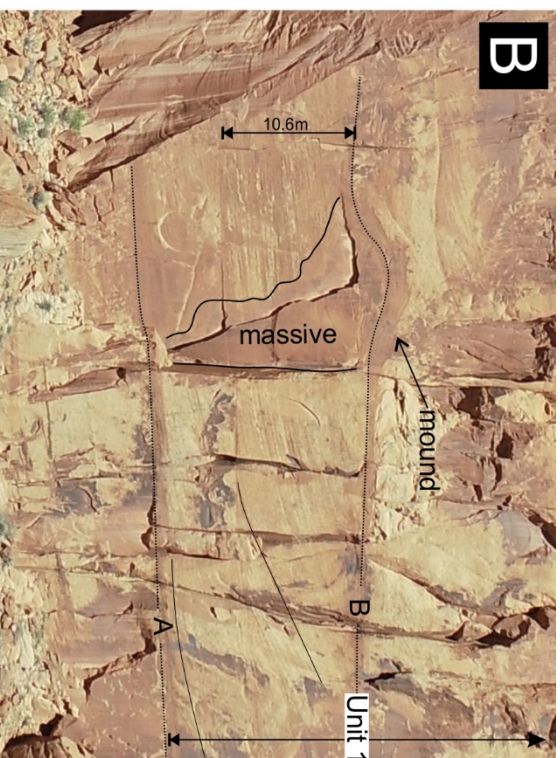
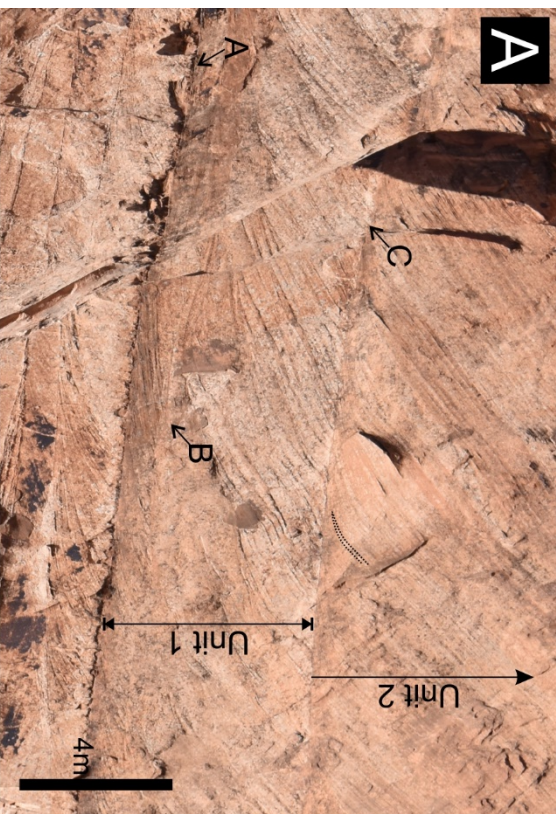


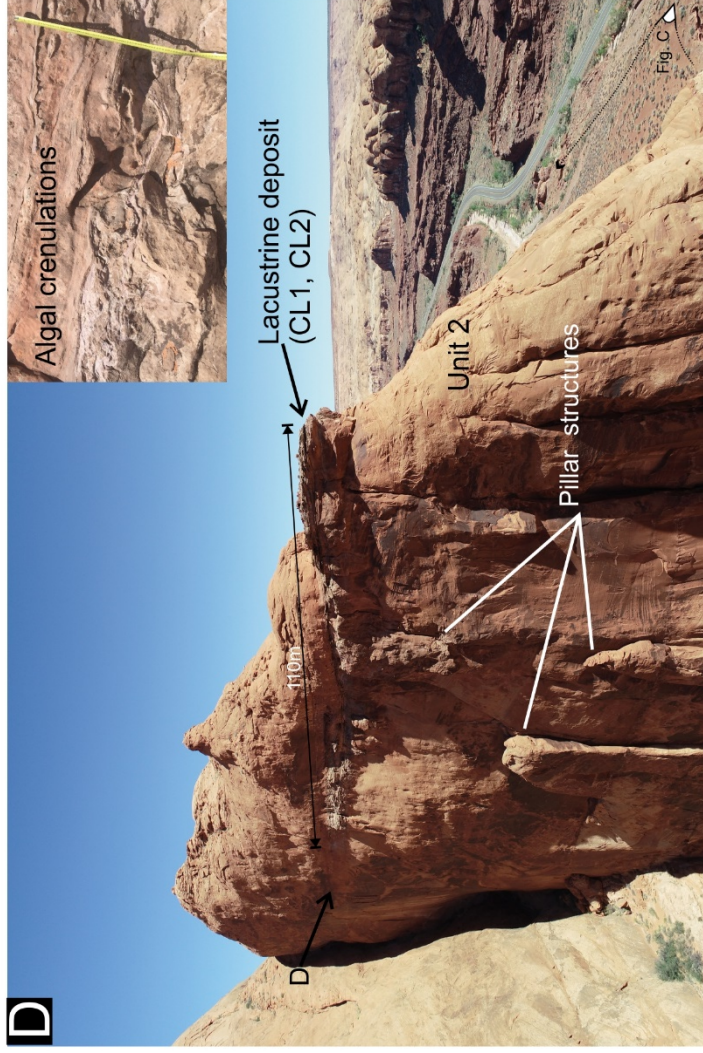
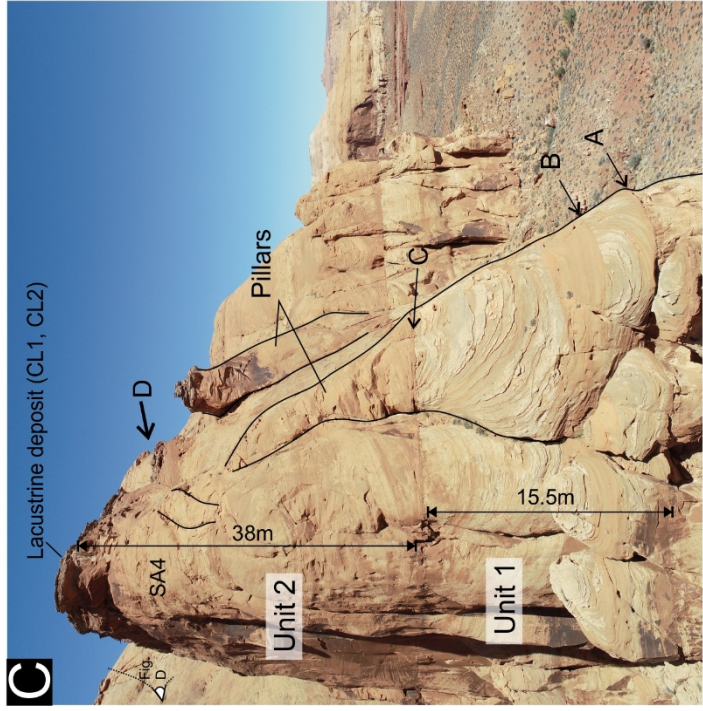
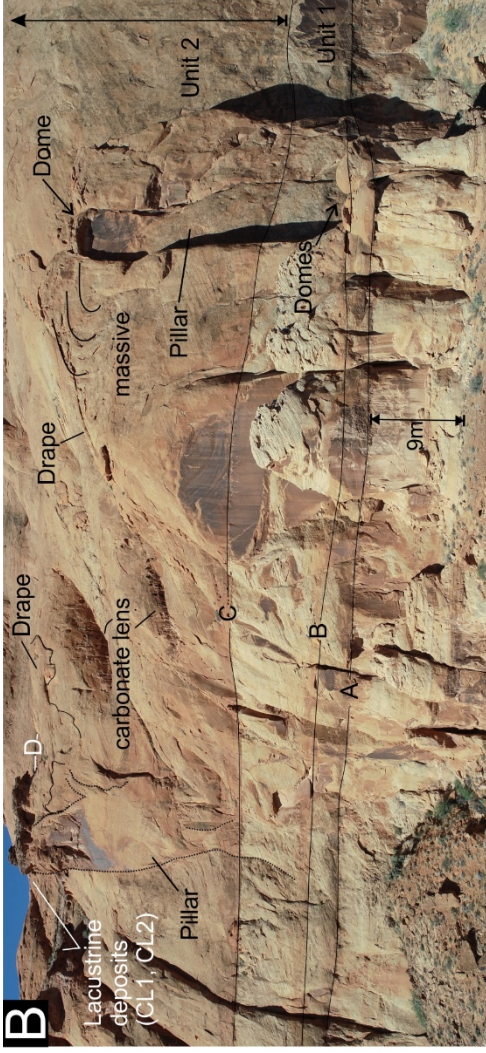
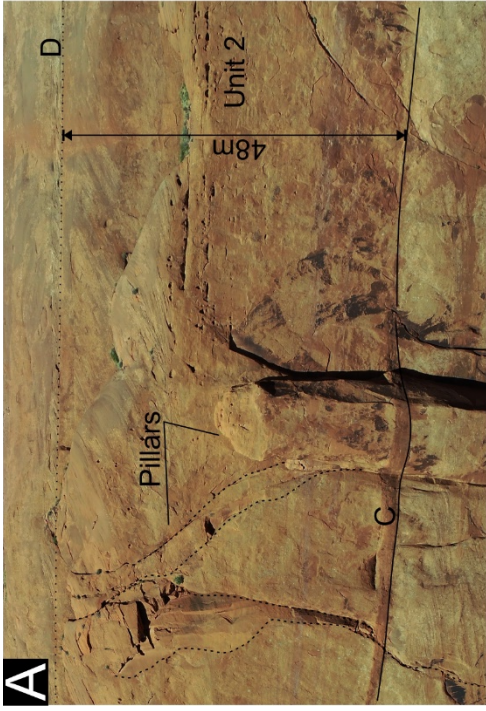
*Figure 10.15: (A) Unit 1 at its thinnest with the preservation of a relatively thin set (<1 m) bound by surface A and B. Surface A shows relatively thin deposits of adhesion strata and is associated with root casts and load structures that cut into and disrupt underlying sets. Interdune deposition of surface B and C is missing in this section and rather interfingering of wind ripple strata and grainflow strata (see annotation) is evident at dune toesets. (B) Surface A and B bounds two tabular planar sets containing tangential cross-strata (select annotated). Surface B forms a mound shape with overlying deposits wrapping around the mound indicative of post depositional deformation. Below the mound massive sands in the shape of a vertical dike cross-cuts the two sets. (C) Typically, interdune deposits of surfaces A-C show a massive and distorted appearance, with load casts into underlying sets, capillary rise draping tangential foresets that downlap into the interdune. In this instance, sand dikes extend from the interdune and cross cut overlying strata. (D) In places, interdune deposits are better bound and consist of wavy-crinkly laminae characteristic of damp interdune (facies SA3). In this example the overlying sets scour into the damp interdune.*

### *Pillar Structures*

Figure 10.17 shows vertical structures that are common throughout the virtual outcrop model. They appear as vertical joints occurring in pairs typically bounding or closely associated with massive and / or contorted strata. Their pillar-like shape shows branching and anastomosing geometries with widths ranging between 8 m and 20 m. The pillars almost always terminate at a surface boundary with features including dome shaped reddish-brown mounds and draped topography. These surfaces always associate with laterally extensive interdune deposits of the same colour (e.g. Figure 10.15B). Within Unit 2, a pillar structure terminates at the massive and contorted sands that drapes the preserved dune topography (Figure 10.16). This is also evident to the southwest of the preserved dune topography in Figure 10.17B where the draping of massive sands overlies an eroded profile above smaller carbonate lenses (~10 m wide). Below where the thick carbonate beds are preserved at the top of Unit 2, pillar structures occur on all visible sides of the outcrop. (Figure 10.17C, D). A higher resolution ground-based photo shows replacement textures of small compound climbing sets (~ 30 – 40 cm thick) preserved in a zone between two pillar-like structures (Figure 10.17E, F). No pillar structures above Unit 2 were evident in the observable outcrop.



Figure 10.16: Interperated sedimentary structures of unit 2. At this outcrop, internal stratification shows well-developed top sets and foresets indicating preservation of dune topography (see tracing and arrows in inset (i) and (ii)). Cross-strata indicates migration to the SE. Vertical pillar structures are evident in at least three places across this image (two labelled here). Features of the pillar structure on the left side of the image is shown in more detail in Figure 10.17B. Letters A-D indicate outcrop scale surfaces. Refer to Appendix A3 for high-resolution figure.



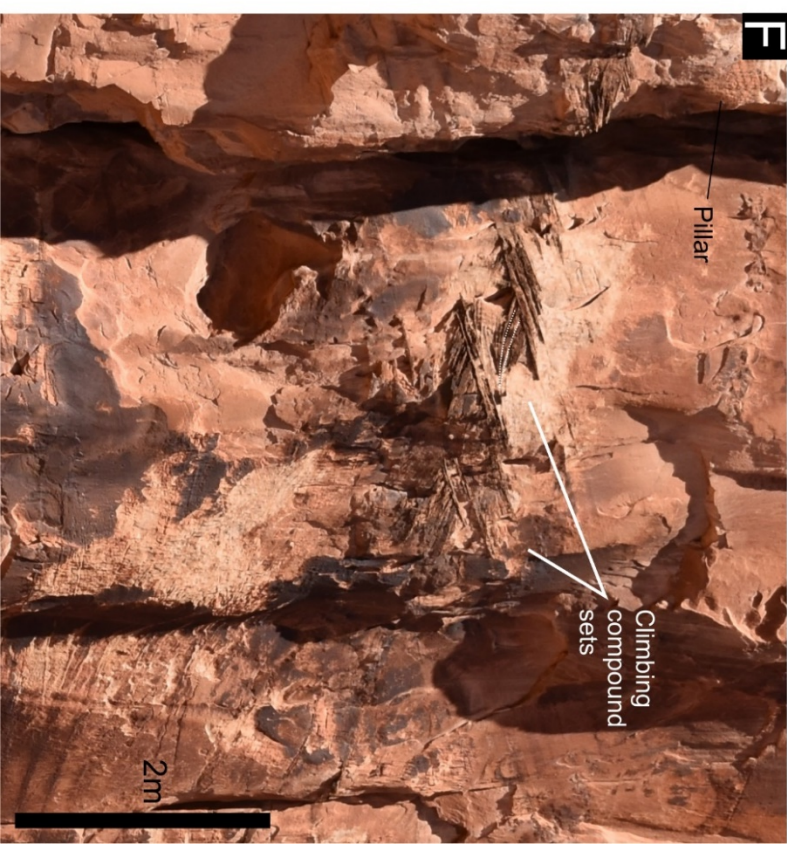
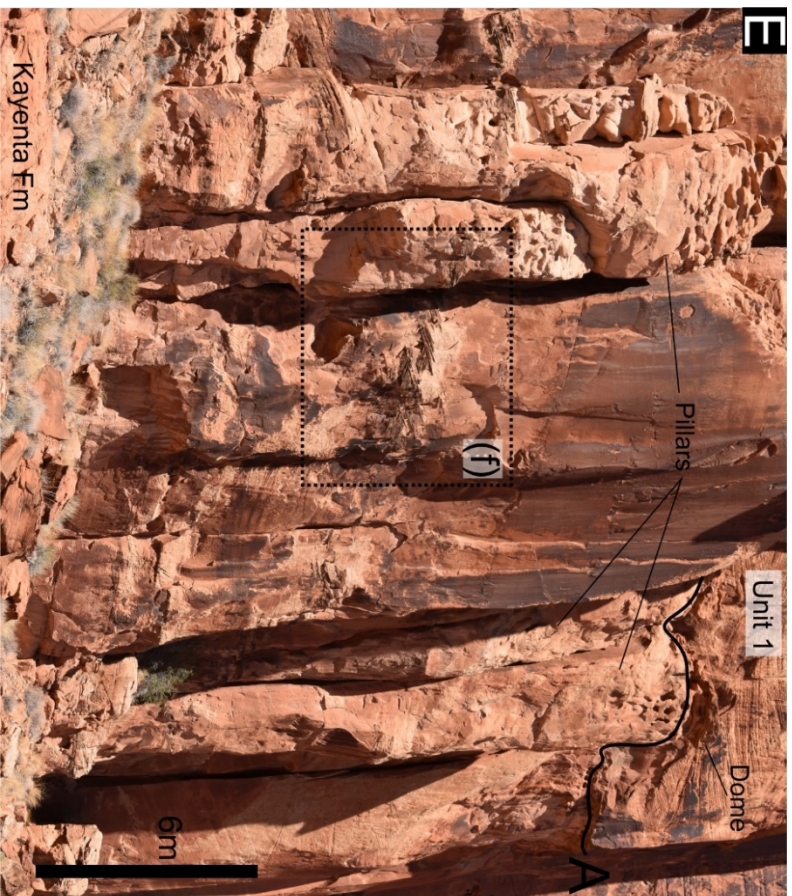


Figure 10.17: Common pillar structures and associated features at the Hite outcrop. (A) Surface D truncates underlying stratigraphy leaving a near planar surface. Pillar structure shows branching geometries and are typically associated with structureless sand or contorted laminae. In this instance two branches terminate at surface D. (B) Two pillar structures cross cut both Units, both of which are associated with massive sands draped over the topography that lies directly above a carbonate lens. On the left of the image the pillar structure terminates at surface D with planar bedded carbonates. (C) and (D) shows the pillar structures leading up to the lacustrine carbonate lens at surface D. The inset of (D) was taken from a carbonate bed at the same stratigraphical level while logging and shows well-preserved algal mats common in the carbonate beds indicating long-standing water. (E) The pillars are crossing sets below Unit 1. Note the intense deformation of the strata on the pillar structures. A dome shaped mound is evident where the pillar structure meets surface A and terminates. Zoomed in image at (f) shows how more permeable strata act as fluid conduits through the relatively small compound climbing sets predominantly consisting of grain-flow strata. Replacement textures of the compound sets are thought to be by carbonate bearing fluids as identified by differential weathering and elephant skin texture common of carbonate deposits.

### 10.3.3 Interpretation and Discussion

Carbonate deposits of the Navajo Sandstone constitute only 2 – 3% of the total volume of the formation (Peterson and Pippingos, 1979), the presence of which is significant in aeolian settings as it indicates the presence of water as groundwater, precipitation, or both, despite the arid setting (Dorney *et al.*, 2017). Precipitation has been evidenced in the Navajo Sandstone by annual monsoon-driven rains recorded by slump masses in annual depositional cycles of aeolian dunes (Loope *et al.*, 2001). Groundwater influences have been recorded by large-scale soft-sediment deformation features and liquefaction of sediments (Bryant and Miall, 2010), artesian-spring deposits (Parrish *et al.*, 2017), and interdune lake systems (Eisenberg, 2003; Dorney *et al.*, 2017).

The studied section of the Navajo Sandstone at Hite is interpreted as having been formed in a wet aeolian system because of the preponderance of features indicating a near surface water-table influence throughout the accumulation of Units 1 and 2 (Figure 10.18). This includes the presence of thick carbonate beds hosting algal mats (facies CL1, CL2), carbonate lenses (facies CL1), contorted strata and draping strata (facies SA4, SA5), crinkly-wavy bedding (facies SA3), capillary rise features and loaded set bases. In addition, palaeohydrological influence, as evidenced by vertical ‘pillars’ interpreted as upward injection of over pressurized water (e.g. Chan *et al.*, 2007), indicates a broader range of water-table conditions during the deformation and preservation of deposits. The most interesting of which occurs within Unit 2 as these influences are associated with preservation at the depositional surface, resulting in conservation of dune topography (Figure 10.16).

Observations of dunes cross-strata within sets from both units indicate sinuous crested dunes with a palaeoflow from the northwest (Rubin and Carter, 2006). Sets of cross-strata bound between surfaces A and C climb towards the southeast are interpreted as a result of migration of dune and interdune areas during periods of a rising water-table (Kocurek and Havholm, 1993). The addition of superimposition surfaces and thickening of Unit 1 in the direction of climb indicates that larger more complex dunes were able to form and preserve as the water-table rose (Figure 10.18).

Water breach at surface level must have occurred periodically as evidence through domes and associated draping strata, lacustrine deposits and carbonate lenses (Figure 10.18). These deposits and accompanying features are likened to observations of subaerial spring deposits or tufa mounds of the Navajo Sandstone found in areas surrounding Moab and Green River, Utah (Dorney *et al.*, 2017; Parrish *et al.*, 2017). The association of these features with the vertical 'pillars' almost always traced to and disappearing below contemporary ground-level indicates fluid escape came from depth under a positive pressure, possibly through the penetration of more impervious strata in the underlying fluvial Kayenta Formation (Figure 10.17E).

The configuration of contorted dune cross-strata increasing upwards within a set, yielding to the structureless (commonly identified as draping) sandstones above, may be related to some triggering event that affects saturated zones in the water-table. Liquefaction and / or fluidisation (as pore-fluid pressure exceeds lithostatic load) is thought to induce a progression of undeformed to deformed to structureless sand and are characteristic of clastic sills, dikes and pipes (Chan *et al.*, 2007). In the instance of Unit 2, the association of fluid escape deformation in direct contact with the unusual preservation of 'frozen' dune-trains indicates these are syndepositional features.

Thick carbonate beds hosting algal mats marks long-standing water accumulation likely forming within interdune troughs (e.g. Bromley, 1992; Eisenberg, 2003). These lacustrine deposits appear to have been fed and / or recharged by underlying dikes (Figure 10.17C,D). The temporal association of these deposits with the laterally extensive and the near-horizontal surface D may indicate an equilibrium of conditions leading to a static water-table and the formation of a super surface (Crabaugh and Kocurek, 1993).

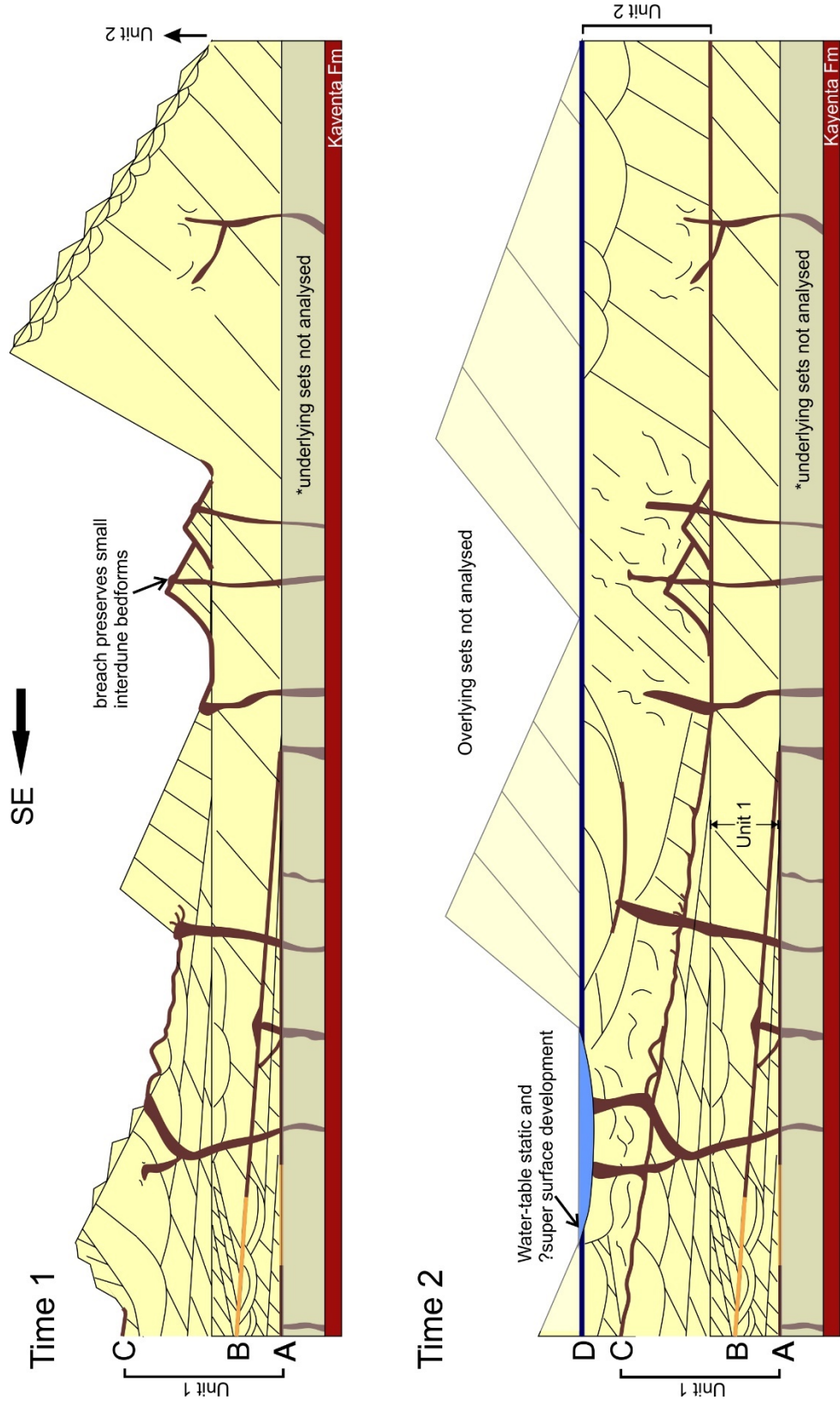


Figure 10.18: Schematic models that envision Hite development (not to scale). Time 1: The stratigraphic record shows sand dikes and associated mounds appear at every major surface on which dune sets climb. Surface C was likely a slowly rising water-table that was periodically static. Renewed deposition occurred with a lower water-table, however, reactivated dikes from lower surfaces brought water-lain sediments that periodically flooded the interdune corridors and in some instances covered and preserved active dunes which were eventually buried by larger downwind dunes. Time 2: Reactivated dikes shows periodic sediment disruption within the larger dunes as they advanced. Reactivated dikes flooded the next generation of interdune corridors. Pondered water deposited up to 4m of lacustrine sediments exposed directly below surface D. As the water-table rose to a new level, it led to large-scale deflation and super surface formation (surface D).

## 10.4 Site 3: Johnsons Canyon

The section presented here focuses on an outcrop located approximately 30 km northeast of the town of Kanab in southern Utah (Figure 10.19). Data acquisition from Johnsons Canyon covers an outcrop of about 600 m in width with a stratigraphical thickness of about 50 m. Previous regional work on the Navajo Sandstone of southern Utah indicates the well-exposed outcrops in the local surroundings can be interpreted as representing the preservation of a dry aeolian system in a central erg setting (Marzolf, 1983; Blakey, 1994; Loope *et al.*, 2012).

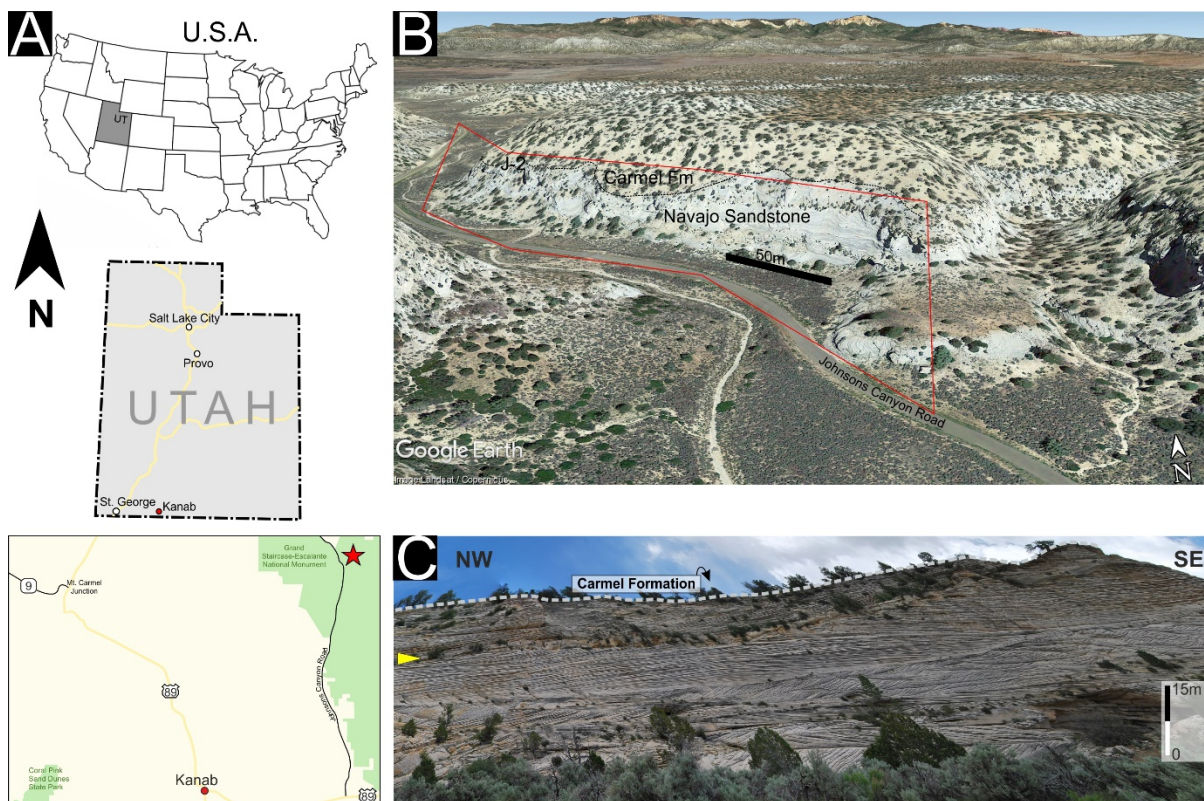


Figure 10.19: (A) Location of the roadside outcrop at Johnsons Canyon (red star). (B) Google earth oblique aerial view to the north. The figure shows the litho-stratigraphy of the site showing the J-2 unconformity that separates the overlying younger dominantly marine Carmel Formation. The red square marks the area where ground-based photogrammetry was acquired. (C) Ground-based photo panel of the outcrop displaying the top ~50 m of the Navajo sequence. The yellow triangle marks a thick dry sandsheet surface.

#### 10.4.1 Study Site and Methods

Johnsons Canyon was selected in order to characterise and interpret the facies architectures of a dry aeolian system. Previous studies local to this area largely focus on the interaction of the Navajo with the Kayenta Formation as the region is famous for well exposed outcrops where the two systems intertongue (e.g. Middleton and Blakey, 1983; Luttrell 1987, 1993; Hassan *et al.*, 2018). The fluvial-aeolian cycles are considered to represent fore-erg advancement over the Kayenta alluvial plains (Herries, 1993). The final fluvial cycle deposited the Tenney Canyon Tongue of the Kayenta Formation and is capped by a prominent bounding surface suggesting a period of nondeposition (Hassan *et al.*, 2018). Following this hiatus aeolian deposition ensued and the erg advanced as evidenced by large-scale aeolian dune sets of a unit termed the 'main body' of the Navajo Sandstone (Figure 10.20). This study focusses on the uppermost 50 m of the main Navajo Sandstone body below the J-2 unconformity that separates the marine Carmel Formation (Figure 10.19).

The near vertical outcrop used for this study was largely inaccessible and as such was captured with ground-based photogrammetry (Figure 10.2). Sedimentological analysis took place on the lower exposed roadside cuttings where possible. Field sketches, photo panels and the 3D virtual outcrop provided the necessary measurements for architectural analysis. A composite log was not produced for this site due to the vertical nature and inaccessibility along the traverse. Focus is placed on large-scale architectures traced using photo-panels and informed using the virtual outcrop model (Figure 10.21).

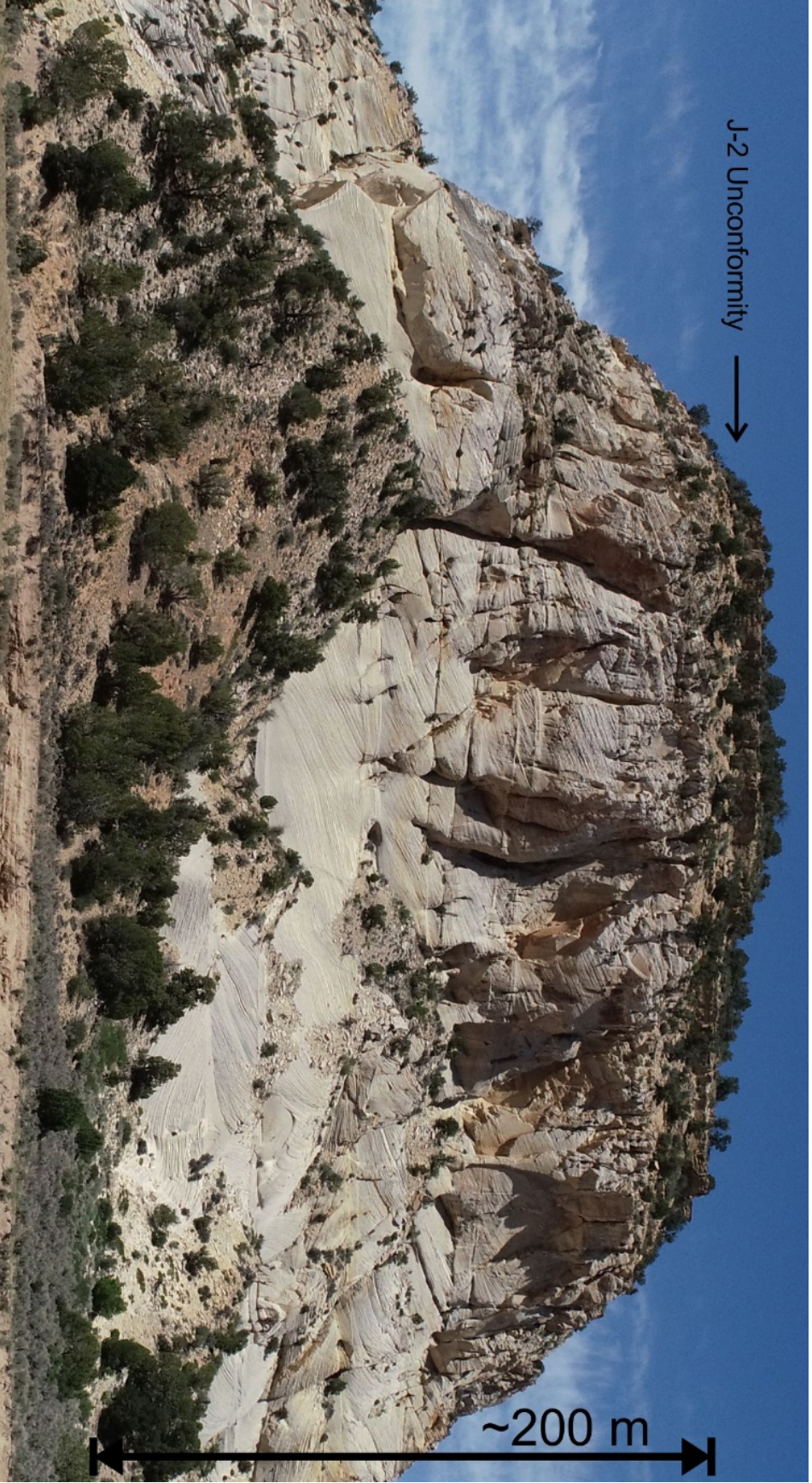


Figure 10.20: The thickness of the 'main body' of the Navajo Sandstone. This outcrop approximately overlies the Tenney Canyon Tongue of the fluvial Kayenta Formation and represents erg advancement and the deposition of large-scale aeolian bedforms. The studied outcrop includes the top ~50 m of this unit in a road exposure about 2 km northwest.

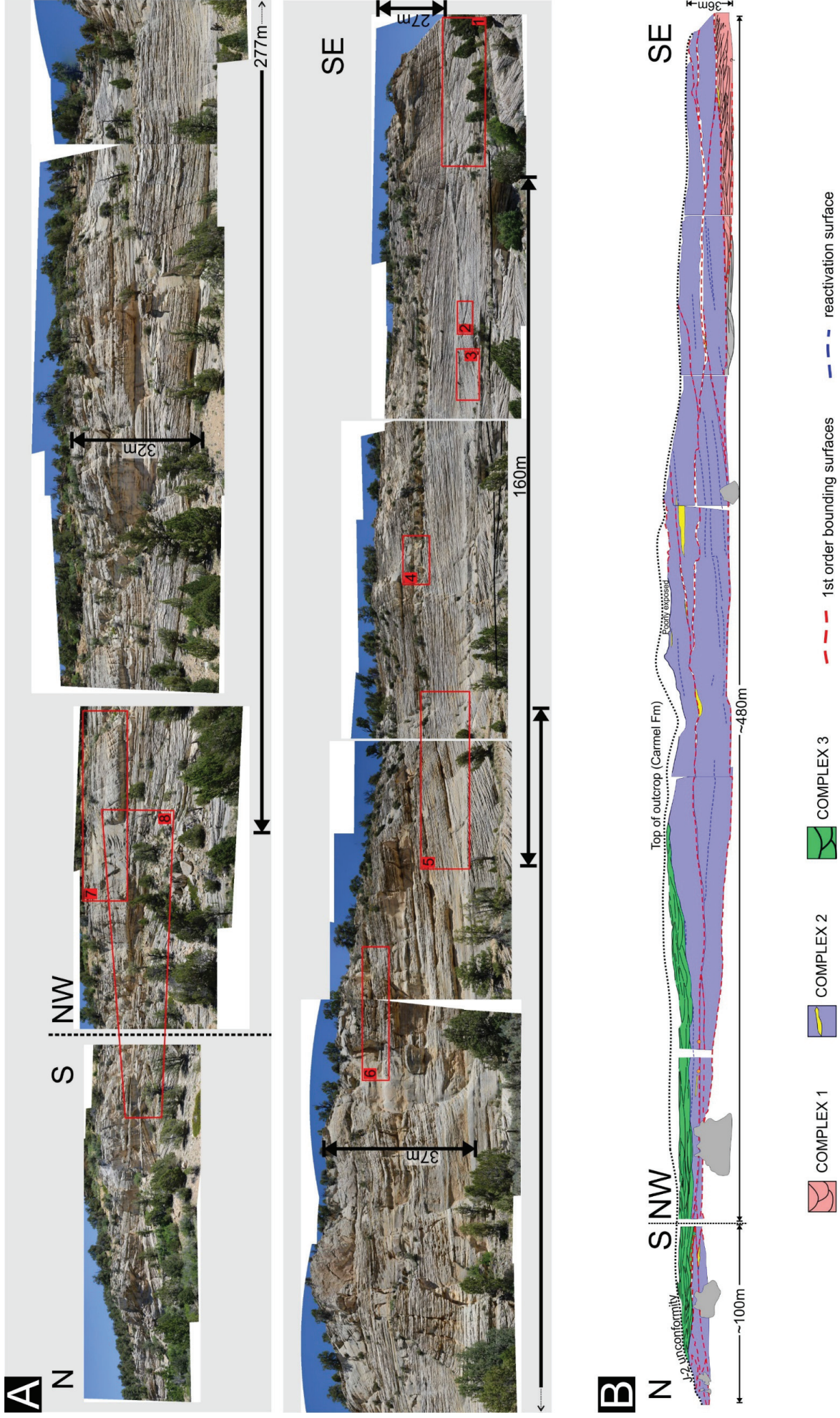


Figure 10.21: (A) Stitched photo panels of the outcrop shown in Figure 10.19. The panels are divided here to fit the page and a continuous length panel is provided in digital Appendix A4. The red numbered boxes are cross-referenced in Figure 10.23, Figure 10.24 and Figure 10.27. (B) Traced and interpreted architectural complexes of photo panels in (A). The schematic diagram is shown in Figure 10.22

## 10.4.2 Results and Interpretations

*Sedimentary architectures observed in the study are separated into three complexes, each with their own architectural style considered in terms of dimensions, shape and distribution of set bodies and orientation of foresets and bounding surfaces (Figure 10.21; Figure 10.22;*

Table 10.4). The differences in the complexes are detailed below by both quantitative and qualitative analysis.

### *Complex 1*

*Description: Complex 1 is characterised by relatively small stacked cross-stratified set bodies (2.4 m average thickness, 19.3 m average width;*

Table 10.4) with a wedge-shaped geometry. The smallest sets occur at the base of the complex and consist of tangential grainflow strata that interfingers with an underlying wind-rippled to adhesion-rippled sub-horizontal surface that is up to 70 cm thick. The surface occasionally follows a low wavelength concave downward pattern in places. At the southeastern limit there is also evidence of the larger sets scouring into underlying sets of cross-strata (not analysed in this study) (Figure 10.23). The set bodies within the complex typically contain asymptotic foresets consisting of wind ripple / grainflow couplets that cyclically scoop into underlying sets forming scalloped bases (Figure 10.23C). Individual sets contain apparent upslope and downslope cross-strata dip directions confirmed by associated dips with a bimodal palaeocurrent distribution from a 260° to 320° mode and a 340° to 80° mode (see stereonet in Figure 10.23). Bounding surface dip directions range between 90° and 260° with dips averaging at 16° (N = 14). The complex occupies a relatively small portion of the outcrop with a maximum observed thickness of 12.9 m at the southeastern extent of the rock face, tapering towards the northwest and to a complete truncation by Complex 2 (Figure 10.21; Figure 10.22).

Table 10.4: Difference in scale, geometry and migration vectors for the three architectural Complexes at Johnsons Canyon.

	SET BODY	MAX THICKNESS		APPARENT WIDTH		PALEOCURRENT		APPROX. MIGRATION	
		RANGE (m)	RANGE (m)	RANGE (m)	RANGE (m)	DISTRIBUTION	DIRECTION	DIRECTION	
<b>COMPLEX 1</b>	SMALL WEDGE PLANAR CROSS-SETS	1.1 – 4.7	6.9 – 37.3	ACCUTE BIMODAL	NNW				
<b>COMPLEX 2</b>	VERY LARGE TROUGH CROSS-SETS	12.9 – 16	154 – 345	OBTUSE BIMODAL	SW & NW				
<b>COMPLEX 3</b>	INTERMEDIATE-SCALE TABULAR CROSS-SETS	1.9 – 3.4	30.5 – 54.7	ACCUTE BIMODAL	WNW				

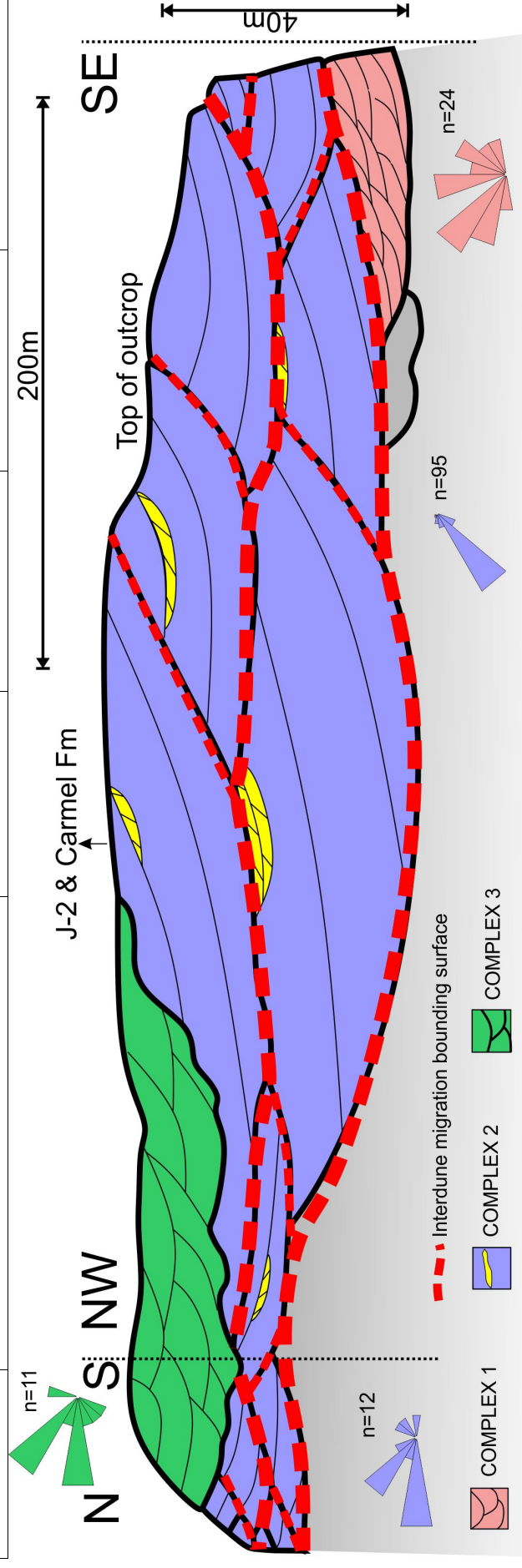


Figure 10.22: Schematic diagram of outcrop at Johnsons Canyon. Rose diagrams are colour-coded to each Complex and contain foreset orientation. The grey base contains sets that are covered by vegetation and do not form part of this study.

*Interpretation:* The wind-rippled planar surface at the base of the complex is interpreted as a sand sheet deposit on which incipient dune growth occurs as evidenced by the horizontal, wind-to-adhesion-rippled surface (Kocurek and Nielsen, 1986) and low-wavelength slipfaceless bedforms interpreted as sand patches or proto-dunes (Kocurek *et al.*, 1991). The larger overlying sets may scour into this surface completely truncating it in places. The upslope and downslope dip directions indicate upslope and downslope migration of superimposed bedforms or along crest migration of three-dimensional bedforms (Rubin and Carter, 2006). The confirmation of these dip directions favours the observations and hypothesis of Rubin and Carter, 2006 (their figure 74; [https://cmgds.marine.usgs.gov/data/seds/bedforms/movie\\_pages/movie74.html](https://cmgds.marine.usgs.gov/data/seds/bedforms/movie_pages/movie74.html)). In their attempt to simulate the architectures of this exact outcrop the simulation required reversing transport directions and an along-crest (longitudinal) component of sediment transport that is nearly as large as the transverse component of transport. The sets architectures were mimicked by two sets of straight-crested superimposed bedforms experiencing thirteen complete cycles of migration during the time the main (straight-crested) bedform completed one wavelength. As a result, the superimposed dunes fluctuate in height, with one set growing while the other diminishes (Rubin and Carter, 2006). Grainflow / wind-ripple couplets that form cyclic basal scallops is indicative of these superimposed bedforms migrating across the lee slope or along the trough of the main bedform. The intersection of the troughs occurs as two sets of bedforms form topographically low scour pits (Rubin, 1987). The set architecture is compared with a contemporary example of two separate trains of superimposed dunes on the flanks of a linear draa of the Namib Sand Sea (Rubin and Carter, their figure 76). Interaction occurs as the dunes are oriented at approximately 45° to the main bedform with one set migrating up-flank and the other down-flank.

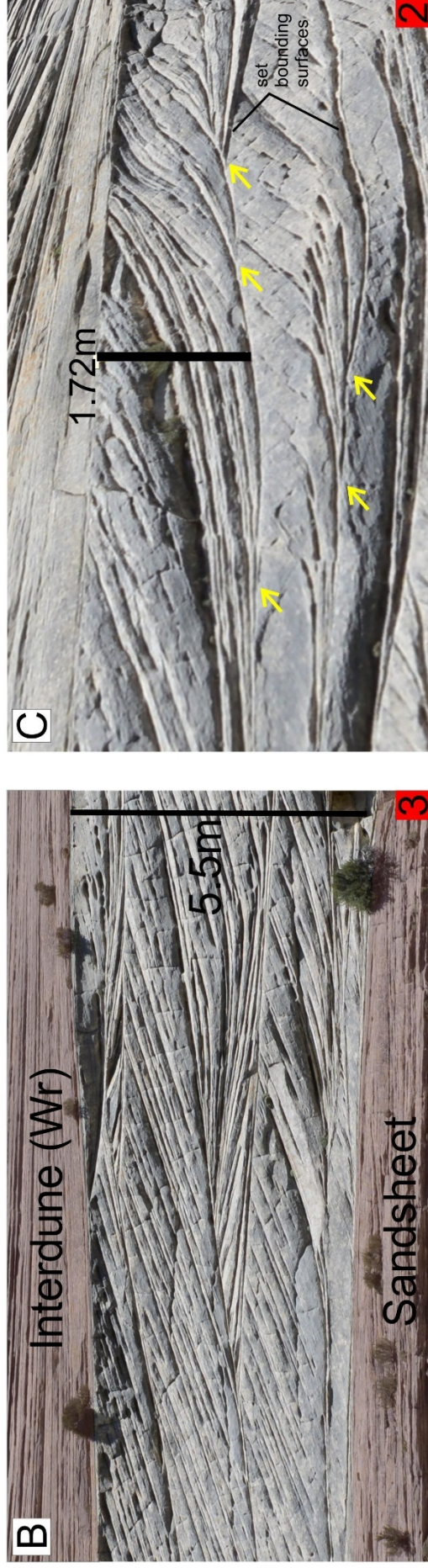
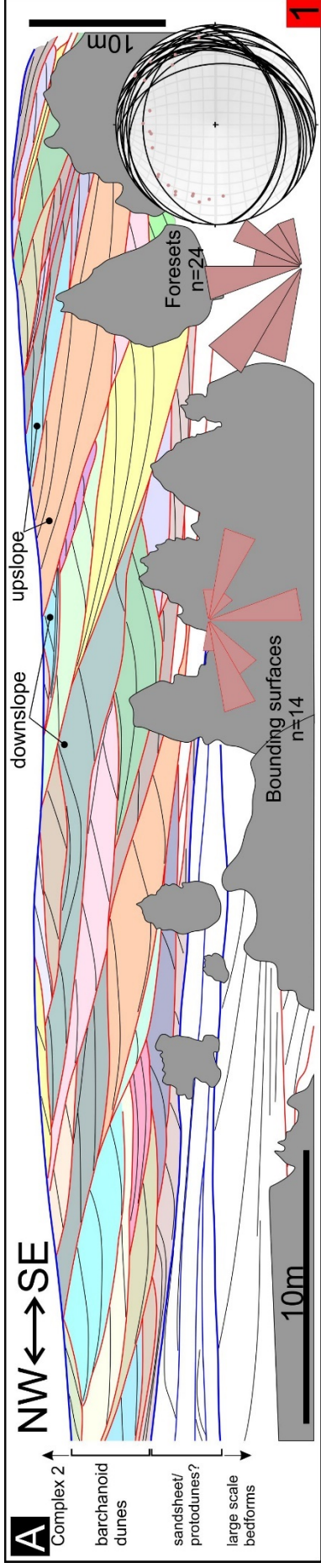


Figure 10.23: (A) Portion of complex 1 showing the geometry of the set bodies with marked examples of individual sets showing apparent upslope and downslope apparent dip directions. The inset stereonet and rose diagram shows this approximate oblique bimodality. Set colours are for visual effect only. (B) The complex is bound by a lower sandsheet deposit hosting protodunes and an upper interdune deposit of the overlying Complex 2. Asymptotic foreset fill scoured basal depressions as the bedforms advanced. (C) Migration of the superimposed bedforms form scalloped surfaces with intersecting troughs (yellow arrows). The red numbers are cross-referenced from Figure 10.21.

## *Complex 2*

*Description: Complex 2 is characterised by the occurrence of very large-scale stacked set bodies (14.3 m average thickness, 234 m average width,*

Table 10.4) with a trough-shape geometry. The complex occupies the full lateral extent of the outcrop with a maximum thickness of about 37 m (Figure 10.21).

Sets are bound by thick (up to 2.5 m) tabular packages hosting thin (mm -to- cm-scale) laminae interpreted as wind-ripple dominated strata (Figure 10.24A, B). These tabular bodies truncate underlying set bodies (not analysed) and follow long-wavelength undulating pattern along the extent of the outcrop forming up to 12 m of topographical relief (note vertically exaggerated schematic in Figure 10.22).

Majority of the sets show a unimodal palaeocurrent with an average foreset dip direction spanning between 203° and 316° (average 234°; N = 95), however, sets on the northern margin of the outcrop deviate from this and show an average foreset dip direction ranging between 082° and 266° (average 324°; N = 12) (Figure 10.22). These set bodies are separated by a zig-zag pattern of set bounding surfaces, which marks the prominent change in dip-azimuths (Figure 10.27B).

Internally tangential foresets consist dominantly of wind-ripple / grainfall couplets, mostly ordered into tabular bodies typically up to 12 cm thick and separated by prominent ~2 cm thick pin-striped laminae (wind-ripple strata) (Figure 10.25). Occasionally these tabular bodies are much thicker, up to 40 cm, and taper towards the set base with a bladed geometry which cross cut surrounding laminae (Figure 10.24A). These bodies are always massive and show polygonal fracturing at their surface. Other features include sporadic wavy-crinkly laminae of facies SA3. Set bases are dominated by wind-ripple strata that interfingers with the asymptotic foresets. Grainflow strata could not be identified at set bases, however this may be due to lack of access to the outcrop face and observations rely on photographic evidence.

Commonly observed at the top of the sets are lenticular bodies consisting of small stacked tabular planar sets of cross-strata superimposed onto the main set (yellow bodies in Figure 10.21 and Figure 10.22, close-up of features in Figure 10.24C). The superimposed sets reach up to 85 cm thick in packages up 3.6 m thick and 20 m wide. Three readings were extracted using the virtual outcrop model and foreset dip directions were unimodal, ranging between 198° and 206° with steep dips between 36° and 42°.

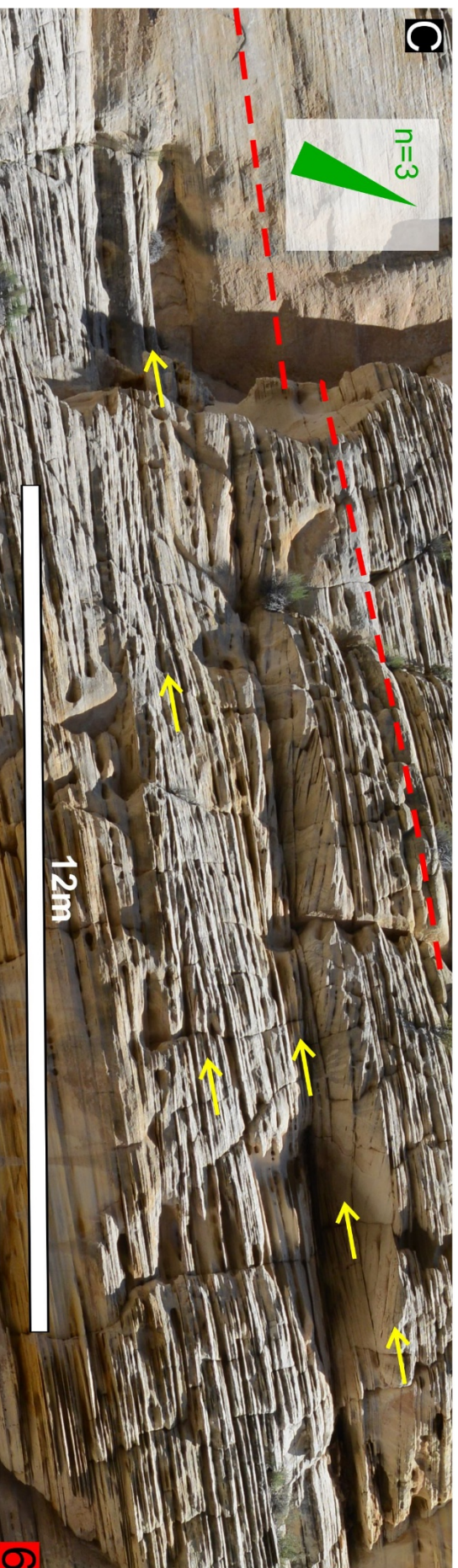
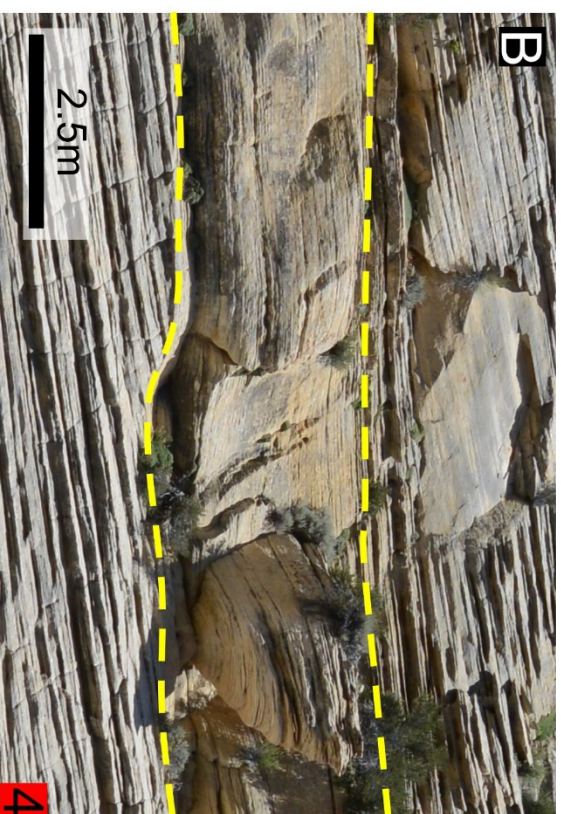
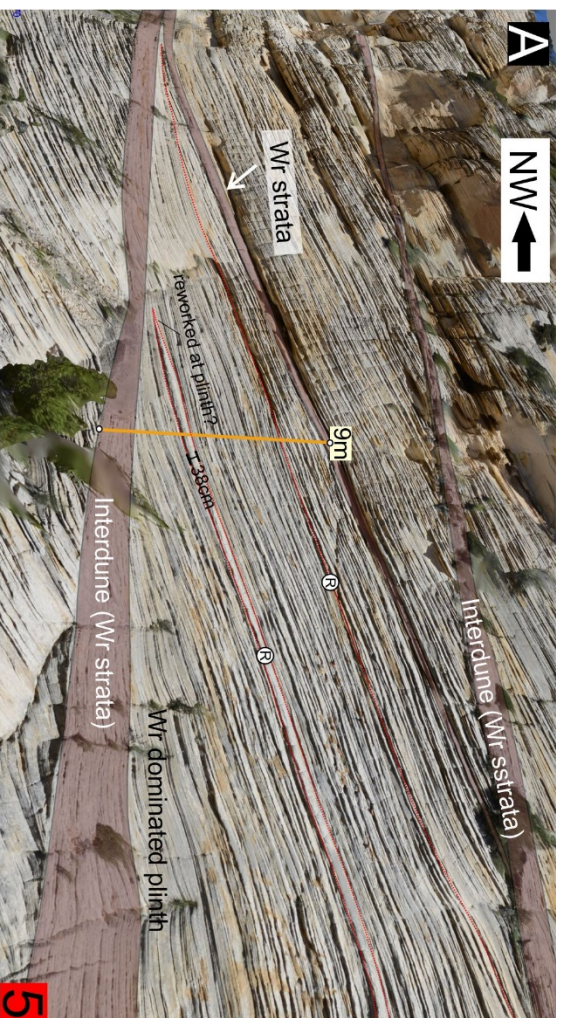


Figure 10.24: (A) Snapshot from the virtual outcrop model looking towards the NW. The data shows these cross-beds dip SW (towards the viewer). The foresets consist dominantly of wind-ripple / grainfall couplets (Wr / Gfl) as shown in detail in Figure 10.25. Reactivation is common in set bodies as a result of opposing winds. (B) Low-angle wind-ripple dominated plinth deposits transition into the thick wind-rippled interdune deposits (~2.5m). (C) Yellow arrows point out downlapping cross-strata indicating active slipface conditions. These sets are lenticular with maximum thicknesses ranging between 10 - 85cm with apparent widths up to 20 m. Cross sets dip steeply (>35°) towards SSW (n=3; inset rose diagram). The red dashed line marks the interpreted overlying bounding surface. The distribution of these bodies is shown in yellow in complex 2 of interpreted panel (Figure 10.21) - note their abundance below interpreted bounding surfaces. The red numbers are cross-referenced from Figure 10.21.

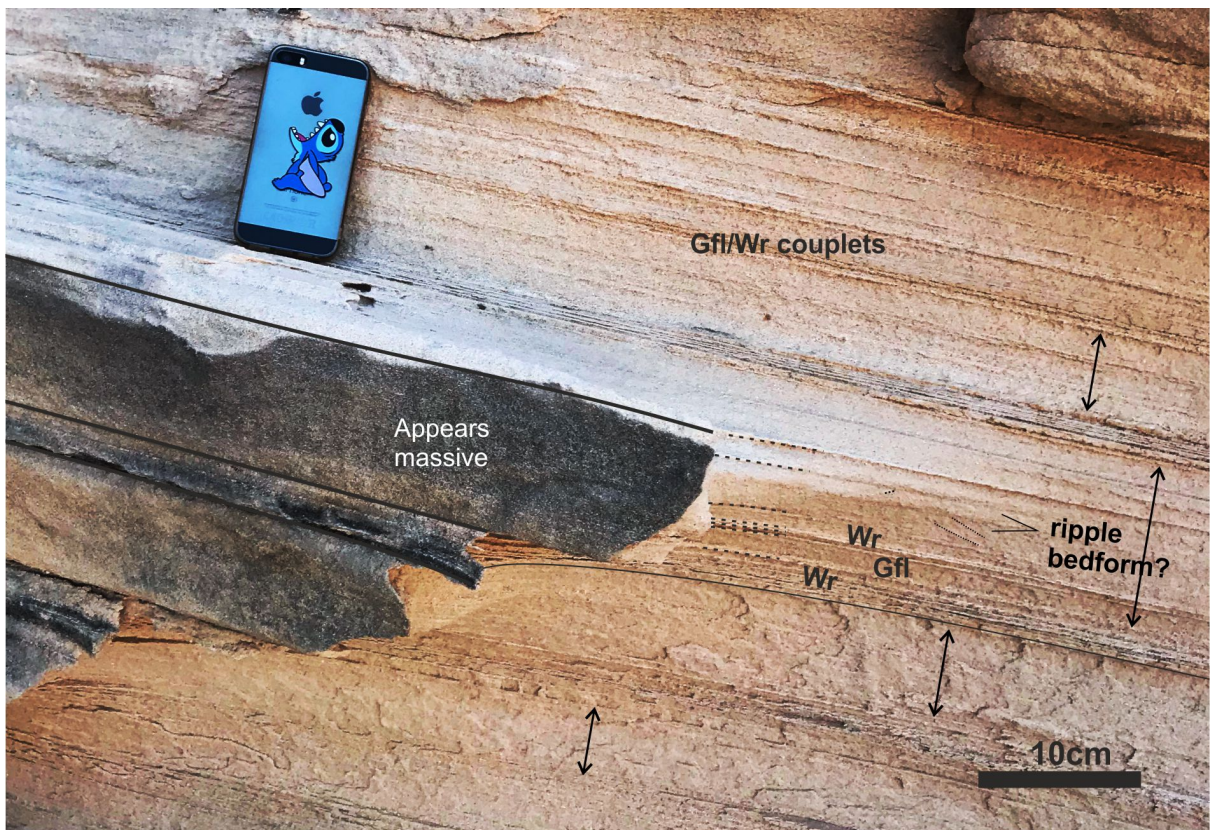


Figure 10.25: Tabular foreset bodies within sets typically appear structureless on their weathered surface, however consist of wind-ripple (Wr) / Grainfall (Gfl) couplets and thicker sets of preserved ripple-foreset cross-laminae. It appears that each 'massive' tabular body is separated by stacked wind-rippled strata (pin-striping) in a pattern that indicates cyclicity (black arrows). The mobile phone used for scale is 146 mm tall by 72 mm wide.

*Interpretation: Preserved 13 to 16 m-thick sets (*

Table 10.4) were likely generated by very large bedforms. The thick packages of wind-ripple strata at the base of these sets are interpreted as interdune-flat elements (Kocurek and Nielson, 1986) representative of the lowermost plinth of the large dunes. The low-wavelength undulation of these packages is attributed to preferential preservation of the plinths as they climb over one another at low angles (Besly *et al.*, 2018).

The largely unimodal palaeocurrent of set units is indicative of transverse migration to the southwest, however, conspicuous wind-rippled zig-zagging patterns associated with sets showing palaeocurrents towards a northeasterly direction indicates more complexity within the system. Observations are consistent with architectures expected for a sinuous, simple linear dune with a longitudinal behaviour (Figure 10.26). This type of migration is considered present in almost all linear bedforms that develop and persist over long time periods (see Bristow *et al.*, 2000, 2007), and is a main reason why the accumulations preferentially show foresets that preserve relatively unimodal distributions (Rubin and Hunter, 1985). Rather than being purely linear bedforms with respect to net sediment transport, this type of bedform is better classified as oblique (Figure 10.26). According to palaeocurrent averages, transverse migration is predicted towards the southwest as indicative of the preservation of primary component of foreset measurements (dominantly towards the viewer in viewing the panels in Figure 10.21). The secondary along-crest component is predicted towards the northwest as indicated by the sets on the northern end of the outcrop and the sinuosity migration surface (zig-zag bounding surfaces; Argüello Scotti and Veiga, 2019 their Fig. 9). Interpretation of this configuration, however, is tentative as it is restricted by the limited exposure of this outcrop face with observations further to the north.

Large tabular bodies with bladed geometries identified within sets are interpreted as reactivation surfaces, typically formed due to highly reworked sands by opposing winds (Kocurek, 1991). Their structureless appearance and polygonal fracturing are interpreted as a result of modern weathering rather than as depositional facies (e.g. Loope and Burberry, 2018). The depositional facies accumulating at the dune brink was likely dominated by grainflow strata as recognised by small cross-

strata dominated bodies at set tops. Fryberger *et al.*, 2017 termed similar features as 'linear dune slipfaces' in the Hopeman Sandstone of Covesea, UK. An alternative interpretation of these tabular sets may be a result of smaller superimposed transverse bedforms forming compound crossbedding (Rubin and Hunter, 1983). Their southerly palaeocurrent indicates oblique downslope migration.

Rare wavy-crinkly strata indicate intermittent damp conditions, the control of which is likely to be related with climatic conditions due to the lack of associated features indicating water-table influence.

Set architecture is interpreted to form part of a very-large draa based on the set sizes, style of cross-strata and evidence of a well-preserved windward slope dominated by wind-ripple facies into the thick dune plinths (Figure 10.25). Similar architectures are found in various simulated models of linear bedforms (Romain, 2014 chapter 5).

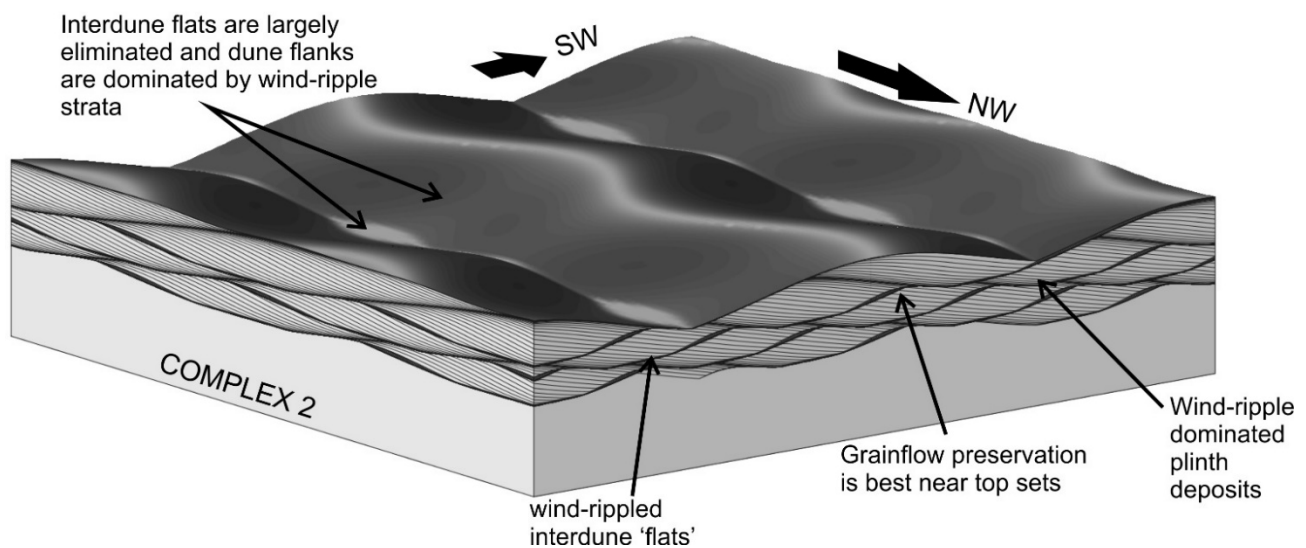


Figure 10.26: Sedimentological model of Complex 2. The simulation of migration and accumulation of a simple linear bedform whereby components of migration occur in a direction parallel to bedform crestline and transverse to crestline. Input parameters are provided in Appendix A5. Produced in BEDFORMS 4.0 (Rubin and Carter, 2006).

### *Complex 3*

*Description:* Complex 3 is characterised by stacked, intermediate-scale sets (3.0 m average thickness, 46.9 m average width,

Table 10.4) with a trough-shaped geometry (Figure 10.21, Figure 10.22, Figure 10.27). The complex occupies about 200 m of the northwestern extent of the outcrop, with a maximum thickness of ~13.8 m. It tapers towards the southeastern extent; however, poor exposure limits this observation.

The trough-shaped sets scour in the underlying Complex 2 forming a sharp erosive undulatory base between the two complexes. Between overlying sets within Complex 3 scour-and-fill geometry is also observed. Tangential cross-strata with bladed geometry are observed tapering towards the base in some sets indicating grainflow. Some sets show wind-ripple / grainflow couplets that pass into a wind-ripple dominated planar base up to 20 cm thick. Palaeocurrent measurements show an acute bimodal distribution with the two modes averaging 320° and 250°. No bounding surface readings could reliably be taken from the virtual outcrop.

Soft sediment deformation is evident in a band approximately 12 m wide and cuts all sets vertically to the outcrop top. It is characterised by contorted strata, massive sets and differential weathering of the outcrop (Figure 10.27). Other features include crinkly-wavy cross-strata (facies SA3) that dominate individual sets (Figure 10.27).

*Interpretation:* The intermediate-scale trough shaped bodies represent, by their size and position within the section, the migration of superimposed dunes over the large scale bedform represented by Complex 2 (e.g. Stage 5 of Bristow *et al.*, 2000). Their bounding surfaces are therefore interpreted as superimposition surfaces. The trough-shaped geometry, scouring nature and palaeocurrent observations indicate a sinuous crestline probably produced by crescentic transverse dune types (Kocurek, 1996). Mean cross-strata dip directions imply these superimposed dunes migrated approximately westwards, oblique to the linear dune longitudinal axis (Figure 10.22).

The soft sediment deformation structure observed cross-cutting sets vertically indicates these structures were likely associated with periodic fluid escape dynamics (e.g. Bryant *et al.*, 2013). Their

association with wavy-crinkly strata of facies SA3 may indicate water-table influences. In the context of Complex 3 representing intermediate-scale superimposed dunes onto Complex 2, its deposition is associated with the development of a large complex draa form (McKee, 1979).

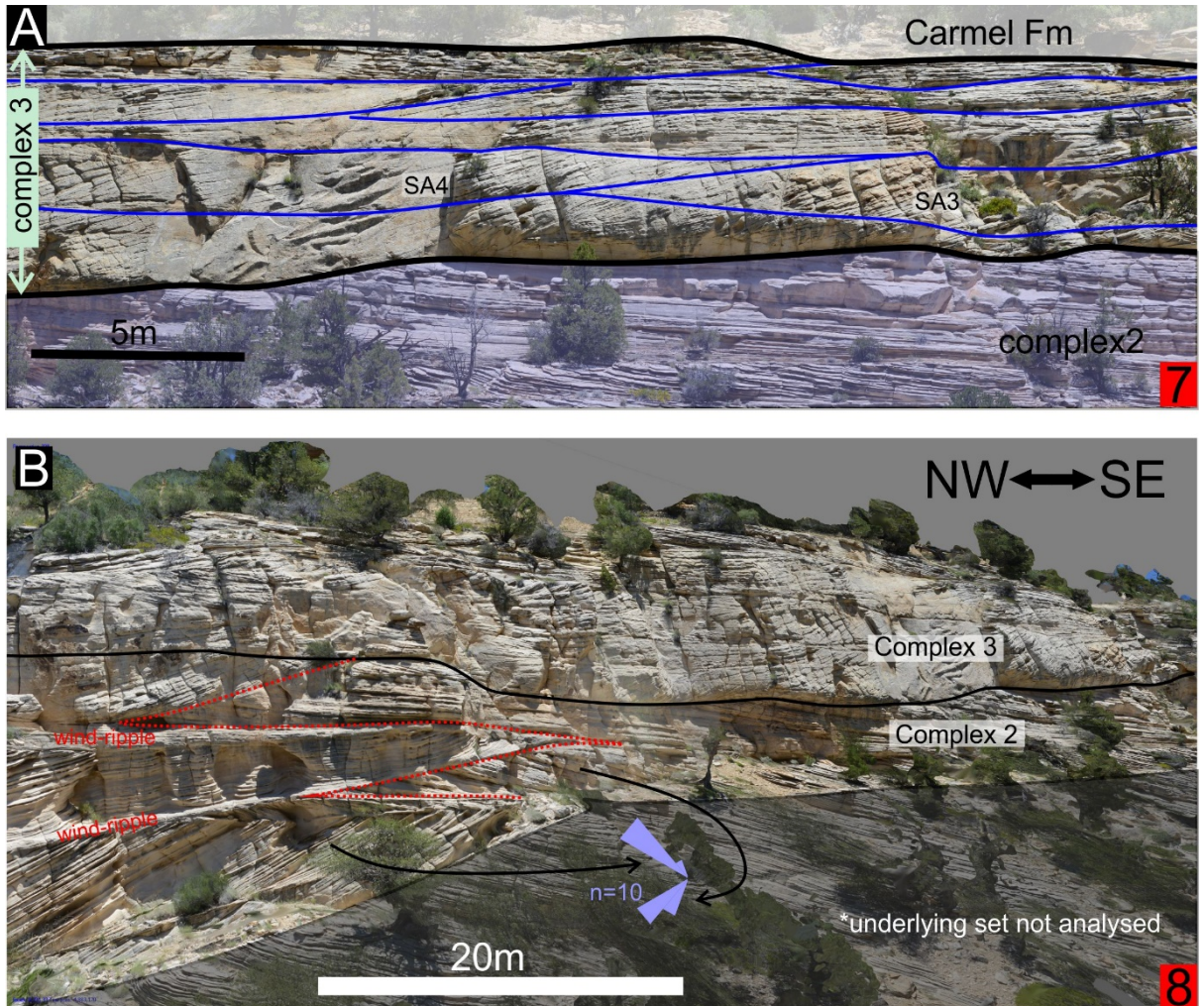


Figure 10.27: (A) Intermediate-scale trough-cross sets of complex 3. The set sizes, position within the section and nature of erosive contact suggests the migration of superimposed dunes over the large-scale underlying Complex. These bounding surfaces may therefore be interpreted as second order (superimposition) surfaces. (B) Nature of the contact between Complex 2 & 3. The superimposed sets of Complex 3 are found best preserved extending over the interpreted sinuosity axis of the linear mega-dune (indicated by the dotted red line). The red numbers are cross-referenced from Figure 10.21.

### 10.4.3 Discussion

Complex dunes such as those of star and linear types are common in modern depositional environments (e.g. Breed *et al.*, 1979; Fryberger and Goudie, 1981). These dunes types are rarely identified in ancient aeolian deposits with much of the Navajo Formation being assigned to bedforms of a transverse nature which record grainflow dominated cross-strata, even in the largest of bedforms (e.g. Loope *et al.*, 2012).

In instances where longitudinal bedforms are not exactly parallel to the long-term sand-transport direction, simulated models show that lateral migration and unimodal cross-strata consequently resemble deposits of transverse dunes (Rubin and Hunter, 1985). The hypothesis is supported by investigations of the internal architectures of linear bedforms in contemporary environments utilising GPR techniques complimented by OSL dating which show that dune construction is indeed accompanied by lateral migration (Bristow *et al.*, 2000, 2007). In aeolian environments where transverse bedforms are subordinate to those of oblique and longitudinal type, sandsheets, undulating hummocks and wind-ripple facies typically dominate the landscape (Nielson & Kocurek, 1987; Kocurek & Nielson, 1986; Rubin & Hunter, 1985). The wind regime in these systems is such that depositional surfaces of large bedforms better preserve low-to-medium angled wind-ripple and reworked wind-ripple strata while pure grainflow facies become increasingly subordinate (e.g. Besly *et al.*, 2018).

Interpretation is limited in the outcrop example at Johnsons Canyon because 1) it only represents a portion of aeolian deposition of the 'main body' of the Navajo (see Figure 10.20), 2) it is at best a 2.5D exposure and 3) is limited by the nature of ground-based photogrammetry over more precise UAV-based methods. Interpretation here instead relies on the architectural complexes displaying significant differences in several aspects of the set bodies and bounding surfaces, such as maximum thickness, apparent width, paleocurrent/bounding surface orientations, and external geometry. Differences are also found in the abundance of aeolian stratification types as well as textural and compositional aspects of the sandstones. Observations are consistent with characteristics of longitudinal to oblique bedforms, with much of the inference relying on previous studies of these bedform types in

contemporary environments (e.g. Bristow *et al.*, 2000, 2007), in examples of preserved ancient aeolian outcrops of linear origin (e.g. Argüello Scotti and Veiga, 2015, 2019; Besly *et al.*, 2018), and in deterministic modelling (e.g. Rubin and Hunter, 1985; Rubin and Carter, 2006; Romain, 2014).

Variations between sets of Complex 1 and 2 should consider that the parameters associated with bedform development are ultimately controlled by the larger dune-field self-organisation that dictates the bedform pattern of the system (Kocurek and Ewing, 2005). Adjacent bedforms in a contemporary central erg setting dominated by large complex draa can show large variabilities in size, morphology and dynamics (e.g. Namib Sand Sea; Livingstone *et al.*, 2010). This could provide an explanation of the different stratigraphic record deposited by the two complexes.

Johnsons Canyon supports a model of a dry aeolian system within the erg-centre. The undulating nature of thick erosional interdune surfaces proposes that interdune 'flats' have been largely eliminated by dune growth typical of dry systems (Kocurek and Havholm, 1993). It is likely that downwind deceleration of airflow over large draa forms was the typical cause of accumulation (positive sediment budget). The association with cross-cutting water escape structures in Complex 3 potentially indicates water-table influences in later development, but probably not near the depositional surface with accumulation.

The hypothesis presented here potentially provides an additional outcrop example in the Navajo Sandstone that was not dominated by transverse dynamics typically identified in the erg centre (i.e. upper deposits of Zion National Park and surrounds). A re-evaluation of these exceptionally exposed Navajo erg-central deposits may reveal the internal dynamics of aeolian bedforms that make up significant portions of contemporary ergs.

## 10.5 Summary

Following the fluvial dominance of the Kayenta Formation and possibly a period of deflation a topographic surface formed. Early erg development was influenced by this topography and controlled its preservation as identified by subsequent larger dunes that scoured into the basal deposits. The larger dunes aggraded with a scour-and-fill geometry indicating their preservation was water-table controlled. Their ultimate preservation was marked by extensive outcrop-scale erosive surfaces that approximately mimic the antecedent topography of the Kayenta, indicating this topography played an additional key role in pattern development and preservation. Overlying these units, evidence suggests a steadily rising water-table dominated as the erg evolved. Laterally extensive horizontal bounding surfaces marking a long-lived static water-table formed surfaces with no evidence of antecedent control marking a switch in which the water-table dominated as the allogenic control on accumulation and deflation. Sevenmile Canyon represents facies association transitions from one in which a fluvial environment dominates (FA1), through erg-margin association (FA5) that includes periods of fluvial incursion (FA2).

Preservation at Hite is controlled by sporadic palaeohydrological influences that breached and inundated the depositional surface resulting in, at times, full preservation of large-scale bedforms. Long-standing ponds below an extensive horizontal surface proposes an equilibrium state was reached as the water-table became static triggering a negative sediment budget and super surface formation. Hite represents facies associations of an erg-centre (FA6) periodically influenced by wet conditions with evidence of a water-table controlled damp association (FA4) and hydrologically controlled flooding in interdune depressions (FA3). The preserved deposits at Hite provide an excellent example for further study of fully preserved aeolian bedforms.

The Johnsons Canyon outcrop supports a model in which three complexes preserve a portion of dune build in a dry aeolian system. Unimodal palaeocurrents indicate transverse migration, however, spatial architectural changes along with the abundance of aeolian stratification types are consistent with longitudinal bedforms. Johnsons Canyon represents facies associations of a dry erg-centre (FA6) with

sporadic evidence for damp conditions (FA4) and some control by the water-table, however, not near to the depositional surface as suggested by a fluid escape structures, soft sediment deformation and spatially restricted damp conditions (FA4). Johnsons Canyon provides a potential example of longitudinal bedforms in the Navajo Sandstone suggesting a re-evaluation of large-scale deposits.



## PART D : SYNTHESIS AND CONCLUSION



## 11 Discussion and Synthesis

This chapter will place focus on integrating the interpretations and discussions presented in Parts B and C in a view to better understand the wider implications of the research ideas presented in the introduction. In some instances, the presentation of new material outlines the broader contribution of this study to the academic discourse.

### 11.1 Study Methods

The use of remote sensing datasets covering the full extent of the Wahiba erg reveals the contemporary configuration of the geomorphic surface that, if preserved, would represent a geological snapshot in time. Unfortunately, the accumulated sedimentary record of most dune fields remains largely unknown with only fragmentary glimpses revealed through techniques such as trenching, coring or GPR studies (Figure 11.1). The opposite is true when observing ancient aeolian successions such as the Navajo Sandstone, described as the largest preserved aeolian system in the stratigraphic record (Blakey *et al.*, 1988). In this case, a vast amount of time is represented vertically, but incurs spatial limitations by the observer. Additionally, relatively few ancient aeolian successions are known that preserve, intact, the original morphologies of the bedforms that gave rise to the architectural complexities inherent in aeolian sequences. To better compare the two aeolian systems a vertical and spatial slice of the Wahiba dune-fields exposing its temporal evolution would be ideal but is unrealistic. A more pragmatic solution involves exploiting the well-exposed laterally continuous outcrops of the Navajo Sandstone.

In studies of other ancient aeolian systems, previous work has shown that broadening spatial observations better reveals the boundary conditions in which the respective systems evolved (Figure 11.2) (e.g. Crabaugh and Kocurek, 1993; Langford *et al.*, 2008; Arguello Scotti and Veiga, 2015, 2019; Cardenas *et al.*, 2019; Kocurek and Day, 2019). Methodologies of the studies cited above included continuous traverses either using a survey tool (i.e. tacheometer) or by recording precise coordinates

extracted directly from the surface of interest, following it as best as possible and between outcrop sites (i.e. differential GPS). The former methodology can be extremely time consuming and requires continuous tracking of the surfaces from ground-view which may be difficult on large, vertical outcrops. The latter methodology requires the user to be in direct contact with the surface, an impractical task if the surface is elevated high up on a vertical outcrop.

To address these constraints and with limited field time, this study opted for a more convenient method to capture the outcrops by way of ground-based and UAV-based remote sensing. This allowed the user to produce georeferenced virtual outcrop models with which to study the key architectural elements off-site and in high detail. UAV-based capture is advantageous and preferred in that it additionally allows parallel access to elevated bounding surfaces on vertical outcrops. In theory, these surfaces can be followed as far as the outcrop allows, in 3D, and with high geographical precision.

The Navajo preserves a variety of depositional styles representing parts of aeolian system evolution which makes it a useful proxy with which to understand depositional architectures in contemporary systems. A comprehensive re-construction of the stratigraphic architecture in the Wahiba Sand Sea is limited by the relative scarcity and complexity of the available data *versus* the spatial extent of the basin and its stratigraphic thickness. By supplementing the available literature with the remote sensing application of this study and in utilising the Navajo Sandstone as an analogue with which to investigate a variety of controls on preservation facilitates the interpretation and speculation surrounding the Wahibas sedimentary record as further discussed in 11.2.

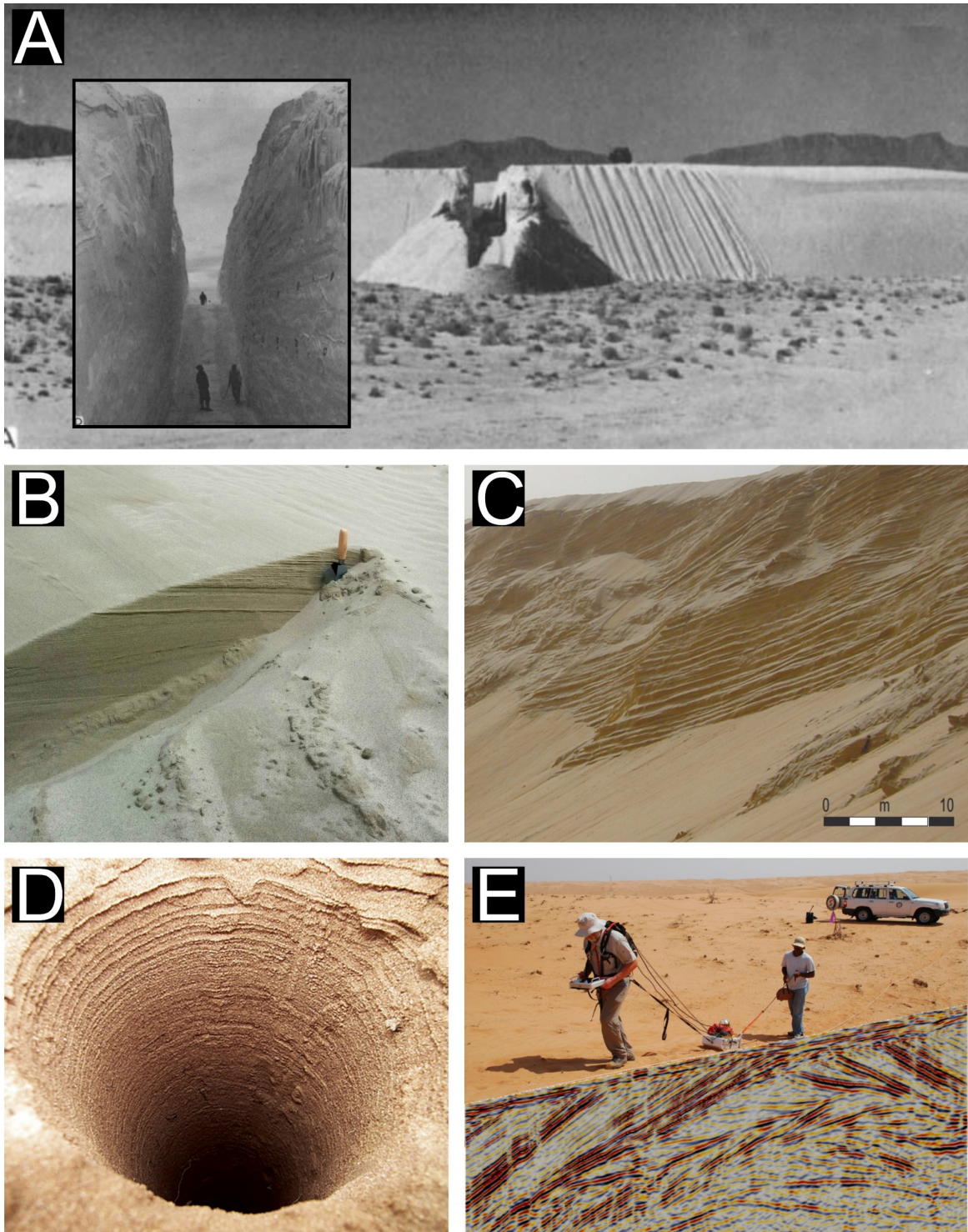


*Figure 11.1: Examples of methods used to investigate the internal structures of contemporary dunes. (A) Large-scale trenching through a dune. In this study, trenches were dug perpendicular and parallel through a transverse dune in White Sands National Monument, USA (after McKee, 1966). (B) Small-scale trenching using a shovel. Multiple trenches were dug along the stoss and lee slope of this dune in Rub' AL-Khali desert, UAE (after Fryberger et al., 2017). (C) Well-developed cross-bedding of a transverse dune exposed by wind-erosion in the Rub'Al-Khali desert, UAE (after Al-Masrahy and Mountney, 2013). (D) Auger hole exposing mm-scale laminations in the Strzelecki desert, South Australia (after Telfer and Hesse, 2013). (E) An example of 2D ground penetrating radar acquisition to image the subsurface of a dune in the Wahiba Sand Sea, Oman (after Tatum et al., 2019).*

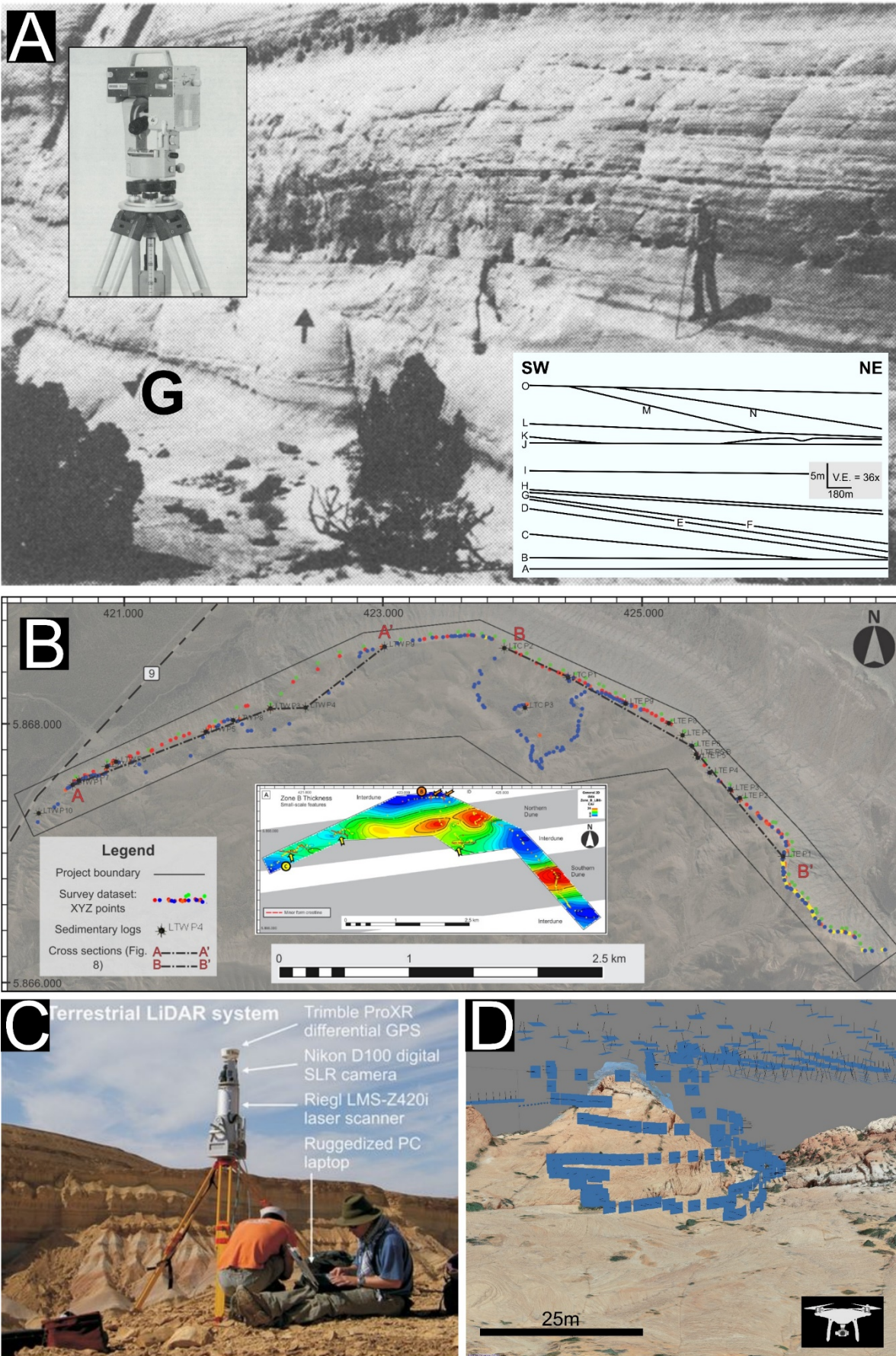


Figure 11.2: Examples of methods used to broaden spatial observations in aeolian outcrops. (A) One of the first studies to accurately measure bounding surfaces used a tacheometer (top left inset) to survey over a continuous

*2.7 km 3D outcrop of the aeolian Entrada Sandstone (USA). This allowed for mathematical planes of correlated surfaces to be determined (bottom right inset) (after Crabaugh and Kocurek, 1993). (B) A Global Positioning System (GPS) is used to track points along bounding surfaces over a continuous outcrop. The study was able to characterise the well-preserved morphology of a linear megadune (inset) in the Troncoso Inferior Member (Argentina) (after Argüello Scotti and Veiga, 2015). (C) Terrestrial Light Detection And Ranging (LiDAR) and (D) UAV photogrammetry capture continuous outcrops in 3D for the production of georeferenced virtual outcrop models. These models can be examined in 3D data visualisation and interpretation software for accurate measurements of sedimentary architectures. Figures (C) after Rarity et al. (2013). Figure (D) shows a virtual outcrop model produced from UAV drone (inset) photogrammetry in the Navajo Sandstone (USA).*

## 11.2 Antecedent Topography

Using the Navajo Sandstone as an analogue to preservation styles, observations at Sevenmile Canyon provide evidence that the Kayenta Formation created an antecedent surface topography in which the initial aeolian system developed (section 10.2). The sets that accumulated during the early-phase of the Navajo dune-field filled the topographically low regions and the strata were preserved. Subsequent larger dunes record variable scour-and-fill in a preservation style that was controlled by the signatures of the antecedent surface topography and a variable water-table.

Within the Wahiba erg, stabilised transversals in the form of large-scale barchan shaped bedforms are suggested to create much of the antecedent topography on which younger strata fills and the linear dunes accrete upon. It can be demonstrated that these mega-crescentic dunes may be 1) closely associated with the linear draa, 2) show partial evidence or remnants of former association, or 3) are apparently absent from linear draa (Figure 11.3).

The example in Figure 11.3 shows that in the instance of (1) and (2) above, the S-N trend of the linear draa maintains a pattern of undulating topography obvious on the contemporary surface and is suggested to be due to the mega-crescentic dunes in train. In the instance of (3), where crescentic bedforms are spatially absent from the linear draa (X-X' in Figure 11.3), the crest still maintains an undulating topography akin to that of transverse bedforms in train (Figure 11.4). If these stabilised mega-crescentic dunes form the core of the linear draa, it is speculated that the translation of their antecedent topography is a dominating allogenic force through the phases of accumulation and scour that is observable on the contemporary geomorphic surface (Figure 11.3, Figure 11.4).

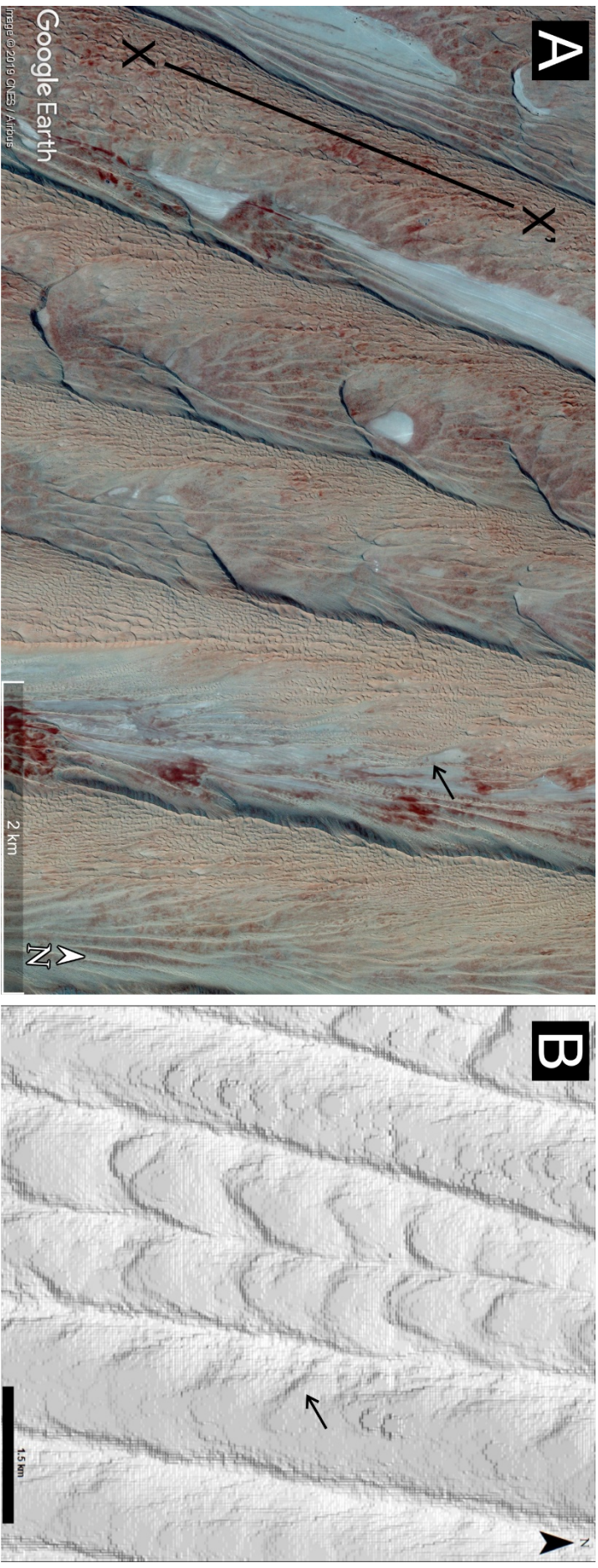
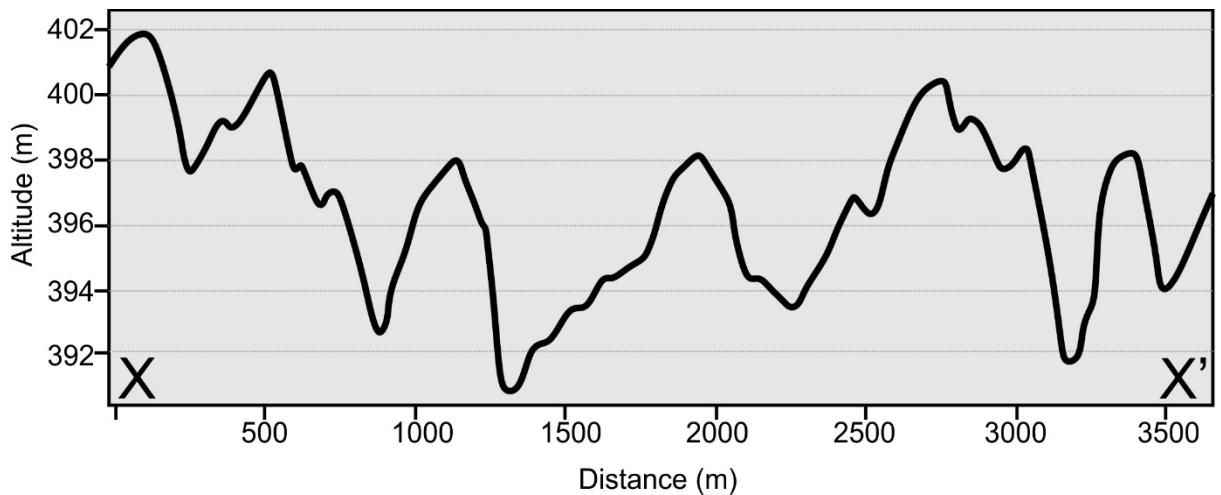


Figure 11.3: Google Earth™ Image in (A) and residual relief map of the same area in (B) shows the intimate relationship between the linear draa and mega-crescentic dunes between N-S trending interdraa corridors. Note under residual relief in (B), the configuration of the crescentic bedforms appear to shape three linear draa crests and create an undulating south-to-north topography on the draa flanks. The arrow in both (A) and (B) points to the east facing stoss flank of a linear draa evidently not containing any mega-crescentic bedforms within the interdraa but showing a similar undulating flank to those that do west of it and possibly indicates partial preservation of antecedent bedforms. South to north profile X-X' is taken on a linear dune not closely associated with the mega-crescentic dunes and is shown in Figure 11.4. Based on evidence provided in chapter 6, this study hypothesises that these mega-crescentic bedforms are antecedent and a subsequent change in the wind regime favoured the linear configuration seen today. The mega-crescentic bedforms were probably well stabilised prior to the growth of the linear draa and their topography played an important role over phases of accumulation that is apparent on the contemporary geomorphic surface. Relief map produced from ALOS AW3D30 DSM dataset (sun azimuth 160° at 20° altitude).



*Figure 11.4: South to North trending topographic profile of a 60 m tall linear draa shown in Figure 11.3. The undulating topography on the draa crests shows up to 10 m of relief. This undulating relief is thought to be translated from the draas core topography suggested to be partial remains of stabilised antecedent crescentic bedforms. A similar style of relief translation was identified in the ancient Navajo Sandstone at Sevenmile Canyon*

This style of preservation was again evident within the GPR profiles representing the top few metres of the Wahiba draa (Figure 11.5). The suggested 'geomorphic container' for subsequent accumulation (i.e. antecedent topography forming the draa core) influence the autogenic processes and ultimately control preservation (Figure 11.5). Deflation and / or stabilisation surfaces create relief onto which successive dune deposits accumulate. Low-lying topography is found to host fully preserved bedforms (section 6.4.4), while truncation occurs at higher reliefs (Figure 11.5). Although this is only a brief snapshot in time, it conforms to the mechanics of the Navajo system apparent at Sevenmile Canyon in that this boundary condition promotes the preservation potential and leads to the formation of a stratigraphic record in the Wahiba Sand Sea.

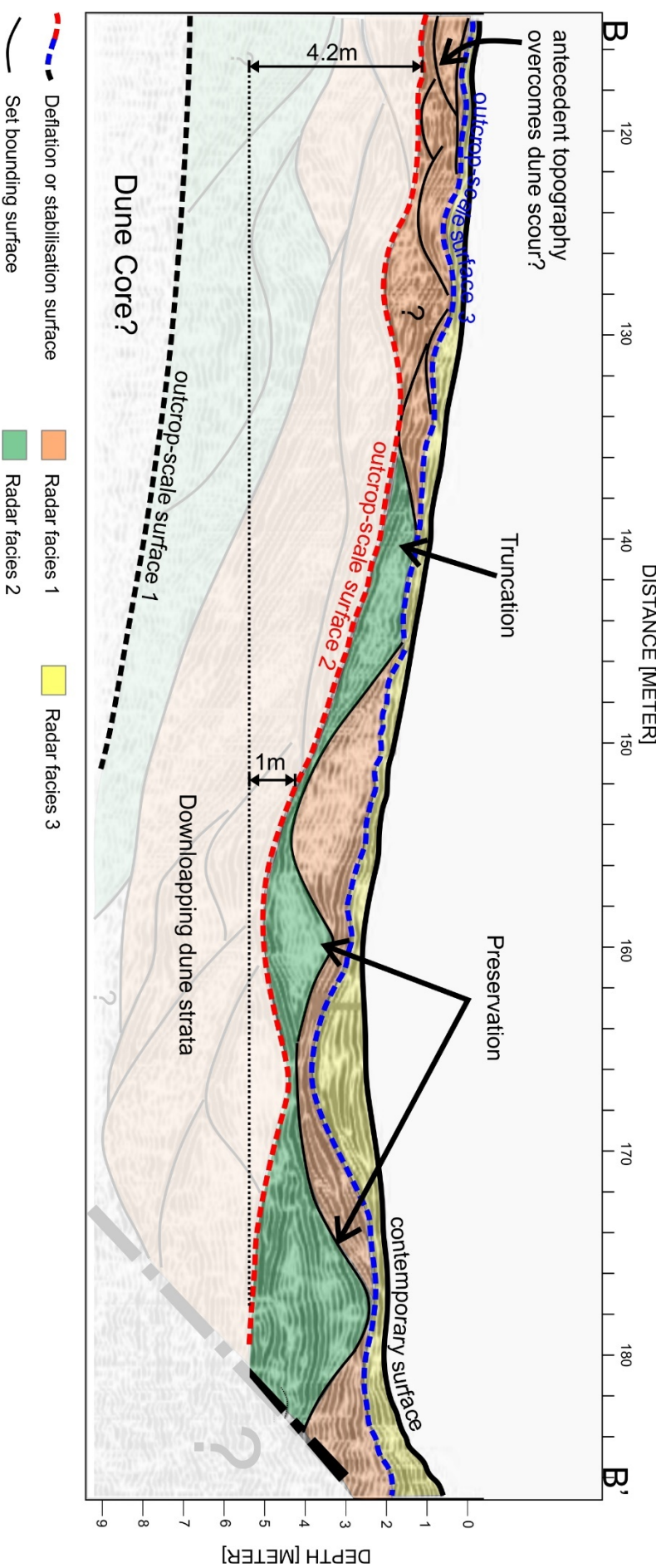


Figure 11.5: Interpreted GPR radargram from the Wahiba Sand Sea near the crest of the draa (refer to section 6.4). Deflation / stabilisation surfaces have been labelled as outcrop-scale surfaces in reference to the observations at Sevenmile Canyon (ancient Navajo Sandstone). As in the Navajo, the individual sets of cross-strata are defined by upper and lower set bounding surfaces that are less continuous than the 'outcrop-scale surfaces'. Focus is placed on the sets above surface 2 which contain up to 4.2 m of relief in this section. The well-preserved bedforms occur in areas of low topographic relief, while those at higher-relief have a lower preservation potential and are deflated by outcrop-scale surface 3. Locally high topographic relief overcomes autogenic tendency of dune scour that would otherwise remove older units. If Surface 1 is a stabilisation surface of the draa core that forms the 'geomorphic container', the above lying configuration is expected as observed in the Navajo architecture at Sevenmile Canyon. Note how all three outcrop-scale surfaces approximately follow the same apparent trend (dipping to the east →B').

### 11.3 Lessons from Linears

The strata of the ancient Navajo Sandstone observed at Johnsons Canyon is consistent with previous studies of large linear draa (section 10.4). Architectures within Complex 1 and complex 2 were analogous to predicted morphologies of deterministic models of bedform climb (Rubin and Carter, 2006; Romain, 2016; Argüello Scotti and Veiga, 2019), all of which found consistencies with studies of linear draa of the Namib Sand Sea (e.g. Bristow *et al.*, 2000, 2007) (Figure 11.6).

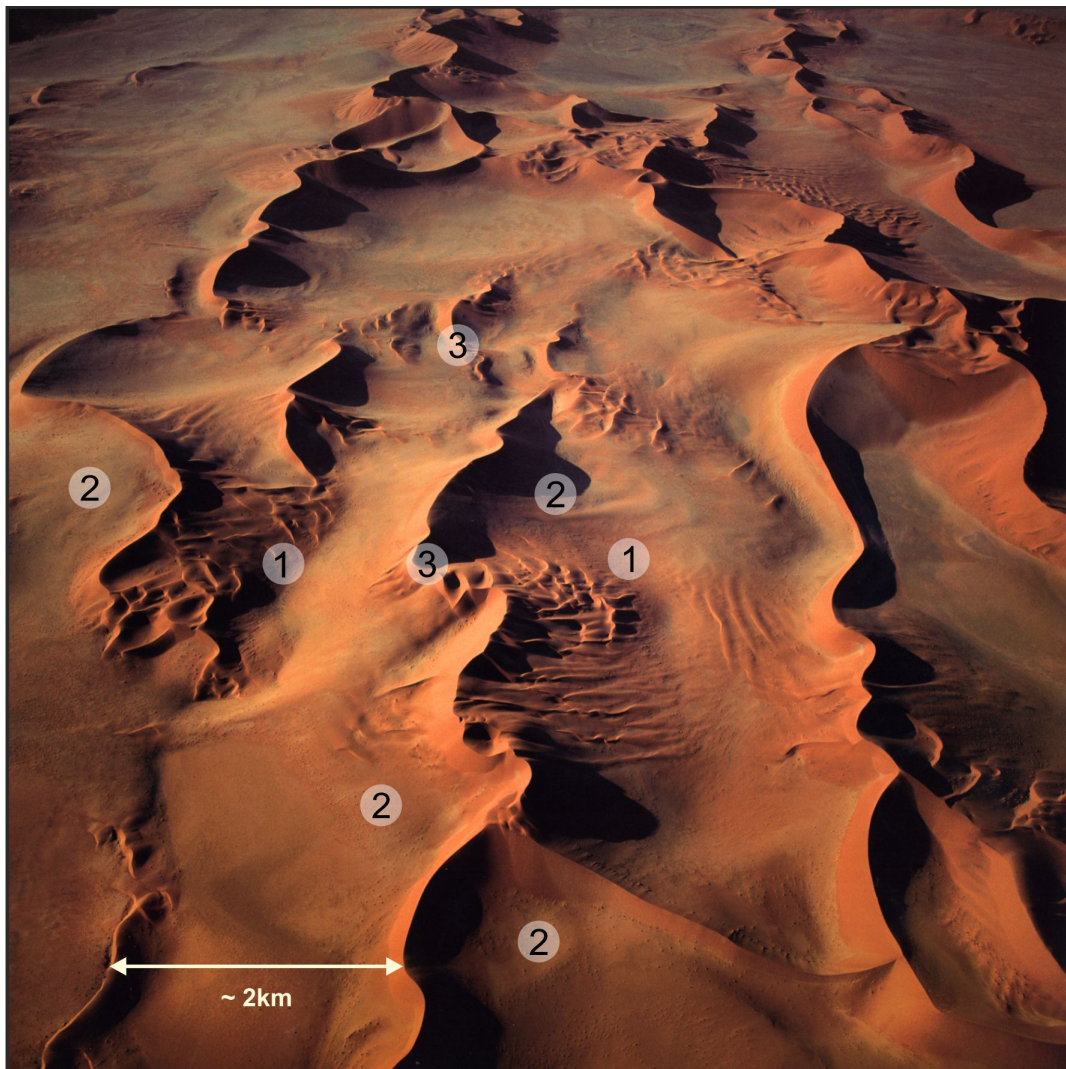


Figure 11.6: Aerial photograph of a complex linear draa of the Namib Sand Sea. The system hosts dune types of linear, transverse and star morphologies. Circled numbers in the foreground are hypothesised contemporary examples of the Complexes (1-3) identified in the study at Johnsons Canyon (section 10.4). Smaller sinuous to linear bedforms show opposing slipfaces and are commonly arranged oblique to the draa crest (Complex 1 type) and rest on the undulating wind-ripple dominated draa flanks. Hypothesised transverse migration of very large undulating bedforms deposit sets of Complex 2 type (wind-ripple dominated slipfaceless draa). Intermediate scale sinuous linear to transverse(?) superimposed dunes of Complex 3 type are observed on the draa crests. The image is modified after Romain, 2016.

With a sand residence time of at least 1 Ma (Vermeesch *et al.*, 2010) and estimates of bedform climb ranging from  $0.003^\circ$  for linear dunes (Lancaster, 1989), the Namib Sand Sea is likely to be a better analogue to the central Navajo erg as sediment availability and long-term pattern development led to draa morphologies and architectures identified and predicted in both systems (i.e. a well-organised dune system). This is especially true at the site of Johnsons Canyon as the suspected linear draa deposits associate with at least 200m of thick, laterally continuous sets with no evidence for super surface development (Figure 10.21). Johnsons Canyon is located towards the southern-central margin downwind of the elongate 'geomorphic container' of the Navajo basin and therefore greater dune-field pattern maturation is expected (compare Figure 7.10 and Figure 8.2).

By contrast to the bedform climb model suggested to develop the longitudinal dunes of the Navajo Sandstone, the Wahiba Sand Sea displays a model in which the 'geomorphic container' is that of relict dune topography superimposed on the basin (Figure 11.3). The irregular topography from early stabilised bedforms may have become the surface from which aggradation occurred. Evidence of intermittent palaeosol horizons (Radies *et al.*, 2004) were important for preservation of older episodes of dune accumulation and growth episodes may have occurred without the complete reworking of former deposits. Substantial dune scour during glacial periods (high sediment supply coupled with increased wind magnitude and a likely shift in direction) may have been overcome by the dominant signature of allogenic boundary conditions associated with antecedent surface topography.

Vertical accretion of linear dunes is recognised in contemporary sand seas. Observations from the largely inactive Strzelecki dune-field in Australia show that linear dune development occurred by vertical accretion from underlying transverse dunes and long-distance transport of sand played no significant role in their formation (Figure 11.7) (Cohen *et al.*, 2010).

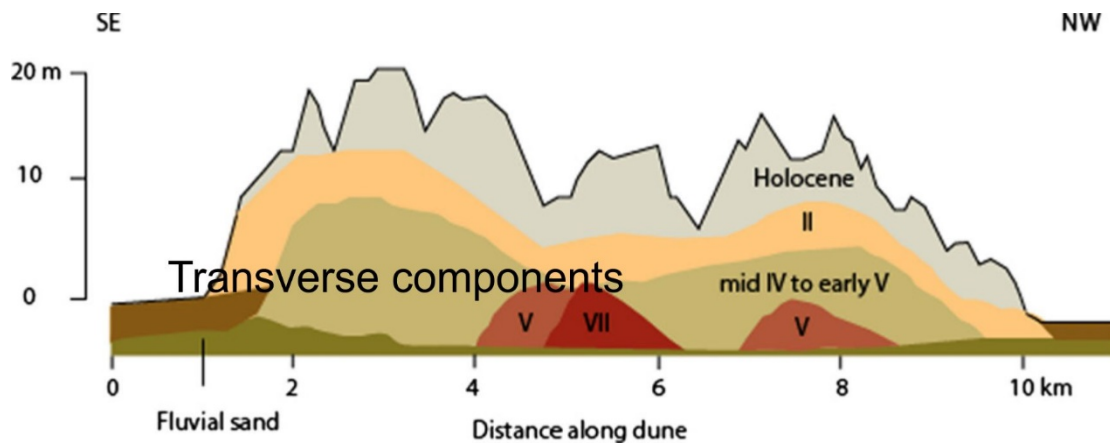


Figure 11.7: Example of the stabilised aeolian system of the Strzelecki Desert, Australia. Linear dune developed from underlying transverse bedforms. The along-dune profile shows multiple episodes of vertical dune accretion spanning the past 120Ka. 'II' to 'VII' indicate marine isotope stages. From Cohen *et al.* (2010). Image modified after Rodríguez-López *et al.*, 2014.

With current datasets, development of a more accurate model for the Wahibas is limiting. Evidence here suggests the linear draa of the Wahiba Sand Sea do not conform to classic models of bedform climb displayed in the Navajo system at Johnsons Canyon. As far as ancient systems are concerned, similar mechanisms for preservation have been recognised in the Permian Cedar Mesa Sandstone of western USA (Langford *et al.*, 2008). The study compared the two models for aeolian aggradation and found evidence within the Cedar Mesa supporting a model in which dunes aggrade laterally from previously stabilised topography in a build-and-fill style (Figure 11.8) (Langford *et al.*, 2008). The study concluded that this form of accretion of aeolian sand to pre-existing large dunes may be a fundamental style in aeolian stratigraphy (Langford *et al.*, 2008). The identification of these features in the rock record is notably difficult, especially when considering draa spacings are typically greater than 1 km. Studying these intervals require large-scale documentation of aeolian architectures and bounding surface recognition.



#### 11.4 Preserved dune topography and stabilisation surfaces

Broadly speaking, migrating dunes that leave an accumulation must move upward or climb with respect to the accumulation surface and in the process typically preserve a small portion of the lower lee slope and dune plinth (Rubin and Hunter, 1982). Fully preserved dune topography is unusual in the ancient record and is typically found as small dunes in wet aeolian systems with a rising water-table (e.g. Crabaugh and Kocurek, 1993; Hassan *et al.*, 2018). In more extraordinary cases, larger dune topography may be preserved. For example, in the Jurassic Entrada Sandstone, palaeotopography of a 35 m tall dune is recorded beneath rapid mass-flow deposits (Benan and Kocurek, 2000). In the Cretaceous Etjo Formation of northwestern Namibia, a fully preserved slipfaceless draa up to 100 m tall is found “drowned” by the rapid emplacement of Etendeka flood basalts (Jerram *et al.*, 1999, 2000). Other cases include partial deformation with net preservation that occur in response to rapid transgression and the submergence of a dune-field (e.g. Glennie and Buller, 1983 – Permian Weissliegend; Huntoon and Chan, 1987 – Permian White Rim Sandstone; Story, 1998 – Jurassic Norphlet Sandstone; Argüello Scotti and Veiga, 2015 – Cretaceous Troncoso Inferior Member). The above cases imply that the preservation is associated with rare extreme events with associated strata that rapidly encase topography termed ‘event beds’ (Chan *et al.*, 2007).

Similarly, evidenced within the Navajo Sandstone at Hite (section 10.3), preservation of dunes up to 24 m tall are associated with clastic dikes that rapidly inundated the dune surface with water-lain sediment and formed a veneer over the pre-existing topography. This veneer acted as a stabilisation surface and, in the case of the observed dune at Hite, was largely resistant to deflation as larger downwind bedforms approached and eventually buried the preserved topography intact (Figure 10.16).

The potential for the preservation of such large bedforms essentially intact is low because they require exceptional circumstances. These rare outcrops therefore provide an opportunity to study original bedform morphologies which would otherwise be fragmentary and therefore difficult to interpret. Furthermore, the investigation of the internal dynamics between preserved topography and

subsequent deflation may have direct application to understanding bedforms in contemporary systems that have been built through stabilisation events. While the mechanism for preservation is different, detailing the interactions between stabilised antecedent bedforms and subsequent deposition is achievable using the ancient record as a proxy. This has the potential to inform contemporary systems that have built through generations of stabilisation, reworking and net accumulation.

## 12 Conclusions

This chapter summarises how the primary research objectives of this study have been addressed and considers the way in which our understanding of the controls on deposition and preservation in aeolian systems has been advanced. Additionally, this chapter proposes recommendations for future research opportunities that have arisen as an outcome of this study.

### 12.1 Research Objectives

This section fulfils the objectives initially proposed in Chapter 0.

12.1.1 To examine, record and interpret the external environmental controls within which a contemporary aeolian dune-field pattern emerges

The methodology and analytical techniques followed in the study of a contemporary dune-field was successful in identifying the dominant role of antecedent topography that appears to have affected the sand sea at multiple scales. At the erg-scale, base-level changes appear consistent with pattern heterogeneity at the geomorphic surface. At the draa-scale, hypothesised antecedent mega-crescentic bedforms appear to conform with draa surface morphometry. At the superimposed dune-scale, small bedforms are influenced by buried, antecedent templates. There appears to be a hierarchy of autogenic processes influenced by antecedent topography that imparts a uniqueness to the emergent dune-field pattern.

12.1.2 To examine and record the sedimentology and architectural elements at three sites across an ancient aeolian system representing spatial and temporal variations of erg evolution. At each site, elucidate the environmental controls in which the system preserved strata and formed a stratigraphic record

The methodology followed in the study of ancient aeolian outcrops was successful in identifying significant differences within the sedimentary architectures at each site. The high-resolution large-scale virtual outcrop models provided a basis from which to examine spatially extensive surfaces and temporal changes within the system.

In the case study of the Navajo succession at Sevenmile Canyon, analysis of gross architecture of preserved accumulations and their bounding surfaces demonstrates that the studied interval does not represent continuous sedimentation within a single, long-lasting sand sea. Rather, the Lower Unit truncates the Basal Unit by landscape-scale deep-scoured troughs. Accumulation of the Basal Unit is consistent with bedform climb in a dry system filling topographic lows. The Lower Unit shows a scour-and-fill geometry with accumulation that appear associated with a rising water-table. A third landscape scale surface is apparent truncating the Lower Unit. Both landscape-scale surfaces are strongly influenced by antecedent conditions and surface configuration. The dominant signatures of allogenic boundary conditions in the lower most outcrops of the Navajo system at Sevenmile Canyon appear associated with antecedent surface topography and a variable water-table. It is apparent that the autogenic tendency of substrate cannibalization by growing dunes are overcome by the allogenic forcings of antecedent topography, thus preserving a stratigraphic record.

In the case study of the Navajo succession at Hite deposition and preservation is commonly associated with 'event-beds' found along interdune surfaces. The unusual occurrence of large preserved dune topography beneath structureless beds argues for the recording of an unusual event within the rock record considered to be formed by complex palaeohydrological influence as evidenced by vertical sand dikes. In the oldest observed succession, dikes fed and / or recharged long standing lacustrine interdune ponds that preserved below a super-surface indicating a static water-table, postulated to represent equilibrium in the hydrodynamic system. The dominant signature of allogenic boundary conditions within the studied interval at Hite appear associated with a rising to static water-table associated with complex and unusual hydrological influence.

In the case study of the Navajo succession at Johnsons Canyon observations of facies architecture are consistent with models of large linear draa. The deposits are analogous to predicted morphologies of deterministic models of bedform climb. The dominant signatures of allogenic boundary conditions appear associated with the areal limits or basin-scale 'geomorphic container' in which a very mature dune-field pattern emerged, probably in its most organised state. The conditions that promoted large linear-draa forms include the absence of a near surface water-table, high sediment availability and wind deceleration as it interacts with the large bedforms.

#### 12.1.3 Compare the controls of preservation and bedform morphology within both systems where applicable

Observation of the contemporary erg reveals that boundary conditions are manifested in both the pattern and its heterogeneity. It is apparent that all aspects of the dune morphology and the dune dynamics results from the influence of boundary conditions upon the autogenic processes. The best analogue for these conditions is apparent at Sevenmile Canyon. The site shows stratigraphy that preserves a record of allogenic boundary conditions, dominated by antecedent topography, locally overcoming an autogenic tendency of larger dunes (i.e. the Lower Unit) to shred their earlier accumulations.

It is apparent that each phase of Wahiba build represents a change in boundary conditions (e.g. tectonic / wind direction / sediment availability). This change may have initiated a new constructional phase of dunes upon an existing, or antecedent, dune pattern. It is apparent that dune interaction at the surface (e.g. migration and scouring of the substrate) have not overcome the dominating allogenic boundary conditions of antecedent topography through evolution and the geomorphic surface represents this. In using the Namib Sand Sea as an analogue to the suggested highly-ordered state of the Navajo system at Johnsons Canyon, the comparison pattern development and bedform morphologies show noticeable contrasts with the Wahiba linear draa, as expected.

The research demonstrates that the ability to extract the signals of allogenic boundary conditions within which autogenic system processes evolved is the basis for the interpretation of geomorphic landforms and their stratigraphic record. Both the Wahiba and the Navajo represent a point on a spectrum of preservation styles most recently observed in aeolian systems (Kocurek and Ewing, 2016; Kocurek and Day, 2018; Cardenas *et al.*, 2019). As such they serve as additional examples with which to understand aeolian systems.

## 12.2 Recommendations

The following section will provide a bulleted summary of recommendations for further study of both the contemporary and ancient ergs detailed herein.

### 12.2.1 Wahiba Sand Sea

In addition to using interpretation from literature this thesis relied greatly on the use of remote sensing datasets. It provides a comprehensive desktop study with which to apply direct ground observations and as such are included in the following proposals:

- In evaluating dune size and spacing, pattern heterogeneity is evident as seen in the low correlation coefficients. The data are certainly sensitive to transect placement and in order to better apply Lancaster's (1988) concept of allometric relationships, segmenting dunes along a north to south trend may improve insight into dune growth and patterns of deposition.
- Changes in base-level topography coincide with changes in Wahiba pattern development (Figure 6.12). Further scrutiny of interdune troughs to base-level surface (e.g. methodologies of Baitus *et al.*, 2014) will further resolve areas of sediment accumulation in relation to base-level changes.
- The 'knick-point' hypothesis (chapter 4; Figure 4.5) provides a basis from which to correlate genetic relict units across the erg. There is a need to evaluate what topographies may be erosional antecedent, and those that may be subsequent (more recent build). The high-resolution DSM reveals a portion of a stabilised bedform with a crescentic morphometry below

an interdune surface connecting two complex linear draa (Figure 6.15). The favoured hypothesis that this is a relict bedform from an ancient dune-field can be tested through sample collection for OSL dating and mineralogical analysis with comparison to the resolved stratigraphy (i.e. Preusser *et al.*, 2002) and mineralogy (Pease *et al.*, 1999; Pease and Tchakerian, 2014) respectively. Additionally, mega-crescentic bedforms above the interdune surface could be augured below active sands into the (speculative) stabilised surface. As shown in section 4.2 (core WDR-1), a mega-crescentic bedform coincides with the 'Al-Hibal' Unit of Radies *et al.* (2004) and as such the author speculates these subdued topographies to be of a similar age (MIS 5d in Radies *et al.*, 2004). Rather, if these dunes are developed under the modern wind regime, the infill between the linear draa perhaps indicate a style of build-and-fill similar to model 2 of Langford *et al.* (2008) (Figure 11.8). This provides the opportunity to detail such mechanisms in a contemporary environment.

- As the full extent of the GPR profile in Figure 6.23 is not in an interpretable resolution, a re-run of the draa-scale acquisition will elucidate relative age of radar facies units. Additional trenching and OSL samples along the transect will reveal absolute ages and resolve draa evolution.
- Additional acquisition of 3D-swath-GPR volumes in the interdraa in Figure 6.15 could better reveal their relationships to the phase of draa / sand sea build. Quantification of relict topography will further clarify the boundary conditions in which the contemporary geomorphic pattern emerged.
- As shown in Chapter 6, dune topographies can be studied in detail with high-resolution DSMs. Ultra-high resolution DEMs (cm-scale) can be cheaply produced via semi-automated UAV-based photogrammetric techniques (section 10.1.2). Areas of interest can be initially surveyed using the medium resolution ASTER DSMs under residual relief inspection. These volumes would be an extremely valuable addition in an instance where a draa is cored and dated from crest to interdraa elevation (e.g. WDR-2 of Preusser *et al.*, 2002).

- Two-dimensional GPR volumes in conjunction with the residual relief maps lead to the interpretation of internal architectures of crescentic dunes. In acquiring three-dimensional GPR volumes these key areas can be re-targeted and allows for interpretation of true dip and azimuth of the cross-strata. Enhanced resolution of the architectures could be compared against computer simulated bedforms (e.g. Rubin and Carter, 2006).
- Vegetation indices tentatively show that vegetation occurs year-round and can be correlated with rainfall patterns, although more data is required to substantiate. This study only looks at four datasets over a five-year period which encompass the earliest to the latest Landsat-8 datasets at the time of this study. Vegetation monitoring, and therefore dune stabilisation, can be expanded to cover longer timeframes using the Landsat imagery from as early as the 1970's.
- Spectral band ratioing allows the production of low-resolution mineralogical distribution maps of the erg. These can be further calibrated with sediment collection and X-ray powder diffraction (XRD) analysis. Time-lapse acquisition has the potential to show temporal sediment dispersion over longer periods. Additionally, hyperspectral datasets can be acquired for more detailed mineralogical analysis. For example, the Compact High-Resolution Imaging Spectrometer (CHRIS) is accessible with registered projects.

### 12.2.2 Navajo Sandstone

As virtual outcrop models expose large-scale observations ready for desk-based interpretation, it is often the case that the user will find areas that are poorly covered or that require supplementary data from direct field observations. First pass models are generally obtained at greater distances from the outcrop wall in a trade-off between operation time and coverage. Areas of high interest identified in desk-based analysis could be scrutinised by closer inspection on additional visits.

- The hypothesised antecedent topography at Sevenmile Canyon (section 10.2) requires extended lateral coverage to better characterise the surface in conjunction with the preserved deposits and truncation between the Basal and Lower Units. The location used in this study is

ideal as the Kayenta / Navajo boundary forms a bench on which ground observations and bounding surface tracking can take place.

- The outcrops at Hite provides the opportunity to study and detail the complex palaeohydrological system of the Navajo Sandstone with comparison to other studied areas and aeolian Formations (e.g. Eisenberg, 2003; Chan *et al.*, 2007; Parrish and Falcon-Lang, 2007; Bryant *et al.*, 2013; Bryant *et al.*, 2016; Dorney *et al.*, 2017; Parrish *et al.*, 2017). Deposits and preservation of this type are scarce in the literature and the Navajo is well-exposed in at least 25 km<sup>2</sup> of accessible outcrop local to this site. Furthermore, the excellent preservation of pre-existing dune topography provides the opportunity to compare their internal architectures with observations acquired in contemporary dune-fields gained through large-scale trenching (e.g. Mckee, 1966) or ground penetrating radar (e.g. Bristow *et al.*, 2000; Bristow, 2019).
- The study at Johnsons Canyon was limiting in that it relied solely on less precise ground-based photogrammetry and was captured largely in 2D. Future studies would benefit from a location where the 'main body' of the Navajo Sandstone is exposed in 3D and accessible for UAV capture.



## 13 Reference List

ADVANCED LAND OBSERVING SATELLITE, 2020, ALOS Global Digital Surface Model "ALOS World 3D - 30m (AW3D30)", viewed 29 January 2020, < <https://www.eorc.jaxa.jp/ALOS/en/aw3d30/index.htm>>

AHMED BENAN, C.A. and KOCUREK, G., 2000. Catastrophic flooding of an aeolian dune field: Jurassic Entrada and Todilto formations, Ghost Ranch, New Mexico, USA. *Sedimentology*, **47**(6), pp. 1069-1080.

ALLABY, M., 2013. *A dictionary of geology and earth sciences*. Oxford University Press.

ALLEN, P.A., 2007. The Huqf Supergroup of Oman: basin development and context for Neoproterozoic glaciation. *Earth-Science Reviews*, **84**(3-4), pp. 139-185.

ALLEN, P.A., VERLANDER, J.E., BURGESS, P.M. and AUDET, D.M., 2000. Jurassic giant erg deposits, flexure of the United States continental interior, and timing of the onset of Cordilleran shortening. *Geology*, **28**(2), pp. 159-162.

AL-MASRAHY, M.A. and MOUNTNEY, N.P., 2013. Remote sensing of spatial variability in aeolian dune and interdune morphology in the Rub'Al-Khali, Saudi Arabia. *Aeolian Research*, **11**, pp. 155-170.

AL-MASRAHY, M.A. AND MOUNTNEY, N.P., 2013. Spatial variability in eolian dune and interdune morphology in the Rub'Al-Khali dunefield, Saudi Arabia. *AAPG Search and Discovery*.

AL-MASRAHY, M.A. and MOUNTNEY, N.P., 2015. A classification scheme for fluvial–aeolian system interaction in desert-margin settings. *Aeolian Research*, **17**, pp. 67-88.

ANDERSON, R.S. and BUNAS, K.L., 1993. Grain size segregation and stratigraphy in aeolian ripples modelled with a cellular automaton. *Nature*, **365**(6448), pp. 740.

ANDERSON, R.S., 1990. Eolian ripples as examples of self-organization in geomorphological systems. *Earth-Science Reviews*, **29**(1), pp. 77-96.

ANDREOTTI, B., CLAUDIN, P. AND POULIQUEN, O., 2010. Measurements of the aeolian sand transport saturation length. *Geomorphology*, **123**(3-4), pp.343-348.

BAARS, D. and STEVENSON, G., 1981. Tectonic evolution of the Paradox basin, Utah and Colorado.

BAARS, D.L., 2000. *The Colorado plateau: a geologic history*. UNM Press.

BAAS, A.C. and NIELD, J., 2007. Modelling vegetated dune landscapes. *Geophysical Research Letters*, **34**(6).

BAGNOLD, R., 1941. Physics of blown sand and sand dunes. *William Morrow and Co., New York*.

BAITIS, E., KOCUREK, G., SMITH, V., MOHRIG, D., EWING, R.C. and PEYRET, A., 2014. Definition and origin of the dune-field pattern at White Sands, New Mexico. *Aeolian Research*, **15**, pp. 269-287.

BARBEAU, D., 2003. A flexural model for the Paradox Basin: implications for the tectonics of the Ancestral Rocky Mountains. *Basin Research*, **15**(1), pp. 97-115.

- BEITLER, B., PARRY, W. and CHAN, M.A., 2005. Fingerprints of fluid flow: chemical diagenetic history of the Jurassic Navajo Sandstone, southern Utah, USA. *Journal of Sedimentary Research*, **75**(4), pp. 547-561.
- BEMIS, S.P., MICKLETHWAITE, S., TURNER, D., JAMES, M.R., AKCIZ, S., THIELE, S.T. and BANGASH, H.A., 2014. Ground-based and UAV-based photogrammetry: A multi-scale, high-resolution mapping tool for structural geology and paleoseismology. *Journal of Structural Geology*, **69**, pp. 163-178.
- BERRY, E., HOUSER, R. K. & LANE, W. G. 1981. *A Wind Energy Assessment of the Southern California Desert, Project Windesert, Final Report, Volume I*.
- BESLY, B., ROMAIN, H.G. and MOUNTNEY, N.P., 2018. Reconstruction of linear dunes from ancient aeolian successions using subsurface data: Permian Auk Formation, Central North Sea, UK. *Marine and Petroleum Geology*, **91**, pp. 1-18.
- BJERRUM, C.J. and DORSEY, R.J., 1995. Tectonic controls on deposition of Middle Jurassic strata in a retroarc foreland basin, Utah-Idaho trough, western interior, United States. *Tectonics*, **14**(4), pp. 962-978.
- BLAKEY, R., 1997. Paleogeographic evolution of the passive-margin to active-margin transition, Early Mesozoic, western North America, *Geological Society of America Annual Meeting Abstracts with Programs*, p. A-202 1997.
- BLAKEY, R.C. and RANNEY, W., 2008. *Ancient landscapes of the Colorado Plateau*. Grand Canyon Assn.
- BLAKEY, R.C. and RANNEY, W.D., 2017. *Ancient landscapes of Western North America: a geologic history with paleogeographic maps*. Springer.
- BLAKEY, R.C., 1994. Paleogeographic and tectonic controls on some Lower and Middle Jurassic erg deposits, Colorado Plateau, 1994, Rocky Mountain Section (SEPM).
- BLAKEY, R.C., 2008. Pennsylvanian–Jurassic sedimentary basins of the Colorado Plateau and southern Rocky Mountains. *Sedimentary Basins of the World*, **5**, pp. 245-296.
- BLAKEY, R.C., HAVHOLM, K.G. and JONES, L.S., 1996. Stratigraphic analysis of eolian interactions with marine and fluvial deposits, Middle Jurassic Page Sandstone and Carmel Formation, Colorado Plateau, USA. *Journal of Sedimentary Research*, **66**(2).
- BLAKEY, R.C., PETERSON, F. and KOCUREK, G., 1988. Synthesis of late Paleozoic and Mesozoic eolian deposits of the Western Interior of the United States. *Sedimentary Geology*, **56**(1-4), pp. 3-125.
- BLECHSCHMIDT, I., MATTER, A., PREUSSER, F. and RIEKE-ZAPP, D., 2009. Monsoon triggered formation of Quaternary alluvial megafans in the interior of Oman. *Geomorphology*, **110**(3-4), pp. 128-139.
- BOGGS, S. and BOGGS, S., 2011. *Principles of sedimentology and stratigraphy*.
- BREED, C.S. and GROW, T., 1979. Morphology and distribution of dunes in sand seas observed by remote sensing. *A study of global sand seas*. US Government Printing Office Washington, DC, pp. 253-302.

- BRISTOW, C., BAILEY, S. and LANCASTER, N., 2000. The sedimentary structure of linear sand dunes. *Nature*, **406**(6791), pp. 56-59.
- BRISTOW, C., LANCASTER, N. and DULLER, G., 2005. Combining ground penetrating radar surveys and optical dating to determine dune migration in Namibia. *Journal of the Geological Society*, **162**(2), pp. 315-321.
- BRISTOW, C., PUGH, J. and GOODALL, T., 1996. Internal structure of aeolian dunes in Abu Dhabi determined using ground-penetrating radar. *Sedimentology*, **43**(6), pp. 995-1003.
- BRISTOW, C.S. and MOUNTNEY, N., 2013. Aeolian landscapes, Aeolian stratigraphy. In: *Treatise on Geomorphology* (Ed. J. Shroder). Elsevier, San Diego, CA, 11, 246–268.
- BRISTOW, C.S., 2019. Bounding surfaces in a barchan dune: annual cycles of deposition? Seasonality or erosion by superimposed bedforms? *Remote Sensing*, **11**(8), pp. 965.
- BRISTOW, C.S., DULLER, G. and LANCASTER, N., 2007. Age and dynamics of linear dunes in the Namib Desert. *Geology*, **35**(6), pp. 555-558.
- BROMLEY, M.H., 1992. Variations in fluvial style as revealed by architectural elements, Kayenta Formation, Mesa Creek, Colorado, USA: evidence for both ephemeral and perennial fluvial processes.
- BROOKFIELD, M., 1977. The origin of bounding surfaces in ancient aeolian sandstones. *Sedimentology*, **24**(3), pp. 303-332.
- BROOKFIELD, M.E., 1992. Eolian systems. *Facies models: response to sea level change*, , pp. 143-156.
- BROTHERS, S.C., KOCUREK, G., BROTHERS, T.C. and BUYNEVICH, I.V., 2017. Stratigraphic architecture resulting from dune interactions: white sands dune field, New Mexico. *Sedimentology*, **64**(3), pp. 686-713.
- BRYANT, G. and MIALL, A., 2010. Diverse products of near-surface sediment mobilization in an ancient eolianite: outcrop features of the early Jurassic Navajo Sandstone. *Basin Research*, **22**(4), pp. 578-590.
- BRYANT, G., CUSHMAN, R., NICK, K. and MIALL, A., 2016. Paleohydrologic controls on soft-sediment deformation in the Navajo Sandstone. *Sedimentary Geology*, **344**, pp. 205-221.
- BRYANT, G., MONEGATO, G. and MIALL, A., 2013. An example of liquefaction-induced interdune sedimentation from the early Jurassic Navajo Sandstone, USA. *Sedimentary Geology*, **297**, pp. 50-62.
- BUCKMAN J. O., FRANCKE J. C., HERN C. Y., TATUM D. I. & WESTERMAN A. R., 2017. Microbially-influenced Architectural Preservation in Aeolian Bedforms , *Geological Society of London, Lyell Meeting 2017: Sticking Together: microbes and their role in forming sediments*, 7, 7 March 2017 2017.
- BURG, J.P., 2018-last update, OMAN: an obduction orogen. Accessed 23 September 2019. Available at: <http://www.files.ethz.ch/structuralgeology/JPB/files/English/Omaneng.pdf>.
- CANNINGS, S., CANNINGS, R. and NELSON, J., 2011. *Geology of British Columbia: a journey through time*. Greystone Books Ltd.

- CARDENAS, B.T., KOCUREK, G., MOHRIG, D., SWANSON, T., HUGHES, C.M. and BROTHERS, S.C., 2019. Preservation of Autogenic Processes and Allogenic Forcings in Set-Scale Aeolian Architecture II: The Scour-and-Fill Dominated Jurassic Page Sandstone, Arizona, USA. *Journal of Sedimentary Research*, **89**(8), pp. 741-760.
- CARR-CRABAUGH, M. and KOCUREK, G., 1998. Continental sequence stratigraphy of a wet eolian system: a key to relative sea-level change.
- CHAICHITEHRANI, N. and ALLAHDADI, M.N., 2018. Overview of Wind Climatology for the Gulf of Oman and the Northern Arabian Sea. *American Journal of Fluid Dynamics*, **8**(1), pp. 1-9.
- CHAN, M., NETOFF, D., BLAKEY, R., KOCUREK, G. and ALVAREZ, W., 2007. Clastic-injection pipes and syndepositional deformation structures in Jurassic eolian deposits: examples from the Colorado Plateau.
- CHESLEY, J., LEIER, A., WHITE, S. and TORRES, R., 2017. Using unmanned aerial vehicles and structure-from-motion photogrammetry to characterize sedimentary outcrops: An example from the Morrison Formation, Utah, USA. *Sedimentary Geology*, **354**, pp. 1-8.
- CLEMMENSEN, L.B. and ABRAHAMSEN, K., 1983. Aeolian stratification and facies association in desert sediments, Arran basin (Permian), Scotland. *Sedimentology*, **30**(3), pp. 311-339.
- CLEMMENSEN, L.B. and BLAKEY, R.C., 1989. Erg deposits in the Lower Jurassic Wingate Sandstone, northeastern Arizona: oblique dune sedimentation. *Sedimentology*, **36**(3), pp. 449-470.
- COHEN, T.J., NANSON, G.C., LARSEN, J.R., JONES, B., PRICE, D.M., COLEMAN, M. and PIETSCH, T., 2010. Late Quaternary aeolian and fluvial interactions on the Cooper Creek Fan and the association between linear and source-bordering dunes, Strzelecki Desert, Australia. *Quaternary Science Reviews*, **29**(3-4), pp. 455-471.
- COLLINSON, J., MOUNTNEY, N. and THOMPSON, D., 2006. Sedimentary structures: England.
- CONDON, S.M., 1997. *Geology of the Pennsylvanian and Permian cutler group and Permian Kaibab limestone in the Paradox Basin, southeastern Utah and southwestern Colorado*. US Government Printing Office.
- CRABAUGH, M. and KOCUREK, G., 1993. Entrada Sandstone: an example of a wet aeolian system. *Geological Society, London, Special Publications*, **72**(1), pp. 103-126.
- CRUDEN, A., VOLLGGER, S., DERING, G. and MICKLETHWAITE, S., 2016. High spatial resolution mapping of dykes using unmanned aerial vehicle (UAV) photogrammetry: new insights on emplacement processes. *Acta Geol.Sin.-Engl*, **90**, pp. 52-53.
- DAVIS, G.H. and BUMP, A.P., 2009. Structural geologic evolution of the Colorado Plateau. *Geological Society of America Memoirs*, **204**, pp. 99-124.
- DECELLES, P.G. and GILES, K.A., 1996. Foreland basin systems. *Basin research*, **8**(2), pp. 105-123.
- DICKINSON, W.R. and GEHRELS, G.E., 2003. U–Pb ages of detrital zircons from Permian and Jurassic eolian sandstones of the Colorado Plateau, USA: paleogeographic implications. *Sedimentary Geology*, **163**(1), pp. 29-66.

- DICKINSON, W.R., 2004. Evolution of the North American cordillera. *Annu.Rev.Earth Planet.Sci.*, **32**, pp. 13-45.
- DIETRICH, J.T., 2016. Riverscape mapping with helicopter-based Structure-from-Motion photogrammetry. *Geomorphology*, **252**, pp. 144-157.
- DONG, Z., QIAN, G., LV, P. and HU, G., 2013. Investigation of the sand sea with the tallest dunes on Earth: China's Badain Jaran Sand Sea. *Earth-Science Reviews*, **120**, pp. 20-39.
- DORNEY, L.J., PARRISH, J.T., CHAN, M.A. and HASIOTIS, S.T., 2017. Petrography and Environmental Interpretation of Tufa Mounds and Carbonate Beds In the Jurassic Navajo Sandstone of Southeastern Utah, USA. *Journal of Sedimentary Research*, **87**(9), pp. 967-985.
- DURÁN, O., CLAUDIN, P. and ANDREOTTI, B., 2011. On aeolian transport: Grain-scale interactions, dynamical mechanisms and scaling laws. *Aeolian Research*, **3**(3), pp. 243-270.
- EASTWOOD, E.N., KOCUREK, G., MOHRIG, D. and SWANSON, T., 2012. Methodology for reconstructing wind direction, wind speed and duration of wind events from aeolian cross-strata. *Journal of Geophysical Research: Earth Surface*, **117**(F3),.
- EDGEHILL, H.S., 2006. *Arabian deserts: nature, origin and evolution*. Springer Science & Business Media.
- EISENBERG, L., 2003. Giant stromatolites and a supersurface in the Navajo Sandstone, Capitol Reef National Park, Utah. *Geology*, **31**(2), pp. 111-114.
- EKDALE, A., BROMLEY, R.G. and LOOPE, D.B., 2007. Ichnofacies of an ancient erg: a climatically influenced trace fossil association in the Jurassic Navajo Sandstone, southern Utah, USA. *Trace Fossils*. Elsevier, pp. 562-574.
- ELBELRHITI, H., CLAUDIN, P. AND ANDREOTTI, B., 2005. Field evidence for surface-wave-induced instability of sand dunes. *Nature*, **437**(7059), pp.720-723.
- EL-HUSSAIN, I., DEIF, A., AL-JABRI, K., TOKSOZ, N., EL-HADY, S., AL-HASHMI, S., AL-TOUBI, K., AL-SHIJBI, Y., AL-SAIFI, M. and KULELI, S., 2012. Probabilistic seismic hazard maps for the sultanate of Oman. *Natural Hazards*, **64**(1), pp. 173-210.
- ELTNER, A., KAISER, A., CASTILLO, C., ROCK, G., NEUGIRG, F. and ABELLÁN, A., 2016. Image-based surface reconstruction in geomorphometry—merits, limits and developments. *Earth Surface Dynamics*, **4**(2), pp. 359-389.
- EWING, R. and KOCUREK, G., 2010. Aeolian dune-field pattern boundary conditions. *Geomorphology*, **114**(3), pp. 175-187.
- EWING, R.C., KOCUREK, G. and LAKE, L.W., 2006. Pattern analysis of dune-field parameters. *Earth Surface Processes and Landforms: The Journal of the British Geomorphological Research Group*, **31**(9), pp. 1176-1191.
- FOOS, A., 1999. Geology of the Colorado Plateau. *Geology Field Trip Guides by Anabelle Foos, University of Akron*. Available online at: <http://www2.nature.nps.gov/geology/education>.

- FOURNIER, M., LEPVRIER, C., RAZIN, P. and JOLIVET, L., 2006. Late Cretaceous to Paleogene post-obduction extension and subsequent Neogene compression in the Oman Mountains. *GeoArabia*, **11**(4), pp. 17-40.
- FREEMAN, W.E. and VISHNER, G.S., 1975. Stratigraphic analysis of the Navajo Sandstone. *Journal of Sedimentary Research*, **45**(3).
- FRYBERGER, S. and GOUDIE, A., 1981. Arid geomorphology. *Progress in Physical Geography*, **5**(3), pp. 420-428.
- FRYBERGER, S.G. and DEAN, G., 1979. Dune forms and wind regime. *A study of global sand seas*, **1052**, pp. 137-169.
- FRYBERGER, S.G. and SCHENK, C., 1981. Wind sedimentation tunnel experiments on the origins of aeolian strata. *Sedimentology*, **28**(6), pp. 805-821.
- FRYBERGER, S.G., HERN, C. and GLENNIE, K., 2016b. Geological studies for petroleum exploration analogues in the Wahiba Sand Sea, Oman, contribute to wind energy development. *Geological Society of America Special Papers*, **520**, pp. 117-123.
- FRYBERGER, S.G., HERN, C.Y. and GLENNIE, K., 2016a. Sedimentology of Reservoir-scale Aeolian-Fluvial Interactions, Wadi Batha, Northern Wahiba Sand Sea, Oman.
- FRYBERGER, S.G., HERN, C.Y. and JONES, N., 2017. Modern and Ancient Analogues for Complex Eolian Reservoirs. *Mountain Geologist*, **12**, pp. 61-73.
- GARDNER, R., 1988. Aeolianites and marine deposits of the Wahiba Sands: character and palaeoenvironments. *The Journal of Oman Studies Special Report*, **3**, pp. 75-95.
- GAWTHORPE, R., COLLIER, R.L., ALEXANDER, J., BRIDGE, J. and LEEDER, M., 1993. Ground penetrating radar: application to sandbody geometry and heterogeneity studies. *Geological Society, London, Special Publications*, **73**(1), pp. 421-432.
- GESCH, D., OIMOEN, M., DANIELSON, J. AND MEYER, D., 2016. Validation of the ASTER global digital elevation model version 3 over the conterminous United States. *The International Archives of Photogrammetry, Remote Sensing and Spatial Information Sciences*, **41**, p.143.
- GHAZANFAR, S.A., 1992. Quantitative and biogeographic analysis of the flora of the Sultanate of Oman. *Global Ecology and Biogeography Letters*, , pp. 189-195.
- GLENNIE, K. and BULLER, A., 1983. The Permian Weissliedend of NW Europe: the partial deformation of aeolian dune sands caused by the Zechstein transgression. *Sedimentary Geology*, **35**(1), pp. 43-81.
- GLENNIE, K. and SINGHVI, A., 2002. Event stratigraphy, paleoenvironment and chronology of SE Arabian deserts. *Quaternary Science Reviews*, **21**(7), pp. 853-869.
- GLENNIE, K., 1970. Developments in Sedimentology. *Nº*, **14**, pp. 78-85.
- GLENNIE, K., FRYBERGER, S., HERN, C., LANCASTER, N., TELLER, J., PANDEY, V. and SINGHVI, A., 2011. Geological importance of luminescence dates in Oman and the Emirates: An overview. *Geochronometria*, **38**(3), pp. 259-271.

- GOGGIN, D., CHANDLER, M., KOCUREK, G. and LAKE, L.W., 1992. Permeability transects of eolian sands and their use in generating random permeability fields. *SPE Formation Evaluation*, **7**(01), pp. 7-16.
- GOUDIE, A., WARREN, A., JONES, D. and COOKE, R., 1987. The character and possible origins of the aeolian sediments of the Wahiba Sand Sea, Oman. *Geographical Journal*, , pp. 231-256.
- GOUDIE, A.S., 2013. *Arid and semi-arid geomorphology*. Cambridge University Press.
- GRIFFITHS, P. G., WEBB, R. H., FISHER, M. & MUTH, A. 2009. Plants and ventifacts delineate late Holocene wind vectors in the Coachella Valley, USA. *Aeolian Research*, **1**, 63-73.
- GUPTA, R.P., 2018. *Remote sensing geology*. Third edition, Springer Nature, Berlin, Germany. <https://doi.org/10.1007/978-3-662-55876-8>
- HANNA, S.S., 1990. The Alpine deformation of the central Oman Mountains. *Geological Society, London, Special Publications*, **49**(1), pp. 341-359.
- HANSMAN, R.J., RING, U., THOMSON, S.N., DEN BROK, B. and STÜBNER, K., 2017. Late Eocene uplift of the Al Hajar Mountains, Oman, supported by stratigraphy and low-temperature thermochronology. *Tectonics*, **36**(12), pp. 3081-3109.
- HAQ, B.U., 2009. Sequence stratigraphy, sea-level change, and significance for the deep sea. *Sedimentation, Tectonics and Eustasy (Ed. Macdonald, DIM) Int.Ass.Sediment.Spec.Publ*, **12**, pp. 3-39.
- HASSAN, M.S., VENETIKIDIS, A., BRYANT, G. and MIALL, A.D., 2018. The Sedimentology of an ERG Margin: The Kayenta–Navajo Transition (Lower Jurassic), Kanab, Utah, USA. *Journal of Sedimentary Research*, **88**(5), pp. 613-640.
- HAVHOLM, K., BLAKEY, R., CAPPS, M., JONES, L., KING, D. and KOCUREK, G., 1993. Aeolian genetic stratigraphy: an example from the Middle Jurassic Page sandstone, Colorado Plateau. *Aeolian Sediments: Ancient and Modern*, , pp. 85-107.
- HAVHOLM, K.G. and KOCUREK, G., 1988. A preliminary study of the dynamics of a modern draa, Algodones, southeastern California, USA. *Sedimentology*, **35**(4), pp. 649-669.
- HAY, A.S., 2018. *The Influence of Complex Topography on Aeolian Sediment Accumulation and Preservation: An Investigation of Morphology and Process History*, .
- HERN, C., TATUM, D., WESTERMAN, R., KOCUREK, G. and FRYBERGER, S., Studies in Contemporary Sand Seas Inform Better Reservoir Models, *AAPG ACE 2018*.
- HERRIES, R.D., 1993. Contrasting styles of fluvial-aeolian interaction at a downwind erg margin: Jurassic Kayenta-Navajo transition, northeastern Arizona, USA. *Geological Society, London, Special Publications*, **73**(1), pp. 199-218.
- HESP, P.A. AND PRINGLE, A., 2001. Wind Flow and Topographic Steering Within a Trough Blowout. *Journal of Coastal Research Special Issue 34*, (ICS 2000 New Zealand). ISSN 0749-0208.
- HILBERT-WOLF, H.L., ROBERTS, E.M. and SIMPSON, E.L., 2016. New sedimentary structures in seismites from SW Tanzania: Evaluating gas-vs. water-escape mechanisms of soft-sediment deformation. *Sedimentary Geology*, **344**, pp. 253-262.

- HILLER, J. and SMITH, M., 2008. Residual relief separation: digital elevation model enhancement for geomorphological mapping. *Earth Surface Processes and Landforms*, **33**(14), pp. 2266-2276.
- HOFFMAN, P.F., 1988. United plates of America, the birth of a craton: Early Proterozoic assembly and growth of Laurentia. *Annual Review of Earth and Planetary Sciences*, **16**(1), pp. 543-603.
- HOROWITZ, D.H., 1982. Geometry and origin of large-scale deformation structures in some ancient wind-blown sand deposits. *Sedimentology*, **29**(2), pp. 155-180.
- HOWARD, A.D., 1977. Effect of slope on the threshold of motion and its application to orientation of wind ripples. *Geological Society of America Bulletin*, **88**(6), pp. 853-856.
- HUGENHOLTZ, C.H. and BARCHYN, T.E., 2010. Spatial analysis of sand dunes with a new global topographic dataset: new approaches and opportunities. *Earth Surface Processes and Landforms*, **35**(8), pp. 986-992.
- HUGENHOLTZ, C.H. and WOLFE, S.A., 2005. Recent stabilization of active sand dunes on the Canadian prairies and relation to recent climate variations. *Geomorphology*, **68**(1-2), pp. 131-147.
- HUGENHOLTZ, C.H., LEVIN, N., BARCHYN, T.E. and BADDOCK, M.C., 2012. Remote sensing and spatial analysis of aeolian sand dunes: A review and outlook. *Earth-Science Reviews*, **111**(3-4), pp. 319-334.
- HUNTER, R.E. and RUBIN, D.M., 1983. Interpreting cyclic crossbedding, with an example from the Navajo Sandstone. *Developments in sedimentology*. Elsevier, pp. 429-454.
- HUNTER, R.E., 1977. Basic types of stratification in small eolian dunes. *Sedimentology*, **24**(3), pp. 361-387.
- HUNTER, R.E., 1981. Stratification styles in eolian sandstones: some Pennsylvanian to Jurassic examples from the western interior USA.
- HUNTOON, J.E. and CHAN, M.A., 1987. Marine origin of paleotopographic relief on eolian White Rim Sandstone (Permian), Elaterite Basin, Utah. *AAPG Bulletin*, **71**(9), pp. 1035-1045.
- INGERSOLL, R.V., 2008. Subduction-related sedimentary basins of the USA Cordillera. *Sedimentary Basins of the World*, **5**, pp. 395-428.
- JENSEN, J.R., 2015. *Introductory digital image processing: a remote sensing perspective*. Prentice Hall Press.
- JOL, H.M. and BRISTOW, C.S., 2003. GPR in sediments: advice on data collection, basic processing and interpretation, a good practice guide. *Geological Society, London, Special Publications*, **211**(1), pp. 9-27.
- JOL, H.M., BRISTOW, C.S. (2003). GPR in Sediments: advice on data collection, basic processing and interpretation, a good practice guide. In *Ground Penetrating Radar in Sediments*; Bristow, C.S., Jol, H.M., Eds.; Geological Society London Special Publication: London, UK, 2003; Volume 211, pp. 9–27.
- JONES, D., COOKE, R. and WARREN, A., 1988. A terrain classification of the Wahiba Sands of Oman. *Journal of Oman Studies*, **3**, pp. 1985-1987.

- JUYAL, N., SINGHVI, A. and GLENNIE, K., 1998. Chronology and paleoenvironmental significance of Quaternary desert sediment in southeastern Arabia. *Quaternary Deserts and Climatic Change*. Rotterdam: Taylor & Francis, , pp. 315-325.
- KELLEY, V.C., 1955. *Regional Tectonics of the Colorado Plateau and Relationship to the Origin and Distribution of Uranium: Prepared in Cooperation with US Atomic Energy Commission, Division of Raw Materials*. University of New Mexico Press.
- KOCUREK, G. and DAY, M., 2018. What is preserved in the aeolian rock record? A Jurassic Entrada Sandstone case study at the Utah–Arizona border. *Sedimentology*, **65**(4), pp. 1301-1321.
- KOCUREK, G. and DOTT, R.H., 1981. Distinctions and uses of stratification types in the interpretation of eolian sand. *Journal of Sedimentary Research*, **51**(2), pp. 579-595.
- KOCUREK, G. and EWING, R.C., 2005. Aeolian dune field self-organization—implications for the formation of simple versus complex dune-field patterns. *Geomorphology*, **72**(1-4), pp. 94-105.
- KOCUREK, G. and FIELDER, G., 1982. Adhesion structures. *Journal of Sedimentary Research*, **52**(4), pp. 1229-1241.
- KOCUREK, G. and HAVHOLM, K.G., 1993. Eolian sequence stratigraphy—a conceptual framework. *MEMOIRS-AMERICAN ASSOCIATION OF PETROLEUM GEOLOGISTS*, , pp. 393-393.
- KOCUREK, G. and LANCASTER, N., 1999. Aeolian system sediment state: theory and Mojave Desert Kelso dune field example. *Sedimentology*, **46**(3), pp. 505-515.
- KOCUREK, G. and NIELSON, J., 1986. Conditions favourable for the formation of warm-climate aeolian sand sheets. *Sedimentology*, **33**(6), pp. 795-816.
- KOCUREK, G., 1981. Significance of interdune deposits and bounding surfaces in aeolian dune sands. *Sedimentology*, **28**(6), pp. 753-780.
- KOCUREK, G., 1988. First-order and super bounding surfaces in eolian sequences—bounding surfaces revisited. *Sedimentary Geology*, **56**(1-4), pp. 193-206.
- KOCUREK, G., 1991. Interpretation of ancient eolian sand dunes. *Annual Review of Earth and Planetary Sciences*, **19**, pp. 43.
- KOCUREK, G., 1996. Desert aeolian systems. , in Reading, H. G., ed., *Sedimentary environments: Processes, facies and stratigraphy*: Oxford, Blackwell Science, p. 125–153.
- KOCUREK, G., 1998. Aeolian system response to external forcing factors—a sequence stratigraphic view of the Saharan region. *Quaternary deserts and climatic change*, , pp. 327-337.
- KOCUREK, G., 1999. The aeolian rock record (Yes, Virginia, it exists, but it really is rather special to create one). *Aeolian environments, sediments and landforms*, , pp. 239-259.
- KOCUREK, G., 2003. Limits on extreme eolian systems: Sahara of Mauritania and Jurassic Navajo Sandstone examples. *SPECIAL PAPERS-GEOLOGICAL SOCIETY OF AMERICA*, , pp. 43-52.
- KOK, J.F., PARTELI, E.J., MICHAELS, T.I. and KARAM, D.B., 2012. The physics of wind-blown sand and dust. *Reports on Progress in Physics*, **75**(10), pp. 106901.

- KUSKY, T., ROBINSON, C. and EL-BAZ, F., 2005. Tertiary–Quaternary faulting and uplift in the northern Oman Hajar Mountains. *Journal of the Geological Society*, **162**(5), pp. 871-888.
- LANCASTER, N. and GREELEY, R., 1990. Sediment volume in the north polar sand seas of Mars. *Journal of Geophysical Research: Solid Earth*, **95**(B7), pp. 10921-10927.
- LANCASTER, N., 1982. Dunes on the Skeleton Coast, Namibia (South West Africa): geomorphology and grain size relationships. *Earth Surface Processes and Landforms*, **7**(6), pp. 575-587.
- LANCASTER, N., 1983. Controls of dune morphology in the Namib sand sea. *Developments in Sedimentology*. Elsevier, pp. 261-289.
- LANCASTER, N., 1988a. Controls of eolian dune size and spacing. *Geology*, **16**(11), pp. 972-975.
- LANCASTER, N., 1988b. The development of large aeolian bedforms. *Sedimentary Geology*, **55**(1-2), pp. 69-89.
- LANCASTER, N., 1989. The Namib Sand Sea: Dune Forms, Processes and Sediments. In: A.A. BALKEMA, ed, *Rotterdam*. pp. 80-200 pp.
- LANCASTER, N., 1992. Relations between dune generations in the Gran Desierto of Mexico. *Sedimentology*, **39**(4), pp. 631-644.
- LANCASTER, N., 2013. *Geomorphology of desert dunes*. Routledge.
- LANCASTER, N., KOCUREK, G., SINGHVI, A., PANDEY, V., DEYNOUX, M., GHIENNE, J. and LÔ, K., 2002. Late Pleistocene and Holocene dune activity and wind regimes in the western Sahara Desert of Mauritania. *Geology*, **30**(11), pp. 991-994.
- LANGFORD, R. and CHAN, M., 1989. Fluvial-aeolian interactions: Part II, ancient systems. *Sedimentology*, **36**(6), pp. 1037-1051.
- LANGFORD, R.P., PEARSON, K.M., DUNCAN, K.A., TATUM, D.M., ADAMS, L. and DEPRET, P., 2008. Eolian topography as a control on deposition incorporating lessons from modern dune seas: Permian Cedar Mesa Sandstone, SE Utah, USA. *Journal of Sedimentary Research*, **78**(6), pp. 410-422.
- LASHKARI, H., MOHAMMADI, Z. and KEIKHOSRAVI, G., 2017. Annual fluctuations and displacements of inter tropical convergence zone (ITCZ) within the range of Atlantic Ocean-India. *Open Journal of Ecology*, **7**(1), pp. 12.
- LEEDER, M.R., 2012. *Sedimentology: process and product*. Springer Science & Business Media.
- LEVIN, N., KIDRON, G.J. and BEN-DOR, E., 2006. The spatial and temporal variability of sand erosion across a stabilizing coastal dune field. *Sedimentology*, **53**(4), pp. 697-715.
- LI, X., KONG, D., TAN, H. and WANG, X., 2007. Changes in soil and vegetation following stabilisation of dunes in the southeastern fringe of the Tengger Desert, China. *Plant and Soil*, **300**(1-2), pp. 221-231.
- LILLESAND, T., KIEFER, R.W. and CHIPMAN, J., 2015. *Remote sensing and image interpretation*. John Wiley & Sons.

- LIU, L. and GURNIS, M., 2010. Dynamic subsidence and uplift of the Colorado Plateau. *Geology*, **38**(7), pp. 663-666.
- LIVINGSTONE, I. AND WARREN, A. (1996). *Aeolian Geomorphology: An Introduction*. London: Longman.
- LIVINGSTONE, I. and WARREN, A., 1996. *Aeolian geomorphology: an introduction*. Longman.
- LIVINGSTONE, I. and WARREN, A., 2019. *Aeolian Geomorphology: A New Introduction*. John Wiley & Sons.
- LIVINGSTONE, I., BRISTOW, C., BRYANT, R.G., BULLARD, J., WHITE, K., WIGGS, G.F., BAAS, A.C., BATEMAN, M.D. and THOMAS, D.S., 2010. The Namib Sand Sea digital database of aeolian dunes and key forcing variables. *Aeolian Research*, **2**(2-3), pp. 93-104.
- LOOPE, D., EISENBERG, L. and WAISS, E., 2004. Navajo sand sea of near-equatorial Pangea: Tropical westerlies, slumps, and giant stromatolites. *Field Guides*, **5**, pp. 1-13.
- LOOPE, D.B. and BURBERRY, C.M., 2018. Sheeting joints and polygonal patterns in the Navajo Sandstone, southern Utah: Controlled by rock fabric, tectonic joints, buckling, and gully. *Geosphere*, **14**(4), pp. 1818-1836.
- LOOPE, D.B. and ROWE, C.M., 2003. Long-lived pluvial episodes during deposition of the Navajo Sandstone. *The Journal of geology*, **111**(2), pp. 223-232.
- LOOPE, D.B., ELDER, J.F. and SWEENEY, M.R., 2012. Downslope coarsening in aeolian grainflows of the Navajo Sandstone. *Sedimentary Geology*, **265**, pp. 156-162.
- LOOPE, D.B., ROWE, C.M. and JOECKEL, R.M., 2001. Annual monsoon rains recorded by Jurassic dunes. *Nature*, **412**(6842), pp. 64-66.
- LOOPE, D.B., STEINER, M.B., ROWE, C.M. and LANCASTER, N., 2004. Tropical westerlies over Pangaeian sand seas. *Sedimentology*, **51**(2), pp. 315-322.
- LUANA, S., HOU, X. AND WANG, Y., 2015. Assessing the accuracy of SRTM dem and Aster Gdem datasets for the coastal zone of Shandong Province, Eastern China. *Polish Maritime Research*, **22**(s1), pp.15-20.
- LUCAS, S. and TANNER, L., 2014. Unconformable contact of the Lower Jurassic Wingate and Kayenta Formations, Utah. *Utah Geological Association Publication*, **43**, pp. 311-320.
- LUCAS, S., TANNER, L., DONOHOO-HURLEY, L., GEISSMAN, J., KOZUR, H., HECKERT, A. and WEEMS, R., 2011. Position of the Triassic–Jurassic boundary and timing of the end-Triassic extinctions on land: Data from the Moenave Formation on the southern Colorado Plateau, USA. *Palaeogeography, Palaeoclimatology, Palaeoecology*, **302**(3), pp. 194-205.
- LUTTRELL, P., 1986. Provenance and basin analysis of the Kayenta Formation (Early Jurassic); central portion Colorado Plateau [abs.]: Geological Society of America, Rocky Mountain Section, *Abstracts with Programs* 1986, pp. 392.

- LUTTRELL, P.R., 1987. *Basin analysis of the Kayenta Formation (Lower Jurassic), central portion Colorado Plateau*. Northern Arizona University.
- LUTTRELL, P.R., 1993. Basinwide sedimentation and the continuum of paleoflow in an ancient river system: Kayenta Formation (Lower Jurassic), central portion Colorado Plateau. *Sedimentary Geology*, **85**(1-4), pp. 411-434.
- MANUEL, R., BRITO, M., CHICHORRO, M. and ROSA, C., 2017. Remote sensing for mineral exploration in central Portugal. *Minerals*, **7**(10), pp. 184.
- MARZOLF, J.E., 1983. Changing wind and hydrologic regimes during deposition of the Navajo and Aztec sandstones, Jurassic (?), southwestern United States. *Developments in Sedimentology*, **38**, pp. 635-660.
- MARZOLF, J.E., 1993. Palinspastic reconstruction of early Mesozoic sedimentary basins near the latitude of Las Vegas: Implications for the early Mesozoic Cordilleran cratonal margin.
- MARZOLF, J.E., 1994. Reconstruction of the early Mesozoic Cordilleran cratonal margin adjacent to the Colorado Plateau, 1994, Rocky Mountain Section (SEPM).
- MASEK, J.G., 2020, NASA Landsat Science, Landsat 8, viewed 29 January 2020, <<https://landsat.gsfc.nasa.gov/landsat-data-continuity-mission/>>
- MCKEE, E.D. and BIGARELLA, J., 1979. Ancient sandstones considered to be eolian. *A study of global sand seas: US Geological Survey Professional Paper*, **1052**, pp. 187-238.
- MCKEE, E.D., 1966. Structures of dunes at White Sands National Monument, New Mexico (and a comparison with structures of dunes from other selected areas) 1. *Sedimentology*, **7**(1), pp. 3-69.
- MIALL, A.D., 1985. Architectural-element analysis: a new method of facies analysis applied to fluvial deposits. *Earth-Science Reviews*, **22**(4), pp. 261-308.
- MIALL, A.D., 1988. Architectural elements and bounding surfaces in fluvial deposits: anatomy of the Kayenta Formation (Lower Jurassic), southwest Colorado. *Sedimentary Geology*, **55**(3-4), pp. 233247-240262.
- MIALL, A.D., 2008. The Paleozoic western craton margin. *Sedimentary Basins of the World*, **5**, pp. 181-209.
- MIALL, A.D., 2016. Stratigraphy: the modern synthesis. *Stratigraphy: A Modern Synthesis*. Springer, pp. 311-370.
- MIDDLETON, L.T. and BLAKEY, R.C., 1983. Processes and controls on the intertonguing of the Kayenta and Navajo Formations, northern Arizona: eolian-fluvial interactions. *Developments in Sedimentology*, **38**, pp. 613-634.
- MILLER, E.L., MILLER, M.M., STEVENS, C.H., WRIGHT, J.E. and MADRID, R., 1992. Late Paleozoic paleogeographic and tectonic evolution of the western US Cordillera. *The Cordilleran orogen: Conterminous US: Boulder, Colorado, Geological Society of America, Geology of North America*, **3**, pp. 57-106.

- MOUNTNEY, N.P. and JAGGER, A., 2004. Stratigraphic evolution of an aeolian erg margin system: the Permian Cedar Mesa Sandstone, SE Utah, USA. *Sedimentology*, **51**(4), pp. 713-743.
- MOUNTNEY, N.P. and RUSSELL, A.J., 2004. Sedimentology of cold-climate aeolian sandsheet deposits in the Askja region of northeast Iceland. *Sedimentary Geology*, **166**(3-4), pp. 223-244.
- MOUNTNEY, N.P. and THOMPSON, D.B., 2002. Stratigraphic evolution and preservation of aeolian dune and damp/wet interdune strata: an example from the Triassic Helsby Sandstone Formation, Cheshire Basin, UK. *Sedimentology*, **49**(4), pp. 805-833.
- MOUNTNEY, N.P., 2006a. Eolian facies models. In: Facies Models Revisited (Eds H. Posamentier and R.G. Walker). SEPM Mem., 84, 19–83.
- MOUNTNEY, N.P., 2006b. Periodic accumulation and destruction of aeolian erg sequences in the Permian Cedar Mesa Sandstone, White Canyon, southern Utah, USA. *Sedimentology*, **53**(4), pp. 789-823.
- MOUNTNEY, N.P., 2012. A stratigraphic model to account for complexity in aeolian dune and interdune successions. *Sedimentology*, **59**(3), pp. 964-989.
- MOUNTNEY, N.P., POSAMENTIER, H. and WALKER, R., 2006. Eolian facies models. *SPECIAL PUBLICATION-SEPM*, **84**, pp. 19.
- MUNTON, P., 1988. Vegetation and forage availability in the sands. *Journal of Oman Studies*, **3**, pp. 241-250.
- MUNYIKWA, K., TELFER, M., BAKER, I. AND KNIGHT, C., 2011. Core drilling of Quaternary sediments for luminescence dating using the Dormer Drillmite. *Ancient TL*, **29**(1), pp.15-23.
- NEAL, A., 2004. Ground-penetrating radar and its use in sedimentology: principles, problems and progress. *Earth-Science Reviews*, **66**(3-4), pp. 261-330.
- NEUENDORF, K.K., MEHL JR, J.P. and JACKSON, J.A., 2005. *Glossary of Geology*. Alexandria, VA: American Geological Institute, .
- NICHOLS, G., 2009. *Sedimentology and stratigraphy*. John Wiley & Sons.
- NOURI, R., JAFARI, M., ARAIN, M. and FEIZI, F., 2012. Hydrothermal alteration zones identification based on remote sensing data in the Mahin Area, West of Qazvin Province, Iran. *World Academy of Science, Engineering and Technology, International Journal of Environmental, Chemical, Ecological, Geological and Geophysical Engineering*, **6**(7), pp. 382-385.
- NURSAIDOVA, R., 2009. *3D architecture of a linear dune revealed by GPR: assessing the impact of heterogeneity*, HERIOT-WATT UNIVERSITY.
- OLSEN, H., DUE, P.H. and CLEMMENSEN, L.B., 1989. Morphology and genesis of asymmetric adhesion warts—a new adhesion surface structure. *Sedimentary Geology*, **61**(3-4), pp. 277-285.
- OLSEN, T.R., MELLERE, D. and OLSEN, T., 1999. Facies architecture and geometry of landward-stepping shoreface tongues: the Upper Cretaceous Cliff House Sandstone (Mancos Canyon, south-west Colorado). *Sedimentology*, **46**(4), pp. 603-625.

PARRISH, J.T., HASIOTIS, S.T. and CHAN, M.A., 2017. CARBONATE DEPOSITS IN THE LOWER JURASSIC NAVAJO SANDSTONE, SOUTHERN UTAH AND NORTHERN ARIZONA, USAJT PARRISH *ET AL.* NAVAJO SANDSTONE CARBONATE DEPOSITS. *Journal of Sedimentary Research*, **87**(7), pp. 740-762.

PARRISH, J.T., HASIOTIS, S.T. and CHAN, M.A., 2017. CARBONATE DEPOSITS IN THE LOWER JURASSIC NAVAJO SANDSTONE, SOUTHERN UTAH AND NORTHERN ARIZONA, USAJT PARRISH *ET AL.* NAVAJO SANDSTONE CARBONATE DEPOSITS. *Journal of Sedimentary Research*, **87**(7), pp. 740-762.

PARRISH, J.T., RASBURY, E.T., CHAN, M.A. AND HASIOTIS, S.T., 2019. Earliest Jurassic U-Pb ages from carbonate deposits in the Navajo Sandstone, southeastern Utah, USA. *Geology*, **47**(11), pp.1015-1019.

PEASE, P. and TCHAKERIAN, V., 2014. Source provenance of carbonate grains in the Wahiba Sand Sea, Oman, using a new LIBS method. *Aeolian Research*, **15**, pp. 203-216.

PEASE, P.P. and TCHAKERIAN, V.P., 2002. Composition and sources of sand in the Wahiba Sand Sea, Sultanate of Oman. *Annals of the Association of American Geographers*, **92**(3), pp. 416-434.

PEASE, P.P., BIERLY, G.D., TCHAKERIAN, V.P. and TINDALE, N.W., 1999. Mineralogical characterization and transport pathways of dune sand using Landsat TM data, Wahiba Sand Sea, Sultanate of Oman. *Geomorphology*, **29**(3-4), pp. 235-249.

PETERSON, F. and PIPIRINGOS, G.N., 1979. *Stratigraphic relations of the Navajo Sandstone to Middle Jurassic formations, southern Utah and northern Arizona*, .

PETERSON, F., 1988. Pennsylvanian to Jurassic eolian transportation systems in the western United States. *Sediment. Geol.* **56**, 207– 260.

PETERSON, F., 1994. Sand dunes, sabkhas, streams, and shallow seas: Jurassic paleogeography in the southern part of the Western Interior Basin, 1994, Rocky Mountain Section (SEPM).

PICHA, F. and GIBSON, R.I., 1985. Cordilleran hingeline: Late Precambrian rifted margin of the North American craton and its impact on the depositional and structural history, Utah and Nevada. *Geology*, **13**(7), pp. 465-468.

PIPIRINGOS, G.N. and O'SULLIVAN, R.B., 1978. *Principal unconformities in Triassic and Jurassic rocks, western interior United States; a preliminary survey*, .

PORTER, M., 1986. Sedimentary record of erg migration. *Geology*, **14**(6), pp. 497-500.

PORTER, M., 1987. Sedimentology of an ancient erg margin: the Lower Jurassic Aztec Sandstone, southern Nevada and southern California. *Sedimentology*, **34**(4), pp. 661-680.

POUR, A.B. and HASHIM, M., 2015. Hydrothermal alteration mapping from Landsat-8 data, Sar Cheshmeh copper mining district, south-eastern Islamic Republic of Iran. *Journal of Taibah University for Science*, **9**(2), pp. 155-166.

PREUSSER, F., 2009. Chronology of the impact of Quaternary climate change on continental environments in the Arabian Peninsula. *Comptes Rendus Geoscience*, **341**(8-9), pp. 621-632.

- PREUSSER, F., RADIES, D. and MATTER, A., 2002. A 160,000-year record of dune development and atmospheric circulation in Southern Arabia. *Science (New York, N.Y.)*, **296**(5575), pp. 2018-2020.
- PREUSSER, F., RADIES, D., DRIEHORST, F. and MATTER, A., 2005. Late Quaternary history of the coastal Wahiba sands, Sultanate of Oman. *Journal of Quaternary Science: Published for the Quaternary Research Association*, **20**(4), pp. 395-405.
- PRIDDY, C.L., PRINGLE, J.K., CLARKE, S.M. and PETTIGREW, R.P., 2019. Application of photogrammetry to generate quantitative geobody data in ephemeral fluvial systems. *The Photogrammetric Record*, .
- PROST, G.L., 2013. *Remote Sensing for Geoscientists: Image Analysis and Integration*. Third Edition edn. Florida: Taylor & Francis Group.
- PYE, K. and TSOAR, H., 2008. *Aeolian sand and sand dunes*. Springer Science & Business Media.
- RADIES, D., 2002. The Development of the Wahiba Sand Sea during the Late Quaternary. Unpublished PhD Thesis. University of Bern, Switzerland
- RAHL, J.M., REINERS, P.W., CAMPBELL, I.H., NICOLESCU, S. and ALLEN, C.M., 2003. Combined single-grain (U-Th)/He and U/Pb dating of detrital zircons from the Navajo Sandstone, Utah. *Geology*, **31**(9), pp. 761-764.
- RAJESH, H., 2004. Application of remote sensing and GIS in mineral resource mapping-An overview. *Journal of Mineralogical and Petrological Sciences*, **99**(3), pp. 83-103.
- RARITY, F., VAN LANEN, X.M.T., HODGETTS, D., GAWTHORPE, R.L., WILSON, P., FABUEL-PEREZ, I. AND REDFERN, J., 2014. LiDAR-based digital outcrops for sedimentological analysis: workflows and techniques. *Geological Society, London, Special Publications*, **387**(1), pp.153-183.
- REYNOLDS, J.M. (2011) *An Introduction to Applied and Environmental Geophysics*; Wiley: Hoboken, NJ, USA, 1997; 796p.
- RIDING, R., 1991. Classification of microbial carbonates. *Calcareous algae and stromatolites*. Springer, pp. 21-51.
- RIGGS, N.R. and BLAKEY, R.C., 1993. Early and Middle Jurassic paleogeography and volcanology of Arizona and adjacent areas.
- ROBINSON, C., EL-BAZ, F., KUSKY, T., MAINGUET, M., DUMAY, F., AL SULEIMANI, Z. and AL MARJEBY, A., 2007. Role of fluvial and structural processes in the formation of the Wahiba Sands, Oman: A remote sensing perspective. *Journal of Arid Environments*, **69**(4), pp. 676-694.
- ROBINSON, M., BRISTOW, C., MCKINLEY, J. and RUFFELL, A., 2013. Ground penetrating radar. *Geomorphological Techniques, Part, 1*, pp. 2047-0371.
- RODGERS, D.W. and GUNATILAKA, A., 2003. Bajada formation by monsoonal erosion of a subaerial forebulge, Sultanate of Oman. *Sedimentary Geology*, **154**(3-4), pp. 127-146.
- RODRÍGUEZ-LÓPEZ, J.P., CLEMMENSEN, L.B., LANCASTER, N., MOUNTNEY, N.P. and VEIGA, G.D., 2014. Archean to Recent aeolian sand systems and their sedimentary record: current understanding and future prospects. *Sedimentology*, **61**(6), pp. 1487-1534.

- ROLLINSON, H.R., SEARLE, M.P., ABBASI, I.A., AL-LAZKI, A.I. and AL KINDI, M.H., 2014. Tectonic evolution of the Oman Mountains: an introduction. *Geological Society, London, Special Publications*, **392**(1), pp. 1-7.
- ROMAIN, H.G. and MOUNTNEY, N.P., 2014. Reconstruction of three-dimensional eolian dune architecture from one-dimensional core data through adoption of analog data from outcrop. *AAPG Bulletin*, **98**(1), pp. 1-22.
- ROMAIN, H.G., 2014. *Controls on aeolian bed-set architecture and implications for reservoir heterogeneity*. Unpublished PhD Thesis. The University of Leeds. September, 2014.
- ROSS, C.A. and ROSS, J.R., 1988. Late Paleozoic transgressive-regressive deposition. : Society of Economic Paleontologists and Mineralogists Special Publication 42, p. 227–247.
- ROSS, G.M., 1983. Proterozoic aeolian quartz arenites from the Hornby Bay Group, Northwest Territories, Canada: implications for Precambrian aeolian processes. *Precambrian Research*, **20**(2-4), pp. 149-160.
- RUBIN, D. and HUNTER, R.E., 1983. Reconstructing bedform assemblages from compound crossbedding. *Developments in Sedimentology*. Elsevier, pp. 407-427.
- RUBIN, D.M. and CARTER, C.L., 2006. *Bedforms and cross-bedding in animation*. Sepm Society for Sedimentary. <https://pubs.usgs.gov/of/2005/1272>.
- RUBIN, D.M. AND HESP, P.A., 2009. Multiple origins of linear dunes on Earth and Titan. *Nature Geoscience*, **2**(9), pp.653-658.
- RUBIN, D.M. and HUNTER, R.E., 1982. Bedform climbing in theory and nature. *Sedimentology*, **29**(1), pp. 121-138.
- RUBIN, D.M. and HUNTER, R.E., 1985. Why deposits of longitudinal dunes are rarely recognized in the geologic record. *Sedimentology*, **32**(1), pp. 147-157.
- RUBIN, D.M., 1987. Formation of scalloped cross-bedding without unsteady flows. *Journal of Sedimentary Research*, **57**(1), pp. 39-45.
- RUBIN, D.M., TSOAR, H. AND BLUMBERG, D.G., 2008. A second look at western Sinai seif dunes and their lateral migration. *Geomorphology*, **93**(3-4), pp.335-342.
- RUNCORN, S., 1964. Palaeowind directions and palaeomagnetic latitudes. *Problems in Palaeoclimatology: London-New York, Interscience Publishers*, pp. 409-421.
- SANSOM, P., 1992. *Sedimentology of the Navajo Sandstone, southern Utah, USA*: Unpublished Ph.D. Wolfson College. DOI: 10.13140/RG.2.2.32239.43686.
- SANSOM, P., Stratigraphic Evolution of the Eolian Navajo Sandstone, SE Utah, *AAPG ACE 2018*.
- SATELLITE IMAGING CORPORATION GEOEYE-1, 2017, GeoEye-1 Satellite Sensor, viewed 29 January 2020, <<https://www.satimagingcorp.com/satellite-sensors/geoeeye-1/>>
- SATELLITE IMAGING CORPORATION WORLDVIEW-3, 2017, Worldview-3 Satellite Sensor, viewed 29 January 2020, <<https://www.satimagingcorp.com/satellite-sensors/worldview-3/>>

- SCHEIDEGGER, A., BORKOVEC, M. and STICHER, H., 1993. Coating of silica sand with goethite: preparation and analytical identification. *Geoderma*, **58**(1-2), pp. 43-65.
- SCOTTI, A.A. and VEIGA, G.D., 2015. Morphological characterization of an exceptionally preserved eolian system: The Cretaceous Troncoso Inferior Member in the Neuquén Basin (Argentina). *Latin American journal of sedimentology and basin analysis*, **22**(1), pp. 29-46.
- SCOTTI, A.A. and VEIGA, G.D., 2019. Sedimentary architecture of an ancient linear megadune (Barremian, Neuquén Basin): Insights into the long-term development and evolution of aeolian linear bedforms. *Sedimentology* (2019) 66, 2191–2213
- SEARLE, M. and COX, J., 1999. Tectonic setting, origin, and obduction of the Oman ophiolite. *Geological Society of America Bulletin*, **111**(1), pp. 104-122.
- SEARS, J.D., 1956. Geology of Comb Ridge and vicinity north of San Juan River, San Juan County, Utah (No. 1021-E). US Geological Survey.
- SHEPHERD, M., 2009. The Role of the Production Geologist.
- SLOSS, L., 1988. Tectonic evolution of the craton in Phanerozoic time. *The Geology of North America*, **2**, pp. 25-51.
- SPATZ, D., 1997. Remote sensing characteristics of the sediment-and volcanic-hosted precious metal systems: imagery selection for exploration and development. *International Journal of Remote Sensing*, **18**(7), pp. 1413-1438.
- STERN, R.J. and JOHNSON, P., 2010. Continental lithosphere of the Arabian Plate: a geologic, petrologic, and geophysical synthesis. *Earth-Science Reviews*, **101**(1-2), pp. 29-67.
- STOKES, W.L., 1976. What is the Wasatch Line? .
- STORY, C., 1998. Norphlet geology and 3-D geophysics: Fairway Field, Mobile Bay, Alabama. *The Leading Edge*, **17**(2), pp. 243-243.
- SWANSON, T., MOHRIG, D., KOCUREK, G., CARDENAS, B.T. and WOLINSKY, M.A., 2019. Preservation of Autogenic Processes and Allogenic Forcings in Set-Scale Aeolian Architecture I: Numerical Experiments. *Journal of Sedimentary Research*, **89**(8), pp. 728-740.
- TAKAKU, J., TADONO, T. AND TSUTSUI, K., 2014. GENERATION OF HIGH RESOLUTION GLOBAL DSM FROM ALOS PRISM. *ISPRS Annals of Photogrammetry, Remote Sensing & Spatial Information Sciences*, **2**(4).
- TATUM, D. and FRANCKE, J., 2012. Constructing hydrocarbon reservoir analogues of aeolian systems using ground penetrating radar. *Journal of Applied Geophysics*, **81**, pp. 21-28.
- TATUM, D., FRANCKE, J., WESTERMAN, R. and HERN, C., 2010. Constructing hydrocarbon reservoir analogues with rapid acquisition long-range GPR, *Proceedings of the XIII International Conference on Ground Penetrating Radar 2010*, IEEE, pp. 1-6.

- TATUM, D., NURSAIDOVA, R., HERN, C., WESTERMAN, A.R., FRANCKE, J. and GARDINER, A.R., 2012. Reservoir Impact of Small-scale Aeolian Dune Architecture-From Acquisition to Simulation in the Wahiba Sands, Oman, *74th EAGE Conference and Exhibition incorporating EUROPEC 2012* 2012.
- TATUM, D., WESTERMAN, R., HERN, C., BUCKMAN, J. and JIANG, Z., 2019. An Integrated Approach to Dune System Analysis, *2019 AAPG Annual Convention and Exhibition*.
- TCHAKERIAN, V. and LANCASTER, N., 2002. Late Quaternary arid/humid cycles in the Mojave Desert and western Great Basin of North America. *Quaternary Science Reviews*, **21**(7), pp. 799-810.
- THOMAS, D.S. and SHAW, P.A., 1991. 'Relict' desert dune systems: interpretations and problems. *Journal of Arid Environments*, **20**(1), pp. 1-14.
- THOME, K., 2020, NASA Terra, The EOS Flagship, viewed 29 January 2020, <<https://terra.nasa.gov/about/terra-instruments/aster>>
- TSOAR, H. (1982) Internal structure and surface geometry of longitudinal (seif) dunes. *J. Sed. Res.*, **52**, 823–831.
- TSOAR, H. and BLUMBERG, D.G., 2002. Formation of parabolic dunes from barchan and transverse dunes along Israel's Mediterranean coast. *Earth Surface Processes and Landforms*, **27**(11), pp. 1147-1161.
- TSOAR, H. and KARNIELI, A., 1996. What determines the spectral reflectance of the Negev-Sinai sand dunes. *International Journal of Remote Sensing*, **17**(3), pp. 513-525.
- TSOAR, H., 2008. Land use and its effect on the mobilization and stabilization of the north-western Negev sand dunes. *Arid Dune Ecosystems*. Springer, pp. 79-89.
- TSOAR, H., BLUMBERG, D.G. and WENKART, R., 2008. Formation and geomorphology of the North-Western Negev sand dunes. *Arid dune ecosystems*. Springer, pp. 25-48.
- VERLANDER, J.E., 1995. The Navajo Sandstone. *Geology Today*, **11**(4), pp. 143-146.
- VIETS, P.W., 1995, Landsat 6 failure attributed to ruptured manifold, NOAA 95-13, viewed 29 January 2020, <[https://landsat.gsfc.nasa.gov/pdf\\_archive/NOAA\\_landsat6.pdf](https://landsat.gsfc.nasa.gov/pdf_archive/NOAA_landsat6.pdf)>
- VISHER, G.S., 1971. Depositional processes and the Navajo Sandstone. *Geological Society of America Bulletin*, **82**(5), pp. 1421-1424.
- VOLLGGER, S.A. and CRUDEN, A.R., 2016. Mapping folds and fractures in basement and cover rocks using UAV photogrammetry, Cape Liptrap and Cape Paterson, Victoria, Australia. *Journal of Structural Geology*, **85**, pp. 168-187.
- WALKER, R. and JAMES, N., 1992. Facies Models. Response to Sea Level Change.—409 pp. *Geol.Assoc.Canada) St.Johns*, .
- WARREN, A. AND KAY, S.A.W. (1987). The dynamics of dune networks. In: *Desert Sediments: Ancient and Modern* (ed. L.E. Frostick and I. Reid), 205–212. Special Publication, 35. Oxford: Geological Society of London, Blackwell.

- WASSON, R. and HYDE, R., 1983. Factors determining desert dune type. *Nature*, **304**(5924), pp. 337-339.
- WERNER, B. and KOCUREK, G., 1999. Bedform spacing from defect dynamics. *Geology*, **27**(8), pp. 727-730.
- WESTOBY, M., DUNNING, S., WOODWARD, J., HEIN, A., MARRERO, S., WINTER, K. and SUGDEN, D., 2015. Sedimentological characterization of Antarctic moraines using UAVs and Structure-from-Motion photogrammetry. *Journal of Glaciology*, **61**(230), pp. 1088-1102.
- WIGGS, G., 2019. Desert Dunes: Form and Process. *Aeolian Geomorphology: A New Introduction*, pp.133-155.
- WILSON, I.G., 1971. Desert sandflow basins and a model for the development of ergs. *Geographical Journal*, , pp. 180-199.
- WILSON, I.G., 1972. Aeolian bedforms—their development and origins. *Sedimentology*, **19**(3-4), pp. 173-210.
- YANG, X., SCUDERI, L., LIU, T., PAILLOU, P., LI, H., DONG, J., ZHU, B., JIANG, W., JOCHEMS, A. and WEISSMANN, G., 2011. Formation of the highest sand dunes on Earth. *Geomorphology*, **135**(1-2), pp. 108-116.
- YOUNG, N.E., ANDERSON, R.S., CHIGNELL, S.M., VORSTER, A.G., LAWRENCE, R. and EVANGELISTA, P.H., 2017. A survival guide to Landsat preprocessing. *Ecology*, **98**(4), pp. 920-932.
- YUAN, Y., KUSKY, T.M. and RAJENDRAN, S., 2016. Tertiary and quaternary marine terraces and planation surfaces of northern Oman: Interaction of flexural bulge migration associated with the Arabian-Eurasian collision and eustatic sea level changes. *Journal of Earth Science*, **27**(6), pp. 955-970.
- ZHAO, G., CAWOOD, P.A., WILDE, S.A. and SUN, M., 2002. Review of global 2.1–1.8 Ga orogens: implications for a pre-Rodinia supercontinent. *Earth-Science Reviews*, **59**(1), pp. 125-162.

## 14 Appendices

**A1:** GPR processing and treatment procedures.

**A2:** Sedimentary logs and facies for all sites in Navajo Sandstone.

**A3:** High-resolution figure of the interpreted sedimentary structures of unit 2 at Hite (Figure 10.16).

**A4:** High-resolution full-length panel and interpretation of the Johnsons Canyon outcrop (Figure 10.21).

**A5:** Input parameters for simulated bedform of Complex 2 (Figure 10.26).

*[Files available at Keele Research Repository: <http://eprints.keele.ac.uk/>]*